Universiteit Antwerpen

Faculteit Wetenschappen

Advanced chemical imaging of artworks – Geavanceerde chemische beeldvorming van kunstwerken

Proefschrift voorgelegd tot het behalen van de graad van doctor in de wetenschappen aan de Universiteit Antwerpen te verdedigen door Stijn LEGRAND

Promotor:
Prof. Dr. Koen Janssens

Antwerpen, 2021

Disclaimer

The author allows to consult and copy parts of this work for personal use. Further reproduction or transmission in any form or by any means, without the prior permission of the author is strictly forbidden.

Table of Contents

Acknowledgements

I would like to express my gratitude to my supervisor Koen Janssens for allowing me to experience the challenging, but also rewarding path of pursuing a PhD. His experience and insight were crucial for guiding me in tackling all challenges that emerged during this work. I am also grateful to him for keeping pushing me out of my comfort zone, I learned much out of that.

I thank Piet Van Espen and Ana Cabal for the many discussions we had, both scientific and beyond. It greatly helped me to grow my problem solving skills.

In a research group you never work alone, therefore I would like to thank the whole former AXI²L and now AXES- group for their support and teamwork. Of course, some people play a special role. My former mentor and later colleague Matthias Alfeld, who introduced me to the world of MA-XRF scanning. Little did I know that this would dominate the next decade of my life. The many hours I spend with Geert Van der Snickt (dis)assembling the MA-XRF scanner, aligning it with unwilling objects, troubleshooting the setup and more seriously interpreting the results, will not easily be forgotten. Nor the days that we together experienced an off-day; what ideally was done within one hour, suddenly took us the better part of a working day. Now that Geert is a professor, his PhD students Nouchka De Keyser, Kirsten Derks and Nina Deleu have taken his place. I would further like to thank: Frederik Vanmeert, Alba Alvarez Martin, Gert Nuyts, Kevin Hellemans, Wout De Nolf, Simone Cagno, Willemien Anaf, Ermanno Avranovich Clerici, Ehab Al-Emam, Olivier Voet, Steven de Meyer and Arthur Gestels, colleagues with whom I have worked closely over the years.

I need to thank the secretaries of both the physics and chemistry departments. I never imagined so much paperwork was involved in working at university, especially when travelling.

Technological instrument development is impossible without experienced technical support; therefore, I would like to thank the technical workshop and more specific Gilles Van Loon and Eddie Schild. Their knowledge, experience and willingness to help were crucial for the instrument development and essential to keep the instruments running. Jaroslav Jordan, not a member of the mechanical workshop, helped much as well.

Being a scientist, the museum world was unknown territory to me when I started to scan artworks in the musea (workshops). Now while writing my PhD thesis during lockdowns, I start to mis the open and friendly atmosphere that is so typical for these institutions. I

Samenvatting

Het onderzoeksveld van de erfgoedwetenschappen is de afgelopen eeuw met onvoorstelbare sprongen gegroeid. Dankzij de uitvindingen van de X-straal radiografie en de infrarood reflectografie werd het mogelijk voor experts om onder het verfoppervlak te kijken. Nog recentere ontwikkelingen hebben geleid tot het ontstaan van hyperspectrale beeldvormingsmethoden, waartoe de in dit werk gebruikte geavanceerde chemische beeldvormingstechnieken, ook toe behoren. Hiermee worden niet enkel de verschillende in kunstwerken aanwezige componenten geïdentificeerd, maar wordt het ook mogelijk om hun verdeling over deze voorwerpen in beeld te brengen. De resulterende distributiebeelden laten het aan een veel breder publiek toe om de wetenschappelijke informatie te interpreteren en om deze resultaten te koppelen aan het kunstwerk zelf.

Voor dit onderzoek werd een reeks aan vlakke kunstvoorwerpen op niet-destructieve wijze onderzocht met behulp van twee macroscopische beeldvormingsmethoden: macroscopische X-straal fluorescentie scanning en macroscopische Fourier getransformeerde midden-infrarood scanning in reflectie mode. In bepaalde gevallen werden de resulterende beelden aangevuld met microscopische technieken op monsters om zo de laagopbouw, samenstelling en de verdeling van deze materialen over de lagen heen te begrijpen.

Aangezien het niet mogelijk was om aanvullende stalen te nemen van verluchte manuscripten, moesten alle vragen op niet-destructieve wijze beantwoord worden. Hiervoor werd de interpretatie van de macroscopische beeldvormingstechnieken tot het uiterste gedreven. Het met chemische beeldvormingstechnieken documenteren van topstukken zoals het *Lam Gods*, hielp het restauratieteam, bijgestaan door de internationale commissie, om de zware beslissing te nemen om alle niet-originele verflagen manueel te verwijderen. Het scannen van glas-in-lood ramen liet experts toe om op basis van deze beelden situatierapporten op te stellen, later ingelegde stukken te identificeren en het gehele restauratieproject veel efficiënter uit te voeren.

Vele bestaande onderzoeks- en restauratievragen konden beantwoord worden door eerst niet-destructieve beeldvormingsmethoden toe te passen. Op basis van de bekomen verdelingskaarten kon met behulp van een beperkt aantal monsters een representatieve verzameling bekomen worden, waarmee de overgebleven vragen beantwoord konden worden. Bij de meeste onderzoeken was het combineren van technieken dus noodzakelijk om de toestand volledig te omvatten. Een gelijkaardige trend kan gezien worden in het onderzoeksveld: een samenwerking tussen uiteenlopende disciplines was vaak noodzakelijk om alle waarnemingen te kunnen verklaren.

Om deze geavanceerde chemische beeldvormingstechnieken volledig te laten doorbreken, is het aangewezen om de meetsnelheid nog te verhogen zodat een aanvaardbare oppervlakte gedurende één werkdag kan worden behandeld. Tegelijkertijd hiermee, moet ook de (basis) dataverwerking nog meer gestroomlijnd worden opdat een grotere groep gebruikers de bekomen resultaten kan gebruiken. Met deze verbeteringen kunnen deze technieken ook door een ruimer publiek gebruikt worden.

Summary

Last century the field of heritage sciences expanded beyond imagination. The inventions of X-ray radiography and infrared reflectography allowed experts to investigate paintings below the surface as well. More recent developments led to the advent of the field of hyperspectral imaging, to which the advanced chemical imaging methods, used in this thesis work, belong. These techniques not only allow to identify the components present in artworks, but also to visualize their distribution over these objects. The resulting distribution maps permit a broader public to interpret the scientific data and to relate these results with the artwork itself.

During this thesis work a range of flat artworks were investigated in a non-destructive manner using mainly two macroscopic imaging techniques: macroscopic X-ray fluorescence scanning and macroscopic Fourier transformed mid-infrared scanning in reflectance mode. The resulting images were sometimes supplemented with microscopic techniques on a minute selection of samples to fully understand the layer build-up, composition and distribution of these materials over the stratigraphy.

Illuminated manuscripts pushed the interpretation of the macroscopic imaging techniques: due to the impossibility of sampling, all answers had to be obtained non-destructively. Documenting masterpieces such as the Ghent Altarpiece by means of chemical imaging techniques, helped the restoration team, assisted by the international commission to make the daring decision of manually removing the non-original paint layers. Scanning stained-glass windows allowed experts to document the panels, create situation reports, identify later infills and guide the restoration process in a more efficient manner.

By initially applying non-destructive imaging techniques, many of the research/conservation questions could already be answered. Based on the resulting distribution maps, only a very limited amount of sampling was required to obtain a representative set to answer the remaining questions. In most cases the combination of multiple methods was necessary to fully understand the situation. A similar trend could be seen in the research field: the collaboration between divergent disciples was often required in order to explain all observations.

In order to completely break through, the scanning speed of these techniques has to increase even more in order to cover an acceptable surface in one workday. Parallel with the operational speed, the (basic) data treatment should also be streamlined more in

order to allow a broader user group to access the results. Once these two improvements are carried out, these techniques become accessible to a larger public.

Introduction

It is often said that the creation of works of art is an important characteristic that distinguishes humanity from the rest of the animal kingdom. The artworks created by master craftsmen and artists may remain a part of human cultural heritage even long after the artist deceased. After a while, these objects might be the only remnants of the society they originate from and are therefore often called "windows on the past". As such, these can provide a wealth of information on the societies they originate from.

Paintings play a special role amongst the fine arts, as not only are the depicted scenes filled with references to the society in which the artist lived, but the application of techniques and materials can be linked with the socio-economic situation the artist found himself in. All the potential wealth of information that is present in these works is the reason why scholars have been studying these objects for ages.

In order to preserve these masterworks for future generations, their conservation and - if needed – restoration is essential. In order to make the right decisions concerning interventions, it is of great importance to document these objects in detail. In Western societies, these objects have received such an unimaginable value, that non-destructive methods are preferred over destructive methods, even when the latter may deliver more information. Originally the documentation consisted mainly of visual (microscopic) inspection of the paintings (surfaces). Apart from local damages or craquelures, it was not possible to observe what was present underneath the surface.

The development of two imaging techniques, based on penetrative radiation: X-ray radiography (XRR) and infrared reflectography (IRR), allowed information, hidden underneath the paint surface, to resurface again without the need of actually removing paint layers. Next to these imaging methods an array of point-based analytical methods has been developed that deliver local (physico-chemical) information.

Over the last decades the combination of an increase in performance and the miniaturization of non-destructive analytical techniques allowed scientists to develop instruments and methods that allowed to move the investigation to the painting, instead of vice versa. Not only did the transportability of analytical instruments increase, the required measurement times decreased sufficiently enough to allow the development of point-by-point raster scanning equipment. These advanced (chemical) imaging methods allow scientists to identify the pigments used, visualize the pigments' distribution over the artwork, identify degradation phenomena and probe under the surface for abandoned compositions.

Two recently developed methods: macroscopic X-ray fluorescence scanning (MA-XRF) and macroscopic Fourier-transformed mid-infrared scanning in reflection mode (MA-rFTIR) can be seen as the further development of XRR and IRR. Where the original techniques only used one (broad) spectral band for imaging, these modern methods allow to visualize the distribution of many adjacent (narrow) spectral bands.

MA-XRF and MA-rFTIR are the main techniques used in this work. One of the main questions is to what extend can these techniques help progressing in the world of art history, conservation sciences and restoration?

At the start of this work MA-XRF became a mature technology that was no longer limited to self-build instruments, since a commercial instrument (M6 Jetstream, Bruker) became available. Initially mainly employed for the analysis of painted art, the scope of MA-XRF was broadened to other flat objects.

MA-rFTIR is the first technique that allows for full spectral macroscopic imaging in the mid-infrared (4000-400 cm^{-1}) range. Some systems using optical fibers or focal plane arrays did already exist, but lacked the potential of the full MIR range. In other bands such as UV, visible or near infrared light, multi- and hyperspectral imaging systems do exist, but these do not record the vibrational (fingerprinting) information that is recorded with MA-rFTIR. This speciation is important since MA-XRF only delivers elemental information.

This thesis is based on published papers and consists of two main parts: The first part discusses the state-of-the-art in chemical imaging of cultural heritage starting with two reviews on hyperspectral (X-ray) imaging methods, followed by two papers discussing the principle of Macroscopic Fourier transform infrared scanning in reflection mode (MA-rFTIR) and the potential to perform clustering-based data-reduction.

The second part focusses on the application of mainly MA-XRF and MA-rFTIR on planar objects of cultural heritage. The showcased applications are grouped into three chapters: illuminated manuscripts, paintings and stained-glass windows. Illuminated manuscripts differ from paintings because of their thinner support, thinner paint layers and limited stratigraphy. Given their general better state of conservation, sampling is rarely allowed, limiting their investigation to non-destructive methods only. The next chapter focusses on two extensive restoration campaigns where non-destructive macroscopic imaging techniques were complemented with microscopic analysis on paint samples. Stained-glass windows benefit from chemical imaging methods as well, since these allow to determine the state and composition of the windows without dismantling the lead came network. The resulting images may even serve as working schemes for restoration campaigns.

By combining the information of different elemental maps (MA-XRF) or multiple techniques (MA-XRF and MA-rFTIR) a new level of information becomes available.

Part one: State of the art in spectroscopic imaging of cultural heritage

Chapter 1 **Spectroscopic and hyperspectral imaging techniques for cultural heritage**

The development of analytical techniques has taken unimaginable leaps forward during the last decades. This chapter will mainly focus on recent developments of X-ray methods and macroscale imaging techniques.

The first paper discusses the application of X-ray based methods from the macroscopic to the (sub)microscopic level on pigments and paintings. In order to completely understand the discovered phenomena, these methods can be complemented by techniques using visible light, infrared radiation or electrochemistry.

The second paper brings a brief overview of recently developed macroscale imaging techniques based on penetrative X-ray or infrared radiation. Given the different interactions of matter with these forms of radiation, the combined use seems to bring complementary information.

This chapter is a modified version of two published papers, adapted with permission from:

● Springer Nature Customer Service Centre GmbH: Springer Nature Topics in Current Chemistry, Non-Invasive and Non-Destructive Examination of Artistic Pigments, Paints, and Paintings by Means of X-Ray Methods, Koen Janssens, Geert Van der Snickt, Frederik Vanmeert, Stijn Legrand, Gert Nuyts, Matthias Alfeld, Letizia Monico, Willemien Anaf, Wout De Nolf, Marc Vermeulen, Jo Verbeeck, Karolien De Wael. Copyright Springer Nature 2016

● Springer Nature Customer Service Centre GmbH: Springer Nature Heritage Science Examination of historical paintings by state-of-the-art hyperspectral imaging methods: from scanning infra-red spectroscopy to computed X-ray laminography, Stijn Legrand, Frederik Vanmeert, Geert Van der Snickt, Matthias Alfeld, Wout De Nolf, Joris Dik, Koen Janssens. Copyright Springer Nature 2014.

1.1 Non-Invasive and Non-Destructive Examination of Artistic Pigments, Paints, and Paintings by Means of X-Ray Methods

Abstract Recent studies are concisely reviewed, in which X-ray beams of (sub)micrometer to millimeter dimensions have been used for non-destructive analysis and characterization of pigments, minute paint samples, and/or entire paintings from the seventeenth to the early twentieth century painters. The overview presented encompasses the use of laboratory and synchrotron radiation-based instrumentation and deals with the use of several variants of X-ray fluorescence (XRF) as a method of elemental analysis and imaging, as well as with the combined use of X-ray diffraction (XRD) and X-ray absorption spectroscopy (XAS). Microscopic XRF is a variant of the method that is well suited to visualize the elemental distribution of key elements, mostly metals, present in paint multi-layers, on the length scale from 1 to 100 µm inside micro-samples taken from paintings. In the context of the characterization of artists' pigments subjected to natural degradation, the use of methods limited to elemental analysis or imaging usually is not sufficient to elucidate the chemical transformations that have taken place. However, at synchrotron facilities, combinations of µ-XRF with related methods such as µ-XAS and µ-XRD have proven themselves to be very suitable for such studies. Their use is often combined with microscopic Fourier transform infra-red spectroscopy and/or Raman microscopy since these methods deliver complementary information of high molecular specificity at more or less the same length scale as the X-ray microprobe techniques. Since microscopic investigation of a relatively limited number of minute paint samples, taken from a given work of art, may not yield representative information about the entire artefact, several methods for macroscopic, non-invasive imaging have recently been developed. Those based on XRF scanning and full-field hyperspectral imaging appear very promising; some recent published results are discussed.

1.1.1 Introduction

Starting from pre-historic times, human artists have always felt the urge to depict their surrounding world on various substrates by using colored materials of different types. Historical paintings, such as, for example, prehistoric cave paintings, are often called ''windows on the past'' and have allowed later generations to imagine how former human societies looked and/or functioned. Historical paintings, therefore, are an enormously valuable part of the cultural legacy we have inherited from past generations.

There is a general belief that paintings are complex, but essentially static assemblages of widely different (in)organic materials. However, at, or just below, the seemingly placid surface of these works of art, chemical reactions are taking place that slowly alter the chemical make-up of the paint layers. While some of these reactions are the result of intimate contact between the different materials, most are driven forward by external physicochemical factors. A prime stimulus for reduction–oxidation (redox) reactions is light absorption by colored substances (molecules) in the ultraviolet (UV) and visible (VIS) range. Such reactions can lead to spontaneous *in situ* formation of secondary chemicals that will often differ in their macroscopic properties (such as color, volume, porosity) from the original materials. Both the organic components of paint (protein-, saccharide- or lipid/oil-based binding media, organic dyes, etc.) and/or the inorganic components (mostly pigments based on metal ions) may be affected. Another important factor in paint degradation is the often cyclic variation in relative humidity, which causes condensation and re-evaporation of minute moisture droplets within the microporous, age-cracked paint layers. The latter can act as miniature galvanic cells in which redox reactions can occur at the interface between pigment grains, binding medium, and water. In addition, phenomena such as crystallization of salts, the leaching of metal cations from pigment grains, and *in situ* formation of metal soaps can gradually undermine the mechanical integrity of paint materials [1]. Cycles of condensation/evaporation may also transport secondary alteration compounds towards the surface, leading to the formation of weathering crusts. These crusts can be partly crystalline; almost all have a color and texture that is quite different from the original material.

When considering the inorganic materials employed as pigments by artists from the fifteenth to the eighteenth century, a relatively limited evolution can be observed over time. This is because the chemistry of pigment synthesis was fairly limited in this period, with the majority of inorganic materials used as pigments still being naturally occurring minerals. Only in a few cases, such as lead white and smalt, the chemical technology was sufficiently advanced that specific colored inorganic materials of high quality and chemical stability could be synthesized in controlled circumstances.

Since the trade in artists' pigments was well spread, it was possible for artists to purchase different varieties of the same pigment, often of significantly different quality and price; in the case of mineral species, these quality differences are related to different geographical origins and/or the grain selection/purification method to convert mineral finds into finely ground pigment powder.

Among the pigments employed by fifteenth to seventeenth century fine art painters in the Low Countries, such as Jan Van Eyck (1390–1441), Hans Memling (1430?–1494), Quinten Matsys (1466–1530), Pieter Brueghel the Elder (1525?– 1569), Pieter Paul Rubens (1577–1640), Anthony Van Dyck (1599–1641), Rembrandt van Rijn (1606–1669), Jan Davidz. de Heem (1606–1684), and Johannes Vermeer (1632–1675), a few fall in a

special category. For these, in many historical paintings, a significant level of chemical alteration of either the pigment grains themselves or of the paint they are part of is observed. It concerns, for example, the pigment smalt (a blue, cobalt-doped type of potassium-rich glass), vermilion red (mercury sulphide, HgS, also known as cinnabar in its mineral form, a pigment used since antiquity), orpiment and realgar (both arsenic sulphides, respectively As_2S_3 and As_4S_4), and lead white (usually a mixture of cerussite, $PbCO_3$, and hydrocerussite, $2PbCO_3 \cdot Pb(OH)_2$). Smalt is a very frequently employed blue pigment that turns greyish/pink upon alteration. Since smalt is often used as part of large surfaces (for example, in a blue sky, in blue clothing of saintly figures, in the darker backgrounds of indoor scenes) its discoloration can have a profound influence of the general outlook and color balance of the painting. This is, for example, the case in a number of paintings by Jan Matsys (1509–1573) and Rembrandt van Rijn. A less strong, but notable change in color can take place with vermilion red, where the originally bright red surface may darken; in addition, the blackened parts of the paint often become covered with white precipitates. In a number of works by the baroque-era painters P.P. Rubens and Pieter Brueghel the Younger (1564–1636), such discolorations have been observed. The yellow/orange pigments composed of arsenic sulphides such as realgar and orpiment have a reputation of being fugitive, i.e., one assumes them to be converted by the action of light and humidity to gaseous/volatile As-containing compounds, supposedly causing the yellow-orange tinting power of these paints to slowly disappear. The seventeenth century painter J. Davidz. de Heem frequently employs the bright orange orpiment as part of his intricate flower pieces while in the Rembrandt *paintings The Nightwatch* and *The Jewish Bride*, realgar is for example employed for painting yellow/golden highlights of the fabrics.

Near the end of the nineteenth century, a number of scientific and technical innovations such as the industrial synthesis of new pigments (with bright, more saturated hues) and the introduction of the paint tube (allowing easy distribution and use of industrially produced artistic paints) set the stage for a significant artistic revolution. Indeed, several masters of modern art, such as Joseph M.W. Turner (1775–1851), John Constable (1776–1837), Camille Pissarro (1830–1903), Paul Cézanne (1839–1906), Vincent van Gogh (1853–1890), George Seurat (1859–1891), and James Ensor (1860–1949) avidly made use of the new possibilities the recently available pigments and paints offered for expressing themselves.

Among the many colors employed by Vincent Van Gogh, the use of yellow pigments becomes very important after 1885. While in his early period (1883–1885/6), he employed mainly Naples yellow (lead antimonate) or light hued earth pigments, in the second half of his career (when he worked in Paris, Arles, and St. Remy, 1885–1890), he frequently employs both chrome yellow and cadmium yellow [2]. As becomes clear from his correspondence [3], chrome yellows are among Van Gogh's favored pigments, featuring in some of his most important paintings from the French period (1886–1890),

such as, for example, the *Sunflowers* series of paintings. Already during his lifetime, Vincent van Gogh was aware of the lack of stability of chrome yellow (see letter nr. 595 from 1898 [3]). In this respect, cadmium yellow had a better reputation; however, recent investigations have revealed that also this pigment may change its hue under the influence of time and environmental agents. Its degradation behavior has been/is being studied in works of art by Vincent Van Gogh, Henri Matisse (1869–1954), and Edvard Munch (1863–1944). The final pigment to be discussed here is minium or red lead (Pb_3O_4); Van Gogh and his contemporaries sometimes employed this orange-red pigment. This substance, frequently used outside artists' workshops to protect metals from corrosion, tends to become either white or black, as a function of its chemical environment.

In order to assess better the current and future state of a painted work of art, it is highly relevant to have a good understanding of the alteration processes that gradually affect the materials it consists of. Many of these alteration phenomena only become visible after an extended period of time and are caused by slow acting (physico-)chemical transformations in multi-component and multi-phase chemical systems that only gradually move towards equilibrium. Redox processes have been identified as being responsible for alteration of a number of inorganic pigments. A lot of these reactions involved include a photo-activation step and, therefore, require (sufficiently energetic) light falling on the painting (surface). The secondary compounds formed in this manner generally are present as micrometer-thin layers, at or just below the paint surface. Advanced analytical methods that allow to distinguish between subtly different compounds or valence states of the same transition metal in these micrometer-thin and superficial alteration layers and that at the same time are able to provide information on the distribution of such secondary compounds, are therefore mandatory tools for art-conservation research [4].

Traditionally, to study the chemical make-up of painted artworks in detail, (minute) paint samples are collected. These tiny samples can be taken using five standard ''microdestructive'' techniques: scalpels or lancets (e.g. [5]); gentle cotton bud (Q-tip) abrasion (e.g. [6]); microdrilling (involving a 100–200 µm diameter bore) (e.g. [7]); or laser ablation, the ablated materials being collected on microscope slides (e.g. [8]). These techniques remove only minute amounts of material and any damage is effectively invisible to the naked eye; they, therefore, do not disturb the esthetic experience of the artwork. Moreover, microdestructive sampling is mostly limited to areas where paint losses have already occurred. The extracted material often comprises the entire stack of micrometer-thick paint layers at a given position. To examine the minute samples, one or more non-destructive microanalytical methods may be employed before undertaking additional analytical investigations that involve the chemical digestion of the sampled material, or any other wet-chemical operation. Prior to microanalysis, multilayered paint samples are typically embedded in resin, cross-sectioned and then polished. Alternatively,

the different materials/layers in a paint sample may be carefully separated from each other under the microscope for separate analysis.

The range of analytical techniques available to painting researchers is now fairly extensive and the methods can be used to characterize a painting's materials in detail. They include the following: optical microscopy (OM), scanning electron microscopy coupled with energy dispersive X-ray spectrometry (SEM-EDX) [9], micro-Fourier transform infrared spectroscopy (μ-FTIR) ([10]), micro-Raman spectroscopy (μ-RS) [11, 12], high-pressure liquid chromatography (HPLC), gas chromatography coupled with mass spectrometry (GCMS), and pyrolysis GCMS (Py-GCMS) [5, 13–15]. To complement these analytical methods there are chemical imaging techniques such as synchrotron radiation (SR)-based micro-X-ray fluorescence (μ-XRF) [16], micro-X-ray absorption near-edge spectroscopy (μ-XANES) spectroscopy ([17]), micro-X-ray powder diffraction (μ-XRPD) [18], and synchrotron radiation micro-Fourier transform infrared spectroscopy (SR-μ-FTIR). SR-based photoluminescence is a relative new addition to this series [19]. Often, combinations of these methods are required to fully understand the paints' chemistry [20, 21]. This was also the case for a number of the investigations described further on.

Micrometers below a painting's surface, a wealth of information may be present about the creative process followed by the artist while making the work of art. The manner in which a painted work of art was created, its conservation, and exhibition history may leave material traces behind, for example, in the layer-by-layer build-up of the artwork. However, this stratigraphic information, comprising structural and compositional aspects, is usually not easy to obtain in a non-invasive manner. Next to the visible surface layers, subsurface layers may include underdrawings, underpaintings, and adjustments made in the course of painting. Together, all these layers determine the current appearance of the work of art. In a growing number of cases conservators have discovered abandoned compositions underneath paintings, illustrating the artist's practice of reusing a canvas or panel. Imaging methods that can "read" this hidden information without any damage to the artwork are, therefore, valuable tools for art-historical research [22]. The standard methods for studying the inner structure of painted works of art are X-ray radiography (XRR) and infrared reflectography (IRR), both penetrative illumination techniques that are optionally complemented with the microscopic analysis of cross-sectioned paint samples. Since these methods all have their limitations, recently, a number of fundamentally new approaches based on X-rays for imaging the buildup of hidden paint layers systems (and for analyzing small samples thereof) have been put into practice. Two major motivations can be discerned for the development of such analytical methods: (a) the desire to know more about the creative process and/or the artist's way of working that have led to a given artefact and (b) the need to assess and predict the current and future condition of a work of art. Motivation (a) is essentially of art-historical nature and seeks to reconstruct (better) the *past/history* of an artwork while motivation (b) is more strongly linked to preventive conservation and to conservation technology and, therefore, mostly

concerned with the *future* of the artwork [17]. It should be duly noted, however, that for conservation, also an understanding of the history of a work of art and the artist's intent is fundamental, since it provides the basis for assessing the current condition of the artwork and for deciding which might be the most appropriate interventions [23].

A comprehensive understanding of the paints used in a work of art, therefore, requires information from across the painting's surface, as well as on their ordering as a function of depth [23]. To complement the detailed information that can be gathered from a limited number of (possibly non-representative) paint cross sections, mobile versions of different non-invasive spectroscopic methods can be used to investigate a (much) larger number of locations on a work of art. By means of portable XRF (PXRF), element signatures can be swiftly recorded from all differently colored areas of a painting, allowing indirect inferences to be made on which pigments were used throughout. Similarly, portable RS and FTIR equipment can be used in a complementary manner to record molecular spectroscopic data and to assess the presence of any organic constituents (e.g. [24]). More recently, several X-ray and visible/near infrared (VIS/ NIR) based non-invasive imaging methods have been developed and successfully employed to document the composition of *complete* paintings [25–27]. They can be considered the state-of-the-art equivalents of the two imaging methods that have been routinely employed in subsurface investigation of paintings for several decades: infrared reflectography (IRR) and X-ray radiography (XRR). Some of these exploit a scanning mode of operation (see Fig. 1) and include the techniques of macroscopic X-ray fluorescence (MA-XRF) [26], macroscopic X-ray diffraction (MA-XRD) [28], macroscopic Fourier transform infrared scanning in reflection mode (MA-rFTIR) [29], and VIS/NIR imaging [30]. Camera-based analytical approaches include hyperspectral imaging in the visible range (350–700 nm), the near-infrared range (NIR; 0.7–1.7 μm), and the short-wave infrared range (SWIR; 1.7–2.5 μm) [27].

In what follows, after outlining a number of X-ray based methods of analysis suitable for studying pigment degradation phenomena, we describe a number of recent studies aimed at unraveling the degradation pathways these pigments are subjected to. Here, the ability to determine the speciation of the inorganic metallic compounds at the (sub)microscopic scale is often highly valuable, as this speciation state often alters during degradation processes. We also briefly describe recently developed methods of chemical imaging by means of which the distribution of pigments in paintings can be visualized. It is often interesting to combine both methods for local (speciation) analysis and large-scale chemical imaging in a study of a particular work of art.
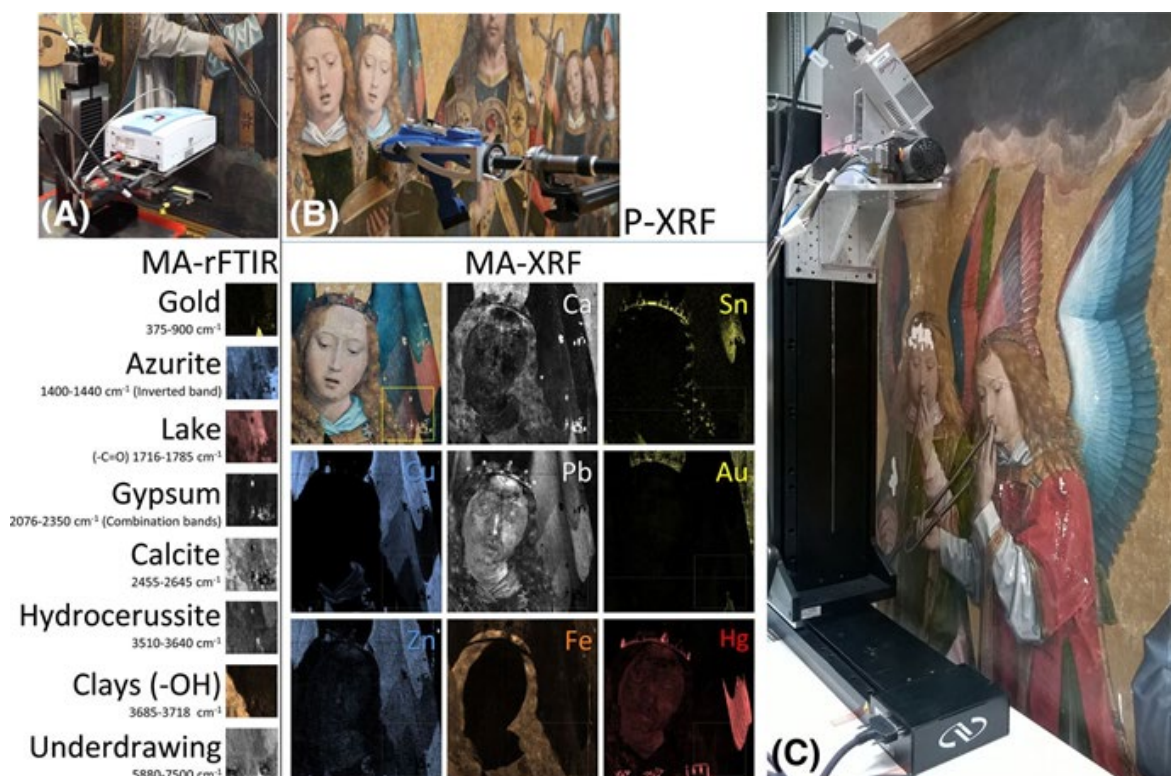
Figure 1: Christ with singing and music-making Angels, Hans Memling (1430–1495, Royal Museum of Fine Arts, Antwerp, Belgium, panels 779, 778, and 780; oil on panel). ***A*** *MA-rFTIR scanner in front of panel 779;* ***B*** *PXRF-analysis of the chest-area of Angel #8, panel 778.* ***C*** *MA-XRF scanner, scanning part of panel 780, and resulting elemental maps. The FTIR maps shown in* ***A*** *correspond to the yellow rectangle in the MA-XRF maps shown in* ***C***. *Adapted from [21]*

1.1.2 X-ray Based Methods of Analysis

X-ray fluorescence analysis (XRF) is a well-established method of (semi)quantitative elemental analysis that is based on the ionization of the atoms of the material being irradiated by an energetic beam of primary X-rays. XRF on heritage and archaeological samples is mainly used in reflection geometry to probe the stratigraphy of polished cross-sections of micro-samples or the exposed surfaces of objects. The energy of the fluorescent photons is the difference in energy between the vacancy that is the result of the ionization process and the electronic state of the electron filling the vacancy [16, 31]. In this manner, the characteristic radiation emitted by the ionized atoms contains information on the nature and the abundance of the elemental constituents present. The technique is particularly efficient for studying high atomic number (high-Z) elements in low-Z matrices. Analysis of the XRF spectra involves identification of the elements present from the fluorescence lines observed and estimation of their net intensity; the latter are in principle proportional to the abundance of the corresponding chemical elements. (Semi)quantitative analysis usually involves more complex calculations as initial absorption of the X-ray beam and absorption of the fluorescent photons in the material

has to be modeled by taking the (expected) matrix composition into account in an iterative fashion [32–34]. Since XRF meets a number of the requirements of the "ideal method" for non-destructive analysis of cultural heritage materials [35], analysis of objects of artistic and/or archaeological value with conventional XRF is fairly common. It is in fact one of the most often applied methods for obtaining qualitative and semi-quantitative information on such objects. Several textbooks cover the fundamental and methodological aspects of the method and its many variants [36].

The variants of XRF that are most relevant for the analysis of painted works of art or of micro-samples taken from such artifacts are (1) PXRF, (2) the X-ray microprobe (XMP), involving the combined use of μ-XRF/μ-X-ray absorption spectroscopy (μ-XAS) and/or of μ-XRF/μ-XRD, usually based on synchrotron radiation, and (3) MA-XRF imaging.

Portable XRF (PXRF): prior to analyzing painted works of art with more sophisticated methods, as a means of first exploration or screening of the artifacts, the use of PXRF, sometimes also called handheld XRF (HXRF or HHXRF) is usually very relevant [37]. Various compact, battery operated devices of this kind are now commercially available [38–43] next to a number of self-built systems [44–47]. One of these is shown in Fig. 1b. Since the interaction of individual photons of a specific energy with single atoms of given atomic number can be very well described, in principle, any form of X-ray fluorescence and, therefore, also PXRF, has the potential of being used for (semi-)quantitative analysis. Several calibration schemes and variants thereof have been developed since the 1970s [48]. Over the past decade, PXRF instruments have allowed non-invasive analyses to be conducted in museums around the world, on virtually any size artifact, producing data for up to several hundred samples per day. However, questions have been raised about the sensitivity, precision, and accuracy of these devices, and the limitations and advantages stemming from performing surface analysis on (often) heterogeneous objects made in obsidian, ceramics, metals, bone, and painted materials have been discussed [49]. In the next paragraph, a number of recently published studies in which PXRF was part of the set of analytical methods employed is outlined. Considering that in PXRF-based studies, the interpretation of the spectral data obtained from complex, multilayered (paint) systems can be problematic, usually the advantages of PXRF have been exploited in combination with other, more surface-specific and/or molecule-specific methods of analysis, in particular vibrational spectroscopies such as Raman and FTIR (micro)spectroscopy.

PXRF has been used extensively both for documentation, as well as for authentication purposes [50] of works of art of different historical periods. The painting materials used in prehistoric rock art have been characterized by PXRF, usually in combination with more specific methods (of molecular spectroscopy) [51–53]. To characterize the materials and stratigraphies of an Egyptian coffin in the Museo Civico Archeologico of Bologna (Italy), restored several times in the past, a two-step approach involving both non-invasive and micro-invasive analysis techniques was used [54]. The *in situ*, portable spectroscopies

employed included XRF, fibre optics reflectance spectroscopy (FORS), and FTIR. This multi-technique approach allowed to reveal many differences in the composition of the (calcite, $CaCO_3$) ground layer and to identify the pigments in the original [cinnabar, orpiment, red clay, Egyptian blue ($CaCuSi_4O_{10}$), and copper-based greens] and restored zones [lead white, Naples yellow ($Pb(SbO_3)_2/Pb_3(SbO_4)_2$), cerulean blue ($CoO \cdot nSnO_2$), azurite ($2CuCO_3 \cdot Cu(OH)_2$)] of the coffin. In order to resolve remaining doubts about the presence of specific pigments in superimposed layers, a few micro-fragments of paint were removed and analyzed using benchtop methods. PXRF was combined with portable RS, Diffuse reflectance infra-red Fourier transform spectroscopy (DRIFTS) and other methods for studying two wall paintings in the Naples Archaeological Museum. The artefacts were extracted ca. 150 years ago from Marcus Lucretius' house in Pompeii, showing the result of the interaction of H_2S gas (expelled during the eruption of Vesuvius) on the painting materials [55]. The efflorescence on the walls of the house and the extracted wall paintings were also studied [56]. The painted surface of plasters withdrawn from different areas of the Villa dei Quintili (Rome, Italy) were examined in a similar manner [57]. A combined XRF/XRD portable instrument was used to study the pigment palette in the paints of the vaults of the Courtyard of Lions in the Alhambra Palace (Granada, Spain), identifying (among others) cinnabar and hematite (Fe_2O_3) in the red hues, in combination with hydrocerussite in the flesh tones while lazurite ($(Na,Ca)_8[(S,Cl,SO_4,OH)_2|(Al_6Si_6O_{24})]$), azurite, and malachite ($CuCO_3 \cdot Cu(OH)_2$) were encountered in, respectively, the blue and green areas [58]. Nubian wall paintings (from churches in southern Egypt and northern Sudan) from the seventh to fourteenth century were analyzed with a combination of PXRF and LA-ICP-MS, allowing the identification of the raw materials employed [59]. On a thirteenth century icon covered by a nineteenth century painting, an extensive campaign of non-invasive analytical investigations was carried out using PXRF, FORS, UV–VIS absorption and emission, allowing the documentation of the gilding techniques employed and formulation new hypotheses regarding thirteenth century painting techniques and materials [60]. To document the use of powdered bismuth (Bi) in Late Gothic paintings and polychromic sculptures, PXRF was used together with SEM-EDX and optical microscopy [61]. A combination of portable FTIR, Raman, and XRF was used to identify the rare minerals crocoite ($PbCrO_4$) and mimetite ($Pb_5(AsO_4)_3Cl$) in medieval Bohemian murals [62], probably as a result of the degradation of the pigments orpiment (As_2S_3) and minium (Pb_3O_4). The same methods were also employed to determine the nature of the painting materials present in Memling's polyptych *Angels Singing and Playing Music* [63] (see Fig. 1), allowing the assessment of the manner in which this painter employed a limited set of pigments and dyes to accomplish a great variety of color and optics effects. With the aim of establishing it better into its historical context, a portable XRF–XRD system was employed to analyze a fifteenth century illuminated parchment from the Archive of the Royal Chancellery in Granada [64]. This revealed the presence of gold and silver, lead tin oxide yellow ($Pb(Sn,Si)O_3/Pb_2SnO_4$), azurite, vermilion, minium, and malachite. Also, the materials employed by Pieter Brueghel the Elder in the painting *Mad Meg* were studied by means of PXRF and other methods [65], identifying the use of copper resinate green, smalt blue,

vermilion red, and lead white; these findings confirm the hypotheses about ''an economic way of painting'' by Brueghel. The gold dust, gold leaf, and the materials used for the gilding of two miniature portraits on copper support from the Evora Museum collection (Portugal) were examined and analyzed by stereomicroscopy, Raman, and FTIR microspectroscopies, SEM-EDX, PXRF, and liquid chromatography coupled to diode array and mass spectrometric detection [66]. The pigments and binding media employed in Sorolla's gouache sketches for the Library of the Hispanic Society of America, New York City, NY, USA have been studied by means of a combination of PXRF, SEM-EDX, and FTIR analysis, showing that a rich palette of pigments was used to manufacture these nineteenth century artists' materials [67]. With the aim of documenting the evolution in the pigment use of the late nineteenth century/ early twentieth century. Belgian painter James Ensor, and to correlate this technical evolution with stylistic developments, a systematic survey was conducted mainly based on PXRF [68]. A series of non-invasive analyses employing PXRF, portable RS, and FTIR were combined with benchtop micro-Raman and SEM-EDX investigations to study the complicated mixtures encountered in paintings by E. Munch and F. Kupka, highlighting the need to employ combinations of methods in order to arrive at unambiguous pigment identifications [69]. Other works of modern painters were examined to verify their authenticity [70] or document their pigment usage [71–75].

Microscopic XRF (μ-XRF) is a branch of XRF that has been developed since 1990 [76], mainly thanks to the use and increasing availability of (a) synchrotron radiation (SR) and (b) various devices for efficient focusing of X-rays [16, 77]. It can obtain information on the local elemental composition of inhomogeneous samples. At synchrotron facilities, a variety of micro- or nanofocus optics, based on refraction [78, 79], diffraction [80, 81], or total reflection [82, 83] of X-rays, is currently in use to create small beams with energies in the 1–100 keV range and with diameters of typically 0.1–1 μm. In laboratory μ-XRF instruments, mostly polycapillary lenses are employed for focusing [84–86], providing focused X-ray beams that usually are 10–30 μm in diameter [87]. Among the commercial apparatus currently available, there are some specifically developed for the local investigation of works of art [88]. By incorporation of additional degrees of freedom of the measuring head, the analysis of Antique manuscripts [89, 90] and bronzes [91, 92], Medieval paintings [93], Chinese porcelain [94], and Baroque-era drawings [95] has become possible.

A specific sub-type of micro-XRF investigations are those employing a confocal excitation-detection geometry [96]. In this case, the recorded XRF signals stem from a well-defined cube-like ''sampling'' volume that is situated at the intersection of the X-ray optical devices positioned between X-ray source and sample (defining the primary beam) and between sample and X-ray detector (defining the direction from which XRF signals can enter the detector) [97]. Often, polycapillary optics are employed for the latter purpose [98, 99]. By moving the sample through this sampling volume, local information on the

elemental composition of the material being investigated can be obtained. Sequential series of confocal XRF measurements along lines and planes allows to visualize the distribution of chemical elements of interest in one or two dimensions, creating, for example, virtual depth profiles, and two- or three-dimensional distributions inside the materials of interest [23, 100, 101]. After its original introduction at synchrotron radiation facilities [97, 101–105], the feasibility of performing confocal XRF measurements using tube sources was demonstrated by several groups around the world [106–110], along with appropriate deconvolution, quantification, and simulation models [111–118]. Several papers have been recently been published where confocal XRF measurements are exploited for sub-surface examination of painted works of art [119–124], next to pottery [125], coins [86], stained-glass [126, 127], painted metal sheet [128], and natural rock samples [129].

About 10–15 years ago, the main advantages of SR-based μ-XRF for the study of archaeological and artistic materials (such as glass, inks, enamel, metals) were considered to be its quantitative and non-destructive character combined with the possibility to perform trace analysis at the 1–10 ppm-level for transition element metals [130]. At that time, the combined use of μ-XRF with μ-XAS and μ-XRD was described as an interesting development [131]. Currently, this multi-modal approach has become standard practice at SR facilities, where the role of μ-XRF is still central, but often no longer of major importance. X-ray microprobes (XMPs), i.e., synchrotron beam lines that allow the combined use of these methods are nowadays present at all SR facilities. Recent review papers [21, 132–134] indicate that they are well established, non-destructive analytical tools that are successfully employed in a large variety of application fields such as materials science/quality control, environmental science, geology, and life sciences, as well as in cultural heritage investigations. Figures 2 and 3 show spectral data and chemical maps derived from degraded paint micro-samples. For the investigation of (altered) paint layer samples, also SR-based μ-FTIR is being increasingly used as a complementary method; in addition to the identification of organic components (binders, varnishes) it provides specific information on the presence of counter ions such as carbonates, sulfates, and oxalates where μ-XRF and μ-XAS mostly yield data on the metal ions themselves.
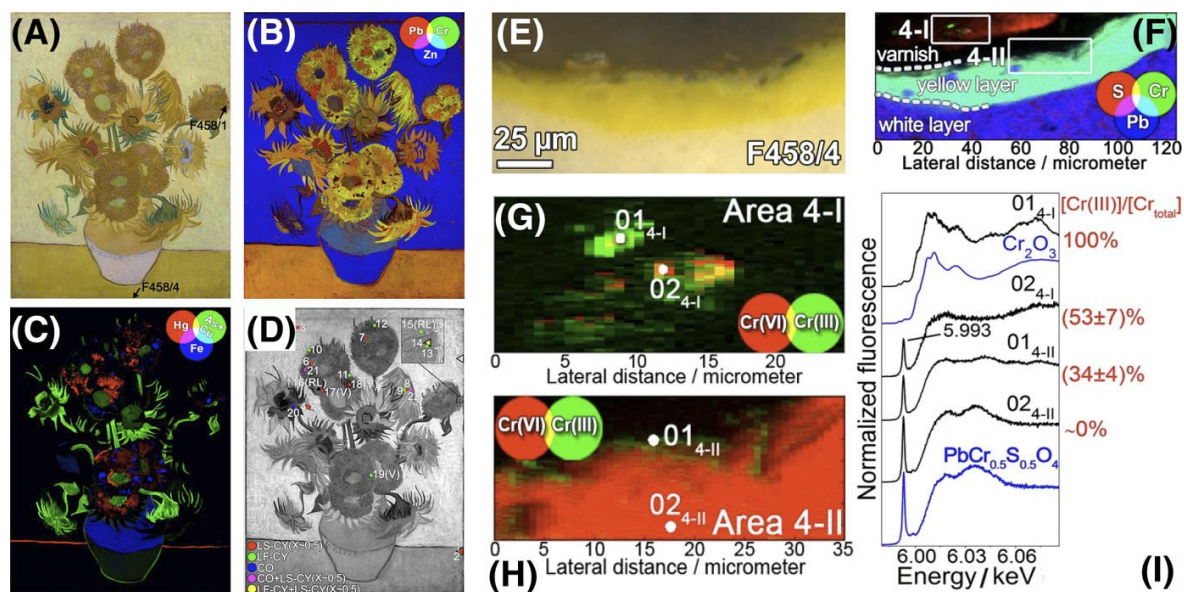
*Figure 2: **A** Photograph of Sunflowers by Van Gogh (Arles, 1889; Van Gogh Museum, Amsterdam, the Netherlands); sampling spots are also shown. RGB composite MA-XRF maps of **B** Pb/Cr/Zn and **C** Hg/As + Cu/Fe. **D** Raman and IR distribution of different CY types (LS-CY: light-sensitive chrome yellow ($PbCr_{1-x}S_xO_4$, with x > 0.4); LF-CY: light-fast chrome yellow (monoclinic $PbCrO_4$); CO: chrome orange [$(1-x)PbCrO_4 \cdot xPbO$]). Triangles show the location of FTIR analyses; ''V'' and ''RL'' indicate spots containing also vermilion and red lead. The white circle denotes the location where only red lead was identified. **E** Photomicrograph detail of sample F458/4 where SR µ-XRF/µ-XANES analysis of **F–I**) were performed. RGB SR µ-XRF images of **F** S/Cr/Pb [map size: 124 x 51.2 µm²; pixel size (h x v): 1 x 0.25 µm²; energy: 6.090 keV]. **G, H** RG Cr(VI)/Cr(III) chemical state maps [pixel size (h x v): 0.7 x 0.2 µm²] and **I** XANES spectra collected from areas indicated in **G, H**. Maps of (**G, H**) were acquired in the regions shown in **F**. Adapted from [156]*

SR-based XMPs have proven their value over more conventional combinations of microanalytical methods, especially for the characterization of degradation products that are formed in thin layers (smaller than 10 µm in thickness) at the surface of weathered archaeological and/or artistic materials and artifacts. Since individual paint layers in paint stratigraphies may be only a few micrometers in thickness, the lateral resolution offered by laboratory µ-XRF is not always sufficient to extract all relevant information; thus, the collection of elemental maps from paint cross sections using SEM-EDX at a typical lateral resolution of 1 µm is still preferred. Occasionally, µ-XRF has been used for this purpose, and then mostly in combination with other laboratory-based methods that provide complementary information [135, 136]. Since the use of (focused beams of) synchrotron radiation exposes the materials under investigation to elevated doses of radiation, not all materials can be examined without beam damage [137]; phenomena such as gradual loss of crystallinity, beam-induced oxidation or reduction have been observed in several cases [138–140].
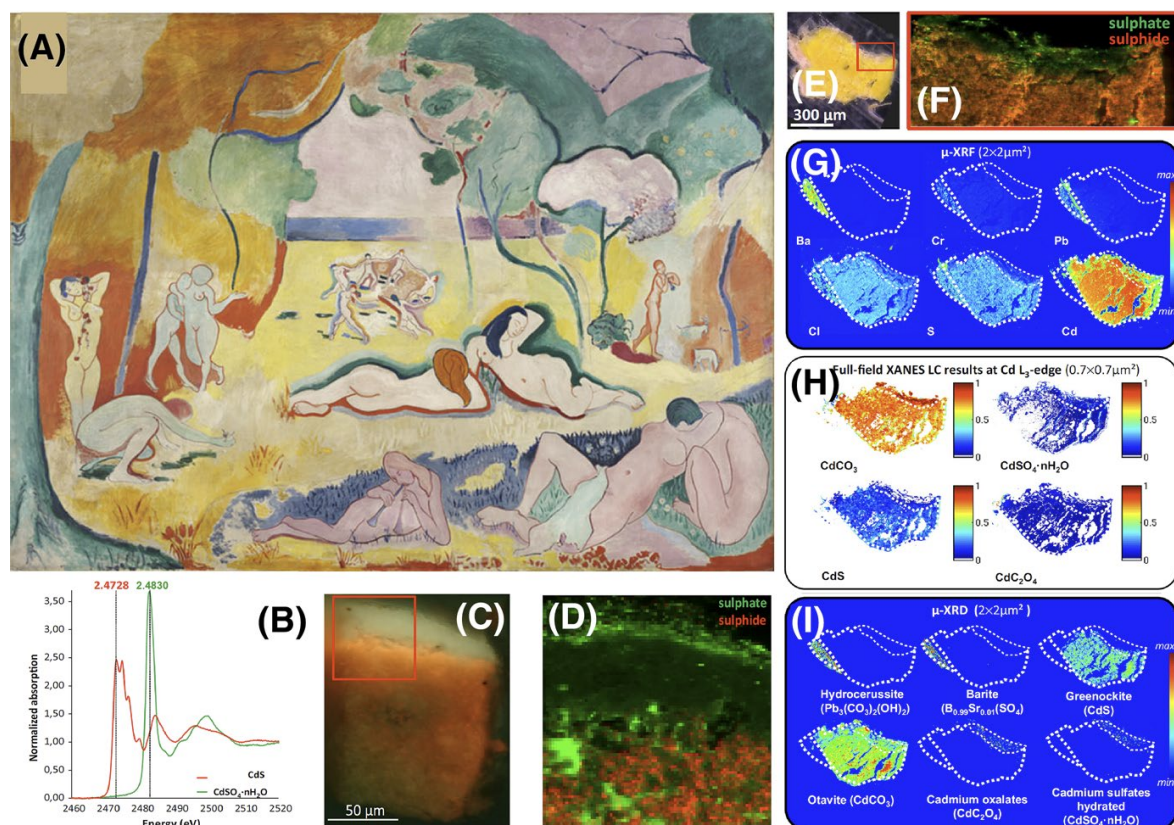
*Figure 3: **A** Le bonheur de vivre (aka The Joy of Life, 1905–1906, oil on canvas, 176.5 x 240.7 cm², The Barnes Foundation, BF719) by Henri Matisse; **B** S-Ka edge XANES of cadmium yellow (CdS, in red) and its transparent/colourless oxidation product (CdSO₄·nH₂O, in green); **C, E** Optical photographs of paint cross sections taken from **A**; **D, F** Compound sulphide (red)/sulphate (green) map of the areas indicated by the red rectangle in c and e (step size: 1 x 1.2 μm²); **G–I** XRF, full-field XANES and XRD maps of the sample shown in **E**. Adapted from [222]*

X-ray absorption spectroscopy (XAS) is based on the absorption of X-rays by materials in the vicinity of the absorption edge of one of its constituting elements. The technique provides chemical speciation, i.e. information on the coordination sphere of the selected absorbing element (the central atom). The tunability of the synchrotron emission with typical bandwidths $\Delta E/E$ smaller than 10^{-3}–10^{-4}, i.e. in the (fractional) eV range for hard X-rays, permits the fine scanning of individual element absorption edges. Synchrotron beam line setups are usually optimized to continuously scan the primary beam energy E with a fixed exit of the beam over the desired energy range (a few tens of electron volts for XANES or a few hundred eV for extended X-ray absorption fine structure (EXAFS) spectroscopy). Due to the high absorbance of many materials encountered at energies below 20 keV most X-ray absorption experiments for cultural heritage and archaeology are performed using XANES in fluorescence detection mode by collecting the X-ray signal typically over some tens of eVs. The XANES fingerprint that is obtained is compared to that of known reference compounds and in many situations the unknown fingerprint spectra can be described by a linear combination of the spectra of the references (see for example Fig. 2i or 3b). By recording μ-XRF maps at a limited number of energies along the

XANES spectrum and appropriate transformation of the resulting intensity distributions, it is possible to obtain species-specific maps (see for example Fig. 3h). Several reviews on the use of XANES for cultural heritage investigations are available [17, 20].

X-ray diffraction (XRD): the main use of XRD for the study of paintings and pigments stems from the fact that identification and quantification of crystalline phases in complex mixtures is possible. Via appropriate optics, an X-ray microbeam of medium to low divergence (typically <3 mrad) is generated that allows a paint sample or an entire artifact either in transmission or in reflection geometry to be irradiated (see Fig. 4). Such beams may be generated at synchrotron facilities using various optics, but also by using laboratory X-ray sources and, e.g., double focusing mirrors. The powder diffraction rings are usually recorded with a two-dimensional detector and then azimuthally integrated (Fig. 4e, f), yielding a radial profile (scattering intensity vs. scattering angle 2ϑ or momentum transfer Q). Each phase inside the sample gives rise to a series of diffraction rings that appear as sharp peaks in the radial profile. This ''fingerprint'' can be compared with databases and used to identify the phases present. A possible overlap between the diffraction peaks makes this process more difficult. In a number of cases, also Rietveld analysis [141] is performed in order to extract quantitative information.

Macroscopic X-ray fluorescence (MA-XRF) imaging is a large scale variant of μ-XRF that has come in use since 2008 when it transpired that hidden/overpainted layers in paintings can be revisualized in this manner; significantly more (pictorial and chemical) information can be obtained than by means of X-ray radiography [142]. It involves the relatively fast scanning of a work of art relative to an X-ray source and XRF-detector assembly. Either the latter assembly is moved in front of the stationary artwork (mobile MA-XRF scanners) or vice versa. With typical dwell times of 50–200 ms per point, a (very) large number of XRF spectra (of the order of one to several million spectra/artwork) are recorded, yielding (after appropriate spectrum evaluation [143]) large-scale elemental maps (see Figs. 1c, 2b, c, 7c, d, 8, 9d, 10b). While its development started at a synchrotron facility [144], at which also the first studies were realized [142, 145–148], relatively soon mobile MA-XRF instruments were developed that allowed performing scanning experiments in the museum or picture gallery where the works of art are normally on display or are conserved [26, 149, 150]. With these MA-XRF scanners, it was possible to examine a great variety of artworks by well-known artists such as Rubens [22], Rembrandt [151–153], Vermeer [154], Goya [155], Van Gogh [145, 156], Magritte [157], Mondriaan [158] and Pollock [159], and to discover new information on their artistic history and on their current state of conservation. Several X-ray instrumentation manufacturers and research institutions have recently described MA-XRF scanners of their own making [27, 160].
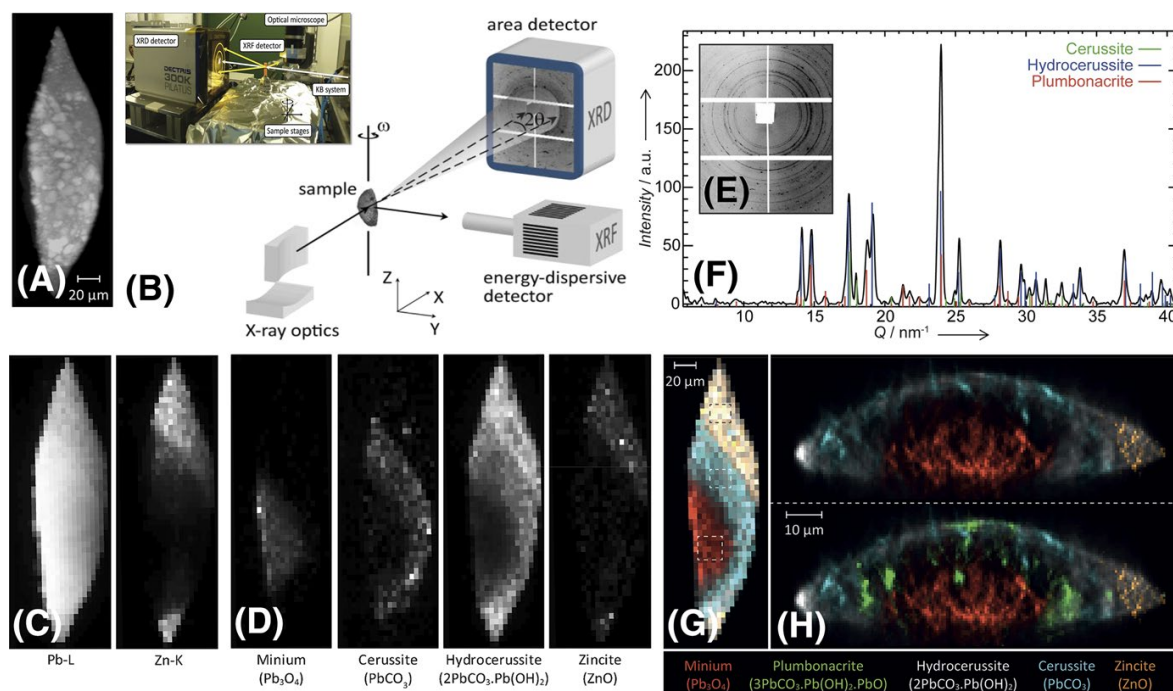
*Figure 4: **A** XRR image (obtained via X-ray absorption tomography) of a minium pustule removed from the surface of ''Wheat stacks under a cloudy sky'', V. van Gogh (Kröller-Müller Museum, Otterlo, the Netherlands). **B** Schematic and photograph of scanning XRF/ XRD setup employed at Beamline P06 of PETRA-III. **C** XRF and **D** XRD 2D distribution images of the severed pustule (map size: 80 x 55 μm²). **E** 2D X-ray diffractogram of a plumbonacrite-rich location and **F** corresponding Q-space spectrum showing the peaks of various lead carbonates. **G** Color reconstructions of the projected and **H** the internal crystalline distribution of the paint sample. Pixel size: 45 μm² (in **C, D**, and **G**); 11 μm² (in **H**). Adapted from [163]*

1.1.3 Multimodal X-ray-Based Identification and Degradation Studies of Artists' Pigments

1.1.3.1 *Pigments As Semi-Conductor Materials*

Most of the artists' pigments of which the spontaneous degradation behavior are described below are semiconductors. These are materials in which, upon absorption of photons, electrons can be promoted from the valence to the conduction band, leaving behind positive holes (see Fig. 5a). As illustrated in Fig. 5b, near the surface of the material, band bending can take place, which may lead to either electrons or positive holes being ''injected'' in the adjacent materials. The (in)stability of these pigments and the nature of the corresponding chemical transformations may be better understood/predicted by considering the positions of the valence band maximum (VBM) and conduction band minimum (CBM) in relation to their thermodynamic oxidation and reduction potential (φ_{ox} and φ_{red}) and that of water (see Fig. 5c) [161, 162].
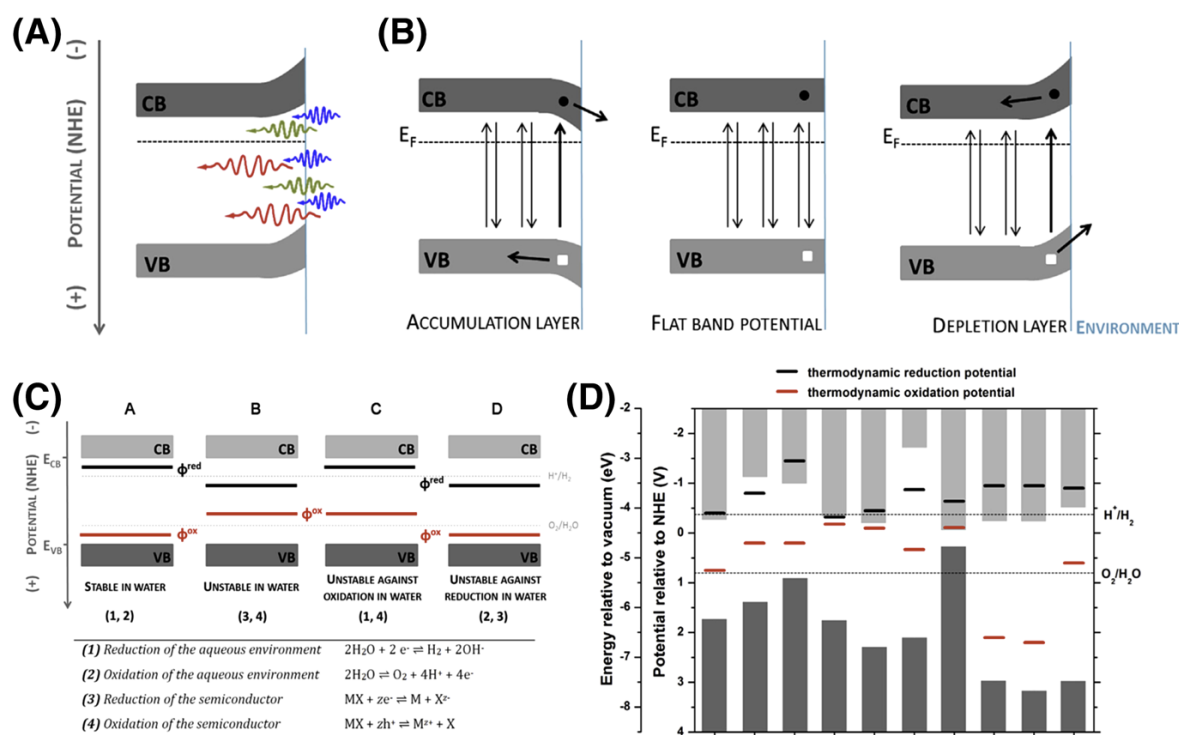
Figure 5: *A* *Indication of the penetration depth of blue (≈450 nm), green (≈510 nm), and red (≈650 nm) light.*
B *Band bending for n-type semiconductors under illumination: accumulation layer (negative surface charge),*
flat band potential and depletion layer (positive surface charge, most common for n-type semiconductors).
Arrows indicate either recombination of generated electron–hole pairs, or charge separation in the presence
of an electric field induced by band bending. *C* *Schematic overview on the stability of semiconductors in*
water. Oxidation and reduction potentials of a semiconductor relative to the oxidation and reduction
potential of H₂O. *D* *Oxidation and reduction potentials relative to the NHE and vacuum level for relevant*
semiconductor pigments or pigment degradation products in aqueous solution at pH 7 (pH 8.5 for ZnO),
plotted versus the valence (dark grey columns) and conduction (light grey columns) band edge positions at
pH 7. Adapted from [161]

In this manner, the positions of φ_{ox} and φ_{red} can be used for a fast screening of the stability of semiconductor pigments towards photo-induced corrosion in an aqueous/humid environment. This theoretical approach corresponds well with experimental data on pigment permanence and degradation phenomena found in the literature. By experimentally recording the photo-induced reduction or oxidation current emitted by the irradiated pigment/paint in an electrochemical setup that mimics the real environment of the degrading paint, the influence of potentially harmful environmental parameters (e.g., the wavelength and intensity of the exciting light, the type of solvent, its pH, the concentration of metal-binding ligands such as Cl⁻and HCO₃⁻) can be rapidly determined. It provides an experimental way of assessing whether or not a semi-conductor pigment is prone to photo-induced oxidation or reduction, with the advantage that it is much faster than more traditional approaches based on artificial ageing of paint model samples. Accelerated weathering experiments on such materials usually are time-

consuming, limiting the number of environmental factors of which the influence can systematically be examined. Moreover, during the long time period of artificial aging, the possibility exists that several chemical transformation processes (e.g. an initial photo-induced redox reaction followed by the precipitation of the released metal ions with suitable anions) may be taking place so that only their compound effect can be observed [163]. As concrete examples, the degradation behavior of the pigments cadmium yellow (CdS) and vermilion (α-HgS) were discussed in greater detail [162, 164, 165].

1.1.3.2 *Pigment Degradation Studies Related to Fifteenth–Seventeenth Century Works of Art*

Vermilion red (α-HgS) is a very frequently used semi-conductor pigment from the neolithic period onwards. It has been mined prehistorically and historically in China, Japan, Europe, and the Americas to extract metallic mercury (Hg^0) for use in metallurgy, as a medicine or preservative, and as a red pigment for (body) painting and in ceramics [166]. It is a pigment that features a complex multistep degradation pathway. Chlorine and sulfur K-edge μ-XANES investigation were combined with μ-XRD to determine the alteration mechanism that causes red pigment to acquire a grayish-black aspect (see Fig. 6) [167]. Paint fragments from Rubens paintings and from wall paintings in the Monastery of Pedralbes in Spain have also been examined [168–170]. Whereas elemental analyses of the degradation products revealed, along with mercury and sulfur, the presence of chlorine, XRD identified (in addition to α-HgS) calomel (Hg_2Cl_2) and the mercury-, sulfur-, and chlorine-containing minerals corderoite (α-$Hg_3S_2Cl_2$) and kenhsuite (γ-$Hg_3S_2Cl_2$). These observations are consistent with S- and Cl-edge XANES data. The resulting maps reveal a clear stratification between the primary mercury compounds (α-HgS) and the secondary species that arose from the interaction with environmental chlorine, leading the authors to hypothesize that α-HgS first takes up Cl, thereby converting into one or more $Hg_3S_2Cl_2$ phases. These light-sensitive compounds, following the loss of sulfur atoms, can be transformed into Hg_2Cl_2, whereas sulfide ions oxidize into sulfate ions. The final step may involve the UV-induced disproportion of Hg_2Cl_2 to $HgCl_2$ and may cause metallic mercury to turn white calomel into a grayish-black substance. No evidence for this transformation could be found with X-ray methods, although some relevant data were recorded via secondary ion mass spectrometry [171]. To study in greater detail the principle environmental factors (light, presence of halides) influencing the instability of red mercury sulfide and to better understand the chemical equilibria governing the formation and evolution of the different degradation compounds, a thermodynamic study of the Hg–S–Cl–H_2O system was made in combination with theoretical considerations and experimental ageing experiments [172]. The latter were performed in O_2-rich and O_2-poor circumstances (see Fig. 6d, e). From these it could be concluded that Hg(0), α-$Hg_3S_2Cl_2$, and Hg_2Cl_2 can be formed from the reaction of α-HgS with ClO(g). Artificial aging experiments were carried out on model samples following the conditions assessed in the first part, in order to reproduce natural ageing observed on red mercury sulfide.
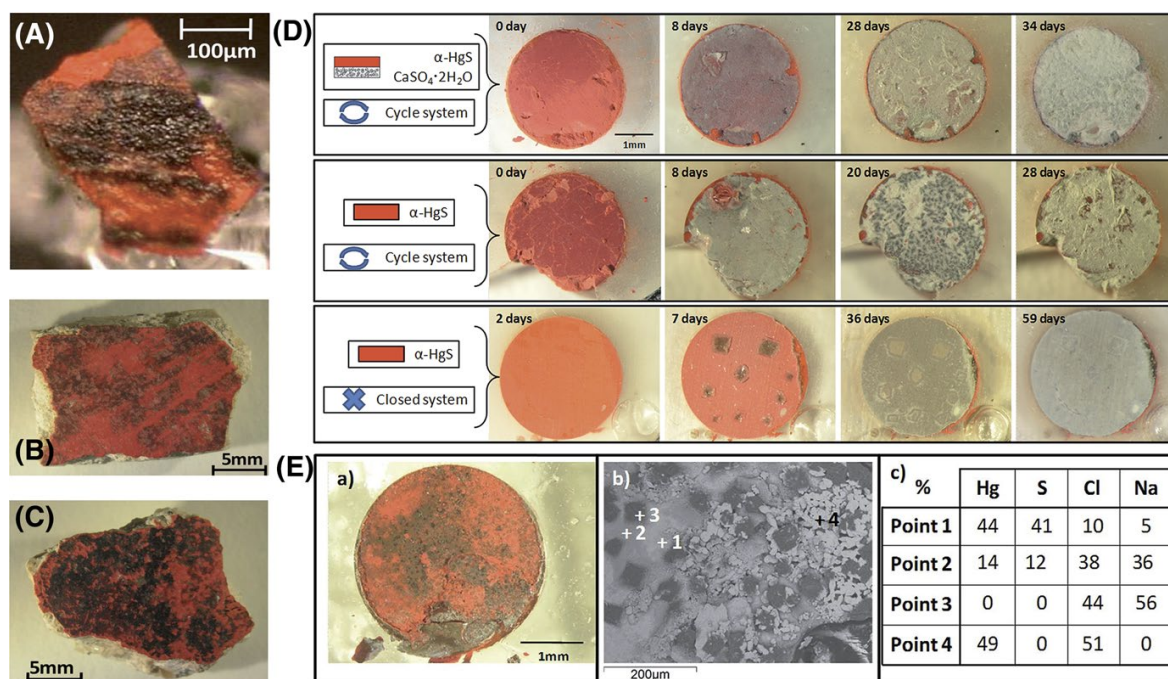
Figure 6: Photographs of paint micro-fragments taken from: **A** The Adoration of the Magi, a painting by P. P. Rubens, Royal Museum of Fine Arts, Antwerp, Belgium; **B, C** a Roman fresco from Villa delle Torre, near Pompeii, Italy. **D** Pellets aged with NaOCl solution and light at different times of ageing: (top panel) two-layered vermilion|gypsum pellet, aged in a cyclic system; single-layered vermilion pellet, aged in (middle panel) cyclic and (bottom panel) closed system; **E** Visible and local backscattered electron (BSE) image of two-layered vermilion|NaCl pellet, aged with NaOCl in a closed system; the table shows quantitative SEM analyses results performed on the four points shown in the BSE image (in atomic percentage; Hg, S, Cl, and Na concentrations were normalized to a total of 100%; C, O, and Al data not shown here). Adapted from [170]

Similarly to degradation compounds detected on original works of art, mercury chlorine compounds such as calomel and corderoite were identified on the surface of α-HgS model samples when exposed to light and a sodium hypochlorite solution. Together with these compounds, sulfates were detected as well, and more particularly gypsum ($CaSO_4 \cdot 2H_2O$) when Ca was originally present in the model sample. These experiments also showed that light is a necessary factor to obtain degradation. From the relevant Pourbaix diagrams, it follows that both calomel and corderoite can be formed at basic pH, which is consistent with their formation in the presence of NaOCl solution (pH 12) during artificial aging experiments. These compounds appear to be formed simultaneously, but the visual aspect of the samples changed during the course of the ageing experiments, showing different steps and colors. In order to remain stable, corderoite needs chlorine to be always available as a reagent. In the case of aging in O_2-rich circumstances, corderoite after some time disappeared and was converted into calomel. It, therefore, appears that corderoite is an intermediate product in the reaction of the formation of calomel from α-HgS. Mapping of cross-sections obtained from the artificially aged samples revealed a multi-layered structure similar to the ones observed on altered works of art, with mercury chloride compounds on top of red mercury sulfide layers and sulfates at the surface of

the samples. Compounds containing both S and Cl are found in intermediate layers. Concerning the visual aspect of the degradation of red mercury sulfide, the different compounds detected on the pellets and on historical paintings (calomel, corderoite, kenhsuite, gypsum) explain the observed white/purple colors, but not the black one. The attribution of the black colour to meta-cinnabar (β-HgS) turned out to be unfounded. Theoretical spectroscopic results have indicated that none of the minerals identified as degradation compounds on mercury sulfide samples is intrinsically gray or black [165]. The presence of elemental mercury was proposed as a by-product of the photo-induced mechanism that causes the darkening of the paintings. In some conditions, the formation of Hg^0 from HgS is indeed thermodynamically favorable. By means of electrochemical methods [164, 173], the formation of metallic mercury from HgS by the joint action of light and chloride ions could be experimentally demonstrated. All the above consideration could be brought together in the following sequence of chemical transformations:

$$HgS \rightarrow \beta\text{-}Hg_3S_2Cl_2 \rightarrow \alpha\text{-}Hg_3S_2Cl_2, \gamma\text{-}Hg_3S_2Cl_2 \rightarrow Hg_2Cl_2 \rightarrow Hg^0 + HgCl_2.$$
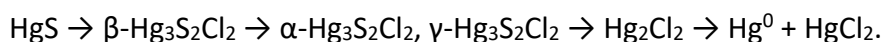
By means of a combination of laboratory-based experiments and thermodynamic modeling, the mechanism(s) and kinetics of cinnabar alteration in fresco applications was further clarified, specifically the role of light, humidity, and chlorine ions. Additionally, possible pathways and preventive and remedial conservation treatments during or immediately following excavation were explored to inhibit or retard darkening of cinnabar pigmented fresco surfaces [174].

Arsenic sulfide pigments (As_xS_y) are yellow (orpiment, As_2S_3) to orange-red (realgar, As_4S_4) p-type semi-conductors that have been used as wall painting pigments since antiquity, especially in Asia or Egypt [175, 176] and in illuminated manuscripts [177–179]. They have been used less extensively in Europe where less toxic or easier-to-use alternatives, such as lead–tin yellow, lead chromate, or cadmium yellow, were available and preferred. Nonetheless, both orpiment and realgar are frequently found in easel paintings, especially during the Venetian renaissance era and in still life or portrait details [180]. It is not also uncommon to find them in sculptures or decorative art objects [181]. Their sensitivity to light and resulting photo-oxidation in works of art is well described and often identified [182–184]: realgar (α-As_4S_4, monoclinic, red) first becomes para-realgar (β-As_4S_4, monoclinic, yellow) which then turns into arsenolite (As_2O_3, white) while orpiment (As_2S_3, yellow-gold) directly turns into arsenolite [176, 180, 182, 185, 186]. In oil paintings, the chemical degradation of emerald green ($Cu(C_2H_3O_2)_2 \cdot 3Cu(AsO_2)_2$) and of arsenic sulfide pigment have arsenic trioxide (As_2O_3) as a common degradation end product. In such paintings where this degradation takes place, arsenic is no longer confined to the pigment particles, but is detected via elemental X-ray analysis throughout the whole paint system, e.g., at layer interfaces, in varnishes, around iron- and aluminium-containing particles, and in the wood structure of a panel painting. The migrated arsenic is thought to be transported within the paint system as arsenic trioxide

in aqueous form (H_3AsO_3) by the same mechanism as its transport in groundwater in the environment. In environmental studies, the oxidation of As(+III) to As(+V) is well documented; dispersed arsenic in paintings released from degraded pigments can, therefore, be a marker for water-linked transport processes [180]. In a cross section from *A Stone Cartouche with a Garland of Flowers* (1655) by the Flemish seventeenth century painter Daniel Seghers (1590–1661), a combination of FTIR and Raman microscopy and XANES investigations was employed to identify and image the two oxidation states of the arsenic sulfide pigment and its secondary compounds—arsenite [As(+III), undegraded] and arsenate [As(+V), degraded]. This painting presented unquestionable signs of alteration as the yellow roses, originally painted using a mixture of arsenic sulfide and ochre, became transparent over time. The As K-edge μ-XANES spectra and maps collected from the cross section left no doubt that As(+V) compounds are effectively present while some of the corresponding Raman data are consistent with this [187]. Some indications are already available that the mineral schultenite ($PbHAsO_4$) can be formed *in situ*; a positive identification of this degradation compound by means of XRD could be realized in several seventeenth century paintings by J. De Heem (unpublished data).

Smalt was commonly used as a pigment by artists between the sixteenth and eighteenth centuries. It is a powdered blue potash glass colored by cobalt ions that easily degrades in oil paint, causing sometimes dramatic chromatic changes in the appearance of oil paintings. In many cases, reflection light microscopy demonstrated the presence of partially discolored smalt particles with a remaining blue core [188] (for an example, see Fig. 9b, c). The composition of smalt can vary considerably depending on the manufacturing process and the elements that are present in the raw materials in addition to the essential glass components silica, potassium oxide, and cobalt. It is known from historical documentary sources that smalt was available to artists in various grades with different color intensities, but it can be difficult to distinguish between pigment that is degraded and that which has always been rather grey in hue. Quantitative analysis of smalt pigment by SEM– EDX has proved to be a useful method of distinguishing between deteriorated and well-preserved pigment based on the potassium content [189]. A typical pattern was encountered in a sample from Paolo Fiammingo's *The Sons of Boreas Pursuing the Harpies* (National Gallery London, NG 5467) [190]. In the upper layer of the cross section, where the smalt is mixed with lead white, it is well preserved and contains around 13–14 w% K_2O. The smalt in the lower layer, which was mixed with only a little lead white, is degraded: the paint appears yellowish; the pigment has lost its color almost entirely and contains only 1–2% K_2O. In order to investigate the changes in the structure and environment around the cobalt ion on deterioration and to further the understanding of the basis of the loss of color, particles of well-preserved and altered smalt in micro-samples from paintings in the National Gallery, London, and the Louvre Museum, Paris, were analyzed using XAS at the Co K-edge [191]. XANES and EXAFS measurements showed that in intense blue particles, the cobalt is predominantly present as Co(+II) in tetrahedral coordination, whereas in colorless, altered smalt the coordination number of Co(+II) in the glass structure is increased, and there is a shift from tetrahedral toward

octahedral coordination. The extent of this shift correlates clearly with the alkali content, indicating that it is caused by leaching of potassium cations, which act as charge compensators and stabilize the tetrahedral coordination of the cobalt ions that is responsible for the blue color. The same samples were analyzed complementarily by using vibrational techniques such as µ-RS and SR-FTIR microscopy [192]. Comparison of the resulting spectra with those from modern smalt, together with spectral decomposition and correlation with quantitative SEM-EDX analysis, shed new light on the role of the various cations in the silicate structure. Important modifications in the structure of the pigment on alteration were revealed, in particular the leaching of alkali ions and the formation of silanol groups, which subsequently condense to create new bridging Si–O–Si bonds and molecular water in the glass. The degradation mechanism and progressive deterioration of smalt were reproduced while also a theoretical explanation for the connection between the discoloration process and structural atomic changes around the Co atom was provided [193].

From antiquity, the pigment ultramarine was prepared by grinding the semiprecious stone lapis lazuli (containing the mineral lazurite) into powder. It was one of the most expensive artists' pigments throughout history. Lapis lazuli is composed of various minerals, among which aluminosilicates of the sodalite group. The most notable is the mineral lazurite $(Na,Ca)_8(Al_6Si_6O_{24})(SO_4,S,Cl)_2$ in which the cations and anions are trapped within the aluminosilicate framework. The pigment obtains its color from the fact that S_2^- and S_3^- anions are present inside the sodalite β-cages. Evidence of entrapment of carbon dioxide in the natural pigment from Afghanistan was found by Miliani et al. [194], indicated by the IR absorption band at 2340 cm^{-1} and a low frequency satellite corresponding to the $^{13}CO_2$ isotopologue. The thermal behavior of natural ultramarine was studied by FTIR, UV–vis spectroscopy, and XRD, from 300 to 1120 K. Measurements showed that CO_2 and the encapsulated S_3^- chromophore behave in the same way during the heating experiment, starting to be released only at about 670 K when the apertures of the sodalite β-cages became larger as an effect of temperature. The absorption at 2340 cm^{-1} can be used as a reliable discriminant between Afghan (the most probable source prior to the nineteenth century for Western artworks) and artificial ultramarine, a fact of great interest when dealing with the authentication of artworks. Recently, the possibility was investigated to distinguish lapis lazuli of different geographic provenance based on their S K-edge XANES spectrum [195]. All examined lapis lazuli samples feature a S-XANES profile consistent with S_3^- being the dominant species (which considered to be the main responsible for the blue colour); however, also indications for the presence of species such as S_4^{2-}, S_4^-, and S_8 are apparent, depending on the origin of the material. However, the heterogeneity of the natural rocks hampers the straightforward association of one specific S K-edge XANES spectrum to a region of provenance. The blue pigments used on altarpieces in the fifteenth century in Catalonia and Crown of Aragon are principally composed of the mineral azurite. To a lesser extent, lapis lazuli was used and occasionally in the background areas and for outlining the principal figures; indigo (of vegetal origin) was used for the chromatic preparation layer. Data from several altarpieces belonging to

well-known artists of that time were analyzed by SR-XRD, benchtop FTIR and SR-FTIR microscopy, RS, and SEM-EDX. XRD and SR-FTIR proved to be especially useful. The application of several layers with decreasing particle size, starting with azurite and finishing with lapis lazuli relates these artworks van Eyck's ''*Adoration of the Mystic Lamb*'' [196]. Synthetic ultramarine shares many properties with its natural form. Both natural and synthetic ultramarine have long been considered to be highly stable to light and compatible with other pigments. With both pigment forms, in some circumstances, a grey-black to greyish/yellow discoloration of ultramarine-containing paint may be observed. In historical paintings, this phenomenon is known as ''ultramarine disease'' and is generally attributed to a break-up of the binding medium. In a recent study on color changes resulting from the interaction of various inorganic pigments with acrylic binding media under UV irradiation, ultramarine blue was found to have a very significant influence on alkyd resin paint, including a loss of blue color [197]. The opening of the sodalite cages of ultramarine [198] can cause its chromophoric S-anions to be released, leading to a loss of color of the pigment itself. Recently, Al K-edge XANES was employed to investigate the white discoloration of synthetic ultramarine in twentieth century paintings [199]. In degraded areas (induced by exposure during 1 min to 3 M HCl), the Al K-edge XANES featured an additional peak, corresponding to octahedral, six coordinated aluminium; in undegraded ultramarine, only the signature from AlO_4 units, part of intact β-cages, are observed. From this difference, it may be possible to conclude that the degradation of ultramarine may involve the removal of Al from the aluminosilicate network.

1.1.3.3 *Alteration of Late Nineteenth/Early Twentieth Century Artists' Pigments*

Below, we describe a number of recent case studies where a combination of X-ray and vibrational spectromicroscopic methods, sometimes together with more conventional laboratory-based analysis techniques, was used to shed light onto the degradation mechanism of pigments employed by artists such as James Ensor, Henri Matisse, Vincent van Gogh, and contemporary artists. The degradation behavior of various yellow pigments such as chrome yellow ($PbCrO_4$ or $PbCr_{1-x}S_xO_4$ with $x \leq 0.8$), zinc yellow ($K_2O \cdot 4ZnCrO_4 \cdot 3H_2O$), cadmium yellow ($CdS/Cd_{1-x}Zn_xS$), and Naples yellow [$Pb(SbO_3)_2 \cdot Pb_3(Sb_3O_4)_2$] were investigated by means of μ-XAS and/or related methods, in addition, the degradation of minium (aka red lead, Pb_3O_4) and Prussian blue [$MFe^{III}[Fe^{II}(CN)_6] \cdot xH_2O$, with M=$K^+$, NH_4^+, or Na^+].

To elucidate the reasons for the darkening of the originally bright chrome yellow (CY) paint in works by Van Gogh (see Fig. 2), a combination of μ-XRF, S, and Cr K-edge μ-XANES together with scanning transmission electron microscopy coupled to energy electron loss spectroscopy (STEM-EELS) was employed [156, 200–207]. This alteration proved to be caused by the surface reduction of Cr(+VI) to Cr(+III), but was very hard to document in a convincing manner using a combination of electron microscopy, Raman, and FTIR spectromicroscopies only. In samples taken from various paintings and in artificially aged

CY paint of that period, Cr(+III) species were found, usually at the boundary between the paint and varnish layers and in sulfur-rich areas (see Fig. 2h). μ-XANES profiling and mapping (Fig. 2e–g) allowed the determination of the superficial brown coating that is 2–3 μm in thickness and contains non-crystalline Cr(III) compounds such as $Cr_2O_3 \cdot 2H_2O$, $Cr_2(SO_4)_3 \cdot H_2O$, and/or $(CH_3CO_2)_7Cr_3(OH)_2$ [200]. The high sensitivity towards darkening of this material could be traced back to the presence of monoclinic and/or orthorhombic $PbCr_{1-x}S_xO_4$ ($0 \leq x \leq 0.8$) co-precipitate phases that are less stable than monoclinic (S-free) $PbCrO_4$ [203–209]. A change from the monoclinic to the orthorhombic structure is observed in $PbCr_{1-x}S_xO_4$ when x exceeds 0.4 [202, 208].

To gain a deeper understanding of the behavior of the different types of chrome yellows, a series of oil paint models was prepared and characterized using a variety of methods before and after photochemical aging. The materials were obtained by employing commercial and in-house synthesized powders of $PbCrO_4$ and $PbCr_{1-x}S_xO_4$ co-precipitates with different x values [202, 203]. Also, samples of 100-year-old commercial paint were subjected to aging and the resulting differences investigated at the micro- and nanoscale [200, 207]. In parallel, a large series of around 20 original chrome yellow paint samples, taken from paintings by Vincent van Gogh and some of his contemporaries were characterized [202]. By combining the results obtained from paint models and original paint samples, a number of conclusions could be reached:

1. Among the aged model oil paints, only those composed of a sulfate-rich orthorhombic $PbCr_{1-x}S_xO_4$ co-precipitate showed a significant darkening after photochemical aging. Cr K-edge μ-XANES investigated the formation of up to about 60% of Cr(+III) species in the outer layer of the most altered sample [203]. On the contrary, negligible alteration effects were observed when sulfate species (such as $PbSO_4$ and $BaSO_4$) were absent from the crystalline structure or were merely mechanically mixed with the original chrome yellow pigment. Only when the sulfate ions are inside the lead chromate crystal structure itself, the darkening phenomenon was apparent. This finding is attributed to a difference in solubility of the chromate compounds that becomes higher when their crystalline structure changes from monoclinic to orthorhombic [203]. By means of XRD, RS, and FTIR, it is possible to make clear the distinction between the different above-mentioned forms of chrome yellows [202, 208].
2. An evaluation of the influence of the wavelength (range) of UV–visible light on the photochemical reduction of the lead chromate-based pigments was also performed. Light-sensitive sulfur-rich/orthorhombic $PbCr_{1-x}S_xO_4$ (x~0.75) co-precipitate was exposed to ranges of UV ($240 \leq \lambda \leq 400$ nm), UVA-VIS ($\lambda \geq 300$ nm), blue ($335 \leq \lambda \leq 525$ nm), and red ($\lambda \geq 570$ nm) light [203]. These experiments demonstrated that it is possible to slow down the darkening of this material by minimizing its exposure to wavelengths shorter than about 525 nm.
3. The above-mentioned forms of chrome yellow (both stable and less stable) were identified on about 20 embedded paint micro-samples originating from paintings by

Van Gogh and some of his contemporaries. It was also possible to demonstrate that the identification of these different forms of chrome yellow is possible by carrying out non-invasive *in situ* analyses, i.e., by employing portable Raman and FTIR instrumentation. For example, in Van Gogh's paintings *Portrait of Gauguin* (Van Gogh Museum, Amsterdam, the Netherlands) and *Falling Leaves* (*Les Alyscamps*, Kröller-Müller Museum, Otterlo, The Netherlands) the presence of the more light-sensitive $PbCr_{1-x}S_xO_4$ type of chrome yellow could be identified [202, 208].

By means of EELS, nanoscale maps of Cr(+VI), Cr(+III), and S(+VI)-containing species before and after light exposure of a historical light-sensitive chrome yellow paint were obtained [207]. This allowed a relatively simple degradation model to be proposed. Considering that this paint originally consists of nanograins of $PbCrO_4$, $PbCr_{1-x}S_xO_4$, and $PbSO_4$ fixed in a porous network of crosslinked oil-based binder in which micro droplets of aqueous solution can be present, this model assumes that the degradation starts via an initial dissolution of CrO_4^{2-} ions into the aqueous phase. In their turn, these ions can react with the organic binder (oil) at those locations where the binder network and the water phase are in contact, thus oxidizing the binder material; this results in a reduction of the chromate ions to Cr(+III) compounds. The redox reaction is followed by precipitation of Cr_2O_3 as nanometer-thin outer layers on the surface of all particles that are present. Because of the leaching of chromate ions from the particles, several core–shell structures can be formed *in situ* on/in the particles.

An integrated approach based on a combination of diffuse reflectance UV–VIS, SR μ-XRF/μ-XANES, and electron paramagnetic resonance (EPR) spectroscopies was used to study the photo-redox process in chrome yellows under the influence of monochromatic light of different wavelengths and several white light sources [205]. EPR spectroscopy was used as a complementary tool to SR-based X-ray methods due to its sensitivity for revealing species containing one or more unpaired electrons and for distinguishing different coordination geometries of paramagnetic centers, such as Cr(+V)-species. Semi-quantitative indications about the darkening of the paint surface were obtained by UV–VIS spectroscopy. The Cr speciation data highlighted that the reduction process was favored not only by (blue) wavelengths in the 400–460 nm range (i.e., where the pigment shows its maximum absorption), but also by (green) light in the 490–530 nm range. The first evidence of the presence of Cr(+V)-intermediates in the Cr(+VI) → Cr(+III) reduction reaction was also gathered; this allowed the risks of inducing photo-degradation of the 490–530 nm wavelength range to be explained.

In order to distinguish between the transformations induced by specific relatively humidity (RH)/temperature conditions (i.e., > 50% RH and a fixed temperature of 40 °C) and exposure to light, monoclinic $PbCrO_4$, and orthorhombic $PbCr_{0.2}S_{0.8}O_4$ were subjected to separate or combined thermal and photo-chemical ageing protocols [206]. Diffuse reflectance UV–VIS and FTIR spectroscopies were used to obtain information associated

with chromatic changes and the formation of organometal degradation products at the paint surface in combination with the abovementioned Cr-speciation techniques. Under the thermal aging conditions employed, Pb(+II)-carboxylates and reduced Cr-compounds (in abundance of up to about 35% at the surface) were identified in the lead chromate-based paints. The tendency of chromates to become reduced increased with increasing moisture levels and was favored for the orthorhombic $PbCr_{0.2}S_{0.8}O_4$ compound. In the case of thermally aged paint models, a higher relative abundance of Cr(+V)-species were observed than in the case of the equivalent photo-degraded material where mainly Cr(+III) species were encountered. In paint models first subjected to a thermal treatment and then exposed to light, compounds ascribable to the oxidation of the organic binder were detected for all chrome yellow types investigated; however, the initial thermal treatment increased the tendency toward photo-reduction of the $PbCr_{0.2}S_{0.8}O_4$ pigment only. For this light-sensitive compound, the variation in thickness of the photo-altered layer (containing ca 70% of reduced forms of Cr) as a function of moisture levels could be attributed to a surface passivation phenomenon taking place prior to photochemical aging.

Three micro-samples from two varnished paintings by Van Gogh and a waxed low relief by Gauguin (all originally uncoated) were examined with the aim of better understanding whether or not the application of the top coating influenced the morphological and/or physicochemical properties of the chrome yellow paint underneath [204, 209]. In all samples studied, regardless of the nature of the coatings (resins or wax), μ-XRF and Cr K-edge μ-XANES measurements showed that Cr(+III) alteration products were present in the form of grains inside the coating (generally enriched in S-species); the Cr(+III) compounds were also homogeneously spread at the paint surface. Inside the coating and within the grains, the alteration compounds were present in abundance up to 70 and 100%, respectively, and were identified as Cr(+III)-sulfates and -oxides. The distribution of Cr(+III) species may be explained by mechanical friction caused by brush-application of the coating that picked up and redistributed superficially formed grains of secondary Cr-compounds, likely already present in the reduced state as result of the photodegradation process. On the basis of the study of varnished chrome yellow paint models, no evidence could be found of an actively Cr-reducing role of the varnish or of superficial S-species.

Firm evidence for the chemical alteration of chrome yellow pigments in Van Gogh's *Sunflowers* (Van Gogh Museum, Amsterdam; see Fig. 2) was recently presented [156]. Non-invasive *in situ* vibrational spectroscopic analysis at several spots on the painting was combined with SR-based μ-XRD, μ-Raman, and μ-FTIR investigations of two paint micro-samples to reveal the presence of lightfast $PbCrO_4$ and light-sensitive $PbCr_{1-x}S_xO_4$ (with *x* approximately equal to 0.5). Cr(+III)-compounds, products of this degradation process, were found at the interface between the paint and the varnish (see Fig. 2h). Selected locations of the painting with the highest risk of color modification by chemical deterioration of chrome yellow were identified; see also Sect. 4 below.

The production records for lead chromate pigments present in the nineteenth century archive database of Windsor & Newton^{TM} (W&N) for the manufacture of their artists' materials, were recently systematically studied [210]. W&N produced essentially three pigment types: (a) lemon/pale chrome yellow, based on solid solutions of lead chromate and lead sulphate [Pb(Cr,S)O$_4$], (b) middle or pure monoclinic lead chromate (PbCrO$_4$), and (c) deep lead chromate that contains the latter admixed with basic lead chromate (Pb$_2$CrO$_5$), accounting for 53, 22, and 21% of the production, respectively. Production recipes for primrose yellow (4%) resulted in mixed crystals with a high percentage of lead sulphate. Each pigment type is characterized by only one or two main synthetic pathways; process variations reveal a systematic and thorough search for a high-quality durable product. A comparison of the chemical composition of pigment reconstructions with early W&N oil paint tubes showed that their records entitled ''pale'' and ''lemon'' correlated with the pigment tubes labelled chrome yellow while the records ''middle'' and ''deep'' corresponded with the tubes labeled ''chrome deep''.

Some of the properties of the chrome yellow varieties containing variable amounts of S have been examined by employing density functional theory (DFT) calculations in order to better understand their photo-degradation behavior [211]. The results show that the mixed PbCr$_{1-x}$S$_x$O$_4$ and the native PbCrO$_4$ share a similar electronic structure, although an energy up-shift of the conduction band is computed by both increasing the amount of sulfate and passing from the monoclinic to the orthorhombic phase. The calculations suggest that, when the degradation would be considered to be purely an electron-exchange phenomenon, the Cr(+VI) photoreduction would more difficult for compounds with high sulfur concentration and an orthorhombic phase. In reality, however, the opposite is true. Thus, it is likely that the degradation is more strongly influenced by other factors, such as a different solubility and/or (nano-)morphology of the PbCr$_{1-x}$S$_x$O$_4$ materials. Another theoretical study attempts to answer the question whether or not the degradation of PbCr$_{1-x}$S$_x$O$_4$ is purely a surface phenomenon; also, the question whether the bulk properties of the sulfur-rich pigment material trigger the process is still open [212]. First-principles calculations were employed to investigate the role of sulfur in defining bulk properties such as structure, stability, and optical properties of the materials. The calculations support the hypothesis that an initial local segregation of lead sulfate could take place. This material would then absorb UV light, thus providing the necessary energy for subsequent reduction of chromate ions into the greenish chromic oxide. To date, no experimental evidence to support this was found.

The darkening of zinc yellow (K$_2$O·4ZnCrO$_4$·3H$_2$O), as observed in *A Sunday at La Grande Jatte* (G. Seurat, 1884, Art Institute of Chicago, Chicago, IL, USA) was studied by a combination of EELS and Cr K-edge XANES on artificially age model paint samples and on original micro paint samples [213, 214]. To observe changes, more corrosive circumstances that needed for chrome yellows were needed, involving a combination of

SO_2 gas, 50/90% humidity and light. Next to Cr(+III) species also dichromate ions [containing Cr(+VI)] were found as degradation products.

Cadmium yellow ($CdS/Cd_{1-x}Zn_xS$) is another class of yellow pigments frequently employed in the early twentieth century by painters such as Henri Matisse, James Ensor, Edvard Munch, and Vincent van Gogh. Cd-based pigments share a common hexagonal wurtzite structure in which cadmium and sulfur can be partially substituted to generate ternary phases with a wide range of colors from pale yellow to deep red. Among them, in $CdS_{1-x}Se_x$ solid solutions, the substitution of sulfur by selenium decreases the valence-to-conduction energy gap, hereby modifying the color toward orange and red tonalities. UV–VIS-NIR and Raman micro-spectroscopies have been used for investigating the composition of ternary $Cd_{1-x}Zn_xS$ and $CdS_{1-x}Se_x$ solid solutions employed as artists' pigments [215, 216]. The goal was the determination of the solid solution stoichiometry of a series of Cd-containing paints, by exploiting the linear dependence of some absorption, emission, and scattering properties with the pigment composition. The high sensitivity of Raman spectroscopy to local compositional and structural heterogeneity permitted to formulate a hypothesis about the possible presence of quaternary solid solutions based on the substitution of cadmium by zinc ($CdS_{1-x}Zn_xS_{1-y}Se_y$) in commercial pigments and by barium ($CdS_{1-x}Ba_xS_{1-y}Se_y$) in historical paints. By employing a combination of S K-edge μ-XANES and μ-XRD, it was established that the oxidation of the pigment cadmium yellow (α-CdS) to cadmium sulphate ($CdSO_4·H_2O$) (white/transparent) was the chemical transformation responsible for the loss of the bright yellow color in a painting by J. Ensor [217]. In a follow-up paper [218], the same authors discovered that another chemical pathway has given rise to the formation of an orange-grey superficial crust in a painting by Van Gogh called *Flowers in a Blue Vase* (1887, KMM), containing the grey/white mineral anglesite ($PbSO_4$) and cadmium oxalate. The chemical and physical alterations of cadmium yellow (CdS) paints in Henri Matisse's *Le bonheur de vivre* (aka *The Joy of Life*, 1905–1906, The Barnes Foundation, Philadelphia, PA, USA), shown in Fig. 3a, have been recognized since 2006, when a survey by portable X-ray fluorescence identified this pigment in all altered regions of the monumental painting. This alteration is visible as fading, discoloration, chalking, flaking, and spalling of several regions of light to medium yellow paint. Similar secondary Cd-compounds (see Fig. 3h), such as $CdCO_3$, $CdSO_4·nH_2O$ (Fig. 3c–f), and CdC_2O_4 (Cd-oxalate) as found in the Ensor and Van Gogh paintings have been identified [219–221]. By using a combination of μ-XRF (Fig. 2g), 2D full-field XANES imaging (Fig. 2h), μ-XRPD (Fig. 3i), and FTIR imaging of the altered paint layers, the question was addressed what the roles of cadmium carbonates and cadmium sulfates are found in the altered paint layers [222]. These compounds have often been assumed to be photo-oxidation products, but could also be residual starting reagents from an indirect wet process synthesis of CdS. In thin sections of altered cadmium yellow paints from *Le bonheur de vivre* the distribution of various cadmium compounds confirms that cadmium carbonates and sulphates are photo-degradation products. On the other hand, in *Flower Piece* (1906, H. Matisse, The Barnes Foundation), the cadmium carbonates appear to be remnants of the CdS manufacturing process, where $CdCO_3$ is the

starting reagent. By employing TOF–SIMS species-specific mapping of degraded paint samples, three categories of inorganic and organic components could also be co-localized throughout i: (1) species relating to the preparation and photo-induced oxidation of CdS yellow pigments, (2) varying amounts of long-chain fatty acids present in both the paint and primary ground layer, and (3) specific amino acid fragments, possibly relating to the painting's complex restoration history [223].

As of the 1840s, cadmium zinc sulfides were extensively employed by nineteenth and twentieth century artists. The direct band gap of CdS is 2.42 eV, but can be modulated by the progressive substitution of Cd with Zn, resulting in pale yellow cadmium zinc sulfide pigments. Rosi et al. developed an analytical methodology for the non-destructive identification of different forms of yellow $Cd_{1-x}Zn_xS$ solid solutions based on electronic and vibrational spectroscopies such as XRF, μ-RS, reflection mode UV–VIS-NIR, VIS–NIR emission spectroscopy, and XRD. Six commercial CdS-based pigments and four historical pigments from the early twentieth century were examined. The reflection behavior in the VIS range and the emission profiles in the VIS and NIR ranges reflected the pigment composition while μ-RS allows to monitor the short range disorder in the CdS lattice caused by Zn substitution. Information on the stoichiometry of the solid solutions and on their local structure could be obtained via XRD and by employing different Raman on/off resonance excitation conditions [215].

Minium or red lead (Pb_3O_4) is another frequently employed pigment by Van Gogh and contemporary artists. This orange–red pigment has been used since Antiquity. It contains both Pb^{2+} and Pb^{4+}-ions and has sometimes been observed to lose its red color. These transformations are either described as darkening of the pigment caused by the formation of either plattnerite (β-PbO_2) or galena (PbS) or as whitening by which red lead is converted into anglesite ($PbSO_4$) or (hydro)cerussite ($2PbCO_3 \cdot Pb(OH)_2$; $PbCO_3$). By examining a degraded paint sample from Van Gogh's *Wheat Stacks under a Cloudy Sky* (1889, KMM) by means of conventional 2D and tomographic XRPD, it was possible to elucidate the degradation mechanism of minium and identify a missing link compound [163]. The degradation process was understood to be induced by absorption of 550 nm (or shorter) wavelengths, promoting electrons from the valence to the conduction band of minium. These electrons may reduce Pb(+IV) to Pb(+II). The *in situ* formed Pb^{2+} (perhaps in the form of PbO) then captures CO_2 (either atmospheric or the result of oxidation of the paint binding medium) to form various lead carbonates. Next to the frequently encountered cerussite and hydrocerussite, a very rare lead mineral, plumbonacrite ($3PbCO_3 \cdot Pb(OH)_2 \cdot PbO$), was revealed to be present. The location of this compound was revealed via XRPD-tomography (Fig. 4b) of a hemispherical paint protrusion, at the centre of which a partially degraded grain of minium was present (see Fig. 4g, h). Evidence for the presence of a series of consecutive equilibria, gradually transforming plumbonacrite into cerussite via hydrocerussite was found. In a follow-up paper, the influence of several parameters on the tendency towards degradation of

minium such as (a) a surplus of PbO inside the red lead material itself, (b) the pH, and (c) the concentration of available HCO_3^- or CO_3^{2-}-ions was investigated [224]. For demonstrating the photoactivity of the pigment, an electrochemical setup with a minium-modified graphite electrode (C | Pb_3O_4) was used. It could be confirmed that minium behaves as a *p*-type semiconductor, photoactive during illumination, and inactive in the dark. Raman measurements confirm the formation of degradation products. The photo-activity of the semiconductor pigment is partly defined by the presence of PbO impurities; these introduce new states in the original band gap. It was experimentally evidenced that the presence of PbO particles in minium leads to an upward shift of the valence band, reducing the band gap. Thus, upon photoexcitation, the electron/hole separation is more easily initialized. The PbO/Pb_3O_4 composite electrodes demonstrate a higher reductive photocurrent compared to the photocurrent registered at pure PbO or Pb_3O_4-modified electrodes. In the presence of bicarbonate ions, a significantly higher photoreduction current is recorded because the PbO that is formed *in situ* reacts further to become hydrocerussite. It could be shown that the presence of bicarbonates in the environment stimulates the photodecomposition process of minium and plays an important role in the degradation process.

The fading of modern pigments based on Prussian blue blues [$MFe^{III}[Fe^{II}(CN)_6]\cdot xH_2O$, with M=$K^+$, NH_4^+ or Na^+], another class of pigments frequently employed by Van Gogh [2] and other artists [69, 225], in the presence of various white pigments has also been investigated [138, 226–230]. Painted samples were studied by UV–VIS, Fe K-edge X-ray absorption, ^{57}Fe transmission Mössbauer spectroscopy, and attenuated total reflectance (ATR) infrared spectroscopy. XAS revealed an effective decrease in the iron coordination number in the aged samples, which, combined with Mössbauer data, suggest a reduction of the surface iron ions in the Prussian blue upon exposure to light.

1.1.4 State-of-the-Art X-ray-Based Chemical Imaging of Painted Works of Art

1.1.4.1 *Macroscopic X-ray Fluorescence Imaging (MA-XRF)*

In a number of recent papers, the results obtained via MA-XRF were compared to those obtained by other methods providing elemental distribution information on the square meter scale. Next to XRR, also neutron activation autoradiography (NAAR) provides information of this kind [231]. Given the differences between XRR, MA-XRF, and NAAR in the fundamental physical phenomena exploited, a theoretical comparison of their capabilities is not straightforward and critical comparisons of their use on the same painting were not available until recently. While NAAR images tend to be more difficult to interpret because they usually contain contributions from more than one element/pigment, MA-XRF maps provide more direct and intuitive information on the distribution of pigments. The different mechanism by which the images are created also effects the sharpness of the resulting image. In NAAR, for example both the copper and mercury radionuclides produce high-energy radiation. In the case the photographic film

not in direct contact with the paint, the path the electrons must bridge between paint and film can cause blurring of the NAAR images. By contrast, MA-XRF images that are obtained by scanning can be much sharper in such cases. However, the absorption of characteristic XRF radiation emitted by elements in underlying paint layers by overlying strata may significantly influence the maps.

During the investigation of Rembrandt's painting *Susanna and the Elders* (Gemäldegalerie, Berlin, Germany), XRR, NAAR, and MA-XRF data were juxtaposed [232]. In the XRR images, which are dominated by the Pb distribution, many *pentimenti* (i.e., intentional changes to the composition, made by the original artist) are visible, but given the complex genesis of the painting, their identification in the radiograph was not straightforward. The painting features a considerable number of overpainted features and a wide range of pigments with different elemental tracers, including earth pigments (Mn/Fe), azurite (Cu), lead white (Pb), vermilion (Hg), and smalt (Co, As) are present. MA-XRF suffers from few spectral overlaps and the scanning of the painting was performed in a few tens of hours and *in situ*, i.e. in the museum itself. NAAR required the stay of the painting at a nuclear research facility for several weeks while inter-element interferences are more difficult to resolve. Moreover, only a limited number of elements contribute to the acquired autoradiographs, most notably Mn, Cu, As, Co, Hg, and P while highly relevant elements such as (K), Ca, Fe, and Pb do not show up in the NAAR images. However, NAAR provides a higher lateral resolution and is less hindered by absorption in covering layers, which makes it the only method capable of visualizing P in lower paint layers. Comparison of the MA-XRF Pb and Hg distribution of *Susanna and the Elders* suggest, for example, that the first Elder's hand was repositioned several times.

Another painting by Rembrandt that was studied by both MA-XRF and NAAR is *An Old Man in Military Costume* (1630–31) in the J. Paul Getty Museum (Los Angeles, CA, USA) [151]. The objective of the study was to virtually reconstruct the hidden portrait below the one that is now visible. The challenge of reconstructing the overpainted figure in *An Old Man in Military Costume* was significantly advanced by the judicious combined use of imaging methods. XRR provided information on part of the face and the area of the eyes since it largely reflects the distribution of lead white. NAAR provided a strong image of the face and cloak of the underlying figure, along with an indication of the chemical composition. The single-element distribution maps produced by MA-XRF provided additional details into the shape of the underlying image and the composition of the pigments used. The underlying figure's face proved to be richer in mercury than the face of the figure on the surface. Likewise, the cloak of the underlying figure was found to be richer in copper than the surface figure although the nature of the copper-containing pigment could not be determined from these data. The use of iron earth pigments, specifically, Si-rich umbers, came forth from complementary information provided by the NAAR and MA-XRF maps; more specifically, the MA-XRF Fe distribution revealed the shape of the first portrait's gorget or collar. These data were used to create a false color

digital reconstruction, yielding the most detailed representation of the underlying painting to date. This new reconstruction, and associated information on the pigments employed in both the upper and lower images serves to invigorate the art-historical discussion on the exact nature of the concealed figure and its significance in Rembrandt's oeuvre.

NAAR and XRF imaging were also used in the investigation of *The Reading Hermit* (1630), allegedly painted by Rembrandt [233].

Gradually, the elemental mapping capabilities of MA-XRF are being employed for the investigation of works of art other than oil paintings. Its applicability for investigating stained-glass windows inside a conservation studio was assessed by analyzing a well-studied late-medieval panel from the City Museum of Bruges (Belgium), showing Saint George and Saint Michael (see Fig. 7) [234]. Although accurate quantification of components is not feasible with this analytical imaging technique, plotting the detected intensities of K versus Ca in a scatter plot allowed distinguishing glass fragments of different compositional types within the same panel (Fig. 7 c1–c4). In particular, clusters in the Ca/K correlation plot revealed the presence of two subtypes of potash glass and three subtypes of high lime-low alkali (HLLA) glass. MA-XRF results proved to be consistent with previous semiquantitative SEM-EDX analyses on two glass micro-samples and theories on glass production in the Low Countries formulated in literature. A bi-plot of the intensities of the more energetic Rb-K versus Sr-K emission lines yielded a similar glass type differentiation and presented a suitable alternative in case the Ca/K signal ratio is affected by superimposed weathering crusts. The MA-XRF maps permitted the identification of the chromophores responsible for the green, blue and red glass colors. In addition, by contrasting MA-XRF maps from the interior with exterior side of the window, it was possible to discriminate between glass panes made in colored pot metal glass (i.e., glass that is colored throughout the pane) and those made in multi-layered flashed glass (i.e., colorless glass covered with one or more thin, intensely colored glass coatings). The benefit of obtaining compositional information from the entire surface, as opposed to point analysis, was illustrated by the discovery of what appears to be a green cobalt glass feature (see Fig. 7d) that was previously missed on this well-studied stained-glass window, both by connoisseurs and spectroscopic sample analysis. Generally, the major benefit is the ability to acquire compositional data from the entire surface in a non-invasive way. In addition, the ensuing chemical data can be presented in a visual way, hence making their interpretation easier for non-XRF specialists. However, in contrast with conventional SEM-EDX and μ-XRF point analyses on samples, MA-XRF experiments do not provide accurate quantitative composition information on the different glass components. Although essentially qualitative in nature, the resulting insights are particularly useful for conservators who are typically interested in an efficient discrimination of the historical phases in one specific window rather than in the exact chemical composition of the different glass types present.
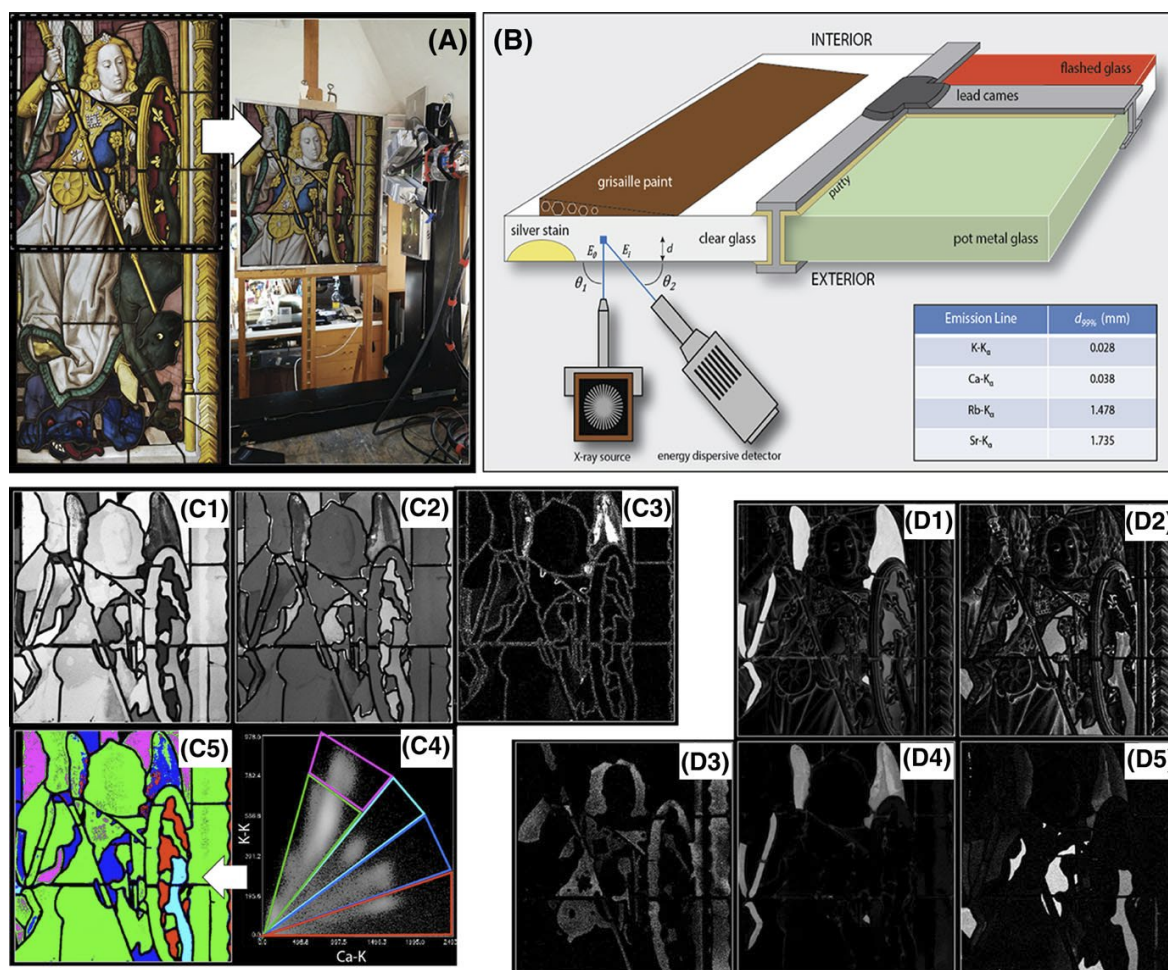
Figure 7: **A** *Stained-glass window from the collection of the City Museum of Bruges showing Saint Michael, dated ca. 1490, in front of the MA-XRF scanner;* **B** *schematic of build-up of a stained-glass window and measurement geometry on interior side. The table lists sampling depths for different XRF energies; Elemental maps collected from the interior side:* **C1** *K,* **C2** *Ca, and* **C3** *S;* **C4** *Ca-K vs K-K intensity scatter diagram with pixels clusters indicated;* **C5** *Locations of color-coded pixel clusters. Elemental maps collected from the interior side:* **D1** *Cu and* **D2** *Co; from the exterior side:* **D3** *Ag,* **D4** *Cu, and* **D5** *Co. Adapted from [234]*

The mobile aspect of the instrument allows performing the experiments directly inside a conservation studio and the ensuing elemental distribution maps can also serve as functional working drawings during the actual treatment. However, the lack of absolute concentration data of the various glass constituents does prevent inter-comparison of MA-XRF data obtained from different stained-glass windows. In this framework, combining the MA-XRF maps with SEM-EDX analyses on a limited number of samples is expected to be particularly relevant. Moreover, by creating MA-XRF maps, sampling locations for SEM-EDX investigations can be selected in a highly substantiated way. Thus, the number of micro-samples required for obtaining a comprehensive compositional overview of the glass types present in a glass window can be minimized and the resulting

sample data can be extrapolated to the rest of the glass surface in a more confident manner.

The benefits and limitations of employing MA-XRF for the study of manuscript illuminations were recently discussed [235]. As a representative example of this type of objects, a fifteenth century Italian manuscript fragment from the collection of the Fitzwilliam Museum in Cambridge (UK) was investigated. MA-XRF scanning of this fragment was undertaken to gain insight into the materials and techniques of Renaissance illuminators and to help answer specific questions regarding its authorship and place of execution, currently considered to be either Bologna or Rome. The non-invasive analysis permitted to reconstruct the palette employed by the anonymous illuminator and highlighted the likely use of two unusual pigments: an arsenic sulphide glass and a manganese (hydr)oxide. Identification of the latter would have been difficult without an elemental Mn map, which showed no overlap with the Fe distribution, excluding the presence of umber pigments, widely used and, therefore, less distinctive of a specific artist or school. The use of manganese oxides as black pigments as hitherto been identified almost exclusively in easel paintings by a number of sixteenth century artists working in northern and central Italy, such as Perugino, with whom the unknown artist of the manuscript fragment shows stylistic affinities. Although MA-XRF could not provide a definite answer to the question of geographic origin, this kind of analysis did offer strong support to securely place the fragment within a specific artistic context. In order to realize a more precise and more reliable pigment identification on these type of artefacts, MA-XRF scanning is best combined with a series of RS or XRD point measurements.

MA-XRF was used together with optical coherence tomography (OCT) for the inspection of a late sixteenth century illuminated parchment manuscript (a gradual), originating from the Convent of the Benedictine Sisters in Lviv (Ukraine) (Fig. 8) [236]. It was employed both for mapping the elemental distribution over large parts of the folios (which included illuminated initials; see Fig. 8a–d), for quantitative analysis of the composition of the smalt pigment, and for documenting changes in the composition of the iron gall ink on different pages. OCT, by providing cross-sectional images of painted details, helped to interpret the XRF results. Of the two non-invasive techniques, MA-XRF appeared to be the more useful. As opposed to the local approach employed with PXRF, the ability of MA-XRF to scan large areas allows for a more general characterization of the object, not restricted to small regions of examination or to the collection of samples from them. OCT also yields images of relatively large structures; Fig. 8e shows virtual OCT cross sections of different locations on the manuscript. However, OCT suffers, due to the high scattering properties of historic parchment, from the drawback that the information retrieved is relatively limited.
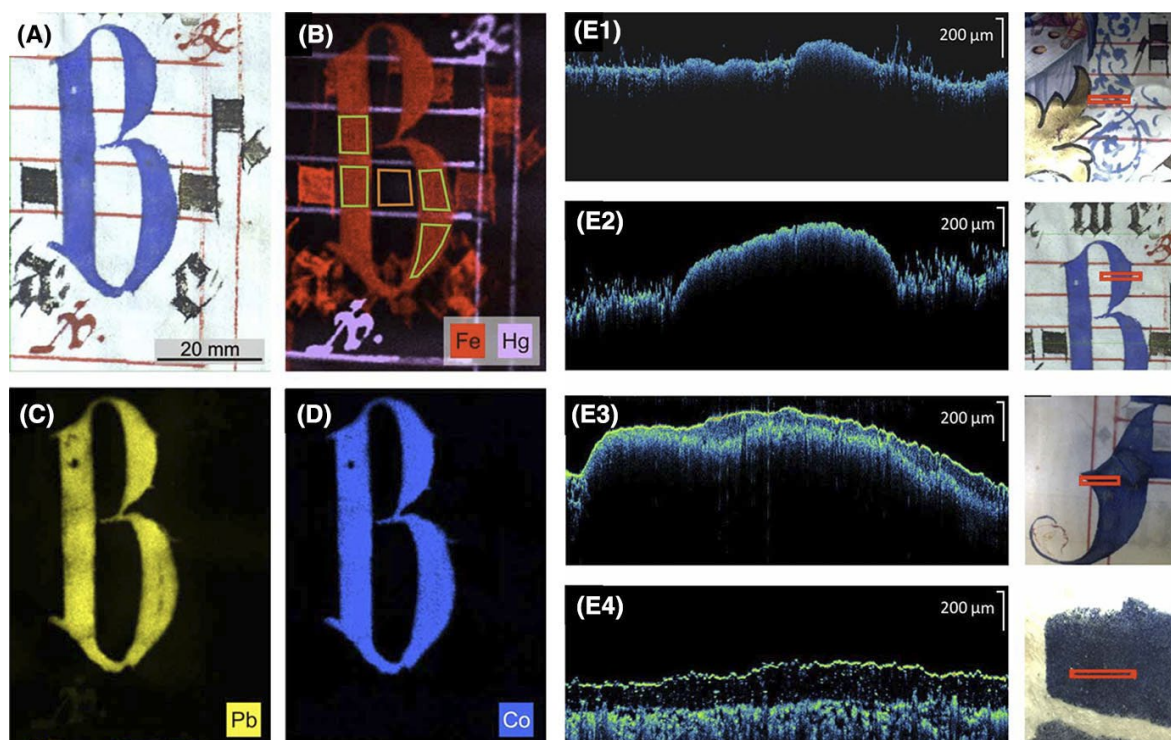
*Figure 8: **A** Optical photograph and elemental maps of **B** Fe, Hg, **C** Pb, and **D** Co a capital ''B'' from a sixteenth century gradual, originating from a Benedictine Convent (Lviv, Ukraine) **E** OCT profiles of several details of blue-lettering (red rectangles). Adapted from [236]*

To illustrate the interplay between spectroscopic methods for non-invasive imaging, for point measurements and for microscopic pigment identification/ imaging, their combined use for a full characterization of the fifteenth century work of art, *Christ with Singing and Music-Making Angels*, by Hans Memling was described [21]. This involved the recording of MA-XRF and MA-rFTIR maps (see Fig. 1), providing information on Memling's painting and colour rendering technique. For example, vermilion red was used in the cloak embroidery and in the bright red parts of the wings of some of the angels, while at a lower concentration level, it was also present in the flesh tones of the faces. In the more purplish tones, madder lake was the major colorant, sometimes mixed with azurite. The latter pigment was also employed in all blueish areas. For the hair of the angels, clay-containing earth pigments (Fe, e.g. from goethite) were employed, with lead tin yellow for the highlights. The worn gilded background features high Au and reflected infrared signals but also Ca and Fe signals, both of which originate from an underlying adhesive bole layer. In Fig. 1c, a composite of the relevant MA-XRF elemental maps is shown. In the examined areas, almost no indications of *pentimenti* were encountered.

1.1.4.2 *Studies Combining Large-Scale Chemical Imaging and Microscopic Paint Sample Analysis*

Next to the use of MA-XRF and related methods for subsurface visualization of overpainted representations, this chemical form of imaging of paintings is also increasing being used as part of pigment degradation studies. Below a number of investigations are described where macroscopic chemical imaging is combined with microscopic analyses of minute paint samples.

1.1.4.2.1 **Identification and Localization of Different Smalt Types in ''*Saul and David*'', Rembrandt**

The painting *Saul and David* shown in Fig. 9, is thought to date from c. 1652 and previously was attributed to Rembrandt van Rijn and/or his studio. It is a complex work of art, recently subjected to an intensive conservation treatment and associated investigation [153]. It was anticipated that its analysis would shed light on authenticity questions and Rembrandt's role in the creation of the painting. The painting was thought to have been started in a colorful style characterized by great detailing and smooth handling of the paint. In contrast, the adjustments made to the painting during the second stage are painted very loosely; some scholars are in doubt whether this second stage was executed by Rembrandt—some of his assistants may have completed the work. It would seem that the painter was experimenting with the use of smalt in this second phase, since it was found over much of the painting, not only in the blue areas of the turban, which belong to the first phase. The extensive use of smalt, especially in mixtures with bone black, lakes, and earth pigments is considered typical of Rembrandt's late painting technique. Its pigment combination was not only useful to create coloristic effects, but also for its drying properties and to give bulk and texture to the paint. As part of the investigation into the authenticity of the curtain area, a number of paint micro-samples were examined with light microscopy (LM) and SEM-EDX. Given that the earth, smalt, and lake pigments used in the painting could not be imaged with traditional imaging techniques, the entire painting was also examined with state-of-the-art non-invasive imaging techniques. Special attention was devoted to the presence of cobalt-containing materials, specifically the blue pigment smalt, considered characteristic for the Rembrandt's late artistic production [152]. The painting and a selected number of MA-XRF distribution maps, recorded prior to removal of overpaint and darkened varnish layers, are shown in Fig. 9a, d, respectively. From the Fe and Co distribution maps, it is immediately clear that the upper right canvas piece (part γ) painted in a monochrome dark tone does not show the same origin as the canvas sections of *Saul and David* (parts α and β, respectively). Both Co and Fe appear to be present throughout the γ area at high abundance; the joins between the various sub-parts, as well as the entire γ-section were uniformly covered with an Fe- and Co-containing paint in order to dissimulate the differences with sections α and β. The Co map of the α-section demonstrates that smalt was extensively used in the areas of the turban, the curtain, Saul's garments and his chair.
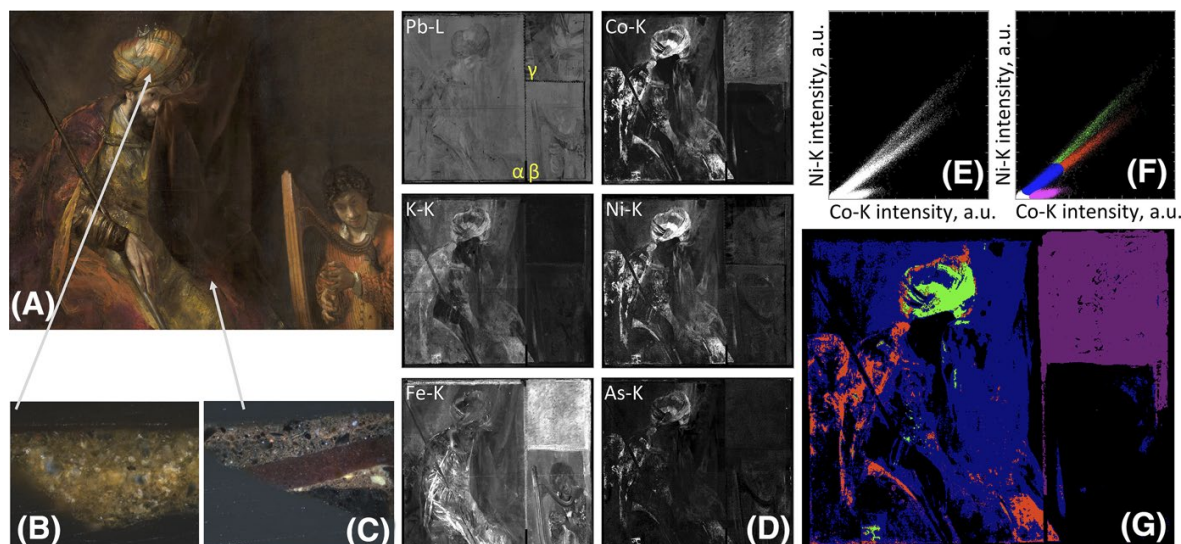
*Figure 9: **A** Saul and David by Rembrandt, (c. 1652, 126 x 158 cm, Royal Museum Mauritshuis, Den Haag, the Netherlands, inv. no. MH621, oil on canvas); **B, C** Optical micrographs of two paint cross sections (locations indicated); **D** MA-XRF maps (1311 x 1656 pixels) of various elements present in the painting; **E** Ni-K vs. Co-K XRF intensity scatter plot; **F** as E, color codes: green: ''high Ni'', red: ''medium Ni'', magenta: ''low Co/Ni'', blue: ''rest''; **G** location map of color-coded pixels. Adapted from [152]*

K is associated with smalt, but also with red lake (likely from alum or KOH added during its production). The Fe-distribution in the α-section is quite different from the other elements since it is dominated by the earth pigment-containing areas, where the Fe concentration is much higher than in smalt (where it is of the order of a few wt%). The Co map has a patchy appearance at the left and bottom of the picture, areas corresponding to Saul's cloak, which initially appears to have extended over the chair. The lighter (higher intensity) areas in the Co map correspond to the thicker/more intact smalt-rich paint. Paint cross-sections (Fig. 9c) from the dark patchy areas in the scans of Saul's show the presence of an incomplete smalt-rich top paint layer applied on top of red lake glazes. The partial removal of the smalt paint from Saul's garment and chair is most likely due to a misinterpretation during a past restoration, where a restorer tried to recover the bright red color of Saul's cloak, obscured by a discolored and darkened smalt layer. In the Ni:Co correlation plot (Fig. 9e, f), the existence of smalt characterized by various distinct Ni:Co ratios is clearly visible. Next to the ''medium Ni'' group of pixels (labeled red in Fig. 9f), a smaller group of pixels (labelled green) is present characterized by a Ni:Co ratio that is ca. 25% higher than in the ''medium Ni'' group. This ''high Ni'' group of pixels is situated in Saul's turban and some small parts of his clothing. The ''medium Ni'' group of smalt pixels corresponds to patchy areas of paint of uneven thickness that are present in Saul's garment in sections α and β. The pixels belonging to the curtain area in the background between the figures of Saul and David, generally showing both a low Co and Ni intensity, were labelled blue. In magenta, a fourth group of pixels, characterized by a very low Ni to Co XRF intensity ratio is also visible in Fig. 9g, corresponding to the paint used to cover the canvas insert γ [153]. Microscopic examination of paint samples from this section

showed that Co is not present in the form of smalt pigment particles but in a more finely divided state, dispersed through the layer. The Co material was likely added to the nineteenth century overpaint as drying agent. In sections α and β however, the Co and Ni are definitely present inside coarsely ground smalt particles. The difference between the ''medium Ni'' and ''high Ni'' areas could also be found back in the quantitative SEM-EDX data of paint samples from both areas (shown in Fig. 9b, c). From analysis of a series individual smalt particles it was possible to infer that (a) the leaching process significantly decreases the K_2O content of the glass, typically from a level of 10–16 to 2–5 wt% while it does not seem to have a large effect on the observed NiO:CoO concentration ratio; (b) the two average NiO:CoO ratios obtained in both areas of the painting are significantly different at the 99% confidence level: the ''turban area'' particles on average show a mean NiO:CoO concentration ratio of 0.35 ± 0.06 (1 s) that is significantly higher than the average ratio of the particles in the ''garment area'' where it is 0.28 ± 0.07. This observation is consistent with the MA-XRF scatter plots of Fig. 9e–g, were in the turban area, a Ni:Co intensity ratio that is ca. 25% higher than that in the garment area is observed. In this manner the combination of quantitative SEM-EDX analysis and MA-XRF scanning revealed that three types of Co-containing materials are present in the *Saul and David* painting.

1.1.4.2.2 Evidence for Pigment Degradation in ''*Sunflowers*'' by V. Van Gogh

The *Sunflowers* painting shown in Fig. 2 was painted by Vincent Van Gogh in Arles in 1888–89 as part of a series of seven, all depicting a bouquet of sunflowers in an earthenware pot. The extent to which spontaneously occurring color changes have influenced today's outlook of the paintings has been questioned, while previous studies showed that CYs ($PbCr_{1-x}S_xO_4$ with variable sulfate content x) are prone to darkening due to (photo-)reduction. The formation of reduced Cr is more favored for sulfate-rich, lemon-yellow, orthorhombic $PbCr_{1-x}S_xO_4$ varieties of the pigment (with $x > 0.4$) than for the orange-yellow, monoclinic $PbCrO_4$ that is the most lightfast of these materials [200, 202, 203, 205, 206]. A combination of non-invasive methods such as MA-XRF, FTIR, and RS were performed *in situ* on the version of *Sunflowers* owned by the Van Gogh Museum (Fig. 2a). Microscopic investigation of minute paint samples was undertaken (1) to assess the extent to which the painting contains lightfast $PbCrO_4$ (henceforth denoted as LF-CY) and light sensitive S-rich $PbCr_{1-x}S_xO_4$ ($x > 0.4$) (LS-CY), and (2) to determine whether or not these pigments have been subject to a reduction process [156]. The MA-XRF maps of the painting (Fig. 2b, c) show that Pb and Cr are the main elemental constituents of the sunflower petals, the orange corollas and the table area. In the pale yellow background, Zn is the predominant element (Fig. 2b), suggesting the presence of zinc white (ZnO), while Pb and Cr are present in a significantly lesser quantities. In some of the ochre and orange tones of the sunflower petals, besides Pb and Cr, Hg, and/or Cu and As were also found (Fig. 2c), due to the presence of vermilion (HgS) and/or emerald green [$3Cu(AsO_2)_2 \cdot Cu(CH_3COO)_2$]. In areas of the sunflower petals and the upper region of the vase with no or very little Pb and Cr, Fe is the main constituent element instead, indicating the use of a yellow ochre (Fe-hydroxide based pigment). All the above-

mentioned pigments are frequently encountered in works by Van Gogh. In the green(ish) areas, besides Cu and As, Pb and Cr are sometimes found together too, suggesting the use of mixtures or overlapping brush strokes of emerald green and CYs. The Pb-Lα:Cr-Kα XRF intensity ratio changes throughout the painting (Fig. 2b), suggesting a distribution of different CY types. However, the presence of other Pb- and/or Cr-based pigments, also frequently used by Van Gogh, such as red lead (Pb_3O_4), lead white [$PbCO_3$, $Pb_3(CO_3)_2(OH)_2$], or viridian green ($Cr_2O_3 \cdot 2H_2O$), and variations of the paint thickness (giving rise to self-absorption of variable magnitude), could also cause a change in the Pb-Lα:Cr-Kα intensity ratio. No meaningful S-distribution maps could be recorded, mainly due to the spectral overlap between the S–K and Pb-M XRF signals and the limited MA-XRF sensitivity for these signals. More reliable insights into the distribution of the different types of CY were obtained by performing vibrational spectroscopic and structural analyses at a select number of points on the surface of the *Sunflowers* painting (see Fig. 2d for a summary of the results). In the light yellow table area, non-invasive Raman and reflection mid-FTIR analyses revealed the presence of LS-CY ($x \approx 0.5$). This finding was confirmed by SR-based μ-XRD and vibrational spectroscopic analysis of a sample from the region (F458/4). In the Zn-rich pale yellow background, Raman spectroscopy (Fig. 2d) again demonstrated the presence of LS-CY ($x \approx 0.5$). For the sunflower petals, various CYs appear to have been used. While in the light yellow areas, a type of LS-CY very similar to that detected in the table and background was identified by Raman spectroscopy, on the other hand, in the ochre-yellow petals, the presence of LF-CY (i.e., monoclinic $PbCrO_4$) was observed. Occasionally, this is mixed with LS-CY or red lead. Chrome orange and vermilion red are sometimes also present in the darker/orange petals. SR-based μ-XRD and μ-Raman mapping experiments of regions of interesting of one of the studied paint samples (F458/1) confirmed the non-invasive analyses: LF-CY is the chief constituent of the orange-yellow shades, while LS-CY ($x \approx 0.5$) is the main phase in the lighter yellow hues. Clear indications for the gradual conversion of Cr(+VI) to Cr(+III) were found. Next to Cr(+III)-rich particles, Cr(+III)-species are present as a 2–3 μm thick layer right at the varnish/paint interface. Here, the relative abundance of Cr(+III) is around 35%, decreasing to 0% when going deeper inside the yellow paint. This pattern is very similar to that previously observed in photochemically aged LS-CY ($x > 0.4$) paint models [200, 203, 205, 206]. In summary, the non-invasive identification and macro-scale level distribution of the light-sensitive chrome yellow in the *Sunflowers* painting in combination with analysis of paint micro-samples has permitted to identify selected locations with the highest probability/risk of color change due to Cr(+VI) reduction and to provide the first evidence on the conservation state of chrome yellow in selected regions of the painting.

1.1.4.2.3 Combining MA-XRF and VNIR Hyperspectral Imaging for the Study of *Le Portrait*, R. Magritte

Diffuse reflectance imaging spectroscopy can be used to separate and identify many artist pigments by virtue of their unique electronic transitions and vibrational features in the visible to reflective near infrared (400–2500 nm) [27, 157, 237–240]. When combined

with MA-XRF scanning results, a more complete identification and mapping of artists' materials is possible [27].

''*Le portrait*'' (*The Portrait*, 1935, The Museum of Modern Art (MoMA), New York City, NY, USA), shown in Fig. 10, is a painting by Belgian surrealist artist René Magritte (1898–1967). It is a classic example of Magritte's imagery, characterized by the realistic representation of ordinary objects made surreal by context or their relationship to each other. In the corresponding XRR image, an underlying composition is visible, showing the head and torso of a female nude. A similarity between the figure in the XRR image and the upper left quarter of a painting by Magritte entitled ''*La pose enchantée*'' (*The Enchanted Pose*), presumed lost, can be recognized. Preliminary *in situ* analyses by means of PXRF suggested the presence of a chromium based pigment in the sky and of an iron oxide based pigment in the darker areas of the female face. To gain a more thorough and overall depiction of the hidden layer, MA-XRF was used to identify and map the distribution of key chemical elements representative of pigments commonly found in artists' paintings, thus revealing information on the color palette employed by Magritte while painting ''*La pose enchantée*''. Secondly, visible and near infrared (VNIR) hyperspectral imaging was performed to complement the information obtained by XRR and MA-XRF, both with respect to the hidden figure and to Magritte's palette in both pictorial layers [157].
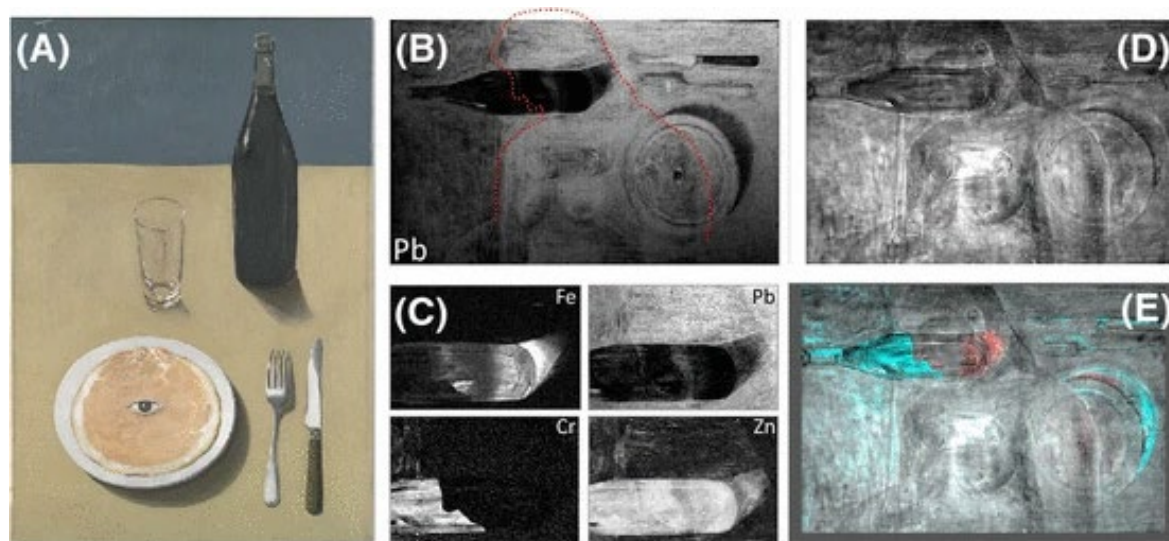
Figure 10: **A** ''*Le portrait*'', *René Magritte (The Portrait, 1935; oil on canvas, 73.3 x 50.2 cm^2; Metropolitan Museum of Modern Art—(c) C. Herscovici/Artists Rights Society (ARS), New York, USA);* **B** *rotated MA-XRF Pb-L map;* **C** *different detailed MA-XRF of the facial area with adjusted contrast;* **D** *first transmission mode NIR eigenimage of 1000–1500 nm spectral region (after histogram equalization);* **E** *composite image obtained by overlaying the image of* **D** *with Cr (light blue), Fe + Hg (red) MA-XRF maps. Adapted from [157]*

The results of these investigations are summarized in Fig. 10. The Pb distribution map (Fig. 10b) bears a significant and expected resemblance to the X-radiography, but is no longer encumbered by the stretcher and hardware and thus easier to interpret. The brushstrokes around the bottle confirm that the bottle was painted right on the top of original painting and that the background around it was painted afterwards. The female figure is visible in the Pb map, showing that this element is more abundant in the highlights of her face and body. The Zn distribution map, looking like the negative of the Pb map, suggests the presence of this element in the ground layer. The dark color used in the bottle appears to stem mainly from carbon black, as Ca and P appear colocalized; Magritte used this pigment also in other paintings. Next to K and Fe, also Cd is detected in the black. It is not unusual for Magritte to modify the tonality of his blacks by mixing with other colors, such as cadmium yellow, in his palette. The same elements are also present in the dark green used to paint the shadow of the plate, the haft of the knife and the top of the bottle. The relative proportions vary slightly as does the green tonality. No other element related to the inorganic green pigment could be identified, suggesting the green was produced by mixing bone black with cadmium yellow, painted over the blue sky of the hidden painting. In subsequent measurements diffuse reflectance spectroscopy (DRS) supports the use of a cadmium yellow in the dark glass of the bottle, its shadow and in the knife handle given the observation of a sharp transition edge at 470 nm, consistent with the presence of CdS [241]. The Cr XRF signals, recorded in the shadow of the plate and knife and in the top half part of the bottle, only, suggest that Magritte did not use a chromium oxide green pigment as part of the top-level blue nor in the dark paint of the bottle and shadows. Rather, this element is present in the sky of the underlying painting, its X-ray fluorescence likely to be totally blocked by the lead white in the top ochre paint while the top blue paint and especially the black and dark green paint are (partially) transparent for Cr XRF radiation. No metallic elements (such as Co, Cu, Fe) were detected that could relate to the blue color on the top half of the painting using the MA-XRF scanning. This rules out many blue pigments such as cobalt, Prussian or cerulean blue; however, ultramarine blue ($Na_{8-10}Al_6Si_6O_{24}S_{2-4}$) cannot be ruled out (Na, Al, Si, and S, characteristic elements of ultramarine, are all difficult or impossible to detect in typical MA-XRF experimental conditions). PXRF measurements using a He flush revealed weak peaks for Al and Si, supportive of the assignment of ultramarine. DRS measurements of the blue background revealed a broad absorption centered at 597 nm and a peak reflectance at 483 nm, also consistent with the presence of ultramarine blue. The green shifted reflectance maximum may in part be due to a contribution of the chrome oxide below. The red color of the slice of ham and of the eyelid were rendered with vermilion red; this pigment was also used in the underlying composition, in highlights over the nose and lips of the nude (Fig. 10c, e). The MA-XRF Fe and Pb maps as well as the diffuse reflectance measurements show that the rest of the figure was painted with an iron oxide based red pigment and lead white for the highlights. NIR hyperspectral imaging of the painting (400–2450 nm wavelength range) in transmission mode was found to give more information about the pictorial features of the prior painted composition than imaging in reflectance mode. Principle component analysis (PCA) analysis, followed by histogram

equalization was used to maximize the clarity of the features from the earlier painting [242, 243]. The appearance of the nude woman corresponds well to the photograph of the prior painting. In the spectral region from 1450 to 1680 nm, Minimum Noise Fraction PCA (MNF-PCA) yields a first eigenimage (Fig. 10d) that shows more of the sketches of the pictorial elements. Figure 10e clearly illustrates the complementary nature of MA-XRF and VNIR imaging. While in the darker areas, the XRF signals from the lower figure can more easily reach the XRF detector that is positioned in a reflection geometry, the opposite is true for the NIR signals that were recorded in transmission. The lighter, more lead white-rich paint is more transparent for the NIR photons while the dark, boneblack-rich areas efficiently absorb the NIR radiation In this particular case, both imaging methods together are capable of revealing all details of the face, showing the characteristic enlarged lips, nose, ears and eyes that are expected. In a similar study on a Degas portrait, it was possible by employing XRF data alone, to faithfully reconstruct the original colours of the overpainted face [244].

1.1.5 Conclusions

In this review, an overview was presented of recent developments regarding the characterization of pigmented materials used by painters from the seventeenth to early twentieth century based on various forms of X-ray-based spectroscopic and imaging analysis. XRF covers a wide range of instrumentation that can be profitable employed for this type of investigations, ranging from fairly compact and cost-effective portable devices to sophisticated synchrotron beam lines where elemental imaging with submicroscopic lateral resolution is possible. Microscopic XRF is well suited to visualize the elemental distribution of key elements, mostly metals, present in paint multilayers on the length scale from 1 to 100 μm inside paint micro-samples taken from paintings. In the context of the characterization of the pigments that suffer from spontaneous degradation, the use of methods limited to elemental analysis or imaging usually is not sufficient to elucidate the chemical transformations that have taken place. However, at synchrotron facilities, combinations of μ-XRF with related methods such as μ-XAS and μ-XRD have proven themselves to be very suitable for such studies. Their use is often associated with μ-FTIR and μ-RS spectroscopy since these methods deliver complementary information on the molecular nature of the materials present, at more or less the same length scale as the X-ray microprobe techniques. The combined use of these methods has allowed elucidating the degradation pathways of some of the pigments frequently employed by fifteenth to twentieth century painters such as P.P. Rubens, Rembrandt van Rijn, V. van Gogh, J. Ensor, and H. Matisse. Some of these studies are now started to being combined with mapping of the distribution of pigments on the square meter scale.

References

1. Cotte M, Checroun E, De Nolf W, Taniguchi Y, De Viguerie L, Burghammer M, Walter P, Rivard C, Salomé M, Janssens K, Susini J (2016) Lead soaps in paintings: friends or foes? Stud Conserv. doi:10.1080/00393630.2016.1232529
2. Hendriks E (2011) Van Gogh's working practice: a technical study. In: Van Tilborgh L, Hendriks E(eds) Vincent Van Gogh Paintings 2: Antwerp & Paris, 1885–1888. Lund Humphries Publishers Ltd., London, pp 90–143
3. Jansen L, Luijten H, Bakker N (2009) Vincent van Gogh—The Letters. http://www.vangoghletters.org. Thames & Hudson Ltd., London
4. Janssens K, Alfeld M, Van der Snickt G, De Nolf W, Vanmeert F, Radepont M, Monico L, Dik J,Cotte M, Falkenberg G, Miliani C, Brunetti BG (2013) The use of synchrotron radiation for the characterization of artists' pigments and paintings. Ann Rev Anal Chem 6(6):399–425
5. Colombini MP, Modugno F (2004) Characterisation of proteinaceous binders in artistic paintings by chromatographic techniques. J Sep Sci 27:147–160
6. Vandenabeele P, Wehling B, Moens L, Dekeyzer B, Cardon B, von Bohlen A, Klockenkamper R (1999) Pigment investigation of a late-medieval manuscript with total reflection X-ray fluorescence and micro-Raman spectroscopy. Analyst 124:169–172
7. Wess TJ, Drakopoulos M, Snigirev A, Wouters J, Paris O, Fratzl P, Collins M, Hiller J, Nielsen K (2001) The use of small-angle X-ray diffraction studies for the analysis of structural features in archaeological samples. Archaeometry 43:117–129
8. Cesaratto A, D'Andrea C, Nevin A, Valentini G, Tassone F, Alberti R, Frizzi T, Comelli D (2014) Analysis of cadmium-based pigments with time-resolved photoluminescence. Anal Methods 6:130–138
9. Antunes V, Jose Oliveira M, Vargas H, Serrao V, Candeias A, Carvalho ML, Coroado J, Mirao J, Dias L, Longelin S, Seruya AI (2014) Characterization of glue sizing under calcium carbonate ground layers in Flemish and Luso-Flemish painting—analysis by SEM-EDS, mu-XRD and mu-Raman spectroscopy. Anal Methods 6:710–717
10. Lluveras A, Boularand S, Roque J, Cotte M, Giraldez P, Vendrell-Saz M (2008) Weathering of gilding decorations investigated by SR: development and distribution of calcium oxalates in the case of Sant Benet de Bages (Barcelona, Spain). Appl Phys Mater Sci Process 90:23–33
11. Bell IM, Clark RJH, Gibbs PJ (1997) Raman spectroscopic library of natural and synthetic pigments (pre-similar to 1850 AD). Spectrochim Acta Part A Mol Biomol Spectrosc 53:2159–2179
12. Van der Snickt G, De Nolf W, Vekemans B, Janssens K (2008) mu-XRF/mu-RS vs. SR mu-XRD for pigment identification in illuminated manuscripts. Appl Phys A Mater Sci Process 92:59–68
13. Andreotti A, Bonaduce I, Colombini MP, Gautier G, Modugno F, Ribechini E (2006) Combined GC/MS analytical procedure for the characterization of glycerolipid, waxy,

resinous, and proteinaceous materials in a unique paint micro-sample. Anal Chem 78:4490–4500

14.   Colombini MP, Andreotti A, Bonaduce I, Modugno F, Ribechini E (2010) Analytical strategies for characterizing organic paint media using gas chromatography/mass spectrometry. Acc Chem Res 43:715–727

15.   Degano I, Ribechini E, Modugno F, Colombini MP (2009) Analytical methods for the characterization of organic dyes in artworks and in historical textiles. Appl Spectrosc Rev 44:363–410

16.   Janssens K, Adams F, Rindby A (2000) Microscopic X-ray fluorescence analysis. Wiley, Chichester

17.   Cotte M, Susini J, Dik J, Janssens K (2010) Synchrotron-based X-ray absorption spectroscopy for art conservation: looking back and looking forward. Acc Chem Res 43:705–714

18.   De Nolf W, Janssens K (2010) Micro X-ray diffraction and fluorescence tomography for the study of multilayered automotive paints. Surf Interface Anal 42:411–418

19.   Thoury M, Echard JP, Refregiers M, Berrie B, Nevin A, Jamme F, Bertrand L (2011) Synchrotron UV-visible multispectral luminescence microimaging of historical samples. Anal Chem 83:1737–1745

20.   Bertrand L, Robinet L, Thoury M, Janssens K, Cohen SX, Schoder S (2012) Cultural heritage and archaeology materials studied by synchrotron spectroscopy and imaging. Appl Phys A Mater Sci Process 106:377–396

21.   Janssens K, Legrand S, Van der Snickt G, Vanmeert F (2016) Virtual archaeology of altered paintings: multiscale chemical imaging tools. Elements 12:39–44

22.   Janssens K, Dik J, Cotte M, Susini J (2010) Photon-based techniques for non-destructive subsurface analysis of painted cultural heritage artifacts. Acc Chem Res 43:814–825

23.   Alfeld M, Broekaert JAC (2013) Mobile depth profiling and sub-surface imaging techniques for historical paintings—a review. Spectrochim Acta Part B 88:211–230

24.   Miliani C, Rosi F, Brunetti BG, Sgamellotti A (2010) *In situ* non-invasive study of artworks: the MOLAB multitechnique approach. Acc Chem Res 43:728–738

25.   Daffara C, Parisotto S, Mariotti PI (2015) Mid-infrared thermal imaging for an effective mapping of surface materials and sub-surface detachments in mural paintings: integration of thermography and thermal quasi-reflectography. In: Pezzati L, Targowski P (eds) Optics for arts, architecture, and archaeology V

26.   Alfeld M, Janssens K, Dik J, De Nolf W, Van der Snickt G (2011) Optimization of mobile scanning macro-XRF systems for the *in situ* investigation of historical paintings. J Anal At Spectrom 26:899–909

27.   Dooley KA, Conover DM, Glinsman LD, Delaney JK (2014) Complementary standoff chemical imaging to map and identify artist materials in an early Italian renaissance panel painting. Angew Chem Int Edit 53:13775–13779

28.   De Nolf W, Dik J, Van der Snickt G, Wallert A, Janssens K (2011) High energy X-ray powder diffraction for the imaging of (hidden) paintings. J Anal At Spectrom 26:910–916

29.   Legrand S, Alfeld M, Vanmeert F, De Nolf W, Janssens K (2014) Macroscopic Fourier transform infrared scanning in reflection mode (MA-rFTIR), a new tool for chemical imaging of cultural heritage artefacts in the mid-infrared range. Analyst 139:2489–2498

30.   Daffara C, Pampaloni E, Pezzati L, Barucci M, Fontana R (2010) Scanning multispectral IR reflectography SMIRR: an advanced tool for art diagnostics. Acc Chem Res 43:847–856

31.   Beckhoff B, Kanngiesser B, Langhoff N, Rainer W, Helmut W (2006) Handbook of practical X-ray fluorescence analysis. Springer, Berlin

32.   Vincze L, Somogyi A, Osan J, Vekemans B, Torok S, Janssens K, Adams F (2002) Quantitative trace element analysis of individual fly ash particles by means of X-ray microfluorescence. Anal Chem 74:1128–1135

33.   Vincze L, Janssens K, Adams F, Jones KW (1995) A general monte carlo simulation of energy-dispersive X-ray fluorescence spectrometers.3. Polarized polychromatic radiation, homogeneous samples. Spectrochim Acta Part B At Spectrosc 50:1481–1500

34.   Vincze L, Janssens K, Vekemans B, Adams F (1999) Monte Carlo simulation of X-ray fluorescence spectra: part 4. Photon scattering at high X-ray energies. Spectrochim Acta Part B At Spectrosc 54:1711–1722

35.   Lahanier C, Amsel G, Heitz C, Menu M, Andersen HH (1986) Proceedings of the international workshop on ion-beam analysis in the arts and archaeology—Pont-A-Mousson, Abbaye Des Premontres, France, February 18–20, 1985—Editorial. Nucl Instrum Methods Phys Res Sect B Beam Interact Mater At 14: R7–R8

36.   Van Grieken R, Markowicz A (2002) Handbook of X-ray spectrometry. Marcel Dekker, New York

37.   Van der Linden V, Meesdom E, Devos A, Van Dooren R, Nieuwdorp H, Janssen E, Balace S, Vekemans B, Vincze L, Janssens K (2011) PXRF, mu-XRF, Vacuum mu-XRF, and EPMA Analysis of Email Champleve Objects Present in Belgian Museums. Microsc Microanal 17:674–685

38.   Carvalho ML, Karydas A, Piorek S (2010) Special issue: the use and application of handheld and portable XRF spectrometers. X-Ray Spectrom 39:77

39.   Potts PJ, Ramsey MH, Carlisle J (2002) Portable X-ray fluorescence in the characterisation of arsenic contamination associated with industrial buildings at a heritage arsenic works site near Redruth, Cornwall, UK. J Environ Monit 4:1017–1024

40.   Jones MC, Williams-Thorpe O, Potts PJ, Webb PC (2005) Using field-portable XRF to assess geochemical variations within and between dolerite outcrops of Preseli, south Wales. Geostand Geoanal Res 29:251–269

41.   Piorek S (1997) Field-portable X-ray fluorescence spectrometry: past, present, and future. Field Anal Chem Technol 1:317–329

42.   Piorek S (2004) Ieee, Portable X-ray fluorescence analyzer for the first level screening of materials for prohibited substances, 2005 International Conference on Asian Green Electronics: Design for Manufacturability and Reliability, Proceedings, pp 7–13

43.   Piorek S, Puusaari E, Piorek E, McCann B (1999) Identification and quantitative analysis of alloys using X-ray fluorescence analyzer with a silicon ''p-i-n'' diode detector. In: Fernandez JE, Tartari A (eds) EDXRS-98: Proceedings of the European Conference on Energy Dispersive X-Ray Spectrometry 1998. Editrice Compositori, Bologna, p 280

44.   Pages-Camagna S, Laval E, Vigears D, Duran A (2010) Non-destructive and *in situ* analysis of Egyptian wall paintings by X-ray diffraction and X-ray fluorescence portable systems. Appl Phys A Mater Sci Process 100:671–681

45.   Eveno M, Moignard B, Castaing J (2011) Portable apparatus for *in situ* X-ray diffraction and fluorescence analyses of artworks. Microsc Microanal 17:667–673

46.   Kriznar A, Munoz V, de la Paz F, Respaldiza MA, Vega M (2011) Portable XRF study of pigments applied in Juan Hispalense's 15th century panel painting. X-Ray Spectrom 40:96–100

47.   Migliori A, Bonanni P, Carraresi L, Grassi N, Mando PA (2011) A novel portable XRF spectrometer with range of detection extended to low-Z elements. X-Ray Spectrom 40:107–112

48.   Kenna TC, Nitsche FO, Herron MM, Mailloux BJ, Peteet D, Sritrairat S, Sands E, Baumgarten J (2011) Evaluation and calibration of a Field Portable X-ray Fluorescence spectrometer for quantitative analysis of siliciclastic soils and sediments. J Anal At Spectrom 26:395–405

49.   Tykot RH (2016) Using non-destructive portable X-ray fluorescence spectrometers on stone, ceramics, metals, and other materials in museums: advantages and limitations. Appl Spectrosc 70:42–56

50.   Galli A, Bonizzoni L (2014) True versus forged in the cultural heritage materials: the role of PXR Fanalysis. X-Ray Spectrom 43:22–28

51.   Beck L, Rousseliere H, Castaing J, Duran A, Lebon M, Moignard B, Plassard F (2014) First use of portable system coupling X-ray diffraction and X-ray fluorescence for *in situ* analysis of prehistoric rock art. Talanta 129:459–464

52.   Pitarch A, Ruiz JF, de Vallejuelo SFO, Hernanz A, Maguregui M, Madariaga JM (2014) *In situ* characterization by Raman and X-ray fluorescence spectroscopy of post-Paleolithic blackish pictographs exposed to the open air in Los Chaparros shelter (Albalate del Arzobispo, Teruel, Spain). Anal Methods 6:6641–6650

53.   Dayer L, d'Errico F, Garcia-Moreno R (2014) Searching for consistencies in Chatelperronian pigment use. J Archaeol Sci 44:180–193

54.   Bracci S, Caruso O, Galeotti M, Iannaccone R, Magrini D, Picchi D, Pinna D, Porcinai S (2015) Multidisciplinary approach for the study of an Egyptian coffin (late 22nd/early 25th dynasty): combining imaging and spectroscopic techniques. Spectrochim Acta Part A Mol Biomol Spectrosc 145:511–522

55.   Madariaga JM, Maguregui M, Castro K, Knuutinen U, Martinez-Arkarazo I (2016) Portable Raman, DRIFTS, and XRF analysis to diagnose the conservation state of two wall painting panels from pompeii deposited in the Naples National Archaeological Museum (Italy). Appl Spectrosc 70:137–146

56.   Madariaga JM (2015) Analytical chemistry in the field of cultural heritage. Anal Methods 7:4848–4876

57.   Crupi V, Galli G, La Russa MF, Longo F, Maisano G, Majolino D, Malagodi M, Pezzino A, RiccaM, Rossi B, Ruffolo SA, Venuti V (2015) Multi-technique investigation of Roman decorated plasters from Villa dei Quintili (Rome, Italy). Appl Surf Sci 349:924–930

58.   Gomez-Moron MA, Ortiz P, Martin-Ramirez JM, Ortiz R, Castaing J (2016) A new insight into the vaults of the kings in the Alhambra (Granada, Spain) by combination of portable XRD and XRF. Microchem J 125:260–265

59.   Syta O, Rozum K, Choinska M, Zielinska D, Zukowska GZ, Kijowska A, Wagner B (2014) Analytical procedure for characterization of medieval wall-paintings by X-ray fluorescence spectrometry, laser ablation inductively coupled plasma mass spectrometry and Raman spectroscopy. Spectrochim Acta Part B At Spectrosc 101:140–148

60.   Daveri A, Doherty B, Moretti P, Grazia C, Romani A, Fiorin E, Brunetti BG, Vagnini M (2015) An uncovered XIII century icon: particular use of organic pigments and gilding techniques highlighted by analytical methods. Spectrochim Acta Part A Mol Biomol Spectrosc 135:398–404

61.   Cechak T, Trojek T, Sefcu R, Chlumska S, Trestikova A, Kotrly M, Turkova I (2015) The use of powdered bismuth in Late Gothic painting and sculpture polychromy. J Cult Herit 16:747–752

62.   Hradil D, Hradilova J, Bezdicka P, Svarcova S, Cermakova Z, Kosarova V, Nemec I (2014) Crocoite $PbCrO_4$ and mimetite $Pb_5(AsO_4)_3Cl$: rare minerals in highly degraded mediaeval murals in Northern Bohemia. J Raman Spectrosc 45:848–858

63.   Van der Snickt G, Miliani C, Janssens K, Brunetti BG, Romani A, Rosi F, Walter P, Castaing J, De Nolf W, Klaassen L, Labarque I, Wittermann R (2011) Material analyses of '*Christ with singing and music-making Angels*', a late 15th-C panel painting attributed to Hans Memling and assistants: part I. non-invasive *in situ* investigations. J Anal At Spectrom 26:2216–2229

64.   Duran A, Lopez-Montes A, Castaing J, Espejo T (2014) Analysis of a royal 15th century illuminated parchment using a portable XRF-XRD system and micro-invasive techniques. J Archaeol Sci 45:52–58

65.   Van de Voorde L, Van Pevenage J, De Langhe K, De Wolf R, Vekemans B, Vincze L, Vandenabeele P, Martens MPJ (2014) Non-destructive *in situ* study of ''Mad Meg'' by Pieter Bruegel the Elder using mobile X-ray fluorescence, X-ray diffraction and Raman spectrometers. Spectrochim Acta Part B At Spectrosc 97:1–6

66.   Veiga A, Teixeira DM, Candeias AJ, Mirao J, Manhita A, Miguel C, Rodrigues P, Teixeira JG (2015) Micro-analytical study of two seventeenth century gilded miniature portraits on copper. Microchem J 123:51–61

67.   Roldan C, Juanes D, Ferrazza L, Carballo J (2016) Characterization of Sorolla's gouache pigments by means of spectroscopic techniques. Radiat Phys Chem 119:253–263

68.   Van der Snickt G, Janssens K, Schalm O, Aibeo C, Kloust H, Alfeld M (2010) James Ensor's pigment use: artistic and material evolution studied by means of portable X-ray fluorescence spectrometry. X-Ray Spectrom 39:103–111

69.   Kosarova V, Hradil D, Hradilova J, Cermakova Z, Nemec I, Schreiner M (2016) The efficiency of micro-Raman spectroscopy in the analysis of complicated mixtures in modern paints: Munch's and Kupka's paintings under study. Spectrochim Acta Part A Mol Biomol Spectrosc 156:36–46

70.   Kajiya EAM, Campos P, Rizzutto MA, Appoloni CR, Lopes F (2014) Evaluation of the veracity of one work by the artist Di Cavalcanti through non-destructive techniques: XRF, imaging and brush stroke analysis. Radiat Phys Chem 95:373–377

71.   Cardeira AM, Longelin S, Costa S, Candeias A, Carvalho ML, Manso M (2014) Multi-analytical characterisation of D'Apres Cormon by Jose Veloso Salgado. Nucl Instrum Methods Phys Res Sect B Beam Interact Mater At 331:271–274

72.   Izzo FC, Capogrosso V, Gironda M, Alberti R, Mazzei C, Nodari L, Gambirasi A, Zendri E, NevinA (2015) Multi-analytical non-invasive study of modern yellow paints from postwar Italian paintings from the International Gallery of Modern Art Ca Pesaro, Venice. X-Ray Spectrom 44:296–304

73.   Trojek T, Trojkova D (2015) Several approaches to the investigation of paintings with the use of portable X-ray fluorescence analysis. Radiat Phys Chem 116:321–325

74.   Cardeira AM, Longelin S, Costa S, Candeias A, Carvalho ML, Manso M (2016) Analytical characterization of academic nude paintings by Jose Veloso Salgado. Spectrochim Acta Part A Mol Biomol Spectrosc 153:379–385

75.   Epley BA, Rogge CE (2015) Prior states: evolution of composition and color in two Barnett Newman paintings. Appl Phys A Mater Sci Process 121:987–998

76.   Janssens K, Vekemans B, Vincze L, Adams F, Rindby A (1996) A micro-XRF spectrometer based on a rotating anode generator and capillary optics. Spectrochim Acta Part B At Spectrosc 51:1661–1678

77.   Vincze L, Janssens K, Adams F, Rindby A, Engstrom P (1998) Interpretation of capillary generated spatial and angular distributions of X-rays: theoretical modeling and experimental verification using the European Synchrotron Radiation Facility Optical beam line. Rev Sci Instrum 69:3494–3503

78.   Schroer CG, Boye P, Feldkamp JM, Patommel J, Samberg D, Schropp A, Schwab A, Stephan S, Falkenberg G, Wellenreuther G, Reimers N (2010) Hard X-ray nanoprobe at beamline P06 at PETRA III. Nucl Instrum Methods Phys Res Sect A Accel Spectrom Detect Assoc Equip 616:93–97

79.   Lengeler B, Schroer CG, Benner B, Gerhardus A, Gunzler TF, Kuhlmann M, Meyer J, Zimprich C (2002) Parabolic refractive X-ray lenses. J Synchrotron Radiat 9:119–124

80.   Gorelick S, Vila-Comamala J, Guzenko VA, Barrett R, Salome M, David C (2011) High-Efficiency Gold Fresnel Zone Plates for Multi-keV X-rays. In: McNulty I, Eyberger C, Lai B (eds) 10th International Conference on X-Ray Microscopy, pp 88–91

81.   Sarkar SS, Sahoo PK, Solak HH, David C, Van der Veen JF (2008) Fabrication of Fresnel zone plates by holography in the extreme ultraviolet region. J Vac Sci Technol B 26:2160–2163

82.   Alianelli L, Sawhney KJS, Barrett R, Pape I, Malik A, Wilson MC (2011) High efficiency nanofocusing kinoform optics for synchrotron radiation. Opt Express 19:11120–11127

83.   Barrett R, Baker R, Cloetens P, Dabin Y, Morawe C, Suhonen H, Tucoulou R, Vivo A, Zhang L (2011) Dynamically-figured mirror system for high-energy nanofocusing at the ESRF. In: Proceedings of SPIE, Advances in X-ray/EUV optics and components VI, vol 8139, p 813904. doi:10. 1117/12.894735

84.   Bichlmeier S, Janssens K, Heckel J, Gibson D, Hoffmann P, Ortner HM (2001) Component selection for a compact micro-XRF spectrometer. X-Ray Spectrom 30:8–14

85.   Trentelman K, Bouchard M, Ganio M, Namowicz C, Patterson CS, Walton M (2010) The examination of works of art using *in situ* XRF line and area scans. X-Ray Spectrom 39:159–166

86.   Buzanich G, Wobrauschek P, Streli C, Markowicz A, Wegrzynek D, Chinea-Cano E, Griesser M, Uhlir K (2010) PART II (Portable ART analyzer)—development of a XRF spectrometer adapted for the study of artworks in the Kunsthistorisches Museum, Vienna. X-Ray Spectrom 39:98–102

87.   Vittiglio G, Bichhneier S, Klinger P, Heckel J, Fuzhong W, Vincze L, Janssens K, Engstrom P, Rindby A, Dietrich K, Jembrih-Simburger D, Schreiner M, Denis D, Lakdar A, Lamotte A (2004) A compact mu-XRF spectrometer for (*in situ*) analyses of cultural heritage and forensic materials. Nucl Instrum Methods Phys Res Sect B Beam Interact Mater At 213:693–698

88.   Bronk H, Rohrs S, Bjeoumikhov A, Langhoff N, Schmalz J, Wedell R, Gorny HE, Herold A, Waldschlager U (2001) ArtTAX—a new mobile spectrometer for energy-dispersive micro X-ray fluorescence spectrometry on art and archaeological objects. Fresenius J Anal Chem 371:307–316

89.   Rabin I, Hahn O (2013) Characterization of the Dead Sea Scrolls by advanced analytical techniques. Anal Methods 5:4648–4654

90.   Wolff T, Rabin I, Mantouvalou I, Kanngiesser B, Malzer W, Kindzorra E, Hahn O (2012) Provenance studies on Dead Sea scrolls parchment by means of quantitative micro-XRF. Anal Bioanal Chem 402:1493–1503

91.   Valerio P, Silva RJC, Araujo MF, Soares AMM, Barros L (2012) A multianalytical approach to study the Phoenician bronze technology in the Iberian Peninsula - A view from Quinta do Almaraz. Mater Charact 67:74–82

92.   Figueiredo E, Araujo MF, Silva RJC, Senna-Martinez JC, Vaz JLI (2011) Characterisation of Late Bronze Age large size shield nails by EDXRF, micro-EDXRF and X-ray digital radiography. Appl Radiat Isot 69:1205–1211

93.   Herm C (2008) Mobile micro-X-ray fluorescence analysis (XRF) on medieval paintings. Chimia62:887–898

94.   Cheng L, Li MT, Youshi K, Fan CS, Wang SH, Pan QL, Liu ZG, Li RW (2011) The study of chemical composition and elemental mappings of colored over-glaze porcelain fired in Qing Dynasty by micro-X-ray fluorescence. Nucl Instrum Methods Phys Res Sect B Beam Interact Mater At 269:239–243

95. Dietz G, Ketelsen T, Hoss M, Simon O, Wintermann C, Wolff T, Rabin I, Hahn O (2012) The Egmont Master phenomenon: X-ray fluorescence spectrometric and paper studies for art history research. Anal Bioanal Chem 402:1505–1515

96. Sun TX, Ding XL (2015) Confocal X-ray technology based on capillary X-ray optics. Rev AnalChem 34:45–59

97. Janssens K, Proost K, Falkenberg G (2004) Confocal microscopic X-ray fluorescence at the HASYLAB microfocus beamline: characteristics and possibilities. Spectrochim Acta Part B At Spectrosc 59:1637–1645

98. Woll AR, Agyeman-Budu D, Choudhury S, Coulthard I, Finnefrock AC, Gordon R, Hallin E, Mass J (2014) Lithographically-fabricated channel arrays for confocal X-ray fluorescence microscopy and XAFS. In: Arp U, Reversz P, Williams GP (eds) 17th Pan-American Synchrotron Radiation Instrumentation Conference (SRI 2013)

99. Bjeoumikhov A, Erko M, Bjeoumikhova S, Erko A, Snigireva I, Snigirev A, Wolff T, Mantouvalou I, Malzer W, Kanngiesser B (2008) Capillary mu Focus X-ray lenses with parabolic and elliptic profile. Nucl Instrum Methods Phys Res Sect A Accel Spectrom Detect Assoc Equip 587:458–463

100. Luhl L, Mantouvalou I, Schaumann I, Vogt C, Kanngiesser B (2013) Three-dimensional chemical mapping with a confocal XRF setup. Anal Chem 85:3682–3689

101. Woll AR, Agyeman-Budu D, Bilderback DH, Dale D, Kazimirov AY, Pfeifer M, Plautz T, Szebenyi T, Untracht G (2012) 3D X-ray fluorescence microscopy with 1.7 μm resolution using lithographically fabricated micro-channel arrays. In: Goto S, Morawe C, Khounsary AM (eds.) Proceedings of SPIE, Advances in X-ray/EUV optics and components VII, vol 8502, p 85020K. doi:10.1117/12.944365

102. Beckhoff B, Fliegauf R, Ulm G, Weser J, Pepponi G, Streli C, Wobrauschek P, Ehmann T, Fabry L, Mantler C, Pahlke S, Kanngiesser B, Malzer W (2003) Ultra-trace analysis of light elements and speciation of minute organic contaminants on silicon wafer surfaces by means of TXRF in combination with NEXAFS. International Society for Optical Engineering, pp 120–128

103. Woll AR, Bilderback DH, Gruner S, Gao N, Huang R, Bisulca C, Mass J (2005) Confocal X-ray fluorescence (XRF) microscopy: a new technique for the non-destructive compositional depth profiling of paintings. In: Vandiver PB, Mass JL, Murray A (eds) Materials issues in art and archaeology VII

104. Woll AR, Mass J, Bisulca C, Huang R, Bilderback DH, Gruner S, Gao N (2006) Development of confocal X-ray fluorescence (XRF) microscopy at the Cornell high energy synchrotron source. Appl Phys A Mater Sci Process 83:235–238

105. Smit Z, Janssens K, Proost K, Langus I (2004) Confocal mu-XRF depth analysis of paint layers. Nucl Instrum Methods Phys Res Sect B Beam Interact Mater At 219:35–40

106. Tsuji K, Matsuno T, Takimoto Y, Yamanashi M, Kometani N, Sasaki YC, Hasegawa T, Kato S, Yamada T, Shoji T, Kawahara N (2015) New developments of X-ray fluorescence imaging techniques in laboratory. Spectrochim Acta Part B At Spectrosc 113:43–53

107. Polese C, Cappuccio G, Dabagov SB, Hampai D, Liedl A, Pace E (2015) 2D and 3D micro-XRF based on polycapillary optics at XLab Frascati. In: Goto S, Morawe C,

Khounsary AM (eds) Proceedings of SPIE, Advances in X-ray/EUV optics and components X, vol 9588, p 95880E. doi:10.1117/12.2189632

108. Smolek S, Nakazawa T, Tabe A, Nakano K, Tsuji K, Streli C, Wobrauschek P (2014) Comparison of two confocal micro-XRF spectrometers with different design aspects. X-Ray Spectrom 43:93–101

109. Nakazawa T, Tsuji K (2013) Development of a high-resolution confocal micro-XRF instrument equipped with a vacuum chamber. X-Ray Spectrom 42:374–379

110. Mantouvalou I, Lange K, Wolff T, Grotzsch D, Luhl L, Haschke M, Hahn O, Kanngiesser B (2010) A compact 3D micro X-ray fluorescence spectrometer with X-ray tube excitation for archaeometric applications. J Anal At Spectrom 25:554–561

111. Tsuji K, Tabe A, Wobrauscheck P, Streli C (2015) Secondary excitation process for quantitative confocal 3D-XRF analysis. Powder Diffr 30:109–112

112. Wrobel P, Wegrzynek D, Czyzycki M, Lankosz M (2014) Depth profiling of element concentrations in stratified materials by confocal microbeam X-ray fluorescence spectrometry with polychromatic excitation. Anal Chem 86:11275–11280

113. Mantouvalou I, Wolff T, Seim C, Stoytschew V, Malzer W, Kanngiesser B (2014) Reconstruction of confocal micro-X-ray fluorescence spectroscopy depth scans obtained with a laboratory setup. Anal Chem 86:9774–9780

114. Czyzycki M, Wrobel P, Lankosz M (2014) Confocal X-ray fluorescence micro-spectroscopy experiment in tilted geometry. Spectrochim Acta Part B At Spectrosc 97:99–104

115. Huber C, Smolek S, Streli C (2014) Simulation of layer measurement with confocal micro-XRF. X-Ray Spectrom 43:175–179

116. Wrobel P, Czyzycki M (2013) Direct deconvolution approach for depth profiling of element concentrations in multi-layered materials by confocal micro-beam X-ray fluorescence spectrometry. Talanta 113:62–67

117. Mantouvalou I, Malzer W, Kanngiesser B (2012) Quantification for 3D micro X-ray fluorescence. Spectrochim Acta Part B At Spectrosc 77:9–18

118. Schoonjans T, Silversmit G, Vekemans B, Schmitz S, Burghammer M, Riekel C, Brenker FE, Vincze L (2012) Fundamental parameter based quantification algorithm for confocal nano-X-ray fluorescence analysis. Spectrochim Acta Part B At Spectrosc 67:32–42

119. Laclavetine K, Ager FJ, Arquillo J, Respaldiza MA, Scrivano S (2016) Characterization of the new mobile confocal micro X-ray fluorescence (CXRF) system for *in situ* non-destructive cultural heritage analysis at the CNA: mu XRF-CONCHA. Microchem J 125:62–68

120. Reiche I, Muller K, Mysak E, Eveno M, Mottin B (2015) Toward a three-dimensional vision of the different compositions and the stratigraphy of the painting *L'Homme bless*, by G. Courbet: coupling SEM-EDX and confocal micro-XRF. Appl Phys A Mater Sci Process 121:903–913

121. Sun TX, Liu ZG, Wang GF, Ma YZ, Peng S, Sun WY, Li FZ, Sun XP, Ding XL (2014) Application of confocal X-ray fluorescence micro-spectroscopy to the investigation of paint layers. Appl Radiat Isot 94:109–112

122.   Woll AR, Mass J, Bisulca C, Cushi-Nan M, Griggs C, Wanzy T, Ocon N (2008) The Unique History of *The Armorer's Shop* an application of confocal X-ray fluorescence microscopy. Stud Conserv 53:93–109

123.   Kanngiesser B, Malzer W, Mantouvalou I, Sokaras D, Karydas AG (2012) A deep view in cultural heritage-confocal micro X-ray spectroscopy for depth resolved elemental analysis. Appl Phys A Mater Sci Process 106:325–338

124.   Reiche I, Mueller K, Eveno M, Itie E, Menu M (2012) Depth profiling reveals multiple paint layers of Louvre Renaissance paintings using non-invasive compact confocal micro-X-ray fluorescence. J Anal At Spectrom 27:1715–1724

125.   Yi LT, Liu ZG, Wang K, Lin X, Chen M, Peng SQ, Yang K, Wang JB (2016) Combining depth analysis with surface morphology analysis to analyse the prehistoric painted pottery from Majiayao Culture by confocal 3D-XRF. Appl Phys A Mater Sci Process 122

126.   Choudhury S, Hormes J, Agyeman-Budu DN, Woll AR, George GN, Coulthard I, Pickering IJ (2015) Application of a spoked channel array to confocal X-ray fluorescence imaging and X-ray absorption spectroscopy of medieval stained-glass. J Anal At Spectrom 30:759–766

127.   Kanngiesser B, Mantouvalou I, Malzer W, Wolff T, Hahn O (2008) Non-destructive, depth resolved investigation of corrosion layers of historical glass objects by 3D Micro X-ray fluorescence analysis. J Anal At Spectrom 23:814–819

128.   Yagi R, Tsuji K (2015) Confocal micro-XRF analysis of light elements with Rh X-ray tube and its application for painted steel sheet. X-Ray Spectrom 44:186–189

129.   Li FZ, Liu ZG, Sun TX, Yi LT, Zhao WG, He JL, Peng S, Wang LL, Zhao GC, Ding XL (2015) Application of three dimensional confocal micro X-ray fluorescence technology based on polycapillary X-ray lens in analysis of rock and mineral samples. Spectrosc Spectr Anal 35:2487–2491

130.   Janssens K, Vittiglio G, Deraedt I, Aerts A, Vekemans B, Vincze L, Wei F, Deryck I, Schalm O, Adams F, Rindby A, Knochel A, Simionovici A, Snigirev A (2000) Use of microscopic XRF for non-destructive analysis in art and archaeometry. X-Ray Spectrom 29:73–91

131.   Terzano R, Spagnuolo M, Vekemans B, De Nolf W, Janssens K, Falkenberg G, Flore S, Ruggiero P(2007) Assessing the origin and fate of Cr, Ni, Cu, Zn, Ph, and V in industrial polluted soil by combined microspectroscopic techniques and bulk extraction methods. Environ Sci Technol 41:6762–6769

132.   Janssens K, De Nolf W, Van Der Snickt G, Vincze L, Vekemans B, Terzano R, Brenker F (2010) Recent trends in quantitative aspects of microscopic X-ray fluorescence analysis. Trac Trends Anal Chem 29:464–478

133.   Fittschen UEA, Falkenberg G (2011) Trends in environmental science using microscopic X-rayfluorescence. Spectrochim Acta Part B At Spectrosc 66:567–580

134.   Salome M, Bleuet P, Bohic S, Cauzid J, Chalmin E, Cloetens P, Cotte M, De Andrade V, Martinez-Criado G, Petitgirard S, Rak M, Tresserras JAS, Szlachetko J, Tucoulou R, Susini J (2009) Fluorescence X-ray micro-spectroscopy activities at ESRF. In: David C, Nolting F, Quitmann C, Stampanoni M, Pfeiffer F (eds) 9th International Conference on X-ray Microscopy Zurich, Switserland, pp 012014

135. Hahn O, Oltrogge D, Bevers H (2004) Coloured prints of the 16th century: non-destructive analyses on coloured engravings from Albrecht Durer and contemporary artists. Archaeometry 46:273–282

136. Paternoster G, Rinzivillo R, Nunziata F, Castellucci EM, Lofrumento C, Zoppi A, Felici AC, Fronterotta G, Nicolais C, Piacentini M, Sciuti S, Vendittelli M (2005) Study on the technique of the Roman age mural paintings by micro-XRF with Polycapillary Conic Collimator and micro-Raman analyses. J Cult Herit 6:21–28

137. Bertrand L, Cotte M, Stampanoni M, Thoury M, Marone F, Schoeder S (2012) Development and trends in synchrotron studies of ancient and historical materials. Phys Rep Rev Sect Phys Lett 519:51–96

138. Gervais C, Thoury M, Reguer S, Gueriau P, Mass J (2015) Radiation damages during synchrotron X-ray micro-analyses of Prussian blue and zinc white historic paintings: detection, mitigation and integration. Appl Phys A Mater Sci Process 121:949–955

139. Bertrand L, Schoeeder S, Anglos D, Breese MBH, Janssens K, Moini M, Simon A (2015) Mitigation strategies for radiation damage in the analysis of ancient materials. Trac Trends Anal Chem 66:128–145

140. Nuyts G, Cagno S, Bugani S, Janssens K (2015) Micro-XANES study on Mn browning: use of quantitative valence state maps. J Anal At Spectrom 30:642–650

141. Rietveld HM (1969) A profile refinement method for nuclear and magnetic structures. J Appl Crystallogr 2:65–71

142. Dik J, Janssens K, Van der Snickt G, van der Loeff L, Rickers K, Cotte M (2008) Visualization of alost painting by Vincent van Gogh using synchrotron radiation based X-ray fluorescence elemental mapping. Anal Chem 80:6436–6442

143. Alfeld M, Janssens K (2015) Strategies for processing mega-pixel X-ray fluorescence hyperspectral data: a case study on a version of Caravaggio's painting *Supper at Emmaus*. J Anal At Spectrom 30:777–789

144. Dik J, Wallert A, Van der Snickt G, Janssens K (2008) Silverpoint underdrawing? A note on its visualization with synchrotron radiation based X-ray fluorescence analysis. Zeitschrift für Kunsttechnologie und Konservierung 22:381–384

145. Struick van der Loeff L, Alfeld M, Meedendorp T, Dik J, Hendriks E, Van der Snickt G, Janssens K, Chavennes M (2012) Rehabilitation of a flower still life in the Kröller-Müller Museum and a lost Antwerp painting by Van Gogh. In: van Tilborgh L (ed) Van Gogh: new findings. Van Gogh Museum, Amsterdam

146. Alfeld M, Janssens K, Appel K, Thijsse B, Blaas J, Dik J (2011) A portrait by Philipp Otto Runge—visualizing modifications to the painting using synchrotron-based X-ray fluorescence elemental scanning. Zeitschrift für Kunsttechnologie und Konservierung 25:157–163

147. Howard DL, de Jonge MD, Lau D, Hay D, Varcoe-Cocks M, Ryan CG, Kirkham R, Moorhead G, Paterson D, Thurrowgood D (2012) High-Definition X-ray fluorescence elemental mapping of paintings. Anal Chem 84:3278–3286

148. Alfeld M, Siddons DP, Janssens K, Dik J, Woll A, Kirkham R, van de Wetering E (2013) Visualizing the 17th century underpainting in *Portrait of an Old Man* by

Rembrandt van Rijn using synchrotron-based scanning macro-XRF. Appl Phys A Mater Sci Process 111:157–164

149. Alfeld M, Pedroso JV, Hommes MVE, Van der Snickt G, Tauber G, Blaas J, Haschke M, Erler K,Dik J, Janssens K (2013) A mobile instrument for *in situ* scanning macro-XRF investigation of historical paintings. J Anal At Spectrom 28:760–767

150. Alfeld M, De Nolf W, Cagno S, Appel K, Siddons DP, Kuczewski A, Janssens K, Dik J, Trentelman K, Walton M, Sartorius A (2013) Revealing hidden paint layers in oil paintings by means of scanning macro-XRF: a mock-up study based on Rembrandt's ''*An old man in military costume*''. J Anal At Spectrom 28:40–51

151. Trentelman K, Janssens K, van der Snickt G, Szafran Y, Woollett AT, Dik J (2015) Rembrandt's *An Old Man in Military Costume*: the underlying image re-examined. Appl Phys A Mater Sci Process 121:801–811

152. Janssens K, Van der Snickt G, Alfeld M, Noble P, van Loon A, Delaney J, Conover D, Zeibel J, DikJ (2016) Rembrandt's '*Saul and David*' (c. 1652): use of multiple types of smalt evidenced by means of non-destructive imaging. Microchem J 126:515–523

153. Noble P, van Loon A, Alfeld M, Janssens K, Dik J (2012) Rembrandt and/or Studio, *Saul and David*, c. 1655: visualising the curtain using cross-section analyses and X-ray fluorescence imaging. Technè 36:35–45

154. Verslype I (2012) The restoration of Woman in Blue Reading a Letter by Johannes Vermeer. Rijksmuseum Bull 60:2–19

155. Bull D, Krekeler A, Alfeld M, Dik J, Janssens K (2011) An intrusive portrait by Goya. Burlingt Mag153:668–673

156. Monico L, Janssens K, Hendriks E, Vanmeert F, Van der Snickt G, Cotte M, Falkenberg G, Brunetti BG, Miliani C (2015) Evidence for degradation of the chrome yellows in van gogh's *Sunflowers*: a study using non-invasive *in situ* methods and synchrotron-radiation-based X-ray techniques. Angew Chem Int Edit 54:13923–13927

157. Van der Snickt G, Martins A, Delaney J, Janssens K, Zeibel J, Duffy M, McGlinchey C, Van Driel B, Dik J (2016) Exploring a hidden painting below the surface of Rene Magritte's Le Portrait. Appl Spectrosc 70:57–67

158. Martins A, Albertson C, McGlinchey C, Dik J (2016) Piet Mondrian's Broadway Boogie Woogie: non-invasive analysis using macro X-ray fluorescence mapping (MA-XRF) and multivariate curve resolution-alternating least square (MCR-ALS). Herit Sci 4:22. doi:10.1186/s40494-016-0091-4

159. Martins A, Coddington J, Van der Snickt G, Van Driel B, McGlinchey C, Dahlberg D, Janssens K, Dik J (2016) Jackson Pollock's Number 1A, 1948: a non-invasive study using macro-X-ray fluorescence mapping (MA-XRF) and multivariate curve resolution— alternating least squares (MCRALS) analysis. Herit Sci 4:33. doi:10.1186/s40494-016-0105-2

160. Ravaud E, Pichon L, Laval E, Gonzalez V, Eveno M, Calligaro T (2016) Development of a versatile XRF scanner for the elemental imaging of paintworks. Appl Phys A Mater Sci Process 122

161. Anaf W, Schalm O, Janssens K, De Wael K (2015) Understanding the (in)stability of semiconductor pigments by a thermodynamic approach. Dyes Pigm 113:409–415

162.   Da Pieve F, Stankowski M, Hogan C (2014) Electronic structure calculations of mercury mobilization from mineral phases and photocatalytic removal from water and the atmosphere. Sci Total Environ 493:596–605

163.   Vanmeert F, Van der Snickt G, Janssens K (2015) Plumbonacrite identified by X-ray powder diffraction tomography as a missing link during degradation of red lead in a Van Gogh painting. Angew Chem Int Edit 54:3607–3610

164.   Anaf W, Trashin S, Schalm O, van Dorp D, Janssens K, De Wael K (2014) Electrochemical photodegradation study of semiconductor pigments: influence of environmental parameters. Anal Chem 86:9742–9748

165.   Hogan C, Da Pieve F (2015) Colour degradation of artworks: an ab initio approach to X-ray, electronic and optical spectroscopy analyses of vermilion photodarkening. J Anal At Spectrom 30:588–598

166.   Emslie SD, Brasso R, Patterson WP, Valera AC, McKenzie A, Silva AM, Gleason JD, Blum JD (2015) Chronic mercury exposure in Late Neolithic/Chalcolithic populations in Portugal from the cultural use of cinnabar. Sci Rep 5

167.   Radepont M, de Nolf W, Janssens K, Van der Snickt G, Coquinot Y, Klaassen L, Cotte M (2011) The use of microscopic X-ray diffraction for the study of HgS and its degradation products corderoite (α-Hg$_3$S$_2$Cl$_2$), kenhsuite (γ-Hg$_3$S$_2$Cl$_2$) and calomel (Hg$_2$Cl$_2$) in historical paintings. J Anal At Spectrom 26:959–968

168.   Cotte M, Susini J, Metrich N, Moscato A, Gratziu C, Bertagnini A, Pagano M (2006) Blackening of Pompeian cinnabar paintings: X-ray microspectroscopy analysis. Anal Chem 78:7484–7492

169.   Cotte M, Susini J, Solé VA, Taniguchi Y, Chillida J, Checroun E, Walter P (2008) Applications of synchrotron-based micro-imaging techniques to the chemical analysis of ancient paintings. J Anal At Spectrom 23:820–828

170.   Radepont M, Coquinot Y, Janssens K, Ezrati J-J, de Nolf W, Cotte M (2015) Thermodynamic and experimental study of the degradation of the red pigment mercury sulfide. J Anal At Spectrom 30:599–612

171.   Keune K, Boon JJ (2005) Analytical imaging studies clarifying the process of the darkening of vermilion in paintings. Anal Chem 77:4742–4750

172.   Da Pieve F, Hogan C, Lamoen D, Verbeeck J, Vanmeert F, Radepont M, Cotte M, Janssens K, Gonze X, Van Tendeloo G (2013) Casting light on the darkening of colors in historical paintings. Phys Rev Lett 111

173.   Anaf W, Janssens K, De Wael K (2013) Formation of Metallic Mercury During Photodegradation/Photodarkening of alpha-HgS: electrochemical Evidence. Angew Chem Int Ed 52:12568–12571

174.   Neiman MK, Balonis M, Kakoulli I (2015) Cinnabar alteration in archaeological wall paintings: an experimental and theoretical approach. Appl Phys A Mater Sci Process 121:915–938

175.   Uda M (2004) *In situ* characterization of ancient plaster and pigments on tomb walls in Egypt using energy dispersive X-ray diffraction and fluorescence. Nucl Instrum Methods Phys Res Sect B Beam Interact Mater At 226:75–82

176.   Daniels V, Leach B (2004) The occurrence and alteration of realgar on ancient Egyptian papyri. Stud Conserv 49:73–84

177.   Muralha VSF, Burgio L, Clark RJH (2012) Raman spectroscopy analysis of pigments on 16-17th c. Persian manuscripts. Spectrochim Acta Part A Mol Biomol Spectrosc 92:21–28

178.   Deneckere A, De Reu M, Martens MPJ, De Coene K, Vekemans B, Vincze L, De Maeyer P, Vandenabeele P, Moens L (2011) The use of a multi-method approach to identify the pigments in the 12th century manuscript Liber Floridus. Spectrochim Acta Part A Mol Biomol Spectrosc 80:125–132

179.   Brown KL, Clark RJH (2004) The Lindisfarne Gospels and two other 8th century Anglo-Saxon/Insular manuscripts: pigment identification by Raman microscopy. J Raman Spectrosc 35:4–12

180.   Keune K, Mass J, Meirer F, Pottasch C, van Loon A, Hull A, Church J, Pouyet E, Cotte M, Mehta A (2015) Tracking the transformation and transport of arsenic sulfide pigments in paints: synchrotron-based X-ray micro-analyses. J Anal At Spectrom 30:813–827

181.   Vermeulen M, Sanyova J, Janssens K (2015) Identification of artificial orpiment in the interior decorations of the Japanese tower in Laeken, Brussels, Belgium. Herit Sci 3:9

182.   Trentelman K, Stodulski L, Pavlosky M (1996) Characterization of pararealgar and other light-induced transformation products from realgar by Raman microspectroscopy. Anal Chem 68:1755–1761

183.   Muniz Miranda M, Sbrana G, Bonazzi P, Menchetti S, Pratesi G (1996) Spectroscopic investigation and normal mode analysis of As_4S_4 polymorphs. Spectrochim Acta Part A Mol Biomol Spectrosc 52:1391–1401

184.   Bindi L, Bonazzi P (2007) Light-induced alteration of arsenic sulfides: a new product with an orthorhombic crystal structure. Am Miner 92:617–620

185.   Kyono A, Kimata M, Hatta T (2005) Light-induced degradation dynamics in realgar: *in situ* structural investigation using single-crystal X-ray diffraction study and X-ray photoelectron spectroscopy. Am Miner 90:1563–1570

186.   Macchia A, Cesaro SN, Campanella L, Maras A, Rocchia M, Roscioli G (2013) Which light for cultural heritage: comparison of light sources with respect to realgar photodegradation. J Appl Spectrosc 80:637–643

187.   Vermeulen M, Nuyts G, Sanyova J, Vila A, Buti D, Suuronen JP, Janssens K (2016) Visualization of As(III) and As(V) distributions in degraded paint micro-samples from Baroque- and Rococo-era paintings. J Anal At Spectrom 31:1913–1921

188.   Boon JJ, Keune K, van der Weerd J, Geldof M, de Boer J (2001) Imaging microspectroscopic, secondary ion mass spectrometric and electron microscopic studies on discoloured and partially discoloured smalt in cross-sections of 16th century paintings. Chimia 55:952–960

189.   Panighello S, Kavcic A, Vogel-Mikus K, Tennent NH, Wallert A, Hocevar SB, van Elteren JT (2016) Investigation of smalt in cross-sections of 17th century paintings using elemental mapping by laser ablation ICP-MS. Microchem J 125:105–115

190. Spring M, Higgitt C, Saunders D (2005) Investigation of Pigment-Medium Interaction Processes in Oil Paint containing Degraded Smalt. Natl Gallery Tech Bull 26:56–70

191. Robinet L, Spring M, Pages-Camagna S, Vantelon D, Trcera N (2011) Investigation of the discoloration of smalt pigment in historic paintings by micro-X-ray absorption spectroscopy at the Co K-Edge. Anal Chem 83:5145–5152

192. Robinet L, Spring M, Pages-Camagna S (2013) Vibrational spectroscopy correlated with element alanalysis for the investigation of smalt pigment and its alteration in paintings. Anal Methods 5:4628–4638

193. Cianchetta I, Colantoni I, Talarico F, d'Acapito F, Trapananti A, Maurizio C, Fantacci S, Davoli I (2012) Discoloration of the smalt pigment: experimental studies and ab initio calculations. J Anal At Spectrom 27:1941–1948

194. Miliani C, Daveri A, Brunetti BG, Sgamellotti A (2008) CO_2 entrapment in natural ultramarine blue. Chem Phys Lett 466:141–148

195. Gambardella AA, Patterson CMS, Webb SM, Walton MS (2016) Sulfur K-edge XANES of lazurite: toward determining the provenance of lapis lazuli. Microchem J 125:299–307

196. Salvado N, Buti S, Aranda MAG, Pradell T (2014) New insights on blue pigments used in 15th century paintings by synchrotron radiation-based micro-FTIR and XRD. Anal Methods 6:3610–3621

197. Pintus V, Wei SY, Schreiner M (2016) Accelerated UV ageing studies of acrylic, alkyd, and polyvinyl acetate paints: influence of inorganic pigments. Microchem J 124:949–961

198. Del Federico E, Shofberger W, Schelvis J, Kapetanaki S, Tyne L, Jerschow A (2006) Insight into framework destruction in ultramarine pigments. Inorg Chem 45:1270–1276

199. Cato E, Borca C, Huthwelker T, Ferreira ESB (2016) Aluminium X-ray absorption near-edge spectroscopy analysis of discoloured ultramarine blue in 20th century oil paintings. Microchem J 126:18–24

200. Monico L, Van der Snickt G, Janssens K, De Nolf W, Miliani C, Verbeeck J, Tian H, Tan H, Dik J, Radepont M, Cotte M (2011) Degradation process of lead chromate in paintings by Vincent van Gogh studied by means of synchrotron X-ray spectromicroscopy and related methods. 1. Artificially aged model samples. Anal Chem 83:1214–1223

201. Monico L, Van der Snickt G, Janssens K, De Nolf W, Miliani C, Dik J, Radepont M, Hendriks E, Geldof M, Cotte M (2011) Degradation process of lead chromate in paintings by Vincent van Gogh studied by means of synchrotron X-ray spectromicroscopy and related methods. 2. Original paint layer samples. Anal Chem 83:1224–1231

202. Monico L, Janssens K, Miliani C, Brunetti BG, Vagnini M, Vanmeert F, Falkenberg G, Abakumov A, Lu Y, Tian H, Verbeeck J, Radepont M, Cotte M, Hendriks E, Geldof M, van der Loeff L, Salvant J, Menu M (2013) Degradation process of lead chromate in paintings by Vincent van Gogh studied by means of spectromicroscopic methods. 3.

Synthesis, characterization, and detection of different crystal forms of the chrome yellow pigment. Anal Chem 85:851–859

203.   Monico L, Janssens K, Miliani C, Van der Snickt G, Brunetti BG, Guidi MC, Radepont M, Cotte M (2013) Degradation process of lead chromate in paintings by Vincent van Gogh studied by means of spectromicroscopic methods. 4. Artificial aging of model samples of co-precipitates of lead chromate and lead sulfate. Anal Chem 85:860–867

204.   Monico L, Janssens K, Vanmeert F, Cotte M, Brunetti BG, Van der Snickt G, Leeuwestein M, Plisson JS, Menu M, Miliani C (2014) Degradation process of lead chromate in paintings by Vincent van Gogh studied by means of spectromicroscopic methods. Part 5. Effects of non-original surface coatings into the nature and distribution of chromium and sulfur species in chrome yellow paints. Anal Chem 86:10804–10811

205.   Monico L, Janssens K, Cotte M, Romani A, Sorace L, Grazia C, Brunetti BG, Miliani C (2015) Synchrotron-based X-ray spectromicroscopy and electron paramagnetic resonance spectroscopy to investigate the redox properties of lead chromate pigments under the effect of visible light. J Anal At Spectrom 30:1500–1510

206.   Monico L, Janssens K, Cotte M, Sorace L, Vanmeert F, Brunetti BG, Miliani C (2016) Chromium speciation methods and infrared spectroscopy for studying the chemical reactivity of lead chromate-based pigments in oil medium. Microchem J 124:272–282

207.   Tan H, Tian H, Verbeeck J, Monico L, Janssens K, Van Tendeloo G (2013) Nanoscale investigation of the degradation mechanism of a historical chrome yellow paint by quantitative EELS mapping of Cr species. Angew Chem Int Ed 52:11360–11363

208.   Monico L, Janssens K, Hendriks E, Brunetti BG, Miliani C (2014) Raman study of different crystalline forms of $PbCrO_4$ and $PbCr_{1-x}S_xO_4$ solid solutions for the non-invasive identification of chrome yellows in paintings: a focus on works by Vincent van Gogh. J Raman Spectrosc 45:1034–1045

209.   Monico L, Janssens K, Alfeld M, Cotte M, Vanmeert F, Ryan CG, Falkenberg G, Howard DL, Brunetti BG, Miliani C (2015) Full spectral XANES imaging using the Maia detector array as a new tool for the study of the alteration process of chrome yellow pigments in paintings by Vincent van Gogh. J Anal At Spectrom 30:613–626

210.   Otero V, Pinto JV, Carlyle L, Vilarigues M, Cotte M, Melo MJ (2016) Nineteenth century chrome yellow and chrome deep from Windsor & Newton. Stud Conserv 61:1–27

211.   Amat A, Miliani C, Fantacci S (2016) Structural and electronic properties of the $PbCrO_4$ chrome yellow pigment and of its light sensitive sulfate-substituted compounds. RSC Adv 6:36336–36344 212.

212.   Munoz-Garcia AB, Massaro A, Pavone M (2016) Ab Initio Study of $PbCr_{(1-x)}S_xO_4$ Solid Solution: an Inside Look at Van Gogh Yellow Degradation. Chem Sci 7:4197–4203

213.   Casadio F, Xie S, Rukes SC, Myers B, Gray KA, Warta R, Fiedler I (2011) Electron energy loss spectroscopy elucidates the elusive darkening of zinc potassium chromate in Georges Seurat's *A Sunday on La Grande Jatte* - 1884. Anal Bioanal Chem 399:2909–2920

214.   Zanella L, Casadio F, Gray KA, Warta R, Ma Q, Gaillard J-F (2011) The darkening of zinc yellow: XANES speciation of chromium in artist's paints after light and chemical exposures. J Anal At Spectrom 26:1090–1097

215.   Rosi F, Grazia C, Gabrieli F, Romani A, Paolantoni M, Vivani R, Brunetti BG, Colomban P, Miliani C (2016) UV–Vis-NIR and micro Raman spectroscopies for the non-destructive identification of $Cd_{1-x}Zn_xS$ solid solutions in cadmium yellow pigments. Microchem J 124:856–867

216.   Grazia C, Rosi F, Gabrieli F, Romani A, Paolantoni M, Vivani R, Brunetti BG, Colomban P, Miliani C (2016) UV–Vis-NIR and microRaman spectroscopies for investigating the composition of ternary $CdS_{1-x}Se_x$ solid solutions employed as artists' pigments. Microchem J 125:279–289

217.   Van der Snickt G, Dik J, Cotte M, Janssens K, Jaroszewicz J, De Nolf W, Groenewegen J, Van der Loeff L (2009) Characterization of a degraded cadmium yellow (CdS) pigment in an oil painting by means of synchrotron radiation based X-ray techniques. Anal Chem 81:2600–2610

218.   Van der Snickt G, Janssens K, Dik J, De Nolf W, Vanmeert F, Jaroszewicz J, Cotte M, Falkenberg G, Van der Loeff L (2012) Combined use of synchrotron radiation based micro-X-ray fluorescence, Micro-X-ray Diffraction, Micro-X-ray absorption near-edge, and micro-fourier transform infrared spectroscopies for revealing an alternative degradation pathway of the pigment cadmium yellow in a painting by Van Gogh. Anal Chem 84:10221–10228

219.   Mass J, Sedlmair J, Patterson CS, Carson D, Buckley B, Hirschmugl C (2013) SR-FTIR imaging of the altered cadmium sulfide yellow paints in Henri Matisse's *Le Bonheur de vivre* (1905–6)— examination of visually distinct degradation regions. Analyst 138:6032–6043

220.   Mass JL, Opila R, Buckley B, Cotte M, Church J, Mehta A (2013) The photodegradation of cadmium yellow paints in Henri Matisse's *Le Bonheur de vivre* (1905–1906). Appl Phys A Mater Sci Process 111:59–68

221.   Uffelman ES, Hobbs PA, Barisas DAG, Mass JL (2013) pXRF analyses of Louise Herreshoff's paintings in relation to CdS and other pigment degradation issues. Appl Phys A Mater Sci Process 111:9–14

222.   Pouyet E, Cotte M, Fayard B, Salome M, Meirer F, Mehta A, Uffelman ES, Hull A, Vanmeert F, Kieffer J, Burghammer M, Janssens K, Sette F, Mass J (2015) 2D X-ray and FTIR micro-analysis of the degradation of cadmium yellow pigment in paintings of Henri Matisse. Appl Phys A Mater Sci Process 121:967–980

223.   Voras ZE, deGhetaldi K, Wiggins MB, Buckley B, Baade B, Mass JL, Beebe TP Jr (2015) ToF-SIMS imaging of molecular-level alteration mechanisms in *Le Bonheur de vivre* by Henri Matisse. Appl Phys A Mater Sci Process 121:1015–1030

224.   Ayalew E, Janssens K, De Wael K (2016) Unraveling the reactivity of minium toward bicarbonate and the role of lead oxides therein. Anal Chem 88:1564–1569

225.   Vila A, Monrad K, Wadum J, Filtenborg T (2014) As time passed by came sunset. Christen Købke's '*View of Lake Sortedam*', its genesis and colour changes. In:

Sgamellotti A, Brunetti BG, Miliani C (eds) Science and art. The painted surface. Royal Society of Chemistry, London, pp 354–372

226. Samain L, Silversmit G, Sanyova J, Vekemans B, Salomon H, Gilbert B, Grandjean F, Long GJ, Hermann RP, Vincze L, Strivay D (2011) Fading of modern Prussian blue pigments in linseed oil medium. J Anal At Spectrom 26:930–941

227. Samain L, Gilbert B, Grandjean F, Long GJ, Strivay D (2013) Redox reactions in Prussian blue containing paint layers as a result of light exposure. J Anal At Spectrom 28:524–535

228. Samain L, Grandjean F, Long GJ, Martinetto P, Bordet P, Strivay D (2013) Relationship between the synthesis of prussian blue pigments, their color, physical properties, and their behavior in paint layers. J Phys Chem C 117:9693–9712

229. Samain L, Grandjean F, Long GJ, Martinetto P, Bordet P, Sanyova J, Strivay D (2013) Synthesis and fading of eighteenth-century Prussian blue pigments: a combined study by spectroscopic and diffractive techniques using laboratory and synchrotron radiation sources. J Synchrotron Radiat 20:460–473

230. Gervais C, Languille M-A, Reguer S, Gillet M, Pelletier S, Garnier C, Vicenzi EP, Bertrand L (2013) Why does Prussian blue fade? Understanding the role(s) of the substrate. J Anal At Spectrom 28:1600–1609

231. Cotter MJ, Meyers P, Vanzelst L, Sayre EV (1973) Authentication of paintings by Blakelock, RA through neutron-activation autoradiography. J Radioanal Chem 15:265–285

232. Alfeld M, Laurenze-Landsberg C, Denker A, Janssens K, Noble P (2015) Neutron activation autoradiography and scanning macro-XRF of Rembrandt van Rijn's *Susanna and the Elders* (Gemaldegalerie Berlin): a comparison of two methods for imaging of historical paintings with elemental contrast. Appl Phys A Mater Sci Process 119:795–805

233. Seim C, Laurenze-Landsberg C, Schroeder-Smeibidl B, Mantouvalou I, de Boer C, Kanngiesser B (2014) Old traces, read anew—*'The Reading Hermit'* painting in the light of X-ray fluorescence. J Anal At Spectrom 29:1354–1360

234. Van der Snickt G, Legrand S, Caen J, Vanmeert F, Alfeld M, Janssens K (2016) Chemical imaging of stained-glass windows by means of macro X-ray fluorescence (MA-XRF) scanning. Microchem J 124:615–622

235. Ricciardi P, Legrand S, Bertolotti G, Janssens K (2016) Macro X-ray fluorescence (MA-XRF) scanning of illuminated manuscript fragments: potentialities and challenges. Microchem J 124:785–791

236. Targowski P, Pronobis-Gajdzis M, Surmak A, Iwanicka M, Kaszewska EA, Sylwestrzak M (2015) The application of macro-X-ray fluorescence and optical coherence tomography for examination of parchment manuscripts. Stud Conserv 60:S167–S177

237. Jackall Y, Delaney JK, Swicklik M (2015) *'Portrait of a woman with a book'*: a 'newly discovered antasy figure' by Fragonard at the National Gallery of Art, Washington. Burlingt Mag 157:248–254

238.   Bacci M, Picollo M (1996) Non-destructive spectroscopic detection of cobalt(II) in paintings and glass. Stud Conserv 41:136–144

239.   Bacci M, Picollo M, Trumpy G, Tsukada M, Kunzelman D (2007) Non-invasive identification ofwhite pigments on 20th-century oil paintings by using fiber optic reflectance spectroscopy. J Am Inst Conserv 46:27–37

240.   Delaney JK, Zeibel JG, Thoury M, Littleton R, Palmer M, Morales KM, de la Rie ER, Hoenigswald A (2010) Visible and infrared imaging spectroscopy of picasso's *Harlequin musician*: mapping and identification of artist materials *in situ*. Appl Spectrosc 64:584–594

241.   Gautier G, Bezur A, Muir K, Casadio F, Fiedler I (2009) Chemical fingerprinting of ready-mixed house paints of relevance to artistic production in the first half of the twentieth century. Part I: Inorganic and organic pigments. Appl Spectrosc 63:597–603

242.   Green AA, Berman M, Switzer P, Craig MD (1988) A transformation for ordering multispectral data in terms of image quality with implications for noise removal. IEEE Trans Geosci Remote Sens 26:65–74

243.   Nielsen AA (2011) Kernel maximum autocorrelation factor and minimum noise fraction transformations. IEEE Trans Image Process 20:612–624

244.   Thurrowgood D, Paterson D, de Jonge MD, Kirkham R, Thurrowgood Howard D (2016) A hidden portrait by Edgar Degas. Scientific Reports 6:29594. doi:10.1038/srep29594

1.2 Examination of historical paintings by state-of-the-art hyperspectral imaging methods: from scanning infra-red spectroscopy to computed X-ray laminography

Abstract The development of advanced methods for non-destructive selective imaging of painted works of art at the macroscopic level based on radiation in the X-ray and infrared range of the electromagnetic spectrum are concisely reviewed. Such methods allow to either record depth-selective, element-selective or species-selective images of entire paintings. Camera-based 'full field' methods (that record the image data in parallel) can be discerned next to scanning methods (that build up distributions in a sequential manner by scanning a beam of radiation over the surface of an artefact). Six methods are discussed: on the one hand, macroscopic X-ray fluorescence and X-ray diffraction imaging and X-ray laminography and on the other hand macroscopic Mid and Near Infrared hyper- and full spectral imaging and Optical Coherence Tomography. These methods can be considered to be improved versions of the well-established imaging methods employed worldwide for examination of paintings, i.e., X-ray radiography and Infrared reflectography. Possibilities and limitations of these new imaging techniques are outlined.

1.2.1 Introduction

Historical paintings are considered to be among the most precious cultural heritage artefacts and have been the subject of intensive studies for decades. Scientific studies on such artefacts are highly relevant, in order to optimize the preservation of the paintings for coming generations and/or to gain more profound insights in their creation process [1-3]. This review focusses on the examination of easel paintings, i.e., painted renditions realized on a moveable substrate. Easel painting consists typically of a support, ground, paint and varnish layers, applied on top of one another. Canvasses and wooden panels are the most popular supports, but also other materials such as thin copper plates, paper, stone and glass have been used. Often the pictorial layers are very thinly painted out, making some of them semi-transparent.

Micrometers below a painting's surface, a wealth of information may be present about the creative process followed by the artist while making the work of art. Many painterly effects can critically depend on the layer build-up: e.g., the translucent shine of colorful tissues, the suggestion of shadow in flesh tones or the convincing illusion of an object's texture may be realized by deliberately including the optical contribution of lower layers. Additionally, knowledge about the stratigraphy of a painting often is highly relevant in

conservation when stability problems such as paint discoloration or delamination are studied. Thus, the study of a painting, its composition and stratigraphy is a common research theme shared by curators, conservators and conservation scientists. However, this information, comprised of structural and compositional aspects, is usually not easy to obtain in a non-invasive manner. Next to the visible surface layers, subsurface layers may include underdrawings, underpaintings, and adjustments made in the course of painting.

Together, all these layers determine the current appearance of the work of art. In a growing number of cases conservators have discovered abandoned compositions underneath paintings, illustrating the artist's practice of reusing a canvas or panel. Imaging methods that can "read" this hidden information without any damage to the artwork are therefore valuable for art-historical research [2] while also being very useful during restoration activities.

The standard methods for studying the inner structure of painted works of art are X-ray radiography (XRR) and infrared reflectography (IRR), penetrative illumination techniques that are optionally complemented with the microscopic analysis of cross-sectioned samples. Both methods are full field imaging methods, employing image plates or cameras that are sensitive in the appropriate range of the electromagnetic spectrum for recording the image data (see Figure 1A). Since these methods all have their limitations, recently, a number of new approaches based on X-ray and Infra-red radiation for imaging the buildup of hidden paint layer systems have been put into practice; some of these methods make use of scanning pencil beams over the painting while recording data either in transmission or reflection mode (see Figure 1B, C). Two major motivations can be discerned for the development of these more advanced versions: (a) the desire to know more about the creative process and/or the artist's way of working that have led to a given work of art and (b) the need to assess and predict the current and future condition of a work of art. Motivation (a) is essentially of art-historical nature and seeks to reconstruct (better) *the past/history* of an artwork while motivation (b) is more strongly linked to preventive conservation and to conservation technology, and therefore mostly concerned with *the future* of the artwork [1]. Of course, for conservation, an understanding of the history of a work of art and the artist's intent is fundamental, since it provides the basis for assessing the current condition of the art work and for deciding which interventions are (not) appropriate [4]. In what follows, we mainly review recent activities that involve the use of strongly penetrative radiation (from either the X-ray or IR range of the EM spectrum); the interested reader is referred to reviews [1-4] for a broader treatment of the topic, including related spectroscopic investigations. Also Liang's 2012 review of multispectral and hyperspectral imaging using mainly visual radiation is a useful complementary resource in this respect [5].
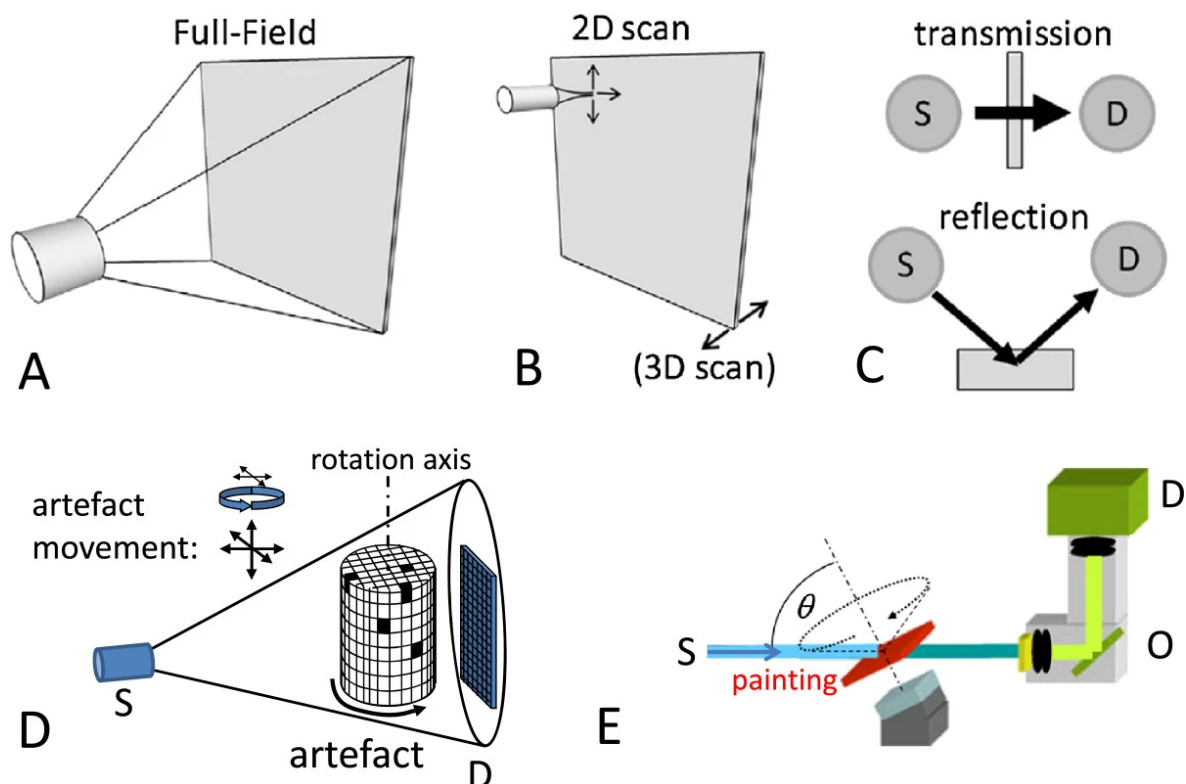
*Figure 1: Schematic representation of (**A**) full field imaging and (**B**) scanning pencil-beam imaging methods: these can operate in either (**C**) transmission or reflection geometry; of (**D**) conventional computed X-ray tomography (employing cone beam illumination) and (**E**) computed X-ray laminography (employing parallel beam irradiation). Adapted from [4] and [2]*

1.2.2 **X-ray based methods**

The variants of XRR that will be discussed below in more detail are called *Macroscopic X-ray fluorescence* (MA-XRF), the related method of *Macroscopic X-ray diffraction* (MA-XRD) and *Computed X-ray laminography* (CXL). All are non-destructive techniques, eliminating the need to remove material from the artefacts for their examination. The first two allow for element- or (crystal) phaseselective imaging at the length scale of the paintings themselves while the third method is suitable for depth selective micro imaging.

1.2.2.1 *Macroscopic X-ray fluorescence analysis (MA-XRF)*

XRF is a well-established method of quantitative element analysis that is based on the ionization of the atoms of the material being irradiated by an energetic beam of primary X-rays [6,7]. Characteristic radiation emitted by the ionized atoms contains information on the nature and the abundance of the elemental constituents present. The technique is particularly efficient for studying high-Z elements in low-Z matrices. Since XRF meets a number of the requirements of the 'ideal method' for non-destructive analysis of cultural heritage materials [8], analysis of objects of artistic and/or archaeological value with conventional XRF is fairly common. Several textbooks cover the fundamental and methodological aspects of the method and its many variants [9]. XRF on cultural heritage

and archaeological materials and artefacts is mainly used in reflection geometry. MA-XRF has recently been implemented to determine the distribution of pigments on easel paintings over large areas. Note that this method is not depth-selective so that *projected* pigment distributions (present at and/or below the visible paint surface) are obtained. In 2008, Dik et al. used a 38.5 keV X-ray beam of 0.5 mm in diameter to record XRF spectra from a 17.5×17.5 cm^2 area of the painting *Patch of Grass* by Vincent van Gogh; this was done to visualize the portrait below the visible landscape [10]. While most of the elemental maps recorded from *Patch of Grass* reflect the individual paint strokes that constitute the multicolored meadow, reconstruction of the flesh tones of the hidden head of a woman was possible by combining the Sb (*yellow-orange, Naples Yellow*) and Hg (*red, vermillion*) distributions. Following this initial and promising result, the MA-XRF setup at the synchrotron facility was employed to examine paintings by Rembrandt van Rijn [11], Philipp Otto Runge [12] and several other paintings by Van Gogh [13,14]. A self-portrait by Australian artist Sir Arthur Streeton (1867–1943) that he covered at a later stage with heavy brushstrokes of lead white paint has been re-visualized by Howard et al. [15] at the Australian Synchrotron radiation facility, making use of a multiple element detector system offering very fast scanning possibilities. One of the developments permitting the use of the MA-XRF method on a larger scale has been the construction of mobile (i.e., X-ray tube based) MA-XRF scanners [14,16-18] that can be used inside the museum or picture gallery where the works of art normally are displayed or conserved. Alfeld et al. [18] has designed and optimized such a device, reporting element sensitivities that are of same order of magnitude as those of the SR-based setup employed to scan *Patch of Grass*. Since the SR setup employed monochromatic 38.5 keV radiation while the mobile device employs the complete *bremsstrahlung* spectrum of Mo- or Rh-anode tubes bombarded with 45–50 keV electrons, the SR setup shows higher Kα-sensitivities for heavy elements (such as Ag, Cd, Sn, Sb) while the reverse is true for elements with atomic number below 40 (Zr). The availability of the mobile MA-XRF scanner permitted the investigation of a number of paintings 'in their native environment' that normally would have been nearly impossible to transport to synchrotron facilities, either because they were too large, too fragile, too valuable or all of these. A MA-XRF scanner is commercially available from Bruker Nano GmbH (Berlin, Germany) under the name 'M6 Jetstream' [19]. Using this device, several paintings by 15th, 17th, 19th and 20th C. artists such as Memling, Rembrandt, Hals, Van Gogh, Magritte, Mondriaan and Pollock could be examined successfully in various museums in The Netherlands, Belgium and the USA.

*Figure 2: **The Moreel Triptych, 1485, H. Memling (Groeninge Museum, Bruges, Belgium). (A)** Photograph; **(B)** the M6 MA-XRF scanning in front of the right panel; **(C-E)** MA-XRF images of part of the left panel, showing Mrs. Moreel and her daughters (ca 60x40 cm²); **(F)** close-up of the right panel, showing W. Moreel and his sons (ca 40x40 cm²); **(G-H)** corresponding MA-XRF images; **(I)** scheme clarifying the shift of the position of the eldest son; step size: 1 mm in both directions; dwell time: 0.5 s/pixel.*

As an example, Figure 2 shows results obtained by scanning the left and right panels of the Moreel triptych, a 15th C altarpiece painted by Hans Memling. It was painted for the highly respected Moreel family of Bruges, whose members had lived in the city since the 13th century. William Moreel, Seigneur of Oost Cleyhem, was one of the wealthiest and most politically active men in Bruges. He served as burgomaster of the city in 1478 and as treasurer in 1489. William Moreel and his second wife Barbara had eighteen children.

Long before their death around 1500, they ordered the altarpiece shown in Figure 2A for their funerary chapel in the Church of St. Jacques in Bruges, founded in 1484. The lower frame of the wings and the center panel bear the same date. On the interior wings, the Moreel family is painted as kneeling devotees; the parents are represented with 16 of their children – the other two presumably were born after 1484. On the left, William Moreel is shown with his five sons behind him and flanked by his name patron saint, William of Acquitaine. On the right panel, Mrs. Moreel and her daughters kneel next to her patron saint St. Barbara. Of the eleven daughters depicted, the oldest wears the habit of a Dominican nun.

Since the X-ray radiographs of the side panels, recorded several decades ago, suggest that changes were made to the representation and position of the minor characters in both wings, MA-XRF was used to vizualise any *pentimenti* in the triptych to allow for a better understanding of its evolution under the hand of Memling. Some of the MA-XRF results obtained with the M6 scanner (see Figure 2B) are shown in Figure 2C-F. Usually, the MA-XRF Pb-Lα distribution (Figure 2C) resembles the XRR image but shows the distribution of lead white (and other lead containing pigments, if any) in a more clear fashion. When considering the copper distribution (green, Figure 2E), we notice that in the original version of the right panel, only four daughters were depicted against a landscaped background, painted with one of more Cu-containing green pigments. Much more of the hill/lawn to the right of Mrs. Moreel was originally visible; in the landscape, positions were left open for her portrait and that of her (first) four daughters. The faces of the additional seven daughters were painted on top of the verdant background in a later phase. The mercury map (red, Figure 2D) shows that initially, Mrs. Moreel's hat was less elongated. Finally, in the lead distribution, it can be seen (grey/white, Figure 2C) that she and her oldest daughter originally wore more revealing dresses, as is still the case for the second daughter (to the right of the nun). In left panel of the Moreel triptych (Figure 2F) changes were made to the positions of the male children behind William Moreel: an additional portrait (of his fourth son) was inserted between that of the two boys already in the background while the eldest son was moved closer to his father (Figure 2I). The latter changes are particularly visible in the Pb and Sr images (Figure 2G and H). From the above we can conclude that the process of creating this altar piece went through at least two major stages, a first in which the relatively young Moreel family was represented in a balanced manner against a green landscape. In order to include in a second phase all the younger children, some of the balance of the representation was sacrified by the artist. This also allowed a number of minor aspects (such as the dress of the eldest daughter) of the painting to be brought up-to-date. The above shows how the use of MA-XRF opens up the possibility for art-historians and conservators alike to explore in greater depth and with unprecedented detail the creative process that led to paintings of this type by Hans Memling and other artists.

1.2.2.2 *Macroscopic XRD (MA-XRD)*

A fundamental limitation of MA-XRF stems from the fact that XRF only provides information that allows distinguishing between different chemical elements, but does not allow making the more subtle difference between, e.g. two different lead-oxide pigments such as minium (Pb_3O_4) and litharge (PbO). By performing macroscopic scans while signals other than X-ray fluorescence emission are recorded, this limitation may be circumvented. The first instance of XRD-based imaging of works of art was reported by Dooryhee et al. [20], making use of synchrotron radiation in reflection mode. De Nolf et al. [21] have employed very high energy radiation (86 keV) for scanning transmission X-ray powder diffraction mapping of the distribution of pigments in mockups and original Netherlandish paintings. They concluded that highly specific identification and visualization of most pigments, even those containing the same characteristic metals (e.g., Fe in hematite and goethite) is possible, provided the angular resolution of the setup is sufficiently high. An additional advantage is that at high energy, absorption of the primary and of the diffracted beams is virtually negligible. Recently, this MA-XRD capability was successfully transferred to the laboratory by making use of a combination of a compact mirror-focused X-ray source (Ag-IµS, Incoatec GmbH, Hamburg, D), emitting monochromatic Ag-Kα radiation of 22 keV and a single photon counting diffraction camera (Pilatus 200 K, Dectris GmbH, Switzerland) [Vanmeert F, Janssens K, De Nolf W, Legrand S, Van der Snickt G, Dik J: Scanning Macroscopic X-ray powder diffraction imaging (MA-XRPD): transfer from the synchrotron to the laboratory, submitted] (see Figure 3A).
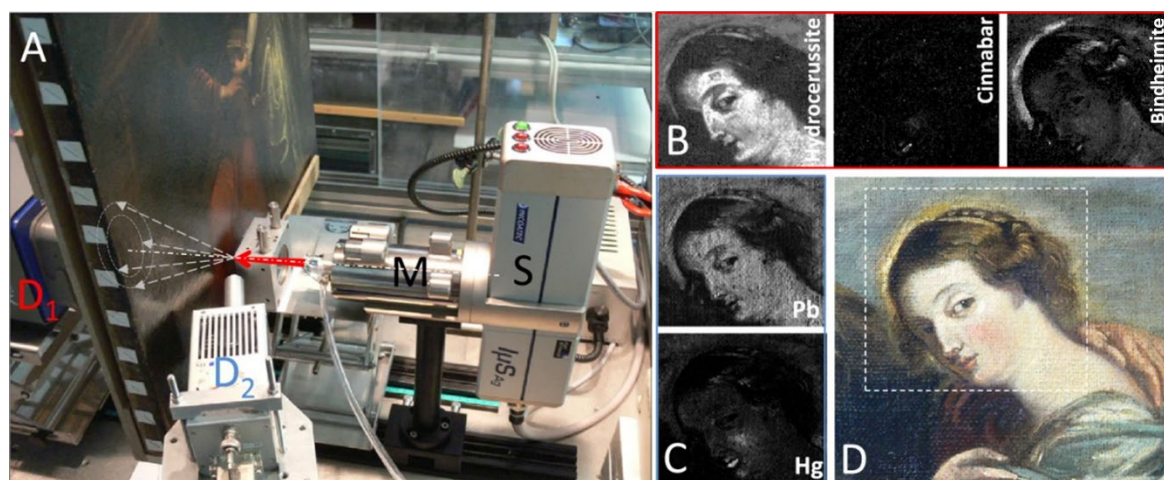
*Figure 3: **Prototype MA-XRD setup at the University of Antwerp. A**) Photograph showing the micro-focus X-ray tube source (S), equipped with a double curved mirror M and detector for recording transmission XRD (D$_1$) and XRF (D$_2$) data: these components are positioned close to a painting mounted on a motorized stage; **B**) MA-XRD and **C**) MA-XRF images obtained by scanning a detail of the painting shown in **D**): scan size: 78×75 mm^2, image step size: 0.5 mm in both directions, Dwell time: 2 s/pixel. Adapted from [Vanmeert F, Janssens K, De Nolf W, Legrand S, Van der Snickt G, Dik J: Scanning Macroscopic X-ray powder diffraction imaging (MA-XRPD): transfer from the synchrotron to the laboratory, submitted].*

As an example of the imaging possibilities of this newly constructed device, Figure 3B shows the distribution of the Pb-containing pigments hydrocerussite [$2PbCO_3 \cdot Pb(OH)_2$] and Naples' yellow [$Pb_2Sb_2O_7$] in a copy of a baroque painting entitled *The Education of Mary* (original painted 1630–1635 by P.P. Rubens). The images have a spatial resolution of 0.5 mm. Both the MA-XRF Hg distribution and the MA-XRD Cinnabar (α-HgS) image show that this red pigment was only used very sparingly to paint Mary's lips and to create a faint blush on her cheeks. The use of lead antimonate (found in nature as the mineral *bindheimite*) to render the halo around Mary's head is consistent with a mid-18th to late-19th century date of origin of this smaller copy of the original Rubens painting. The higher specificity of XRD allows readily distinguishing and identifying the pigments in a direct and positive manner while this is only possible in an indirect manner on the basis of the corresponding MA-XRF images (Figure 3C). The higher energy of the diffracted X-rays as opposed to that of the characteristic XRF radiation also allows to probe deeper for representations that may be hidden below the surface.

1.2.2.3 *Computed X-ray Laminography (CXL)*

A limitation shared by MA-XRF, MA-XRD and XRR is the fact that they provide projection images, i.e., they do not reveal information on the distribution of (one or more) pigments in a single layer but rather in a series of superimposed paint layers. To separate out the contributions from the different paint layers, a tomographic data collection approach [22,23] or, in the case of (MA-)XRF, a confocal detection geometry [24,25] may be employed. Computed X-ray tomography (CXT) involves the recording of a series of two-dimensional radiographies under many different orientations of the sample relative to the X-ray source-detector axis; the principle is illustrated in Figure 1D for the case of cone-beam illumination [26]. For CXT, the shape of artefacts being examined should be such that under all observation/irradiation angles, the total path length the transmitted radiation must follow through the absorbing material does not vary more than, say, an order of magnitude. In case of paintings and other objects that are much more extended along two dimensions (length, width) than along the third (depth), conventional CXT therefore cannot be employed; during the rotating motion of the painting relative to the source-detector axis, in a particular orientation, its entire length or width would be in the radiation path, blocking all transmission. A way of circumventing this problem is to employ the related method of computed X-ray laminography (CXL), originally developed for inspection of complex, flat, multilayered objects such as printed circuit boards [27-29]. CXL makes use of a rotation around an axis that is not perpendicular to the radiation source/detector axis but that is tilted relative to it (Figure 1E). By performing experiments on mock-up paintings, Krug et al. [30] demonstrated that voids and hidden compartments inside paintings can be inspected in a non-destructive manner via this technique.
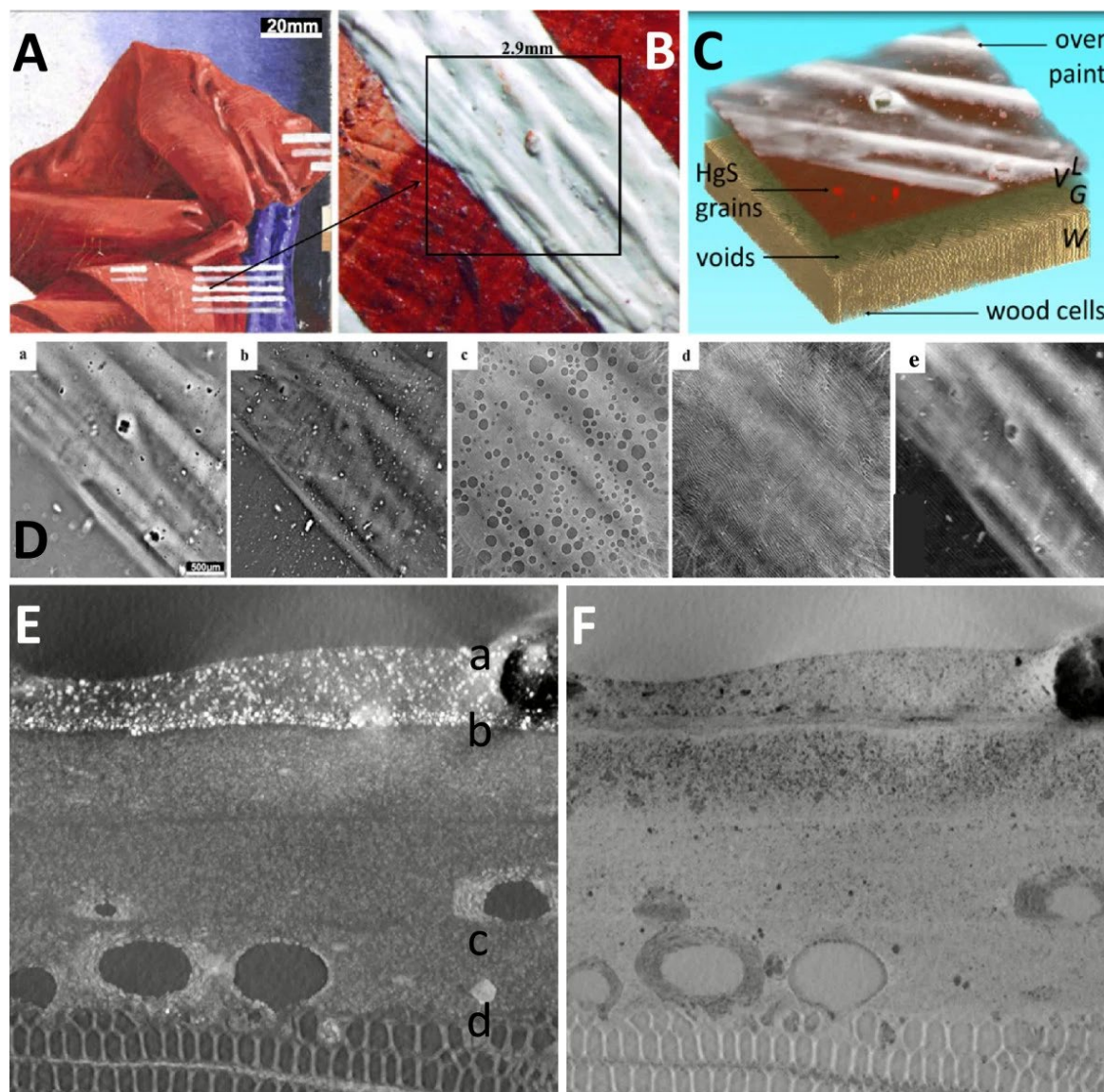
*Figure 4: **Mockup painting used for evaluating CXL. A:** Visual photograph; **B:** detail of A, showing a stroke of lead white covering the red surface of the painting; **C:** 3D rendering of CXL data, showing the reconstructed volume; **D:** series of virtual laminographic sections a-d, parallel to the wood/paint surface at the depth indicated in E: (a) superficial lead white, (b) pigment particles in the red paint; (c) spherical voids in the ground layer; (d) cells in the wood support; panel (e) shows the corresponding radiography of the volume shown in **C**; **E, F:** virtual cross sections obtained by applying a maximum (**E**) or a minimum (**F**) filter of 750 images, oriented perpendicular to the axis of the wood cells. Adapted from [32].*

Figure 4 illustrates how CXL allows high-resolution imaging of the local sub-surface microstructure in paintings in a non-invasive and non-destructive way. Results of feasibility tests on a painting mockup (consisting of an oak panel, a chalk ground superimposed with vermilion and lead white paint layers, see Figure 4AB) show that achieving lateral and depth resolutions of up to a few micrometers is possible. Based on absorption and phase contrast, the method can provide high-resolution 3D maps of the paint stratigraphy (Figure 4C), including the wooden substrate, and visualize small

features, such as pigment particles, voids, cracks, cells in the wood support etc. (Figure 4D). In resulting virtual cross sections (Figure 4EF) the local density and chemical composition of the different paint layers are visible due to increased attenuation of X-rays by elements of higher atomic number. A typical CXL scan consists of 1000 to 3600 radiographs, each with a size of 2048 by 2048 pixels and a pixel size of 0.28 to 1.4 micrometers. While each image is only exposed for 0.1 s, the speed with which the painting can be rotated is limited; thus, per data set of the order of 1 h of total collection time was required.

Thus, this method is well adapted to study the temporal evolution of the stratigraphy in test specimens and offers an alternative to destructive sampling of original works of art. In a fashion very similar to that used with high magnification optical microscopes, the laminographic technique allows to obtain detailed morphological images at any depth in an (optically opaque) paint layer stack [31,32]. CXL thus presents a non-invasive and non-destructive alternative to sampling and polishing where such fine structure needs to be preserved. The technique has a high potential in studying conservation problems on test specimens or original works of art, where the microstructure of carrier, ground or paint is of importance but sample removal is to be avoided.

1.2.3 Methods based on infrared radiation

IRR was introduced in the 1960's by J.R.J. van Asperen de Boer, using PbS-based Vidicon tubes as recording devices and has seen important technological improvements over the past years [33-35]. An infra-red (IR) source of around 1.2 µm is used to illuminate objects; this radiation will readily penetrate through a number of commonly occurring paint constituents such as lead white, while becoming strongly absorbed by others such as carbon black. The radiation (0.9-1.7 µm) reflected by the illuminated objects is now typically recorded with an InGaAs (or equivalent) camera, allowing for rapid acquisition of high definition images with a resolution up to 0.1 mm, covering areas of typically 0.5×0.5 m^2. Over the past decades, IRR has become a routine form of analysis in many painting collections, almost exclusively for the study of carbon-based underdrawings in paintings from the 16th century and earlier. In such artefacts, IR-absorbing carbon black tracery is often applied on IR-reflective chalk or gypsum grounds, resulting in a strong contrast in the reflectograms. Examination of 17th or 18th century paintings with IRR tends to be less rewarding because these later paintings often were set up in sketchy touches of earth pigments, or underdrawn in white chalk. These pigments are very poor infrared absorbers. Furthermore, many 17th century paintings were painted on colored grounds that poorly reflect IR. Another limiting factor is that many of the paints contain infrared absorbing pigments, such as carbon black, that make it hard to distinguish the underlying drawings from the covering paint layers. Next to the acquisition of full field reflection images by IR-sensitive cameras, scanning may also be employed. Already in 2006, Saunders et al. [35] devised a camera system that acquired 25 Mpixel IRRs with a lateral

resolution of 100 μm; it incorporated a small (320 × 256 pixel) moving InGaAs sensor of which the images were stitched together. This lightweight camera, suitable for in-situ measurements, is commercially available (OSIRIS camera) and is sensitive in the 0.9-1.7 μm wavelength range. The camera itself does not offer any means of wavelength dispersion or selection, but via absorption filters the spectral range effectively acquired can be adjusted to optimize the vizualisation of underdrawing material. Daffara et al. have described an advanced scanner that records 14 bands from 0.7 to 2.3 μm and that allows for multispectral imaging of large paintings, achieving a spatial resolution of 0.5 mm [36]. Fast movement of the scanner head in front of the painting allows recording IRR maps of 1 m^2 areas within a period of several hours at maximum resolution.

Delaney et al. have more recently described a novel near-infrared (NIR) system that allows for hyperspectral imaging in 342 narrow wavelength bands situated in the 1.0-2.5 μm (4000–10000 cm^{-1}) range [37-41]. The system incorporates a scan mirror, an imaging lens, a transmission grating spectrometer + relay lens and a cryo-cooled (640 × 512 pixel) InSb sensor. The area examined is scanned one-dimensionally by rotation of the mirror while the other camera dimension is used for wavelength dispersion. In a number of cases where the results of MA-XRF do not significantly differ from those obtained by XRR, for example in the case where very thick overpainted layers of lead white are present, this system has allowed to obtain contrast-rich imaging information. This complementarity was recently underscored during the examination of a painting by R. Magritte, called *Le Portrait* (1934, Museum of Modern Art, New York City, USA) by means of a combination of traditional XRR, MA-XRF and NIR-hyperspectral imaging [Van der Snickt G, Martins A, Duffy M, McGlinchey C, Coddington J, Delaney JK, Janssens K, Dik J: Multimodal examination of '*Le portrait*' by R. Magritte by means of X-ray and Infrared hyperspectral imaging methods reveals an overpainted representation, submitted]. The combined use of the resulting images allowed art historians of MoMA to identify the work present below the surface as *La Pose Enchantée*, a painting erroneously believed lost that was made by Magritte in 1927 but overpainted in 1935.

Also in the mid infrared (MIR) range, a tendency towards hyperspectral imaging and even full spectrum recording at all pixel positions is discernable. Promising results have been recently reported by Rosi et al. [42] using a novel hyperspectral imaging system (Hi90, Bruker Optics), originally developed for the remote identification and mapping of hazardous compounds. It is based on a focal-plane array mercury cadmium telluride (FPA-MCT) detector having 256×256 pixels. This device operates in the 900–1300 cm^{-1} (7.7-11.0 μm) spectral range and allows for the parallel recording of series of MIR spectra (with adequate spectral resolution -4 cm^{-1}), corresponding to each pixel of the investigated area. It was successfully used for mapping of both organic and inorganic compounds in a painting by A. Burri. Daffara et al. also have reported on a device operating in the 2000–3000 cm^{-1} (3.3-5.0 μm) range [43].

In view of these promising results, and in analogy of the MA-XRF and MA-XRD scanners discussed above, Legrand et al. [44,45] have recently explored the possibilities and limitations of a prototype macroscopic MIR-FTIR scanner, based on the Alpha Bruker FTIR spectrometer. The latter is a compact, light-weight FTIR spectrometer operating in the 400–7500 cm^{-1} (1.3-25.0 µm) range, incorporating a globar IR-source and a deuterated triglycine sulphate (DTGS) detector that can be fitted with a reflection mode accessory. The curved mirrors in the latter produce a roughly circular IR beam of ca 2×2 mm^2 with which a single spot on a painting may be interrogated. During the scanning operation, the entire spectrometer is moved in an XY fashion in front of the painting while series of FTIR spectra are recorded in reflection mode from many points.
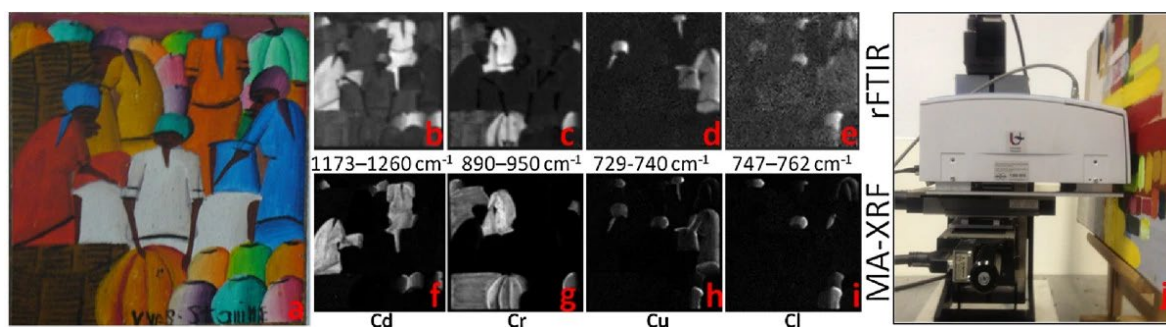

*Figure 5: **Antillean folk art painting (8×8 cm^2), of assumed 20th Century origin. a)** Visual image; MA-rFTIR chemical distribution images: **b)** cadmium lithopone (1173–1260 cm^{-1}), **c)** chrome yellow (890–950 cm^{-1}), **d)** phthalocyanine blue (729–740 cm^{-1}) and **E)** phthalocyanine green (747–762 cm^{-1}); MA-XRF elemental distribution maps of **f)** cadmium, **g)** chromium, **h)** copper and **i)** chlorine: lighter tones indicate higher levels of net pseudo absorbance or X-ray fluorescence intensity; **j)** Photograph of MA-rFTIR device in front of a large canvas, scanned area: 76×76 mm^2, step size: 1 mm in both directions, dwell time: 8 s/pixel. Adapted from [44].*

Figure 5 compares results obtained by MA-rFTIR and MA-XRF from a small (8 × 8 cm^2) 20th century, unvarnished folk-art panel painting of Antillean origin. It is built up of a number of strongly contrasting coloured areas and has a fairly simple stratigraphy, in most cases consisting of only one paint layer applied on a calcite ground. MA-XRF analysis of this painting (see Figure 5, lower row) reveals the presence of the elements cadmium, selenium and barium in the red and orange regions, strongly suggesting that the pigment employed here is cadmium lithopone (CdSe + BaSO$_4$). Cadmium-based pigments have, due to the heavy atomic mass of cadmium, their fundamental bands in the far-IR (FIR) region and therefore cannot be detected with the MIR setup. The map in Figure 5B (1173–1260 cm^{-1}) however, shows that the distribution of the sulphate ion via its symmetric stretching vibration mode (v_3-SO$_4^{2-}$) is strongly correlated to the Cd MA-XRF maps of Figure 5F, corroborating the hypothesis about the presence of cadmium lithopone in the orange areas. The MA-XRF-data also show that the main yellow pigment present in this painting contains the elements lead and chromium; in the FTIR spectra, it is identified by its chromate- (v_4-CrO$_4^{2-}$ at 888 cm^{-1}) and sulphate- (v_4-SO$_4^{2-}$ at 604 and 630 cm^{-1}) ion bands as chrome yellow (in its pale PbCr$_{1-x}$S$_x$O$_4$ form), a pigment that is in

use since the 19th century [46]. Accordingly, the map in Figure 5C, based on the CrO_4^{2-} asymmetric stretch (890–950 cm^{-1}) shows a good correlation with the chromium XRF image (Figure 5G). By means of the rFTIR maps, it was also possible to identify the blue and green pigments present in this painting in an unambiguous manner as phthalocyanine-based compounds. Since this group of pigments was only discovered in the 1930s, their presence confirms the presumed 20th century origin of the painting. The metal-ligand band at 898 cm^{-1} suggest that copper is the metal ion in the complex, a hypothesis that is confirmed by the MA-XRF copper map of Figure 5H. The phthalocyanine-blue (PB15 – Colour Index Generic Name) distribution (Figure 5D) can be visualized by means of its C-H out-of-plane bending mode at 729–740 cm^{-1}. Phthalocyanine green (PG7) is a partially chlorinated version of PB15 and this substitution results in a shift of the C-H out-of-plane bending mode band of this pigment towards higher wavenumbers, in this case to 747–762 cm^{-1} (Figure 5E). For confirmation, the copper and chlorine XRF-maps are also shown in Figure 5H and I. While the MA-XRF copper map resembles the sum distribution of both pigments, the chlorine distribution of Figure 5I only resembles the FTIR map of PG7. It is possible to conclude from the above that the species-specific MA-rFTIR maps allow visualization of the distribution of these highly similar pigments in a straightforward and reliable manner, even though in its current implementation, very long acquisition times are required for this. Considering these results, that illustrate the advantages of recording full spectral data at all positions of an examined painting area may entail, it is expected that hyper- and full spectral imaging of paint surfaces in the IR fingerprint region will open up new and broad perspectives for non-invasive analysis.

It must be mentioned here that the mid-FTIR based methods are severely hampered by the presence of varnish (or other organic cover) layers and in practice can only be employed on paintings that are not varnished or those where the varnish has been temporarily removed. This important limitation is not present with the X-ray based imaging methods discussed above where both primary and secondary (XRF) radiation can easily penetrate any cover layers.

A related and notable development of recent years is the depth selective variant of NIR-based imaging called Optical Coherence Tomography (OCT) [47,48]. OCT is a point scanning system based on the use of a NIR source coupled to a Michelson interferometer. The source, similar to those used for conventional IRR, illuminates both a reference mirror and the object under examination. Constructive interference occurs when the length of the optical path of the light that is backscattered within the object matches, within the coherence length, the length of the optical path of the radiation reflected by the mirror. The interference measurement therefore enables the determination of the depth at which the reflection took place within the object. This adds depth-resolution to the infra-red investigation of paintings, allowing mapping of the distribution of specific materials and material interfaces throughout the paint stratigraphy. The technique proves

to be a powerful imaging tool in the study of thinly painted layers as found in 16th century and earlier paintings [49,50]. The technique is particularly valuable for the study of near-surface features, notably translucent layers such as glazes and varnish [51].

In order to compare the possibilities of MA-XRF, MA-rXRPD and MA-rFTIR, an area depicting a monk in prayer on the *Fragment from an altarpiece: The Visitation* panel, attributed to the Master of the view of Saint Gudula (65.5 x 96.4 cm², Inv. 4348, King Baudouin Foundation on long-term loan to the RMFAB, Brussels, Belgium) was analyzed. The results of the three methods are shown in figure 6.

A first difference between the techniques is the larger pixel size of MA-rFTIR (1 x 1 mm²) and MA-rXRPD (1.2 x 1.2 mm²) compared to MA-XRF (0.5 x 0.5 mm²). This has a twofold reason: (1) the irradiating beam is larger in the first two techniques and (2) the relative long dwell time per point (around 10 s in both cases) compared to the 0.2 s for MA-XRF pushed towards larger step sizes to keep the total scanning time acceptable.

In case of MA-XRF, all lead based components are visualized together in the distribution of lead, only lead-tin-yellow can be separated by using the distribution of tin. Oftentimes, the comparison between Pb-L and Pb-M allows to differentiate sub-surface from surface information. The characteristic radiation of Pb-L is more energetic than Pb-M, as a result the Pb-L radiation that reaches the detector can emerge from below the paint surface, while the Pb-M detected Pb-M lines are limited to the surface. MA-rXRPD manages to separate the Pb contribution into 4 components: lead tin yellow (Pb_2SnO_4,), hydrocerussite ($2PbCO_3 \cdot Pb(OH)_2$), cerussite ($PbCO_3$) and plumbonacrite ($3PbCO_3 \cdot Pb(OH)_2 \cdot PbO$), the latter being a degradation product of lead white. In reflected FTIR spectra, peaks are generally broader and shifted compared to transmission spectra. As a result the subtle shift between the different lead carbonates, identified by MA-rXRPD is difficult to capture. In this example two bands, assigned to lead white, are visualized. These two distributions do not completely match, because the carbonate band at 1445 - 1495 cm^{-1} is influenced by other carbonates.

Copper based pigments are very well detected by MA-XRF. However, being an elemental technique it cannot differentiate between the broad variety of copper-based pigments that has been used throughout history. The crystalline segment of these pigments can be detected by MA-rXRPD; in this example azurite ($2CuCO_3 \cdot Cu(OH)_2$) and some malachite ($CuCO_3 \cdot Cu(OH)_2$) as an impurity were detected. Being both carbonates, MA-rFTIR, can detect these as well. When comparing the malachite distributions, these do not match completely. In the zone of the azurite rich mantle, the paint is relatively rough, inhibiting the specular reflection of light and enhancing the diffuse reflection of light. Since the malachite band is the result of specular reflected light its signal decreased significantly in this area, while the diffuse reflected light enhances the combination bands used to map the azurite distribution. Zinc is an impurity that is often found in copper ores. The

absence of zinc-components in both MA-rFTIR and MA-rXRPD showcases the better detection limit of MA-XRF for these elements.

The distribution of the applied gold foil is clearly visible in the MA-XRF distribution. Given the higher energy of Au-L than the Cu-Ka radiation used in MA-rXRPD, also the overpainted part of the gold foil adjacent to the hale is visible in the MA-XRF distribution, while this is not the case in the XRD-distribution. Metallic gold has good reflecting properties for mid-infrared light and no absorption bands in this spectral range. However, it is possible to map its surface distribution using the total reflected intensity, rather than the baseline-subtracted pseudo-absorbance intensity that is used for chemical mapping. In such distributions that resemble classical infrared reflectography (IRR), the local increased of reflected light is attributed to the polished gold foil.

Three different uses of iron can be discerned in the iron distribution map: brown earth pigments in the tree trunk, skin tones and hair, as a bole layer underneath the gold foil and as an impurity in azurite. When comparing the iron and gold distributions, a similar damage pattern can be discerned. This means that the damaged gilding is probably caused by the cracking of the bole layer and not by a worn down leaf. If the latter was true, the iron signal should increase where the gold layer is damaged, while this is not the case. Earth pigments contain crystalline water, either in the iron (hydr)oxides or in other minerals present such as clays. By plotting the distribution of these water vibrations, the distribution corresponds to the iron distribution that can be assigned to earth pigments in the trunk, hair and skin. Given the strong IR-reflectance of gold, it is not possible to analyze the bole layer where the gilding is intact. Only at the edges and damages of the halo, an increase in intensity can be seen. For these compounds no distribution maps could be created by means of MA-rXRPD. It must be commented that during this experiment, the geometry and Q-space range were optimized for the detection of oxalates and other degradation products.

Calcium is another element that can be present in multiple components: gypsum ($CaSO_4 \cdot 2H_2O$) or chalk ($CaCO_3$) as preparatory or ground layers, filler or lake substrate, or bone black in darker passages. The identification of the latter by MA-XRF can be more firmly if the co-presence of phosphorus is found. Unfortunately, this is often hindered by the presence of a thick, P-K radiation absorbing, varnish. With the advent of chemical imaging methods, it became clear that calcium is not only present as gypsum, chalk or bone black, but often present at the surface as the degradation product calcium oxalate ($CaC_2O_4 \cdot x(H_2O)$). This is visible in the MA-rFTIR distribution, while after fitting, no distribution was available for MA-rXRPD. Two possibilities arise: either the amount of calcium oxalate, present in this area was too low to be detected by MA-rXRPD or the calcium oxalate was not present in a crystalline form.

*Figure 6: a comparison between MA-XRF (**top row**), MA-rFTIR (**middle row**) and MA-rXRPD (**bottom row**) on a detail of Fragment from an altarpiece: The Visitation panel by The master of the view of Saint Gudula (inv. 4348, King Baudouin Foundation on long-term loan to the RMFAB, Brussels, Belgium) (**top left**), the orange rectangle indicates the zone scanned by MA-XRF and MA-rXRPD and the red rectangle indicates the zone scanned by MA-rFTIR*

1.2.4 Conclusions

In this paper a brief overview was presented of recent methodological and instrumental developments regarding the characterization of painted works of art based on either penetrative X-ray or Infrared radiation. Macroscopic XRF is a variant of the general method of X-ray fluorescence analysis that is well suited to visualize the elemental distribution of key elements, mostly metals, present in areas of around 0.5-1 m^2 or more. This method is not depth-selective so that *projected* pigment distributions (at and/or below the visible paint surface) are obtained. For *depth-selective* imaging of the individual layers in a painting, on the other hand X-ray laminography, a variant of computed X-ray tomography that is more suitable for examination of flat panels, appears promising.

Also by means of OCT, depth resolved imaging appears possible, albeit in materials that retain a certain transparency. By means of infrared radiation, either in the NIR or in the MIR ranges, camera-based or scanning based reflection mode imaging can be performed. The information obtained in this manner is often complementary to that obtained by means of the X-ray based methods. The combined use of MA-XRF/XRD scanning with NIR/MIR hyperspectral imaging or MA-rFTIR scanning appears to be a very promising new direction for non-invasive imaging of paintings.

References

1.   Cotte M, Susini J, Dik J, Janssens K: Synchrotron-Based X-ray Absorption Spectroscopy for Art Conservation: Looking Back and Looking Forward. Acc Chem Res 2010, 43:705–714.

2.   Janssens K, Dik J, Cotte M, Susini J: Photon-based techniques for non-destructive subsurface analysis of painted cultural heritage artifacts. Acc Chem Res 2010, 43:814–825.

3.   Janssens K, Alfeld M, Van der Snickt G, De Nolf W, Vanmeert F, Radepont M, Monico L, Dik J, Cotte M, Falkenberg G, Miliani C, Brunetti BG: The use of synchrotron radiation for the characterization of artists' pigments and paintings. Annu Rev Anal Chem 2013, 6:399–425.

4.   Alfeld M, Broekaert JAC: Mobile depth profiling and sub-surface imaging techniques for historical paintings - A review. Spectrochim Acta B At Spectrosc 2013, 88:211–230.

5.   Liang H: Advances in multispectral and hyperspectral imaging for archaeology and art conservation. Appl Phys A Mater Sci Process 2012, 106:309–323.

6.   Janssens K, Adams F, Rindby A: Microscopic X-ray fluorescence analysis. Chichester, UK: John Wiley & Sons; 2000.

7.   Beckhoff B, Kanngiesser B, Langhoff N, Rainer W, Helmut W: Handbook of Practical X-ray Fluorescence Analysis. Berlin, Heidelberg, Germany: Springer Verlag; 2006.

8.   Lahanier C, Amsel G, Heitz C, Menu M, Andersen HH: Proceedings of the International Workshop on Ion-Beam Analysis in the Arts and Archaeology - Pont-A-Mousson, Abbaye des Premontres, France, February 18–20, 1985 - Editorial. Nucl Instrum Methods Phys Res B Beam Interact Mater Atoms 1986, 14:R7–R8.

9.   Van Grieken R, Markowicz A: Handbook of X-ray Spectrometry. New York, USA: Marcel Dekker; 2002.

10.   Dik J, Janssens K, Van der Snickt G, van der Loeff L, Rickers K, Cotte M: Visualization of a lost painting by Vincent van Gogh using synchrotron radiation based X-ray fluorescence elemental mapping. Anal Chem 2008, 80:6436–6442.

11.   Dik J, Alfeld M, Janssens K, van de Wetering E: Nouveau type d'examen aux rayons x d'un Rembrandt dissimule. In Un Nouveau regard sur Rembrandt. Edited by van de Wetering E. Amsterdam, The Netherlands: Local World; 2009.

12.   Alfeld M, Janssens K, Appel K, Thijsse B, Blaas J, Dik J: A portrait by Philipp Otto Runge - visualizing modifications to the painting using synchrotron-based X-ray fluorescence elemental scanning. Zeitschrift für Kunsttechnologie und Konservierung 2011, 25:157–163.

13.   Struick van der Loeff L, Alfeld M, Meedendorp T, Dik J, Hendriks E, van der Snickt G, Janssens K, Chavannes M: Rehabilitation of a flower still life in the Kröller-Müller Museum and a lost Antwerp painting by Van Gogh. In Van Gogh: New Findings. Edited by van Tilborgh L. Amsterdam, The Netherlands: Van Gogh Museum; 2012.

14.   Alfeld M, Van der Snickt G, Vanmeert F, Janssens K, Dik J, Appel K, van der Loeff L, Chavannes M, Meedendorp T, Hendriks E: Scanning XRF investigation of a Flower Still

Life and its underlying composition from the collection of the Kroller-Muller Museum. Appl Phys A Mater Sci Process 2013, 111:165–175.

15.   Howard DL, de Jonge MD, Lau D, Hay D, Varcoe-Cocks M, Ryan CG, Kirkham R, Moorhead G, Paterson D, Thurrowgood D: High-definition X-ray fluorescence elemental mapping of paintings. Anal Chem 2012, 84:3278–3286.

16.   Hocquet FP, del Castillo HC, Xicotencatl AC, Bourgeois C, Oger C, Marchal A, Clar M, Rakkaa S, Micha E, Strivay D: Elemental 2D imaging of paintings with a mobile EDXRF system. Anal Bioanal Chem 2011, 399:3109–3116.

17.   Bull D, Krekeler A, Alfeld M, Dik J, Janssens K: An intrusive portrait by Goya. Burlingt Mag 2011, 153:668–673.

18.   Alfeld M, Janssens K, Dik J, de Nolf W, van der Snickt G: Optimization of mobile scanning macro-XRF systems for the *in situ* investigation of historical paintings. J Anal At Spectrom 2011, 26:899–909.

19.   Alfeld M, Pedroso JV, Hommes MV, Van der Snickt G, Tauber G, Blaas J, Haschke M, Erler K, Dik J, Janssens K: A mobile instrument for *in situ* scanning macro-XRF investigation of historical paintings. J Anal At Spectrom 2013, 28:760–767.

20.   Dooryhee E, Anne M, Bardies I, Hodeau JL, Martinetto P, Rondot S, Salomon J, Vaughan GBM, Walter P: Non-destructive synchrotron X-ray diffraction mapping of a Roman painting. Appl Phys A Mater Sci Process 2005, 81:663–667.

21.   De Nolf W, Dik J, Van der snickt G, Wallert A, Janssens K: High energy X-ray powder diffraction for the imaging of (hidden) paintings. J Anal At Spectrom 2011, 26:910–916.

22.   Ferreira ESB, Boon JJ, van der Horst J, Scherrer NC, Marone F, Stampanoni M: 3D Synchrotron X-ray Microtomography of Paint Samples. In O3a: Optics for Arts, Architecture, and Archaeology, Proceedings SPIE 7391. Edited by Pezzati L, Salimbeni R. Bellingham, WA, USA: Int. Soc. for Optical Engineering; 2009.

23.   De Nolf W, Janssens K: Micro X-ray diffraction and fluorescence tomography for the study of multilayered automotive paints. Surf Interface Anal 2010, 42:411–418.

24.   Mass JL, Woll A, Bisulca C: Confocal X-ray fluorescence of paintings: Imaging a missing NC Wyeth. Abstr Pap Am Chem Soc 2009, 238:1.

25.   Mass J, Bisulca C: Revealed, a Lost Illustration by N.C. Wyeth. In Antiques and Fine Art. Summer/Autumn 2010 ed. Watertown, MA, USA: Pure Imaging Inc; 2010.

26.   Zhang X, Blaas J, Botha C, Reischig P, Bravin A, Dik J: Process for the 3D virtual reconstruction of a microcultural heritage artifact obtained by synchrotron radiation CT technology using open source and free software. J Cult Herit 2012, 13:221–225.

27.   Helfen L, Baumbach T, Cloetens P, Baruchel J: Phase-contrast and holographic computed laminography. Appl Phys Lett 2009, 94:104103.

28.   Helfen L, Baumbach T, Mikulik P, Kiel D, Pernot P, Cloetens P, Baruchel J: High-resolution three-dimensional imaging of flat objects by synchrotron-radiation computed laminography. Appl Phys Lett 2005, 86:071915.

29.   Helfen L, Xu F, Suhonen H, Cloetens P, Baumbach T: Laminographic Imaging Using Synchrotron Radiation - Challenges and Opportunities. In Proceedings 11th International Conference on Synchrotron Radiation Instrumentation. Edited by Susini J, Dumas P. 2013.

30.   Krug K, Porra L, Coan P, Wallert A, Dik J, Coerdt A, Bravin A, Elyyan M, Reischig P, Helfen L, Baumbach T: Relics in medieval altarpieces? Combining X-ray tomographic, laminographic and phase-contrast imaging to visualize thin organic objects in paintings. J Synchrotron Radiat 2008, 15:55–61.

31.   Dik J, Reischig P, Krug K, Wallert A, Coerdt A, Helfen L, Baumbach T: Threedimensional imaging of paint layers and paint substructures with synchrotron radiation computed mu-laminography. J Am Inst Conserv 2009, 48:185–197.

32.   Reischig P, Helfen L, Wallert A, Baumbach T, Dik J: High-resolution non-invasive 3D imaging of paint microstructure by synchrotron-based X-ray laminography. Appl Phys A Mater Sci Process 2013, 111:983–995.

33.   Van Asperen de Boer J: Scientific Examination of Early Netherlandish Painting. In An Introduction to the Scientific Examination of Paintings. Edited by Filedt Koj JP. Bussum,The Netherlands: Fibula - van Dishoeck; 1976:1–40.

34.   Liang H, Saunders D, Cupitt J: A new multispectral imaging system for examining paintings. J Imaging Sci Technol 2005, 49:551–562.

35.   Saunders D, Billinge R, Cupitt J, Atkinson N, Liang H: A new camera for high-resolution infrared imaging of works of art. Stud Conserv 2006, 51:277–290.

36.   Daffara C, Pampaloni E, Pezzati L, Barucci M, Fontana R: Scanning multispectral IR reflectography SMIRR: an advanced tool for art diagnostics. Acc Chem Res 2010, 43:847–856.

37.   Delaney JK, Zeibel JG, Thoury M, Littleton R, Palmer M, Morales KM, de la Rie ER, Hoenigswald A: Visible and Infrared imaging spectroscopy of Picasso's Harlequin musician: mapping and identification of artist materials in Situ. Appl Spectrosc 2010, 64:584–594.

38.   Thoury M, Delaney JK, Rene de la Rie E, Palmer M, Morales K, Krueger J: Near-infrared luminescence of cadmium pigments: in Situ identification and mapping in paintings. Appl Spectrosc 2011, 65:939–951.

39.   Ricciardi P, Delaney JK, Facini M, Zeibel JG, Picollo M, Lomax S, Loew M: Near infrared reflectance imaging spectroscopy to map paint binders in Situ on illuminated manuscripts. Angewandte Chemie Int Ed 2012, 51:5607–5610.

40.   Dooley KA, Lomax S, Zeibel JG, Miliani C, Ricciardi P, Hoenigswald A, Loew M, Delaney JK: Mapping of egg yolk and animal skin glue paint binders in Early Renaissance paintings using near infrared reflectance imaging spectroscopy. Analyst 2013, 138:4838–4848.

41.   Muir K, Langley A, Bezur A, Casadio F, Delaney J, Gautier G: Scientifically investigating Picasso's suspected use of Ripolin house paints in still life, 1922 and the red armchair, 1931. J Am Inst Conserv 2012, 52:156–172.

42.   Rosi F, Miliani C, Braun R, Harig R, Sali D, Brunetti BG, Sgamellotti A: Non-invasive analysis of paintings by mid-infrared Hyperspectral imaging. Angewandte Chemie Int Ed 2013, 52:5258–5261.

43.   Daffara C, Ambrosini D, Pezzati L, Mariotti PI: Mid-Infrared Reflectography for the Analysis of Pictorial Surface Layers in Artworks. In Proceedings 3rd International Topical Meeting on Optical Sensing and Artificial Vision. Edited by Gurov I. 2013:68–75.

44.   Legrand S, Alfeld M, Vanmeert F, De Nolf W, Janssens K: Macroscopic reflection Fourier Transformed Mid-Infrared (MA-rFTIR) scanning, a new technique for *in situ* imaging of painted cultural heritage artifacts. Analyst 2014, 139:2489–2498.

45.   Legrand S: Ontwikkeling van een macroscopische Mid-Infrarood scanner. Antwerp, Belgium: University of Antwerp; 2012.

46.   Monico L, Janssens K, Miliani C, Brunetti BG, Vagnini M, Vanmeert F, Falkenberg G, Abakumov A, Yinggang L, Tian H, Verbeeck J, Radepont M, Cotte M, Hendriks E, Geldof M, Van der Loeff L, Salvant J, Menu M: The Degradation Process of Lead Chromate in paintings by Vincent van Gogh studied by means of Spectromicroscopic methods. 3: Synthesis, characterization and detection of different crystal forms of the chrome yellow pigment. Anal Chem 2012, 85:851–859.

47.   Liang H, Cid MG, Cucu RG, Dobre GM, Podoleanu AG, Pedro J, Saunders D: En-face optical coherence tomography - a novel application of non-invasive imaging to art conservation. Opt Express 2005, 13:6133–6144.

48.   Liang H, Peric B, Hughes M, Podoleanu A, Spring M, Saunders D: Optical Coherence Tomography for Art Conservation and Archaeology. In O3a: Optics for Arts, Architecture, and Archaeology, Proceedings of the SPIE 6618. 2007:05–12.

49.   Targowski P, Iwanicka M, Tyminska-Widmer L, Sylwestrzak M, Kwiatkowska EA: Structural examination of easel paintings with optical coherence tomography. Acc Chem Res 2010, 43:826–836.

50.   Targowski P, Iwanicka M, Sylwestrzak M, Kaszewska EA, Frosinini C: OCT Structural Examination of 'Madonna dei Fusi' by Leonardo da Vinci. In Optics for Arts, Architecture, and Archaeology IV, Proceedings of the SPIE 8790. Edited by Pezzati L, Targowski P. 2013.

51.   Targowski P, Iwanicka M: Optical Coherence Tomography: its role in the non-invasive structural examination and conservation of cultural heritage objects-a review. Appl Phys A Mater Sci Process 2012, 106:265–277.

Chapter 2 **Macroscopic Fourier transformed Infrared scanning in reflectance mode (MA-rFTIR)**

In this chapter the development of a MA-rFTIR instrument, using a compact Fourier transformed-mid infrared spectrometer is presented. By analyzing an enlarged mock-up version of the vegetal pattern in a $15^{th}/16^{th}$ century illuminated manuscript, a 20th century Antillean painting and a more complex 19th century icon, the possibilities and limitations of this technique are demonstrated.

In order to improve the elaborate data treatment process and to allow non-experts to obtain and interpret the results of MA-rFTIR scans in a relative fast manner, the use of clustering based automated data-reduction was tested on corroded bronze samples that were (partially) covered by protective layers. In a second stage this method was applied on data acquired on a 16th century bronze statue in Bologna.

This chapter is a modified version of two published papers, adapted with permission from:

- S. Legrand, M. Alfeld, F. Vanmeert, W. De Nolf, K. Janssens, "Macroscopic Fourier transform infrared scanning in reflection mode (MA-rFTIR), a new tool for chemical imaging of cultural heritage artefacts in the mid-infrared range", *Analyst,* 139 (10), **2014**, 2489-98, 10.1039/c3an02094k. With permission from The Royal Society of Chemistry
- G. Sciutto, S. Legrand, E. Catelli, S. Prati, C. Malegori, P. Oliveri, K. Janssens, R. Mazzeo, "Macroscopic mid-FTIR mapping and clustering-based automated data-reduction: An advanced diagnostic tool for in situ investigations of artworks", *Talanta,* 209, **2020**, 120575, 10.1016/j.talanta.2019.120575. Copyright 2020 Elsevier B.V.

2.1 Macroscopic Fourier transform infrared scanning in reflection mode (MA-rFTIR), a new tool for chemical imaging of cultural heritage artefacts in the mid-infrared range

Abstract In this paper we demonstrate that by means of scanning reflection FTIR spectroscopy, it is possible to record highly specific distribution maps of organic and inorganic compounds from flat, macroscopic objects with cultural heritage value in a non-invasive manner. Our previous work involved the recording of macroscopic distributions of chemical elements or crystal phases from painted works of art based on respectively macroscopic X-ray fluorescence or X-ray powder diffraction analysis. The use of infrared radiation instead of X-rays has the advantage that more specific information about the nature and distribution of the chemical compounds present can be gathered. This higher imaging specificity represents a clear advantage for the characterization of painting and artist materials. It allows the distribution of metallo-organic compounds to be visualized and permits distinguishing between pigmented materials containing the same key metal. The prototype instrument allows the recording of hyperspectral datacubes by scanning the surface of the artefact in a contactless and sequential singlepoint measuring mode, while recording the spectrum of reflected infrared radiation. After the acquisition, spectral line intensities of individual bands and chemical distribution maps can be extracted from the datacube to identify the compounds present and/or to highlight their spatial distribution. Not only is information gained on the surface of the investigated artefacts, but also images of overpainted paint layers and, if present, the underdrawing may be revealed in this manner. A current major limitation is the long scanning times required to record these maps.

2.1.1 Introduction

In the study of historical paintings and more specifically as a preparation for restoration activities of such artefacts, it usually is of great relevance to investigate which pigments are present and how these are distributed at or below the painting surface. A large number of analytical techniques have been developed that can be used for the identification of artists' materials. However, many of these techniques require destructive sampling or some form of sample preparation. Therefore, such analyses are restricted to point measurements while the number of investigated locations is usually limited to a minimum. Moreover, in many cases, most of the analysed positions are chosen in the background areas or at the edges of the painting and not in the important pictorial

regions in order to minimise any damage to the cultural heritage (CH) artefact being examined.

During the last few decades the continued development of non-destructive analytical techniques resulted in instruments with a higher performance and in the miniaturization of such devices. When bench top equipment is employed for works of art, the objects or samples to be analysed need to be moved to a (science or conservation) laboratory. Due to all the necessary precautions regarding transport, safety, climate control and insurance, this kind of transportation for objects of cultural heritage usually is fairly costly and difficult to undertake. In the case of artefacts that are not possible or very difficult to move, the increased mobility of analytical instruments has made it possible to analyse such objects *in situ*.[1–7] Since this *modus operandi* barely requires manipulating the object to be analysed, conservators are more willing to give scientists access to works of art for *in situ* measurements.

Some of these non-destructive *in situ* methods, including X-ray fluorescence (XRF), X-ray diffraction (XRD), fibre optics reflectance spectroscopy (FORS) and Raman spectroscopy commonly, are only used for spot analyses and, on average, require several minutes to record a spectrum from a single sample position. After the point analysis campaign, and on the basis of visual information and extra data such as knowledge about the artist's painting technique, the obtained results may be extrapolated to the entire painting. However, making such extrapolations is error prone. Thus, hyperspectral analysis methods, where a spectral response is obtained from all points of the examined surface rather than from a limited number of (hopefully) representative spots, are preferred; such methods have only become recently available. An example of this class of analytical methods is macroscopic X-ray fluorescence (MA-XRF) analysis.[8] While it is possible to perform *in situ* imaging at decimeter to meter length scales by means of this method, the elemental distribution maps acquired lack the possibility of differentiating between pigments that consist of similar key elements (to see, *e.g.*, the difference between hematite, goethite and limonite) and to detect low Z-elements that are characteristic of many organic pigments and dyes.

Infrared-based analytical methods use radiation of energy comparable to that of the vibrational levels present in molecules. Therefore, these techniques are better suited than others for differentiating between (similar) chemical compounds. In addition, infrared measurements in reflection mode allow the performance of analyses in a non-contact and a non-destructive manner.

With the development of infrared reflectography,[9] instrumental imaging of cultural heritage materials in the infrared region of the electromagnetic spectrum became possible. An IR-transparent lens can be used to capture radiation reflected by the object under study and refocus it on an IR-sensitive camera. Initially vidicon imaging systems,

sensitive to infrared light, were used for this purpose. Nowadays these are mostly replaced by focal plane arrays (FPA), sensitive in the same or adjacent spectral regions; these devices allow direct recording of IR-intensity images.

At first, only one or a few spectral bands could be used for imaging. Their spectral region was optimized in order to minimize the absorption of IR light by the overlying paint layers and thus to enhance the contrast between the underdrawing and the overlying painting. To obtain more than one spectral band with the same FPA, filters can be placed in front of the FPA. While the first generations made use of manually placed filters, liquid tuneable filters[10] were employed in later generations. In cases where only a few to a few tens of spectral bands are used, the term multispectral imaging is employed. The use of large spectral bands results in a good signal-to-noise contrast ratio in the obtained images, but yields only a limited spectral resolution. Thus, identification of the chemical compounds present, based solely on the recorded image data, is not possible. However, it may still be possible to differentiate between two adjacent pigment areas when their reflectance characteristics in the IR region are different.

2.1.1.1 *NIR imaging*

Detectors for imaging in the NIR range of radiation may comprise arrays of thousands and thousands of individual detector elements. These detectors are often modified charged coupled devices (CCD),[10] photo-detectors or thermal detectors. Since it is more difficult to create detector arrays, sensitive towards the longer wavelengths of IR-light, with comparable lateral resolution and spectral response as those available for visible light, the FPAs used in IR camera systems mostly comprise only tens up to maximum a few hundreds of pixels in each dimension. In order to analyse macroscopic objects such as paintings with a sufficiently high lateral resolution, mosaic assemblies of smaller images are then recorded.

The use of lenses in combination with flat detectors such as FPAs introduces distortions in the resulting images. To avoid such problems, an alternative approach[11,12] was developed, based on point-by-point rather than full-field scanning (or a whisk-broom approach) of the object. This solution involves the use of fibre-optics for guiding the reflected IR radiation to the detectors. The moving head of the scanner contains only the main optical system, responsible for emitting the primary radiation and capturing the reflected radiation. The reflected radiation is focused at the entrance of the optical fibres and guided towards the detectors present in the stationary part of the scanner. This approach makes the scanning setup lighter, enables the use of higher scanning speeds and avoids vibrations that are passed along from the moving scanner to the detectors.

Every optical fibre directs radiation to a different interference filter/detector combination. In this instrument, three silicon (Si) and 12 indium gallium arsenide (InGaAs) detectors are used for near infrared (NIR)-imaging resulting in a fast scanning capability

with a maximum rate of 2 kHz at a 250 mm step size, covering almost the whole NIR-band (800–2300 nm or 12 500–4350 cm^{-1}). However, since this spectral range is only divided into a limited number of bands, datasets with only a limited spectral resolution are obtained.

Recent instrumental evolution has resulted in imaging systems that can record data over an increased number of spectral bands; to differentiate these systems from the older multispectral systems they are called hyperspectral imaging systems. No exact boundary between the two imaging systems can be found in the literature, but general convention states that multispectral systems possess a number of bands that is distinctly lower than the number of steps used in the spatial dimension. On the other hand, in hyperspectral systems, the number of bands is of the same order as the number of spatial steps.[13,14]

Improvements in the spectral resolution of multi- or hyperspectral NIR imaging systems can be realised via the use of a dispersive element such as a grating.[15] The grating disperses the radiation depending on its wavelength and the intensity of the dispersed bundle of radiation is recorded by different rows of the array. The number of spectral bands in these systems is therefore determined by the number of elements in the FPA. The second dimension of the detector can still be used for the spatial domain and thus allows the acquisition of line scans, allowing faster scanning speed.

2.1.1.2 *MIR imaging*

The previously cited imaging devices are all active in the near infrared (NIR) region, where overtone and combination bands of the functional groups of chemical compounds are present. This spectral region allows differentiation to a certain degree between the compounds present in analysed objects, but lacks the specificity that can be obtained from mid-infrared (MIR) spectral data. Until recently,[16] it has not been possible to perform macroscopic non-destructive MIR imaging on macroscopic artefacts such as paintings. Rosi et al. recently employed a hyperspectral imaging system to record distribution images over a limited region of the MIR-range (900–1440 cm^{-1}) with a spectral resolution of 4 cm^{-1}. The system employed combines a 256 x 256 pixel FPA detector coupled to an interferometer, allowing the recording of a complete hyperspectral data cube in one measurement. The investigation of an area of 9 x 9 cm^2 required a collection time of 80 s.

In what follows, we describe a mobile point-by-point NIR-MIR (7500–375 cm^{-1}) reflection mode scanning device for non-invasive and non-destructive hyperspectral imaging of macroscopic two-dimensional objects such as paintings. Contrary to previously described systems, this scanning setup does not employ a (costly) FPA, but a single point detector incorporated into a compact and inexpensive FTIR spectrometer. Thus, FTIR data over the full spectral range are recorded at each position. The entire infrared spectrometer is part

of the moving scanning head. This avoids the use of chalcogenide fibre optics that have a spectral cut-off at ca. 900 cm^{-1}.

2.1.2 Experimental

2.1.2.1 *MA-rFTIR setup*

Local irradiation of the examined artifacts and spectrum acquisition were performed by means of a Bruker Alpha FTIR spectrometer, equipped with a frontal reflection module (20°/20° geometry) and a coaxial visual camera. The spectrometer incorporates a globar IR-source and a deuterated triglycine sulphate (DTGS) detector. Such a detector has a slower response time and is less sensitive than a mercury cadmium telluride (MCT) detector, but it has the advantage of operating at room temperature, making it more useful for *in situ* measurements. In addition, DTGS-detectors have an increased spectral response towards the far infrared (FIR) region than most MCT-detectors.

Spectra acquisition and storage are done with the Bruker OPUS 6.0 software package. The instrument is calibrated using a polystyrene film at room temperature on a weekly basis. Before every scan, the background is recorded for 15 minutes by placing a gold coated mirror in front of the reflection module. This background spectrum is then used to correct each spectrum for atmospheric absorptions during the scan.

During most scans, the infrared spectra are recorded during an interval of *ca.* 3 seconds per point, where an individual spectrum is saved roughly every second, having a spectral resolution of 4 cm^{-1}. When consecutive spectra in one point differ too much, the spectrometer's control software automatically rejects the last spectrum, resulting in a lower number of spectra in such locations. This is often the case when the analysed surface is not smooth.

Since the actual measuring time is the most time-consuming component in the total scan time, it is important to keep it as short as possible. The above-mentioned spectrum acquisition time of *ca.* 3 s per point corresponds to a compromise between spectral quality and scanning speed. Longer measurement times per point result in an improved spectral quality, but the latter usually only results in a marginal improvement of the final image quality. In addition to the time devoted to spectrum acquisition, per recorded position, an additional 3.5 to 6.5 s are required for spectrum saving, and for moving to the next point. Thus, it generally does not make sense to use acquisition times per pixel that are shorter than ca. 3 s with this system. When a better spectral quality is required than what can be recorded during such an interval, spectra of adjacent or similar points can be combined *a posteriori.*

In this scanning setup (Fig. 1), the FTIR spectrometer is mounted on a motorized scanning stage (Newport Corporation, Irvine, CA, USA). During the scan operation, the

spectrometer is moved in the X (maximum travel range: 100 mm) and Y (250 mm range) directions by motorized stages, while the Z (100 mm range) stage allows the positioning of the focal point of the scanner at the surface of the painting prior to the XY movement. This Z-position is determined at the centre of the area to be analysed as the distance where the reflected radiation is detected at the maximum intensity. The entire scanning operation, including stage movement and spectrometer triggering, is controlled by in-house written software. The processing of the individual spectra and the hyperspectral data treatment are performed with self-written routines using the data analysis software package IDL 8.2. The measured reflectance intensity (R) is a combination of both specular and diffuse reflectance components because the infrared radiation impinges on and reflects back from the surface under an angle of 20 degrees. Because both components contribute to the spectra, neither the Kramers–Krönig nor the Kubelka–Munk transformations can be applied to the spectra. Instead, the reflectance spectra are converted to a pseudo-absorbance (A') form using the relation $A' = log(1/R)$. Unless otherwise noted, all data in this paper are in the pseudo-absorbance form.

*Figure 1: Photographs of the MA-FTIR scanning setup: (**a**) side- and (**b**) front view.*

The beam size at the spectrometer focal point was determined by performing a line scan measurement across a sharp edge between two sample areas made up of calcite ($CaCO_3$) and Prussian blue ($Fe_4[Fe(CN)_6]_4$). After the scan, an error function was fitted to the sigmoidal shape obtained by plotting the band intensity of the cyanide group (1900–2120 cm^{-1}) against the lateral coordinate. The full width at half maximum of this function was taken as a measure of the effective size of the IR-beam in the scan direction: values of 1.80 mm (horizontal) x 2.10 mm (vertical) were obtained. The increased beam size in the vertical plane results from the reflection geometry since the IR beam impinges on the analysed surface at an angle. Even though these dimensions were found, smaller details could be visualised, which is probably due to the fact that the beam intensity is not equally distributed over the irradiated spot. As a result, smaller step sizes than the beam dimensions are being used in the imaging experiments.

Table 1: Scan parameters employed during MA-FTIR examinations of three paintings

Painting	Step size (H x V) (mm²)	Area examined (cm²)	Dwell time per pixel (s)	Spectral range (cm⁻¹)
Replica	1 x 1	5.5 x 8.0	7.7	375–7500
Antillean painting	1 x 1	7.6 x 7.6	7.7	375–7500
Russian icon	1 x 1	10.2 x 17.2	18.4	375–7500

In Table 1, an overview of the scan parameters employed to investigate the 3 paintings described below is provided. The third painting was scanned using a longer spectral acquisition time, resulting in a longer dwell time.

2.1.2.2 *Processing of FTIR hyperspectral data*

After each scan, the series of reflectance infrared spectra are arranged into a three-dimensional data cube and converted to pseudo-absorbance values.

Next to the local chemical composition, the recorded reflectance intensity is a function of the local physical parameters of the irradiated area such as grain size and surface roughness. These last two parameters primarily result in an intensity modulation of the total reflection FTIR spectrum, and less in a change of the spectral features that are recorded. To maximise the chemical contrast in the distribution images, the integrated intensity of the peaks in the pseudo-absorbance spectra is calculated followed by the subtraction of the background relative to a baseline running through the integration limits. As a result, also negative intensities can be obtained. This is typically for bands inverted by the *reststrahlen*-effect, usually observed for antisymmetric stretching of silicate, sulphate and carbonate pigments. When these bands are used for imaging, the distribution image will be reversed so that the most intense pixels correspond with the most negative intensity. A typical feature of reflectance infrared spectra is that they may show derivative shaped features when the absorption index of the irradiated material is small (see Fig. 3a–c). The centre of these features is situated near the wavenumber where the maximum of the corresponding band would be in a transmission FTIR spectrum. When referring to these bands, the centre wavenumber is used, but the integration limits used for creating the chemical distribution images are shifted towards higher wavenumbers with respect to those appropriate for transmission FTIR imaging. By subtracting the *A'* baseline value, the reflectance intensity modulation due to surface artefacts is largely eliminated. This procedure is performed on all pixels, resulting in two dimensional distributions of the baseline-subtracted pseudo-absorbance values, one map for each spectral feature of interest, reflecting the distribution of (a class of) chemical compound(s) in the area examined.

To identify the compounds present, spectra from similar points can be combined into one averaged spectrum of high signal-to-noise ratio. Since published spectra in the literature usually are (converted into) transmission spectra, the averaged pseudo-absorption spectra are mostly compared with transmission databases[17,18] even though they do not show exactly the same features. Only a few papers identify and assign a collection of pigments in pseudo-absorbance mode without any additional data manipulation.[19,20]

2.1.2.3 *Comparative measurements*

The artefacts discussed below were also examined using other macroscopic scanning methods in order to compare characteristics such as the lateral resolution and the chemical specificity of the resulting distributions. To record MA-XRF images, a self-built scanner was used,[8] comprised of a Mo anode X-ray tube, running at 50 kV and 1.0 mA, equipped with a dedicated polycapillary lens, as a primary radiation source and four Vortex EX detectors, mounted under different angles relative to the primary excitation beam, to detect the XRF signals emitted by the analysed painting. The resulting XRF-spectra were analysed with PyMca[21] and converted to elemental distribution maps, using in-house written software.

Macroscopic X-ray powder diffraction scanning (MA-XRPD) measurements were performed during experiment EC-764 at ID15B beamline of the European Synchrotron Radiation Facility (ESRF) in Grenoble, France. A high energy 87.08 keV, 300 x 300 µm² primary beam was used for an exposure time of 0.5 seconds per point. Step sizes of 0.8 mm and 0.4 mm were employed. The obtained series of 2D XRD-patterns were analysed and converted to species-specific maps using the XRDUA software package.[22]

2.1.2.4 *Examined artefacts*

To determine the capabilities and limitations of the MA-rFTIR scanner, a series of painted artefacts of various natures were investigated. The first artefact consisted of a replica (8 x 5 cm²) of a vegetal pattern present in a decorative border of a 15th century breviary;[23] the replica was prepared using modern and well-documented oil paint materials (see Fig. 2a). Chemical distribution maps were recorded by means of the MA-rFTIR and MA-XRPD systems. A second artefact, a relatively simple 20th century panel painting (8 x 8 cm² in size, see Fig. 4a), was analysed by means of MA-rFTIR and MA-XRF, allowing for a comparison between the chemical and elemental distribution maps resulting from both methods. The third artefact was a painting with more complex paint stratigraphy, *i.e.*, a 19th century icon (14 x 18 cm² in size, see Fig. 6a). The MA-rFTIR distributions recorded from this painting were compared with those obtained by IRR, MA-XRF and MA-XRPD.
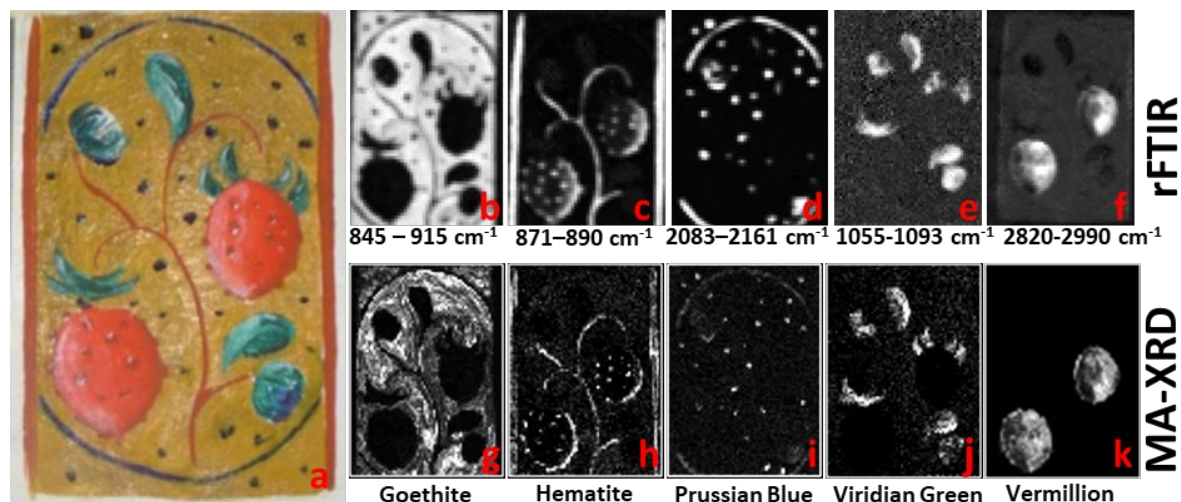
Figure 2: (a) Visual image of the replica; upper row: MA-rFTIR chemical distribution images of (b) goethite (845–915 cm^{-1}), (c) calcite (871–890 cm^{-1}), (d) Prussian blue (2083–2161 cm^{-1}), (e) viridian green (1055–1093 cm^{-1}), and (f) organic binder (2820–2990 cm^{-1}); lower row: MA-XRPD results of (g) goethite, (h) hematite, (i) Prussian blue, (j) viridian green, and (k) vermillion. Lighter tones indicate higher levels of net pseudo-absorbance or diffraction intensity.

2.1.3 Results and discussion

2.1.3.1 *Analysis of a replica painting*

In the painted replica shown in Fig. 2, three different iron-based pigments were employed: hematite (Fe_2O_3, dark red), goethite (α-FeOOH, ochre) and Prussian blue ($Fe_4[Fe(CN)_6]_4$, dark blue). Besides these iron containing pigments, zinc white (ZnO) was used for the preparation layer, vermillion (HgS) for the brighter red in the fruits and viridian green ($Cr_2O_3 \cdot 2H_2O$) in the green foliage.

In Fig. 2, a photograph of the replica and a number of FTIR images (upper row) are shown. The wavenumber region used for the net intensity integration is indicated per FTIR image. For comparison, a number of distribution images obtained by MA-XRPD (lower row) are included as well. Fig. 3 shows the spectra corresponding to the high intensity areas in the MA-rFTIR distribution maps. To obtain these spectra, an average of 16 spectra, belonging to pixels in the high intensity parts of the corresponding areas, was calculated.
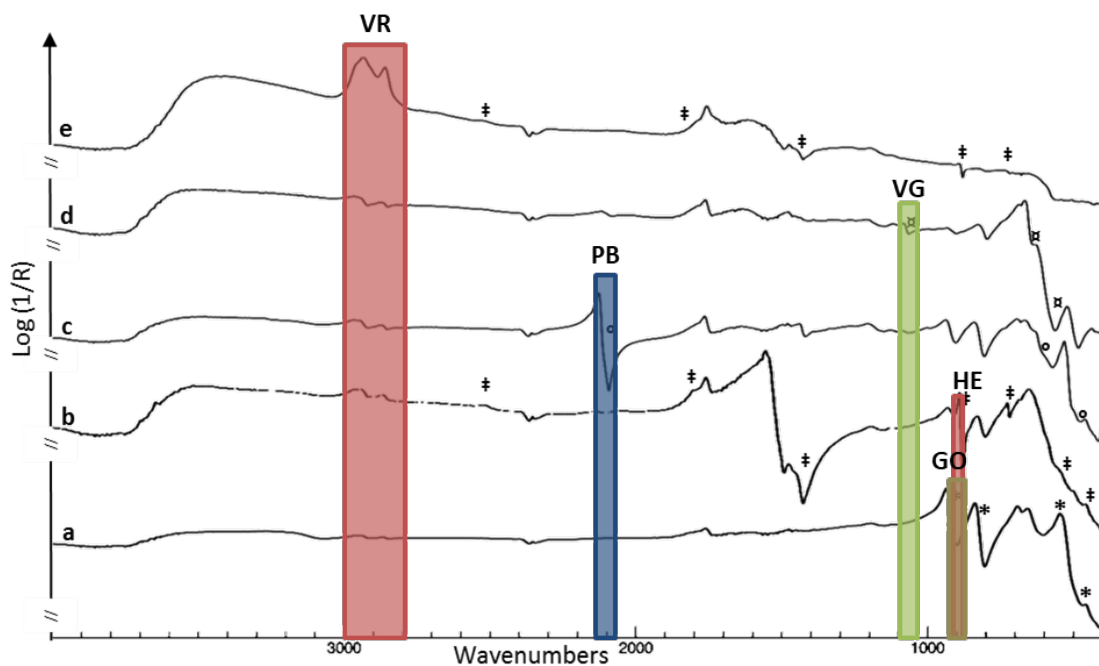
Figure 3: Averaged spectra of highlighted zones in Fig. 2; (a) goethite, (b) calcite/hematite, (c) Prussian blue, (d) viridian green and (e) vermillion.

A feature that allows the differentiation of goethite from hematite is the presence of an – OH group in goethite. This bond results in intense bands (γ-OH: 795 and δ-OH: 892 cm^{-1}, marked by "*" in Fig. 3a) that are observed with the mineral goethite. The inverted δ-OH band of goethite ("GO" in Fig. 3) is used for visualising the goethite distribution. Since this is an inverted band, the resulting intensities were inverted in order to correlate the brightest pixels with the most intense (inverted) bands. This resulting distribution (Fig. 2b) shows a strong correlation with the ochre background colour and, albeit only in the qualitative sense, with the MA-XRPD distribution of goethite shown in Fig. 2g. (The difference between Fig. 2b and g reflects the sampling depth of both methods.) This spectral region is an example of the instrument's ability to discern between products with (partial) overlapping bands. As visible in Fig. 3a, the δ-OH bending band of goethite ("GO" in Fig. 3a) overlaps with the v_2– CO$_3^{2-}$ bending mode of calcite ("HE" in Fig. 3b), however this does not result in interfering distribution maps between these compounds (Fig. 2b and c).

It should be noted that the oxide-related bands of hematite (nominally at 458 and 545 cm^{-1}) and of goethite (at 458 and 566 cm^{-1}) are situated close to each other. Furthermore, the exact position of the bands is prone to shifts in wavenumber due to the pigment's grain size and shape.[24] This explains why the exact wavenumber of these oxide bands is cited in the literature to be in a range of a few tens of wavenumbers wide. Due to the partial mutual overlap between the two minerals, these bands are not well suited for chemical imaging in this painting. Moreover, some of the Cr–O bending bands of viridian

green (marked by "¤" in Fig. 3d) of which the distribution is shown in Fig. 2e and j overlap with those of hematite and goethite. The viridian green distribution (Fig. 2e) was obtained by using the Cr=O stretching band ("VG") and shows a good correlation with the corresponding MA-XRPD distribution in Fig. 2j.

Another way of distinguishing the pigment hematite from goethite in this particular case is to make use of the fact that only hematite has been mixed with calcite ($CaCO_3$), resulting in strong carbonate signals at 713, 875, and 1430 cm^{-1} and the combination bands[19] $v_1 + v_4$ at 1795 cm^{-1} and $v_1 + v_3$ at 2518 cm^{-1}, marked by "‡" in Fig. 3b. Accordingly, in the distribution of Fig. 2c, to which calcite contributes, the same highlights as visible in the MA-XRPD distribution of hematite (Fig. 2h) can be observed.

Prussian blue is chemically and structurally very different from the previous two iron containing pigments, resulting in an IR spectrum that is fairly specific and is characterized by v(CN) at 2097, v(FeC) at 605 and δ(FeCN) bands at 494 cm^{-1} (see "°" in Fig. 3c). The most intense band, as can be seen in Fig. 3c near 2100 cm^{-1}, corresponding to the cyanide group, can be used for chemical imaging (band "PB" in Fig. 3), as shown in Fig. 2d, since there is no danger of interference with signals of other pigments present. An equivalent distribution as that obtainable with MA-XRPD (Fig. 2i) is obtained.

Vermillion itself could not be identified using MA-rFTIR since it has its characteristic bands in the FIR-range due to the heavy atomic mass of mercury, but the presence of this compound appears to have an influence on the shape of the observed MIR spectra in the areas where it is present. As a result, the distribution in Fig. 2f, reflecting the intensity of the C–H stretch vibration corresponding to the organic binder of the pigment (band "VR" in Fig. 3), strongly correlates with the MA-XRPD distribution of vermillion in Fig. 2k. In the area with high intensity, some mixture of calcite and hematite is also present. As a result, the major calcite related bands are visible in the averaged "vermillion" spectrum shown in Fig. 3e, marked by "‡".

In general, finer details can be discerned in the MA-XRPD images, since a smaller spot size (0.3 x 0.3 mm^2) was used in the synchrotron-based MA-XRPD experiment than with the MA-rFTIR scanner. Nevertheless, from Fig. 2 it can be concluded that species-specific distribution images of good image quality and in which most of the details of the painted representation are visible can be recorded with the mobile MA-rFTIR scanner. Note that when comparing the different spectra in Fig. 3, the two OH-bending bands of goethite (795 and 892 cm^{-1}) seem to appear in most of the averaged spectra. This is a result of the fact that the spot size of the IR-beam is larger than the examined features; this does not seem to disturb the resulting distribution map overly much, however.

2.1.3.2 *Analysis of an Antillean painting*

As a second case study, we consider a small (8 x 8 cm²) 20th century, unvarnished Antillean panel painting shown in Fig. 4a. It consists of a number of coloured areas of appropriate sizes to be imaged by the scanner; in addition, its stratigraphy is fairly simple, in most cases consisting of only one paint layer applied on a calcite ground. As a result, the ($v_1 + v_3$) combination band of calcite (shown in Fig. 5) is visible in all recorded FTIR spectra.

Red and orange areas: MA-XRF analysis of this painting (see Fig. 4, lower row) reveals the presence of the elements cadmium, selenium, sulphur and barium (last three distributions are not shown in this article) in the red and orange regions, strongly suggesting that the pigment employed here is cadmium lithopone ($CdSe + BaSO_4$). Cadmium-based pigments have, due to the heavy atomic mass of cadmium, their fundamental bands in the far-IR (FIR) region and therefore cannot be detected with the MIR setup. However, these pigments are often adulterated with the less expensive barium sulphate ($BaSO_4$). The sulphate ions present in this filler are well visible in the MIR-range ($v_4–SO_4^{2-}$ at 612 and 640 cm⁻¹, $v_1–SO_4^{2-}$ at 983 cm⁻¹ and $v_3–SO_4^{2-}$ at 1079, 1126 and 1202 cm⁻¹).[19,25] These vibrational bands confirm the presence of barium sulphate and thus cadmium lithopone in the orange areas. The map in Fig. 4b (1148–1200 cm⁻¹) shows the distribution of the sulphate ion *via* its inverted antisymmetric stretching vibration mode ($v_3–SO_4^{2-}$) which is strongly correlated with the Cd MA-XRF maps of Fig. 4f.
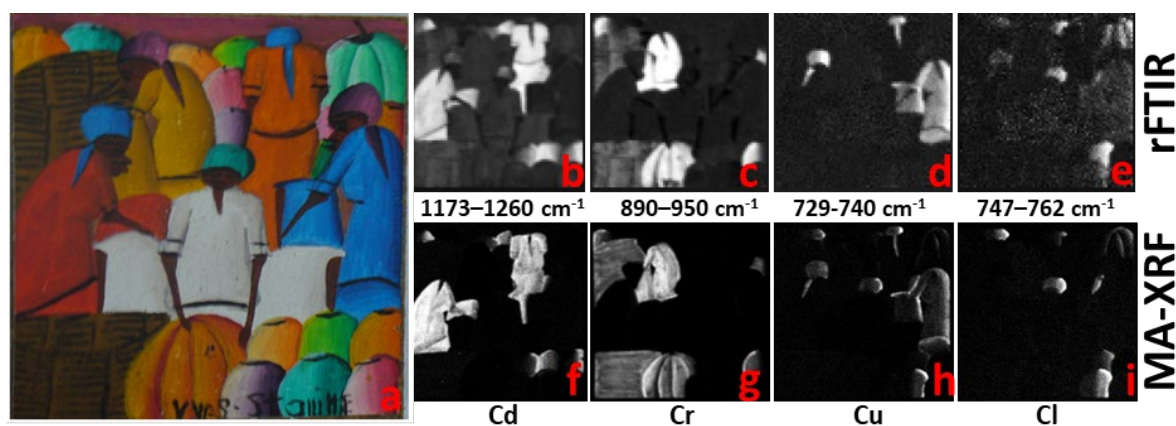

Figure 4: (a) Visual image of the Antillean painting; MA-rFTIR chemical distribution images: (b) barium sulphate (1148–1200 cm⁻¹), (c) chrome yellow (770–895 cm⁻¹), (d) phthalocyanine blue (729–740 cm⁻¹) and (e) phthalocyanine green (747–762 cm⁻¹); elemental distribution maps of (f) cadmium, (g) chromium, (h) copper and (i) chlorine. Lighter tones indicate higher levels of net pseudo-absorbance or X-ray fluorescence intensity.

Yellow areas: based on the MA-XRF-data, the main yellow pigment present in this painting contains the elements lead and chromium and in the FTIR spectra it is identified by its chromate ($v_4–CrO_4^{2-}$ at 888 cm⁻¹) and sulphate ($v_4–SO_4^{2-}$ at 604 and 630 cm⁻¹) ion bands as chrome yellow ($PbCr_{1-x}S_xO_4$), a pigment that is in use since the 19th century. The

map in Fig. 4c is based on the CrO_4^{2-} inverted asymmetric stretch (770–895 cm^{-1}) and shows a good correlation with the chromium XRF image (Fig. 4g). Even though the fact that both barium sulphate and chrome yellow comprise sulphate groups in their molecules, no hindering interference between these distributions occurred. The presence of heavier lead instead of barium resulted in a shift towards lower wavenumbers for sulphate bending and stretching bands for the chrome yellow pigment. Besides this shift, the sulphate bands in chrome yellow are of lesser intensity and broadened in comparison to those of barium sulphate. The combination of these effects resulted in interference-free distribution images.
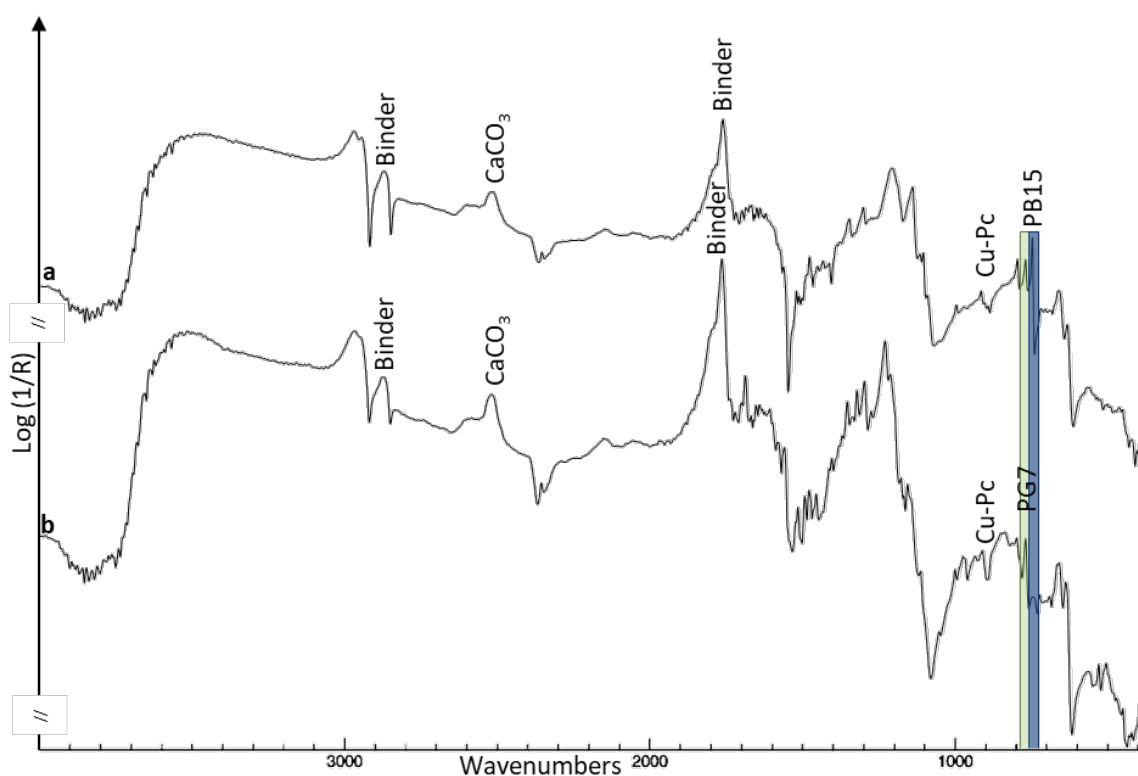

*Figure 5: Pseudo-absorption converted reflectance spectra of the phthalocyanine pigments (**a**) PB15 and (**b**) PG7; "Cu–Pc" marks the band assigned to the copper–phthalocyanine vibration; "PB15" marks the band used for imaging the blue pigment, while "PG7" marks the band used for the green pigment; "CaCO₃" marks the most intense calcite band and "Binder" marks those due to the binding medium.*

Blue and green areas: the blue and green pigments present in this painting could be identified as phthalocyanine-based pigments. Since this group of pigments was only discovered in the 1930s, their presence confirms the presumed 20th century origin of the painting. The absence of the N–H bending band at 1003 cm^{-1} (Fig. 5b) suggests that the phthalocyanine molecules are present as organo–metalo complexes. Together with the presence of the metal–ligand vibration at 898 cm^{-1}, typical for copper, these pigments are

identified as copper–phthalocyanine. This identification is confirmed by the copper distribution image obtained by MA-XRF (see Fig. 4h).

The phthalocyanine-blue (PB15) distribution (Fig. 4d) can be visualized by means of its C–H out-of-plane bending mode at 729–740 cm^{-1} (see Fig. 5a). Phthalocyanine green (PG7) is a partially chlorinated version of PB15. This substitution results in a shift of the C–H out-of-plane bending mode band towards higher wavenumbers, in this case to 747–762 cm^{-1} (see Fig. 5b). Therefore, these modes can be used for imaging the distribution of PG7 (Fig. 4e) as well as that of PB15 (Fig. 4d). As a comparison, the copper and chlorine XRF-maps are given in Fig. 4h and i. Since copper is present in both PB15 and PG7, the MA-XRF copper map resembles the sum distribution of both these pigments. It is possible, however, to distinguish between these two pigments in the MA-XRF data by considering the chlorine distribution (Fig. 4i) since the latter element is only present in PG7. The species-specific MA-rFTIR maps, however, allow the visualization of the distribution of these two highly similar pigments in a more straightforward and reliable manner.
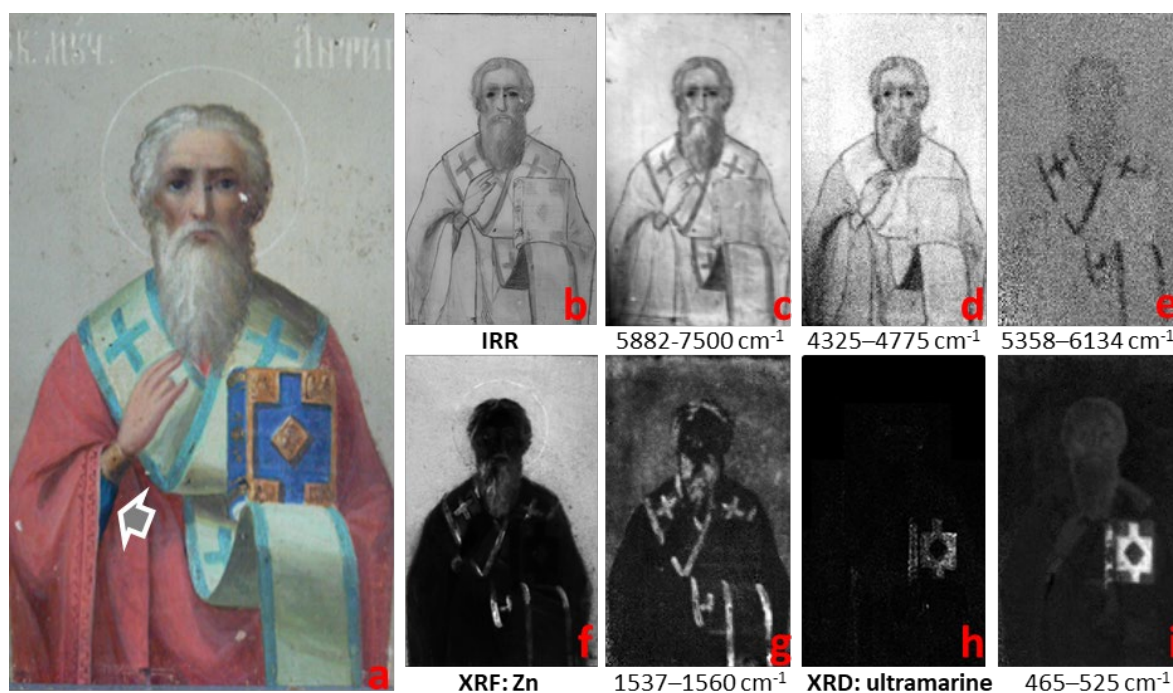

*Figure 6: (**a**) Visual photograph of the Saint Nicholas' icon; the arrow indicates the blue sleeve of the saint; (**b**) corresponding IRR image; (**c**) total MA-rFTIR reflectance image in the spectral range corresponding to the IRR image; (**d**) underdrawing (MA-rFTIR); (**e**) decorative bands on the stole (MA-rFTIR); (**f**) Zn distribution (MA-XRF); (**g**) asymmetric carboxylate stretching mode of zinc soap (MA-rFTIR); (**h**) ultramarine (MA-XRPD) and (**i**) ultramarine (MA-rFTIR distribution, Al, Si–O bending mode). Lighter tones indicate higher levels of net pseudo-absorbance or diffraction intensity.*

2.1.3.3 *Analysis of a 19th century Saint Nicholas icon*

As a third case study with a more complex stratigraphy, MA-rFTIR images from a 19th century Russian house icon depicting Saint Nicholas of Myra, painted on a wooden panel (14 x 18 cm), were recorded. This artefact, visible in Fig. 6a, was subjected to different non-destructive imaging methods.

The visualization of hidden underdrawings in paintings is traditionally performed *via* IRR imaging, as illustrated in Fig. 6b. This reflectogram was obtained with a SIRIS camera system,[26] sensitive in the NIR-range (900–1700 nm or 11 111– 5882 cm^{-1}). Since there is a spectral overlap (1333–1700 nm or 7500–5882 cm^{-1}) between the SIRIS camera system and the MA-rFTIR scanner, similar results can be obtained with the latter setup when the recorded FTIR spectra are treated in a similar manner as done by the SIRIS camera software: the reflectance spectra are used in total reflection mode, no baseline subtraction is performed and the total reflectance intensity is summed within a wide spectral range (7500–5882 cm^{-1} in this case). The result is shown in Fig. 6c; comparison with the IRR image of Fig. 6b shows that even at a lower lateral resolution, the MA-rFTIR result shows most of the details present in the IRR. Since a wide spectral band is used for such imaging techniques, more components rather than solely the underdrawing may contribute to the resulting images. An advantage of the MA-rFTIR scanner is that simultaneously using the wide NIR range, several narrower spectral ranges in the MIR part of the spectrum can be used for the imaging of specific compounds, and that these spectral ranges do not need to be specified prior to the measurements (as is the case when filters are employed in NIR-imaging setups). Narrowing a spectral range for imaging purposes has the advantage that this allows scientists to separate the different contributions to wideband images. For example, a detailed examination of the light green decorative lines and crosses on the stole of the Saint that are visible in the IRR image shows that these are likely features that were added in the final phase of the painting and do not correspond to any carbon-based drawing made in the initial phases. When considering more narrow spectral bandwidths in the NIR, the chemical distribution image of Fig. 6e (5358–6134 cm^{-1}) can be obtained that only shows the details of the stole, while the carbon-based underdrawing (without stole details) is present in another non-overlapping spectral range (4325–4775 cm^{-1}, Fig. 6d; note that in order to obtain the maps 6d and e, the intensity of the reflection spectra was employed without the usual conversion to pseudo-absorbance form). The NIR-band to which these spectral ranges belong is known for the presence of combination and overtone bands of the fundamental MIR bands. Recently, these bands have successfully been used for mapping paint binders in Early Renaissance paintings.[27] Even though this paper shows the possible use of those bands, they were not used as such for this experiment. The narrower NIR bands were solely used for their ability to differentiate between the underdrawing and the overpainted detail.

The distribution of zinc white (ZnO), present in the grey background, the beard of the figure and the decorations of the stole can be obtained *via* the intense (and perturbed) reflection FTIR band around 500 cm^{-1}; in transmission spectra this band is present as a broad spectral feature between 400 and 500 cm^{-1}. Because multiple metal-oxide bands belonging to different metals are present close to each other in this spectral region, distribution images with good contrast are difficult to obtain based on the Zn–O stretching mode. A better result can be obtained by using the asymmetric COO$^-$ stretching mode, as shown in Fig. 6g (1537–1560 cm^{-1}). This band is shifted in the spectrum due to the saponification of the binding medium under the influence of zinc ions.[28] When comparing the distribution of the element zinc (Fig. 6f) with the distribution of the zinc soap (Fig. 6g), one can see that the intensity of the zinc soap is lower in the grey background area than what would be expected based on the intensity in the MA-XRF Zn distribution image. This may be due to the fact that the zinc oxide in the stole decoration is not present in the form of pure zinc white, but as cobalt green (CoO·ZnO) mixed with chromium oxide (Cr$_2$O$_3$). This is consistent with the correlated presence of zinc, cobalt and chrome in the blue-green decorative stripes and crosses of the stole as revealed by MA-XRF (resulting Co and Cr elemental distributions are not shown in Fig. 6). The data suggest that the different chemical environments of the zinc ions in the blue-green and grey areas of the painting have resulted in a different spectral response and possibly in different degrees of saponification of the binding medium.

One of the limitations of MA-XRF is that it is insensitive to low Z-elements. These elements have low energetic XRF-signals that are absorbed by ambient air; consequently, generally it is not possible to visualize any elements lighter than potassium. This absorption can be avoided by working under vacuum or (more realistically) by replacing ambient air by helium flow; however, the latter method may induce stress into the painting, which can result in damage. Because of their lower atomic mass, chemical bonds between low Z-elements and oxygen have their fundamental bands in the MIR range of the electromagnetic spectrum, making MA-rFTIR a possible complementary technique to MA-XRF. The pigment ultramarine (Na$_{8-10}$Al$_6$Si$_6$O$_{24}$S$_{2-4}$) is well suited to demonstrate this complementarity since this inorganic pigment consists only of low Z-elements and thus is hard to be detected by means of MA-XRF. Fig. 6i demonstrates that by using the pseudo-absorbance in the 465–525 cm^{-1} range (Al, Si–O bending mode[29]), MA-rFTIR allows the creation of a clear map (Fig. 6i) of the distribution of this pigment. The presence of artificial ultramarine is consistent with the 19th century origin of the icon. This pigment is chemically identical to the expensive medieval ultramarine pigment which was obtained from the semi-precious stone lapis lazuli, exclusively mined in the Afghan mountains at that time. In Fig. 6i and h, the ultramarine distributions obtained by MA-rFTIR and MA-XRPD are compared. Both distributions show that only the blue part of the gospel book was painted with this pigment; the Saint's sleeve (see the arrow in Fig. 6) even though being painted in a similar blue is not highlighted in these distributions, since it was rendered using Prussian blue.

2.1.4 **Conclusion**

By means of the prototype MA-rFTIR scanner that is described in this paper, we demonstrate that the scanning reflectance Fourier transform mid-infrared technique is useful for *in situ* non-destructive chemical imaging of planar cultural heritage artifacts. Since this device scans the object point-by-point, while recording full spectra over an extended MIR-range (7500– 375 cm^{-1}) at each position, it is possible to identify the compounds present and visualize their distribution based on their MIR fingerprint features.

When compared to MA-XRF elemental distributions, the obtained chemical distributions show a good correlation with the elemental maps when the chemical element in question is only present in one pigment. MA-rFTIR can deliver complementary information for pigments that cannot be detected or identified in a unique manner by means of MA-XRF. When differentiating between multiple pigments that contain the same characteristic elements, the chemical distribution maps obtained by MA-rFTIR show good agreement with those obtained by MA-XRPD.

By analysing different works of art of increasing complexity in terms of paint stratigraphy and pigment variety, the possibilities and some of the drawbacks of MA-rFTIR could be inventoried: the investigation of a replica of a vegetal decoration was useful to demonstrate the ability of the method to differentiate between various iron-containing pigments. Since these pigments are available in different colours, distinguishing between these pigments can help to understand the artist's techniques and to restore altered paintings back to their original status. The analysis of an Antillean panel painting highlighted the ability of MA-rFTIR to imagine the distribution of different phthalocyanine pigments. This is important since many pigments developed during the last century are organic. Moreover, some organic dyes such as lakes are in use since antiquity and are hard to identify by non-destructive methods. The analysis of a 19th century Russian icon allows the demonstration of the capability of the instrument to visualize overpainted underdrawings and to record the distribution of pigments based on light Z-elements such as ultramarine.

Based on these first results, future analysis campaigns on old masterpieces should be undertaken to obtain a better understanding of the chemical imaging of pigments and overpaintings.

A major important limitation of the prototype MA-rFTIR instrument described above is the time required to record a hyperspectral dataset. However, many possibilities are available to improve this aspect, including the use of a more powerful source of MIR radiation and of larger beam focusing and/or collection optics for the reflected radiation.

Another limiting factor in this process is the fact that the majority of historic paintings is covered by a varnish layer to protect and saturate the underlying painting. Such layers absorb most of the MIR radiation and as a result strongly disturb the results. Fortunately not all paintings are covered by a varnish layer and from many paintings under restoration, the varnish is removed in the preliminary phases of the treatment. Similar to other forms of mobile FTIR, MA-rFTIR could then be used under optimal conditions once or several times during a restoration campaign. Beside these unvarnished paintings, it is also relevant to investigate in greater detail the possibilities and limits of MA-rFTIR investigations of thinly varnished paintings; experience has shown that, in a number of such cases, by means of portable FTIR devices such as the Bruker Alpha, meaningful spectral features can still be recorded.

Acknowledgements

References

1. C. Miliani, F. Rosi, B. G. Brunetti and A. Sgamellotti, Acc. Chem. Res., 2010, 43, 728–738.
2. C. Miliani, F. Rosi, I. Borghia, P. Benedetti, B. G. Brunetti and A. Sgamellotti, Appl. Spectrosc., 2007, 61, 293–299.
3. L. De Viguerie, P. Walter, E. Laval, B. Mottin and V. A. Solé, Angew. Chem., Int. Ed., 2010, 49, 6125–6128.
4. A. Romani, C. Clementi, C. Miliani and G. Favaro, Acc. Chem. Res., 2010, 43, 837–846.
5. G. Chiari, Nature, 2008, 453, 159.
6. F. Rosi, C. Miliani, C. Clementi, K. Kahrim, F. Presciutti, M. Vagnini, V. Manuali, A. Daveri, L. Cartechnini, B. G. Brunetti and A. Sgamellotti, Appl. Phys. A: Mater. Sci. Process., 2010, 100, 613–624.
7. F. Rosi, V. Manuali, T. Grygar, P. Bezdicka, B. G. Brunetti, A. Sgamellotti, L. Burgio, C. Seccaroni and C. Miliani, J. Raman Spectrosc., 2011, 42, 407–414.
8. M. Alfeld, K. Janssens, J. Dik, W. de Nolf and G. van der Snickt, J. Anal. At. Spectrom., 2011, 26, 899–909.
9. J. R. J. Van Asperen de Boer, Appl. Opt., 1968, 7, 1711–1714.
10. J. R. Mansfield, M. Attas, C. Majzels, E. Cloutis, C. Collins and H. H. Mantsch, Vib. Spectrosc., 2002, 28, 59–66.
11. C. Bonifazzi, P. Carcagni, R. Fontana, M. Greco, M. Mastroianni, M. Materazzi, E. Pampaloni, L. Pezzati and D. Bencini, J. Opt. A: Pure Appl. Opt., 2008, 10, 064011.

12.   C. Daffara, E. Pampaloni, L. Pezzati, M. Barucci and R. Fontana, Acc. Chem. Res., 2010, 43, 847–856.

13.   C. Fisher and I. Kakoulli, Rev. Conserv., 2006, 7, 3–16.

14.   H. Liang, Appl. Phys. A: Mater. Sci. Process., 2011, 106, 309– 323.

15.   J. K. Delaney, J. G. Ziebel, M. Thoury, R. Litteton, K. M. Morales, M. Palmer and E. Rene de la Rie, Proc. SPIE, 2009, 7391.

16.   F. Rosi, C. Miliani, R. Braun, R. Harig, D. Sali, B. G. Brunetti and A. Sgamellotti, Angew. Chem., Int. Ed., 2013, 52, 1–5.

17.   S. Vahur, A. Teearu and I. Leito, Spectrochim. Acta, Part A, 2010, 75, 1061–1072.

18.   K.   Castro,M.   Perez, M.   D.   Rodrieguez-Laso   and J. M. adariaga, Anal. Chem., 2003, 75, 214–221.

19.   C. Miliani, F. Rosi, A. Daveri and B. G. Brunetti, Appl. Phys. A: Mater. Sci. Process., 2012, 106, 295–307.

20.   D. Buti, F. Rosi, B. G. Brunetti and C. Miliani, Anal. Bioanal. Chem., 2013, 405, 2699–2711.

21.   V. A. Solé, E. Papillon, M. Cotte, Ph. Walter and J. Susini, Spectrochim. Acta, Part B, 2007, 62, 63–68.

22.   W. De Nolf and K. Janssens, Surf. Interface Anal., 2010, 42, 411–418.

23.   G. Van Der Snickt, W. De Nolf, B. Vekemans and K. Janssens, Appl. Phys. A: Mater. Sci. Process., 2008, 92, 59–68.

24.   J. L. Rendon and C. J. Serna, Clay Miner., 1981, 16, 375– 381.

25.   V. Ramaswamy, R. M. Vimalathithan and V. Ponnusamy, Adv. Mater. Lett., 2012, 3, 29–33.

26.   D. Saunders, R. Billinge, J. Cupitt, N. Atkinson and H. Liang, Stud. Conserv., 2006, 51, 277–290.

27.   K. A. Dooley, S. Lomax, J. G. Zeibel, C. Miliani, P. Ricciardi, A. Hoenigswald, M. Loew and J. K. Delaney, Analyst, 2013, 138, 4838–4848.

28.   L.   Robinet   and   M.   Corbeil, Stud. Conserv.,   2003, 48, 23–40.

29.   C. Miliani, A. Daveri, B. G. Bruinetti and A. Sgamellotti, Chem. Phys. Lett., 2008, 466, 148–151.

2.2 Macroscopic mid-FTIR mapping and clustering-based automated datareduction: An advanced diagnostic tool for *in situ* investigations of artworks

Abstract The present study describes a multivariate strategy that can be used for automatic on-site processing of reflection mode macro FTIR mapping (MA-rFTIR) data obtained during investigation of artworks. The chemometric strategy is based on the integration of principal component analysis (PCA) with a clustering approach in the space subtended by the three lowest-order principal components and allows to automatically identify the regions of interest (ROIs) of the area scanned and to extract the average FTIR spectra related to each ROI. Thanks to the automatic data management, in-field HSI (hyperspectral imaging)-based analyses may be performed even by staff lacking specific advanced chemometric expertise, as it is sometimes the case for conservation scientists or conservators with a scientific background. MA-rFTIR was only recently introduced in the conservation field and, in this work the technique was employed to characterize the surface of metallic artefacts. The analytical protocol was employed as part of a rapid procedure to evaluate the conservation state and the performance of cleaning methods on bronze objects. Both activities are commonly part of restoration campaigns of bronzes and require an on-site analytical procedure for efficient and effective diagnosis. The performance of the method was first evaluated on aged standard samples (bronzes with a layer of green basic copper hydroxysulphate, treated with different organic coatings) and then scrutinized *in situ* on areas of the 16th century Neptune fountain statue (Piazza del Nettuno, Bologna, Italy) by Gianbologna.

2.2.1 Introduction

Non-invasive techniques are essential tools for analysis in the field of conservation, because they preserve the integrity of the artwork and allow an extensive documentation of its surface to be acquired. Several miniaturized devices have been developed that allow for *in situ* examinations. In this way, the risks and costs related to handling artworks are reduced. Spectroscopic hyperspectral-based analyses allow for easy and extensive investigations on the surface of an object, providing the possibility to obtain chemical images related to the distribution of a single molecular species/moiety or of a single chemical element. Data acquisition can be carried out by full field or pencil-beam imaging methods, which produce, in both cases, a 3D data matrix [1]. This 3D data matrix contains the spatial information in two (x and y) dimensions, while the spectral information is present in the third (z) dimension. To date, macroscopic X-ray fluorescence scanning (MA-

XRF) [2,3] and visible-near infrared (VNIR) or short-wave infrared (SWIR) devices are the most widely used hyperspectral instruments for the in-situ analysis of paintings [4,5] and illuminated manuscripts [6,7]. The use of the mid infrared (MIR) spectral region for macroscopic imaging or mapping analysis in the reflection mode (MA-rFTIR) represents a quite attractive but poorly explored approach, due to limitations concerning instrument costs. The imaging systems so far proposed for the analysis of paintings [8,9] operates in a reduced spectral subregion of MIR: 1400-900 cm^{-1} [8] and 3700-1800 cm^{-1} [9]. Additionally, a low-noise MIR imaging spectrometer operating in the region 1240-760 cm^{-1} for fast acquisition of paintings has been presented [10]. The high cost of these instruments, together with the limit in terms of detectable spectral range, make a wide application in museums or private laboratories prohibitive. As a powerful alternative to avoid the use of an expensive focal plane array (FPA) detector, an in-house portable point-scan FTIR spectrometer mounted on a motorized 3D stage has been recently proposed for the mapping of chemical species on paintings. This compact and cost-effective spectrometer has also the advantage to cover the entire MIR range and a portion of the NIR range (7500-375 cm^{-1}) [11,12].

In the present research, an innovative chemometric strategy was developed to improve the processing of hyperspectral data. The automated approach proposed allows to reduce the time required for data processing. By maximizing the degree of automation of the procedure, data analysis is rendered easier and becomes more directly applicable by personnel that does not have advanced chemometric insights; often, such is the case for conservation scientists or conservators. The strategy allows to automatically identify (sub)regions of interest (ROIs) in the area scanned, after application of principal component analysis (PCA) on the FTIR spectral 3D data matrix. In a second phase, the PC score maps are automatically clustered by the density-based spatial clustering of applications with noise (DBSCAN) algorithm [13]. In the present study, the DBSCAN algorithm was integrated with PCA for the processing of hyperspectral data. The DBSCAN algorithm presented peculiar advantages, compared with other clustering algorithms: (i) minimal requirements of domain knowledge to determine the input parameter, (ii) identification of clusters of irregular shape, (iii) good efficiency on large databases. Most important, DBSCAN does not require neither the a-priori definition of the number of clusters nor a decisional intervention by the operator. This allowed a more efficient extraction of information, in an automatic way, which was the purpose of the strategy proposed. In this manner, for each ROI, the corresponding average FTIR spectrum is obtained. Evaluation of the spectral profiles can then be performed to achieve a better understanding of the chemical variability within the selected area. With a single-step approach, the automatic algorithm allows to obtain: (i) the proper selection of the most representative areas (in terms of spectral information and number of pixels), (ii) the automatic extraction of the most significant spectra from all the investigated areas.

PCA-based chemometrics approaches coupled with MIR spectroscopy have already been proposed for the investigation of micro cross-sections of paintings [14,15]. Different statistical methods have been also presented for the data management and reduction of reflectance 3D data matrices obtained in visible – near infrared (V-NIR) and shortwave infrared (SWIR) ranges. Among others, methods that enable the identification and mapping of most representative spectra ("endmembers") in the 3D data matrix are well established in the field of cultural heritage. In particular, methods based on the use of the so-called hourglass paradigm (ENVI software, Harris Corporation, Melbourne, FL, USA) to extract the endmembers and combined with the spectral angle-mapping (SAM) algorithm, to visualize the pigment distributions, have been successfully employed for the study of illuminated manuscripts and paintings [4,5]. Nevertheless, the complexity of these chemometric data processing requires a deep expertise in multivariate analysis and a lot of super-vised/manual interpretation efforts [16]. These requirements are not always compatible with on-site diagnostic campaigns and cannot guarantee that the results will be obtained in real time.

The chemometric strategy here presented was developed to quickly and easily obtain chemical information from complex dataset. In particular, application of MA-rFTIR mapping analysis on metal patinas is described. The results provide information on the state of conservation to support the on-site development of appropriate conservation treatments, during ongoing restoration campaigns. Indeed, although MA-rFTIR systems usually required a long acquisition time for the analysis of rather small areas, the application of a fast data processing method may help in reducing the overall investigation time.

Recently, in-situ hyperspectral imaging in the short-wave infrared (SWIR) region was successfully used to map two bronze corrosion products, brochantite and antlerite, on the surface of the outdoor bronze sculpture the "*Man with the Key*" by Auguste Rodin in Oslo [17]. In that study, two areas of the corroded bronze were analyzed and data were successively processed by an "ad hoc" multivariate approach based on singular value decomposition (SVD), iterative key set factor analysis (IKSFA) and spectral angle mapping (SAM). The approach first seeks and extracts the purest spectra from the 3D data matrix (SVD and IKSFA). Successively, by means of overtones and combination bands, the purest spectra are assigned to a pertinent corrosion product. Spatial distribution of the identified corrosion compounds is eventually obtained by the SAM algorithm. Although combination bands and higher overtones of fundamental vibrations proved to be useful in the identification of corrosion products, they suffer from lower selectivity in comparison to the bands in the fingerprint MIR range, with the risk of loss of important information.

Here, the proposed analytical protocol was tested as a time-efficient manner of evaluating the conservation state of bronze objects, by identifying both corrosion products and coatings and exploiting the diagnostic and selective character of mid-IR

range, and the performance of associated cleaning methods. These two activities are commonly part of restoration campaigns and need to be supported in real time with an easy and suitable analytical procedure. The MA-rFTIR approach combined with automated data elaboration proved to be efficient in showing the distribution of organic treatment residuals as well as the presence of the corrosion product brochantite. The distribution maps obtained can clearly offer a valid help to restorers in taking important decision on the restoration of the sculpture. The information acquired is meaningful and the millimeter-size spatial resolution, low compared to a SWIR-NIR hyperspectral camera, does not highly affect the information that can be extracted.

Subsequently, analysis of MA-rFTIR data obtained from standard copper coupons, with a green copper hydroxysulfate (brochantite) patina and different protective coatings, is discussed. After that, the application of the data reduction procedure to hyperspectral maps obtained from the 16th century Neptune fountain in Bologna, Italy, and collected *in situ* during the last restoration campaign in 2016, is described. The first aim of the latter investigation was to understand and document the state of conservation of the bronze surface by considering the distribution of corrosion products and the presence of residual treatment compounds applied during the all-but-last restoration in 1989–1990 [18]. As a second goal, the suitability of the MA-rFTIR system for *in situ* monitoring of the efficacy of cleaning procedures aimed at removing deteriorated coatings from the metal surface was evaluated.

2.2.2 Materials and methods

2.2.2.1 *Samples*

Two copper plates (5 × 7 cm²), named R6 and R57, were selected as test samples (Figs. 1a and 2a). The copper substrate is covered by a thin layer of brochantite ($Cu_4SO_4(OH)_6$) formed naturally by exposure to the urban atmosphere of Munich (Germany) for almost 80 years. Each sample has been divided in three equally-sized rectangular areas of dimension 1.6 × 7.0 cm². The first area, denoted with letter *B* was untreated with plain brochantite as a reference; the second area, denoted as *I*, was covered with a protective layer of Incralac, an acrylic resin-based formulation; the third area, denoted as *W* was treated first with Incralac and, successively, with a layer of microcrystalline wax. R6 was prepared in 2005 and exposed for 8 months in the urban atmosphere of Venice [19]. R57 was prepared in 2011 but never exposed to the outside atmosphere. The two coupons were preserved over the years in a controlled indoor laboratory environment. Incralac and microcrystalline wax R21 were purchased from Phase Srl (Bologna, Italy). The real case under examination was the famous renaissance bronze sculpture of Neptune by the sculptor Gianbologna, situated in Piazza del Nettuno, Bologna, Italy.
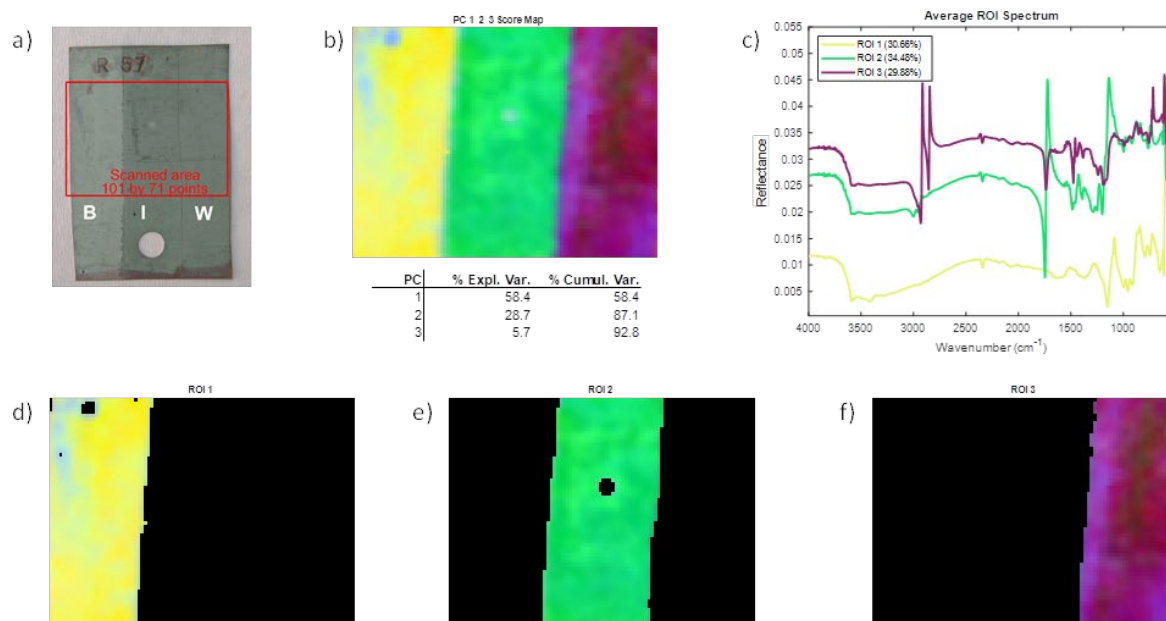
*Figure 1: Sample R57. **a**) RGB picture – the red rectangle indicates the area submitted to MA-rFTIR mapping analysis. R57 was scanned over an area of 50.5 by 35.5 mm²; **b**) PC1,2,3 score map; **c**) average spectra extracted from the ROIs; **d**) ROI 1; **e**) ROI 2; **f**) ROI 3. ROI 1 describes the distribution of brochantite, ROI 2 the distribution of Incralac and ROI 3 the distribution of wax applied over the Incralac layer. (For interpretation of the references to color in this figure legend, the reader is referred to the Web version of this article.)*

2.2.2.2 *FTIR macro mapping*

MA-rFTIR scans were performed, using an in-house portable point-scan FTIR spectrometer mounted on a motorized 3D stage [11]. The core of the instrument is an Alpha FTIR spectrometer (Bruker, Billerica, MA, USA), equipped with a frontal reflectance module (20°/20° geometry), controlled by OPUS 6.0 software (Bruker, Billerica, MA, USA). The spectra were acquired in reflection mode in the range 375–7500 cm⁻¹ with a spectral resolution of 4 cm⁻¹. The spectrometer is positioned during the scan on a $100 \times 250 \times 100$ mm³ motion system (Newport Corporation, Irvine, CA, USA). X and Y stages are employed for the actual scanning motion, while the Z stage is used to bring the XY scanning plane parallel to the object under investigation. Prior to each scan, a background measurement of 15 min was performed to compensate for infrared-absorbing compounds in the environment atmosphere. Approximately 10 min was necessary to position the instrument probe-head in front of the sample to be analyzed, at 1.5 cm distance. The copper plates were analyzed by scanning an area of 50.5×35.5 mm² on sample R57 and 51.5×33 mm² on sample R6, with the acquisition time per pixel of 3 s, following a 0.5×0.5 mm² grid. The acquisition time of each area was approximately 15 h. Regarding the scanning of the Neptune sculpture, the acquisition time per pixel was 3 s, using a 1×1 mm² grid. The analyzed areas have dimension 42×40 mm² and 22×22 mm²; the acquisition time was 4 h for the first area and 1 h and 10 min for the second area.

119

2.2.2.3 *Data processing*

Three-dimensional data arrays corresponding to hyperspectral maps were preliminarily unfolded to two-dimensional data matrices, in which the rows correspond to pixels while the columns refer to spectral variables, to allow direct processing by means of principal component analysis (PCA). The unfolded 2D matrices were pre-processed by means of the standard normal variate (SNV) transform [20,21] to correct for undesired physical variations within spectra, and by column mean-centering. PCA was then applied, resulting in a score matrix, with as many rows as the pixels of the map and as many columns as the principal components (PCs) retained [22]. Score values (i.e. the magnitude of the various PCs in each pixel) were used to construct a composite score map as a false-color image in which the red, green and blue channels are encoded by the PC1, PC2 and PC3 score values, respectively, under the assumption that the three lowest-order PCs embody the most relevant information. This is reasonable for highly inter-correlated variables, such as spectral ones. Score values were preliminarily scaled between 0 and 255 in each channel. This type of combined maps allows to efficiently identify areas characterized by different score values and, thus, by a different spectral response thanks to their different colors. To recognize the regions of interest (ROIs, a specific spatial region identified within the analyzed area) in an automated manner, the density-based spatial clustering of applications with noise (DBSCAN) algorithm [13] was applied, using PC1-to-PC3 scaled score values as the input variables and pixels as the objects to be clustered. The DBSCAN algorithm identifies groupings of pixels that have similar sets of scores and, therefore, similar false colors in the composite map. Other clustering approaches were previously used for automated clustering of spectral data in a reduced PCA space [23]. DBSCAN identifies non-linearly separable clusters, defined as groupings of objects that are mutually close to each other within a high-density region in the multivariate space. Two parameters must be set: minPts (the minimum number of objects that may define a cluster) and ε (the maximum radius of the neighborhood from an object in which other objects are considered as belonging to the same cluster). In the present study, minPts was set equal to N/120, where N is the total number of pixels in the map, and ε was set equal to 19, from empirical evaluations. The choice of the clustering parameters has been optimized for this type of spectral data and the user does not have to change these settings while operating. These parameters can be, in fact, reasonably maintained constant for analyzing data of the same typology.

Clusters of pixels identified by DBSCAN, corresponding to relevant ROIs in the area mapped can be directly highlighted. Clustering is a necessary step in the proposed strategy, to automatically provide the operator with the chemical information (from the averaged spectrum) related to the regions of interest within the map. Simultaneously, the average spectral profile of the pixels constituting each ROI can be computed and plotted, with a color-coded indication of the correspondence ROI-spectrum. This combination of automatic identification of ROIs performed by DBSCAN – with ROI visualization on the map – and of the extraction of their average spectra constitutes a very efficient data reduction and exploration procedure, in which the intervention of the user is essentially

unnecessary. Multivariate data processing and analysis of graphical outputs were performed by means of ad hoc in-house Matlab routines (The MathWorks, Inc., Natick, USA, Version 2018a).

2.2.3 Results and discussion

2.2.3.1 *Model bronze samples*

The automatic chemometric processing developed for MIR macro mapping data was tested to quickly solve some diagnostic problems, which usually occurs during a restoration campaign on historical metal artefacts. Before defining the appropriate conservation strategy, it is relevant to identify the state of conservation of an artwork in terms of occurrence of degradation products and the distribution of previous coatings. These two points allow to decide whether it is necessary to remove any residual coatings applied during past treatments and to apply (one or more) new ones, and if the object must be treated with a corrosion inhibitor (for example, in case of active corrosion processes due to the presence of chlorides). These two restoration activities usually need to be supported by results of analytical investigations that can be performed relatively quickly on site, and at the same time/just prior to the actual restoration activities.

The new analytical method was first tested on model bronze samples R6 and R57, naturally aged in urban environments and treated with traditional protective coatings. For each copper plate, a scan area encompassing the three different regions was selected and mapped by MA-rFTIR (Figs. 1a and 2a). After the acquisition of the MIR chemical maps, the 3D data matrices were submitted to the automatic multivariate data processing. PCA combined with clustering allowed an automatic selection of characteristic ROIs in the mapped area.

From the 3D data matrix obtained from sample R57 (only exposed to indoor atmosphere), the automatic data analysis produced an RGB false color PC1,2,3 score map, in which three different ROIs were identified that could be associated with the three different regions of the sample (Fig. 1b). The use of the three lowest-order PCs allowed to guarantee a minimal intervention by technical operators. In fact, for data – such as spectroscopic ones – in which variables are highly inter-correlated, the most relevant information is usually concentrated in the first two or three PCs [24]. Nevertheless, this screening approach does not exclude the possibility of deepener investigations, exploring the higher-order PCs by using more conventional multivariate approaches.

Each ROI was visualized individually (Fig. 1d-f), to better assess its position. Subsequently, the average reflection-mode FTIR spectrum was extracted to chemically characterize the selected area, also thanks to the comparison with the spectral signatures of pure standard materials (Figs. S2 and Supplementary Material) shows the effect of the standard normal variate (SNV) transform applied on spectral profiles of sample R57. It can

be easily observed how this transform minimizes unwanted systematic effects present within the spectral profiles, such as baseline shift and global intensity amplification (Fig. S3, Supplementary Material). ROI 1 (yellow area, Fig. 1d) shows a homogeneous distribution of brochantite. The extracted spectrum showed distorted bands induced by specular and/or diffuse reflection (Fig. S1a, Supplementary Material). The *reststrahlen* band at 1086 cm^{-1} and the bands between 3600 and 3400 cm^{-1} refer to SO$_4^{2-}$ and O–H stretching modes, respectively. Several weak bands in the spectral region between 2500 and 1600 cm^{-1} are likely ascribable to overtone and combination bands, visible thanks to the diffuse reflection contribution [25]. ROI 2 labeled with a green color (Fig. 1e) is characterized by the presence of Incralac, owing to the strong derivative-like shaped band in the range 1770–1700 cm^{-1}, ascribable to the C=O stretching mode. C–H bending bands in the range 1340–1450 cm^{-1} were well recognizable together with the C–O stretching band at about 1140 cm^{-1} (Fig. S1b, Supplementary Material). Brochantite, which is present underneath Incralac, remains detectable due to the presence of a weak O–H stretching band up to 3500 cm$_{-1}$. ROI 3 (violet area, Fig. 1f) evidences the presence of wax applied over the Incralac layer. The so-called "double coating system" of bronze statues in Mediterranean countries is traditionally used to extend the lifetime of the protective coatings [26]. This is probably the mostly used coating system applied to protect surface of outdoor sculptures from corrosion. The spectrum extracted from ROI 3 is characterized by the vibrational modes typical of long-chained carbon compounds such as wax (Fig. S1c, Supplementary Material). Derivative-like shaped bands in the spectral range between 2820 and 2940 cm^{-1} refer to the C–H stretching modes, while the double bands at 715 and 727 cm^{-1} are ascribable to C–H bending (methylene rocking) and are indicative of the presence of long aliphatic chains [25]. The contribution of the ester C=O stretching mode (band with a derivative-like shape at 1737 cm^{-1}) is ascribable to the underlying synthetic resin.

In sample R6 (exposed to outdoor urban atmosphere for 8 months), four different ROIs were identified by the algorithm (Fig. 2). The green ROI 1 (Fig. 2c) is ascribable to brochantite, as confirmed by the average spectrum (data not shown). Brochantite is situated in area B and in those zones of area I where the Incralac layer was degraded/eroded during exposure. Both ROI 2 and ROI 3 (pink region, Fig. 2. e and red-brown region, Fig. 2. f, respectively) are located in the area treated with Incralac. The automatic plotting of the average spectra easily allowed a prompt comparison among the different clusters/ROIs. ROI 2 showed the presence of the acrylic diagnostic bands (Fig. 1Sd), while the spectral profile obtained from ROI 3 revealed the co-presence of brochantite and Incralac with a higher contribution of brochantite. In fact, intense and well-defined O–H stretching modes at 3560-3590 cm^{-1} were more intense, as well the *reststrahlen* band at 1083 cm^{-1}, if compared with the C–O stretching band of Incralac at 1140 cm^{-1}. The inhomogeneous distribution of Incralac resulted from the deterioration of this layer induced by aging. The yellow ROI 4 (Fig. 2g) is associated to the undamaged layer of wax (Fig. 2c). It can be concluded from the discussion above that the evaluation

of the analytical procedure on standard samples allows to establish the potentialities of the protocol for the easy and quick identification of different compounds on a surface.
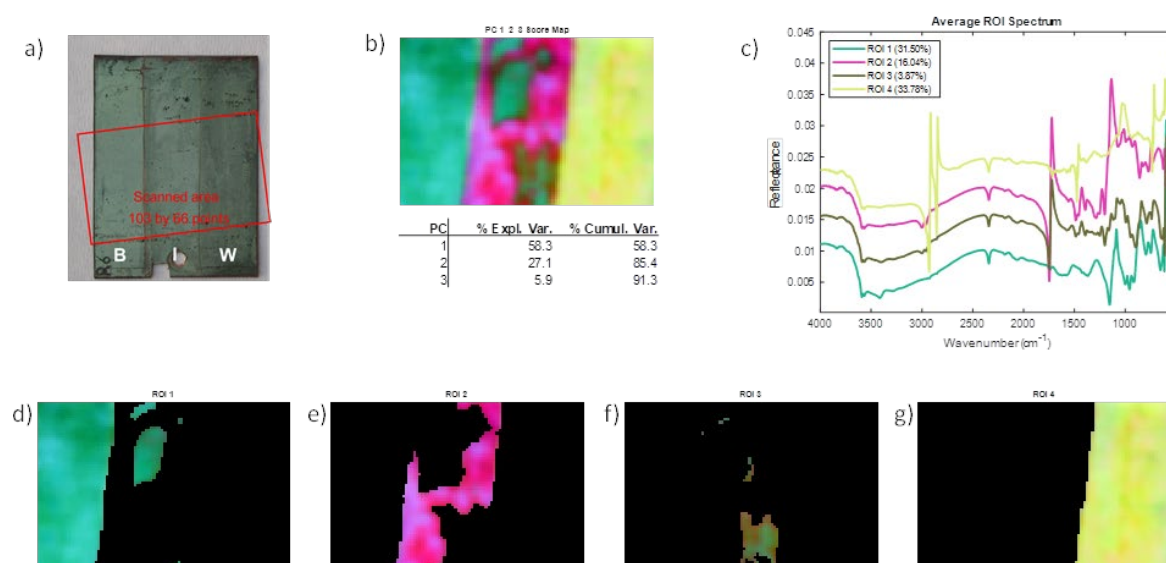

*Figure 2: Sample R6. **a**) RGB picture – the red rectangle indicates the area submitted to MA-rFTIR mapping analysis. R6 was scanned over an area of 51.5 by 33 mm²; **b**) PC1,2,3 score map; **c**) average spectra extracted from the ROIs; **d**) ROI 1; **e**) ROI 2; **f**) ROI 3; **g**) ROI 4. ROI 1 describes the distribution of brochantite, ROI 2 the distribution of a well-preserved Incralac layer, while ROI 3 describes an area with the co-presence of brochantite and Incralac with a higher contribution of brochantite. ROI 4 describes the distribution of wax applied over the Incralac layer. (For interpretation of the references to color in this figure legend, the reader is referred to the Web version of this article.)*

2.2.3.2 *Neptune statue*

The MA-rFTIR imaging protocol was then employed to obtain information on the state of conservation of the Bologna Neptune statue during its restoration campaign in 2016. These analyses were aimed at characterizing the type of degradation products present on the surface, and at documenting the permanence of the coatings applied in the previous restoration, which dates back to 1989–1990. The corroded surface of the sculpture was then covered with a protective double layer coating made of Incralac and microcrystalline wax. Fig. 3a shows an altered area located on the gluteus of the Neptune sculpture that was submitted to MA-rFTIR mapping.

The PC1,2,3 score map (Fig. 3b) shows a heterogeneous situation that allowed to identify three different ROIs within the scanned area (Fig. 3d-f). The scanned area is mainly included in ROI 1 (Fig. 3d), whose averaged spectrum (Fig. S4a, Supplementary Material) shows the presence of a discontinuous layer of wax (bands at 2820 and 2940 cm⁻¹ and at 715 and 727 cm⁻¹). Indeed, the intense carbonyl bands at about 1725 cm⁻¹ and the band at 1140 cm⁻¹ reveal the diffuse presence of Incralac. The derivative-like shape of the main absorption bands suggests a strong contribution of the specular components. This indicates that, in this area, the wax layer maintained its texture during time.
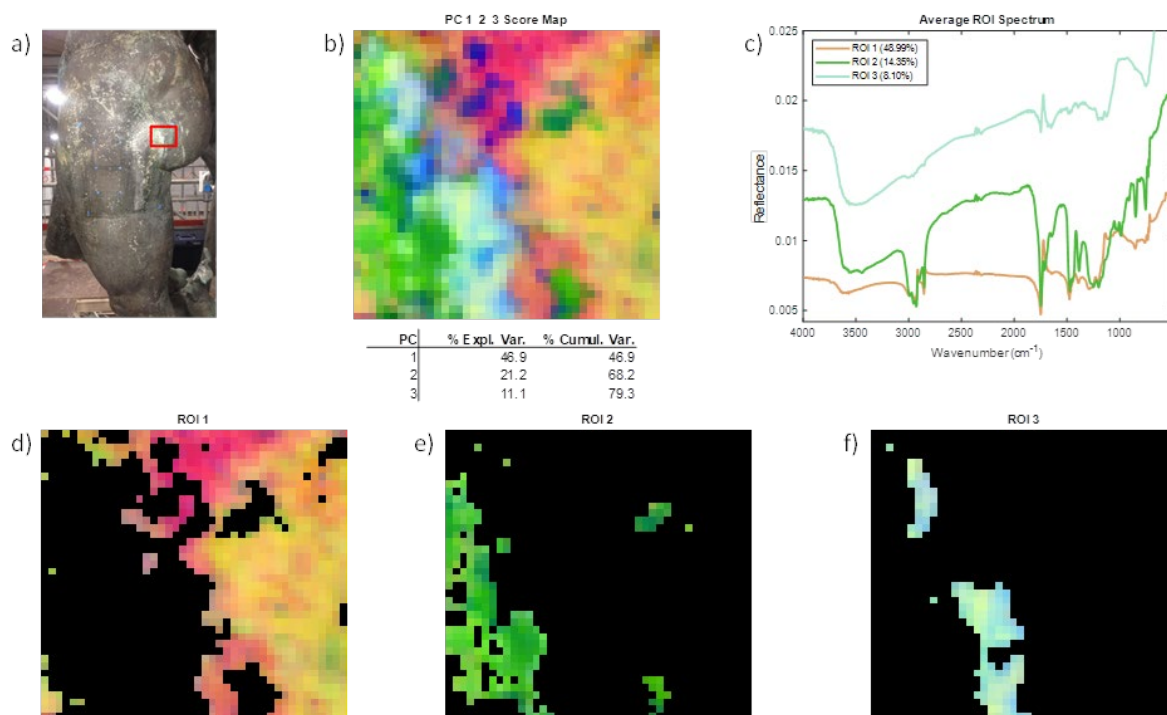
*Figure 3: Detail of the gluteus of the Neptune sculpture. **a)** RGB picture, the red rectangle indicates the area submitted to MA-rFTIR mapping analysis. The glutes area was 42 by 40 mm²; **b)** PC1,2,3 score map; **c)** average spectra extracted from the ROIs; **d)** ROI 1; **e)** ROI 2; **f)** ROI 3. ROI 1 describes an inhomogeneous layer of wax, while ROI 2 describes the co-presence of wax and Incralac with a higher contribution of Incralac. ROI 3 describes a strongly corroded surface in which it is possible to detect the presence of alteration products with some traces of Incralac. (For interpretation of the references to color in this figure legend, the reader is referred to the Web version of this article.)*

On this basis, a limited spread of alteration products in this area can be assumed. The average spectrum (Fig. S4b, Supplementary Material) extracted from ROI 2 (green region, Fig. 3e) did not show any evident deformation of the bands. This suggests that the diffuse reflection components are predominant in this area, indicating a more irregular and degraded surface. MIR signals from both protective coatings (wax and Incralac) are still visible, although those from the synthetic resin appear to dominate the spectrum.

This suggests that the external wax layer was partially degraded in this ROI. Moreover, the broad OH band at about 3500 cm⁻¹ and the shoulder at about 1160 cm⁻¹ may suggest the presence of traces of corrosion products such as copper hydroxyl sulfates (Fig. S4b, Supplementary Material). Associated with ROI 3 (light-blue region, Fig. 3f) is an averaged spectrum in which broad and weak bands are present, probably affected by diffuse reflection (Fig. S4c, Supplementary Material). This corresponds to a coarse, strongly corroded surface. Only few traces of Incralac are still visible (band around at 1730 cm⁻¹). Additionally, in the spectrum presented in (Fig. S4c Supplementary Material), it is possible to observe a broad band at 3500 cm⁻¹ due to the OH stretching and a broad band at around 1000 cm⁻¹ that might be tentatively assigned to the stretching modes of sulfates

or silicates. The bands, however, are too broad to securely assign them to a defined inorganic compound, probably due to some effects of overlapping. Micro-destructive analysis performed with micro FTIR, revealed the presence in the patina of copper hydroxysulfates, gypsum and silicates [25], which might be possible candidates to explain these bands.
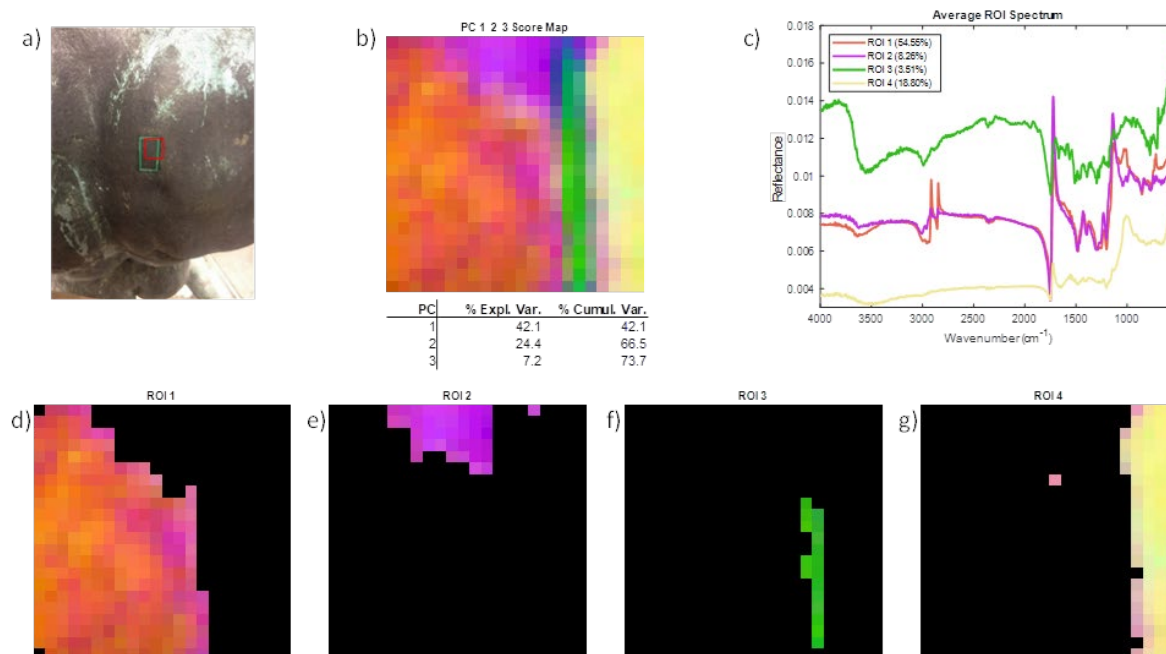

*Figure 4: Detail of the shoulder of the Neptune sculpture. **a)** RGB picture, the red rectangle indicates the area submitted to MA-rFTIR mapping analysis. The shoulder area was 21 by 21 mm^2; **b)** PC1,2,3 score map; **c)** average spectra extracted from the ROIs; **d)** ROI 1; **e)** ROI 2; **f)** ROI 3; **g)** ROI 4. ROI 1 and ROI 2 describe the uncleaned area and they are differentiated by a different amount of wax. ROI 3 describes the tape used to limit the untreated area and ROI 4 describes the acetone-cleaned area. (For interpretation of the references to color in this figure legend, the reader is referred to the Web version of this article.)*

From the results reported above, it is possible to conclude that the MA-rFTIR imaging method allows to distinguish the subregions of the mapped area by locating intact coatings and partially degraded regions. To further assess the applicability of the method, MA-FTIR mapping in combination with the automatic pixel clustering was used to monitor the cleaning procedures that were employed on the Neptune statue. Restoration protocols often include the removal of aged coatings to be re-placed with new treatment layers. A region cleaned with acetone was analyzed, comparing the results with a neighboring and untreated area (Fig. 4a). The automatic clustering applied on the hyperspectral map resulted in four spatial ROIs. ROI 1 and ROI 2 (Figs. 4d and 4e) are in the uncleaned area and they can be differentiated by a different amount of wax, confirming the inhomogeneity of the coatings as previously described. In both regions, Incralac was well recognizable due to the derivative-like shape band of the carbonyl stretching at about 1730 cm^{-1}, while ROI 1 showed a higher contribution of wax with

respect to ROI 2, due to the presence of bands at 2918-2845 cm^{-1} and at 731-721 cm^{-1} (data not shown). ROI 3 is ascribable to the tape used to limit the un-treated area (Fig. 4f) and ROI 4 corresponds the acetone-cleaned area (Fig. 4g). The average spectra of the cleaned area confirmed the total removal of wax and the drastic reduction of the thickness of the Incralac layer (Fig. S4d, Supplementary Material), which was still partially present. Thus, CH stretching and bending modes were no longer present in the average spectrum extracted from ROI 4, while the C–O modes were still recognizable. Additionally, a broad and intense band at 1006 cm^{-1}, together with a band at 912 cm^{-1}, suggested the presence of silicate-based components, probably ascribable to a local deposition of dust. From this last hyperspectral map, it can be concluded that MA-rFTIR in combination with the automated spectral clustering method, can provide conservators with on-site monitoring information on the efficacy of the coating removal interventions they are applying.

2.2.4 Conclusions

In the present study, a new on-site analytical approach for the rapid and simple processing of hyperspectral data cube is proposed, based on macroscopic reflection mode FTIR scanning analysis. The approach allows in real time for the sorting of complex spectra data sets into a limited number of sub areas of the mapped region, each characterized by a distinct average spectrum.

The system was tested both on naturally corroded mockup samples and on surface areas of the 16th century Neptune statue and allowed to obtain information related to the metal patina of the investigated bronze surfaces. The method was proposed for the characterization of coatings applied as protective agents.

Even if, in the last decades, the relevance of scientific analyses in the conservation field has been acknowledged, the related time and expertise required are often not bearable. The automated approach proposed in the present study allows to reduce the time required for data processing by maximizing the degree of automation of the procedure. Data analysis becomes applicable on site during diagnostic campaigns to quickly obtain information for the definition of proper conservation actions. Additionally, the approach can be also suitable for the processing of data obtained from forensic and environmental analytical measurements, which usually aim to achieve reliable results in the shortest time possible.

References
1.   S. Legrand, F. Vanmeert, G. Van der Snickt, M. Alfeld, W. De Nolf, J. Dik, K. Janssens, Examination of historical paintings by state-of-the-art hyperspectral imaging methods: from scanning infra-red spectroscopy to computed X-ray laminography, Herit. Sci. 2 (1) (2014), https://doi.org/10.1186/2050-7445-2-13.

2.   A. Martins, J. Coddington, G. Snickt, B. Driel, C. McGlinchey, D. Dahlberg, K. Janssens, J. Dik, Jackson Pollock's Number 1A, 1948: A non-invasive study using macro-X-ray fluorescence mapping (MA-XRF) and multivariate curve resolution alternating least squares (MCR-ALS) analysis, Herit. Sci. 4 (1) (2016), https://doi.org/10.1186/s40494-016-0105-2.

3.   G. Sciutto, T. Frizzi, E. Catelli, N. Aresi, S. Prati, R. Alberti, R. Mazzeo, From macro to micro: an advanced macro X-ray fluorescence (MA-XRF) imaging approach for the study of painted surfaces, Microchem. J. 137 (2018) 277–284, https://doi.org/10.1016/J.MICROC.2017.11.003.

4.   J.K. Delaney, J.G. Zeibel, M. Thoury, R. Littleton, M. Palmer, K.M. Morales, E.R. De La Rie, A. Hoenigswald, Visible and infrared imaging spectroscopy of picasso's harlequin musician: mapping and identification of artist materials *in situ*, Appl. Spectrosc. 64 (6) (2010) 584–594.

5.   C. Cucci, J.K. Delaney, M. Picollo, Reflectance hyperspectral imaging for investigation of works of art: old master paintings and illuminated manuscripts, Acc. Chem. Res. 49 (10) (2016) 2070–2079, https://doi.org/10.1021/acs.accounts. 6b00048.

6.   P. Ricciardi, S. Legrand, G. Bertolotti, K. Janssens, Macro X-ray fluorescence (MA-XRF) scanning of illuminated manuscript fragments: potentialities and challenges, Microchem. J. 124 (2016) 785–791, https://doi.org/10.1016/J.MICROC.2015.10. 020.

7.   P. Ricciardi, J.K. Delaney, M. Facini, J.G. Zeibel, M. Picollo, S. Lomax, M. Loew, Near infrared reflectance imaging spectroscopy to map paint binders *in situ* on illuminated manuscripts, Angew. Chem. Int. Ed. 51 (23) (2012) 5607–5610, https://doi.org/10.1002/anie.201200840.

8.   F. Rosi, C. Miliani, R. Braun, R. Harig, D. Sali, B.G. Brunetti, A. Sgamellotti, Non-invasive analysis of paintings by mid-infrared hyperspectral imaging, Angew. Chem. Int. Ed. 52 (20) (2013) 5258–5261, https://doi.org/10.1002/ange. 201209929.

9.   A. Daveri, S. Paziani, M. Marmion, H. Harju, A. Vidman, M. Azzarelli, M. Vagnini, New perspectives in the non-invasive, *in situ* identification of painting materials: the advanced MWIR hyperspectral imaging, TrAC Trends Anal. Chem. (Reference Ed.) 98 (2018) 143–148, https://doi.org/10.1016/J.TRAC.2017.11.004.

10.   F. Gabrieli, K.A. Dooley, J.G. Zeibel, J.D. Howe, J.K. Delaney, Standoff mid-infrared emissive imaging spectroscopy for identification and mapping of materials in polychrome objects, Angew. Chem. Int. Ed. 57 (25) (2018) 7341–7345, https://doi.org/10.1002/anie.201710192.

11.   S. Legrand, M. Alfeld, F. Vanmeert, W. De Nolf, K. Janssens, Macroscopic Fourier transform infrared scanning in reflection mode (MA-rFTIR), a new tool for chemical imaging of cultural heritage artefacts in the mid-infrared range, Analyst 139 (10) (2014) 2489–2498, https://doi.org/10.1039/C3AN02094K.

12.   K. Janssens, S. Legrand, G. Van Der Snickt, F. Vanmeert, Virtual archaeology of altered paintings: multiscale chemical imaging tools, Elements 12 (1) (2016) 39–44, https://doi.org/10.2113/gselements.12.1.39.

13.   M. Ester, H.-P. Kriegel, J. Sander, X. Xu, A Density-Based Algorithm for Discovering Clusters in Large Spatial Databases with Noise, Kdd, 1996, pp. 226–231.

14. G. Sciutto, P. Oliveri, S. Prati, M. Quaranta, S. Lanteri, R. Mazzeo, Analysis of paint cross-sections: a combined multivariate approach for the interpretation of μATR-FTIR hyperspectral data arrays, Anal. Bioanal. Chem. 405 (2–3) (2013) 625–633, https://doi.org/10.1007/s00216-011-5680-1.

15. F. Rosi, A. Federici, B.G. Brunetti, A. Sgamellotti, S. Clementi, C. Miliani, Multivariate chemical mapping of pigments and binders in easel painting cross-sections by micro IR reflection spectroscopy, Anal. Bioanal. Chem. 399 (9) (2011) 3133–3145, https://doi.org/10.1007/s00216-010-4239-x.

16. S. Buratti, C. Malegori, S. Benedetti, P. Oliveri, G. Giovanelli, E-nose, e-tongue and e-eye for edible olive oil characterization and shelf life assessment: a powerful data fusion approach, Talanta 182 (2018) 131–141, https://doi.org/10.1016/j.talanta.2018.01.096.

17. E. Catelli, L. Randeberg, H. Strandberg, B. Alsberg, A. Maris, L. Vikki, Can hyperspectral imaging be used to map corrosion products on outdoor bronze sculptures? J. Spectr. Imaging 7 (1) (2018) a1, https://doi.org/10.1255/jsi.2018.a10.

18. G. Guida, M. Marabelli, R. Mazzeo, G. Morigi, Chemical and physical examination of the bronze sculptures of the fountain of Neptune in relation to the restoration, the identification of the construction technique and previous restoration work, Sci. Technol. Cult. Herit. (3) (1994) 75–88.

19. E. Joseph, P. Letardi, R. Mazzeo, S. Prati, M. Vandini, Innovative treatments for the protection of outdoor bronze monuments, Proceedings of the Interim Meeting of the ICOM-CC Metal WG, 2007, pp. 71–77. Amsterdam, Netherlands.

20. R.J. Barnes, M.S. Dhanoa, S.J. Lister, Standard normal variate transformation and de-trending of near-infrared diffuse reflectance spectra, Appl. Spectrosc. 43 (5) (1989) 772–777, https://doi.org/10.1366/0003702894202201.

21. P. Oliveri, C. Malegori, R. Simonetti, M. Casale, The impact of signal pre-processing on the final interpretation of analytical outcomes – a tutorial, Anal. Chim. Acta 1058 (2019) 9–17, https://doi.org/10.1016/J.ACA.2018.10.055.

22. P. Oliveri, C. Malegori, M. Casale, E. Tartacca, G. Salvatori, An innovative multivariate strategy for HSI-NIR images to automatically detect defects in green coffee, Talanta 199 (2019) 270–276, https://doi.org/10.1016/J.TALANTA.2019.02.049.

23. B. Vekemans, K. Janssens, L. Vincze, A. Aerts, F. Adams, J. Hertogen, Automated segmentation of μ-XRF image sets, X Ray Spectrom. 26 (6) (1997) 333–346, https://doi.org/10.1002/(SICI)1097-4539(199711/12)26:6<333::AID-XRS231>3.0. CO;2 (D).

24. R. Bro, A.K. Smilde, Principal component analysis, Anal. Methods 6 (2014) 2812–2831, https://doi.org/10.1039/C3AY41907J.

25. E. Catelli, G. Sciutto, S. Prati, Y. Jia, R. Mazzeo, Characterization of outdoor bronze monument patinas: the potentialities of near-infrared spectroscopic analysis, Environ. Sci. Pollut. Res. 25 (24) (2018) 24379–24393, https://doi.org/10.1007/ s11356-018-2483-3.

26. D.A. Scott, Copper and Bronze in Art: Corrosion, Colorants, Conservation, Getty publications, Los Angeles, 2002.

2.2.5 Appendix A. Supplementary data

Supplementary data to this article can be found online at https://doi.org/10.1016/j.talanta.2019.120575.
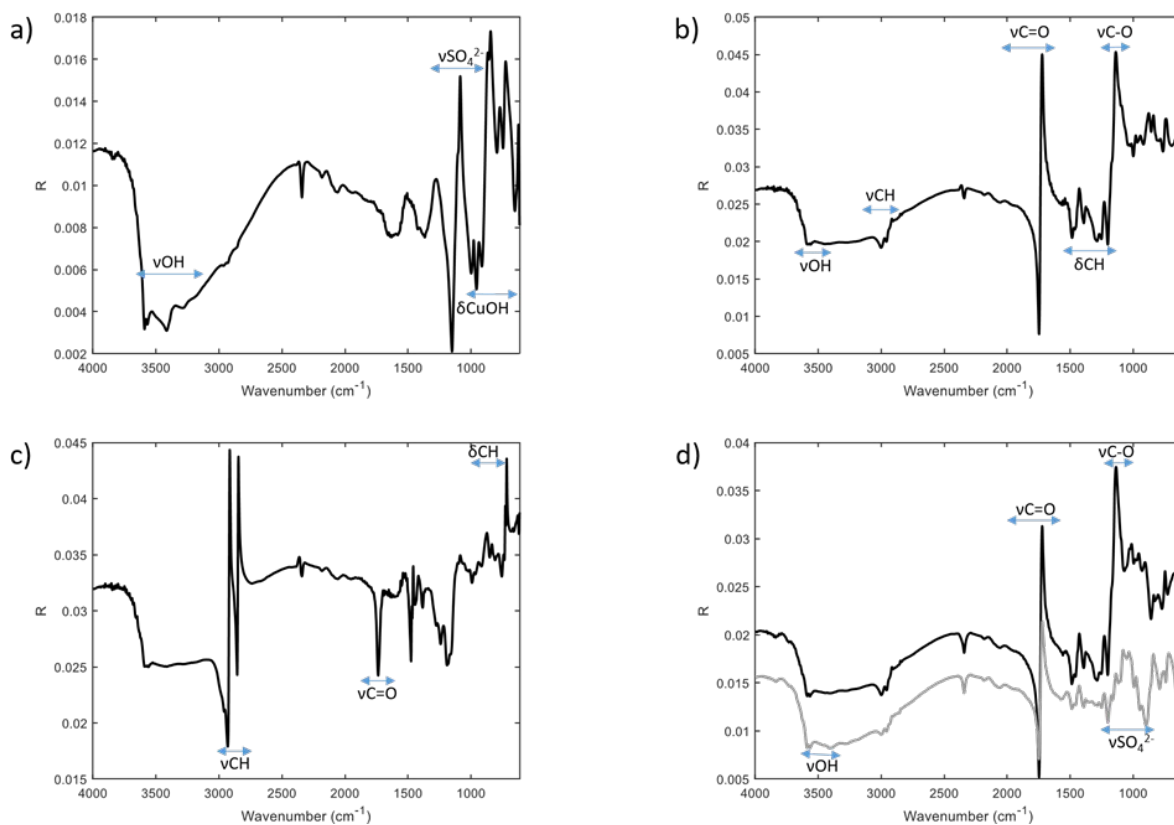

*Figure S1: Investigated areas on R57 and R6 samples. **a)** Average spectrum extracted from ROI 1 (R57); **b)** averaged spectrum extracted from ROI 2 (R57); **c)** average spectrum extracted from ROI 3 (R57); **d)** comparison between average spectra extracted from ROI 2 and ROI 3 (R6).*
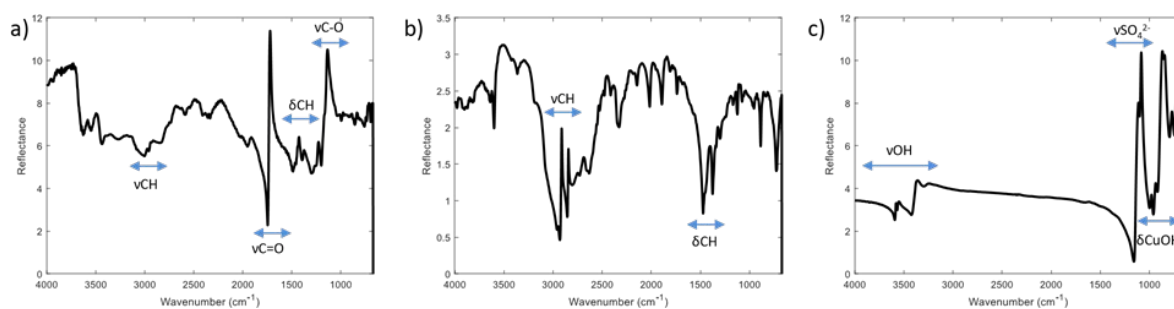

*Figure S2: Spectra of standard materials, for comparison with Figure S1. **a)** Incralac; **b)** microcrystalline wax; **c)** brochantite.*
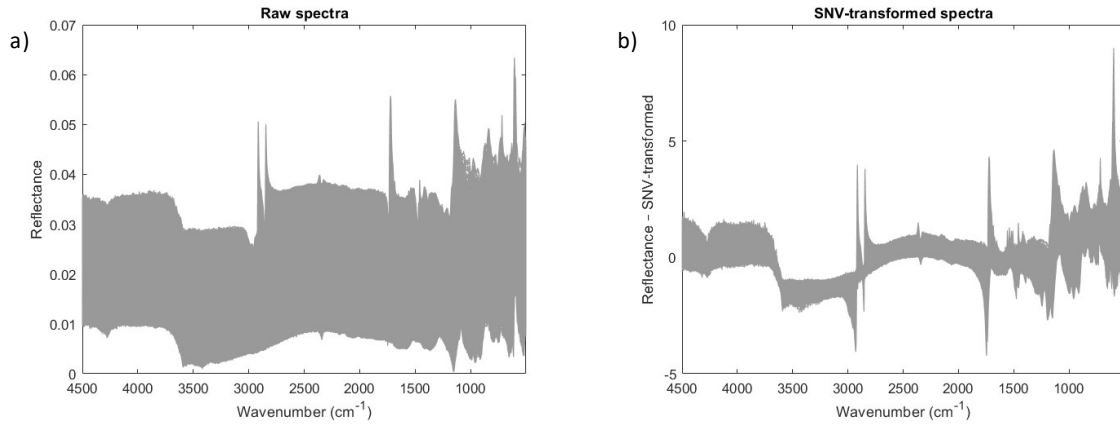
*Figure S3: Spectra from all the pixel of the hyperspectral image of sample R57. **a)** raw signals; **b)** signals after application of the standard normal variate (SNV) transform.*
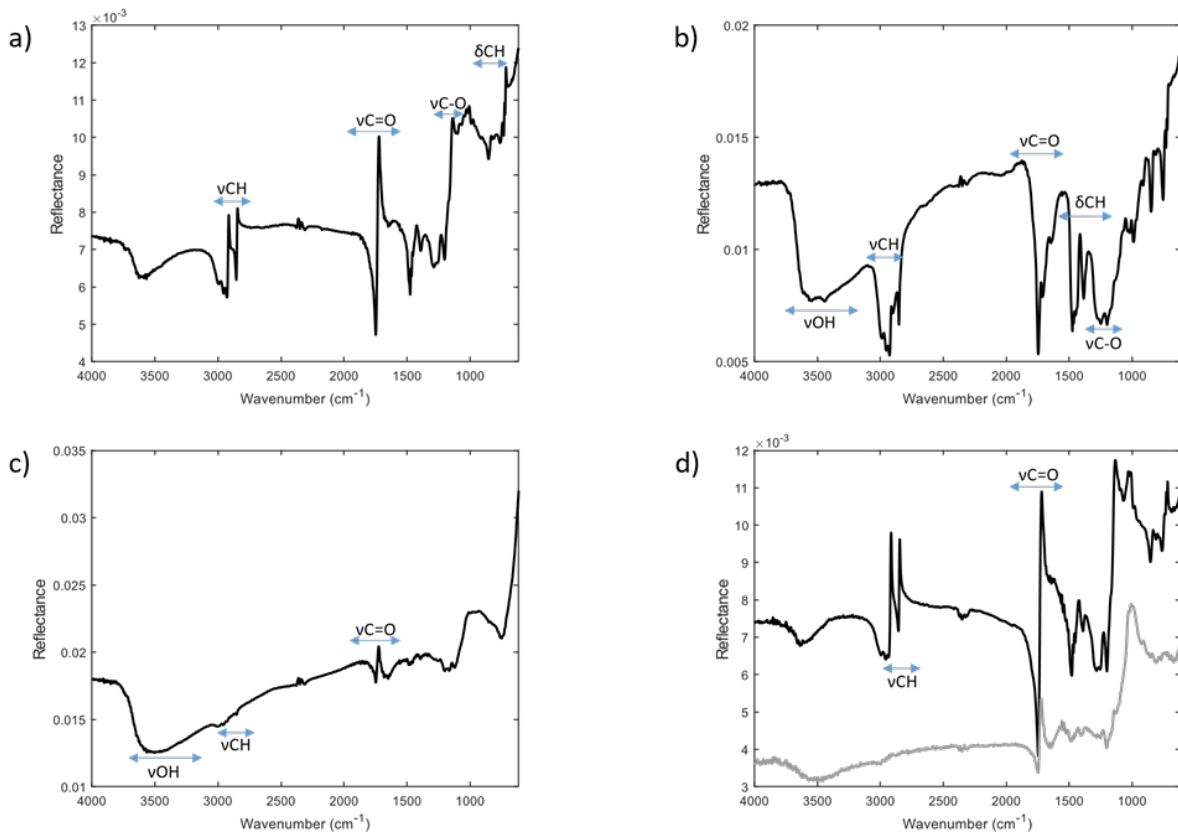

*Figure S4: Investigated areas on gluteus and shoulder of the Neptune sculpture. **a)** Average spectrum extracted from ROI 1 (gluteus); **b)** average spectrum extracted from ROI 2 (gluteus); **c)** average spectrum extracted from ROI 3 (gluteus); **d)** comparison between averaged spectra extracted from ROI 2 and ROI 3 (shoulder).*

Part 2: Case studies

Chapter 3 **Illuminated manuscripts**

Illuminated manuscripts are highly appreciated for their level of detail and the fact that these are often in a better state of conservation than paintings of a similar age. This can be explained by the fact that these were protected by their parent volume against the environment for a large part of their history.

In a first stage an illuminated manuscript fragment was analyzed by MA-XRF only in order to identify the pigment usage, technique and help to retrace its origin, now lost since it was excised from its parent volume and sold separately. The MA-XRF distribution maps added valuable information to this discussion that was deducible from XRF point measurements.

In a second stage a combined MA-XRF/MA-rFTIR analysis was performed on an illuminated manuscript fragment in order to allow more speciation of the materials present and to reconstruct the verso side (which is currently not accessible). The revisualization of the hidden text on the back side allowed scholars to identify this fragment's location in the original volume.

3.1 Macro X-ray fluorescence (MA-XRF) scanning of illuminated manuscript fragments: potentialities and challenges

Abstract Macro X-ray fluorescence scanning (MA-XRF) is gradually becoming an established technique for the non-invasive analytical investigation of painted surfaces. This paper discusses some of the benefits and limitations of employing MA-XRF for the study of manuscript illuminations. Art historical research on this type of artefacts that is based on scientific measurements is often limited by the fact that usually no sampling can take place. Hence there is a need for non-invasive analytical tools that make it possible to conduct systematic investigations.
As a representative example of this type of objects, a 15th century Italian manuscript fragment from the collection of the Fitzwilliam Museum in Cambridge (UK) is investigated. The aims of the study were to gain insight into the materials and techniques employed by Renaissance illuminators and to help answer specific questions regarding the fragment's authorship and geographic origin. The complementarity and advantages of MA-XRF mapping versus site-specific analyses are discussed. For this purpose, MA-XRF data are evaluated and compared with the results of other analytical techniques. The interpretation of the elemental maps is discussed along with the challenges faced during the analysis.

3.1.1 Introduction

Macro X-ray fluorescence scanning (MA-XRF) is gradually becoming an established technique for the non-invasive and element-specific imaging of painted surfaces. It allows the determination of the spatial distribution of chemical elements over large areas, thus enabling researchers to infer the presence of certain pigments or mixtures thereof across the entire surface of a work of art. Initially, MA-XRF has been mainly used to study easel paintings [1,2], but recently its scope has been broadened to other two-dimensional (i.e., 'flat') cultural heritage objects such as stained-glass windows [3] and illuminated manuscripts [4]. The analytical study of manuscripts is often hindered by the very limited possibilities for sampling, which is rarely considered acceptable for this type of artwork by current conservation standards, meaning that only non-invasive methods can be used. Removing manuscripts from their permanent locations in museum collections for analysis in scientific laboratories is also hardly ever allowed due to the intrinsically high sensitivity of these artefacts to changes in environmental conditions, which may lead to physical damage and accelerate aging and degradation of the painted surfaces. The availability of 'portable' or at least 'mobile' instrumentation is therefore crucial.

Many of the illuminations which are found today in museum collections are in the form of manuscript *fragments*, i.e. single decorated pages or portions thereof which were excised from bound volumes usually during the 18th and 19th century in order to be sold individually and displayed as small paintings. Technical analysis of such fragments can be an invaluable resource to manuscript scholars, as research on this type of objects is often made difficult by the lack of contextual information, lost when the illuminations were separated from their parent volume.
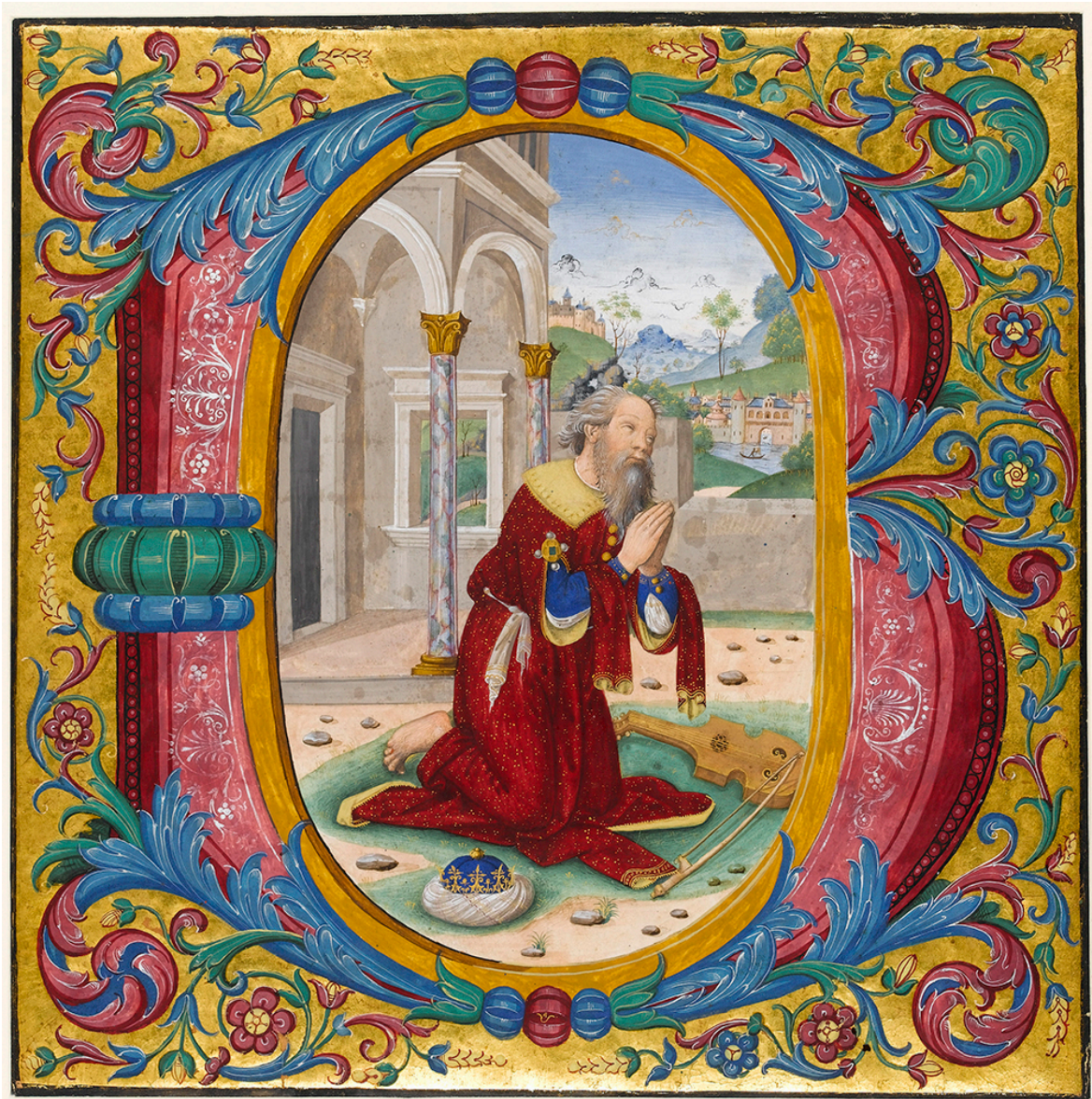

Figure 1: Fitzwilliam Museum, Marlay Cutting It 25. Bologna or Rome, c. 1490–1500. © Fitzwilliam Museum, Cambridge.

The manuscript fragment discussed here (Fitzwilliam Museum, Marlay Cutting It 25, see Fig. 1) was probably made in Bologna or Rome in the last decade of the fifteenth century. The historiated initial B, representing King David in prayer, would have introduced Psalm 1 ('*Beatus vir*') in the Antiphoner from which it was excised. The style of illumination finds parallels in the work of several leading artists active in both cities at the time, including Perugino and Pinturicchio, but despite these affinities, the name of the illuminator remains unknown [5]. Technical analyses were undertaken in the hope that they may help in identifying the individual artist or painting workshop who decorated this fragment, or at least in firmly establishing its geographic origin. Prior to MA-XRF scanning, 39 micro-XRF spectra and 54 fibre-optics UV–VIS-NIR reflectance (FORS) spectra were acquired on this illuminated fragment, yet several questions remained about the identity of certain pigments, as further discussed in Section 3.

3.1.1.1 *Advantages of MA-XRF scanning over single-point XRF analysis*

Due to the wide availability of relatively inexpensive portable instrumentation, XRF is – together with Raman spectroscopy – amongst the most commonly used methods for the technical study of manuscript illumination [6,7]. However, the selection of sites for single-point analysis has to be done carefully in order to obtain information that is ideally limited to only one feature per spectrum (one pigment or mixture, one color, one sequence of layers, …), without potential interference from nearby areas. This is often a difficult task due to the small-scale details of a vast majority of manuscript illuminations. Additionally, since only a limited number of single-point spectra are acquired, these have to be of great quality, resulting in relative long acquisition times, usually of the order of minutes per point. Enough spectra must be acquired to ensure that the results are representative of all the pigments, mixtures or painting techniques used on the illumination under study, or at least sufficient to provide a reliable answer to the question that the technical analysis is trying to answer. This can rapidly become a very time-consuming task, which can occupy a researcher for multiple days. MA-XRF scanning is also time consuming, but input from the researcher is only required during set-up; once started, the MA-XRF scan runs independently. In order to scan an illumination within a reasonable time period, the measurement time per point has to be kept low (usually a fraction of a second), resulting in a lower signal-to-noise ratio for each individual spectrum. It is however possible to combine the recorded spectra from similar points *a posteriori* to obtain an averaged spectrum with improved statistics.

An advantage of performing two-dimensional scans over single-point analyses is that subtle differences in peak intensities between different points can be hard to interpret while comparing two or more single-point spectra; however, their meaning is often immediately clear in elemental distribution images. This can, for example, be the case for trace elements only present in some of the spectra which can be attributed to a specific pigment, which may point to two different sources or two different 'grades' of the same material, used on separate parts of the illumination.

Parchment was used as a substrate material for most of Western European illuminations. Due to its proper composition and to the preparation treatments it was subjected to before it was painted upon, it gives rise to an XRF spectrum of its own. In most cases it is possible to record *'blank'* XRF spectra of the parchment at a few positions, but these may not be truly representative of the entire area investigated. In many cases, fragments were cut so close to the edges of the illumination that no bare parchment is actually available. As a result it can be very difficult to correctly evaluate the influence of the parchment signal in the individual XRF spectra of painted areas. In the distribution images resulting from MA-XRF scans, however, contributions deriving from the support usually are clearly distinguishable from those originating from the painting materials.

MA-XRF analysis of illuminated manuscript *fragments* is less challenging than the examination of illuminations found in bound volumes, because they are already relatively 'flat'. They can therefore be easily and safely set-up for a 2D scan, without causing any physical stress or any possible risk to their integrity. The absence of other pages situated behind the scanned surface also simplifies the interpretation of the resulting XRF data, as all the recorded XRF signals clearly originate from a single page. However, in some instances manuscript fragments have been pasted onto paper, cardboard or wood, which may interfere with the XRF signals and can hide any text and decoration present on the verso side. The latter can also contribute to the XRF data recorded. The contribution of hidden materials from the verso side is usually rather hard to evaluate when single-point spectra are acquired, but much easier to understand when elemental maps of an entire illumination are available (see Sections 2.2 and 3.3). Whenever fragments are pasted onto a support which cannot be penetrated by visible or infrared light, the penetrating nature of the X-rays and the resulting contribution of materials present on the reverse is in fact no longer a hindering side effect but becomes an asset. MA-XRF scanning allows the visualization of information which would otherwise be hidden and which can aid significantly in identifying a fragment's parent manuscript or even its original position within the manuscript.

3.1.2 Materials and Methods

3.1.2.1 *MA-XRF instrumentation*

The MA-XRF scan of Marlay Cutting It 25 was performed by means of a dedicated instrument, developed at the University of Antwerp and described in detail elsewhere [1,2]. This instrument is equipped with a 10 W Moxtek 50 kV "Magnum" X-ray tube with a Rh target, operated at 45 kV and 200 µA. The emitted X-ray beam is defined by means of a Pb pinhole collimator of 0.8 mm diameter. Two Vortex EX-90 detectors (each with a 50 mm^2 active area) are mounted under an angle of 20 degrees relative to the primary beam to detect the created XRF-radiation under a large solid angle.

In order to obtain optimum results, the fragment was positioned relatively close to the scanning head, at an approximate distance of 1.5 cm, parallel to the scanner's plane of movement. To ensure its safety during scanning, the fragment was in-set in a thin archival board which was hinged into a conservation-grade mount. The mount itself extended several cm on each side of the fragment allowing it to be secured upright on a vertical paintings easel. The extended mount as well as the absence of rims or other edges on the easel, which could have interfered with the scanner's movements, allowed scanning the entire surface of the fragment. In Fig. 2, a photograph of the MA-XRF setup is shown while examining another illuminated fragment in the Fitzwilliam Museum's collection.

The scan was run at a dwell time of 275 ms per pixel and with a step size of 500 μm. In order to cover the entire surface of the fragment (263 x 260 mm^2), a dataset of 584,000 spectra was acquired over 22 consecutive hours.

Figure 2: Detail of the MA-XRF scanning head in front of a mounted manuscript fragment (Fitzwilliam Museum, Marlay Cutting It 13ii).

3.1.2.2 *MA-XRF data processing and interpretation: from spectra to pigments, via elemental maps*

The dataset derived from Marlay Cutting lt 25 was processed using a combination of two data processing packages, described elsewhere: 'Datamuncher' [8] and PyMca [9]. This process, discussed in further detail by Alfeld and Janssens [8], was initiated by creating a global fitting model using non-linear least squares fitting. To obtain improved counting statistics, this model was fitted to an artificial sum spectrum of all the individual spectra. The model was then used to perform least squares fitting by single matrix multiplication (dynamic analysis). This process results in a three dimensional matrix where x and y are the spatial coordinates of the analyzed object and z corresponds to the fitted elemental lines. Elemental distribution images (greyscale maps, cf. for example Fig. 3f) can be extracted from this matrix for each element ($Z > 15$) present in the object. In MA-XRF images, the most interesting information is often present in the middle tones. These middle tones can be obscured by local hotspots, for example due to damages or to previous retouches and conservation treatments. To improve the readability of the distribution maps, the 0.5% most extreme values for each distribution map can be omitted, resulting in a broader dynamic range for the middle tones. The elemental information provided by these elemental maps is used to infer the presence of individual pigments based on the knowledge of their chemical composition. To properly interpret these maps, some knowledge about XRF theory and instrumentation is necessary. Since these spectra are recorded using an energy dispersive X-ray detector, the peaks in the spectra are relatively broad, resulting in possible mis-fits. This is most likely to happen when the XRF signal in the high-intensity areas of one element gives rise to an additional contribution in the distribution image of the one which follows it in the periodic table. For example, the element Mn, via its K_β line may contribute to the apparent intensity of Fe since the Mn-K_β (at 6.49 keV) overlaps with the Fe-K_α line (at 6.40 keV). Additionally, the different depth of penetration of X-rays of different energies has to be taken into account, considering that most painted surfaces have a multilayered structure. As a result of this, the distribution of lighter elements (Si, S, K, Ca, Ti, …) – which only emit low-energy radiation (typically in the 1–6 keV range) that is significantly absorbed when it originates from deep inside the material – predominantly resembles the surface layer. On the other hand, the distribution of heavier elements such as Cu, Sr, Pb and Hg, which can emit higher energy radiation (typically above 6 keV) that is less easily absorbed, can contain information that originates from underlying layers. Therefore the interpretation of each elemental map needs to take into account the information derived from the maps of other elements: the apparent absence of light elements in sub-surface structures, for example, might be due simply to their signal being absorbed by more superficial paint layers.

Several greyscale maps can also be combined to form RGB composite images (cf. Fig. 3b-e), highlighting the presence of two or more chemical elements in the same area, thus facilitating the identification of certain pigments. The correlation between multiple elements present in the same area can be difficult to infer from a limited number of single-point spectra, but it is usually clearly apparent in the elemental maps (see examples in Section 3).

It is worth noting that knowledge of the date and geographical origin of the object under analysis greatly helps in limiting the number of possible pigments which may be present on a certain object, although unexpected occurrences can, of course, occasionally be identified. The following discussion illustrates the inference process which allows to link the presence of one or more chemical elements to a specific pigment (or class of pigments), with examples chosen because of their relevance to the manuscript fragment discussed here. Sections 2.2.1 through 2.2.7 are based on the comprehensive list of pigments used throughout history compiled by Eastaugh et al. [10], as well as the extensive discussions of the use of XRF for the analysis of painted surfaces in general, and of illuminated manuscripts in particular, published by Seccaroni and Moioli [11] and by Trentelman *et al.* [7].

3.1.2.2.1 Copper

Copper is the main constituent of the blue mineral pigment azurite ($Cu_3(CO_3)_2(OH)_2$), isomorphous with the green mineral malachite. It also occurs in a number of other natural green pigments – mainly sulphates and chlorides, in addition to other carbonates – and synthetic ones, the latter of very variable composition but often grouped under the umbrella term 'verdigris'. For this reason, elemental analysis alone cannot be used to precisely identify copper-containing pigments, although the co-presence of certain other elements can help restrict the range of possibilities. For example, the identification of zinc in a Cu-rich area could indicate the presence of rosasite, a Cu-Zn carbonate hydroxide mineral often found in association with malachite and azurite [10,11], or alternatively might suggest that a synthetic green pigment was used, derived from brass (an alloy of Cu and Zn) as the raw material [11]. The additional identification of elements such as arsenic and/or antimony may further specify the natural origin of the copper pigment, as these elements are common impurities in copper-bearing minerals, especially in green ones [11].
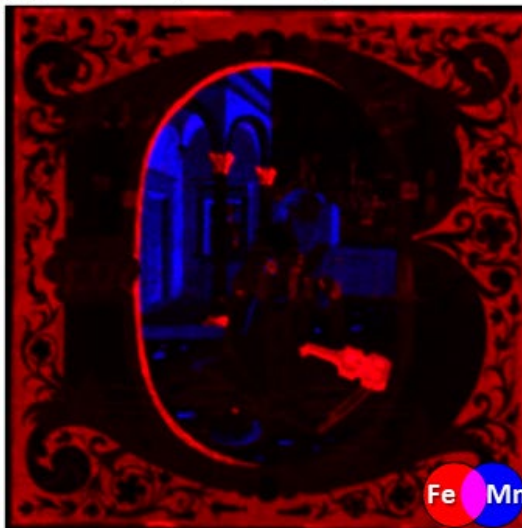
(a) Marlay Cutting It 25
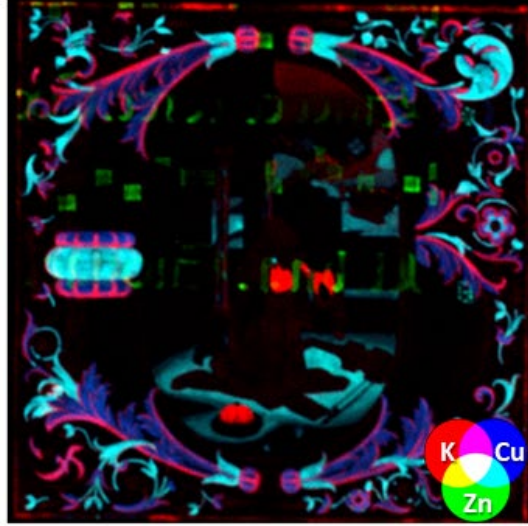
(b) R=K-K, G=Zn-K, B=Cu-K
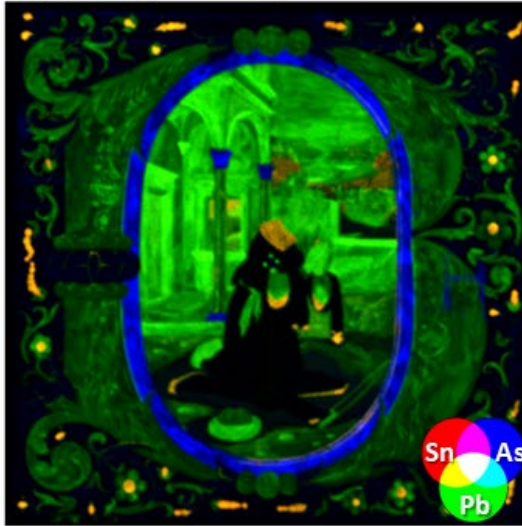
(c) R=Sn-K, G=Pb-L, B=As-K

(d) R=Ca-K, G=Sr-K, B=S-K

(e) R=Fe-K, G=n/a, B=Mn-K

(f) Au-L

*Figure 3: (**a**) Marlay Cutting It 25, visible image and elemental distribution maps. (**b**) RGB composite where R = K-K, G = Zn-K, B = Cu-K (**c**) RGB composite where R = Sn-K, G = Pb-L, B = As-K (**d**) RGB composite where R = Ca-K, G = Sr-K, B = S-K (**e**) RGB composite where R = Fe-K, G = unassigned, B = Mn-K (**f**) Au-L.*

3.1.2.2.2 **Potassium**

The blue pigment ultramarine, frequently employed in manuscript illuminations, is obtained from the semi-precious gemstone lapis lazuli. The main component of lapis lazuli, the mineral lazurite, is a complex aluminosilicate sulfate with composition $(Na,Ca)_8[(Al,Si)_{12}O_{24}](S,SO_4)$, belonging to the sodalite group of minerals. In view of the low atomic number and low XRF emission energies of elements such as Na, Al and Si, it is difficult to directly map their presence with MA-XRF. Calcium and sulphur maps suffer from other interpretation-related issues, as discussed in Section 2.2.5. Despite the fact that potassium does not enter into the generally accepted chemical formula of lazurite, it is often present as an interstitial cation in the molecular structure of hauyne (ideal formula $(Na,Ca)_{4-8}[Al_6Si_6O_{24}](SO_4,S,Cl)_{1-2}$), another member of the sodalite group, which is commonly found in association with lazurite. Hauyne predominates in the lapis lazuli mined in Afghanistan, the main source of ultramarine blue for over six thousand years [12]. A high concentration of potassium has been recently identified directly in Afghan lapis lazuli stone samples [13]. The presence of high levels of potassium in blue areas of illuminated manuscripts may therefore be used to (tentatively) infer the presence of ultramarine. Its use as the main elemental marker for ultramarine is also made possible by the fact that K is absent in other historic blue pigments.[1] However, care should be taken with the use of this association between ultramarine and potassium. When K is identified in areas of yellow, red, pink or purple paint, the K-K XRF signal usually indicates the presence of a lake pigment, prepared by adsorption of an organic dye onto an inorganic compound. In the vast majority of western European recipes for the manufacture of red lake pigments from the 12th through the 18th century, the inorganic substrate is alum, generally indicating potassium aluminium sulphate $(AlK(SO_4)_2 \cdot 12H_2O)$ [14].

---

[1] The only exception to this is smalt, a blue pigment obtained by grinding a potassiumbased, cobalt-containing glass. The co-presence of potassium and cobalt would therefore suggest that smalt, rather than ultramarine, was used.

3.1.2.2.3 Lead and tin

Lead is often identified ubiquitously in manuscripts, where it indicates the presence of the white lead carbonates cerussite ($PbCO_3$) and hydrocerussite ($2PbCO_3 \cdot Pb(OH)_2$), the orange-colored lead oxide commonly called 'red lead' (Pb_3O_4), or one of a few yellow lead oxides such as massicot and litharge (PbO). XRF analysis alone cannot be used to distinguish between these compounds, two or more of which may be mixed together or with other colorants; moreover, the latter may be organic in nature and therefore (very) difficult to identify by XRF. Hypotheses can occasionally be put forward based on the visual appearance of the paint layers in question, but only additional analyses by means of Raman spectroscopy or other molecular/structural 'fingerprinting' techniques such as X-ray diffraction can confirm the identity of the lead-based pigment or pigments identified.

The co-related presence of lead and tin may point to the use of one of two types of lead-tin yellow: either 'type I', a lead-tin oxide of composition Pb_2SnO_4, or 'type II', a lead-tin-silicon oxide of more uncertain composition. If MA-XRF scans are performed at low enough voltage, the resulting silicon map may help distinguish between the two types of lead-tin yellow, which can anyway only be reliably differentiated by using supplementary analytical methods [15].

3.1.2.2.4 Arsenic and sulphur

The co-presence of arsenic and sulphur may point to the presence of one or more arsenic sulphide pigments: yellow orpiment (As_2S_3), orange-red realgar (As_4S_4), or orange-yellow pararealgar (AsS, which can occur as a light-induced alteration product of realgar, but may also have been used as a pigment in its own right). Since the observed As-K_α/S-K_α intensity ratio may be strongly influenced by different factors (such as the thickness of the paint layer and absorption therein) other than the As:S elemental ratio, this is another case where additional analytical methods are needed in order to ascertain which of these arsenic sulphide pigments is present in the analysed area.

3.1.2.2.5 Calcium, sulphur and strontium

White compounds containing calcium, in the form of calcium oxide (CaO) or more likely calcium carbonate ($CaCO_3$), are almost ubiquitous in illuminated manuscripts, often having been used as part of the preparatory treatment to make the parchment sheets suitable for writing and painting [7]. For this reason, it is difficult to link the presence of calcium to the use of a specific pigment. The high levels of calcium observed in pink, red, or yellow-colored areas of illuminated manuscripts, however, can be an indirect indication of the presence of lake pigments, as both lime and calcium carbonate may have been used during their preparation [14].

The co-presence of calcium and sulphur is suggestive of the occurrence of gypsum ($CaSO_4 \cdot 2H_2O$), a material seldom used as a white pigment but often present in preparatory layers under gold leaf or in combination with organic dyes as a substrate for lake pigments. MA-XRF can be very useful in identifying gypsum in painted layers where lead is also present, because the overlap of the S-K and the Pb-M lines may hinder the unequivocal identification of the former from a single XRF spectrum. The availability of data across an entire area, however, combined with a robust spectral deconvolution algorithm, can yield sufficiently reliable sulphur distribution maps. The co-related presence of strontium and calcium may indicate the presence of celestite ($SrSO_4$) or strontianite ($SrCO_3$) as impurities of the calcium-containing minerals, rather than being evidence of modern retouches using strontium yellow ($SrCrO_4$).

3.1.2.2.6 Mercury

The occurrence of mercury in art objects is usually linked to the presence of vermillion (HgS), or its mineral equivalent cinnabar, both of which have been prized as bright red pigments throughout history. As already discussed, the presence of lead, even in moderate amounts, can hinder the identification of sulphur, but until the 19th century, no other mercury compounds are known to have been used as pigment, so that the identification of Hg alone is sufficient to indicate the presence of mercury sulphide.[2] However, mercury can also be present in small quantities in areas which contain the shiny pigment known as 'mosaic gold' (SnS_2) due to its production method which involved an amalgam of tin and mercury.

3.1.2.2.7 Iron and manganese

Iron oxide and hydroxides are the main components of a large group of naturally occurring red, yellow and brown compounds broadly termed 'earth pigments'. Some of these also contain variable amounts of manganese, up to ~20% in brown 'umbers', and up to ~50% in dark brown to black 'wads'. The identification of manganese alone, i.e. in the absence of iron, suggests instead the presence of one of numerous naturally occurring manganese oxides and hydroxides which have been used as black pigments.

The presence of iron may also suggest the presence of iron-gall ink, the most common type of ink used in medieval manuscripts, which often incorporates variable amounts of zinc and copper.

---

[2] A yellow mercury oxide sulphate ($Hg_3SO_4O_2$) appears to have also been occasionally used as a pigment during the 17th and possibly the 18th century [10]. Elemental analysis, however, would not allow the discrimination of this pigment from mercury sulphide.

3.1.3 Results and Discussion

MA-XRF scanning of Marlay Cutting It 25 yielded 32 elemental maps in addition to a 'continuum' map; the latter derives from Compton and Rayleigh scattering of the primary radiation towards the XRF detector. Some of these were combined in RGB composites to highlight the presence of two or more elements in the same areas. The most significant greyscale and RGB maps are presented in Figs. 3–5 and discussed in Sections 3.1–3.6.

3.1.3.1 *Blue and green pigments*

The presence of potassium in certain blue areas such as King David's sleeves and hat, as well as the sky within the initial (red map in Fig. 3b) is attributed to the use of ultramarine blue. Azurite, identified by the presence of copper (blue map in Fig. 3b), is used instead for the light blue areas in the foliate decoration. The presence of ultramarine and azurite had already been hypothesized based on the features of the FORS spectra collected in these areas (data not shown). What the reflectance spectra had not revealed, however, was the fact that the darker blue outlines of the foliage contain ultramarine, as suggested by the presence of both Cu and K in these areas (blue + red = magenta map in Fig. 3b). These thin dark blue lines were too small to be distinguished by the FORS set-up employed, which collected information from areas 3–4 mm in diameter.

The combined presence of copper and zinc in all green areas suggests the use of malachite which is likely to contain impurities of rosasite (blue + green = cyan map in Fig. 3b). As discussed in Section 2.2.1, MA-XRF alone cannot be used to unequivocally identify copper-based pigments; in this case, the proposed identification is based on the availability of FORS spectra which show the characteristic spectral features of this mineral.

Throughout the fragment, Cu and Zn appear to be highly correlated. The only areas in which Zn is not related to the presence of Cu (green map in Fig. 3b) correspond to the text and musical notes visible on the reverse of the fragment, where zinc is present as an impurity of the iron gall ink (cf. Fig. 3e, discussed in Section 3.5).

3.1.3.2 *Yellow and white pigments*

Two different yellow pigments can be identified: lead-tin yellow (green + red = yellow map in Fig. 3c) was used for the flowers which surround the initial but also for King David's collar and the inner lining of his crimson robe. Lead-tin yellow was also added to the green grass and trees in the landscape. Difficult to spot in Fig. 3c, which is an RGB composite map including the Sn-K distribution, but much clearer if the Sn-L map is considered (cf. Fig. 4), is the presence of this pigment on the thin yellow highlights of the green leaves and ring-like decoration on the left side of the initial. The inner portion of the oval outline of the initial is also highlighted in lead-tin yellow on the right-hand side.
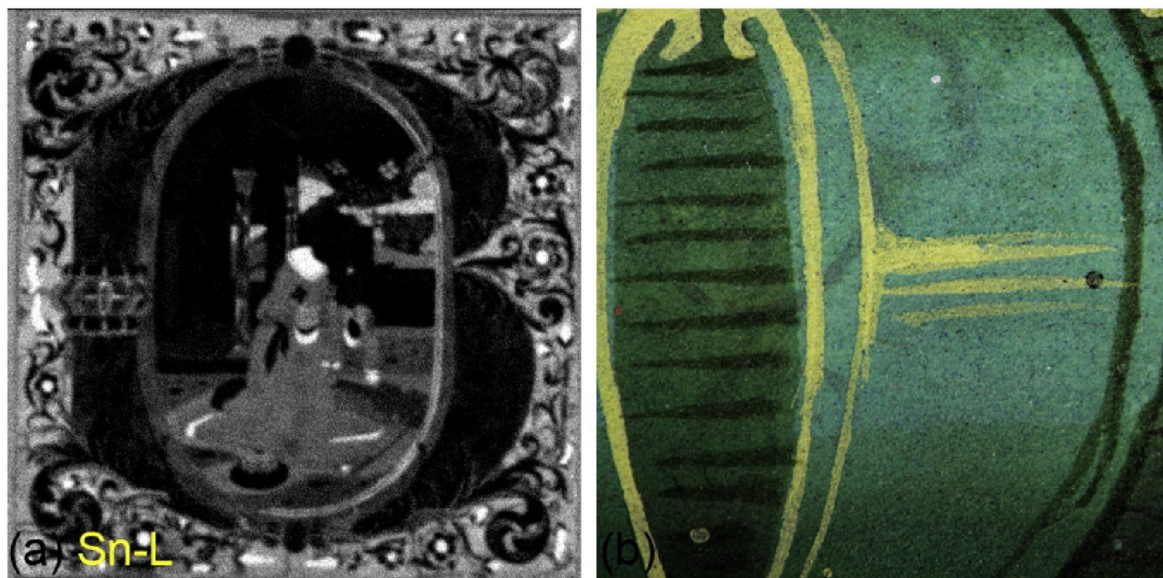
*Figure 4: **(a)** Sn-L map **(b)** microphotograph of green foliage with yellow highlights.*

 In contrast to the above, an arsenic-based pigment (blue map in Fig. 3c) was used for the capitals and base of the columns and also for the inner outline of the initial. Raman spectroscopy allowed to specify the nature of this material as an arsenic sulphide glass, a hitherto almost unknown pigment, only recently identified securely on painted objects [16,17].[3]

The fact that the As-K map appears to include the large letter A, present on the reverse of the fragment and actually containing mercury (cf. Fig. 5 and Section 3.3) is a clear example of how XRF emission lines related to different elements but very close in energy – as is the case for the As-K_β line at 11.73 keV and the Hg-L_β line at 11.82 keV – can cause mis-fits in the elemental maps.

Lead white (green map in Fig. 3c) was used extensively in the white and flesh tone areas, and was also mixed with other pigments to modify their hue. For example, lead white was added abundantly to the light pink of the initial, but not to the deep red robe of David, both of which were painted with organic dyes, as discussed in the following section.

---

[3] Raman spectra were collected and interpreted by Prof. Andrew Beeby (Dept. of Chemistry, University of Durham) and Dr. Kate Nicholson (Dept. of Applied Sciences, Northumbria University) with a fiber-based instrument employing a 632.8 nm laser whose power was kept below 0.3 mW at the sample throughout the measurements. Measured areas are estimated to be about 50 μm in diameter

3.1.3.3 *Red and pink pigments*

The Hg-L map (Fig. 5a) cannot easily be interpreted based on the visual appearance of the illumination, as the penetrating nature of the X-rays induced a strong signal from the mercury present in the musical stave and letters painted in red on the reverse side of the fragment (Fig. 5b, flipped left-to-right to facilitate a comparison with the elemental map),[4] to reach the detector. Areas where the mercury signal is less intense, suggesting the presence of vermillion in small quantities and most likely in mixtures with other materials, include King David's face, hands and foot, his viol, the darker portions of the grey-brown architecture, as well as the light brick-red floor and buildings in the landscape, all of which also contain large amounts of lead – most likely in the form of lead white.

Figure 5: (a) Hg-L map (b) visible image of the reverse side of the fragment, flipped left-to-right.

The deep red robe of David and the pink of the initial B with its floral decoration do not appear to contain any mercury, excluding the presence of vermillion. They do, however, contain calcium, whose content is especially high in David's robe (red map in Fig. 3d), suggesting the use of an organic dye. This hypothesis is supported by the absorption bands observed at about 526 and 560 nm in the reflectance spectra of these areas (data not shown) which are characteristic of insect-derived dyes such as kermes.

---

[4] At some point in the past, this fragment was - after its excision from the original bound volume - pasted onto paper, which was later largely removed. Fig. 5b shows the reverse side of the fragment in its present partially uncovered state.

3.1.3.4 *Calcium compounds*

Apart from David's red robe, in which the presence of calcium indicates the use of a lake pigment, the highest concentration of calcium corresponds to areas of high strontium and sulphur (Sr + Ca + S = white map in Fig. 3d). These three elements together suggest that presence of gypsum, with its common impurity of celestite, was used as a ground for the gold leaf (see also Sections 3.5 and 3.6). It is worth noting that the sulphur map (blue) is noisy in the central area due to the spectral overlap of the $S-K_\alpha$ peak at 2.31 keV and the $Pb-M_\alpha$ peak at 2.34 keV, which may result in a mis-fit in regions where lead is especially abundant.

3.1.3.5 *Earth pigments*

An iron-rich ochre pigment (red map in Fig. 3e) was used to paint David's viol, and mixed or layered with the arsenic sulphide glass identified in the columns' capitals and base. Ochre was also used to shadow the left side of the inner outline of the initial, and as part of the preparation layer for the gold leaf (see also Sections 3.4. and 3.6). The letters and musical notes present on the reverse side of the fragment and painted with iron gall ink are only faintly visible in the Fe-K map, but more readily apparent in the Zn-K map (cf. Fig. 3b, discussed in Section 3.1).

Rather unexpectedly, the elemental maps for iron and manganese (blue map in Fig. 1e) do not overlap, as would be the case if an umber pigment had been used. Instead, manganese is assumed to be present in the form of a manganese oxide or hydroxide, mixed with lead white and in some areas with vermillion, resulting in the grey-brown color of the building to the left of David, the wall directly behind him, and the stones scattered on the floor. It is in this context relevant to point out that the use of pyrolusite, a naturally-occurring black manganese dioxide, has been reported in easel paintings by a number of 16th century artists working in Rome, Bologna, and other Northern Italian cities, including Perugino [18].

3.1.3.6 *Gold*

Possibly, illuminated manuscripts are best known for their lavish use of gilded decorations. Gold could be applied as 'shell gold' or gold paint (finely ground gold particles held together by a binding medium) or as gold leaf (small thin sheets of hammered gold, laid side by side over a preparatory layer) [19]. Both techniques were used in this fragment (Fig. 3f). Fine details such as David's crown and jewels and the highlights of his robe were painted with shell gold, while the area around the initial was decorated using gold leaf, laid over a ground containing gypsum and a red ochre (Fig. 3d and e) and then highly burnished. Fig. 3f clearly shows the sites where two adjacent gold leaves overlap, as the double thickness of metal results in higher greyscale values in the $Au-L_\alpha$ map.

3.1.4 **Conclusions**

MA-XRF scanning of a 15th century Italian manuscript fragment was undertaken to gain insight into the materials and techniques of Renaissance illuminators and to help answer specific questions regarding its authorship and place of execution, currently considered to be either Bologna or Rome.

The non-invasive analysis allowed to reconstruct the palette employed by the anonymous illuminator and highlighted the likely use of two unusual pigments: an arsenic sulphide glass and a manganese (hydr)oxide. Identification of the latter would have been difficult, had it not been for the availability of an elemental map for manganese, which showed no overlap with the map for iron, excluding the presence of umber pigments, widely used and therefore less distinctive of a specific artist or school.

The use of manganese oxides as black pigments as hitherto been identified almost exclusively in easel paintings by a number of 16th century artists working in Central and Northern Italy, including Perugino, with whom the unknown artist of the manuscript fragment shows stylistic affinities. Therefore, while it could not provide a definite answer to the question of geographic origin, the technical analysis did offer a strong support to securely place the fragment within a specific artistic context.

In order to allow for more precise and more reliable pigment identification, MA-XRF scanning is best combined with a series of point measurements of a 'fingerprinting' method such as Raman spectroscopy or X-ray diffraction.

References

1. M. Alfeld, K. Janssens, J. Dik, W. de Nolf, G. Van der Snickt, Optimization of mobile scanning macro-XRF systems for the *in situ* investigation of historical paintings, J. Anal. At. Spectrom. 26 (2011) 899–909, http://dx.doi.org/10.1039/c0ja00257g.

2. M. Alfeld, G. van der Snickt, F. Vanmeert, K. Janssens, J. Dik, K. Appel, L. van der Loeff, M. Chavannes, T. Meedendorp, E. Hendricks, Scanning XRF investigation of a Flower Still Life and its underlying composition from the collection of the Kröller-Müller Museum, Appl. Phys. A 111 (2013) 165–175, http://dx.doi.org/10.1007/s00339012-7526-x.

3. G. Van der Snickt, S. Legrand, J. Caen, F. Vanmeert, M. Alfeld, K. Janssens, Chemical imaging of stained-glass windows by means of Macro X-Ray Fluorescence (MA-XRF) scanning, Microchem. J. (2015) (in this issue).

4. N. Turner, K. Trentelman, C.S. Patterson, J. Dik, G. Van der Snickt, K. Janssens, Macro-XRF Scanning of Illuminations: An improved method for non-invasive analysis of illuminated manuscripts, Proceedings of "INSIDE ILLUMINATIONS. Art Technical Research & the Illuminated Manuscript", KIK-IRPA, Brussels, 5 June 2014, Corpus of Illuminated Manuscripts of Illuminare, KU Leuven, Peeters Publishers, Leuven, 2015 (forthcoming).

5. S. Panayotova (Ed.), Colour: the art and science of illuminated manuscripts, Harvey Miller/Brepols, London and Turnhout, 2016 (forthcoming).

6. M. Clarke, The analysis of medieval European manuscripts, Rev. Conserv. 2 (2001) 3–17.

7. K. Trentelman, C. Schmidt Patterson, N. Turner, XRF analysis of manuscript illuminations, in: A.N. Shugar, J.L. Mass (Eds.), Studies in Archaeological Sciences, Handheld XRF for art and archaeology Leuven University Press, Leuven 2012, pp. 159–189.

8. M. Alfeld, K. Janssens, Strategies for processing mega-pixel X-ray fluorescence hyperspectral data: a case study on a version of Caravaggio's painting *Supper at Emmaus*, J. Anal. At. Spectrom. 30 (2015) 777–789.

9. V.A. Solé, E. Papillon, M. Cotte, Ph. Walter, J. Susini, A multiplatform code for the analysis of energy-dispersive X-ray fluorescence spectra, Spectrochim. Acta Part B 62 (2007) 63–68.

10. N. Eastaugh, V. Walsh, T. Chaplin, R. Siddall, Pigment Compendium: a dictionary and optical microscopy of historical pigments, Elsevier Butterworth-Heinemann, Oxford, 2008.

11. C. Seccaroni, P. Moioli, Fluorescenza X, Prontuario per l'analisi XRF portatile applicata a superfici policrome. , Nardini Editore, Florence, 2004.

12. M.R. Derrick, D. Stulik, J.M. Landry, Infrared spectroscopy in conservation science, The Getty Conservation Institute, Los Angeles, 1999 134–138.

13. A. Re, A. Lo Giudice, D. Angelici, S. Calusi, L. Giuntini, M. Massi, G. Pratesi, Lapis lazuli provenance study by means of micro-PIXE, Nucl. Inst. Methods B 269 (2011) 2373–2377, http://dx.doi.org/10.1016/j.nimb.2011.02.070.

14.   J. Kirby, M. Spring, C. Higgitt, The technology of red lake pigment manufacture: study of the dyestuff substrate, Natl. Gallery Tech. Bull. 26 (2005) 71–87.

15.   D. Hradil, T. Grygar, J. Hradilová, P. Bezdička, V. Grűnwaldová, I. Fogaš, C. Miliani, Microanalytical identification of Pb-Sb-Sn yellow pigment in historical European paintings and its differentiation from lead tin and Naples yellows, J. Cult. Herit. 8 (2007) 377–386.

16.   G. Grundmann, N. Ivleva, M. Richter, H. Stege, C. Haisch, The rediscovery of sublimed arsenic sulphide pigments in painting and polychromy: applications of Raman microspectroscopy, in: M. Spring, H. Howard, C. Christensen, S.Q. Lomax, M. Palmer, S. Wilcox (Eds.), Studying Old Master Paintings: Technology and Practice, Postprints of The National Gallery Technical Bulletin 30th Anniversary Conference, London, UK, 16–18 September 2009, Archetype Publications Ltd., London 2011, pp. 269–276.

17.   M. Vermeulen, J. Sanyova, K. Janssens, Identification of artificial orpiment in the interior decorations of the Japanese tower in Laeken, Brussels, Belgium, Herit. Sci. 3 (2015) 9, http://dx.doi.org/10.1186/s40494-015-0040-7.

18.   M. Spring, R. Grout, R. White, "Black Earths": A Study of Unusual Black and Dark Grey Pigments used by Artists in the Sixteenth Century, Natl. Gallery Tech. Bull. 24 (2003) 96–114.

19.   D.V. Thompson Jr., G.H. Hamilton, De Arte Illuminandi. The technique of manuscript illumination, Yale University Press, New Haven, 1933.

3.2 Non-invasive analysis of a 15ᵗʰ century illuminated manuscript fragment: point-based vs imaging spectroscopy

Abstract Illuminated manuscript fragments are some of the best preserved objects of Western cultural heritage. Therefore, scholars are limited to non-invasive - often point-based - methods, to answer questions on material usage, technique, origin and previous treatments. These powerful methods yield specific information; however, the information is limited to the number of points analyzed. Imaging spectroscopies such as MA-XRF and MA-rFTIR combine specificity with the power of imaging, resulting in distribution images that are interpretable by non-spectroscopists and the public at large. In this paper the possible added value of using imaging spectroscopy is discussed. Do these methods yield the same results as an extensive point-based spectroscopic campaign and can they bring novel information? As a case study, a 15ᵗʰ century illuminated manuscript fragment is employed in order to explore the differences between these approaches and present an inventory of their advantages and limitations.

3.2.1 Introduction

Of all objects of Western cultural heritage, Medieval and Renaissance manuscript illuminations have most frequently retained their original color appearance in an optimal manner. Often well protected within volumes, inside their heavy bindings, they were less exposed to environmental variations, pollutants, vandalism and other causes of damage and degradation. As a result, they can provide scholars with detailed insights into Medieval and Renaissance artists' materials and techniques, showing geographic variation as well as their evolution over time.

Due to their smaller size and generally better state of preservation than easel paintings, sampling of illuminated manuscripts is rarely allowed. Thus their scientific analysis has to be limited to non-invasive techniques. Point-based techniques such as X-ray fluorescence (XRF) spectroscopy, Raman spectroscopy and ultraviolet visible and near-infrared (UV–VIS-NIR) fiber optics reflectance spectroscopy (FORS) are all routinely employed for this purpose [1,2,3,4,5]. Microspectrofluorimetry and X-ray diffraction have also been used successfully in several cases [6,7,8,9]. One of the oldest and most widely used imaging methods for the examination of works of art is X-ray radiography (XRR). Contrary to the case of easel paintings, XRR is used much less frequently to investigate illuminated manuscripts due to the thinner build-up of the paint layers and the lower occurrence of significant *pentimenti*. The use of NIR reflectance (IRR) and UV (fluorescence) imaging systems has long allowed scholars to visualize underdrawings and to identify past

---

conservation treatments. More recently, hyperspectral imaging systems have become an appreciated set of tools in the field of cultural heritage science. Originating from the field of remote sensing [10], such systems record reflected or emitted UV, visible and NIR radiation in a large number of narrow contiguous spectral bands, resulting not only in (hundreds of) images, but also in a full spectral response curve to become available at each imaged pixel [11,12,13,14,15]. The most recent generation of hyperspectral imaging systems not only employs camera systems, but often incorporates spectroscopic techniques such as FORS, XRF, XRD, and FTIR also used in scanning mode [16,17,18]. Methods of this type that are employed in this paper are macroscopic XRF (MA-XRF) [19,20] and macroscopic reflection mode FTIR (MA-rFTIR) scanning [21].

The main purpose of this paper is to describe which additional benefits can be obtained by collecting a combination of spectroscopic data across the entire surface of the work of art, rather than limiting the (multimode) spectroscopic analysis to a discreet number of locations that are considered a priori to be representative of the entire artefact. To do so, we will consider a 15th century illuminated manuscript fragment (Fig. 1), which had initially been characterized by means of various point-based spectroscopic methods, allowing to make a hopefully complete list of the paintings materials employed for its creation in a non-invasive manner. The fragment was recently part of a major exhibition at the Fitzwilliam Museum [22], in preparation for which scanning MA-XRF and MA-rFTIR analyses were performed in Cambridge during two successive measurement campaigns in 2014 and 2016.

By selecting a fragment from a 15th century illuminated manuscript as a case study, rather than a more complex artwork such as an oil painting, we opt to investigate an object with a simpler layer stratigraphy and in which less complex pigments mixtures are presumably employed. These two factors should allow to focus on the problem of pigment identification via a multi-modal spectroscopic approach, while avoiding limitations imposed by the presence of covering varnishes, oily binding media and overpaint layers that strongly absorb and scatter radiation.

We will first discuss the information which can be gleaned from the elemental maps generated by means of MA-XRF imaging of the fragment. In addition to the elemental maps themselves, we will show that employing inter-element correlation among MA-XRF distributions can be very useful to distinguish between various types of artists' pigments having similar but (sometimes subtly) different elemental profiles. Since this approach does not always suffice to extract all relevant information on the nature of the materials present, we will then discuss the combined use of MA-XRF and MA-rFTIR to obtain maps with higher chemical specificity. We will conclude by making a critical assessment of the advantages and limitations of the combined use of MA-XRF and MA-rFTIR when compared to point-based multimodal spectroscopic materials identification.

Figure 1: Don Silvestro dei Gherarducci, St Clement in a historiated initial D, Florence, c. 1370–1375, 170 × 165 mm². Fitzwilliam Museum, MS 5–1979 © The Fitzwilliam Museum, Cambridge, UK.

3.2.2 Materials and methods

3.2.2.1 *The manuscript fragment: St Clement in a historiated initial D*

The manuscript fragment studied (Fitzwilliam Museum, MS 5-1979, Fig. 1) shows St Clement in a historiated initial D. It is one of four initials in the Fitzwilliam Museum's collection which were originally part of a set of choir books illuminated between 1370 and 1506 by successive generations of artists in the scriptorium of the Camaldolese monastery of Santa Maria degli Angeli in Florence [22]. These volumes were mutilated during the Napoleonic campaigns (1797–1809), with many of their images cut out to be sold as individual 'paintings' and therefore subsequently scattered all over the world. The

volumes remain at the Biblioteca Laurenziana in Florence, labelled as *Corali* 1–19. The image with St Clement was excised from *Corale* 2, the earliest work of the head of the scriptorium Don Silvestro dei Gherarducci, dated to 1370–1371. The initial would have opened the Introit to the Mass for St Clement's feast on 23 November beginning *Dicit dominus sermones mei*, originally on folio 159 of the book [23]. When excised from its parent book, the initial, measuring approximately 150 × 145 mm², was trimmed very closely to its edges (the entire fragment only measures 170 × 165 mm²) and then glued to a cardboard support, which currently obscures the reverse side.

3.2.2.2 *MA-XRF instrumentation*

MA-XRF is based on the sequential recording of a very large number of XRF spectra while a two-dimensional motorized stage moves the artwork relative to the measuring head, or vice versa. The latter consists of (a) an X-ray tube equipped with either a collimator or a polycapillary lens to define the primary X-ray beam and (b) one or more energy dispersive detectors to record the XRF signals emitted by the irradiated spot on the work of art. Due to the relative low energy of the secondary X-rays, measurements must be performed in reflection mode: the X-ray source and the detector capturing the secondary X-rays are positioned on the same side of the object.

Using such a setup, distribution information can be obtained for chemical elements heavier than K. Lighter elements such as S, P, Na, Mg, and Si emit low energetic XRF signals (< 3 keV), which are significantly absorbed by the object itself and in the air path between object surface and detector. Another limitation of the method is related to the use of energy dispersive (ED) detectors, which have a broader energy resolution than the intrinsic bandwidth of the secondary X-rays. This causes overlaps between element-specific XRF signals with approximately the same energy levels. Careful evaluation of the spectra by fitting them to analytical models allows to resolve most of these overlaps, but may lead to artefacts in the resulting images if the overlap is not correctly dealt with.

The MA-XRF scan recorded in this work was obtained using version F of a dedicated instrument, described in detail elsewhere (Fig. 2a) [20]. This instrument consists of a 50 watt molybdenum anode X-ray tube (XOS, USA), equipped with a polycapillary lens with a focal spot size of 50 μm at a distance of 3 mm. During scanning, the manuscript fragment was placed parallel to the scanning plane at a distance of approximately 6 mm from the front of the lens, resulting in a larger spot size than defined by the polycapillary. The tube ran at 50 kV and 1 mA. One Vortex EX-90 detector (Hitachi, USA) was used, at an angle of 50 degrees relative to the primary beam.

With MA-XRF, every 333 μm, an XRF spectrum is recorded during a period of 365 ms, resulting in an overall scanning time of approximately 22 h for this object.

The MA-XRF dataset was processed by means of a combination of three data processing packages: Datamuncher [24], PyMca [25] and bAxil [26,27]. The results of this data treatment are three dimensional (x, y, E) data cubes, where x and y are the spatial or pixel coordinates of the scanned area. The third dimension (E) represents the net XRF intensities of the different elemental contributions (Z > 15) to the recorded XRF spectra. Fig. 3 shows a series of elemental maps recorded from the manuscript fragment.

For more quantitative analysis and in order to distinguish between multiple combinations of the same two elements, correlation biplots can be used (see e.g. Figs. 6 and 8). In these graphs, each pixel is plotted against its fitted intensity for two elemental lines. If there are multiple pixels with a similar composition, these will appear correlated and can be seen as clusters. By selecting these clusters, it is possible to mark the corresponding pixels in an elemental distribution image.

3.2.2.3 *MA-rFTIR instrumentation*

MA-rFTIR also works in a point-by-point scanning mode; it operates in the mid infrared range. The measurement head, a compact Alpha FTIR spectrometer (Bruker, Germany) [21] emits a polychromatic beam of infrared radiation of 1–2 mm diameter via the Michelson interferometer. This beam is focused on the surface under examination by a spherical gold mirror. A second mirror of this kind captures the radiation reflected by the surface and leads it toward the DTGS detector of the FTIR spectrometer. A 20°/20° irradiation/collection geometry is employed. Due to the low energy of infrared radiation, for most of the artists' materials present in illuminated manuscripts, it has much lower penetration capabilities than X-ray radiation. In order to use this technique in a non-invasive manner, it has to be applied in reflectance mode (contrary to classic IR-spectrometers which usually operate in transmission mode). The resulting reflected infrared spectra are more complex than regular absorption FTIR spectra, as absorption bands can appear inverted or show a derivative shape [28].

*Figure 2: (**a**) MA-XRF scanning of MS 5–1979; (**b**) MA-rFTIR scanning of MS 5–1979. In both cases, the measuring head is positioned on a motorized two-dimensional stage while the manuscript fragment is securely mounted on an easel and remains stationary.*

Fig. 2b shows a photograph taken during the MA-rFTIR scanning of the manuscript fragment. Spectral acquisition was done using the Bruker OPUS 6.0 software package in the range 7500–375 cm^{-1} (~1.3–26.7 µm). A spectral background was recorded during 30 min prior to scanning the manuscript fragment by placing a gold coated mirror in front of the instrument. A coaxial camera allowed to monitor the scanning process and helped with the alignment of the instrument with the artefact. The fragment was placed in the instrument's focal point at a distance of 1.5 cm from the external reflection module. During a scan, an FTIR spectrum was recorded each millimeter over a period of 3 s, resulting in a total scanning time of 56 h.

All subsequent MA-rFTIR data treatment was performed in the scientific programming package IDL 8.3. Individual rFTIR spectra were combined into a three dimensional data cube, with x and y being the spatial coordinates and z the measured reflectance intensity. The reflectance intensities (*R*) are converted to pseudo absorbance (*A' = log(1/ R)*). The chemical distribution images display the baseline-subtracted, integrated intensity of the infrared band of interest. This subtracted baseline runs through the first and the last point of the integrated interval. In order to obtain qualitative spectra for identification, nine spectra from similar data points are combined when extracting spectra from the dataset in order to reduce the noise that is inherently present when measuring only briefly in each point.

3.2.3 Results and discussion

3.2.3.1 *Preliminary results*

Table 1 shows an overview of pigments present in the differently colored areas of the fragment, identified using a combination of non-invasive site-specific techniques including FORS, XRF, FTIR and Raman spectroscopy accompanied by near-infrared imaging and observation under magnification. This work was carried out prior to the macroscanning experiments [29]. The palette is fairly standard for 14th century Florentine illumination and includes carbon black, lead white (used both on its own and mixed with other pigments to modify their hue), vermilion, red lead, ultramarine, azurite and organic pinks. Small amounts of ultramarine were also added to the white areas in order to obtain a cooler hue. A dark red earth pigment was used to outline the glittering bronze-colored decorations painted in mosaic gold (SnS_2). A yellow lead oxide (PbO, massicot) was likely mixed with azurite to provide green hues whereas the yellow oval surrounding St Clement was painted with lead tin yellow. Gold leaf was laid over a gypsum-based ground and a red bole and then burnished to a high shine. The flesh tones were painted by mixing and layering different amounts of lead white and vermillion on a green earth base, using a technique that closely resembles contemporary easel painting. Egg yolk appears to have been used as a binding medium for the red lead paint, and possibly for vermilion as well [30,31].

Table 1: Palette identified on MS 5-1979 prior to MA-XRF and MA-rFTIR scanning.

Colour	Pigments
Black	Carbon-based black
White	Lead white (ultramarine mixed in)
Red	Vermilion
	Red lead (orange hue)
	Fe-oxide pigment
Pink	Gypsum, organic dye
Yellow	Lead tin yellow (type II?)
	lead oxide or lead white and organic dye
Blue	Ultramarine mixed with azurite
	Ultramarine
Green	Azurite mixed with lead oxide or lead white and organic dye
Flesh tones	Green earth mixed with lead white and vermilion
Metals	Gold
	Mosaic gold
Bole	Gypsum, Fe-oxide pigment
Ink	(Brown) Fe-gall ink
	(Red) vermilion

The pink leaves and the yellow initial, as well as the white highlights over the orange leaves and ornaments, have darkened significantly. This is most likely linked to the presence of lead white. In the pink and yellow areas the discoloration appears to have started not on the surface but rather in the lower portion of the paint layers. If this is indeed the case, the degradation process may have been catalyzed by the materials used to glue the fragment to its modern cardboard support. Microscope images acquired in raking light provide evidence of the previous existence on the front side of the image of a brown cardboard mat, stamped with flowers and other decorative elements. The impressions left by these flowers are still visible, especially along the lower edge of the fragment.

The following sections discuss in detail the artists' materials and techniques used for the decoration of the manuscript fragment and focus specifically on how these can be identified through a combination of different MA-XRF and MA-rFTIR images.

3.2.3.2 *Gilded areas*

With respect to the gilded parts of the fragment, several questions can be answered by means of chemical imaging: what type of gilding method was used? Is real gold actually employed in all areas which appear gilded? What is their overall state of conservation?

As shown in Table 1, metallic gold (Au) is present, predominantly in the background of the fragment but also to depict the gilded edge of the saint's robe. A form of imitation gold is also present, in the roundels above and below the saint and in the shiny bronze-looking leaf in the top left corner. This is tin sulphide (SnS_2), usually called 'mosaic gold'.

In the 15th century, illuminated manuscripts were gilded either by painting with 'liquid' gold (so-called 'shell gold') or by applying thin gold sheets ('gold leaf'). Shell gold was prepared by grinding small gold flakes in a shell and by mixing the resulting powder with a binding medium, after which it could be used as regular paint. In order to make thinly hammered gold foils adhere to a manuscript page, a colored preparatory layer was usually painted first onto the parchment substrate. This facilitates adhesion of the gold foil and also allows to modify its color, shape and surface texture and permits burnishing of the surface.

Fig. 4a represents a schematic cross section of gold leaves (yellow) applied using a bole (red) on parchment (tan). From left to right, along the top, one can see first the most common situation with a single leaf present; followed by a damaged area where the bole is exposed; then details painted in blue and orange on top of the gold leaf (as is the case e.g. along the edge of the Saint's mantle); and finally a double layer of gold, indicating areas where two leaves overlap.
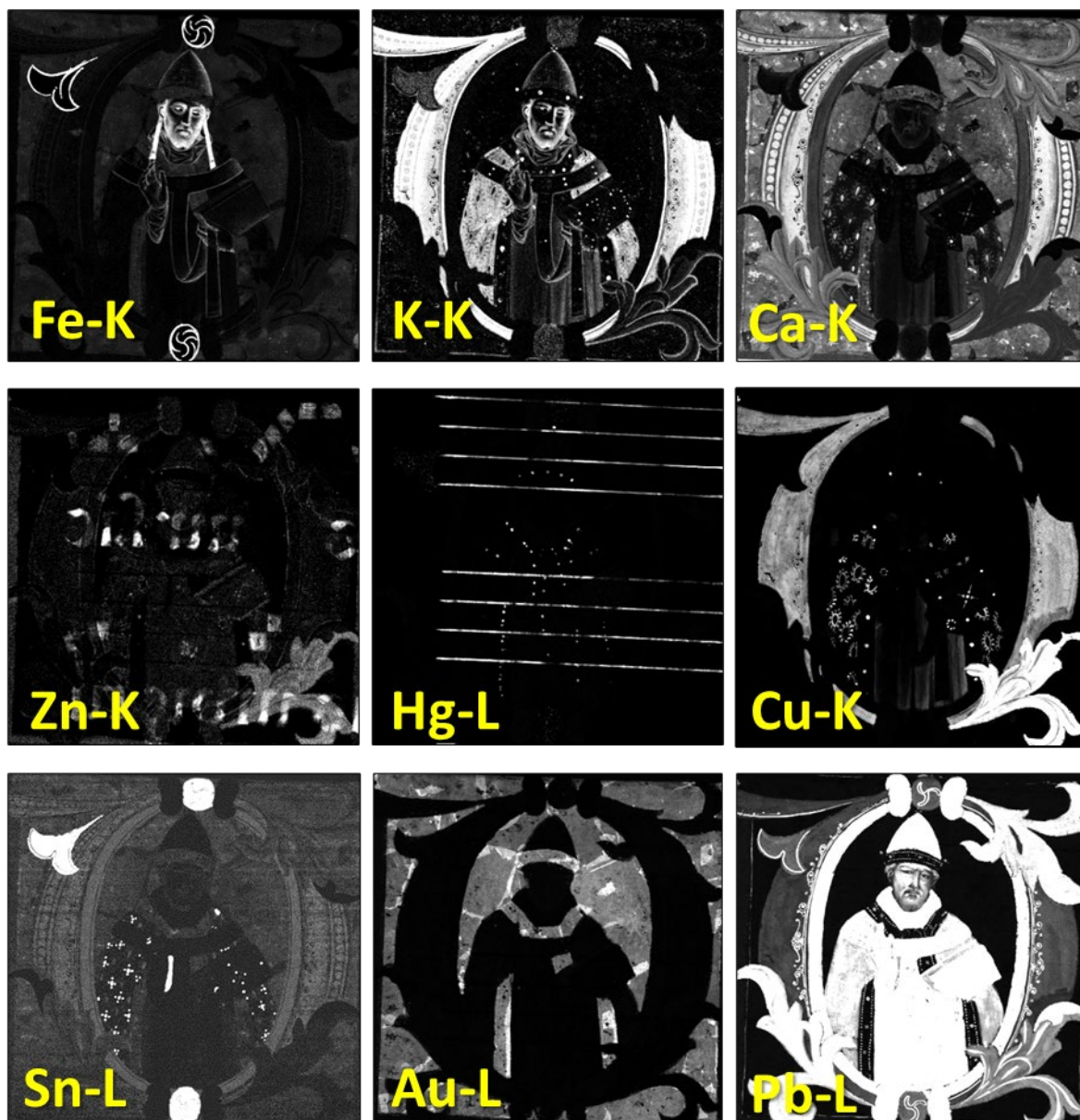
Figure 3: Elemental maps obtained by MA-XRF scanning of MS 5–1979. Each image consists of 202,500 pixels (total scan time: 21 h and 26 min).

The Au-L maps in Figs. 3 and 5d illustrate how MA-XRF can be used to specifically identify the gilding technique used. In those areas where two gold foils were made to overlap, the Au-L intensity is approximately twice as high as that observed in other gilded areas (yellow areas in Fig. 6a). In the Au-L map, the location of the multi-colored decorations painted over the gilded edge of the robe are visible as darker spots, since the painted-on details partially absorb the Au-L XRF signals emerging from the gold foil (see Figs. 3 and 5d). The Fe and Ca maps in Fig. 4 allow to see that wherever gold leaf was employed, faint Ca-K and Fe-K signals are also present, emerging from the bole layer used as a ground for the gold foil. In both of the maps, where a double thickness of gold leaf is present, the

159

signal from calcium and iron is lower, confirming that these two elements are situated in a paint layer below the gold. Small areas of gold leaf loss (Fig. 5a) can be identified as bright 'spots', especially visible in the Ca-K map, and marked in red in the false-color image shown in Fig. 5b. The same areas in the gilded background that appear as hotspots in the Ca-K map, show an increase in intensity for the sulphate stretching band visualized in Fig. 4e, supporting the presence of gypsum in the bole layer as can be seen in the proposed cross-section in Fig. 4a. This gypsum can only be detected when the gold layer is damaged, as the thin gold foil otherwise reflects the IR radiation before it can reach the underlying gypsum.

When considering the Au-L, Ca-K and Fe-K distributions more in detail, for example in the upper left portion of the gilded background, above the initial D, it becomes also clear that these elemental images can be used to map and quantitatively estimate the fraction of the leaf-gilded area that has lost its gilding. These areas can be identified by employing the Au-L vs Ca-K XRF intensity scatter plot of Fig. 6b. In this scatter plot, two main features can be seen: a narrow vertical cluster (circled in blue, on the left) consisting of pixels showing no gold and a large group of pixels featuring an anti-correlation between gold and calcium. This anti-correlation means that with increasing Au-L intensity, the detected Ca-K intensity decreases. The bulk of the pixels in this anti-correlation groups - circled in green and corresponding to areas covered with a single gold leaf - appear over a net Au-L intensity range of 600 to 1700 counts. Another group (in red), which contains a relatively small number of points, appears to be an extension of the green group towards lower Au-L intensities; this group corresponds to areas where the gold leaf has detached. Above 1700 net Au-L counts, a different anticorrelation between Au-L and Ca-K is observed, suggesting that the stratigraphy is different than in the above-described areas; the resulting group of pixels, circled in yellow, represent areas where two gold leaves overlap. These four color-coded pixel groups are shown in the form of a false color image in Fig. 6a (where the white rectangle indicates the detail shown in Figs. 5a and b). The "red coded" pixels in the background area amount to ca 6% of the total single leaf-covered area (green in Fig. 6a). As mentioned above, the "red coded" pixels are characterized by a higher Ca signal, since in these locations the gold leaf that absorbs the Ca-K XRF signal is no longer intact. Other Ca-rich pixels in areas that do not contain gold are "blue coded" and relate to the blue initial "D" surrounding the saint rather than to the gilding.
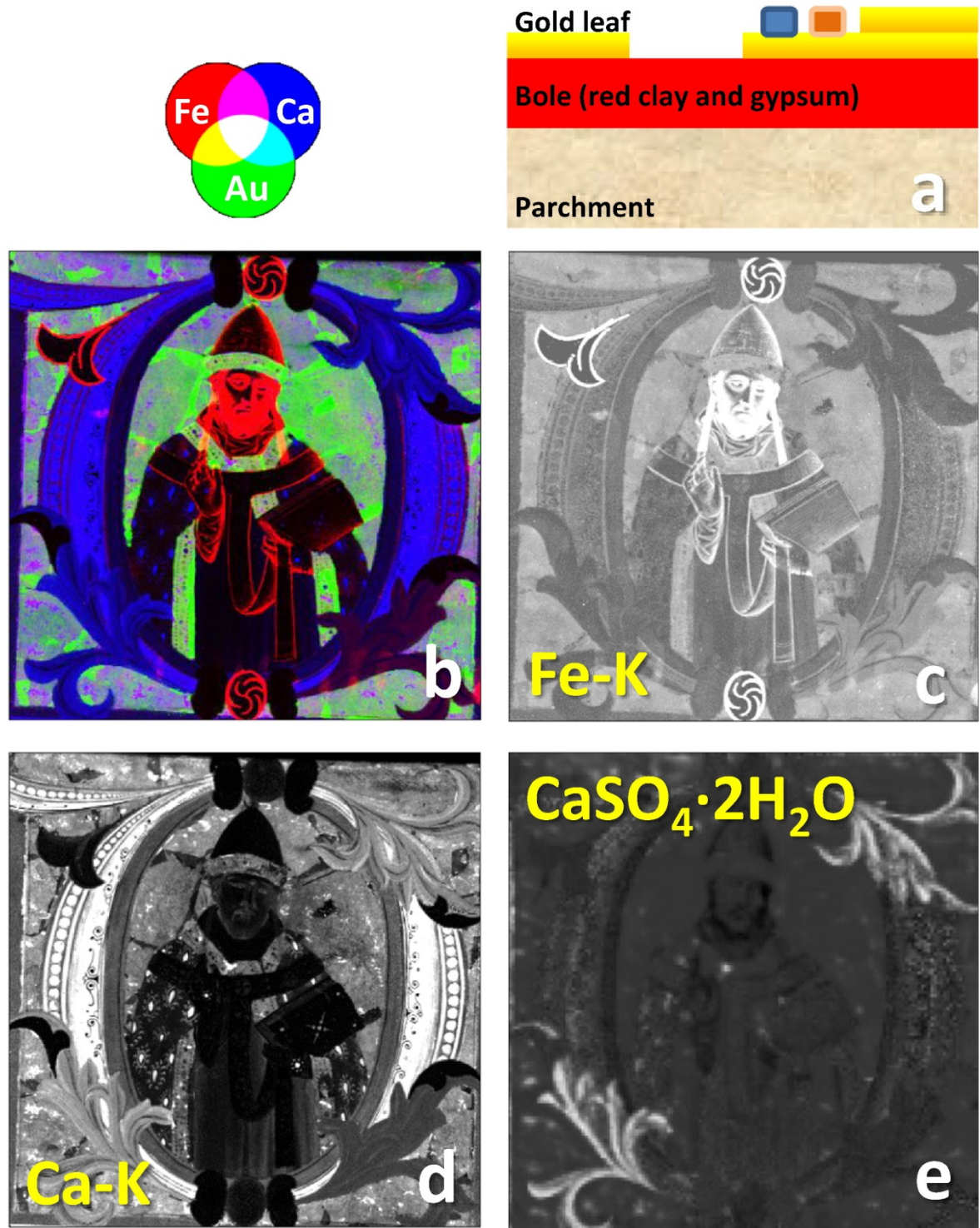
Figure 4: (a) Schematic cross-sectional buildup of gilded areas; (b) RGB composite image where R: Fe-K, G: Au-L and B: Ca-K MA-XRF distributions; (c-d) Fe-K and Ca-K distributions, with grey scale adjusted relative to Fig. 3 to increase visibility of the lower-intensity areas; (e) MA-rFTIR intensity distribution of the 1090–1174 cm^{-1} band, attributed to the sulphate stretching of gypsum ($CaSO_4 \cdot 2H_2O$).
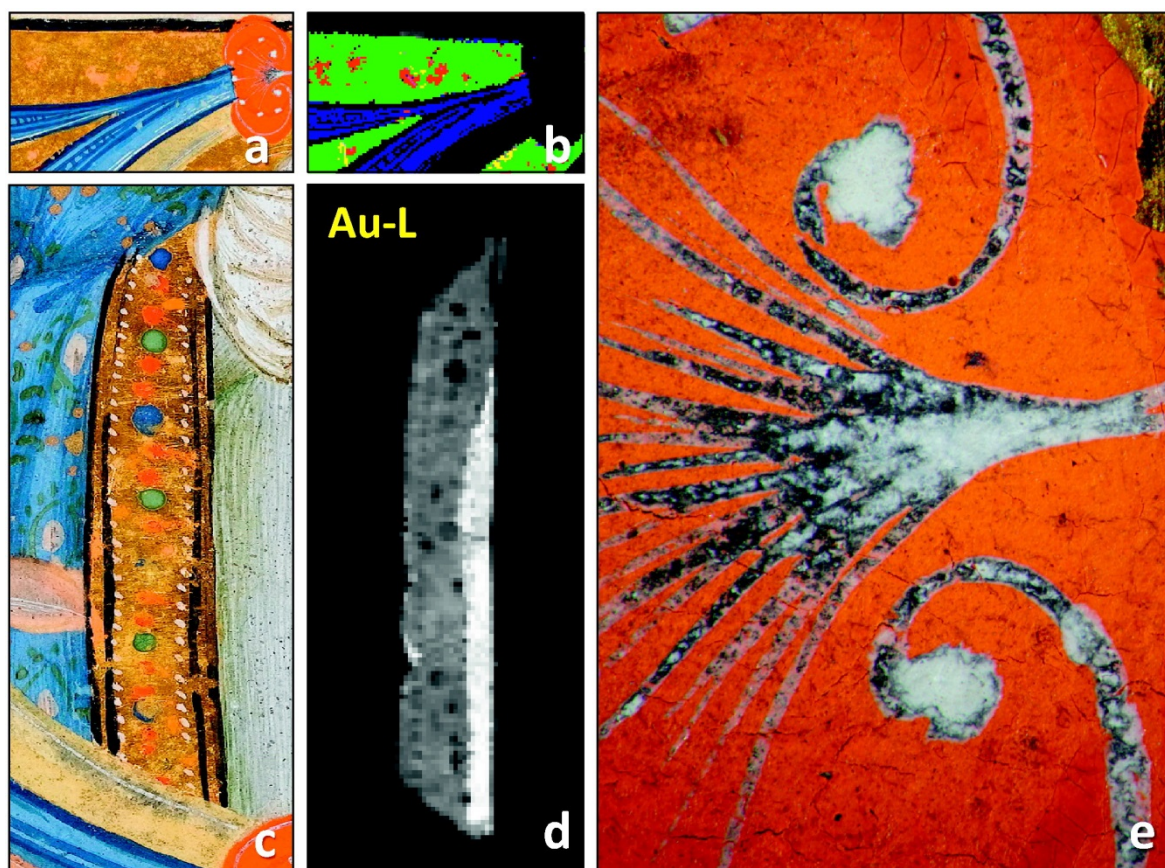
Figure 5: *(a)* detail of gilded background in the upper left corner; *(b)* corresponding false-color map showing locations; in green: covered with a single gold leaf; in yellow: covered with a double thickness of gold leaf; in red: no longer covered by gold leaf, showing an increased Ca-K signal and in blue: other Ca-rich areas (see also Fig. 6); *(c)* detail of the gilded edge of the Saint's robe; *(d)* corresponding Au-L elemental distribution; *(e)* detail of orange decoration with lead white highlights showing a dark degradation product. (For interpretation of the references to color in this figure legend, the reader is referred to the web version of this article.)

Areas painted with mosaic gold, characterized by the presence of Sn, can easily be identified from (the higher intensity portions of) the Sn–L map in Fig. 3 and the blue color-coded pixels in Fig. 8c. The small gilded portion of the robe's edge next to the saint's proper right hand also appears to be painted in mosaic gold instead of real gold, and shows no bole preparation either (virtually no Ca or Fe are present). Gold leaf was usually applied first, before the rest of the decoration was painted. The artist must have realized belatedly that this area needed to appear gilded, and used mosaic gold to simulate the appearance of the precious metal which he had forgotten to lay down. All mosaic gold elements of the illumination are outlined with a Fe-rich, dark reddish paint, which can be identified as red earth by the presence of hematite and clay minerals in the FT-IR maps. The fact that sulfides [32,33] and presumably mosaic gold as well can act as a local source of H_2S, a gas which can react with lead white to form galena (black lead sulphide, PbS) [34,35] might help to explain the black degradation product that has formed on top of the white highlights over the orange decorations (Fig. 5e).

From these considerations it is possible to conclude that in addition to the nature of the materials employed for gilding, the distribution of real and imitation gold conveys information on the specific techniques of application of these materials. As shown by Turner et al. [36] also the size and shape of the individual gold leaf squares employed can be estimated in this manner.
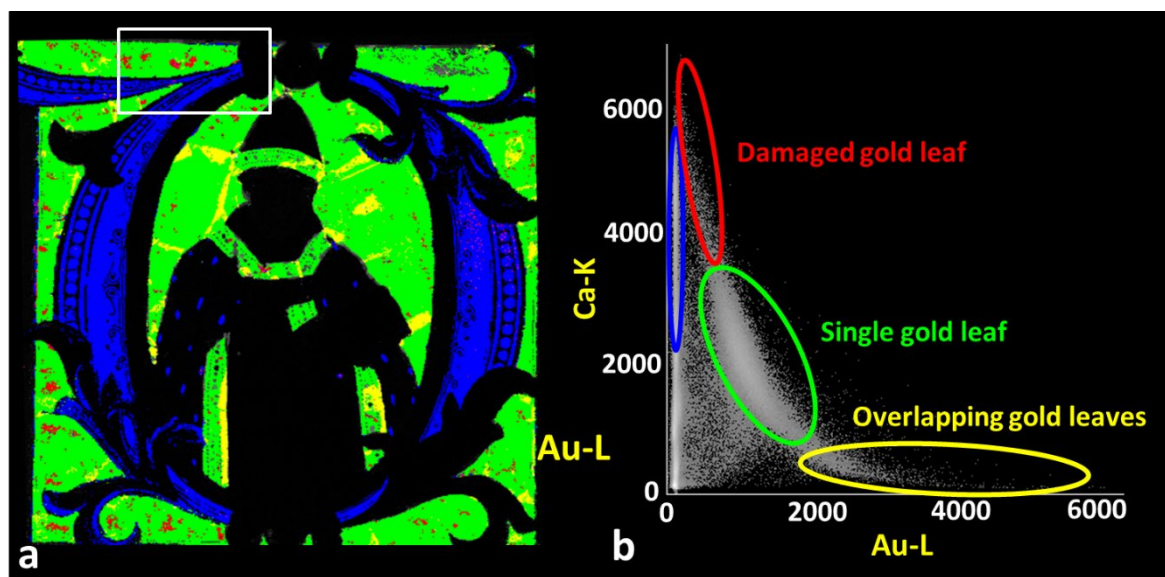

Figure 6: (a) False color map and (b) Au-L vs. Ca-K correlation plot highlighting the different types and conditions of gilded areas: green pixels: covered with a single gold leaf; yellow: covered with a double thickness of gold leaf; red pixels: losses in the gold leaf, showing low Au and high Ca signals; blue pixels: other high-Ca signal locations. (For interpretation of the references to color in this figure legend, the reader is referred to the web version of this article.)

3.2.3.3 *Information from the reverse side*

Since MS 5–1979 was originally part of a choir book, it is not surprising that a musical score is present on the reverse side of the fragment. This can be observed in the Fe-K, Zn-K and Hg–L maps (see Fig. 7), even though the fragment has been glued over thick cardboard. These maps correspond to fairly energetic XRF radiation (6.4 keV for Fe–Ka, 8.6 keV for Zn–Ka and 9.99 keV for Hg-La) so that when irradiating the parchment fragment, painted on both sides, the XRF radiation from both the recto and the verso can reach the XRF scanner detector without being completely absorbed along the way. The Zn and Hg maps can be read as a superimposition of contributions from both painted surfaces, on the recto and on the verso. Contributions from the recto include the green acanthus leaf in the lower right corner, visible in the Zn map, which are linked to zinc impurities in the azurite blue pigment used in the green mixture. Vermilion red dots, which decorate the saint's paraments, are visible in the Hg map. Also visible are traces of mercury in the areas painted with mosaic gold; these are remnants of the starting material used for the preparation of this synthetic pigment. Once these contributions are taken into account, one can identify what is present on the reverse side: in the Hg–L

image, vermilion red musical lines are clearly visible, whereas the Zn-K image clearly shows lettering as well as square and diamond-shape musical notes. Zinc is a common impurity in ferro-gallic inks, used for the text and musical notation in the majority of medieval and Renaissance illuminated manuscripts in Europe. One would expect to be able to identify the same lettering and musical notes in the Fe-map where, however, these contributions from the verso are not at all well visible. This is a common problem, also observed in other manuscript fragments (see for example the other three objects shown at http://www.fitzmuseum.cam.ac.uk/ illuminated/manuscript/discover/initials-from-choir-books). It is partly due to the contribution of Fe signals originating from the green earth underpaint of the saint's face and beard of the saint, the abovementioned hematite used to outline the mosaic gold areas and to paint the mitre's lappets, and the red clay used as a ground layer for the gold leaf. The intense Fe-signals emerging from the recto side combined with the object's stratigraphy, with rich paint layers as well as gold leaf, result in a recorded intensity for Fe which is lower than would be expected for iron gall ink. It is however still partially possible to visualize the lettering on the verso, by adjusting the grey scale of the Fe-K map to maximize the lower intensity levels, shown in Fig. 4c.
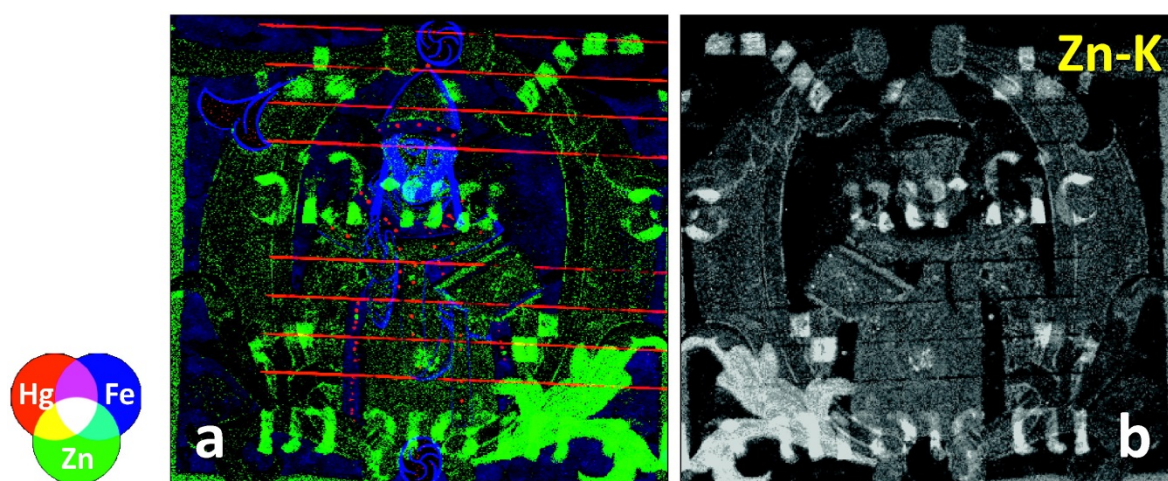

*Figure 7: (**a**) RGB composite of MA-XRF maps with R: Hg-L, G: Zn-K and B: Fe–K; (**b**) horizontally mirrored Zn-K map with adjusted contrast settings, improving the readability of the writing on the verso.*

The Zn map, which contains the most information about the text on the reverse of the fragment, can be horizontally mirrored and contrast adjusted to improve its readability (Fig. 7b). It is thus possible to read the Latin text: "*s vir sāc*" on the first line, followed by "*s Urbis tu*" on the second one. Considering the presence of missing text on both the left and the right side, the entire sentence can be read as "*[Beatu]s vir sa(n) c[tus Martinu]s urbis tu[tonis Episcopus]*", or "Beatus Saint Martin Bishop of the city of Tours". This is a significant discovery, as it allows to confirm the position of the St Clement fragment within its parent book, and to establish that the image was originally on the verso of a page [37].

These observations clearly show that in addition to providing information on the visible side of an illuminated fragment, a MA-XRF investigation is occasionally also able to provide relevant data on the reverse, often inaccessible side, which may reveal significant information about the original context of the object. At the same time, it should be pointed out that this advantage of the method, sometimes is also a limitation: in the case of illuminations in a bound volume being examined, care must be taken to isolate the illustration under examination from those on the adjacent pages in order to eliminate unwanted contributions from neighboring folios. This can be done by placing e.g. a lead sheet below the page being scanned or by suitable positioning of this page relative to the rest of the book.

3.2.3.4 *(Un)specific mapping of lead-based pigments of different colours*
Fig. 8b shows the MA-XRF distribution map of Pb, obtained by recording the Pb-L XRF radiation. A comparison with the visible image of the fragment (Fig. 1) shows that lead is present, in variable amounts, in all non-gilded areas and thus corresponds to white, yellow, red, pink, green, blue and flesh-colored areas. Clearly the filigree details painted on top of the mosaic gold areas and the blue exterior of the initial D appear to be painted with lead white. However, the nature of the other lead compounds present is not immediately obvious. The Pb-L/Sn-L correlation biplot of Fig. 8a (with the pixels mapped in Fig. 8c) allows to distinguish at least three subgroups: the blue pixel cluster corresponding to a high Sn-L signal but very low Pb-L signal, corresponding to the mosaic gold areas; the yellow cluster, situated just above the main (red color-coded) cluster, corresponding to areas where the Pb dominates over the Sn-L signal, but the latter is not zero. These pixels correspond to the inner part of the initial D, which was painted with lead tin yellow type I ($PbSnO_4$) or type II ($Pb(Sn,Si)O_3$). Finally, the largest cluster of pixels shows a high Pb–L signal, without detectable Sn-L response. This corresponds to the mitre, the stole, the alb and the book. It also includes the orange leaves and decorations surrounding the initial.

While it would be reasonable to suppose the presence of minium in these orange-red lead-based areas, it is not possible to derive the distribution of this pigment from the MA-XRF maps of Pb alone. In order to distinguish lead white ($PbCO_3$ and/or $2PbCO_3 \cdot Pb(OH)_2$) from minium (Pb_3O_4) the MA-rFTIR distributions of Figs. 8d and e must also be considered. Fig. 8d shows the intensity of the stretching vibration band (680–720 cm^{-1}) of the carbonate group attached to a Pb^{2+} ion [38, 28], while Fig. 8e maps the intensity of the Pb-O stretching band (530–585 cm^{-1}) [39], characteristic for minium, confirming that this pigment was used to paint the book cover and some of the acanthus leaves and other marginal decorations. The images of Fig. 8 allow to clearly map the distribution of the various lead-bearing species, in a manner which is consistent with the visible colours of the illumination.
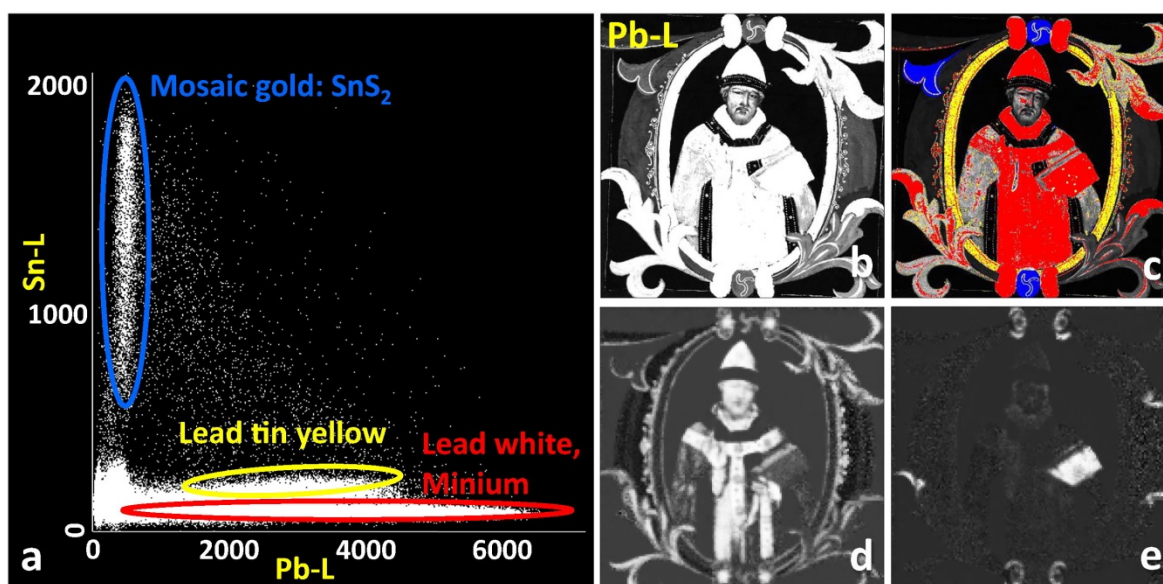
Figure 8: (**a**) Correlation biplot of Pb-L and Sn-L MA-XRF intensity values in MS 5–1979; (**b**) Pb-L elemental distribution; (**c**) false color Pb-L image, based on the groups indicated in the correlation biplot; (d-e) MA-rFTIR intensity maps attributed to (**d**) carbonate bending mode of Lead White (680–720 cm^{-1}) and (**e**) Pb-O stretch of Minium (530–585 cm^{-1}).

Although the spatial resolution of the MA-rFTIR maps is not high enough to reveal all the fine details of the painting, the map in Fig. 8d does correspond very well to the lighter areas of the fragment, where lead white is either present by itself (e.g. in the white draperies and paraments, the flesh tones, and in the filigree decoration over the blue initial and the orange and mosaic gold areas) or mixed with red lakes in the pink acanthus leaves in the upper right and lower left corners).

3.2.3.5 *Mapping of blue pigments: azurite and ultramarine*

In the blue parts of the initial, several color tones can be distinguished, ranging from the pale blue of the background to the darkest blue outlines (Fig. 9a). Fig. 9b shows a virtual cross-section of the blue initial, based on the MA-XRF results. A pale blue base layer was applied on the parchment. White details were applied on top of this layer, while the darker hues were obtained by superimposing multiple blue brush strokes over the base layer.

As shown in Fig. 9c, the blue initial shows a quasi-uniform Cu-K XRF intensity, with the exception of the areas where the signal is strongly absorbed by the superimposed lead white filigree patterns. This would suggest that an azurite base layer was painted for the initial as a whole. It is worth noting that in the blue portions of the saint's clothing, no Cu and therefore no azurite is present, with the exception of the small green decorations (see Cu-K map in Figs. 9c and 11c).
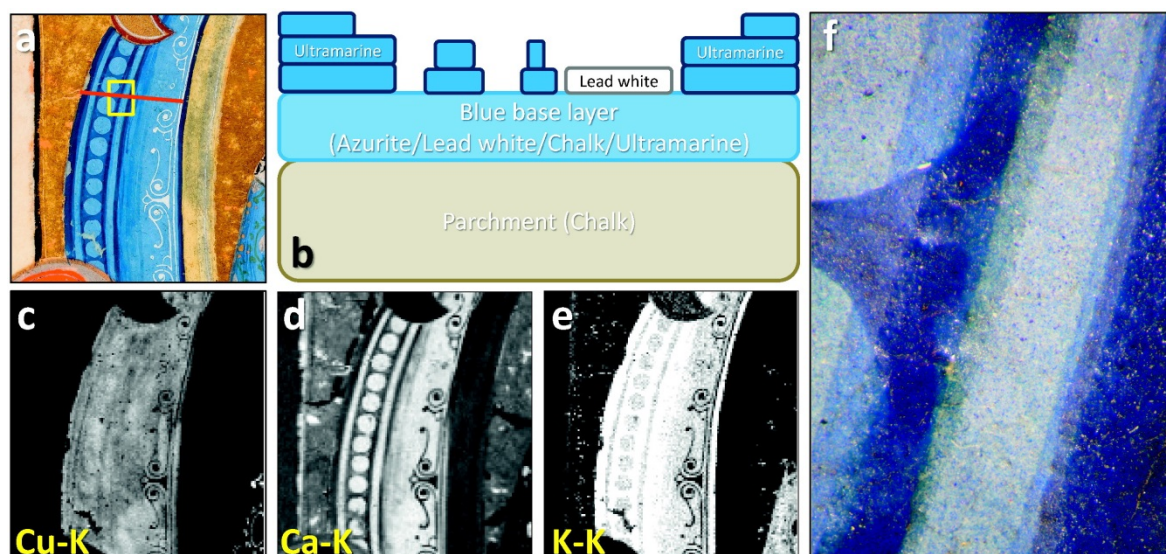
*Figure 9: (**a**) Detail of left side of the initial D showing different blue tones; (**b**) virtual cross-section over the red line indicated in (a), representing the layer buildup in this area; (**c-d-e**) corresponding Cu-K, Ca-K and K-K MA-XRF maps; (**f**) microphotograph of area indicated by yellow rectangle in (a). (For interpretation of the references to color in this figure legend, the reader is referred to the web version of this article.)*

The Ca- image (Fig. 9d), on the other hand, shows a distribution similar to the visible image, with lighter areas emitting a higher Ca signal, suggesting the use of chalk or gypsum. This could misinterpreted as if this Ca was used to create a lighter blue. However, careful comparison of the Ca-K, Cu-K and Pb-L distributions (Figs. 11a,c,e) shows similar brush marks for all three elements, an indication that these are all present in the same (base) layer. The relative low energetic Ca-K XRF radiation is absorbed to a higher degree than the more energetic Cu-K and Pb-L radiation by the K-rich pigment in the dark blue parts.

The overall K- MA-XRF map in Fig. 10a shows that both the blue mantle of the saint and the darker tones in the blue areas of the initial (Fig. 9e) were painted with a K-containing pigment, which is likely to be natural ultramarine (see Table 1). Since the K-K intensity does not drop down to zero in the pale blue circular holes, probably some ultramarine was already mixed with the azurite base layer. (Since low energetic K-K radiation is significantly absorbed by the ultramarine paint layers themselves, the K-K image does not reflect the thickness variations among the ultramarine brushstrokes present.) However, since the presence of the element potassium is only consistent with, but not conclusive proof for, the presence of ultramarine, the MA-rFTIR data were examined to seek confirmation. This could be found in three spectral regions within the FTIR datacube. The MA-XRF K-K distribution (Fig. 10a) turns out to be very similar to the intensity map of the

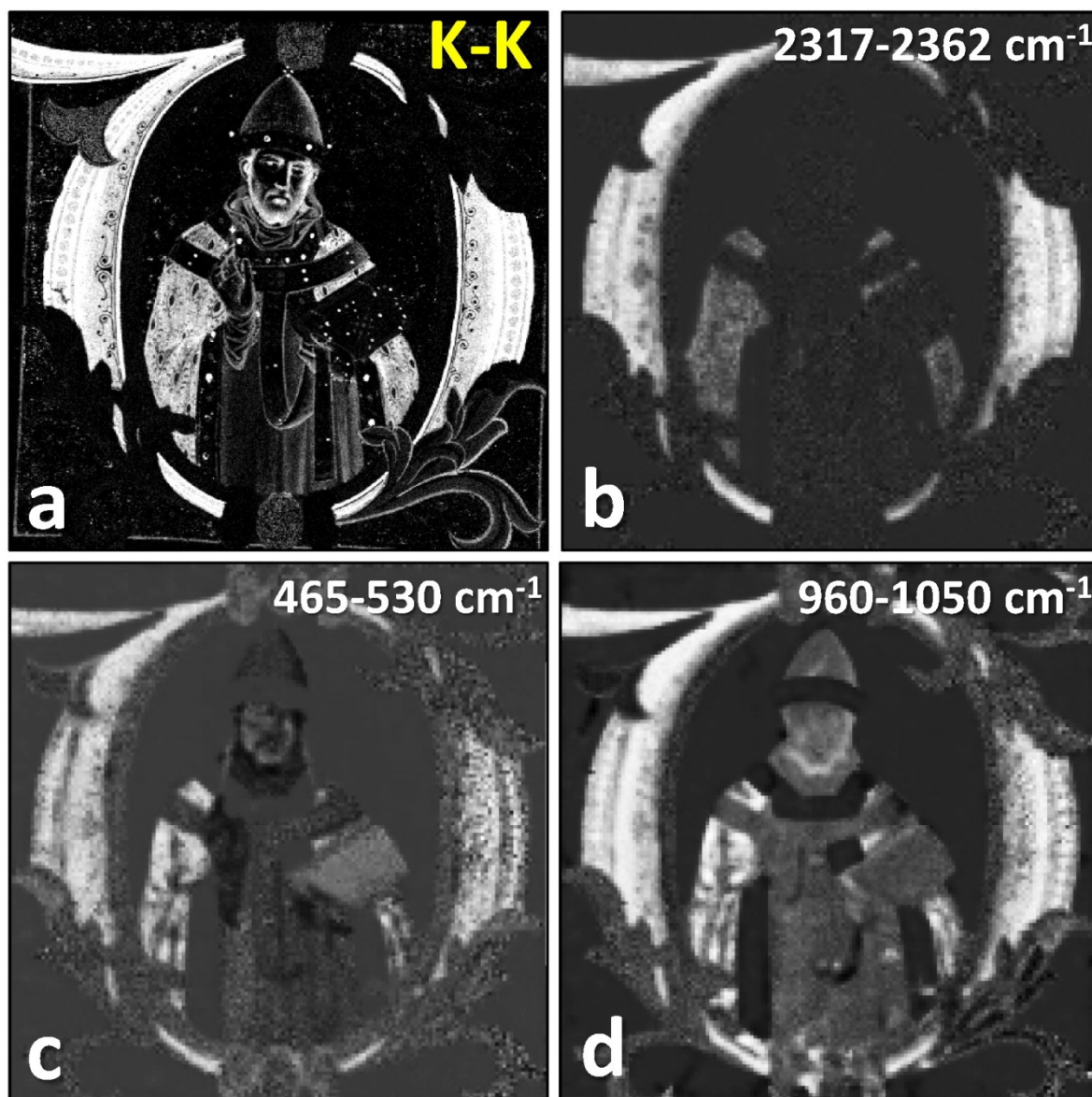FTIR band at 2317–2362 cm^{-1} (Fig. 10b) which can be regarded as a specific signal for Afghan ultramarine.

*Figure 10: Fitzwilliam Museum, MS 5–1979: (**a**) MA-XRF K-K distribution; (**b-c-d**) MA-rFTIR intensity distributions: (**b**) CO_2 or HS_3^- stretching (2317–2362 cm^{-1}), signaling the presence of Afghan ultramarine; (**c**) Si-O bending (465–530 cm^{-1}) and (**d**) Si-O stretching (960–1050 cm^{-1}), both attributed to ultramarine blue and/or other silicates.*

As described by Miliani et al. [40], a distinctive sharp peak at 2341 cm^{-1} can be observed (Fig. 12a) and attributed to the presence of CO_2 in the aluminosilicate cages of the mineral lazurite. Another interpretation for the origin of this peak is that it is caused by vibration of HS_3^- species inside the aluminosilicate cages [41]. While the MA-rFTIR map is more blurred than the K-K MA-XRF map due to the larger beam employed during MA-

rFTIR scanning, taken together, the two distributions clearly indicate that natural ultramarine was used in all blue areas of the illumination, and consistently with the layer structure schematically shown in Fig. 9b. Additional MA-rFTIR maps support the identification of ultramarine in these areas: the presence of silicate-rich material is confirmed by the intensity distributions of the bands at 460–530 cm^{-1} (Si-O bending vibration, Fig. 10d) and at 960–1050 cm^{-1} (Si-O stretching vibration, Fig. 10e).

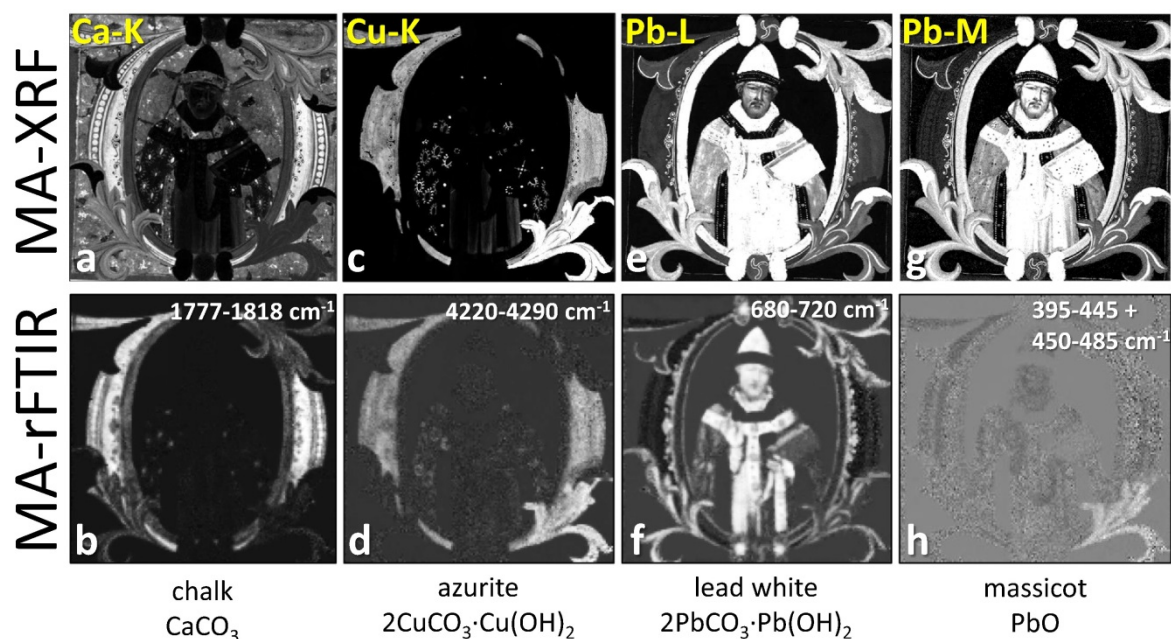|			
chalk	azurite	lead white	massicot
$CaCO_3$	$2CuCO_3 \cdot Cu(OH)_2$	$2PbCO_3 \cdot Pb(OH)_2$	PbO

Figure 11: Fitzwilliam Museum, MS 5–1979; Top row: MA-XRF elemental distributions: (**a**) Ca–K; (**c**) Cu–K; (**e**) Pb–L; (**g**) Pb–M; Bottom row: MA-rFTIR intensity distributions: (**b**) carbonate combination band of chalk (1777–1818 cm^{-1}); (**d**) carbonate combination band of azurite (4220–4290 cm^{-1}); (**f**) carbonate bending mode of lead white (680–720 cm^{-1}); (**h**) combination of two Pb-O stretching bands of massicot (395–445 and 450–485 cm^{-1}).

3.2.3.6 *Florentine green: an azurite mixture*

Fig. 11 shows the XRF- and FTIR-derived distributions of three metal carbonate species, i.e. chalk ($CaCO_3$), azurite ($2CuCO_3 \cdot Cu(OH)_2$) and lead white – here assumed to be predominantly present in its hydrocerussite form, $2PbCO_3 \cdot Pb(OH)_2$, based on the clear – OH signal observed at 3540 cm^{-1} (data not shown). The direct comparison between the XRF and FTIR maps shows that all Cu (Fig. 11c) appears to be present as azurite (Fig. 11d) whereas, as already discussed above, Ca and Pb are also present as chemical species other than carbonates. The main difference between the Ca map of Fig. 11a and the chalk map of Fig. 11b appears to reside in the gilded background and in the pink-colored acanthus leaves where $CaSO_4 \cdot 2H_2O$ is present, respectively in the bole layer and as a likely substrate for the pink lake (see Fig. 4e). If we focus the attention on the green acanthus leaf in the lower right corner, then the lead white highlights are clearly visible in Figs. 11e-f, whereas the presence of azurite throughout the leaf is evident from Figs. 11c-d. The Pb map of Fig. 11e also demonstrates that a significant amount of lead is (fairly uniformly) present, alongside copper, in the green areas of this leaf. The Pb content of this leaf is

169

visible in the Pb–M MA-XRF maps as well (see Fig. 11g), suggesting that the Pb is present at or close by the paint surface, in a mixture with other materials. Faint bands can be isolated in the FTIR data near 450–485 cm^{-1} (and also at 395–445 cm^{-1}); their intensity distribution (Fig. 11h) matches the shape of the green portion of this acanthus leaf. This suggests that the green paint was obtained by mixing blue azurite with a yellow pigment, in this case massicot (PbO), a standard practice employed in 15th C. Florentine workshops.

3.2.3.7 *Binding media*

FORS analysis found spectral evidence for the use of a lipidic binder in areas painted with red lead. The spectral signature is characterized by two relatively weak bands at 2311 and 2352 nm [30], possibly suggesting that whole egg was used rather than egg yolk, or else that a small amount of egg yolk was added to another type of binder, perhaps to improve the handling properties of the paint.

(MA-)rFTIR was employed to support and possibly refine this identification. All point-based FTIR spectra show intense bands in the 1900–1400 cm^{-1} range, where the absorptions of the main groups in lipids, proteins and polysaccharides can be identified [42]. These spectra differ due to the physical properties of the pictorial layer; sometimes two sharp, almost derivative like signals are present, sometimes they show only a broad peak, with two or more relative maxima. In both cases, these signals can be attributed to the presence of a protein containing binder. The absence of distinctive peaks at 4329 and 4259 cm^{-1}, attributable to the combination of CH_2 stretching and bending vibrational modes [43] in lipid fatty chains, exclude the use of a pure lipidic binder such as egg yolk.

In the spectra where the derivative-like distortion is predominant (Fig. 12b), the two peaks with inflection point at 1652 and 1549 cm^{-1} can be attributed to the amide I and II stretching in proteinaceous binders. These bands are well detectable as relative maxima in the spectra where the derivative distortion is less evident (Fig. 12c). When comparing Fig. 12a with 12c, no striking differences can be seen between a spectrum that is recreated from the MA-rFTIR datacube (Fig. 12a) and one obtained by measuring over a longer period in only one position (Fig. 12c).

Further analysis does not reveal the presence of strong C=O stretching absorption, centered around 1740 cm^{-1}, superimposed to the Amide I band. A weak band at 1738 cm^{-1} can be assigned to the $v_1 + v_4$ carbonate combination band of lead white [28].
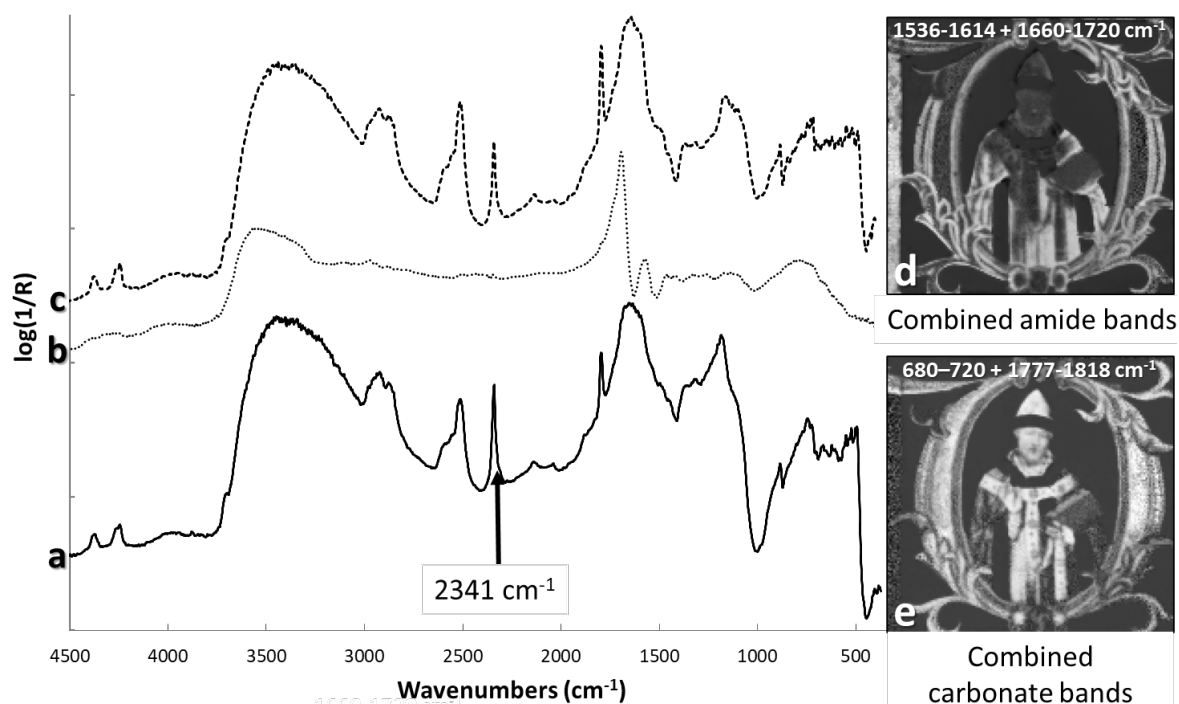
*Figure 12: Reflection mode spectra in the region 4500–375 cm^{-1} of (**a**) the blue initial (spectrum extracted from the MA-rFTIR datacube), the arrow points out the distinctive peak for genuine Afghan ultramarine; (**b**) the green earth over the white alb; (**c**) the blue region in the initial; MA-rFTIR intensity distributions of (**d**) combined intensities of Amide I and Amide II bands; (**e**) combined intensities of the carbonate bending mode of lead white (680–720 cm^{-1}) and the carbonate combination band of chalk (1777–1818 cm^{-1}).*

When these amide bands are employed to map the distribution of the binding medium in Fig. 12d, surprisingly not all painted areas appear. Mainly the carbonate rich zones (calcite, lead white and azurite) show low amide intensities. When combining the two most abundant carbonate species in Fig. 12e: lead white and calcite, the painted areas appear as the inverse of the combined amide band distribution. This is not a surprise since carbonates have active bands in the same spectral region as the amides. Contrary to ATR and transmission spectra, external reflectance bands are often broader because the instrument captures not only specularly reflected radiation, but diffuse reflected radiation as well. The presence of the carbonates changes the physical properties of the pictorial layers and increases the diffuse reflection component. This diffuse reflection enhances the CO_3^{2-} overtone and combination bands which overlap with the amide bands, making it more difficult to map the amide bands.

This case illustrates that the method to map chemical bands, obtained by MA-rFTIR still has room for improvement. Especially in areas where overlapping bands occur while in the same locations also the spectral background changes, the separation of the net signals of all molecular contributions is difficult to perform in a reliable manner.

3.2.4 Conclusions

By employing MA-XRF and MA-rFTIR scanning as complementary, non-invasive spectroscopic means of investigation, we obtained several new types of information about a 15th century Florentine illuminated fragment used as a case study. In general, while MA-XRF allows to image the distribution of the different painters' materials with sufficient lateral detail, it lacks in specificity to unambiguously identify all materials present. For this purpose, a combined investigation with more specific spectroscopic methods based on vibrational interactions such as FTIR or Raman spectroscopy is recommended.

Specifically for this case, the combination of MA-XRF and MA-rFTIR imaging allowed to obtain information on the different types of gilding employed, which included mainly gold leaf applied on a bole substrate, complemented by painting of smaller areas with mosaic gold. Several different lead compounds were identified, such as lead white and minium in addition to lead tin yellow and massicot. The latter was employed in a mixture with azurite to obtain a green hue, consistent with the Florentine tradition of that period. Two types of blue were identified: azurite as a base layer for the blue areas of the initial and natural (Afghan) ultramarine for St Clement's robe and for dark blue shades and outlines in the initial.

The elemental map for Zn allowed the identification of the Latin text present on the reverse side of the fragment, currently obscured by a cardboard support. This, in turn, revealed significant contextual information about this object, which has been physically separated from its parent book for the last two hundred years.

As our ability to record this type of chemical information about entire illuminations, or series of illuminations, increases, exciting new possibilities open up to study the way in which the use of artists' materials and painting techniques evolved over time and geographically. This without having to rely on physical samples removed from these precious objects. As recent research projects, academic conferences and specialist publications prove, the future of manuscript studies (and of heritage science as a whole) lies in the application of cutting-edge non-invasive imaging methods, and on close collaboration between all parties concerned: from chemists to art historians, from conservators to imaging scientists.

complementary Raman analyses. The warm hospitality of the Hamilton Kerr Institute is also gratefully acknowledged. The Esmée Fairbairn Collections Fund and Cambridge University's Returning Carers Scheme provided funding for part of this research. SL and KJ acknowledge support from project METOX (contract BR/165/A6/MetOx), BELSPO, Brussels.

References

1. M. Aceto, A. Agostino, G. Fenoglio, A. Idone, M. Gulmini, M. Picollo, P. Ricciardi, J.K. Delaney, Characterisation of colourants on illuminated manuscripts by portable fibre optic UV-visible-NIR reflectance spectrophotometry, Anal. Methods 6 (2014) 1488–1500 https://doi.org/10.1039/c3ay41904e.

2. C. Anselmi, P. Ricciardi, D. Buti, A. Romani, P. Moretti, K.R. Beers, B.G. Brunetti, C. Miliani, A. Sgamellotti, MOLAB® meets Persia: non-invasive study of a sixteenth century illuminated manuscript, Stud. Conserv. 60 (2015) 185–191 https://doi.org/10.1179/0039363015Z.000000000223.

3. B. Doherty, A. Daveri, C. Clementi, A. Romani, S. Bioletti, B. Brunetti, A. Sgamellotti, C. Miliani, The book of Kells: a non-invasive MOLAB investigation by complementary spectroscopic techniques, Spectrochim. Acta A 115 (2013) 330–336 https://doi.org/ 10.1016/j.saa.2013.06.020.

4. D. Lauwers, V. Cattersel, L. Vandamme, A. Van Eester, K. De Langhe, L. Moens, P. Vandenabeele, Pigment identification of an illuminated mediaeval manuscript De Civitate Dei by means of a portable Raman Equipment, J. Raman Spectrosc. 45 (2014) 1266–1271 https://doi.org/10.1002/jrs.4500.

5. W. Faubel, S. Staub, R. Simon, S. Heissler, A. Pataki, G. Banik, Non-destructive analysis for the investigation of decomposition phenomena of historical manuscripts and prints, Spectrochim. Acta B 62 (2007) 669–676 https://doi.org/10.1016/j.sab.2007.03.029.

6. M.J. Melo, A. Claro, Bright light: microspectrofluorimetry for the characterization of lake pigments and dyes in works of art, Acc. Chem. Res. 43 (2010) 857–866 https://doi.org/10.1021/ar9001894.

7. G. Van der Snickt, W. De Nolf, B. Vekemans, K. Janssens, μ-XRF/μ-RS vs. SR μ-XRD for pigment identification in illuminated manuscripts, Appl. Phys. A Mater. Sci. Process. 92 (2008) 59–68 https://doi.org/10.1007/s00339-008-4447-9.

8. A. Duran, J.L. Perez-Rodriguez, T. Espejo, M.L. Franquelo, J. Castaing, P. Walter, Characterization of illuminated manuscripts by laboratory-made portable XRD and micro-XRD systems, Anal. Bioanal. Chem. 395 (2009) 1997–2004 https://doi.org/10.1007/s00216-009-2992-5.

9. A. Duran, A. López-Montes, J. Castaing, T. Espejo, Analysis of a royal 15th century illuminated parchment using a portable XRF-XRD system and micro-invasive techniques, J. Archaeol. Sci. 45 (2014) 52–58 https://doi.org/10.1016/j.jas.2014.02.011.

10. M. Borengasser, W.S. Hungate, R. Watkins, Hyperspectral Remote Sensing — Principles and Applications, CRC press, 2007.

11.   C. Balas, V. Papadakis, N. Papadakis, A. Papadakis, E. Vazgiouraki, G. Themelis, A novel hyper-spectral imaging apparatus for the non-destructive analysis of objects of artistic and historic value, J. Cult. Herit. 4 (2003) 330–337 https://doi.org/10.1016/S1296-2074(02)01216-5

12.   K.C. Gross, K.C. Bradley, G.P. Perram, Remote identification and quantification of industrial smokestack effluents via imaging Fourier-transform spectroscopy, Environ. Sci. Technol. 44 (2010) 9390–9397 https://doi.org/10.1021/es101823z.

13.   F. Rosi, C. Miliani, R. Braun, R. Harig, D. Sali, B.G. Brunetti, A. Sgamellotti, Non-invasive analysis of paintings by mid-infrared hyperspectral imaging, Angew. Chem. Int. Ed. 52 (2013) 1–5 https://doi.org/10.1002/anie.201209929.

14.   K.A. Dooley, D.M. Conover, L.D. Glinsman, J.K. Delaney, Complementary standoff chemical imaging to map and identify artist materials in an early Italian renaissance panel painting, Angew. Chem. 126 (2014) 13995–13999 https://doi.org/10.1002/ange.201407893.

15.   K.A. Dooley, J. Coddington, J. Krueger, D.M. Conover, M. Loew, J.K. Delaney, Standoff chemical imaging finds evidence for Jackson Pollock's selective use of alkyd and oil binding media in a famous 'drip' painting, Anal. Methods 9 (2017) 28–37 https://doi. org/10.1039/c6ay01795a.

16.   M. Alfeld, K. Janssens, J. Dik, W. De Nolf, G. Van der Snickt, Optimization of mobile scanning macro-XRF systems for the *in situ* investigation of historical paintings, J. Anal. At. Spectrom. 26 (2011) 899–909 https://doi.org/10.1039/c0ja00257g.

17.   S. Legrand, F. Vanmeert, G. Van der Snickt, M. Alfeld, W. De Nolf, J. Dik, K. Janssens, Examination of historical paintings by state-of-the-art hyperspectral imaging methods: from scanning infra-red spectroscopy to computed X-ray laminography, Herit. Sci. 2 (2014) 13 https://doi.org/10.1186/2050-7445-2-13.

18.   W. Vetter, M. Schreiner, A fiber optic reflection-UV/Vis/NIR-system for non-destructive analysis of art objects¸ Adv, Chem. Sci. 3 (2014) 7–14.

19.   M. Alfeld, G. Van der Snickt, F. Vanmeert, K. Janssens, J. Dik, K. Appel, L. van der Loeff, M. Chavannes, T. Meedendorp, E. Hendriks, Scanning XRF investigation of a Flower Still Life and its underlying composition from the collection of the Kröller–Müller Museum, App. Phys. A 111 (2013) 165–175 https://doi.org/10.1007/s00339-0127526-x.

20.   G. Van der Snickt, H. Dubois, J. Sanyova, S. Legrand, A. Coudray, C. Glaude, M. Postec, P. Van Espen, K. Janssens, Large-area elemental imaging reveals Van Eyck's original paint layers on the *Ghent Altarpiece* (1432), rescoping its conservation treatment, Angew. Chem. 56 (2017) 4797–4801 https://doi.org/10.1002/anie.201700707.

21.   S. Legrand, M. Alfeld, F. Vanmeert, W. De Nolf, K. Janssens, Macroscopic Fourier transform infrared scanning in reflection mode (MA-rFTIR), a new tool for chemical imaging of cultural heritage artefacts in the mid-infrared range, Analyst 139 (2014) 2489–2495 https://doi.org/10.1039/c3an02094k.

22.   S. Panayotova (Ed.), Colour. The Art and Science of Illuminated Manuscripts. Harvey Miller/Brepols, London and Turnhout 2016, pp. 139–142. See also

http://www.fitzmuseum.cam.ac.uk/illuminated/manuscript/discover/initials-from-choir-books

23. M. Levi D'Ancona, The Illuminators and Illuminations of the Choir Books from Santa Maria Degli Angeli and Santa Maria Nuova in Florence, vol. 1, 1994, 91 Centro Di, Florence.

24. M. Alfeld, K. Janssens, Strategies for processing mega-pixel X-ray fluorescence hyperspectral data: a case study on a version of Caravaggio's painting *Supper at Emmaus*, J. Anal. At. Spectrom. 30 (2015) 777–789 https://doi.org/10.1039/c4ja00387j.

25. V.A. Solé, E. Papillon, M. Cotte, Ph. Walter, J. Susini, A multiplatform code for the analysis of energy-dispersive X-ray fluorescence spectra, Spectrochim. Acta Part B 62 (2006) 63–68 https://doi.org/10.1016/j.sab.2006.12.002.

26. Brightspec NV, http://www.brightspec.be, Belgium.

27. A. Cabal, S. Legrand, B. Van den Bril, K. Toté, K. Janssens, P. Van Espen, Study of the uniformity of aerosol filters by scanning MA-XRF, X-Ray Spectrum. 46 (2017) 461-466 https://doi.org/10.1002/xrs.2767.

28. C. Miliani, F. Rosi, A. Daveri, B.G. Brunetti, Reflection infrared spectroscopy for the non-invasive *in situ* study of artists' pigments, App. Phys. A 106 (2012) 295–307 https://doi.org/10.1007/s00339-011-6708-2.

29. P. Ricciardi, MS 5-1979 — Summary of Analytical Results, Unpublished Technical Analysis Report, 10, August 2015.

30. P. Ricciardi, J.K. Delaney, M. Facini, J.G. Zeibel, M. Picollo, S. Lomax, M. Loew, Near-infrared reflectance imaging spectroscopy to map paint binders *in situ* on illuminated manuscripts, Angew. Chem. Int. Ed. 51 (2012) 5607–5610 https://doi.org/10. 1002/anie.201200840.

31. P. Ricciardi, M. Facini, J. Delaney, in: D. Saunders, M. Spring, A. Meek (Eds.), Painting and Illumination in Early Renaissance Florence: The Techniques of Lorenzo Monaco and His Workshop, The Renaissance Workshop 2013, pp. 1–9 London.

32. M. Vermeulen, J. Sanyova, K. Janssens, G. Nuyts, S. De Meyer, K. De Wael, The darkening of copper- or lead-based pigments explained by a structural modification of natural orpiment: a spectroscopic and electrochemical study, J. Anal. At. Spectrom. 32 (2017) 1331–1341 https://doi.org/go10.1039/c7ja00047b.

33. D. Goltz, J. McClelland, A. Schellenberg, M. Attas, E. Cloutis, C. Collins, Spectroscopic studies on the darkening of lead white, Appl. Spectrosc. 57 (2003) 1393–1398.

34. G. Smith, A. Derbyshire, R.J.H. Clark, *In situ* spectroscopic detection of lead sulphide on a blackened manuscript illumination by Raman microscopy, Stud. Conserv. 47 (2002) 250–256 https://doi.org/10.1179/sic.2002.47.4.250.

35. A. Coccato, L. Moens, P. Vandenabeele, On the stability of mediaeval inorganic pigments: a literature review of the effect of climate, material selection, biological activity, analysis and conservation treatments, Herit. Sci. 5 (2017) https://doi.org/10.1186/s40494-017-0125-6.

36.   N. Turner, K. Trentelman, C. Patterson, J. Dik, G. Van der Snickt, K. Janssens, Macro-XRF Scanning of Illuminations: an improved method for non-invasive analysis of illuminated manuscripts, proceedings of INSIDE ILLUMINATIONS, Art Technical Research & the Illuminated Manuscript, KIK-IRPA, Brussels, 5 June 2014, Corpus of Illuminated Manuscripts of Illuminare, KU Leuven, Peeters Publishers, Leuven, 2015 (forthcoming).

37.   S. Legrand, P. Ricciardi, K. Janssens, The benefits of scanning illuminated manuscripts with MA-XRF and MA-rFTIR, S. Panayotova, P. Ricciardi (Eds.), Manuscripts in the Making: Art and Science, vol. 2, Harvey Miller/Brepols, London and Turnhout, 2018 forthcoming.

38.   W.B. White, The carbonate minerals, V.C. Farmer (Ed.), Mineralogical Society of Great Britain and Ireland 1974, pp. 227–283 https://doi.org/10.1180/mono-4.

39.   S. Vahur, U. Knuutinen, I. Leito, ATR-FT-IR spectroscopy in the region of 500–230 cm^{-1} for identification of inorganic red pigments, Spectrochim. Acta Part A 73 (2009) 764–771 https://doi.org/10.1016/j.saa.2009.03.027.

40.   C. Miliani, A. Daveri, B.G. Brunetti, A. Sgamellotti, CO_2 entrapment in natural ultramarine blue, Chem. Phys. Lett. 466 (2008) 148–151 https://doi.org/10.1016/j.cplett. 2008.10.038.

41.   M. Bacci, C. Cucci, E. Del Federico, A. Lenco, A. Jerschow, J.M. Newman, M. Picollo, An integrated spectroscopic approach for the identification of what distinguishes Afghan lapis lazuli from others, Vib. Spectrosc. 49 (2009) 80–83 https://doi.org/10.1016/j.vibspec.2008.05.002.

42.   R. Arbizzani, U. Casellato, E. Fiorin, L. Nodari, U. Russo, P.A. Vigato, Decay markers for the preventive conservation and maintenance of paintings, J. Cult. Herit. 5 (2004) 167–182 https://doi.org/10.1016/j.culher.2003.12.003.

43.   M. Vagnini, C. Miliani, L. Cartechini, P. Rocchi, B.G. Brunetti, A. Sgamellotti, Anal. Bioanal. Chem. 395 (2009) 2107–2118 https://doi.org/10.1007/s00216-009-3145-6.

Chapter 4 **Paintings**

Paintings are considered to be the most precious form of cultural heritage. As a result, these objects are studied more often than other forms of art. In this chapter two altarpieces of famous Flemish Primitives, Christ with singing and music-making Angels by Hans Memling and the Ghent Altarpiece by the brothers Hubert and Jan Van Eyck, are subjected to a series of analytical (imaging) techniques during an extensive restoration campaign.

The first article showcases that the combination of non-destructive macroscopic (imaging) techniques with a minute selection of well-chosen samples for microscopic analytical methods is often needed to get a full comprehension of the applied materials and techniques, as well as to understand the present degradation processes and their distribution in the paint stratigraphy.

The second article describes in-depth the identification and removal process of a disfiguring crust present on the Memling panels. This is a good example to demonstrate that the collaboration between multiple research fields is often required to solve the questions that emerge during the restoration and conservation of paintings and to be able to associate these with the complex history of the piece of art.

When true masterpieces such as the Ghent Altarpiece are being restored, these paintings are subjected to an array of non-destructive techniques to help the restorers and the supporting committee in taking the right decisions in this process. A lengthy MA-XRF scanning campaign allowed to document that underneath most of the painting's surface another (more refined) version of this artwork was present and that this hidden version was in a good condition. Paint cross-sections indicated that between the two stacks of paint layers, an intermediate varnish layer was present, essential for a safe removal of the overpaint. These objective

arguments helped in the decision to remove the non-original overpaint layers and bring the original composition back to the surface.

In the second phase of this phenomenal restoration campaign the lower register of the inner panels was treated by the experts. Based on the findings on the outer panels and the more finely detailed composition compared to the outer panels more non-destructive macroscopic chemical imaging methods were applied to these panels. In this process a special attention was given to the central theme of this polyptych: The Lamb of God. By combining complementary imaging techniques, it was possible to visualize multiple versions of this lamb's head and some other compositional changes in the central theme.

This chapter is a modified version of four published papers, adapted with permission from:

- The Mineralogical Society of America: K. Janssens, S. Legrand, G. Van der Snickt, F. Vanmeert, "Virtual Archaeology of Altered Paintings: Multiscale Chemical Imaging Tools", *Elements,* 12 (1), **2016**, 39-44, 10.2113/gselements.12.1.39. copyright 2016 MSA
- Springer Nature: Springer eBook, Characterization and Removal of a Disfiguring Oxalate Crust on a Large Altarpiece by Hans Memling, Lizet Klaassen, Geert van der Snickt, Stijn Legrand, Catherine Higgitt, Marika Spring, Frederik Vanmeert, Francesca Rosi, Brunetto Giovanni Brunetti, Marie Postec, Koen Janssens. Copyright 2019 Springer Nature
- John Wiley and Sons: G. Van der Snickt, H. Dubois, J. Sanyova, S. Legrand, A. Coudray, C. Glaude, M. Postec, P. Van Espen, K. Janssens, "Large-Area Elemental Imaging Reveals Van Eyck's Original Paint Layers on the *Ghent Altarpiece* (1432), Rescoping Its Conservation Treatment", *Angew Chem Int Ed Engl,* 56 (17), **2017**, 4797-4801. Copyright 2018 John Wiley and Sons
- G. Van der Snickt, K.A. Dooley, J. Sanyova, H. Dubois, J.K. Delaney, E.M. Gifford, S. Legrand, N. Laquiere, K. Janssens, "Dual mode standoff imaging spectroscopy documents the painting process of the Lamb of God in the *Ghent Altarpiece* by J. and H. Van Eyck", *Science Advances,* 6 (31), **2020**, eabb3379, 10.1126/sciadv.abb3379. Reprinted with permission from AAAS.

4.1 Virtual Archaeology of Altered Paintings: Multiscale Chemical Imaging Tools

Adapted from: K. Janssens, S. Legrand, G. Van der Snickt, F. Vanmeert, "Virtual Archaeology of Altered Paintings: Multiscale Chemical Imaging Tools", *Elements,* 12 (1), **2016**, 39-44, 10.2113/gselements.12.1.39.

Abstract Understanding how painted works of art were constructed, layer-by-layer, requires a range of macroscopic and microscopic X-ray and infrared-based analytical methods. Deconstructing complex assemblies of paints horizontally across a picture and vertically through it provides insight into the detailed production process of the art work and on the painting techniques and styles of its maker. The unwanted chemical transformations that some paint pigments undergo are also detectable; these changes can alter the paint's optical properties. Understanding the chemistry behind such paint degradation gives conservators vital clues to counter these effects and is an invaluable asset in protecting these cultural artefacts for future generations.

4.1.1 Introduction

From prehistoric times, man has felt the urge to depict the surrounding world on various substrates by using coloured materials. Historical paintings, such as prehistoric cave paintings, are often called 'windows on the past' and have allowed later generations to imagine how former human societies looked and/or functioned. Historical paintings are, therefore, considered to be a very valuable part of the cultural legacy we have inherited from past generations.

There is a general belief that paintings are complex but essentially static assemblages of widely different (in)organic materials. However, at, or just below, the seemingly placid surface of these works of art, chemical reactions are taking place that are slowly altering the make-up of the paint layers. While some of these reactions are the result of intimate contact between the different materials, they are mainly propelled by external physicochemical factors. Light absorption by coloured substances (molecules) in the ultraviolet (UV) and the visible range is a prime stimulus for reduction–oxidation (redox) reactions. These reactions can lead to spontaneous *in situ* formation of secondary compounds that will often differ in their macroscopic properties (colour, volume, porosity) from the original materials. Such reactions may significantly alter the organic component of a paint (the protein-, saccharide- or lipid/ oil-based binding media, organic dyes, etc.) and some of the inorganic components (mostly mineral pigments based on metal ions). Another important factor in paint degradation is the often cyclic variation in relative humidity, which causes condensation and re-evaporation of minute moisture droplets within the microporous, age-cracked paint layers. The latter processes can function as miniature galvanic cells where redox reactions occur at the interface between

the pigment grains, binding media and water. In addition, phenomena such as crystallization of salts and leaching of metal cations from pigment grains can gradually undermine the mechanical integrity of paint materials. Cycles of condensation/ evaporation may also transport alteration compounds towards the surface, leading to the formation of weathering crusts. These crusts can be partly crystalline and almost all have a colour and texture that is quite different from the original material.

Traditionally, to study the chemical make-up of painted artworks in detail, (minute) paint samples are collected. These tiny samples can be taken using five standard 'microdestructive' techniques: scalpels or lancets (e.g. Colombini and Modugno 2004); gentle cotton bud (Q-tip®) abrasion (e.g. Vandenabeele et al. 1999); microdrilling (involving a 100–200 μm diameter bore) (e.g. Wess et al. 2004); or laser ablation, the ablated materials being collected on microscope slides (e.g. Cesaratto et al. 2014). These techniques remove only minute amounts of material and any damage is almost invisible to the naked eye.

Microdestructive sampling is limited to areas where paint loss has already occurred. The extracted material ideally comprises the entire stack of micrometer-thick paint layers at a given position. One or more non-destructive microanalytical methods may be employed before undertaking additional analytical investigations that might involve the chemical digestion of the sampled material, or any other wet-chemical operation. Prior to microanalysis, multilayered paint samples are typically embedded in resin, cross-sectioned and then polished. Alternatively, the different materials/layers in a paint sample may be carefully separated from each other under the microscope for separate analysis.

The range of analytical techniques available to painting researchers is now fairly extensive, and the methods can be used to characterize a painting's materials in great detail. They include the following: optical microscopy (OM); scanning electron microscopy coupled with energy dispersive X-ray spectrometry (SEM-EDX) (Antunes et al. 20 14); micro-Fourier transform infrared spectroscopy (μ-FTIR) (Lluveras et al. 2008); micro-Raman spectrometry (μ-RS) (Bell et al. 1997; Van der Snickt et al. 2008); gas chromatography coupled with mass spectrometry (GCMS); and pyrolysis GCMS (Py-GCMS) (Andreotti et al. 2006; Colombini et al. 2010). To complement these chemical analytical methods there are chemical imaging techniques such as synchrotron radiation (SR)-based micro-X-ray fluorescence (μ-XRF) (Janssens et al. 2000), micro-X-ray absorption near edge spectroscopy (μ-XANES) (Cotte et al. 2010), micro X-ray powder diffraction (μ-XRPD) (De Nolf and Janssens 2010), and synchrotron radiation micro-Fourier transform infrared spectroscopy (SR-μ-FTIR). Often, combinations of these methods are required to fully understand a paints' chemistry (Bertrand et al. 2012a,b; Janssens et al. 2013).

A comprehensive understanding of the paints used in a work of art requires data from across the painting's surface, as well as depth profiles through the paint layers themselves. To complement the detailed information that can be gathered from the small number of (possibly non-representative) paint cross sections, mobile versions of different non-destructive spectroscopic methods are used to investigate a greater number of locations on an artwork. By means of a portable XRF (PXRF), element signatures can be swiftly recorded from all differently coloured areas of a painting, allowing indirect inferences to be made on which pigments were used throughout. Similarly, portable RS and FTIR probes can be used to collect complementary vibrational data and so assess the presence of any organic constituents (e.g. Miliani et al. 2010). More recently, several non-invasive imaging methods have been developed and successfully employed to document the composition of a complete painting (e.g. Ricciardi et al. 2012; Alfeld et al. 2013). They can be considered the spectroscopic equivalents of the two imaging methods that have been routinely employed in subsurface investigation of paintings for several decades: infrared reflectography (IRR) and X-ray radiography (XRR). Some of these exploit a scanning mode of operation and include the techniques of macroscopic X-ray fluorescence (MA-XRF) (Alfeld et al. 2013), macroscopic X-ray diffraction (MA-XRD) (De Nolf et al. 2011), macroscopic Fourier transform infrared scanning in reflection mode (MA-rFTIR) (Legrand et al. 2014) and visible/ near-infrared (Vis/NIR) imaging (Daffara et al. 2005). Camera-based analytical approaches include hyperspectral imaging in the visible range (Vis; 350–700 nm), the near-infrared range (NIR; 0.7–1.7 μm) and the short-wave infrared range (SWIR; 1.7–2.5 μm) (Ricciardi et al. 2012; Dooley et al. 2014).

To illustrate the interplay between spectroscopic methods for macroscopic, mobile and microscopic pigment identification and imaging, we offer an example of their combined use for the full characterization of the fifteenth century work of *art Christ with singing and music-making Angels* (Royal Museum of Fine Arts Antwerp, Belgium, inventory numbers 779, 778 and 780), by Hans Memling (ca. 1430–1494) (FIG. 1A). This painting was commissioned by Spanish merchants for the monastery of Santa Maria la Real de Nájera (Spain) and is currently under restoration.

4.1.2 Macroscopic imaging and multiple point analysis of *Christ with singing and music-making angels* by Hans Memling

The panels of *Christ with singing and music-making Angels* (Royal Museum of Fine Arts, Antwerp) were extensively analyzed by means of portable and non-invasive FTIR, XRF and XRPD (Van der Snickt et al. 2011). The relatively short acquisition times for PXRF and PFTIR meant that they could be used as quick screening tools; on a more limited number of locations XRPD patterns were recorded using significantly longer measuring times. Together, these techniques provided a comprehensive overview of Memling's pigment usage.
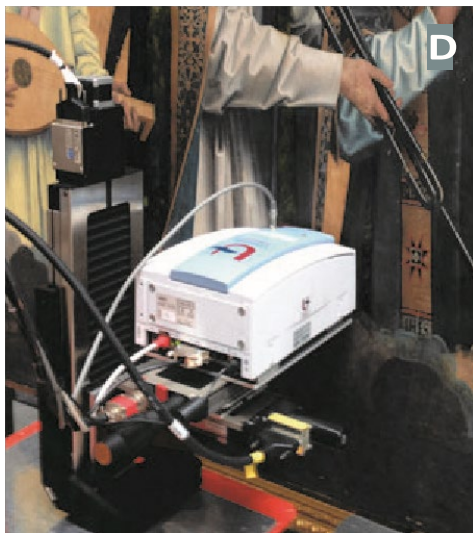
*Figure 1: (**A**) Fifteenth century painting Christ with singing and music-making Angels in three panels (inventory numbers 779, 778 and 780) by Hans Memling (1430–1495), held in the Royal Museum of Fine Arts, Antwerp (Belgium) and measuring 1.70 m x 6.70 m. The depicted angels are numbered 1 to 16. PHOTO BY RENÉ GERRITSEN. (**B**) Portable XRF (PXRF) analysis of the chest area of angel 8 in panel 778. (**C**) Macroscopic (MA-)XRF scanner analyzing part of angels 12 and 13 in panel 780. (**D**) MA-rFTIR scanner in front of angel 5 in panel 779. (**E**) Close-up of the heads of angels 6, 7 and 8 in panel 778; the green arrow indicates the original position of the paint micro-sample shown in figure 5.*

The following pigments were found to be present: lead tin yellow (type 1, Pb_2SnO_4), azurite [$Cu_3(CO_3)_2(OH)_2$], ultramarine ($Na_7Al_6Si_6O_{24}S_3$), lead white {hydrocerussite [$Pb_3(CO_3)_2(OH)_2$] and cerussite [$Pb(CO_3)$]}, a green organo-copper complex, brown and yellow earths (containing goethite [$FeO(OH)$]), vermilion (HgS) and madder lake (containing the red dyes purpurin and alizarin). Compared to the inorganic substances, the presence of the dyes (in areas coloured pink to burgundy) was more difficult to ascertain but was accomplished via reflection mode UV–Vis fluorimetry. A striking observation was the omnipresence of azurite as the blue pigment; only for the blue gems on Christ's cloak did Memling apply a thin glaze of costly ultramarine over the azurite. In all the panels' ground layers, both chalk and gypsum were found. The presence of gypsum was unexpected because this is a grounding material more closely associated with Southern European easel painting than with the fifteenth century Northern European painting tradition. The presence of quartz and goethite in the gilded areas suggested the use of water gilding, involving the application of a thin gold foil on a red clay substrate layer.

Figure 2 shows an area of the central panel where Memling succeeded in creating a wide range of colours and optical effects: the wing of angel #8 is rendered in dark blue over blueish green to purple and red tones. The PXRF spectrum of blue area A revealed only Cu (as azurite) and Pb (as lead white) as the colour-determining elements; in the green blue area B, it is a mixture of azurite and lead tin yellow that appears responsible for the colour. In the bright red area, HgS (vermilion red) is present, but visual inspection also revealed a transparent red overglaze layer (madder lake). The PXRF/PFTIR spectra of area C only indicates azurite: a combination of madder lake and azurite appears to be responsible for the purple tone. Finally, in area D, a simple madder root glaze that covers a lead white modelling layer appears to have been used to obtain the reddish pink tone.

The MA-XRF and MA-rFTIR maps of figure 3 provide more information on Memling's painting and colour rendering technique. The spectra were recorded using the devices shown in figures 1C and 1D, respectively; they consists of a moveable XRF or rFTIR measuring head mounted on a motorized X–Y stage (Alfeld et al. 2013; Legrand et al. 2014). The MA-XRF head consists of an X-ray tube fitted with an X-ray polycapillary lens and an energy dispersive detector; the MA-rFTIR device employs curved mirrors, which focus the external IR beam into a millimeter-sized spot, a Michelson interferometer and a deuterated triglycine sulfate (DTGS) detector.
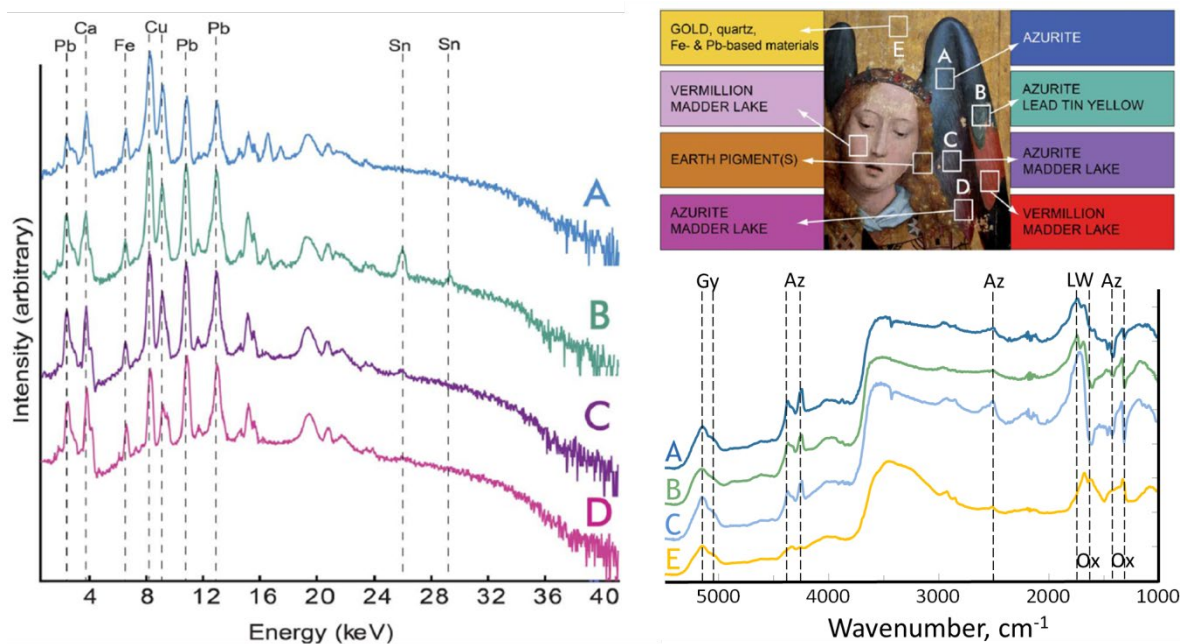
*Figure 2: Detailed analysis of angel 8 in panel 778 (see Fig. 1). (**LEFT**) Relative X-ray fluorescence (XRF) signal intensity versus energy, showing characteristic peaks for Pb, Ca, Fe, Cu and Sn. The four spectra marked A, B, C, D correspond with areas marked on the upper-right figure. (**UPPER RIGHT**) Areas in the angel 8 painting subjected to analysis and identified by lettered boxes. The primary pigment(s) used in each zone are indicated by the colored boxes to the left and right of the image. (**LOWER RIGHT**) Fourier transform infrared (FTIR) spectra [pseudo absorbance (A'=log[1/R]) versus wavenumber] for the analysed areas A, B, C and E of angel 8.Gy: Gypsum; Az: Azurite; LW: Lead White; Ox: oxalates.*

Museum professionals, including art historians and painting conservators who are less familiar with spectroscopic techniques, find these XRF and rFTIR maps easier to interpret than large series of spectral data from many single points. The maps permit them to intuitively associate key chemical elements or compounds (and the corresponding pigments) with areas of a specific colour. In the case of *Christ with singing and music-making Angels*, the following six conclusions from the maps can be drawn:

1. Vermilion red (HgS) was used in the cloak embroidery and in the red parts of the wing of angel #8; it was used at a lower concentration level in the flesh tones of the face in a mixture with lead white.
2. In the more purplish tones of angel #8's wing, madder lake is the major colourant, sometimes together with azurite.
3. Azurite was employed in all blueish areas, but is contaminated with Zn.
4. The hair of angel #8 was mostly painted using clay containing earth pigments (Fe, e.g. from goethite), with lead tin yellow used in the light yellow highlights.
5. Missing portions in the pictorial layer are evident from areas lacking XRF signals of Pb, Sn and Cu/Zn and rFTIR signals of carbonate. These losses show an intense Ca signal and somewhat elevated Fe signals (from XRF) that originate from the ground layer

184

and/or filling material and that coincide with elevated sulfate rFTIR signals indicative of gypsum.

6. The worn gilded background features high Au and reflected infrared signals but also Ca and Fe signals, both of which originate from an underlying adhesive bole (?) layer.
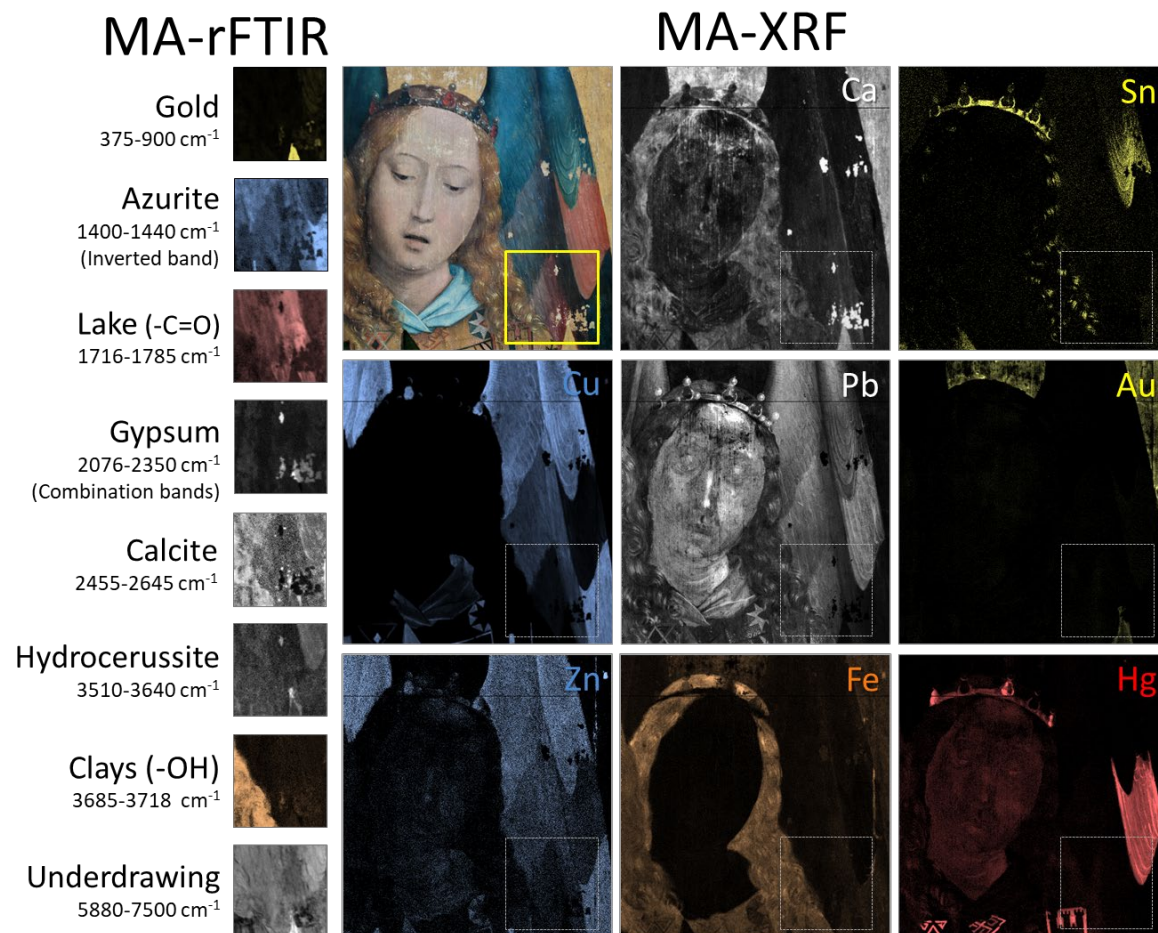

Figure 3: Elemental distribution maps from part of angel 8 in panel 778 (see Fig. 1) obtained using macroscopic X-ray fluorescence (MA-XRF) and macroscopic Fourier transform infrared spectroscopy in reflection mode (MA-rFTIR). The 8 large elemental maps are the MA-XRF distributions of Ca, Sn, Cu, Pb, Au, Zn, Fe and Hg. The yellow square indicates the location of the 8 smaller MA-rFTIR maps shown on the left. The distribution of pigments used in the painting are highlighted in the smaller MA-rFTIR maps.

In the indicated areas, almost no indications of *pentimenti* (intentional changes made by the painter) were encountered. This is not the case for other Memling panels where sometimes very substantial changes to the positioning of figures, or even the entire composition, could be revealed by means of chemical imaging.

4.1.3 Paint cross sections analysed by multimodal X-ray techniques

Paint cross sections are conventionally embedded in resin and morphologically and compositionally characterized by SEM-EDX in combination with optical microscopy. Separate layers are relatively easy to distinguish from each other by using secondary electron imaging (SEI) and/or backscatter electron imaging (BEI), with contrast and colour information delivered by visual and fluorescent light microphotography. Figure 5A shows an optical micrograph of a paint fragment (see FIG. 1D for the sampling position) in which one can see several layers containing coloured mineral grains of different type and size. Figures 5B and 5C show the corresponding SEI image and SEM-EDX element maps reflecting the major compositions of the various layers. The distributions of Ca suggests that the ground consists of a central layer (layer 2, FIG. 5E) of chalk ($CaCO_3$) – a grounding material traditionally employed by Netherlandish painters of the fifteenth to sixteenth centuries – but that an additional layer (layer 1) is present, containing both Ca and S: this spatial coincidence suggests gypsum, which is a type of ground more typically associated with the Mediterranean region, including the Iberian Peninsula (Rodríguez et al. 2010; Antunes et al. 2014). In addition, two thin P-containing layers appear to be present: the first one is situated directly on top of the preparation layer and contains black particles (see the P-K map as part of FIG. 5C), suggesting the use of bone black as underdrawing material. Note, however, that the second P-rich layer is actually an artefact that stems from spectral overlap with the Au-M emission line. Below the gold foil (see Au-L map as part of FIG. 5C) is a preparatory Fe- and Pb-based adhesive bole (?) layer. At the sampling spot, the purplish paint of the angel's clothing overlaps with the golden background so that the paint stratigraphy contains two additional strata; the later appear in the SEM-EDX maps as a single Pb-rich layer. One of these contains large bright blue Cu-rich grains, suggesting the presence of azurite. In combination with red madder lake, the presence of azurite results in the purple colour of the angel's dress: the presence of madder itself can only be deduced indirectly from the distribution of potassium, part of the alum substrate on which the organic dye was precipitated. Even though the SEM-EDX data do not permit a detailed determination of the (inorganic) species that are present in each layer, the combination of element content, colour and contextual and historical knowledge allows us to infer a great deal about a given layer's (major) composition.
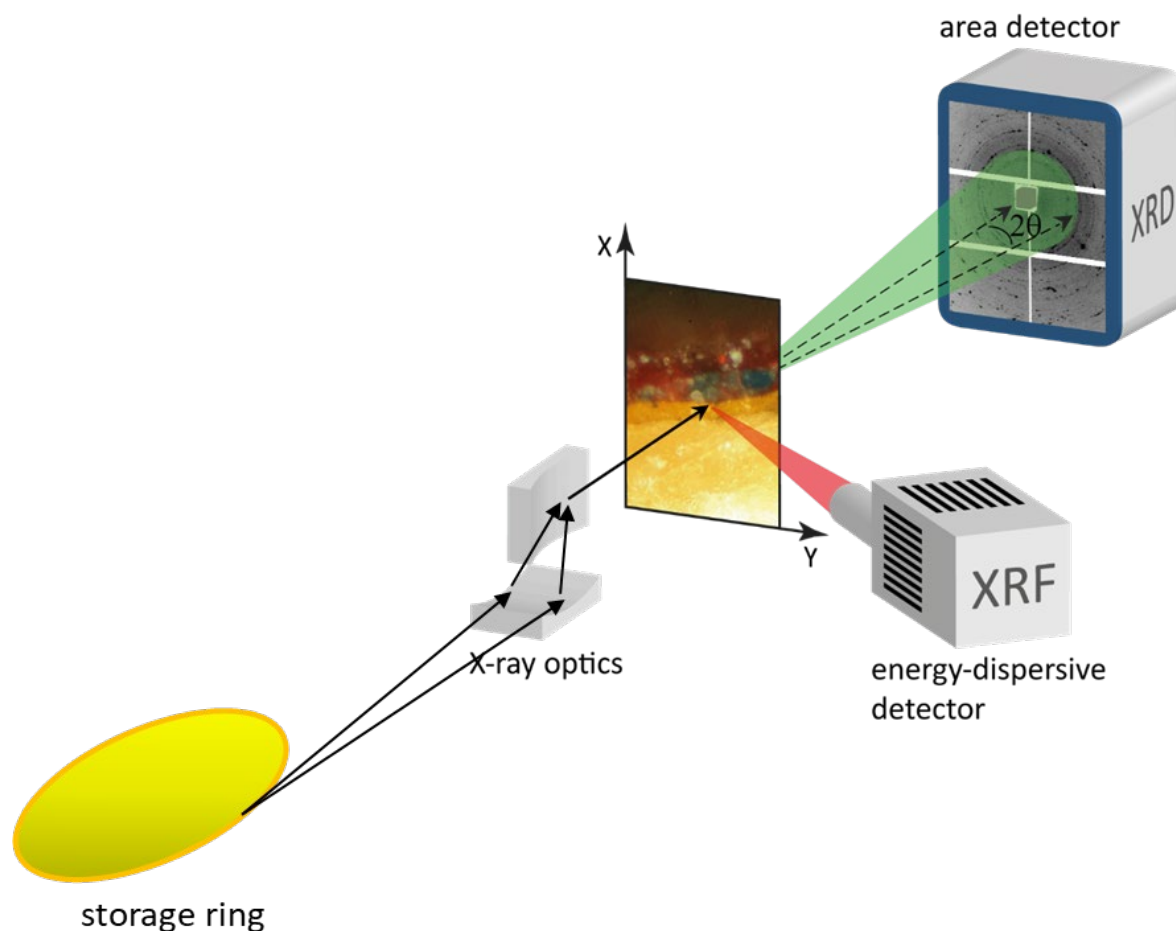
Figure 4: Schematic of a synchrotron-based micro-X-ray fluorescence/X-ray powder diffraction (μ-XRF/μ-XRPD) combined scanning experiment. The primary X-ray beam (21 keV, focused to 0.4 × 0.4 μm² diameter) scans the paint cross section and irradiates a cylinder of material from which XRF and XRD signals emerge. These are recorded in reflection and transmission mode, respectively, by the appropriate detectors.

Though not directly visible in the maps of figure 5C, two shortcomings of the SEM-EDX technique are (a) that the effective lateral resolution is mainly determined by the size of the interaction volume of the primary electron beam with the material, which here is on the order of several micrometers, which may be insufficient to sharply visualize the thinnest strata; (b) the information obtainable via SEM-EDX spectra or maps is limited to the major constituents. For example, the Zn contamination of azurite documented by the MA-XRF maps was not detected. To distinguish by means of SEM-EDX alone between two Cu-containing pigments, one of which has a low-level of Zn (<1,000 ppm) is difficult to impossible. To make the analysis of these complex multilayered samples more material- and layer-specific, several complimentary methods must be employed. Raman microscopy (possibly in confocal mode) is one such method that can chemically distinguish between very thin paint layers, but it requires a judicious selection of the laser wavelength to avoid high fluorescence backgrounds and a careful adjustment of the laser intensity to eliminate unwanted laser-induced chemical transformations.
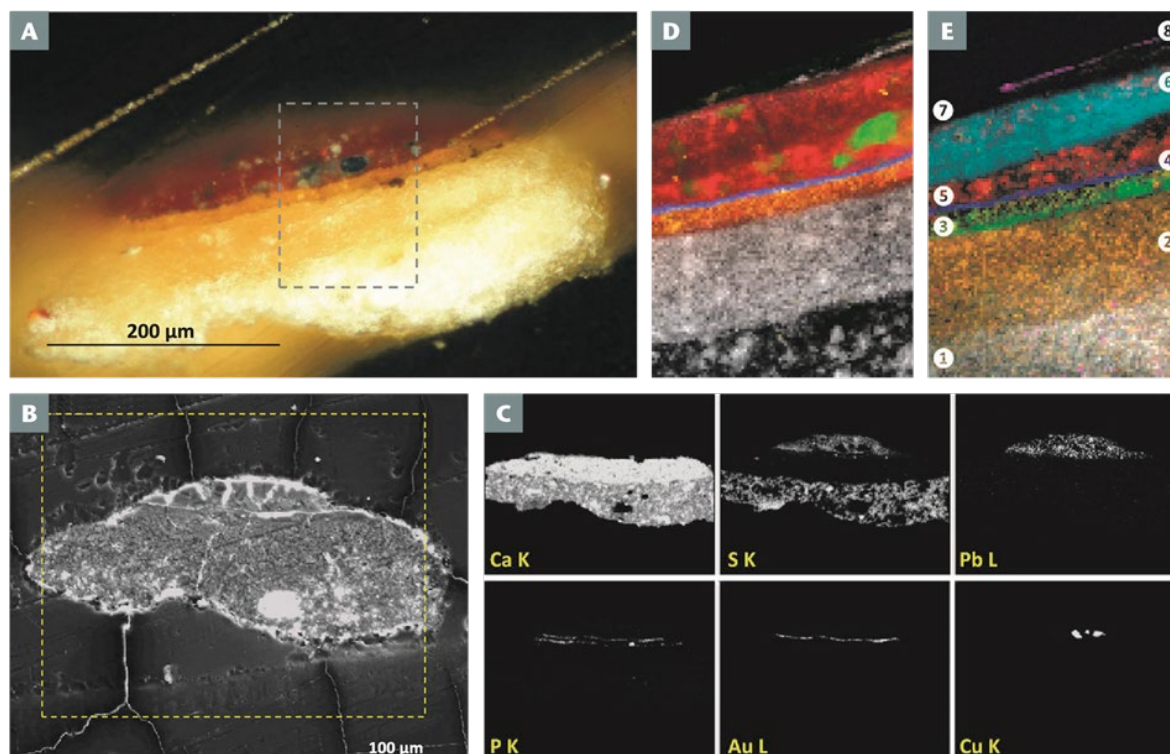
*Figure 5: (**A**) Optical micrograph of an embedded paint cross section, taken from the location of the arrow in figure 1E (panel 780). (**B**) Secondary electron image of the paint cross section shown in (A). (**C**) Scanning electron microscope–energy dispersive X-ray spectroscopy (SEM-EDX) element maps, using selected elements' K and L spectral lines, of the cross section outlined in yellow in (B): Ca-K, S-K, Pb-L, P-K, Au-L and Cu-K. (**D**) Composite micro-X-ray fluorescence maps of cross section shown in (A) where red = Pb; green = Cu; blue = Au; yellow = Fe; white = Ca. (**E**) Micro- X-ray powder diffraction maps of cross section shown in (A) where magenta = weddellite; cyan = anglesite; red = the sum of hydrocerussite and cerussite; blue = gold; yellow = goethite; green = hydroxylapatite; orange = calcite; white = gypsum. Numbers 1 to 8 represent layers discernable in (E).*

Figures 5D and 5E summarise the results of a combined µ-XRF/XRPD scanning experiment over the area indicated in figure 5A (127×90 µm^2). This involved moving a highly monochromatic (21 keV) and intense (10^{11} photons per second) X-ray beam (generated in the PETRA-III synchrotron in Hamburg, Germany) of 0.4 µm diameter in steps of 1 µm in the x- and y direction. At each beam position, X-ray fluorescence data were collected in reflection mode. Simultaneously, behind the sample, an X-ray sensitive camera recorded the diffraction pattern produced by the irradiated material (see FIG. 4 for a schematic of the apparatus set-up).

In figure 5D, a composite of the resulting µ-XRF elemental maps is shown. This contains essentially the same information as the SEM-EDX maps of figure 5C, except that the effective resolution is now defined by the step size of the scan. Along its path, the primary beam broadens only to a negligible extent as a result of scattering interactions. In the µ-XRF maps, the higher resolution also allows us to see a difference in texture between layers 1 and 5–6, the lower one composed of coarser grains (gypsum) than the upper one

composed of calcite. Near the top of the paint stack, one or more thin layers are visible (layer 7) of a Ca-containing material, which appears to have precipitated on the outer surface of the original (Pb-containing) layer. The unambiguous identification of most inorganic materials in the paint stratigraphy is possible by employing the information summarized in figure 5E. The distinction between layers 2 [calcite, $Ca(CO_3)$] and 1 [gypsum, $Ca(SO_4) \cdot 2H_2O$] is clear. In layer 3, hydroxylapatite [$Ca_5(PO_4)_3(OH)$] can be identified, confirming the suspicion that one or more layers of bone-black are present. Immediately on top of these layers we find a thin layer of goethite [$FeO(OH)$] (the bole layer). The XRPD maps confirm that the purplish paint covering the gold foil is in two layers. The lower layer (layer 5) has a lead white matrix (mainly hydrocerussite in this case), with large blue-green grains of a Cu-rich material. Although no XRPD signals of azurite were detected, we know from PFTIR that this blue pigment is omnipresent in this area. Surprisingly, in layer 6, Pb was present only in a minor amount as a carbonate but was mostly found as $PbSO_4$, the greyish mineral anglesite. As anglesite is not a painting material (Eastaugh et al. 2008), it is plausible that this is a degradation product formed from available Pb^{2+} ions that were already present in the same layer and meeting (highly mobile) SO_4^{2-} ions that originated either from inside the paint stratigraphy (e.g. from the gypsum ground) or from an exterior source. To complete the complex stratigraphy, on top of the outermost (varnish) layer 7, the XRPD maps show a thin precipitation layer of weddellite [calcium oxalate, $Ca(C_2O_4) \cdot 2H_2O$]. This compound possibly resulted from a natural degradation phenomenon: oxidative splitting of long aliphatic fatty-acid chains, which are present in the oil, gives rise to shorter, more oxidized, molecules such as oxalates. Oxalates of the metal ions Ca^{2+}, Cu^{2+}, Pb^{2+}, and Cd^{2+} have been encountered in many (degraded) works of art of the same or more recent periods (Salvadó et al. 2009); PFTIR spectra and macroscopic maps (FIG. 3) from *Christ with singing and music-making Angels* revealed these compounds to be abundantly present on the surface as well. The less-specific μ-XRF maps, which are generated simultaneously with the XRPD distributions, serve to link up with other microscopic data (e.g. the SEM-EDX maps) and are useful for pinpointing non-crystalline materials in the paint (such as the blue/green Cu-rich grains present in layer 5). In this case, most layers are flat and can be oriented relative to the primary beam such that the interface between the layers can be sharply imaged. In case of more complex paint morphologies, the related method of XRPD tomography (e.g. Vanmeert et al. 2015) can be employed. This method allows for a better separation of the XRPD contributions of various layers present in a paint stratigraphy from each other, leading to increased insights about the composition of each layer (De Nolf and Janssens 2010). The technique of confocal XRF can potentially do the same type of analysis (Janssens et al. 2010; Kanngießer et al. 2012).

4.1.4 Conclusions

Examination of works of art by painters from various time periods such as Van Eyck, Goya, Rembrandt, Rubens, Van Gogh and others by means of constituent-specific macroscopic hyperspectral methods (e.g. MA-XRF, Vis–NIR and/ or MIR imaging) have demonstrated

that these new tools are very useful for art historians and for art restorers alike, revealing information hitherto inaccessible. To complement the *in plane* information with *in depth* data, the use of highly-specific microscopic imaging methods such as combined μ-XRF/XRPD and/or vibrational spectroscopies is very appropriate. Thus, a far more complete overview can be constructed for the presence/usage of the various (crystalline) minerals or other pigments that were originally used to produce a painting. The new methodologies also allow us to see the *in situ* secondary products that often develop inside paint layers as they age and/or interact with their local environment.

References

Alfeld M and 9 coauthors (2013) A mobile instrument for *in situ* scanning macro-XRF investigation of historical paintings. Journal of Analytical Atomic Spectrometry 28: 760-767

Andreotti A and 5 coauthors (2006) Combined GC/MS analytical procedure for the characterization of glycerolipid, waxy, resinous, and proteinaceous materials in a unique paint micro-sample. Analytical Chemistry 78: 4490-4500

Antunes V and 10 coauthors (2014) Characterization of glue sizing under calcium carbonate ground layers in Flemish and Luso-Flemish painting – analysis by SEM-EDS, μ-XRD and μ-Raman spectroscopy. Analytical Methods 6: 710-717

Bell IM, Clark RJH, Gibbs PJ (1997) Raman spectroscopic library of natural and synthetic pigments (pre- ≈1850 AD). Spectrochimica Acta Part A 53: 2159-2179

Bertrand L and 5 coauthors (2012a) Cultural heritage and archaeology materials studied by synchrotron spectroscopy and imaging. Applied Physics A 106: 377-396

Bertrand L and 5 coauthors (2012b) Development and trends in synchrotron studies of ancient and historical materials. Physics Reports 519: 51-59

Cesaratto A and 5 coauthors (2014) Detection of Organic Colorants in Historical Painting Layers Using UV Laser Ablation Surface-Enhanced Raman Microspectroscopy. Angewandte Chemie 53: 14373-14377

Colombini MP, Modugno F (2005) Characterisation of proteinaceous binders in artistic paintings by chromatographic techniques. Journal of Separation Science 27: 147-160

Colombini MP, Andreotti A, Bonaduce I, Modugno F, Ribechini E (2010) Analytical strategies for characterizing organic paint media using gas chromatography/mass spectrometry. Accounts of Chemical Research 43: 715-727

Cotte M, Susini J, Dik J, Janssens K (2010) Synchrotron-based X-ray absorption spectroscopy for art conservation: looking back and looking forward. Accounts of Chemical Research 43: 705-714

Daffara C, Pampaloni E, Pezzati L, Barucci M, Fontana R (2010) Scanning multispectral IR reflectography SMIRR: An advanced tool for art diagnostics. Accounts of Chemical Research 43: 847-856

De Nolf W, Janssens K (2010) Micro X-ray diffraction and fluorescence tomography for the study of multilayered automotive paints. Surface and Interface Analysis 42: 411-418

De Nolf W, Dik J, Van der Snickt G, Wallert A, Janssens K (2011) High energy X-ray powder diffraction for the imaging of (hidden) paintings. Journal of Analytical Atomic Spectrometry 26: 910-916

Dooley KA, Conover DM, Glinsman LD, Delaney JK (2014) Complementary standoff chemical imaging to map and identify artist materials in an early Italian Renaissance panel painting. Angewandte Chemie 53: 13775-13779

Eastaugh N, Walsh V, Chaplin T, Siddall R (2013) Pigment Compendium: A Dictionary of Optical Microscopy of Historical Pigments. Butterworth Heinemann, Oxford, 958pp

Janssens K and 13 coauthors (2000) Use of microscopic XRF for non-destructive analysis in Art and Archaeometry. X-Ray Spectrometry 29: 73-91

Janssens K, Dik J, Cotte C, Susini J (2010) Photon-based techniques for non-destructive subsurface analysis of painted cultural heritage artifacts. Accounts of Chemical Research 43: 814-825

Janssens K and 11 coauthors (2013) The use of synchrotron radiation for the characterization of artists' pigments and paintings. Annual Review of Analytical Chemistry 6:399-425

Kanngießer B, Malzer W, Mantouvalou I, Sokaras D, Karydas AG (2012) A deep view in cultural heritage—confocal micro X-ray spectroscopy for depth resolved elemental analysis. Applied Physics A 106: 325-338

Legrand S, Alfeld M, Vanmeert F, De Nolf W, Janssens K (2014) Macroscopic Fourier transform infrared scanning in reflection mode (MA-rFTIR), a new tool for chemical imaging of cultural heritage artefacts in the mid-infrared range. Analyst 139: 2489-2498

Lluveras A and 5 coauthors (2008) Weathering of gilding decorations investigated by SR: development and distribution of calcium oxalates in the case of Sant Benet de Bages (Barcelona, Spain). Applied Physics A 90: 23-33

Miliani C, Rosi F, Brunetti BG, Sgamellotti A (2010) In situ non-invasive study of artworks: the MOLAB multitechnique approach. Accounts of Chemical Research 43: 728-738

Ricciardi P and 6 coauthors (2012) Near infrared reflectance imaging spectroscopy to map paint binders in situ on illuminated manuscripts. Angewandte Chemie 51: 5607-5610

Rodríguez A and 6 coauthors (2010) Characterization of calcium sulfate grounds and fillings of applied tin-relief brocades by Raman spectroscopy, Fourier transform infrared spectroscopy, and scanning electron microscopy. Journal of Raman Spectroscopy 41: 1517-1524

Salvadó N and 5 coauthors (2009) Identification of reaction compounds in micrometric layers from gothic paintings using combined SR-XRD and SR-FTIR. Talanta 79: 419-428

Vandenabeele P, Wehling B, Moens L, Dekeyzer B, Cardon B, von Bohlen A, Klockenkämper R (1999) Pigment investigation of a late-medieval manuscript with total reflection X-ray fluorescence and micro-Raman spectroscopy. Analyst 124: 169-172

Van der Snickt G, De Nolf W, Vekemans B, Janssens K (2008) µ-XRF/ µ-RS vs. SR µ-XRD for pigment identification in illuminated manuscripts. Applied Physics A 92: 59-68

Van der Snickt G and 11 coauthors (2011) Material analyses of '*Christ with singing and music-making Angels*', a late 15th-C panel painting attributed to Hans Memling and assistants: Part I. non-invasive *in situ* investigations. Journal of Analytical Atomic Spectrometry 26: 2216-2229

Vanmeert F, Van der Snickt G, Janssens K (2015) Plumbonacrite identified by X-ray powder diffraction tomography as a missing link during degradation of red lead in a Van Gogh painting. Angewandte Chemie 54: 3678-3681

Wess TJ and 8 coauthors (2001) The use of small-angle X-ray diffraction studies for the analysis of structural features in archaeological samples. Archaeometry 43: 117-129

4.2 Characterization and Removal of a Disfiguring Oxalate Crust on a Large Altarpiece by Hans Memling

Abstract During the conservation treatment of Memling's *Christ with Singing and Music-making Angels*, three panel paintings that are among the most monumental works in early Netherlandish art, the conservators came across insoluble surface layers containing calcium oxalates. A very thin and irregular layer of this type, hardly visible to the naked eye, was spread across the surface of all three panels. A much thicker layer forming an opaque and highly disfiguring crust that obscured the composition (Figs. 1 and 7) was locally present on areas of dark copper-containing paint, where multiple layers of old discolored coatings and accretions remained in place before the most recent cleaning.

This article describes the application of a wide range of analytical techniques in order to fully understand the stratigraphy and composition of the crusts on the Memling paintings. FTIR spectroscopy in transmission and reflection mode, micro-ATR-FTIR imaging and macro-rFTIR scanning, SEM-EDX, mobile XRD, and SR-µXRD showed that the crusts contained two related Ca-based oxalate salts, whewellite and weddellite, and were separated from the original paint surface by varnish, indicating that they did not originate from degradation of the original paint but from a combination of microbial action and a thick accumulation of dirt. Supported by the results from these different analytical techniques, which when used together proved to be very effective in providing complementary information that addressed this specific conservation problem, and aided by the presence of the intermediate varnish layer(s), the conservators were able to remove most of the crusts with spectacular results.

4.2.1 Introduction

One of the highlights in the collection of the Royal Museum of Fine Arts Antwerp is three large panel paintings entitled *Christ with Singing and Music-making Angels*, attributed to Hans Memling and assistants (Fig. 1). This paper deals with its extraordinary conservation treatment, which took from 2001 until 2017 and involved a team of conservators and scientists.
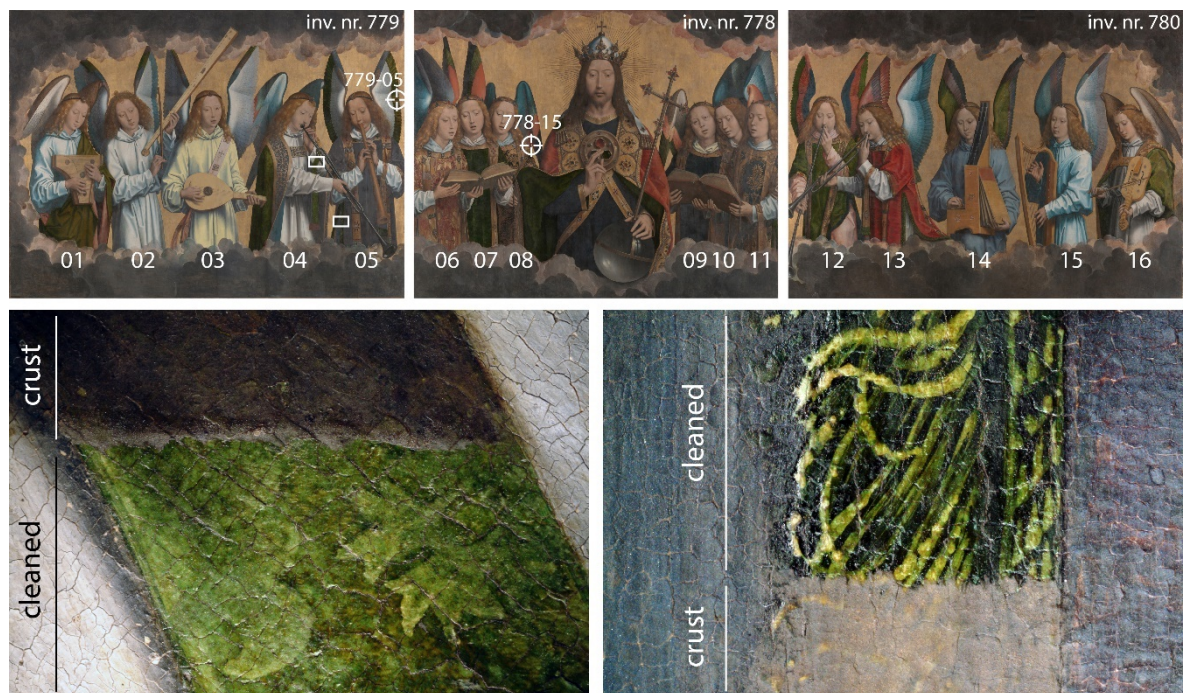
*Figure 1: **Top row**: Christ with Singing and Music-making Angels attributed to Hans Memling and assistants. Collection of the Royal Museum of Fine Arts Antwerp (KMSKA), with numbering of the angels and indication of sample locations (crosshair). The white rectangles indicate the location of the details shown in the bottom row. **Bottom row**: two macrophotographs showing two areas on panel 779 where oxalate crusts on green paint had been partly removed. Photos top row: KMSKA © Photo Rik Klein Gotink. Photos bottom row: KMSKA © Arcobaleno, Adri Verburg*

4.2.2 Memling's Retablo Major

Christ with Singing and Music-making Angels consists of three large panel paintings: the central panel measures 170 × 213 cm², and the two side panels are 170 × 231 cm² each. The panels are attributed to Hans Memling and assistants and were made at the end of the fifteenth century, so late in Memling's career (Fransen 2018). Despite their sizeable dimensions, the panels are only a fragment of the original work of art. Originally, they formed the upper row of what must have been a very large polyptych, created for the high altar of the monastery of Santa Maria la Real in Nájera, Spain. The panels were described in 1795 by the Spanish writer Gaspard David Jovellanos who saw them, together with a large *Assumption of the Virgin*, two apostles, and the Saints Benedictus, Prudentius, Vitalis, and Agricola, on his visit to Nájera. According to Jovellanos, all of the artworks were by the same artist and belonged to the same altarpiece. Jovellanos saw the different parts in various places in the Monastery, the altarpiece having already been dismantled by 1795, but the *Assumption of the Virgin* was probably originally placed below Christ and flanked by the saints (Vandenbroeck 1985; Borchert 1993; De Vos 1994).

Although the Antwerp panels are undoubtedly among the most monumental works in early Netherlandish painting, not much is known about their history. As indicated above, the polyptych had already been dismantled by 1795, and when the panels were rediscovered around 1880 by Spanish art dealers, the central panel, *Christ with Singing Angels*, was placed above an altar, and the side panels, *Music making Angels*, formed part of an organ decoration. After a stay of almost 400 years in Nájera, in 1886 the panels were sold to art dealers and finally bought by the Royal Museum of Fine Arts Antwerp in 1895.

The different retouching campaigns visible on the paint surface and the cradles on the back, probably attached in the 1950s or 1960s, indicated that there must have been several interventions in the past. However, there is very little documentation on the conservation history of the panels. Before they entered the art dealer circuit, they were brought to Madrid and "cleaned."[5] In the museum archives just a few, very short notes were found describing only minor interventions executed after their purchase.[6]

4.2.3 The Need for Intervention in 2001

The poor condition of the paintings was the impetus for the extensive conservation treatment that began in 2001. By that time there was severe flaking of the paint layers, the cradles were blocked, and the surface was extremely dirty. The consolidation of the paint layers and the unblocking of the cradles were the first steps of the treatment, and both could be executed without major problems. The cleaning, however, turned out to be problematic and took years to complete. Yellowed varnishes, discolored retouching, and layers of dirt subdued the bright colors and greatly reduced the legibility and the three-dimensionality of the composition. It was only through technical imaging, including infrared photography, infrared reflectography (IRR),[7] and X-ray radiography (XRR),[8] that

---

[5] "Llegó a Madrid, donde, tras su limpieza, se intentó que lo comprara la Reina Maria Christina," (Gómara 2013). Many thanks to Sara Mateu for providing the article.

[6] Flaking paint was noted in February and May 1901, in different areas. It was mentioned that the panels were covered by a layer of dust that adhered to the surface and diminished the brightness of the colors. Consolidation and surface cleaning with bread crumbs was proposed, but the charge made for the work was only for consolidation. In 1952, 1977, and 1980, the panels occur in lists among other paintings that were treated, but details were not specified. Although nothing is mentioned about the cradles, judging from their appearance, it is thought that they were attached in the 1950s or 1960s when the panels were already in the museum. In addition, a synthetic varnish (isobutyl acrylate) was found on the surface which must also have been applied in the museum.

[7] Infrared imaging was carried out twice: at the beginning of the project by Adri Verburg, using a phase I scanning back (4 × 5 inch) with spectral range 1000–1100 nm, and during the project by Claudia Daffara …

the conservators became aware that underneath some of the plain, flat brown areas, decorative details, as well as modelling of the volume and folds in the draperies were present.

Cleaning tests showed that underneath the uppermost soluble varnish layers, a grey-brown opaque crust was present in the darkest, most obscured areas, in particular over the copper-containing blue and green paint and the grey clouds surrounding the figures, which also contain a copper-based pigment in the form of azurite.[9]

Unfortunately, this crust turned out to be highly insoluble in the extensive range of solvents and cleaning systems that were tested. It reacted to the cleaning tests by blanching but appeared impossible to dissolve. To gain more insight into its composition and with the hope of finding a safe method to remove it, scrapings of it were first analyzed by transmission FTIR microscopy and SEM-EDX. Further non-invasive investigations and detailed analysis of samples mounted as cross sections were also undertaken subsequently, in order to gain a more precise understanding of the chemical composition of the crusts, their location in the layer structure, and their distribution across the paint surface.

4.2.4 Experimental

Transmission Fourier transform infrared (FTIR) microscopy (mid-IR range) spectra were acquired using a Nicolet 710 Series FTIR spectrometer with a NicPlan infrared microscope, fitted with a mercury-cadmium-telluride (MCT) type A detector (cooled with liquid nitrogen). Small subsamples of the scrapings of the crusts were placed between the windows of a Spectra-Tech micro-compression diamond cell for analysis. Measurements were made in transmission mode over the range 4000–650 cm^{-1}, using a Spectra-Tech Reflachromat Cassegrain ×15 objective. One hundred twenty-eight or 256 scans were made at a resolution of 4 cm^{-1} with HappGenzel apodization. Both spectrometer and microscope were purged with water and CO_2-free air.

---

and Mattia Patti, using a multispectral scanner, spatial resolution 4 pt./mm (250 micron), InGaAs with spectral range 800–1700 nm, C.N.R.–I.N.O.A (Istituto Nazionale di Ottica Applicata).

[8] X-radiography was undertaken by Guido van de Voorde, Royal Institute for Cultural Heritage, Parc du Cinquantenaire 1, B-1000 Brussels.

[9] SEM-EDX detected copper in the blue and green paints, suggesting the use of azurite and a copper-containing green pigment (most probably originally verdigris). The grey paint layer depicting the clouds consists mainly of a mixture of lead white and a black pigment (probably a carbon-based black), mixed with a little azurite, identified by SEM-EDX and FTIR microscopy.

Mobile reflection mid-infrared (reflection mid-FTIR) spectrometry point measurements were performed by means of a portable JASCO VIR 9500 spectrophotometer, made up of a Midac Illuminator IR radiation source, a Michelson interferometer, and a liquid nitrogen-cooled MCT detector. The probe was a 4 mm bifurcated cable containing 19 chalcogenide glass fibers allowing collection of spectra in the range 4000–900 cm^{-1} at a resolution of 4 cm^{-1}. The noncontact probe was kept perpendicular to the painting surface (0°/0° geometry) at a distance of about 3 mm. The total reflectance was collected over 400 scans using the spectrum from an aluminum mirror plate for background correction. The reflectance spectra (R) were converted to pseudo-absorbance (A' = *log(1/R)*).

The instrument used for the macroscopic FTIR scanning measurements in reflection mode (MA-rFTIR scanner) was a Bruker Alpha FTIR spectrometer, equipped with a frontal reflection module (20°/20° geometry) and a coaxial visual camera (Legrand et al. 2014). The spectrometer incorporates a globar IR source, Michelson interferometer, and a deuterated triglycine sulfate (DTGS) detector. Spectra acquisition and storage were carried out using the Bruker OPUS 6.0 software package. Before each scan a spectral background was recorded over 30 min by placing a gold-coated mirror in front of the reflection module. During scanning mode, spectra were recorded for 3 s on each point at a resolution of 4 cm^{-1} over the range 7500–375 cm^{-1}. For scanning purposes, the spectrometer was mounted on a motorized X (10 cm), Y (25 cm), and Z (10 cm) motor stage setup (Newport Corporation, Irvine, CA, USA). The X and Y stages are used during scanning, while the Z stage helps to bring the setup in focus (2 mm spot) prior to the scan. The processing of the hyperspectral datasets was performed by self-written routines using the data analysis software package IDL 8.3. For most chemical distributions and spectra, the recorded reflectance was converted to pseudo-absorbance. The resulting FTIR maps have a lateral resolution in the mm range.

For mobile X-ray diffraction (MXRD) measurements combined with XRF, a 30 W air-cooled iMOXS-MFR (IFG, Adlershof, Berlin, Germany) X-ray tube was used with a voltage of 40 kV and a current of 700 µA. The source is equipped with a polycapillary semi-lens providing a 4 mm (3.8–4.4 mm) diameter parallel X-ray beam (total exit divergence of 0.25° or 4.36 mrad). The copper anode provides, through a 0.1 mm beryllium window, polychromatic X-rays necessary for XRF measurements. The source is equipped with a 15 µm Ni filter to strongly attenuate the Cu K_β-line and avoid the presence of secondary diffraction peaks. XRD is therefore performed with the usual monochromatic radiation (Cu-K_α; E = 8.047 keV

(= 0.154 nm)). Diffractograms are collected in reflection mode using an incident angle ω of 10° to the specimen surface allowing 2ϑ values larger than 10° to be reached. Fine-grain alumina samples were used for the calibration. The relatively prolonged acquisition times, amounting up to 30 min, limited the number of measurements. The FIT 2D software[10] was used to transform the two-dimensional diffraction images into 2ϑ spectra. Based on the latter and a database of X-ray powder diffraction patterns, the EVA[11] and XRDUA[12] software were used to determine the crystalline phases that were present. The technical features and analytical performance of this instrument are discussed elsewhere (Gianoncelli et al. 2008).

At the University of Antwerp, embedded paint cross sections were analyzed by means of a Jeol 6300 electron microprobe system equipped with an energy dispersive Si (Li) X-ray detector (SEM-EDX) (Princeton Gamma Tech). Elemental distribution maps were collected from the surface of paint cross sections at 20 kV, a magnification of 500x, a beam current of 1 nA, and a recording time of 3600 s.

The elemental analysis and mapping that was carried out at the National Gallery on paint cross sections and scrapings was done using a Carl Zeiss EVO® MA10 variable pressure scanning electron microscope (SEM) coupled to an Oxford Instrument X-Max 80 mm^2 energy dispersive X-ray spectrometer (EDX), using INCA 350 software. The operating parameters were 20 kV, 200 pA beam current, and 30 Pa chamber pressure (the minimum necessary to limit charging) with air as the chamber gas. Optical microscopy was carried out using a Leica DM4000 M microscope and a Zeiss AxioCam HRc camera for recording images. A filter system A (BP 340–380 nm, dichromatic mirror: 300 nm, suppression filter: LP 425 nm) was used for UV excitation.

Attenuated total reflection Fourier transform infrared (ATR-FTIR) microspectroscopic imaging spectra were acquired from embedded cross sections by using a Bruker Tensor 27 FTIR spectrometer connected to a Hyperion 3000 Series microscope, fitted with a 64 × 64 (4096 pixels) FPA detector (range = 4500– 900 cm^{-1}), cooled with liquid nitrogen. The microscope was fitted with a CCD camera, X-Y stage (adjustment accuracy of 0.1 μm), and a dedicated ATR objective (20× magnification). The ATR had a germanium crystal with a tip size of 250 μm. Both spectrometer and microscope were purged with water- and CO_2-free air. One hundred twenty-eight scans were collected at a resolution of 4 cm^{-1}. The 64

---

[10] http://www.esrf.eu/computing/scientific/FIT2D/. Accessed February 2017.
[11] http://www.bruker-axs.de/eva.html. Accessed February 2017.
[12] http://xrdua.ua.ac.be/. Accessed February 2017.

× 64 pixel focal plane array collects image data from a 32 × 32 µm² square. An effective (diffraction limited) lateral resolution of 3–5 µm is achieved.

Combined synchrotron radiation-based micro X-ray fluorescence and micro X-ray diffraction (SR µ-XRF/µ-XRD) imaging experiments were performed at the microprobe station of the P06 Hard X-ray Micro/Nano-Probe beamline (PETRA III, DESY, Germany). A photon energy of 21 keV was selected by means of a Si(111) double crystal monochromator. The beam was focused to 0.4 × 0.4 µm² (hor. × vert.) employing a Kirkpatrick-Baez mirror optic. Fluorescence radiation was recorded by a Vortex-EM silicon drift detector placed perpendicular to the incident X-ray beam. Simultaneously diffraction signals were recorded in transmission geometry using a Pilatus 300 K area detector at a distance of approximately 15 cm behind the sample. Initial calibration of the diffraction setup was performed using a LaB_6 reference sample. The software package PyMca was used for spectral fitting of the fluorescence data (Solé et al. 2007), while whole pattern fitting of the diffraction data was performed using XRDUA (De Nolf and Janssens 2010). This software package provides several methods for obtaining crystalline-specific distributions from a large number of diffraction patterns typically obtained in µ-XRPD imaging experiments (De Nolf et al. 2014).

4.2.5 Analytical Results

4.2.5.1 *Analysis of Scrapings of the Crust*

Since rapid identification of the crusts was vital for the continuation of the conservation treatment, a number of samples in the form of scrapings were taken and analyzed after local removal of the upper varnish layers. These were collected from each panel, concentrating in particular on the crusts on the blue and green paint and on the grey clouds. The resulting powders were analyzed using FTIR microscopy in transmission mode and SEM-EDX at the National Gallery, London. All of the samples of the crusts had a similar composition, consisting essentially of calcium oxalate (bands at c. 1650, 1327, and 783 cm^{-1}), with some calcium carbonate (c. 1414, 875, and 712 cm^{-1}) and calcium sulfate (c. 3401, 1120, and 671 cm^{-1}). In addition, when interpreted with the SEM-EDX results, the broad band at c. 1090 (together with the doublet at c.800/780 cm^{-1}) indicates the presence of various silicates, and the band at c. 1041 cm^{-1} shows the presence of calcium phosphate (and/or silicates such as phyllosilicates with bands at c. 1040 and 915 cm^{-1})

(Farmer 1974). This composition suggests that the layer most probably resulted from an accumulation of dirt on the surface.[13]

4.2.5.2 *Non-invasive Analysis*

In cooperation with the University of Antwerp and as part of a MOLAB campaign (Miliani et al. 2010),[14] the crusts were further investigated using mobile analytical equipment (Van der Snickt et al. 2011). The noncontact and non-invasive approach typical of MOLAB allowed a large number of measurements to be performed all over the vast paint surface of all three panels. In this way it was possible to assess the extent to which the local data obtained from a few scrapings was representative of the rest of the large surface.

Monico et al. demonstrated the usefulness and sensitivity of reflection mid-FTIR spectroscopy for the non-invasive identification of various oxalate salts on the surface of polychrome works of art (Monico et al. 2013). Interestingly, MOLAB reflectance FTIR point measurements, performed with the same instrument that was employed in that study, indicated the presence of oxalates across the entire paint surface. As exemplified by the spectrum in Fig. 2, characteristic calcium oxalate bands at around 1320 and 1640 cm^{-1} were observed in all FTIR measurements, including those collected in areas where no crusts were visible to the naked eye. At the end of the campaign, it was evident that there was an oxalate-containing layer distributed across the whole paint surface of all three panels but so thin that it was hardly visible to the naked eye.

The numerous non-invasive reflectance FTIR measurements on the thicker crust present above areas of dark copper-containing paint also revealed exclusively calcium oxalates, with no evidence of the formation of the analogous compounds with copper, in agreement with the transmission FTIR analyses of the scrapings. Measurements performed on the crusts with the mobile X-ray diffraction (XRD) instrument from the

---

[13] C. Higgitt and M. Spring, Preliminary EDX and FTIR microscopic examination of samples, National Galley, unpublished research report. For comparable spectra see the appendix in Higgitt and White (2005). For the chemical composition of dirt, see Van Grieken et al. (2000).

[14] MOLAB is a mobile laboratory composed of a unique collection of portable equipment which is available to cultural heritage researchers across Europe, including art historians, conservators, and conservation scientists. The MOLAB analyses presented here were funded under the EU CHARISMA project (FP7, grant no. 228330). MOLAB can currently be accessed through the Horizon 2020 IPERION project (www.iperionch.eu, Grant No. 654028).

C2RMF (Gianoncelli et al. 2008) confirmed the presence of two related Ca-based oxalate salts: whewellite and weddellite.[15]
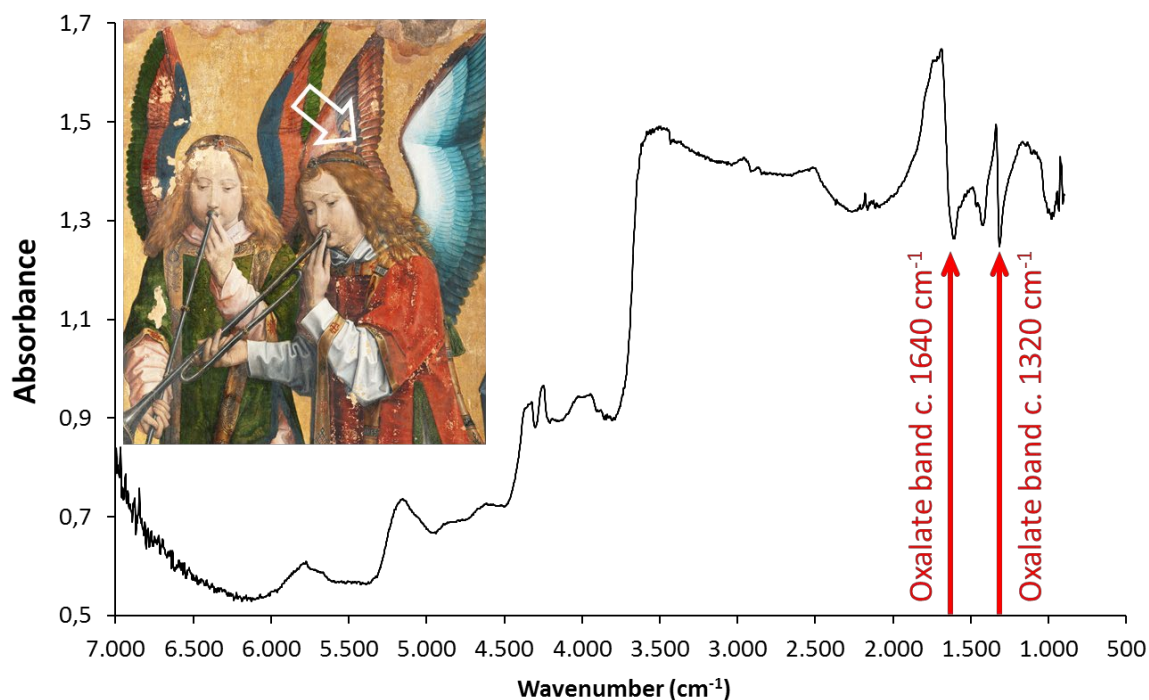

Figure 2: Reflection mid-FTIR spectrum recorded on a reddish feather of angel 13 in an area where no crusts were observed. **Insert**: a white arrow indicates the exact spot where the spectrum was collected. Characteristic calcium oxalate bands around 1320 and 1640 cm^{-1} are indicated by red arrows

4.2.5.3 *Analysis of Paint Cross Sections*

While the characterization of scrapings and non-invasive analysis of the paintings allowed identification of the surface materials, more detailed information about the layer structure of the paint and coatings was considered essential in order to assess the feasibility of removal of the crusts. The extensive non-invasive analysis guided the selection of sample locations and reduced the number of samples that were needed. The samples were taken both from areas where the thick, opaque crusts were evident and from areas where the oxalate-containing layer was hardly visible to the naked eye. The

---

[15] In principle, whewellite and weddellite can also be distinguished on the basis of their FTIR spectra (although there is some disagreement in the literature about precise band positions), but in practice this is difficult, particularly when the salts are present in mixtures or in combinations with other compounds, see, for example, Garty et al. (2002), Conti et al. (2010), and Leroy (2016).

main objective was to compare these areas through the examination of paint cross sections and to gain insight into the location of the oxalate-containing layers within the overall layer structure.
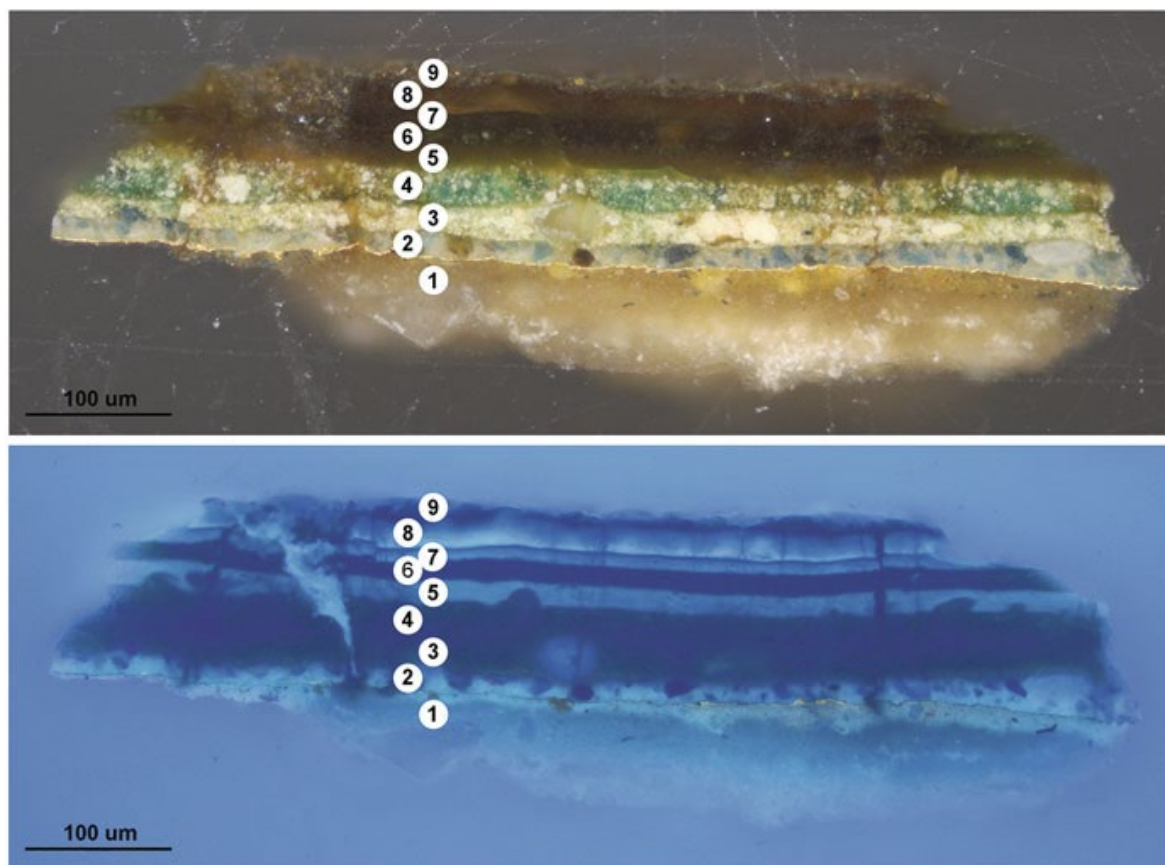

Figure 3: Top: optical microscopy (OM) image of the cross section prepared from sample 779-05, removed from the green wing of angel 5, taken with visible illumination, and showing the sample stratigraphy. Bottom: photomicrograph of the same cross section taken under UV illumination

Figure 3 shows the stratigraphy of the cross section prepared from a sample taken from the crust on top of the green feathers of the wing of angel 5 on panel 779. Figures 4 and 5 show the results of SEM-EDX analysis and micro-ATR-FTIR imaging of this sample. ATR-FTIR microspectroscopic imaging (Fig. 5) is a technique that was not available at the time of the first FTIR analyses on scrapings but since its introduction has proved very valuable for chemical imaging at high resolution (up to about 3 µm is achievable) directly on cross sections. It is especially suited to the characterization and location of oxalate-containing accretions.
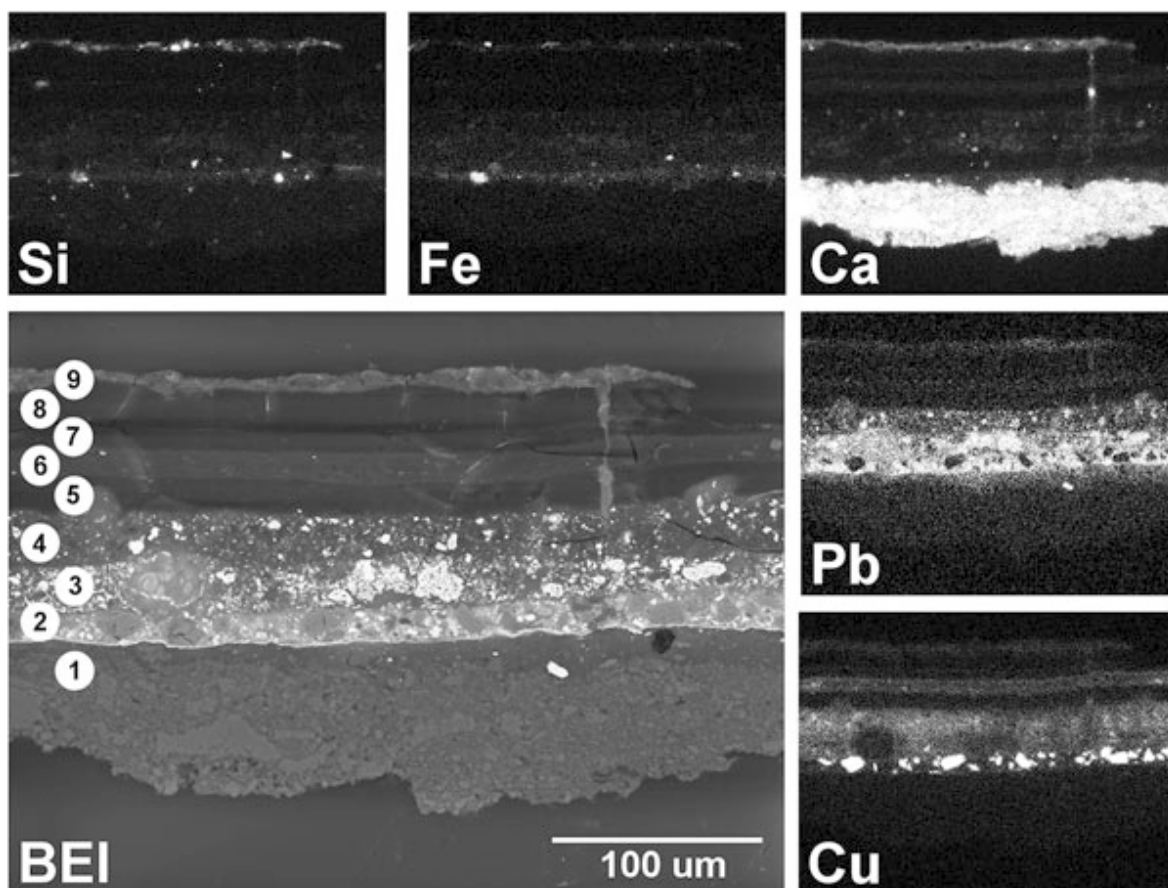
*Figure 4: SEM-EDX measurements on sample 779-05 taken from the green wing of angel 5. **Bottom left**: backscattered electron image (BEI) showing the sample stratigraphy. **Top**: elemental distribution maps of silicon (crust and mordant) and iron (crust and mordant). **Right, top to bottom**: elemental distribution maps of calcium (crust and ground, plus smaller quantities in the paint layers and the intermediate copper-containing layer), lead (paint layers), and copper (paint layers and intermediate layer between varnish layers)*

At the bottom of the cross section are the ground layers on top of which are a thin brownish mordant and a layer of gold leaf (all layers labelled together as "1" in Figs. 3, 4, and 5). The ground in this sample consists of a first thin gypsum-rich layer followed by a thick chalk-rich layer. The gilded background extends beneath the paint in this area. The next layer (labelled 2) contains a mixture of lead white and azurite and appears to correspond to the paint used to create the inner part of the wing. Over the blue paint is a light yellow-green paint (labelled 3) composed of a copper-containing pigment (probably verdigris or a related copper salt of an organic acid), lead white and lead-tin yellow (type I). This is covered with a more deeply colored green paint (labelled 4), containing a similar mixture to layer 3 but with rather less lead white and lead-tin yellow.
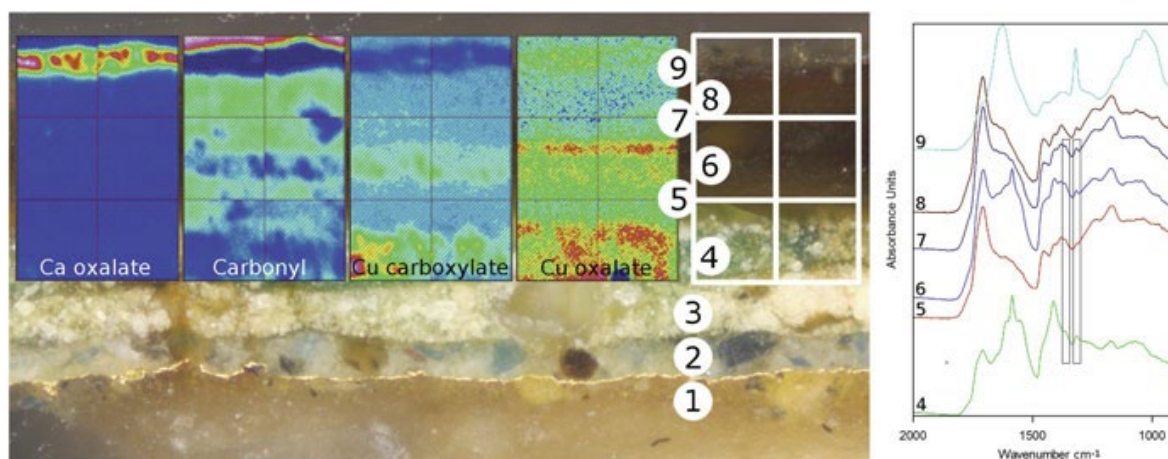
*Figure 5: **Left**: series of ATR-FTIR images produced by integration of IR spectral bands revealing the location of different materials within sample 779-05 taken from the green wing of angel 5. **From left to right**: the image produced by integration of the band between 1333 and 1302 cm^{-1} shows the distribution of calcium oxalates; between 1741 and 1674 cm^{-1} shows the distribution of carbonyl groups associated primarily with the oil-resin varnish layers, the paint, and the polyester mounting resin; between 1599 and 1564 cm^{-1} shows the distribution of copper carboxylates (and the green copper-containing pigment(s)); and between 1371 and 1345 cm^{-1} shows the distribution of copper oxalates. The scan window is 64 μm wide and 96 μm tall, i.e., 2 × 3 32 μm squares. **Right**: series of FTIR spectra from the different layers extracted from the ATR-FTIR imaging data. (9) Surface crust (calcium oxalate at c. 1650 and 1321 cm^{-1}), (8) varnish layer directly below crust (oil-resin varnish at c. 1733, 1711, 1435, 1414, 1318, 1254, and 1166 cm^{-1}), (7) varnish layer directly above copper-containing intermediate layer (possibly same layer as layer 8), (6) copper containing intermediate layer (strong asymmetric carboxylate stretch at 1587 cm^{-1}), (5) varnish layer directly above paint (as above), and (4) upper green paint layer (copper-based pigment and copper carboxylates at c. 1615, 1586, 1546, and 1414 cm^{-1}). Copper oxalates can be detected in layers 4–7 only (determined by the presence of the highlighted bands at c. 1364 and 1319 cm^{-1})*

Detailed examination of a series of FTIR spectra extracted from the ATR-FTIR imaging data confirmed that the copper-containing pigment in this layer is some form of (basic) copper acetate and revealed the presence of copper carboxylates (strong asymmetric carboxylate stretch at 1586 cm^{-1}), presumably from reaction of the pigment with the oil binder, and copper oxalates. Directly over the green paint is a very brown oil-resin varnish layer (labelled 5), which also contains some copper oxalate, suggesting migration of copper from the paint layer below. Over this varnish is a layer with a greenish color (labelled 6), which can be seen in the EDX maps to contain copper (both dispersed throughout the layer and in discrete copper-rich particles) and a little calcium. ATR-FTIR indicates that at least some of the copper in this layer is present in the form of copper carboxylates and oxalates. Since it lies over varnish, it is not completely clear whether this copper-

containing layer is overpaint or an original glaze,[16] but it is covered by at least one, or possibly two, further oil-resin varnish layers (labelled 7 and 8). Copper oxalates were detected in the lower part of the varnish on top of the intermediate green layer (corresponding to layer 7) but not further up within the stratigraphy.[17] The calcium EDX map (Fig. 4) shows a thick calcium-rich layer (labelled 9) at the very top of the stratigraphy, corresponding to the calcium oxalate containing crust, as can be seen in the ATR-FTIR imaging results (Fig. 5). The elemental distribution maps reveal the heterogeneous nature of the crust which contains, in addition to calcium, distinct particles rich in silicon and iron.

Another sample was taken from the red lake-containing glaze in the feathers of the wing of angel 8 on panel 778. This was an area where the oxalate-containing surface layer was hardly visible to the naked eye. The sample was imaged using synchrotron radiation-based μ-XRF/μ-XRD mapping, and a number of the resulting chemical images are shown in Fig. 6. The XRD mapping shows a very thin layer (less than 1 μm) containing weddellite at the very top of the stratigraphy. Compared to the oxalate layers in the cross section that include the thick crust (see Figs. 3, 4, 5), this layer is much thinner, which explains why the oxalate deposits are hardly visible to the naked eye in this area. The oxalate layer might seem to be directly on top of the red lake-containing paint, but in fact – although this is not very clear in Fig. 6 – other chemical images of this cross section show that the weddellite-containing layer is separated from the original paint by an organic layer, presumably varnish (Janssens et al. 2016). At the very bottom of the cross section, the preparation layers are visible: the ground appears to consist of two layers, a layer rich in chalk applied over a layer rich in gypsum. The technique allowed the detected calcium fluorescence signal to be resolved into four separate species: gypsum and calcite in the ground, hydroxylapatite on top of the ground (not shown), and a thin layer of weddellite at the top.

---

[16] Although the conservators were of the opinion that the copper-containing paint on top of the varnish layer was probably overpaint, it was left on the surface during cleaning as no certain proof for this could be found in the cross sections or on the surface of the paintings. It was not present as a continuous layer but more as local spots.

[17] The location of the copper oxalates suggests that some degree of migration of copper ions into adjacent layers has occurred but not all the way up into the surface crust. These results clarify why only calcium oxalates were detected at the surface of the paintings in the scrapings and using the MOLAB non-invasive reflectance FTIR equipment. It should be noted that calcium oxalates may also be present in those layers containing copper oxalates, but this cannot be confirmed because of the overlap of the spectral bands and the 900 cm^{-1} cutoff for the micro-ATR-FTIR imaging equipment.
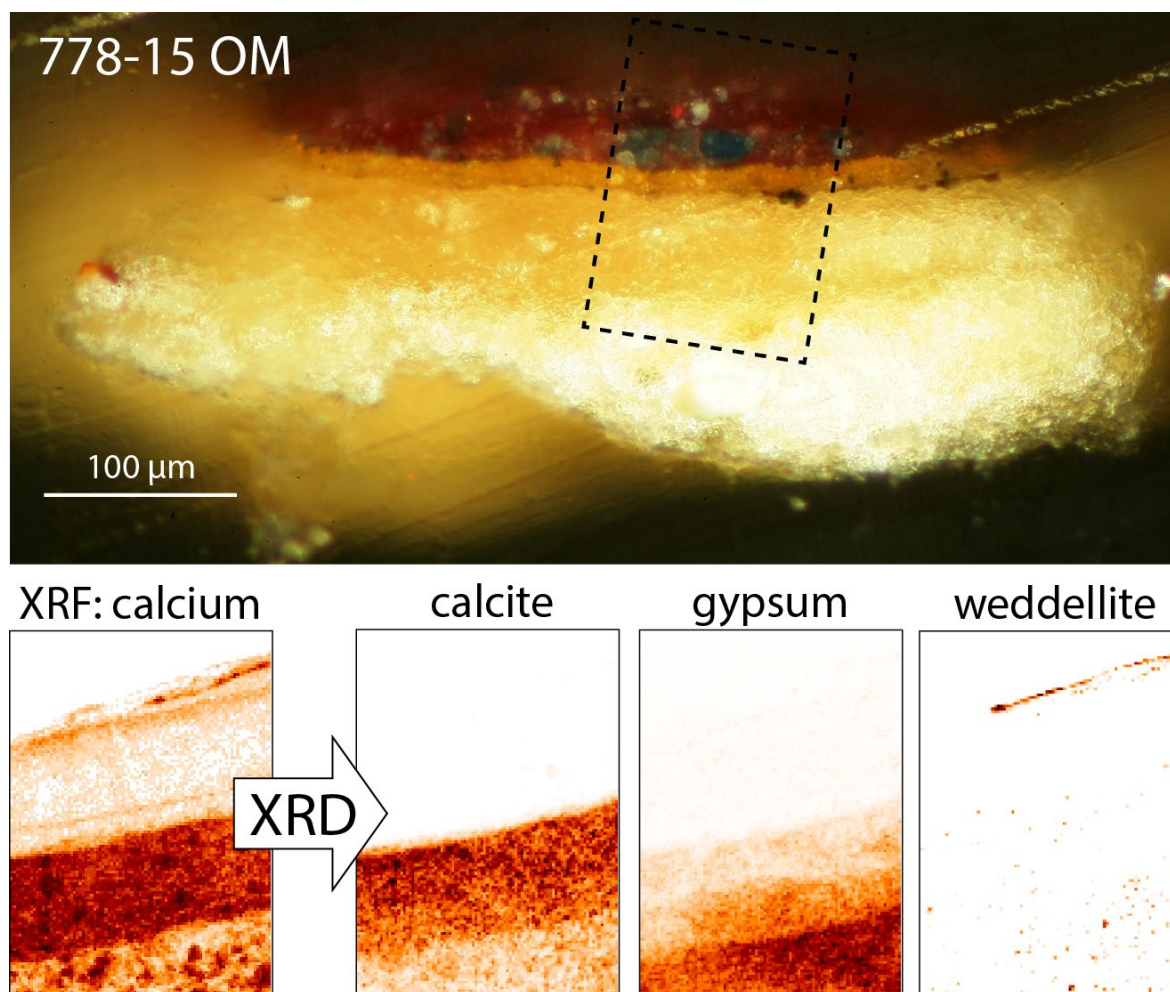
Figure 6: *Top*: micrograph of sample 778–15 taken from the feathers of angel 8. The black rectangle indicates the area that was chemically imaged. *Below*: chemical images obtained by means of synchrotron radiation-based μ-XRF/μ-XRD. *Bottom left*: μ-XRF map of calcium collected in reflection mode. *Bottom right*: corresponding μ-XRD maps (transmission mode) of three calcium species: calcite, gypsum, and weddellite

4.2.6 Discussion

The formation of metal oxalates, and particularly oxalate-rich surface layers, is commonly observed for a wide range of artworks including stone and bronze sculpture, wall paintings, and stained-glass (Zoppi et al. 2010). Such oxalate-rich crusts, which are essentially inorganic in composition and highly insoluble, induce scatter and can be highly disfiguring. As oxalate and other salts form on surfaces, colored components of dirt (e.g.,

carbon-containing particles) can also become trapped within the crust, as observed on building stone (Potgieter-Vermaak et al. 2005). In recent literature, oxalate-containing layers on the surface of easel paintings are being reported with increasing frequency.[18] Although on easel paintings these layers are generally thin, their scattering effect gives an unsaturated appearance and can be optically very disturbing, especially in the dark areas. Nevertheless, during conservation treatments, these oxalate-containing layers are often left essentially undisturbed on the surface as their insolubility and strong adhesion to underlying layers make it impossible to remove them selectively.

The origin and formation of oxalate salts is complex and not fully understood. A number of different mechanisms may be involved depending on the exact materials and environment, but in general, oxalate salts form when oxalic acid reacts with metal ions. In paintings, the metal cations may originate from the paint layers (e.g., pigments or driers (Van der Snickt et al. 2012)), from the ground/substrate, or from particulate matter such as dirt deposited on the paint surface, but the source of the oxalic acid is still a subject of debate (Spring and Higgitt 2006). Microbiological activity and some form of extreme chemical deterioration of organic substances, either within the paint (e.g., the binder) or on the paint surface (e.g., protective or other coatings), have both been suggested in the literature (Mendes et al. 2008; Zoppi et al. 2010). It appears that either or both of these processes can be a source, but it is also clear that oxalate formation can occur even in the absence of an organic material (or where only small amounts are present).

In the case of Memling's *Christ with Singing and Music-making Angels*, a calcium oxalate-containing layer was found over the entire surface of the paintings, but in most areas, over light colors, this layer was so thin (less than 1 μm) that it was hardly visible to the naked eye. The oxalate-containing crusts on the darkest areas of the painting, however, were exceptionally thick, with an opaque grey-brown appearance, and highly disfiguring. Such crusts were present primarily over dark copper-containing paints, including the green garments painted with verdigris, and to a lesser extent over the azurite-rich garments and the grey clouds, which also contain a little azurite.

In the literature, copper-based pigments are noted to be one of the types of pigments with which oxalate formation seems to be particularly pronounced (Higgitt and White 2005; Spring and Higgitt 2006; Salvadó et al. 2013). Zoppi et al. reported that calcium- and

---

[18] For examples of the detection of calcium oxalate in easel painting, see Matteini et al. (2002), Higgitt and White (2005), Noble and Van Loon (2007), Van Loon (2008), Kahrim et al. (2009), and Salvadó et al. (2009, 2013).

copper-containing pigments show the highest reactivity toward oxalic acid, due to their high solubility in an acid environment (Zoppi et al. 2010). In this case, however, analysis showed that although some copper oxalates were detected lower in the stratigraphy in certain green passages, the surface crusts only contain calcium oxalates. Examination of cross sections and UV-induced visible fluorescence imaging on the painting during cleaning showed that the crust was not directly adjacent to the original paint surface but separated from it by one or more varnish layers, strongly suggesting that its formation is unrelated to the degradation of the underlying paint. The heterogeneous composition of the crust, which contains compounds that are typical of airborne particles, suggests instead that its formation is linked to dirt deposition and that the calcium is primarily of atmospheric origin. Supporting this suggestion is the fact that the panels spent a long period in the Spanish monastery in Nájera where – more than in a museum environment – they are likely to have accumulated high levels of calcium-containing dust and been exposed to microbial action (Kontozova-Deutsch et al. 2011). The thickest crust formation was found over the dark-colored copper-containing paint layers. Such areas are likely to have been left untouched during past selective cleaning when varnish(es) might only have been removed from the light colors to obtain a quick result, allowing dirt to build up most over these passages. These conditions would favor the formation of calcium oxalate salts which have effectively "cemented" the dirt to the surface of the painting, creating the thick, highly insoluble, and disfiguring surface crusts. The presence of multiple layers of very discolored and dirty oil-resin varnish and overpaint below the crust in the dark paint passages further obscured the composition. The dark passages may also have benefitted from local varnishing to (re)saturate the colors, with such additional organic layers perhaps further enhancing the oxalate formation, in a similar way as suggested by some authors for stone monuments (Lazzarini and Salvadori 1989; Rampazzi et al. 2004).

4.2.7 Removal

As the thick crusts concealed every hint of color and every pictorial detail over large areas, they were very disturbing, reducing the artistic quality and legibility of the paintings. To be able to fully appreciate again the original quality of the paintings, their removal was an essential part of the ongoing cleaning of the panels. The varnish layers in between the crust and the original paint indicated that the crusts were not part of the original paint stratigraphy. Together with the international advisory committee that oversaw the conservation process, it was therefore decided to undertake this time-consuming operation.

The presence of an intermediate varnish layer made it possible to separate the crusts from the original paint surfaces. In the green areas, where solvents might damage the vulnerable glazes, this could only be done mechanically, with a scalpel under the microscope. Working under magnification and progressing only millimeter by millimeter, the conservators were able to remove the disfiguring crust. Time-consuming as it was, the results were spectacular as can be seen in Figs. 1 and 7. Underneath the dull, plain brown

surface appeared lush green draperies with three-dimensional folds, brocade patterns in different green hues, and decorative details such as fringes applied using lead-tin-yellow, as predicted by the imaging techniques. In the UV-induced visible fluorescence photograph (Fig. 7), it can be seen that the fluorescent varnish layer located between the crust and the original paint surface was revealed after removal of the crust, again confirming the observations made from paint samples.
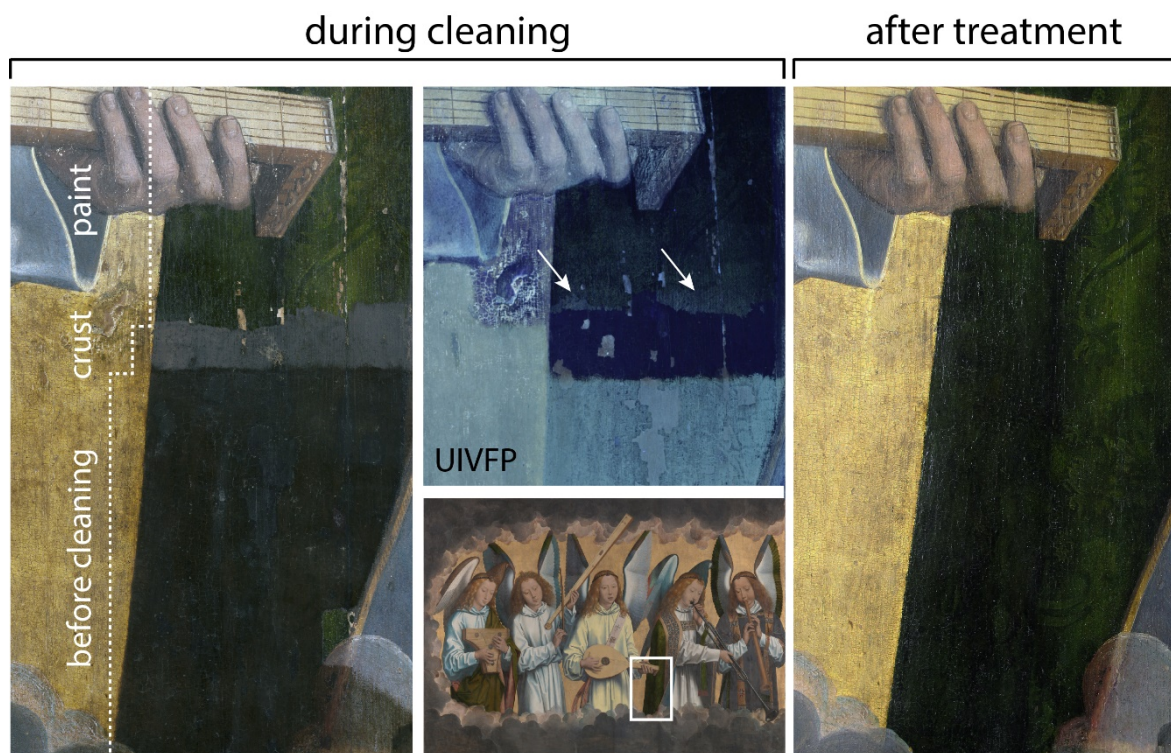

Figure 7: Photo showing a detail of panel 779, as indicated by the white rectangle (middle, bottom). **Left**: *cleaning staircase illustrating the gradual removal of the aged surface varnish(es) and the oxalate crust on the green paint.* **Middle, top**: *UV-induced visible fluorescence photograph (UIVFP) of the same area showing the typical fluorescence of the aged surface varnish(es) while the oxalate crusts appear dark in UV where exposed. Between the crust and the original paint surface, a fluorescent layer is visible (indicated by two white arrows), confirming the presence of an intermediate varnish layer.* **Right**: *the same area after treatment. Photo left: KMSKA © Arcobaleno, Adri verburg. Photo right: KMSKA © Rik Klein Gotink*

Figure 8 illustrates how the gradual removal of the surface varnish layers and the underlying crust was documented *in situ* during the ongoing treatment by means of macroscopic FTIR scanning and spectroscopy in reflection mode.
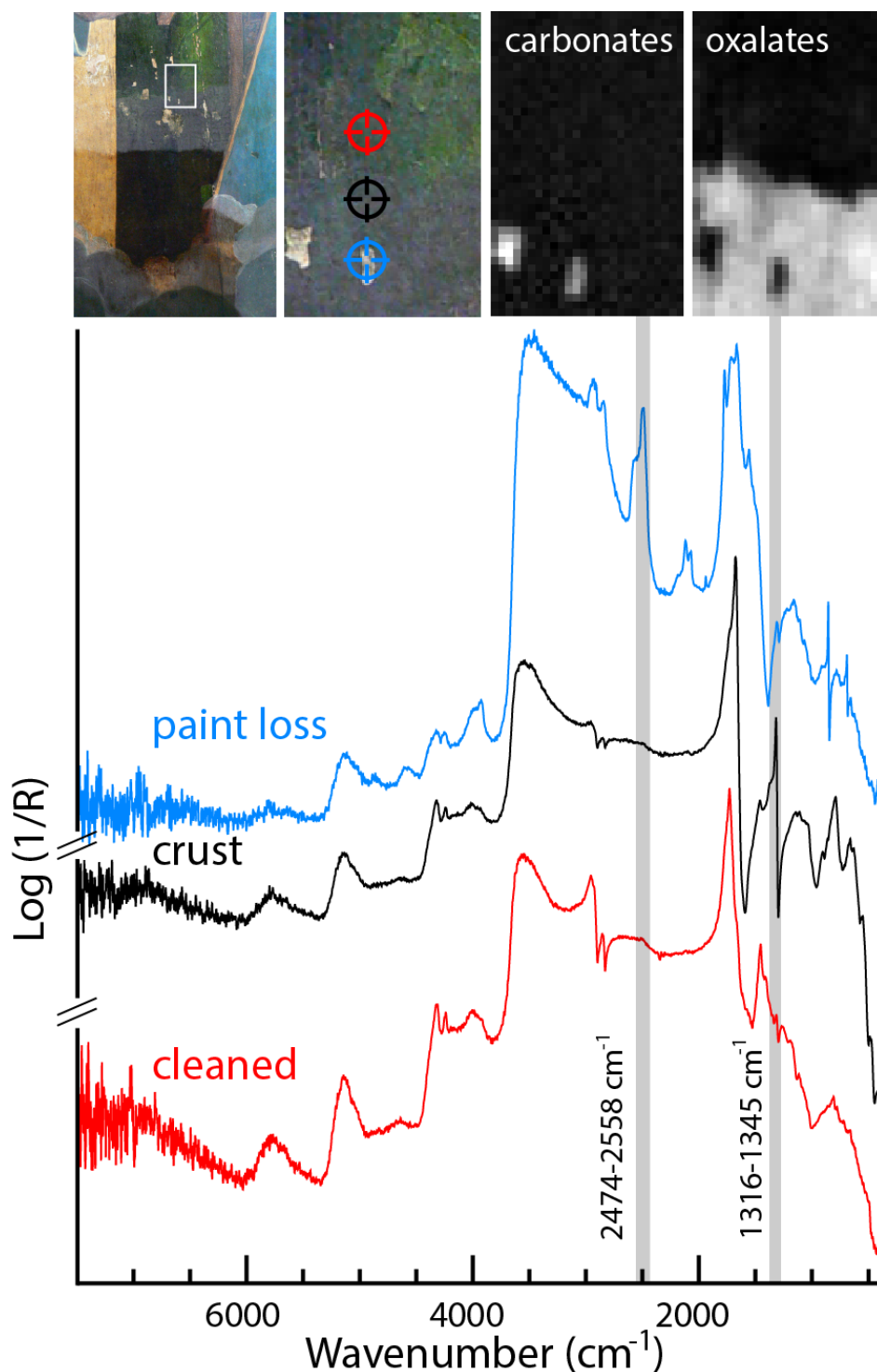
*Figure 8: **Top, left**: detail of the garment of angel 4 showing sequential cleaning tests. The white rectangle indicates an area where the crust was partially removed and imaged by means of macroscopic FTIR scanning in reflection mode. **Top right**: corresponding FTIR maps showing the distribution of carbonates in the paint losses and calcium oxalates in the crust. **Bottom**: FTIR spectra isolated from the hyperspectral data cube, with indication of the bands that were used to generate the chemical maps*

The aim of these scans was to show the effectiveness of the (mechanical) cleaning procedure. As shown in the FTIR maps in Fig. 8, the distribution of the v_s (CO) band of calcium oxalate clearly coincides with the crust, while the signal is absent where the green paint is revealed. The spectra in Fig. 8 were obtained in the latter cleaned area, proving what can be concluded from the oxalate distribution map: the intensity of the band at 1320 cm^{-1}, related to calcium oxalate, has dropped significantly after cleaning. Two paint losses appear as hot spots in the distribution maps for calcium carbonate, one of the materials employed in the preparation layers.

Although mechanical cleaning was possible on the smooth surface of the green colors, it was impossible on the more grainy blue colors and grey clouds. Removal of the crusts over the blue colors was possible to a certain degree by repeat applications of mixtures of dimethyl sulfoxide in ethyl acetate in different concentrations. On the grey clouds, a combination of solvent action and mechanical removal could be used. However, the vulnerability of the grey paint layer made it impossible to remove the oxalate-containing crusts completely, and some material had to be left on the surface. Over the lighter colors, the oxalate-containing layers are very thin and hardly visible, for example, over the red feathers discussed above. In such areas, since the layers were not optically disturbing, they were left on the surface.

4.2.8 Conclusion

During the recent conservation of the three panels of Memling's *Christ with Singing and Music-making Angels*, an insoluble calcium oxalate-containing layer was found over the entire surface of the paintings. This crust was particularly thick, opaque, and disfiguring on the dark, copper-containing paint passages. The crust obscured the underlying composition but was extremely insoluble and posed a major conservation challenge.

A wide range of non-invasive and micro-invasive analytical techniques were employed to determine the composition and distribution of the crusts and to establish the stratigraphy and nature of the underlying layers. Each contributed in a significant and complementary way to achieving as full an understanding as possible of the accretions on the paint surface, which was essential in informing the treatment of the paintings. The analytical results revealed that the crusts contained oxalate salts in the form of two related Ca-based oxalate salts, whewellite and weddellite, and a range of other components consistent with surface dirt deposition.

Oxalate salts have been found associated with a wide range of different artworks, and the mechanism of their formation is complex, possibly quite variable, and not fully understood. In the case of the Memling panels, the oxalates associated with the surface crusts did not appear to originate from degradation of the original paint but possibly from a combination of microbial action and a thick accumulation of dirt, particularly over the

darker paint passages, where in addition a buildup of older varnishes had been left in place. The dirt deposits are likely to have accumulated during the period, while the panels were in the Nájera monastery.

The presence of intermediate varnish layer(s) between the crust and the original paint surface, as revealed by the analyses, indicated that the crusts were not part of the original paint stratigraphy and made it possible to remove most of them mechanically. The removal was a difficult and time-consuming process, and its progress was carefully monitored using macroscopic FTIR scanning and spectroscopy in the reflection mode. The treatment has, however, yielded spectacular results and has allowed the original colors and spatial depth of the composition to be recovered.

References

Borchert T (1993) Memling's Antwerp "God the Father" with music-making angels. In: Verougstraete H, Van Schoute M (eds) Le dessin sous-jacent dans la peinture, Colloque X, September 1993, vol 1995. Le dessin sous-jacent dans le processus de creation, Louvain-laNeuve, pp 153–168

Conti C, Brambilla L, Colombo C et al (2010) Stability and transformation mechanism of weddellite nanocrystals studied by X-ray diffraction and infrared spectroscopy. Phys Chem Chem Phys 12:14560–14566

De Nolf W, Janssens K (2010) Micro X-ray diffraction and fluorescence tomography for the study of multilayered automotive paints. Surf Interface Anal 42:411–418

De Nolf W, Vanmeert F, Janssens K (2014) XRDUA: crystalline phase distribution maps by two-dimensional scanning and tomographic (micro) X-ray power diffraction. J Appl Crystallogr 47:1107–1117

De Vos D (1994) Hans Memling. Het volledige oeuvre. Mercatorfonds, Antwerpen

Farmer V (1974) The layer silicates. In: Farmer V (ed) The infrared spectra of minerals. Mineralogical society monograph, vol 4. Mineralogical Society of Great Britain and Ireland, London, pp 331–363

Fransen B (2018) Hans Memling's Nájera altarpiece: new documentary evidence, The Burlington Magazine. Feb 2018. CLX 101–105

Garty J, Kunin P, Delarea J et al (2002) Calcium oxalate and sulphate-containing structures on the thallial surface of the lichen Ramalina lacera: response to polluted air and simulated acid rain. Plant Cell Environ 25:1591–1604

Gianoncelli A, Castaing J, Ortega L et al (2008) A portable instrument for *in situ* determination of the chemical and phase compositions of cultural heritage objects. X-Ray Spectrom 37:418–123 Gómara E (2013) Las tablas Najerinas del Muro de Amberes. Arte e Historia 21:16–19

Higgitt C, White R (2005) Analyses of paint media: new studies of Italian paintings of the fifteenth and sixteenth centuries. Natl Gallery Tech Bull 26:88–97

Janssens K, Legrand S, Van der Snickt G et al (2016) Virtual archaeology of altered paintings: multiscale chemical imaging tools. Elements 12:39–44

Kahrim K, Daveri A, Rocchi P et al (2009) The application of *in situ* mid FTIR fibre-optic reflectance spectroscopy and GC-MS analysis to monitor and evaluate painting cleaning. Spectrochim Acta A 74:1182–1188

Kontozova-Deutsch V, Cardell C, Urosevic M et al (2011) Characterization of indoor and outdoor atmospheric pollutants impacting architectural monuments: the case of San Jerónimo Monastery (Granada, Spain). Environ Earth Sci 63:1433–1445

Lazzarini L, Salvadori O (1989) A reassessment of the formation of the patina called 'scialbatura'. Stud Conserv 34:20–26

Legrand S, Alfeld M, Vanmeert F et al (2014) Macroscopic Fourier transform infrared scanning in reflection mode (MA-rFTIR), a new tool for chemical imaging of cultural heritage artefacts in the mid-infrared range. Analyst 139:2489–2498

Leroy C (2016) Oxalates de calcium et hydroxyapatite: des matériaux synthétiques et naturels étudiés par techniques RMN et DNP. PhD thesis in Chemistry, Université Pierre et Marie Curie, Paris. https://tel.archives-ouvertes.fr/tel-01443727. Accessed Feb 2017

Matteini M, Moles A, Lanterna G et al (2002) Characteristics of the materials and techniques. In: Ciatti M, Seidel M (eds) Giotto. The crucifix in Santa Maria Novella. Edifir, Florence, pp 387–403

Mendes N, Lofrumento C, Migliori A et al (2008) Micro-Raman and particle-induced X-ray emission spectroscopy for the study of pigments and degradation products present in 17th century coloured maps. J Raman Spectrosc 39:289–229

Miliani C, Rosi F, Sgamellotti A et al (2010) *In situ* non-invasive study of artworks: the MOLAB multitechnique approach. Acc Chem Res 43:728–738

Monico L, Rosi F, Miliani C et al (2013) Non-invasive identification of metal-oxalate complexes on polychrome artwork surfaces In reflection mid-infrared spectroscopy. Spectrochim Acta A 116:270–280

Noble P, Van Loon A (2007) Rembrandt's Simeon's song of praise, 1631: pictorial devices in the service of spatial illusion. Art Matters 4:19–35

Potgieter-Vermaak S, Godoia R, Van Grieken R et al (2005) Micro-structural characterization of black-crust and laser cleaning of building stones by micro-Raman and SEM techniques. Spectrochim Acta A 61:2460–2467

Rampazzi L, Andreotti A, Bonaduce I et al (2004) Analytical investigation of calcium oxalate films on marble monuments. Talanta 63:967–977

Salvadó N, Butí S, Nicholson J et al (2009) Identification of reaction compounds in micrometric layers from gothic paintings using combined SR-XRD and SR-FTIR. Talanta 79:419–428

Salvadó N, Butí S, Cotte M et al (2013) Shades of green in 15th century paintings: combined microanalysis of the materials using synchrotron radiation XRD, FTIR and XRF. Appl Phys A 111:47–57

Solé V, Papillon E, Cotte M et al (2007) A multiplatform code for the analysis of energy-dispersive X-ray fluorescence spectra. Spectrochim Acta B 62:63–68

Spring M, Higgitt C (2006) Analyses reconsidered: the importance of the pigment content of paint in the interpretation of the results of examination of binding media. In: Nadolny J (ed) Medieval paintings in northern Europe: techniques, analysis, art history. Studies in commemoration of the 70th birthday of Unn Plahter. Archetype, London, pp 223–229

Van der Snickt G, Miliani C, Janssens K et al (2011) Material analyses of '*Christ with singing and music-making Angels*', a late 15th-C panel painting attributed to Hans Memling and assistants: Part I. non-invasive *in situ* investigations. J Anal At Spectrom 26:2216–2229

Van der Snickt G, Janssens K, Dik J et al (2012) Combined use of synchrotron radiation based micro-X-ray fluorescence, micro-X-ray diffraction, micro-X-ray absorption near-edge, and micro-Fourier transform infrared Spectroscopies for revealing an alternative degradation pathway of the pigment cadmium yellow in a painting by Van Gogh. Anal Chem 84:10221– 10228

Van Grieken R, Gysels K, Hoornaert S et al (2000) Characterization of individual aerosol particles for atmospheric and cultural heritage studies. Water Air Soil Pollut 123:215–228

Van Loon A (2008) Color changes and chemical reactivity in seventeenth-century oil paintings. Dissertation, University of Amsterdam. MOLART Reports, vol. 14
Vandenbroeck P (1985) Catalogus schilderijen 14e en 15e eeuw. Ministerie van de Vlaamse Gemeenschap/Koninklijk Museum voor Schone Kunsten, Antwerpen, pp 138– 143

Zoppi A, Lofrumento C, Mendes N et al (2010) Metal oxalates in paints: A Raman investigation on the relative reactivities of different pigments to oxalic acid solutions. Anal Bioanal Chem 397:841–849

4.3 Large-Area Elemental Imaging Reveals Van Eyck's Original Paint Layers on the *Ghent Altarpiece* (1432), Rescoping Its Conservation Treatment

Adapted from: G. Van der Snickt, H. Dubois, J. Sanyova, S. Legrand, A. Coudray, C. Glaude, M. Postec, P. Van Espen, K. Janssens, "Large-Area Elemental Imaging Reveals Van Eyck's Original Paint Layers on the *Ghent Altarpiece* (1432), Rescoping Its Conservation Treatment", *Angew Chem Int Ed Engl,* 56 (17), **2017**, 4797-4801, 10.1002/anie.201700707.

Abstract: A combination of large-scale and micro-scale elemental imaging, yielding elemental distribution maps obtained by, respectively non-invasive macroscopic X-ray fluorescence (MA-XRF) and by secondary electron microscopy/energy dispersive X-ray analysis (SEM-EDX) and synchrotron radiation-based micro-XRF (SR µ-XRF) imaging was employed to reorient and optimize the conservation strategy of van Eyck's renowned *Ghent Altarpiece*. By exploiting the penetrative properties of X-rays together with the elemental specificity offered by XRF, it was possible to visualize the original paint layers by van Eyck hidden below the overpainted surface and to simultaneously assess their condition. The distribution of the high-energy Pb-L and Hg-L emission lines revealed the exact location of hidden paint losses, while Fe-K maps demonstrated how and where these lacunae were filled-up using an iron-containing material. The chemical maps nourished the scholarly debate on the overpaint removal with objective, chemical arguments, leading to the decision to remove all skillfully applied overpaints, hitherto interpreted as work by van Eyck. MA-XRF was also employed for monitoring the removal of the overpaint during the treatment phase. To gather complementary information on the in-depth layer build-up, SEM-EDX and SR µ-XRF imaging was used on paint cross sections to record microscale elemental maps.

4.3.1 Introduction

 Several methods for obtaining information about the distribution of pigments and other chemical constituents of artworks have been developed;[1] such methods are necessarily non-invasive and employ radiation in the infrared, visible, ultraviolet or X-ray range. Traditionally, the spectroscopic characterization of artworks was done on a point-by-point basis, an approach that has inherent limitations with respect to representativeness. The recent transformation of spectroscopic instrumentation into mobile scanning systems[2–5] that allow the examination of all locations on the surface of (flat) artworks, proved to have a significant added-value for the study of cultural heritage objects. These forms of (spectro)chemical imaging allow the consideration of large and complex spectroscopic datasets as (hyperspectral) image stacks that are (more) easily understandable by non-chemists such as art conservators and art historians than extensive series of spectral data derived from individual points.
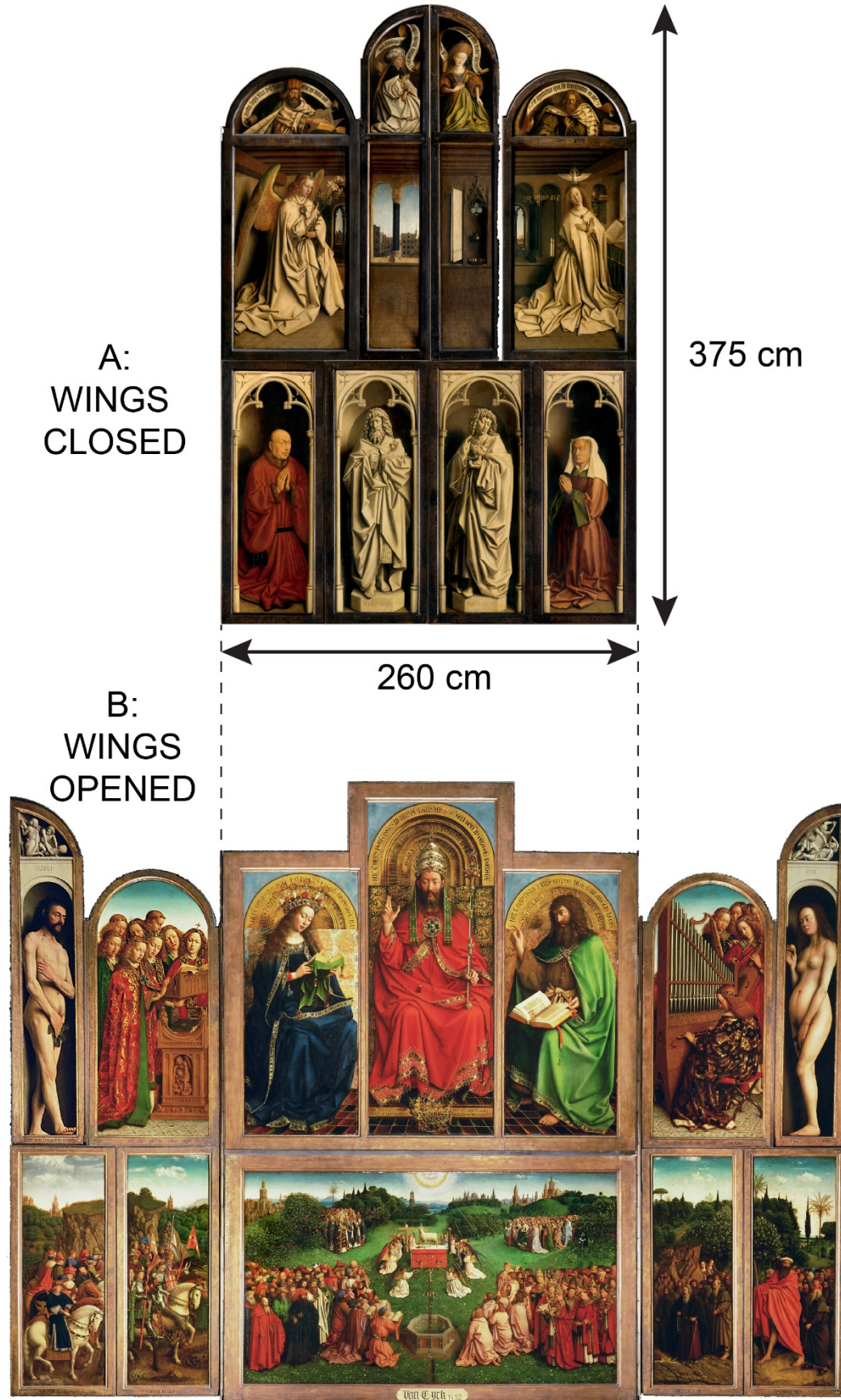
A:
WINGS
CLOSED

375 cm

260 cm

B:
WINGS
OPENED

*Figure 1: The Ghent Altarpiece by the van Eyck brothers (Cathedral of Saint Bavo, Ghent, Belgium) in **A)** closed position and **B)** opened position. The verso side of the wing panels (A), was imaged by means of MA-XRF scanning.*

Whereas subtle point-to-point variations in the spectral response may be hard to notice and even more difficult to interpret correctly, gradual compositional variations that become apparent in large-scale chemical or elemental maps are usually much easier to link to (in)visible features of the paint surface and/or its conservation state.

Since its introduction by Alfeld et al.,[2] mobile MA-XRF scanning has met with considerable attention and success, for example, by supplying new and pivotal arguments for authentication of high-profile works of art in cases in which more conventional analytical and/or imaging techniques led only to ambiguous information.[6–8]

The vast retable by the van Eyck brothers, shown in figure 1, finished in 1432, is considered by many to be the pinnacle of European mediaeval painting, attracting up to 200 000 visitors per year.[9] Chemical imaging of the entire altarpiece was considered to be particularly challenging in view of its large surface and the corresponding wealth of spectral data. Up to now, compositional information was collected from the verso side of the eight wing panels shown in figure 1A. This painted surface, measuring circa 8 m^2 was divided into 37 separate scan areas (see the Supporting Information, figure S1). More than 16 million XRF spectra were collected. In this manner, a large (>1 GB) hyperspectral XRF data cube was obtained per panel. Next to the lengthy data collection, an additional challenge was the time-efficient and artefact-free processing of the data set. The set of wooden support beams (from the cradle) attached to the backside of the thin wooden panels gave rise to a strong pixel-to-pixel fluctuation of the spectral background. By adapting existing deconvolution software (AXIL),[10] a robust and time-efficient combination of background subtraction and net X-ray line intensity determination could be realized.[11]

The sum XRF spectrum in figure 2C of one of the panels illustrates the various spectral overlaps that are caused by the many characteristic lines emitted by the elements in the paint layer stack. These can be associated with the inorganic painting materials employed by the artist(s), including Pb (lead white), Hg (vermilion red), Ca (mainly chalk or gypsum), K (alum, red dye substrate), Fe (earth pigments), and Cu (azurite or verdigris). Next to these major peaks, weaker emission lines of Mn and Zn are present, both associated with the shadow areas of the folds of Vyds cloak.
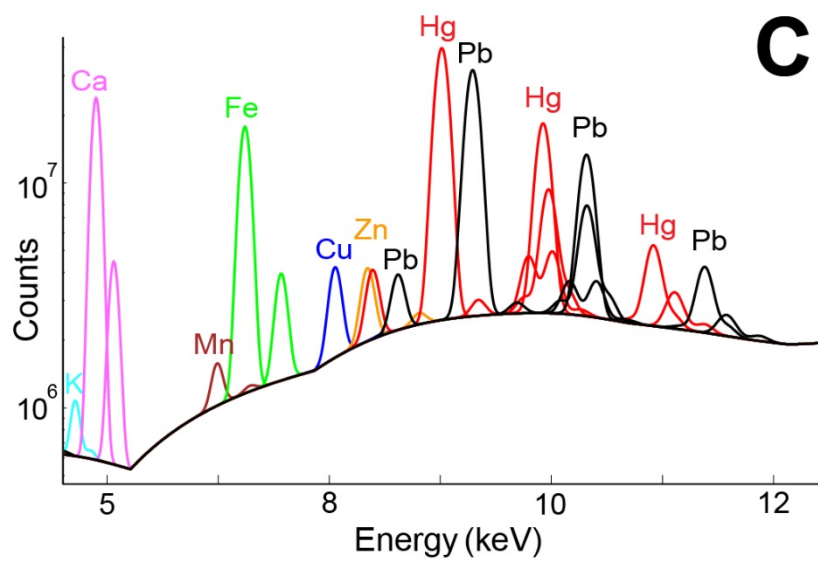
*Figure 2: **A**) Donor portrait of Joos Vyd. **B**) Corresponding composite elemental image showing the distribution of Hg (red), Fe (green) and Pb (white). **C**) MA-XRF sum spectrum of circa two million spectra recorded on this panel with indication of the subtracted background and the fit model used, illustrating the overlapping emission lines from the various artists' materials.*

The distribution images of the heavier elements (with atomic number ≥26, Fe) proved to be very informative regarding the presence and state of conservation of the hidden paint layers. Since the XRF emission associated with these elements (having energies >6 keV) is able to readily penetrate the upper paint layers, the structure of the underlying strata could be observed without great difficulty. The composite elemental map in figure 2B shows extensive damage in some parts of the red coat of Joos Vyd, the donor (sponsor) of the altarpiece. In a visually pristine area, that is, in the rightmost folds of the lower part of the coat rendered with vermilion red (HgS), numerous discrete paint losses become visible. The latter can be clearly observed in the Fe-K and Hg-L XRF maps of figure 2B and figure S5 (Supporting Information) because the gaps in the original red paint (corresponding to a lower Hg-L intensity) were filled up with a reddish Fe-containing paste (green spots in figure 2B) before they were covered with a thin layer of red HgS paint (see the Supporting Information, figure S2) to hide them from view. The filling material, present in 10.4% of the total red area of the coat, was a reddish paste, colored with hematite (Fe_2O_3). Moreover, the Hg-L and Pb-L maps revealed additional highlights and sharper forms than those that were visible to the naked eye. The former were considered by van Eyck scholars to be more typical for the painting style of the master than the forms rendered in the upper, visible stratum. The MA-XRF maps therefore supported and strengthened the conclusion of the conservators that the panels were largely overpainted during a previous intervention. The extent of overpainting was never suspected during earlier conservation campaigns;[12] thus, for centuries, scholars attributed the visible brushwork to the van Eyck brothers, while in reality, the original Eyckian forms and rendering were hidden from sight by less sophisticated overpaint. A similar pattern as in figure 2B could be discerned in several of the other panels that were examined.

Figure 3 and figure S3 (see the Supporting Information) show MA-XRF maps recorded from the panel of Elisabeth Borluut, wife of Joos Vyd. The red dress of Borluut does not derive its color from an inorganic (opaque) pigment such as vermilion or hematite. The burgundy shade, the translucency, and the deep saturation are indicative of a (semi-transparent) organic red dye. Alum, the inorganic substrate on which the dyestuff was precipitated ($KAl(SO_4)_2 \cdot 12H_2O$) is observed in the potassium MA-XRF (figure S3) and SEM-EDX distribution images (figure 4C).
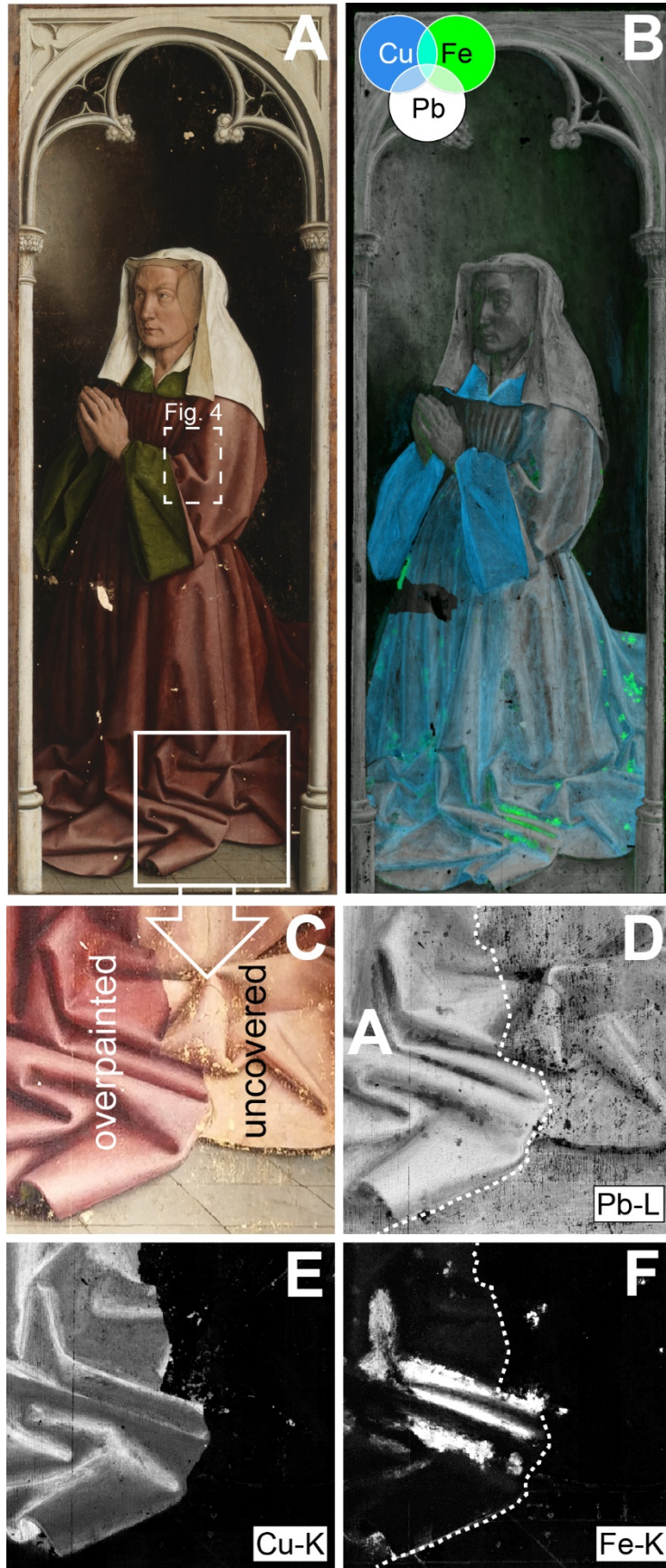
*Figure 3: **A**) Donor portrait of Elisabeth Borluut. The white rectangle indicates the location of the detail maps shown in (C–F). **B**) Composite elemental image showing the distribution of copper (blue), iron (green), and lead (white). **C**) Detail of the paint surface when the removal of the overpaint was halfway. The interface between the original composition and the darker overpaint is clearly visible and reflected in the corresponding **D**) lead, **E**) copper, and **F**) iron distributions. The dashed line in (D) and (F) indicates this treatment.*

The green lining of the sleeves of the dress were rendered with a Cu-containing pigment such as verdigris or a derivative copper-organo complex. Yet, the red parts of the dress also contain Cu.

In the high-resolution scan of the zone indicated in figure 4A, well-defined dark areas can be observed in the Pb-L map, clearly revealing a number of significant paint losses in the underlying paint system. Also in this panel, the cavities were first filled with an iron-containing material (Fe-K maps in figure 4A and figure S3) before an additional layer of paint was superimposed on van Eyck's composition. The Fe-rich patches correspond to 11.4% of the total red area of the dress. The cross section in figure 4B establishes that the overpaint (layer nr. 4), besides containing a red dye similar to that employed by van Eyck, also contains Cu-rich grains (see Cu map in figure 4C). In Early Netherlandish painting, azurite blue ($2CuCO_3 \cdot Cu(OH)_2$) was often added to red dye paint to obtain a purplish hue.[13] While the overall Cu-K map (figure 3B and figure S3), collected prior to removal of the overpaint layer, shows that Cu is present throughout the entire dress, in the detailed Cu map of figure 4A, the concealed paint losses are not visible. This indicates that the detected Cu is exclusively present in the upper layer and therefore not part of the original van Eyck paint. As azurite was progressively abandoned after the invention of Prussian blue in 1704,[14] the presence of this basic copper(II) carbonate in the overpaint suggests, together with other indications, that this intervention pre-dates at least the 18th century.

The evidence gathered by the macroscopic and microscopic elemental mapping described above, strengthened both the conservators and the members of the supervising International Advisory Board in their opinion that the non-Eyckian overpaint should be removed from the outer panels, to the extent this could be carried out without damaging the original composition. The macroscopic elemental images allowed for the first time the quantitative estimation of the percentage of the area of the underlying original paint that was still intact. After a careful deliberation, this lead to the joint decision of all stakeholders involved to uncover the original, Eyckian paint layers that had been obscured from view for several centuries.

When this process was at the halfway mark, MA-XRF maps were again recorded from selected areas (figures 3D–F and the Supporting Information, figures S4 and S6) to verify the interpretation of the previous scans. The treatment front is clearly discernible in the Cu-K map of figure 3E and figure S4; the fact that the Cu-K signal has dropped to virtually zero in the uncovered areas shows that all the azurite-containing overpaint on Elisabeth Borluut's robe was removed. After the overpaint removal, reddish fillings surfaced in the

original paint layer exactly at the locations anticipated by the non-invasive scanning and the Fe-K distribution.
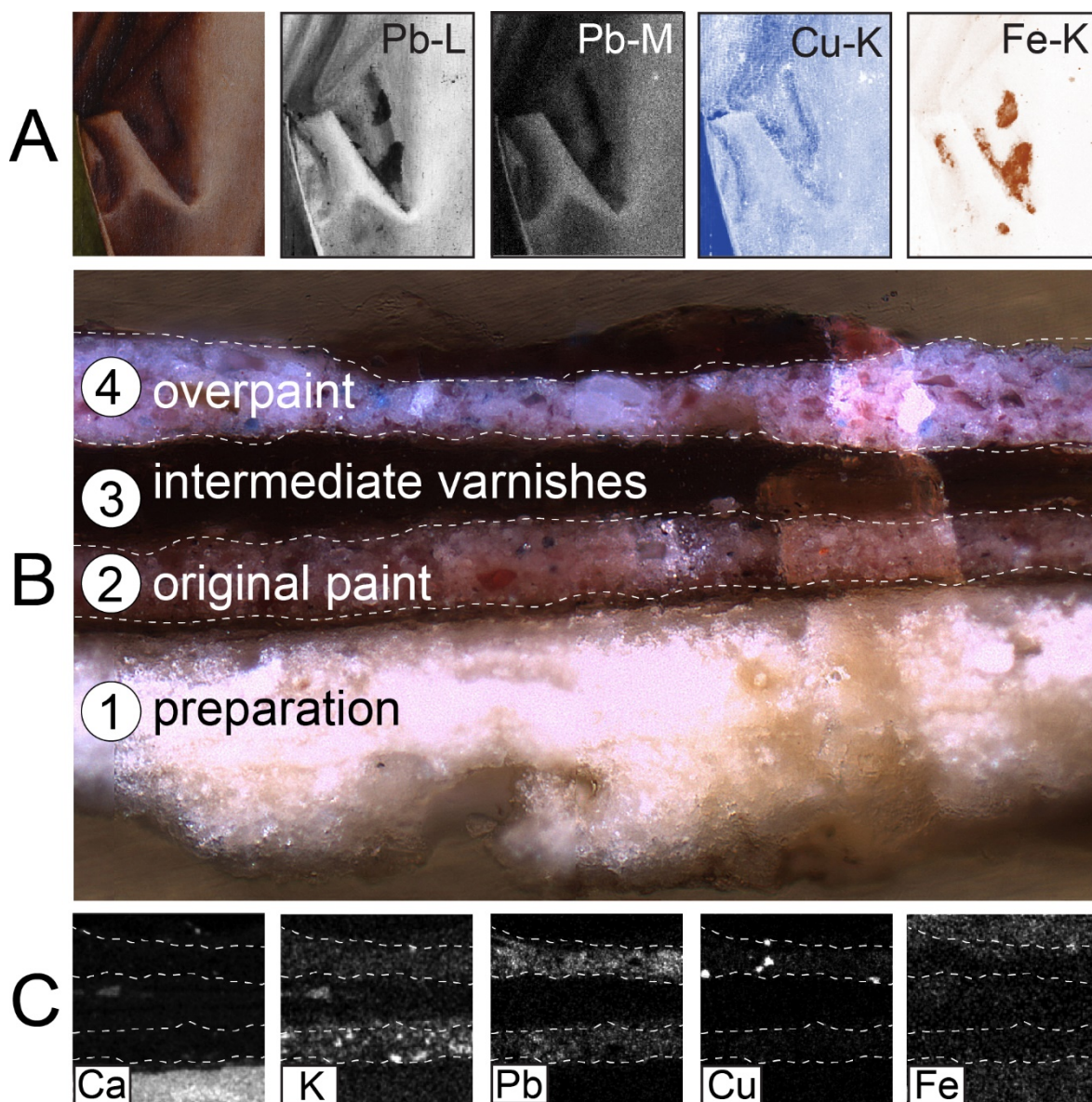
Figure 4: **A)** High resolution MA-XRF maps recorded on a visually pristine area on Borluut's dress (see figure 3), revealing an underlying, lead containing paint layer with paint losses (Pb-L map), first filled with an Fe-rich material (Fe-K map) and subsequently overpainted with a Cu- and Pb-containing paint (Cu-K, Pb-M maps). **B)** Optical micrograph of a paint sample extracted from the area shown in (A), adjacent to a paint loss/filling area, revealing a bipartite paint system on top of the preparation, with both paint layers separated by intermediate varnish layers and non-original glazes (older restorations); **C)** SEM-EDX maps collected from the paint cross-section, showing the elemental depth distribution at this location.

On the other hand, the Pb-L maps in figure 3 and figure S4 demonstrate the limitations of the elemental "see-through" imaging technique; namely, that after overpaint removal, numerous minute paint losses became visible that could not be discerned before, because they were masked by Pb-containing overpaint.

4.3.2 Conclusion

In conclusion, in this study we have shown how elemental mapping by MA-XRF of the outer panels of the *Ghent Altarpiece* was used to objectively underpin the conservators assertion that extensive overpainting was present. At the same time, the chemical maps demonstrated in a quantitatively reliable manner that van Eyck's worn, overpainted composition was in sufficiently good condition to justify full removal of the non-original layer(s). The MA-XRF results enriched the intensive scholarly debate with unbiased chemical arguments in the form of easily interpretable images and helped to clarify its conclusions. The non-invasive macro-imaging data had a significant impact on the conservation procedure, as the decision to remove all overpaint added two additional years to the treatment procedure and lead to a considerable increase in the project budget. After careful deliberation, a decision to uncover the original work of van Eyck by removing all non-Eyckian paint was arrived at. This process finally brought the original Eyckian paint layers back to the surface throughout the verso side of the wing panels. The authors expect that integral chemical imaging of paintings by MA-XRF and/or other means will soon become a standard procedure during major restorations of painted artworks. As objectification of decisions, elaborate documentation, and public motivation of treatments become increasingly important in modern conservation, so does detailed elemental/chemical imaging of the artworks before, during, and after the conservation treatments.[15] Future efforts will focus on reducing the total required MA-XRF scanning time by enhancing the sensitivity of the analyzer and by implementing complimentary imaging techniques in the same setup (for example, based on the reflectance of visible and infrared radiation) with the aim of corroborating the deduced paint layer sequence versus depth and collecting information on organic paint components.[16]

References
1.   K. Janssens, S. Legrand, G. Van der Snickt, F. Vanmeert, Elements 2016, 12, 39–44.

2.	M. Alfeld, K. Janssens, J. Dik, W. De Nolf, G. Van der Snickt, J. Anal. At. Spectrom. 2011, 26, 899–909.

3.	K. A. Dooley, D. M. Conover, L. Deming Glinsman, Angew. Chem. Int. Ed. 2014, 53, 13775–13779; Angew. Chem. 2014, 126, 13995–13999.

4.	S. Legrand, M. Alfeld, F. Vanmeert, W. De Nolf, K. Janssens, Analyst 2014, 139, 2489–2498.

5.	F. Rosi, C. Miliani, R. Braun, R. Harig, D. Sali, B. G. Brunetti, A. Sgamellotti, Angew. Chem. Int. Ed. 2013, 52, 1–5; Angew. Chem. 2013, 125, 1–1.

6.	M. Alfeld, G. Van der Snickt, F. Vanmeert, K. Janssens, J. Dik, K. Appel, L. van der Loeff, M. Chavannes, T. Meedendorp, E. Hendriks, Appl. Phys. A 2013, 111, 165–175.

7.	K. Janssens, G. Van Der Snickt, M. Alfeld, P. Noble, A. van Loon, J. Delaney, D. Conover, J. Zeibel, J. Dik, Microchem. J. 2016, 126, 515–523.

8.	M. Alfeld, J. A. C. Broekaert, Spectrochim. Acta Part B 2013, 88, 211–230.

9.	S. Nash, Northern Renaissance Art. Oxford History of Art, Oxford University Press, Oxford, 2008.

10.	P. Van Espen, K. Janssens, J. Nobels, Chemom. Intell. Lab. Syst. 1986, 1, 109–114.

11.	M. Alfeld, K. Janssens, J. Anal. At. Spectrom. 2015, 30, 777–789.

12.	P. Coremans, L'Agneau mystique au Laboratoire. Contributions l'étude des Primitifs flamands, 2, Sikkel, Antwerp, 1953.

13.	G. Van der Snickt, C. Miliani, K. Janssens, B. G. Brunetti, A. Romani, F. Rosi, P. Walter, J. Castaing, W. De Nolf, L. Klaassen, I. Labarque, R. Wittermann, J. Anal. At. Spectrom. 2011, 26, 2216–2229.

14.	N. Eastaugh, V. Walsh, T. Chaplin, R. Siddall, Pigment Compendium, Butterworth-Heinemann, Oxford, 2008.

15.	P. Dredge, S. Ives, D. L. Howard, K. M. Spiers, A. Yip, S. Kenderdine, Appl. Phys. A 2015, 121, 789–800.

16.	K. A. Dooley, A. Kathryn, S. Lomax, J. G. Zeibel, C. Miliani, P. Ricciardi, A. Hoenigswald, M. Loew, J. K. Delaney, Analyst 2013, 138, 1364–5528.

4.3.3 Supporting Information

4.3.3.1 *Experimental Section*

4.3.3.1.1 MA-XRF scanning

The verso panels of the *Ghent altarpiece* were analysed in reflection mode by means of a MA-XRF scanning instrument (Fig. S1) developed within the AXES group of the University of Antwerp. This in-house device is an optimised variant of the setup described by Alfeld et al.[1] In particular, the instrument was improved by adjusting the path of the fluorescence signal to the detector. Decreasing the path between the detector and the sample reduced attenuation of the fluorescence signal by ambient air. This intervention enhances count rates significantly for emission lines of low energy (e.g. K-K or Ca-K). The detector geometry was adjusted by enlarging the take-off angle. The latter improves the information depth as the travel path of fluorescence signal through the sample material is shortened.

The measurement head consists of a compact 10W Rh anode transmission tube (Moxtek, UT, USA) operated at 45 kV and 200 μA and a Vortex EX-90 SDD (SII, Northridge, CA, USA) detector with a 50 mm² active area positioned close to the incident X-ray beam. The diameter of the diverging primary beam is reduced by means of a 0.8-mm lead pinhole collimator. The XRF measurement head is mounted on software controlled X-Y motor stage with an ESP 301 3-Axis Motion Controller (Newport Corporation, Irvine, CA, USA) with a maximum travel range of 57 x 60 cm² (h x v). MA-XRF scans are performed by sweeping the measuring head systematically over the paint surface. Careful positioning and alignment of the scanner ensures a stable distance of ca. 1.5 cm in between the snout and the panel. Alignment was obtained by manually adjusting the distance between the X motor stage and the paint surface while moving the measuring head along the X-axis. To do so, the position of the X-motor on the table top was adjusted while painting and easel remained immobile. During the movement, XRF spectra are recorded every 700 μm (step size) with a dwell time of 200 ms (real time) for each spectrum, using a DXP-XMAP multi-channel analyser (XIA LLC, Hayward, CA, USA).

The resulting spectral data cube was processed through an optimised version of the AXIL software package[2]. The AXIL spectral deconvolution software was found capable of rapid data handling when the profiles of the spectral peaks and the background shape were first defined on the basis of a sum spectrum; this allows to fix a number of the non-linear parameters in the fitting model. The linear parameters of the fit were the only ones remaining free during the subsequent least-squares batch fitting process[2]. Although this approach permits large hyperspectral data cubes to be processed in a time-efficient manner, disturbing artefacts can emerge in the resulting distribution images when strong fluctuations of the spectral background are encountered. In the present case, this was indeed the case, the cause being the supporting latticework, attached to the backside of the wooden panels that gave rise to significant variations of the spectral background intensity, caused by scattering of the primary radiation. This complication was addressed by adapting the existing AXIL deconvolution software in such a way that the background was first subtracted from all spectra before performing a swift linear fit.

As the panel dimensions exceeded the travel range of the motors, each scene was divided into overlapping scan areas as indicated in Fig S1. After spectral deconvolution, for each panel, the separate elemental distribution images were seamlessly compiled by means of the Datamuncher software, hereby removing geometric and intensity mismatches caused by slight variations of the position of the scan plane relative to the panel surface.[3] For practical reasons, the scans were spread over a fairly long time period, comprising four scan campaigns between March 2014 and May 2015. In this way, the total painted surface of the verso panels measuring over 8 m² was analysed in 60 working days, making it the largest polychromed surface that was entirely scanned by means of MA-XRF so far.

*Figure S1: **Left**: the panel with the donor portrait of Joos Vyd during MA-XRF scanning in the conservation studio. **Right**: The closed retable showing the verso sides of the panels. The dashed white rectangles illustrate how the painted surface was divided into 37 areas for scanning.*

4.3.3.1.2 **SEM-EDX analysis**

A number of samples, dating from the previous conservation treatment in 1950-1951, still available in the laboratory archive of KIK-IRPA, were re-examined during the present campaign. A number of new samples also had to be taken to understand fully the layer buildup of both original and overpaint. The multi-layered paint samples were embedded in resin and cross-sectioned to allow for a detailed study of the layer sequence (stratigraphy) and its composition. The polished cross-sections were first observed with an AxioImager stereomicroscope (Carl Zeiss, Germany) in polarized and UV light and subsequently analysed by means of a JEOL JSM6300 SEM equipped with an Oxford-Link Pentafet Si(Li) energy-dispersive X-ray spectrometer (EDX) and BSE detector (Tetra Link). The EDX-analyses were run at an acceleration voltage at 15 kV after gold sputter-coating of the cross-sections. Analytical results were correlated with the optical images and the MA-XRF elemental distribution images, permitting a more accurate interpretation of the macroscopic elemental maps.

4.3.3.1.3 Synchrotron Radiation based μ-XRF (SR μ-XRF) imaging

A selection of paint micro-samples was investigated at beamline ID21 of the European Synchrotron Radiation Facility (ESRF, Grenoble) by means of μ-XRF imaging. A highly monochromatic primary beam (with $\Delta E/E$ = 10-4) of 7.2 keV was produced using a Si(220) fixed-exit double crystal monochromator. For the paint cross-section shown in Fig. S2, the incident beam was focused with Fresnel zone plates down to 0.8 × 0.3 μm² (h × v). XRF signals were collected in the horizontal plane and at 69° relative to the incident beam by means of a single energy-dispersive silicon drift detector (Xflash 5100, Bruker). μ-XRF experiments were performed in vacuum in order to minimize air absorption. Two-dimensional μ-XRF maps were obtained via raster scanning of the samples using a focused X-ray beam and with 300 ms/pixel dwell times. The PyMca software package was used in batch fitting mode to deconvolute the X-ray fluorescence spectra and to separate the different elemental contributions in the spectrum corresponding to each pixel of the two-dimensional (2D) maps. Both the setup[4] and the XRF spectrum evaluation[5] procedure are discussed more in detail elsewhere.

4.3.3.2 *Supplementary data*

4.3.3.2.1 SR μ-XRF imaging

As discussed in the main part of the paper, interpretation of the non-destructive MA-XRF images indicated a bipartite paint system on the panels. SEM-EDX measurements on a cross-section from the dress of Elisabeth Borluut confirmed the presence of an (original) paint stratum underneath the visible paint, both separated by several varnishes and a thin, even older restoration layer. This bipartite paint system is again encountered in Fig. S2 during SR μ-XRF imaging on a micro-sample extracted from the other donor portrait (Joos Vyd). In the red dress area, two vermillion-based paint layers (see Fig. S2C) are present, separated by varnishes that fluoresce under UV light (see Fig. S2B). In this case no intermediary restorations are present. Interestingly, the first paint layer by Van Eyck and the intermediate varnishes contain jagged particles rich in Si, K, Ca and/or Mn. These might be due to the addition of powdered calco-potassic glass to the paint with the aim to assist its drying and/or to improve its transparency, a practice in Early-Netherlandish painting that was reported earlier by Spring et al.[6]
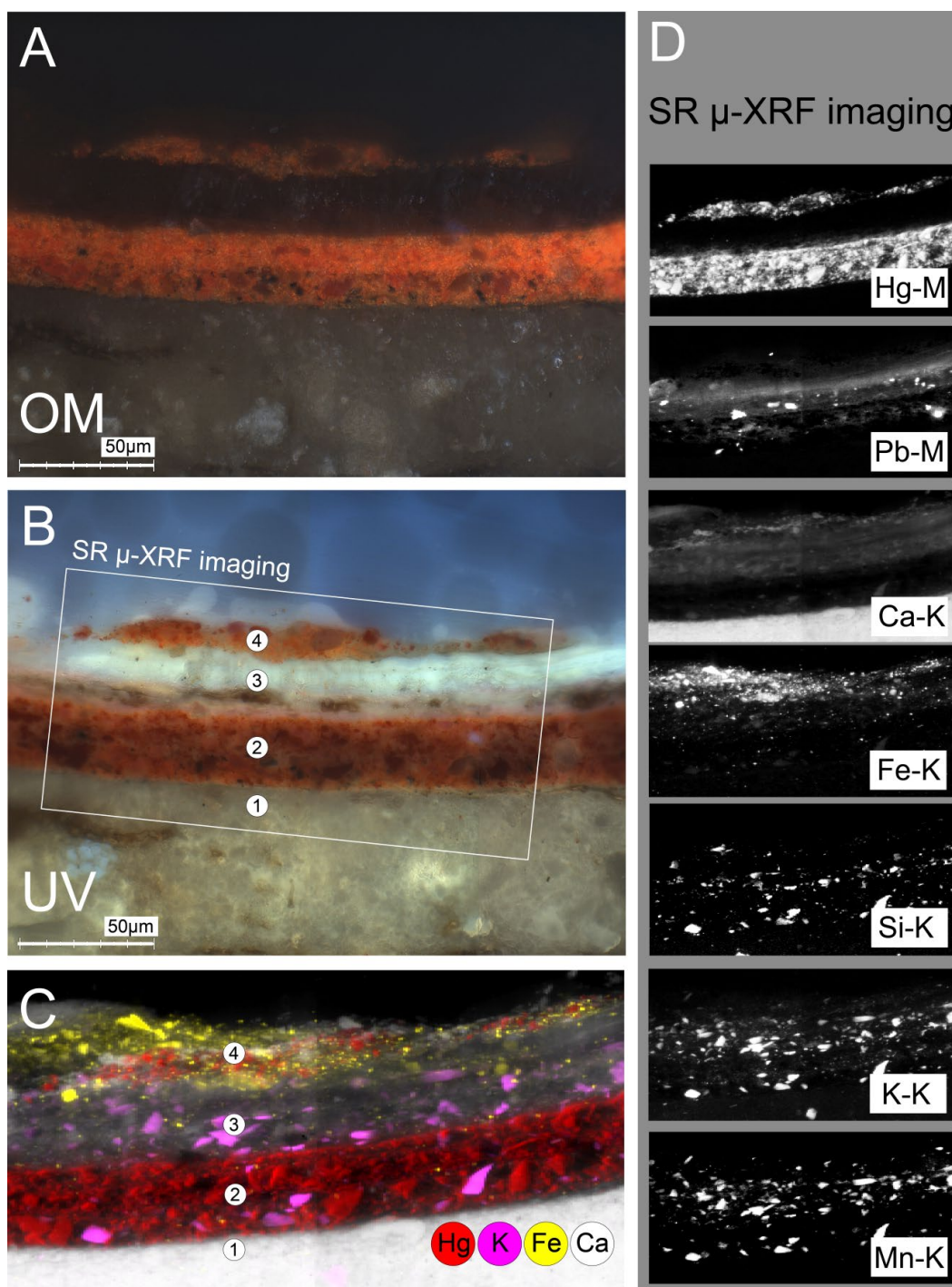
Figure S2: *A: Optical micrograph of a paint cross-section extracted from the red garment of Joos Vyd (see Fig. S1). B: Optical micrograph of the sample shown in A under UV light, revealing a bipartite system with two red paint layers (nrs. 2 and 4) separated by a (fluorescing) varnish layer (nr. 3), on top of a chalk ground (nr. 1). C: Composite elemental distribution map of the sample area shown in A and B, collected by means of SR µ-XRF imaging at the ID21 beam line (ESRF) showing the distribution of mercury (in red), potassium (in pink), iron (in yellow), calcium (in white). D: Separate SR µ-XRF elemental distribution maps of Hg-M, Pb-M, Ca-K, Fe-K, Si-K, K-K and Mn-K. Map size 200 × 100 µm^2 (h x v), step size 0.8 × 0.3 µm^2 (h x v), primary energy 7.2 keV. White: high X-ray intensity; black: low X-ray intensity.*

4.3.3.2.2 MA-XRF elemental distribution maps

The main paper features a selection of the MA-XRF maps recorded on the donor portraits that are relevant for the discussion. Figs S3 to S6 complete these images by showing the distribution of all elements that were identified.

Fig. S4 presents the more detailed MA-XRF images that were recorded when the overpaint removal on the Borluut panel was halfway. The visual image reveals a clear difference in colour between the uncovered and still overpainted areas. This contrast is equally reflected in the elemental distribution maps. The Pb-L maps shows that both the overpaint and the original paint layers contain lead. After removal, it becomes clear that the original paint displays numerous minute defects that previously could not be completely detected below the lead-containing overpaint that had been applied to hide them. The same defects show up in the Ca-K image as the paint losses expose the underlying chalk ground layer. The Cu-K signal gradually disappears as the cleaning procedure progresses, proving that the copper pigment is only present in the upper paint layer. The Fe-K map shows the iron fillings that were applied to fill the larger paint losses in the original paint prior to overpainting. At the same time, the Fe-K map gives evidence that these fillings were abundantly applied as the iron area exceeds the outline of the actual gaps as seen in the Pb-L map. The iron signal is mostly absent in the area on the right as conservators removed the fillings along with the overpaint during cleaning. Potassium is present both in the uncovered and overpainted areas. The source for K is most likely alum, a hydrated potassium aluminium sulphate that was commonly employed as inorganic substrate for precipitation of organic red dyes.

In the report of the International Expert Commission accompanying the Restoration of the *Ghent Altarpiece* of March 14, 2015, the experts recommended removing the overpaint following research including MA-XRF. Their report states the following: "The International Committee recommends that while the remaining conservation work on the exterior panels continues and is brought to completion, additional investigation of the interior panels be carried out simultaneously. In this new study the existing paint samples should be re-examined and Macro-XRF of the interior panels undertaken. When interpreted in the light of the important new discoveries made during the first phase (conservation treatment of the exterior panels), the results will refine the team's understanding of what to expect next when undertaking treatment of the interior panels".[7]

*Figure S3: MA-XRF maps recorded from the donor portrait of Elisabeth Borluut (**top left**) showing the intensity distribution of the following X-ray emission lines: Pb-L, mostly correlated with the pigment lead white; Ca-K, mostly stemming from Ca-based fillings in paint losses, from bone black or from a chalk additive to the paint; Hg-L, correlated to vermillion; Zn-K, correlated with the red lake pigment in the original paint (in which Zn most probably was present as a drier); Fe-K, present in fillings of paint losses in the original paint; Cu-K, correlated with a green (verdigris) and blue copper (azurite) pigment; and K-K, associated with red lake. Arrows in Cu map indicate locations of "observation windows" where the upper layer of overpaint was already removed.*

Figure S4: Detailed MA-XRF maps recorded on the bottom part of Borluut's dress when the removal of the overpaint was halfway. Distribution of the Pb-L, Ca-K, Cu-K, Fe-K, K-K, Zn-K, Mn-K and Hg-L emission lines. The dashed line encircles the area where overpaint is still present.

*Figure S5: MA-XRF maps recorded on the donor portrait of Joos Vyd (**top left**) showing the intensity distribution of the Pb-L, Ca-K, Hg-L (**top row**), K-K, Fe-K, and Cu-K (**bottom row**) X-ray emission lines. The Hg-L map reveals a series of paint losses in the bottom right corner of the red dress, while the Fe-K map highlights the corresponding fillings, containing a reddish (hematite type) material. The fillings exceed the outlines of the paint losses (see Fe-K vs Hg-L maps). Zn, possibly associated with siccative additives, is present here in glazes in original layers and old restorations.*
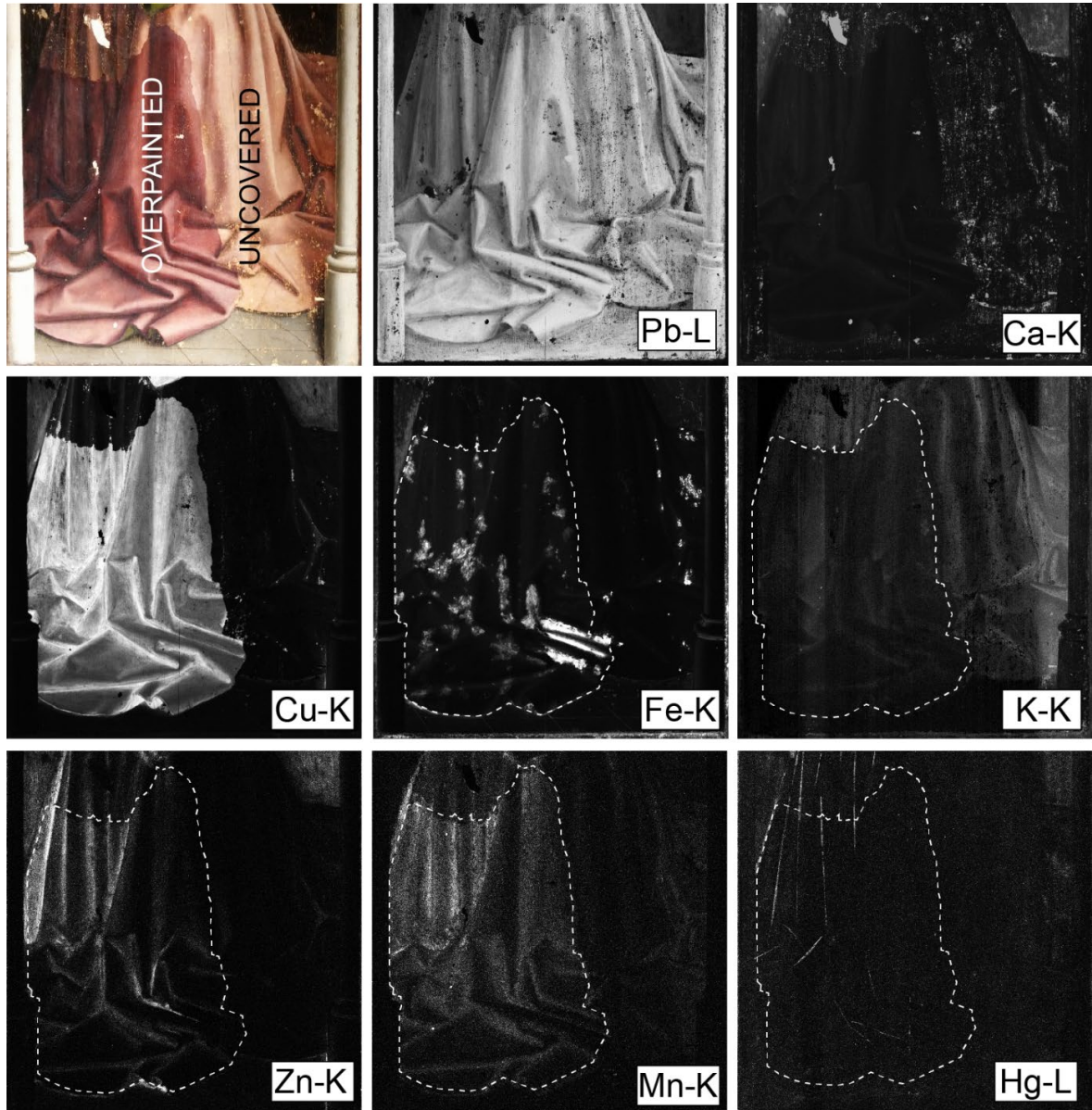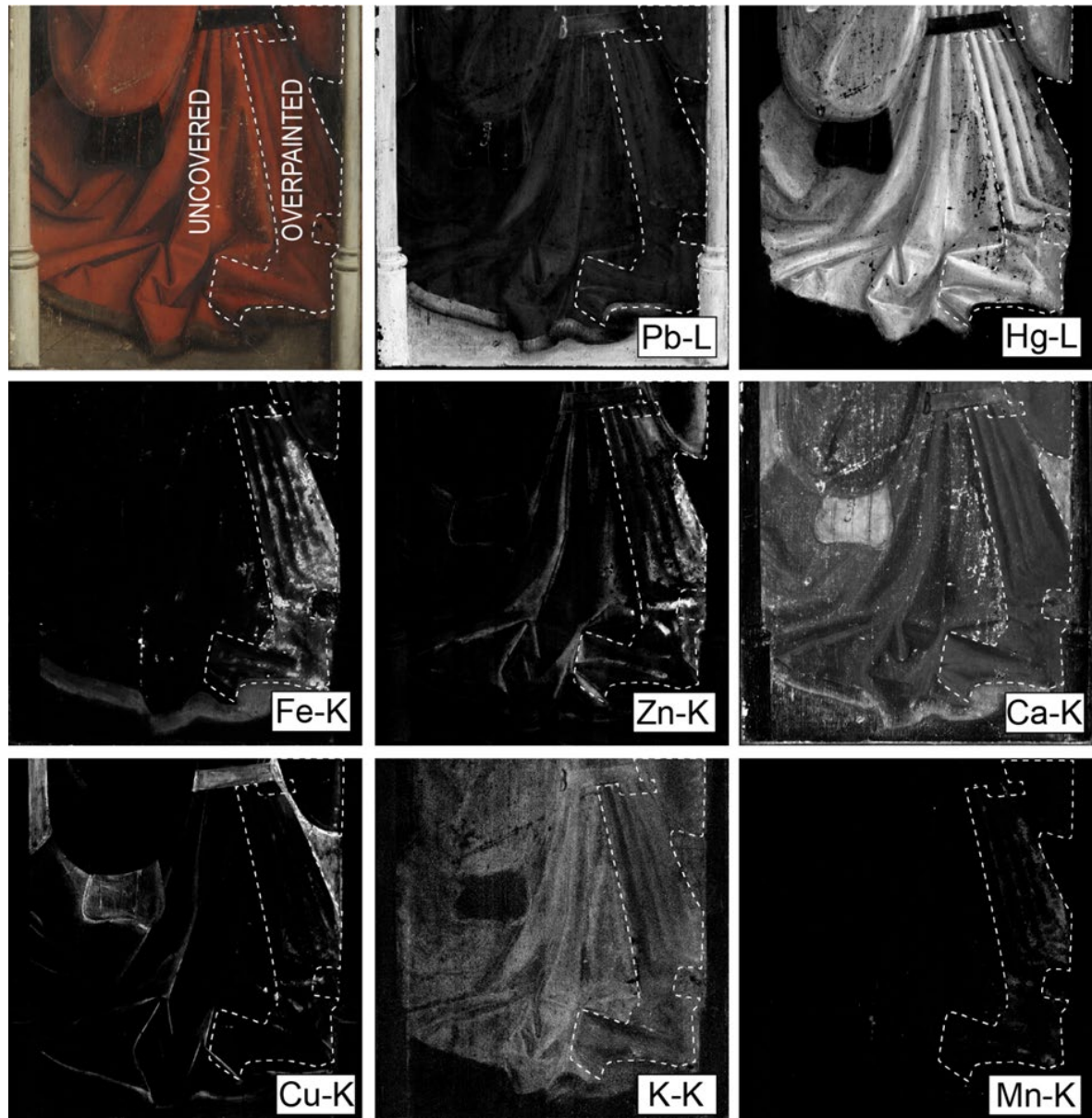
Figure S6: Detailed MA-XRF maps recorded on the bottom part of Vyd's dress when the removal of the overpaint was halfway. Distribution of the Pb-L, Hg-L, Fe-K, Zn-K, Ca-K, Cu-K, K-K and Mn-K emission lines. The dashed line encircles the area where overpaint is still present.
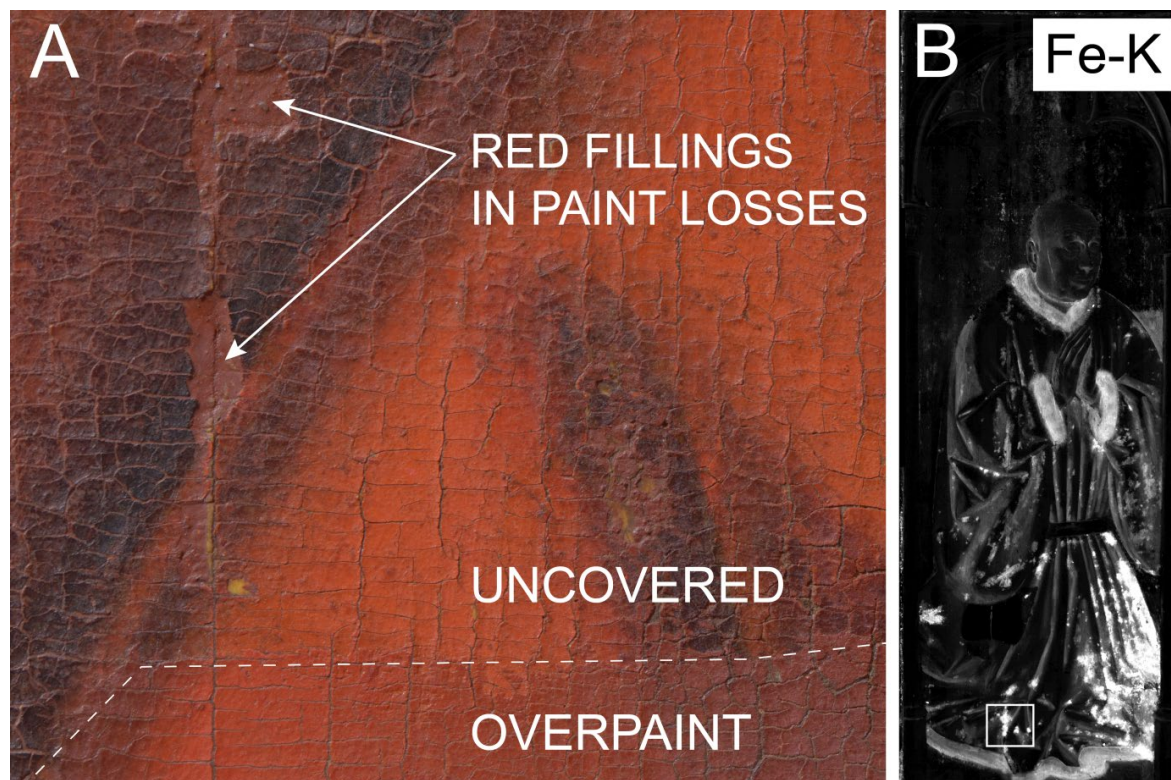
*Figure S7: **A**: detail of the dress of Joos Vyd during treatment. After removal of the overpaint, the paint losses in the original Van Eyck paint and their red fillings emerge as predicted by the MA-XRF scans. **B**: distribution map of iron. The white rectangle indicates the area shown in A.*

4.3.3.3 *Supplementary References*

1. M. Alfeld, K. Janssens, J. Dik, W. De Nolf, G. Van der Snickt, J. Anal. At. Spectrom., 2011, 26, 899-909.

2. P. Van Espen, K. Janssens, J. Nobels, Chemometr. Intell. Lab., 1986, 1, 109-114.

3. M. Alfeld, K. Janssens, J. Anal. At. Spectrom., 2015, 30, 777-789.

4. M. Salomé, M. Cotte, R. Baker, R. Barrett, N. Benseny-Cases, G. Berruyer, D. Bugnazet, H., Castillo-Michel, C. Cornu, B. Fayard, E. Gagliardini, R. Hino, J. Morse, E. Papillon, E. Pouyet, C. Rivard, V. A. Solé, J. Susini, G. Veronesi, J. Phys.: Conf. Ser. 2013, 425, 182004.

5. V. A. Solé, E. Papillon, M. Cotte, Ph. Walter, J. Susini, Spectrochim. Acta, Part B, 2007, 26, 63–68.

6. M. Spring. Nat. Gallery Techn. Bull., 2012, 33, 4-26.

7. Conservation Dossier "*Ghent Altarpiece* Project", KIK-IRPA, Brussels.

4.4 Dual mode standoff imaging spectroscopy documents the painting process of the Lamb of God in the Ghent *Altarpiece* by J. and H. Van Eyck

Abstract The ongoing conservation treatment program of the *Ghent Altarpiece* by Hubert and Jan Van Eyck, one of the iconic paintings of the west, has revealed that the designs of the paintings were changed several times, first by the original artists, and then during later restorations. The central motif, The Lamb of God, representing Christ, plays an essential iconographic role, and its depiction is important. Because of the prevalence of lead white, it was not possible to visualize the Van Eycks' original underdrawing of the Lamb, their design changes, and the overpaint by later restorers with a single spectral imaging modality. However, by using elemental (X-ray fluorescence) and molecular (infrared reflectance) imaging spectroscopies, followed by analysis of the resulting data cubes, the necessary chemical contrast could be achieved. In this way, the two complementary modalities provided a more complete picture of the development and changes made to the Lamb.

4.4.1 Introduction

The *Ghent Altarpiece* (1432) (Fig. 1) by the brothers Hubert and Jan Van Eyck is considered one of the founding masterpieces of Western European painting and of Early Netherlandish painting in particular, bearing witness to a visual acuity and painterly skills unequalled at the time. Verses inscribed on the original frames of the outer wings record that the altarpiece was begun by Hubert van Eyck and completed after his death by his brother, Jan. We know of no other surviving works by Hubert, but Jan's paintings have been so influential that, for centuries, a long-standing myth credited him as the "inventor" of oil painting. The *Ghent Altarpiece* reveals the remarkable potential of the oil medium to evoke tangible materials from living plants to glittering jewels to soft fleece and, in the process, transform a sacred scene into a vivid extension of the real world. When the wings of the altarpiece are open (Fig. 1), the viewer is drawn into the central panel, *The Adoration of the Lamb*, which represents the sacrifice of Christ with a depiction of the Lamb of God, standing on an altar, blood pouring into a chalice.

This iconic work is not only associated with the flowering of oil painting but also with the birth of cultural heritage science over 500 years later. Already in 1950, the panel paintings were protagonists of the first wave of scientific restoration treatments (*1*), i.e., art

conservation interventions consistently supported by chemical research and analytical measurements, with the ensuing insights published in the emerging domain-specific journals of that time (*2*). Today, the panels are again the subject of an extensive conservation and research campaign, and as was the case 70 years ago, state-of-the-art diagnostic instrumentation has been exhaustively exploited.

In the mid-20th century, the extraction and characterization of micro-samples by light microscopy and microchemical testing were pivotal developments (*3, 4*) toward a better understanding of the material used by the artists. During the extensive technical investigation that guided the conservation treatment undertaken in 1950 to 1951, researchers made use of minute paint samples mounted in cross section for microscopic analysis of the paintings' material composition and layer sequence. This research was undertaken with a twofold aim: to understand the original paint structure of the altarpiece and to identify areas where overpaints applied by earlier restorers obscured the Eyckian original (*5*).

The paint samples studied during the 1950s treatment showed the layer structure typical of an early Netherlandish panel painting. The wood panel, typically oak, was prepared for painting with a "ground" layer of chalk bound with glue. The artist drew the planned image on the white ground layer with a black underdrawing. He then sealed the ground layer and drawing with a translucent priming (or isolation layer) of drying oil tinted with small amounts of lead white, chalk, carbon black, and traces of earth pigments, which ensured that the absorbent glue-bound layer would not drain the oil medium from the subsequent paint layers. Guided by the design laid out in the underdrawing, the artist applied one or more layers of underpaint to define the colors of the design in schematic fashion. In the final paint stage, he completed the image with subtle details and rich colors. Ultimately, after the paint had dried for a year or so, a varnish layer typically was applied to saturate the colors of the final painting. For illustration purposes, these layers can be seen in Fig. 3 in a cross section taken from the Lamb's body in 1950 to 1951; the reanalysis of this cross section is discussed in Results.

In the 1950 to 1951 study, conservation researchers recognized in this cross section the presence of restorers' overpaint, separated from the original paint layers by varnish layers built up in multiple restorations. In their magnified visual and X-ray radiography (XRR) examination of the painting, they also saw evidence of this overpaint in the region of the Lamb's head. However, it was not possible with the techniques available at that time to localize the extent of all the old restorers' overpaint with precision. When faced with insufficient information, conservators and curators err on the side of caution, choosing to leave areas of possible overpaint in place until further research provides definitive evidence on their origin. For this reason, along with time limitations, it was decided to remove overpaint only from the area immediately surrounding the head of the Lamb. The result was that in the 1950 to 1951 treatment only, the gilded rays and ears of

the original Lamb were uncovered, leading to the unexpected effect of a head with four ears (*5*).

Figure 1: The Ghent Altarpiece by the Van Eyck brothers (1432, Cathedral of Saint Bavo, Ghent, Belgium) with the wings opened. The white rectangle indicates the area featuring the Lamb of God, the central motif of this polyptych and subject of this paper. Color image taken after the 1950s treatment and before the 2019 treatment (© Lukasweb.be - Art in Flanders vzw).

Since the 1950s, many new in situ analytical tools and data analysis algorithms (*6*) have been developed and applied to the conservation and study of artworks. Of particular interest here is the development of mobile instrumentation that allows for non-invasive microscale and macroscale chemical imaging directly on the paint surface. The ultimate goal of microscale imaging analysis is to provide virtual cross sections (i.e., the non-invasive mining to obtain stratigraphic and compositional information on the paint layers at any site of the painting) using modalities such as optical coherence tomography (*7*), confocal elemental mapping (*8–10*), and femtosecond pump-probe spectroscopy (*11*). While these methods have shown promising preliminary results, they currently lack sufficient chemical specificity to identify artists' pigments conclusively and, in some cases, show a limited depth or lateral resolution. For the macroscale methods, several are based on imaging spectroscopy (*12, 13*), the collection of hundreds of narrow spectral band images over a continuous portion of the electromagnetic spectrum. The focus of

macroscale methods on spectral information has provided reasonable chemical specificity, but currently, they are without the capability to provide as detailed information about the paint layer structure as cross-sectional methods.

Within the field of conservation science, macro X-ray fluorescence (MA-XRF) imaging (*12*) and infrared reflectance imaging spectroscopy (RIS) (*13*) currently are important to art historical scholars and conservators who seek to document and understand the composition (*14*), (long-term) chemical reactivity (*15*), and hidden structure of paintings (*16*). Infrared RIS and MA-XRF may be regarded as improvements of infrared reflectography (IRR) and XRR, respectively, two (broad spectral band) conventional imaging techniques that are used on a routine basis for the study of paintings and of which the imagery recorded on the *Ghent Altarpiece* is available online (http://closertovaneyck.kikirpa.be/). As illustrated below, the key added value of imaging spectroscopy lies in the fact that many of the constituent artists' materials can be identified in situ and without sampling, and their macroscale distribution can be plotted with high spatial resolution (200 to 750 µm per pixel). The resulting distribution images allow for a direct comparison with visual features on the paint surface such as paint strokes, degradation fronts, and other defects (*14, 17*). In addition, the penetrative properties of the primary radiation permits probing for subsurface modifications; this can give insight into both the painting process and the restoration history of paintings (*12, 13, 16*). While MA-XRF and infrared RIS were initially developed separately, it is now becoming clear that their combined use allows for a mutual compensation of the drawbacks of each method (*13, 18*). That is, each method provides some level of chemical contrast in cases where the other does not. In particular, each technique can reveal materials to which the counterpart is insensitive, for example, overlying layers that strongly attenuate X-rays can prove transparent for infrared radiation and vice versa (*16*). The implementation of chemical imaging techniques on the macro level can reveal changes in the artistic design, but specifying the specific paint layer(s) in which the artist made modifications is challenging. By comparison, microscale imaging of the paint stratigraphy through paint samples does offer information on the complex sequence of paint layers—both the work of the original artists and layers of overpaint added by later restorers in the course of almost six centuries—but localized to a specific point (*3*).

The first phase of the current conservation treatment of the *Ghent Altarpiece*, begun in 2012, focused on the reverse side of the wing panels, which are only visible to the visitor when the altarpiece is closed. During the first phase of treatment, MA-XRF imaging, supplemented with the analysis of a limited number of paint cross-sectional samples, facilitated the identification and accurate localization of extensive overpaints. Combined with historical evidence, this research documented an extensive restoration campaign dating to the middle of the 16th century that encompassed all panels (*19*). This combined analysis contributed objective chemical evidence to the scholarly debate on conservation treatment decisions. With a much more complete understanding of the extent of

overpaints and the state of preservation of the original paint below, it was decided to fully remove these 16th century non-original layers, bringing to light the exquisite quality of the original Eyckian paint surface (20).

Given the success of combining the MA-XRF results with traditional methods (IRR, XRR, and magnified visual examination) during the first treatment phase to map the areas of overpaint, this combined approach was also adopted for the second phase of the conservation program that began in 2016 during which the lower tier of panels on the interior of the altarpiece were treated. It was considered likely that the set of 16th century overpaints identified during the first phase of treatment would also be present on the interior panels. This paper uses the motif of the Lamb of God in the central panel depicting *The Adoration of the Lamb* (Fig. S1) to demonstrate the utility of the methods applied in documenting different stages of the painting's history and the results of removing the 16th century overpaint. Because of lingering questions raised during the 1950 to 1951 treatment regarding the remaining overpaint on the Lamb, we sought a more complete understanding of the distribution of the overpaint and a clearer distinction between the overpaint and the original paint structure of the Eyckian Lamb and altar. Thus, both MA-XRF and infrared RIS data were collected and analyzed from the Lamb of God. Although the macroscale chemical imaging provides limited information on stratigraphy, the visualization of material differences helped to separate different painting stages.

4.4.2 Results

MA-XRF and infrared (970 to 1680 nm) RIS image cubes of the Lamb of God and surrounding area were collected with a spatial resolution of 0.75 and 0.17 mm per pixel, respectively. These image cubes were collected in early 2018 before removal of all the 16th century overpaint. From the infrared RIS cube, false-color images were made along with a map of the distribution of basic lead white (hydrocerussite). Elemental maps were extracted from the MA-XRF cube. These new MA-XRF and infrared RIS images provided the required chemical contrast to go beyond the 1950 to 1951 study and begin to assign the extent of the overpaint layers compared to the original Eyckian paint layers. This new chemical imaging data, combined with the conservators' magnified surface examinations, allowed restorers to distinguish between more than one early campaign of restoration. Specifically, the MA-XRF and infrared RIS image products contributed to separating the visual characteristics of the 16th century overpainted Lamb from the Eyckian Lamb, as well as deriving information on how the Eyckian Lamb was painted. To demonstrate this, we present images of painted design features such as the head of the Lamb, its body, and the altar: color images made after the 1950s treatment and then after the treatment completed in 2019 (which removed all 16th century overpaint), along with images obtained by spectroscopic analysis.
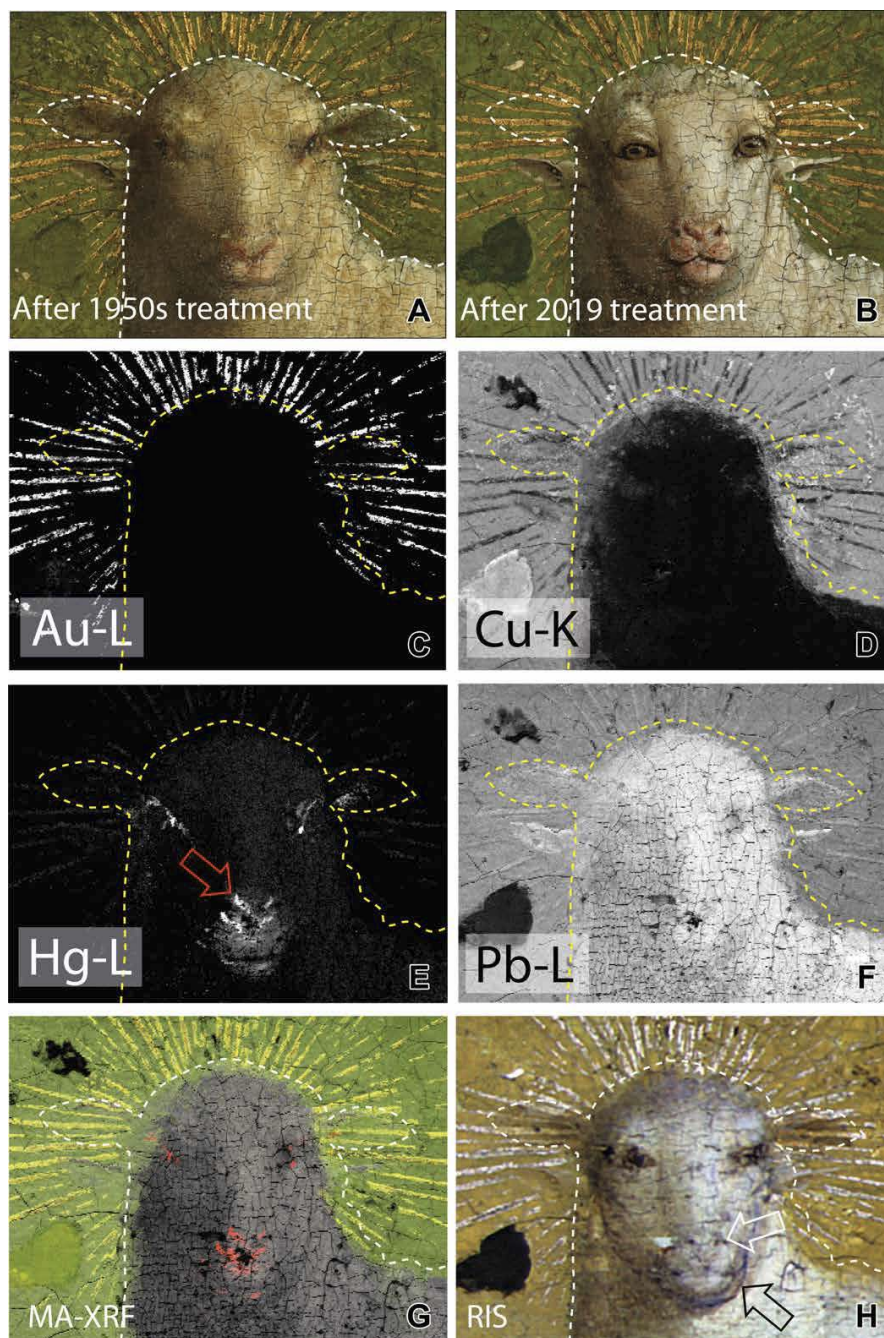
*Figure 2: Detail of the head of the Lamb. Color image (**A**) before the removal of all 16th century overpaint and (**B**) after the removal of all 16th century overpaint, revealing the face of the Eyckian Lamb. The dotted lines indicate the outline of the head before treatment (© Lukasweb.be - Art in Flanders vzw). MA-XRF elemental maps showing the distribution of (**C**) gold, (**D**) copper, (**E**) mercury with a red arrow indicating the position of the Eyckian Lamb's nostrils and (**F**) lead. (**G**) Colorized composite MA-XRF elemental map showing the elemental distribution of copper (in green), mercury (in red), gold (in yellow), and lead (in gray). (**H**) Composite false-color infrared RIS image (B, 1000; G, 1350; R, 1650 nm) shows underdrawn lines, indicating the position of the facial features of the Eyckian Lamb. The white arrow indicates the nostrils, whereas the black arrow indicates the jawline. All chemical images were collected after varnish removal but before 16th century overpaint removal.*

As noted in Introduction, only some overpaint around the head of the Lamb was removed in the 1950 to 1951 treatment, revealing the original Eyckian ears (color image after 1950s treatment; Fig. 2A) (*5, 19, 21*). MA-XRF elemental maps displaying the distribution of gold, copper, mercury, and lead are shown in Fig. 2 (C to F), along with a colorized composite of these MA-XRF maps in Fig. 2G. The corresponding false-color infrared RIS image is shown in Fig. 2H. The outline of the overpainted head of the Lamb, as it appeared before the recent removal of the 16th century overpaint, is shown as a dashed line. This makes it clear that the copper paint of the green meadow extends inside the outline of the Lamb's head. To produce a clean edge of the head of the Lamb against the green meadow, standard Netherlandish painting practice in the 15th century dictated that the copper green underpaint would have extended into the area planned for the head, later to be covered by the final white paint of the Lamb (Fig. 2, D and F). After completion of the Lamb, the artist's final touch was the gilded rays of the halo applied right up to the contour of the Lamb's head and ears. The gold distribution in the elemental map (Fig. 2, C and G) shows that the rays continue inside the dotted line on the right-hand side and are also situated underneath the paint depicting the upper set of ears. These findings demonstrate that the restorer's 16th century overpaint enlarged the Lamb's head along the right side of the neck and shoulder and also added the upper ears. The false-color infrared RIS image (Fig. 2H) shows similar information, as the background (light brown color) extends inside the dotted line on the right-hand side, and the rays of the halo are present underneath the upper set of ears. The MA-XRF and RIS chemical images show that the gold rays are not present underneath the lower set of ears but instead were applied only up to the outer edges of those ears.

The MA-XRF map for mercury (Fig. 2, E and G), an element associated with the red pigment vermilion (HgS), reveals the presence of two sets of nostrils that are roughly v-shaped. The lower set aligns with the nostrils of the Lamb with the 16th century overpaint (Fig. 2A), whereas the upper set (red arrow in Fig. 2E) is smaller and coincides with dark underdrawing "dots" (Fig. 2H, white arrow), likely associated with the Eyckian Lamb. In the infrared RIS image, dark lines of the preparatory underdrawing that delineate the division between the lips and the jawline (Fig. 2H, black arrow) are also visible. In addition, in the infrared RIS image, design features from two sets of eyes can be seen. Dark, irregularly shaped spots align with the pupils of the overpainted eyes. Comparison with the mercury map shows that vermilion also is likely associated with the overpainted eyes. The other set of eyes is characterized in the infrared RIS image by some drawing lines and dark pupils and is slightly lower on the face. In contrast to the outward-looking eyes of the Lamb depicted in the 16th century overpaint, this set looks forward toward the viewer. Collectively, these facial features indicate that the Eyckian face of the Lamb had forward-gazing eyes and effectively a shorter muzzle than the 16th century restorer's overpainted face. During the recent conservation treatment that was completed in 2019, conservators were able to safely remove the 16th century overpaint that completely obscured the head and patches of the body in the Lamb of God. The head of the Lamb

that emerged (Fig. 2B) has many of the facial features that previously could be elucidated from analysis of the chemical imaging data.
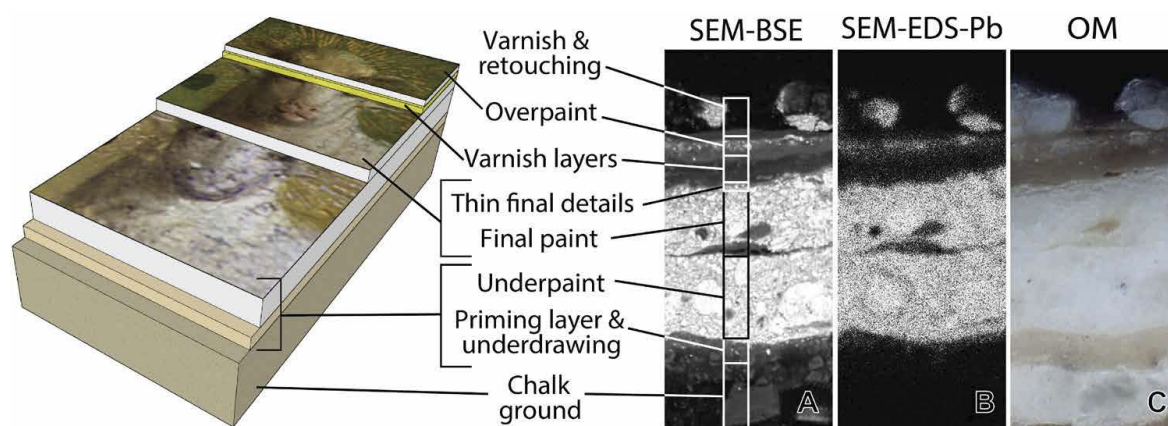

*Figure 3: Paint micro-sample extracted from the body of the Lamb. The scheme on the left illustrates the stratigraphy observed in the paint cross section collected in 1950 to 1951 and reanalyzed here. An area of the cross section is shown on the right, recorded with three different methods (**from left to right**): (**A**) Backscattered electron image recorded with a scanning electron microscope (SEM-BSE) and (**B**) lead distribution image recorded with an SEM equipped with an energy dispersive X-ray spectrometer (SEM-EDS-Pb), followed by (**C**) an optical microscopy (OM) image. The uppermost "varnish and retouching" layer, but not the overpaint, was removed before imaging spectroscopy was done. Size of micrographs: 95 μm by 42 μm.*

In the 1950 to 1951 study, evidence for overpaint on the body of the Lamb came most conclusively from a paint cross section (Fig. 3) extracted from the Lamb's body, of which the location is identified in Fig. 4A. The results from reexamination of this cross section by means of optical microscopy (OM) and scanning electron microscopy with energy dispersive X-ray spectroscopy (SEM-EDS) analysis confirmed many of the findings from the 1950s analysis. In summary, the stratigraphy consists of a chalk ground, priming layer, and two thick applications of lead white–based paint (corresponding to the underpaint and final paint of the Eyckian Lamb), as well as thin traces of a discontinuous third lead white layer (newly reported here) that may correspond to final details such as the curls of the fleece. The absence of dirt and varnish in between these strata strengthens the hypothesis that these layers were applied within only a short interim and, thus, likely were painted by the Van Eyck brothers. On top of the Eyckian paint layers, several thick varnish layers are present, which must have originated in multiple restorations, followed by a series of interleaved layers of overpaint (rich in lead white) and more varnish.

The contrast seen in MA-XRF and infrared RIS images derives from differences in chemical composition. However, since the paint cross section from the body of the Lamb (Fig. 3) confirms that it was both painted and overpainted using superimposed layers of lead white, the information obtained from MA-XRF was expected to be limited because the high X-ray absorption coefficient of lead restricts the depth information that can be

obtained. In contrast, infrared RIS has a more extended penetration depth in lead white–rich paints. The absorption coefficient of lead white is negligible in the visible and infrared spectral regions; however, its scattering coefficient, while large in the visible, decreases markedly at infrared wavelengths. The differences in penetration of the lead white–rich layers can be seen in Fig. 4 (C to F), which compare the MA-XRF elemental maps and the false-color infrared RIS of the entire Lamb.

In the body of the Lamb, the lead map (Fig. 4C) shows the same shape of the animal as seen in the image before removal of 16th century overpaint (Fig. 4A); the intensity variation also appears to show denser areas of lead white corresponding to the final details of curly fleece. Because RIS was restricted to the infrared spectral region, better transmission of light through the paint layers was expected, the latter including any overpaint, final, and underpaint layers. Compared to the MA-XRF maps (Fig. 4, C to E) and the image before removal of all 16th century overpaint (Fig. 4A), the false-color infrared RIS image (Fig. 4F) shows a slightly smaller form of the Lamb's body that appears opaque, as well as a translucent, thinly painted region along the back and hindquarters. Further evidence for these changes to the size of the Lamb can be seen in principal component images from the RIS data (see fig. S8), although such images rarely represent contributions from a single pigment. A focus on the spectral features that directly relate to pigments used in the Lamb is discussed further below. The false-color infrared RIS image also shows the presence of underdrawing, including lines that define the smaller, opaque body (white arrows, Fig. 4F) and "wavy" brown lines used to model the Lamb's torso and suggest the texture of the fleece (black arrows). The brown lines are most apparent on the Lamb's chest and underside of the belly. The lines are not present in the images before or after 16th century overpaint removal in Fig. 4 (A and B), suggesting that they are below the surface and are likely underdrawing. Also, visible in the false-color infrared RIS image are underdrawing lines that denote the legs and hooves of the Lamb. Whereas some of the lines are brown (near the Lamb's tail), others are wider, black lines (such as that delineating the front of the proper left front leg) that are visually similar to the black underdrawn line that reinforces the jawline of the Eyckian Lamb in Fig. 2H.
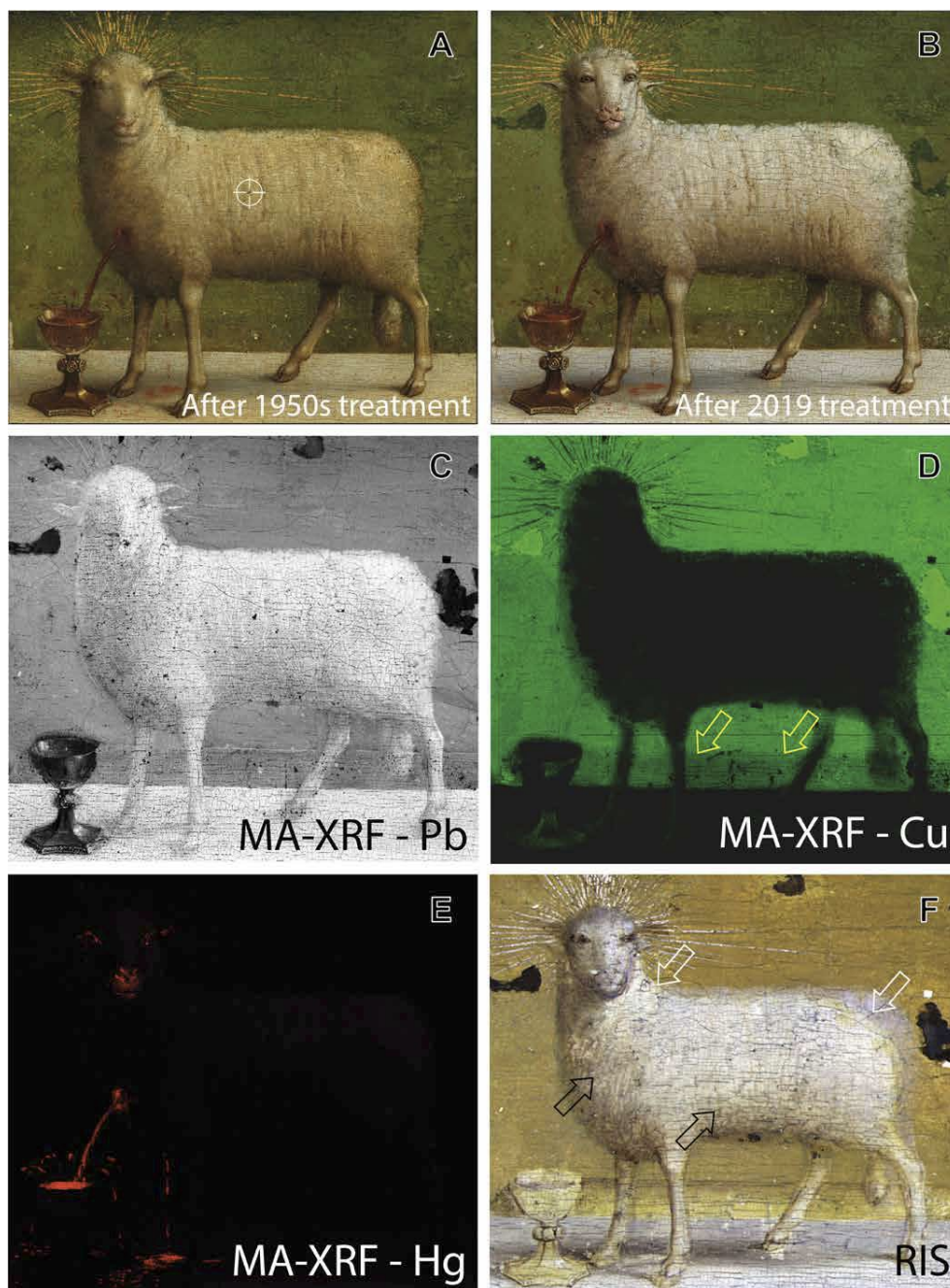
*Figure 4: The Lamb of God. (**A**) Color image of the Lamb before removal of all 16th century overpaint; the location of the paint sample discussed in Fig. 3 is indicated by a white reticle. (**B**) The Lamb after removal of all 16th century overpaint in 2019 (© Lukasweb.be - Art in Flanders vzw). (**C to E**) MA-XRF elemental maps recorded before removal of all 16th century overpaint showing the distribution of (**C**) lead (in white), (**D**) copper (in green), and (**E**) mercury (in red). The yellow arrows in (**D**) indicate the edge of the larger altar. (**F**) False-color infrared RIS image (B, 1000; G, 1350; R, 1650 nm) revealing underdrawing that denotes the size of the smaller version of the Eyckian Lamb's back and tail, more rounded hindquarters, repositioning of the hooves, and the larger size of the altar. The white arrows indicate underdrawing lines defining a smaller body, whereas the black arrows point to wavy underdrawing lines applied for torso modelling and fleece texture.*

The difference between these two drawing types (thinner brown lines or thicker black lines) can be better understood by looking at a detail from the angel to the left of the Lamb (Fig. 5). Infrared RIS can be used to distinguish between different underdrawing materials owing to changes in their absorption and scattering coefficients as a function of wavelength in the infrared. This can only be exploited by using hundreds of narrow spectral bands, as is done in RIS. In contrast, since broad spectral band traditional IRR is the sum of all these spectral bands, the ability to distinguish artist materials is substantially limited. In the IRR image (Fig. 5B), the underdrawing lines are only distinguishable based on their relative intensity. The false-color infrared RIS image (Fig. 5C) shows two types of underdrawing materials. One type consists of thin, brownish lines that appear to have been rendered using a fine brush and a liquid medium (Fig. 5C, brown arrows). The other type is thicker, black lines that were likely more heavily applied, also in a liquid medium (Fig. 5C, black arrows). These two types of underdrawing are clearly also present in the Lamb (Figs. 2H and 4F). Together, these results indicate that the infrared RIS image is dominated by the underdrawing, priming layer, and underpaint layer of the Eyckian Lamb.

As seen in the infrared RIS image of the Lamb in Fig. 4F, a sharp, crisp boundary is not observed between the light brown background (corresponding to the green meadow) and the white Lamb along the back and hindquarters. Instead, this area appears as a translucent, hazy white that is clearly on top of the light brown background. Underdrawing lines are present at the top of the hindquarters and along the neck and shoulder (Fig. 4F, white arrows) and are found along the boundary between the opaque and hazy translucent white paint. This suggests that there was a version of the Lamb that had a more naturalistic build with a slightly sagging back and more rounded hindquarters.

The MA-XRF copper map shown in Fig. 4D indicates that changes were made to the altar as well. The areas of lower intensity of copper along the back edge of the altar coincides with an underdrawing line seen in traditional IRR images, also visible in the false-color infrared RIS image in Fig. 4F. A larger section of the infrared RIS false-color image (Fig. 6A) shows the extent of the underdrawing of the altar. The drawn altar was deeper and with a slightly different perspective than the final painted altar, indicated by the edge of the white plane that extends beyond the drawing lines on the left and right. The abandoned part of the altar is characterized by having a lower copper intensity and higher reflectance intensity, which suggests the change occurred during a paint campaign and not directly after the underdrawing was completed. To confirm that the deeper altar was painted, the reflectance spectra from different areas on the altar were examined. The paint of the altar is rich in lead white as indicated by the MA-XRF lead map (Fig. 4C) and the presence of a strong hydroxyl absorption feature at 1446 nm in the RIS spectra, indicative of basic lead white (hydrocerussite) (Fig. 6B, blue and green spectra). The finished altar likely consists of two paint layers containing lead white: the underpaint and the final paint. The depth of the 1446-nm feature is indicative of the amount of basic lead white present and

is most pronounced in the upper (blue) spectrum of Fig. 6B. In contrast, the average spectrum from the green meadow (Fig. 6B, yellow spectrum) shows that much less lead white is present, along with a broad absorption from ~967 to 1375 nm, indicative of copper green pigments. In this region of the green meadow, the contribution from lead white may be from small amounts of lead white added to the green paint of the meadow or in the priming layer. The average reflectance spectrum from the abandoned region of the altar (Fig. 6B, red spectrum) has an absorption feature at 1446 nm whose depth is less than that of the finished altar but greater than that of the green meadow, indicating that at least the underpaint layer of the altar extended to the underdrawn line. This suggests that the larger drawn altar was underpainted with lead white before it was abandoned. This is consistent with the MA-XRF Cu image in Fig. 4D revealing a less intense copper signal, likely from a thinner build-up of green paint in this area (as indicated by the yellow arrows).
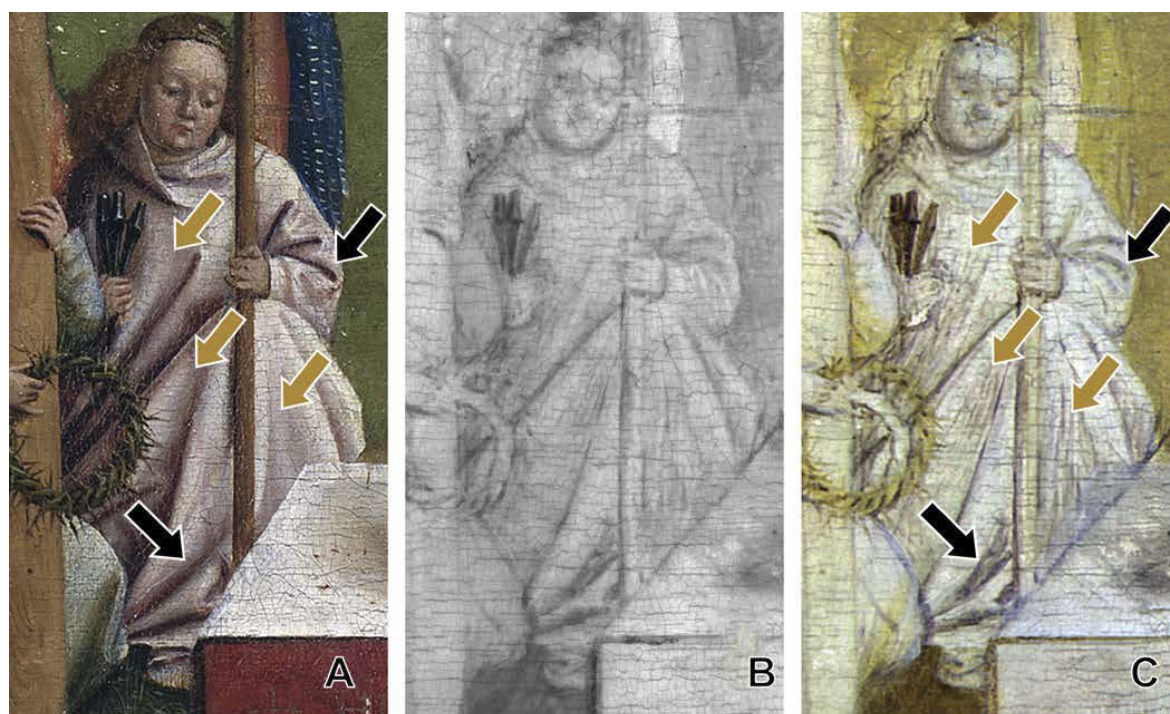

*Figure 5: Detail of the angel to the left of the Lamb. (**A**) Color image after 2019 cleaning and during retouching (© Lukasweb.be - Art in Flanders vzw). The brown and black arrows indicate the position of the underdrawing lines shown in (**C**). (**B**) IRR image (http://closertovaneyck.kikirpa.be, © KIK-IRPA, Brussels) revealing the infrared- absorbing underdrawing. (**C**) The corresponding false-color infrared RIS image (B, 1000; G, 1350; R, 1650 nm) allows further distinction of the types of underdrawing: (i) Brown arrows indicate the finer lines of the first stage of underdrawing, which appear brownish in the RIS image, and (ii) black arrows show the thicker lines in a liquid medium from the second stage of underdrawing, which appear blackish in the image. The yellow color in the background is a result of partial penetration of copper-containing green paint in the infrared.*

The paint of the Lamb itself is mostly dominated by lead white, including the overpaint. The expected stratigraphy of the Eyckian Lamb is composed of an underpaint layer and a

final paint layer whose thicknesses are much larger than the overpaint layers (see cross section in Fig. 3). A map derived from RIS data indicating the integrated area of the hydroxyl absorption at 1446 nm was obtained by fitting each reflectance spectrum in the image cube with a convex hull function, the intensity of the resulting map (Fig. 6C) being proportional to the amount of basic lead white present. In comparison to the 16th century overpainted Lamb (Fig. 4A), the lead white map clearly shows the more naturalistic shape of the Lamb's sagging back, rounded hindquarters, smaller tail, and the larger altar.

Duly informed by the MA-XRF and infrared RIS imagery, as well as by extensive magnified examination of the paint surface, the second phase of conservation treatment of the *Ghent Altarpiece* undertook the complete removal of the 16th century (and later) overpaint, as shown in the resulting images of the Lamb in Figs. 2B and 4B. This resulted in changes to the Lamb's face that had many of the facial characteristics identified with the MA-XRF and infrared RIS analysis. The body of the Lamb retained the same shape as the image before 16th century overpaint removal. The difference between the body of the Lamb after removal of the 16th century overpaint (Fig. 4B) and the body recovered from the infrared RIS analysis here (Fig. 6C) indicates that the lead white paint layer used to define the larger squared-off hindquarters was applied before the 16th century restoration.

An interesting question is whether this layer was applied during the Eyckian painting process or at some later time. After removal of the 16th century overpaint, two observations suggest that the paint may have been applied after a smaller version of the Lamb was painted with a high degree of finish and possibly considered completed. This small Eyckian Lamb would likely have been considered finished once the fine, tight curls of the fleece were applied. One observation comes from visual examination of the paint, and the other comes from examination of the X-ray radiograph. Close visual examination of the paint surface shows that the texture of the added paint extending the upper contour of the Lamb's back and hindquarters differs substantially from the paint in the center of the body. The X-ray radiograph shows vertical "fuzzy" columns of opaque paint (Fig. 6D, lower black arrow) that are likely from the curls of the fleece, and these curly features end at a thin horizontal opaque ridge, which corresponds with the upper contour of the small Eyckian Lamb (Fig. 6D, upper black arrow). Outside of that upper contour, the X-ray radiograph shows an additional zone of thin, opaque paint (white arrows), which coincides with the translucent, hazy white revision shown in the infrared RIS image (Figs. 4F and 6A). Magnified examination of the paint surface confirms that the paint used to revise the Lamb to give it squared-off hindquarters shows less finesse in its application: It was dabbed on in a single tone of white paint, without the surface variations that define the texture of the fleece. Together, these observations support the hypothesis that the small Eyckian Lamb had the boundaries shown in the infrared RIS lead white map (Fig. 6C)

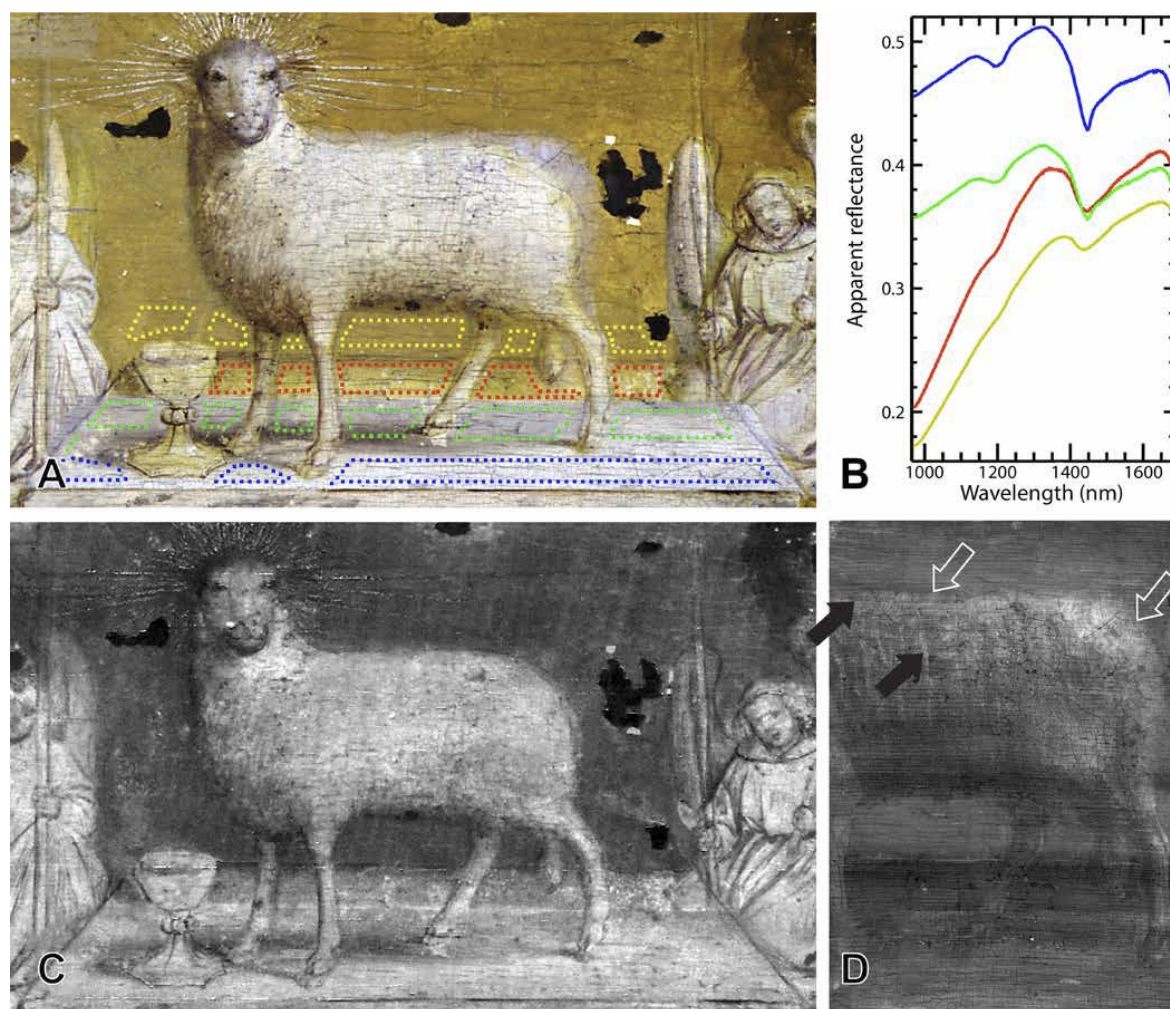and that this highly finished version was subsequently reworked to modify the shape of the Lamb's body.

*Figure 6: RIS images and map of the Lamb derived from processing the infrared reflectance image cube. (**A**) Infrared RIS false-color image (B, 1000; G, 1350; R, 1650 nm) and (**B**) associated average infrared RIS spectra collected from the colored dashed shapes shown in (**A**). (**C**) RIS lead white map derived from processing the infrared RIS image cube. Brighter areas of the map indicate stronger absorption from the –OH group of lead white. (**D**) X-ray radiograph detail (http://closertovaneyck. kikirpa.be, © KIK-IRPA, Brussels) after removal of all 16th century overpaint in 2019. The white arrows indicate where the body of the Lamb was revised, whereas the black arrows point to fleece texture.*

4.4.3 Discussion

The combination of two imaging spectroscopic techniques, MA-XRF and infrared RIS, allowed studying the painting process of the Lamb of God with chemical specificity. In summary, the combined results established the presence of three versions of the Lamb: a first, highly finished, small Eyckian version, a second version whereby the hindquarters were enlarged and squared off (revealed after overpaint removal), and a third, 16th

century version that extensively modified the head but respected the shape of the body from the second version. The second version could have been either a very late change by the original artist(s) or an early intervention by another painter. This identification of three versions is strengthened when historical information and conservation treatment details are integrated with the chemical imaging results.

The known drawing and painting style of the Van Eyck brothers can be used to further support the assignment of what was above referred to as the small Eyckian Lamb. The Van Eyck style of underdrawing is characterized by a first stage of fine lines that define design features as well as parallel hatching (rather than cross-hatching) to model the forms and a second stage of heavier lines that reinforce or revise the forms (*22, 23*). This characteristic drawing style is clearly seen in the angels (see Fig. 5). In the Lamb, the wavy parallel hatching that models the body while also evoking its fleece is characteristic of the first Van Eyck drawing stage. In the legs, both drawing stages can be seen. The dark underdrawing lines in the face appear characteristic of the second stage. The drawing defining the shoulder and the rounded hindquarters is narrow and possibly associated with the first drawing stage, but the drawing stage is difficult to conclusively categorize because the drawing is covered by lead white paint and likely overlaps with the copper paint of the green meadow. An important characteristic of the Van Eyck painting style is the finesse for which they render final details. Thus, the finding of the curly fleece only within the boundaries of the smaller Lamb is consistent with it having been painted by the Van Eyck brothers.

There are some other painted and drawn features revealed by the chemical imaging analysis that are unexpected, such as the forward- looking eyes of the Lamb and the change in the size and perspective angle of the top of the altar. The interpretation of the forward-looking eyes is part of an ongoing, unpublished scholarly debate (*24*). Some scholars have proposed that the Lamb was deliberately rendered less true to life to obtain a more intense and confronting appearance. Since the Lamb is an embodiment of Christ, the forward-gazing eyes could have a religious connotation. A simpler explanation may be that the painting of animals with forward-facing eyes is typical of an older style that was still present in the 15th century but disappeared as artists mastered a more naturalistic depiction of animals. The team treating the altarpiece noted that animals with both forward- and outward-looking eyes are seen in the panels of the *Ghent Altarpiece*. For example, in the panel of The Just Judges (stolen in 1934 but documented in photographs), there are horses with eyes that look forward, whereas in the panel of The Knights of Christ, the horses are depicted more naturalistically with outward-looking eyes. Thus, it is not unexpected that the Van Eyck brothers would have painted the Lamb with forward-facing eyes that directly engage the viewer.

Chemical imaging also revealed that the planned larger altar was at least painted with an underpaint layer of lead white and then abandoned before completion of the painting.

Supporting this is a report on the presence of white paint beneath the green paint in the abandoned section of the altar determined from optical stereomicroscopy (*25*). This change was likely made by the Van Eyck brothers during the painting process. This is not surprising since there is ample evidence for many changes to the design that were made during the painting process and so were not indicated in the drawing. This design change may have been made for two reasons. Looking at the position of the small Eyckian Lamb on the originally planned altar in Fig. 6C, the Lamb is not centered along the depth direction of the altar, which makes it seem unbalanced. To correct for this, the depth of the altar was reduced. This also results in another benefit in that it provides more space between the altar and the nearby angels. The infrared RIS images also show that the edges of the altar were revised in paint to effectively change the tilt of the altar, as has been noted in the previous study (*25*). Because Netherlandish painters at this time did not use vanishing points to define the perspective but instead rendered three-dimensional objects intuitively, the change in the tilt of the altar may have been done to make the design more pleasing.

After the removal of the 16th century overpaint by mechanically shearing it from the thick buildup of old varnish (as seen in the paint cross section in Fig. 3), it became clear that the enlargement of the Lamb was done in paint applied over the green meadow. The research here cannot definitively establish whether this paint is a change (*pentimento*) by the original artist(s) or a very early restoration. There is evidence for very old damages that precede the 16th century overpainting campaign (*21*). One clue that has emerged is the observation that this paint lacks the texture and detail expected for Eyckian paint. However, because the material evidence available at the time of the current conservation treatment could not establish whether this was original paint or an early restoration, the enlarged contour of the Lamb was not removed. From the early 19th century, there has been an ongoing scholarly debate on the respective contributions of the two brothers, Hubert and Jan Van Eyck (*26*). Here, too, the material evidence currently available does not allow conclusions to be drawn.

From a more technical point of view, the added value of MA-XRF and infrared RIS with respect to conventional XRR and IRR was demonstrated in this research. In particular, the element specificity of MA-XRF imaging permitted examining the complex structure and composition in a more selective way as compared to XRR. Whereas XRR cannot distinguish between heavy elements like lead and mercury, MA-XRF permits identifying and mapping chemical elements separately, which enabled the visualization of the nostrils of the Eyckian Lamb underneath the 16th century overpainted Lamb. In an analogous way, classic IRR can detect a variety of different IR-absorbing materials, such as carbon black, umber, or copper pigments, but cannot distinguish among them. Infrared RIS makes use of the materials' different spectral signatures, which allowed for the separation between two underdrawing campaigns, as well as a separation of copper

pigments from lead white. The spectral information provides the capability to discriminate among artists' materials.

The sensitivity of MA-XRF and infrared RIS to distinguish and map pigments is not the same and varies with the pigments used and the paint layering structure. Using both methods together, these differences can be exploited for a more robust and comprehensive identification and mapping of pigments in layered structures. For both modalities, the degree of depth penetration depends on the absorbance and scattering properties of the pigments within the paint layers. Both modalities helped to visualize the facial features of the Eyckian Lamb. The MA-XRF map of mercury (associated with vermilion) showed the placement of the nostrils, whereas infrared RIS revealed the infrared-absorbing underdrawing in the face, as well as the boundary between the copper green landscape and the lead white associated with the head and neck of the Lamb. Together, these maps and images provided the shape and position of the key facial features that defined the head and neck of the Eyckian Lamb.

In conclusion, we have demonstrated that the combination of infrared RIS and MA-XRF, now in the vanguard of heritage science, expands our possibilities for resolving complex conservation and art historical issues. These imaging technologies can be used to predict the characteristics of specific painted features before the removal of overpaint. Combined with the conservators' thorough optical examination informed by years of experience and insights derived from paint cross sections, chemical imaging methods will no doubt be central to furthering interdisciplinary research and contributing to resolving art historical and theological issues on the *Ghent Altarpiece* and other works of art.

4.4.4 **Materials and methods**

The chemical imaging campaign was divided into two phases and done in the conservation studio. First, the entire panels were imaged with an in-house MA-XRF scanning instrument. Next, the ensuing elemental distribution maps were used to define areas of interest, such as the Lamb of God, that would benefit from complementary infrared RIS experiments. All chemical images discussed in this work were collected in the early stages of the conservation treatment, when only the surface varnish had been removed.

4.4.4.1 *Macroscopic X-ray fluorescence imaging*
The MA-XRF instrument (Fig. S2) is an optimized variant of the very first mobile MA-XRF setup, built and described by Alfeld et al. as "Instrument B" (*27*). The measurement head consists of a 50-W XOS Xbeam micro tube with Mo anode (XOS, USA) operated at 50 kV and 1 mA and one Vortex EX-90 SDD detector with an active area of 50 mm^2 positioned at 45° relative to the surface normal. The excitation beam was normal to the painting

251

surface and was focused to a focal spot of ca. 50 μm by means of a polycapillary X-ray lens.

This measurement head is mounted on a software-controlled X-Y motor stage with a maximum travel range of 57 cm by 60 cm. MA-XRF scans were performed by sweeping the measuring head systematically over the paint surface at a constant speed. Careful positioning and alignment of the scanner ensured that the detector remained ca. 1 cm away from the panel painting. Retaining this constant instrument-to-painting distance maintained the anticipated spot size and prevented fluctuation of the attenuation of the X-ray fluorescence signals in ambient air. During the movement, the detector was read out every 200 ms, which, given the scan speed of ca. 3.75 mm/s, gave a collection footprint of ca. 0.75 mm × 0.75 mm for each pixel in the image cube. The resulting spectral data cube was processed through dynamic analysis using the bAxil (*28*) software package. The grayscale of the resulting images is linear to the detected intensities. However, after spectral deconvolution, the levels in the histogram of each individual image were manually moved or stretched to optimize contrast and readability by means of the Datamuncher software (*29*).

4.4.4.2 *Reflectance imaging spectroscopy*

Infrared reflectance image cubes were collected with a line-scanning imaging spectrometer (modified SOC-720SWIR, Surface Optics Corp., CA, USA) shown in Fig. S3 that uses a transmission grating prism spectrometer and a 640 × 512-pixel InGaAs focal plane array (640SDV-1.7RT, Sensors Unlimited, NJ, USA). The line-scanning imaging spectrometer has optimal signal-to-noise ratio from 967 to 1680 nm, with a spectral sampling of 3.4 nm, resulting in 209 spectral bands. The painting was illuminated with two lamps containing 125-W quartz halogen bulbs (Lowel Pro-light with Impact 3000 K FSH bulb) placed at ±45° to the surface normal. A rheostat was used to adjust the intensity of the lights to be no more than 1000 lux at the surface of the artwork. Image cubes were collected at an integration time of 33 ms per line, and the line field of view was changed by rotation of a scan mirror positioned at the front of the optical system. The spatial sampling at the artwork was 0.17 mm per pixel. The dark current was subtracted from the image cubes, and non-uniformities in illumination were corrected by dividing by a dark-subtracted image cube of a diffuse reflectance standard (99% reflector, 30 cm by 30 cm Spectralon panel, Labsphere, NH, USA). This procedure also converted the cubes to relative reflectance. The 14 reflectance image cubes collected in the region of the Lamb were then mosaicked and registered using a point-based algorithm to spatially align the cubes to a reference color image (*30*). The false- color images shown in the paper were created by placing the spectral band images specified into the red, green, and blue color channels of an RGB color image. Maps displaying the distribution of lead white were calculated from the reflectance image cube by integrating the area of a characteristic absorption at 1446 nm.

4.4.4.3 *Optical microscopy and scanning electron microscopy with energy dispersive X-ray spectroscopy*

The microscopic paint sample presented in this paper was taken from the Lamb during the previous conservation treatment in 1950 to 1951. The sample was embedded in acrylic resin and cross-sectioned to allow for detailed study of the layer structure and pigment composition. During the present campaign, the cross section, still available in the laboratory archive of the Royal Institute for Cultural Heritage (KIK-IRPA), was repolished and reexamined. It was first observed with OM using a polarizing light microscope on an Axio Imager M1 (Carl Zeiss, Oberkochen, Germany) with ultraviolet illumination (excitation band-pass filter from 390 to 420 nm) at magnifications up to ×500. Subsequently, the pigment compositions of the ground and paint layers were analyzed by means of SEM-EDS on a Zeiss EVO LS15 microscope with backscattered electron (BSE) and EDS detectors (Oxford Instruments X-MaxN 80 mm^2, AZtec Oxford Instruments Software). EDS analyses were run at an acceleration voltage of 15 kV. Analytical results were correlated with the optical images and the MA-XRF elemental distribution images, permitting a more accurate interpretation of the MA-XRF maps.

4.4.4.4 *Infrared reflectance reflectography*

The broadband infrared reflectogram was collected using a Lion Systems IRR camera, equipped with an InGaAs detector having a 640 × 512-pixel focal plane array and a spectral response of 1100 to 1700 nm. A micro-Nikkor 55-mm lens, fitted with a narrow bandwidth filter of 1500 to 1730 nm was mounted on the camera. The camera was moved by a motorized stage that maintained a constant distance between the lens and the painting surface, compensating for any warping in the wooden panel. Individual IRR images, each recording an area of 5 cm by 4 cm on the paint surface, were digitally assembled into larger images via Adobe Photoshop. Lighting was provided by two freestanding halogen lights, one placed at either side of the painting.

4.4.4.5 *X-ray radiography*

XRR images were taken using a Baltospot 110 generator from Balteau NDT using a 50-kV voltage and a current of 12 mA. AGFA Structurix D4 analogue X-ray film strips of 35-cm wide were cut to the desired length and placed against the painted side of the panels. The generator was positioned at a distance of 7 m from the artwork, and the film was irradiated for 10 min. After exposure, the films were developed and digitized using a high-resolution Laser Film Digitizer (Array Corporation, 2905HD). The resulting digital images were assembled using Adobe Photoshop software.

4.4.5 Supplementary materials

Supplementary material for this article is available at http://advances.sciencemag.org/cgi/content/full/6/31/eabb3379/DC1

Figure S1: Central panel of the Ghent Altarpiece: The Adoration of the Lamb. The white rectangles indicate the area of the Lamb of God, discussed in figures 2 and 4 and the angel, discussed in figure 5. Color image taken after the 1950s treatment and before the 2019 treatment (© Lukasweb.be - Art in Flanders vzw).

Figure S2: Experimental setup. The MA-XRF instrument during experiments on the central panel (Adoration of the Lamb). "Geert Van der Snickt at University of Antwerp".

Figure S3: Experimental setup. Near-infrared reflectance imaging spectroscopy (~980-1680 nm). "Kathryn Dooley at National Gallery of Art".
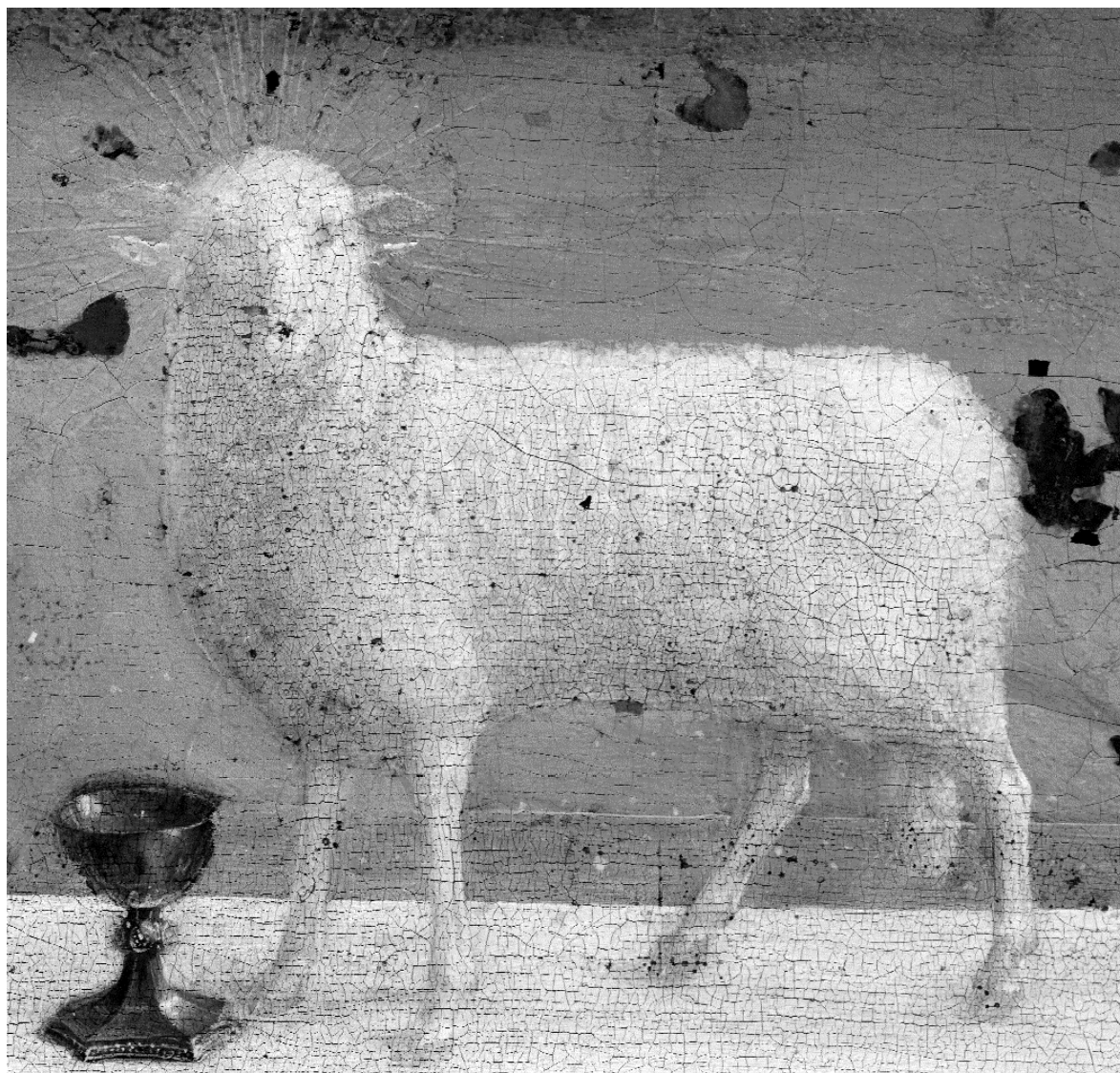
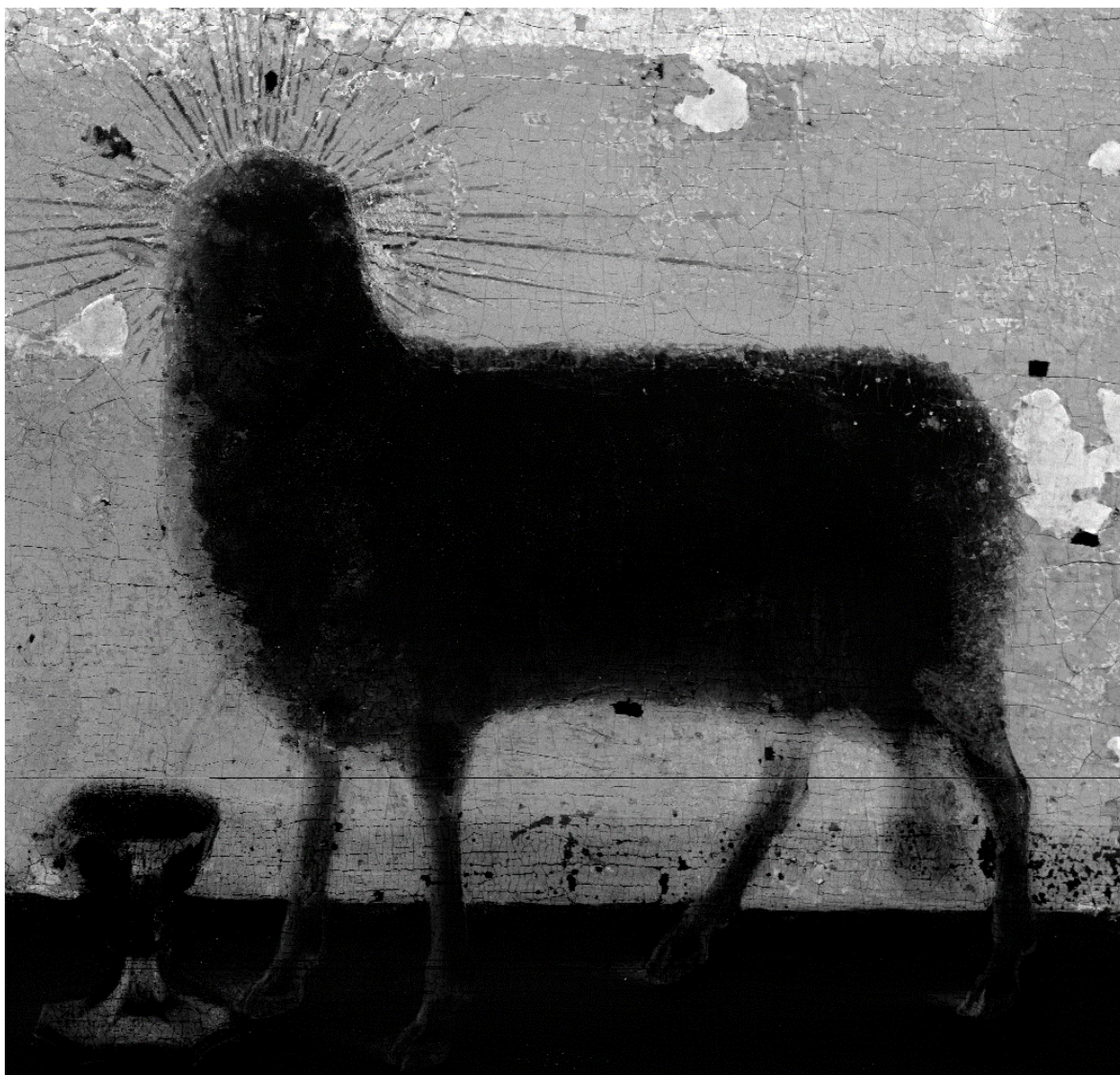*Figure S4: MA-XRF image showing the distribution of lead (Pb-L).*

Figure S5: MA-XRF image showing the distribution of copper (Cu-K).

Figure S6: MA-XRF image showing the distribution of mercury (Hg-L).

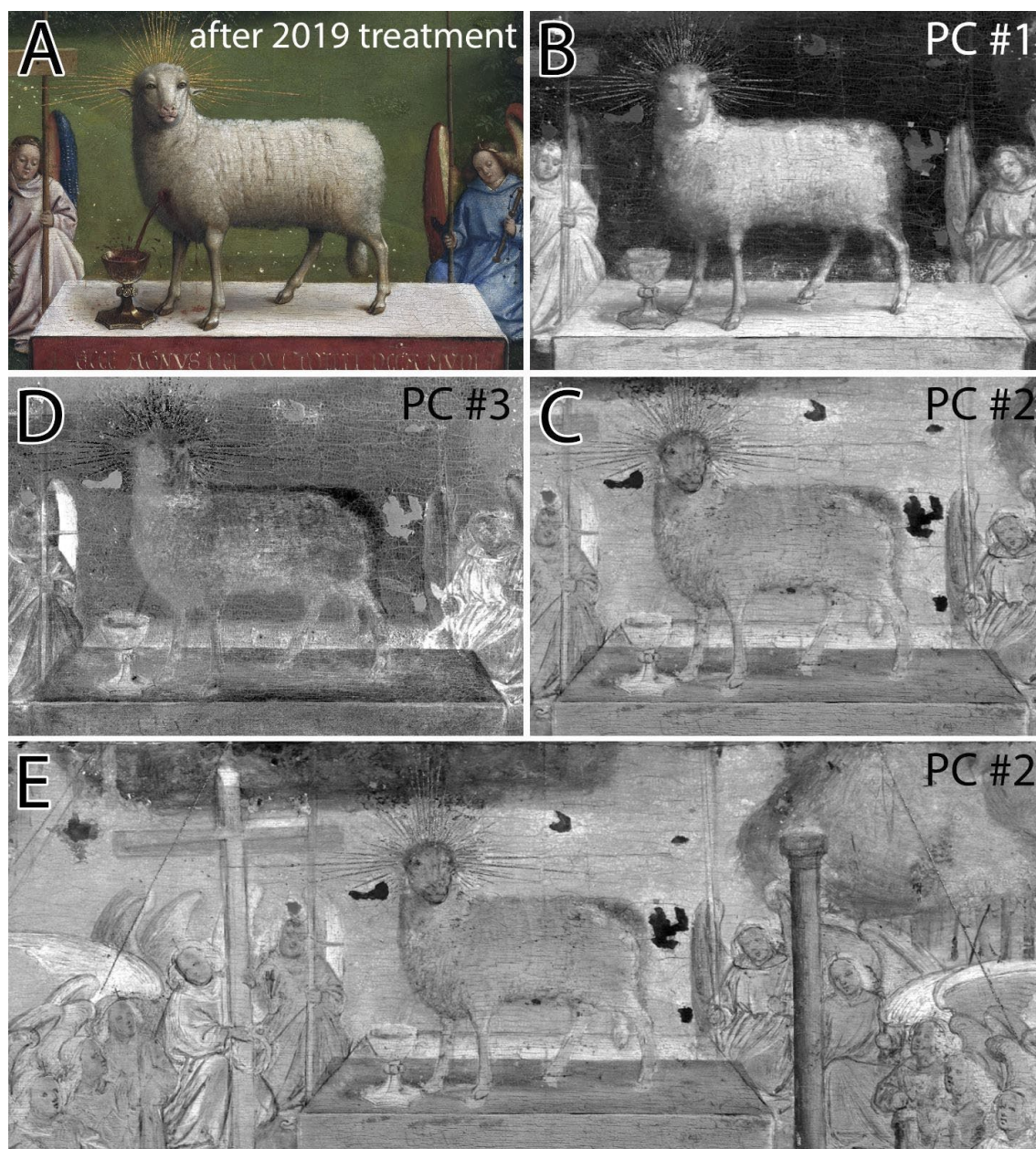*Figure S7: MA-XRF image showing the distribution of gold (Au-L).*

Figure S8: Comparison among principal component (PC) images. (A) Color image detail taken after the 2019 treatment (© Lukasweb.be - Art in Flanders vzw). (B-D) Detail of PC images #1-3, calculated from the RIS data set (spectral range 967-1680 nm) over the spatial area shown in (E) using the Minimum Noise Fraction algorithm in ENVI hyperspectral image analysis software (Harris Geospatial Solutions, Inc.). Generally, if revisions made to a painting can be seen in false-color infrared RIS images (see for example, figures 4F and 6A), then one or more of the PC images often emphasize such features more clearly. The revisions to the Lamb are visible in PC images #1-3, but appear most prominently in PC image #3. PC image #3 also shows marked differences between the robes and wings of the angels, clearly illustrating the fact that PC images do not necessarily represent a specific pigment or set of pigments, and thus do not provide information about the chemical composition directly. To investigate the chemical composition of the Lamb, the hydroxyl absorption feature at 1446 nm in the RIS spectra, characteristic of basic lead white, was used to make a map showing the distribution of this particular pigment (see figure 6C). (E) PC image #2 is dominated by drawing, including underdrawn lines in the altar, angels, and cross.

References and notes

1.   S. Muñoz Viñas, Contemporary Theory of Conservation (Butterworth-Heinneman, 2005).

2.   P. Coremans, La technique des "Primitifs flamands": Etude scientifique des matériaux, de la structure et de la technique picturale. III. Van Eyck: *l'Adoration de l'Agneau Mystique* (Gand: Cathedrale Saint-Bavon). Stud. Conserv. 1, 145–161 (1954).

3.   J. Plesters, Cross-sections and chemical analysis of paint samples. Stud. Conserv. 2, 110–157 (1956).

4.   P. Coremans, R. J. Gettens, J. Thissen, La technique des "Primitifs flamands". Stud. Conserv. 1, 1–29 (1952).

5.   P. Coremans, L'agneau Mystique au Laboratoire: Examen et Traitement (De Sikkel, 1953).

6.   Z. Sabetsarvestani, B. Sober, C. Higgitt, I. Daubechies, M. R. D. Rodrigues, Artificial intelligence for art investigation: Meeting the challenge of separating X-ray images of the *Ghent Altarpiece*. Sci. Adv. 5, eaaw7416 (2019).

7.   P. Targowski, M. Iwanicka, M. Sylwestrzak, C. Frosinini, J. Striova, R. Fontana, Using optical coherence tomography to reveal the hidden history of The Landsdowne Virgin of the Yarnwinder by Leonardo da Vinci and studio. Angew. Chem. Int. Ed. Engl. 57, 7396–7400 (2018).

8.   I. Reiche, M. Eveno, K. Müller, T. Calligaro, L. Pichon, E. Laval, E. Mysak, B. Mottin, New insights into the painting stratigraphy of L'Homme blessé by Gustave Courbet combining scanning macro-XRF and confocal micro-XRF. Appl. Phys. A 122, 947 (2016).

9.   A. R. Woll, J. Mass, C. Bisulca, M. Cushi-Nan, C. Griggs, T. Wanzy, N. Ocon, The unique history of the Armorer's Shop: An application of confocal X-ray fluorescence microscopy. Stud. Conserv. 53, 93–109 (2008).

10.   T. Lachmann, G. van der Snickt, M. Haschke, I. Mantouvalou, Combined 1D, 2D and 3D micro-XRF techniques for the analysis of illuminated manuscripts. J. Anal. At. Spectrom 31, 1989–1997 (2016).

11.   T. E. Villafana, W. P. Brown, J. K. Delaney, M. Palmer, W. S. Warren, M. C. Fischer, Femtosecond pump-probe microscopy generates virtual cross-sections in historic artwork. Proc. Natl. Acad. Sci. U.S.A. 111, 1708–1713 (2014).

12.   J. Dik, K. Janssens, G. Van der Snickt, L. van Der Loeff, K. Rickers, M. Cotte, Visualization of a lost painting by Vincent van Gogh using synchrotron radiation based X-ray fluorescence elemental mapping. Anal. Chem. 80, 6436–6442 (2008).

13.   K. A. Dooley, D. M. Conover, L. D. Glinsman, J. K. Delaney, Complementary standoff chemical imaging to map and identify artist materials in an early Italian Renaissance panel painting. Angew. Chem. Int. Edit. 53, 13775–13779 (2014).

14.   K. A. Dooley, E. M. Gifford, A. van Loon, P. Noble, J. G. Zeibel, D. M. Conover, M. Alfeld, G. Van der Snickt, S. Legrand, K. Janssens, J. Dik, J. K. Delaney, Separating two painting campaigns in *Saul and David*, attributed to Rembrandt, using macroscale reflectance and XRF imaging spectroscopies and microscale paint analysis. Herit. Sci. 6, 46 (2018).

15. S. A. Centeno, C. Hale, F. Carò, A. Cesaratto, N. Shibayama, J. K. Delaney, K. A. Dooley, G. Van der Snickt, K. Janssens, S. A. Stein, Van Gogh's Irises and Roses: The contribution of chemical analyses and imaging to the assessment of color changes in the red lake pigments. Herit. Sci. 5, 18 (2017).

16. G. Van der Snickt, S. Legrand, I. Slama, E. Van Zuien, G. Gruber, K. Van der Stighelen, L. Klaassen, E. Oberthaler, K. Janssens, In situ Macro X-ray fluorescence (MA-XRF) scanning as a non-invasive tool to probe for subsurface modifications in paintings by P.P. Rubens. Microchem. J. 138, 238–245 (2018).

17. K. Janssens, G. Van der Snickt, M. Alfeld, P. Noble, A. van Loon, J. Delaney, D. Conover, J. Zeibel, J. Dik, Rembrandt's 'Saul and David' (c. 1652): Use of multiple types of smalt evidenced by means of non-destructive imaging. Microchem J. 126, 515–523 (2016).

18. J. K. Delaney, D. M. Conover, K. A. Dooley, L. Glinsman, K. Janssens, M. Loew, Integrated X-ray fluorescence and diffuse visible-to-near-infrared reflectance scanner for standoff elemental and molecular spectroscopic imaging of paints and works on paper. Herit. Sci., 6, 31 (2018).

19. H. Dubois, The Art of conservation XV. The conservation history of the Ghent Altarpiece. Burlingt. Mag. 160, 754–765 (2018).

20. G. Van der Snickt, H. Dubois, J. Sanyova, S. Legrand, A. Coudray, C. Glaude, M. Postec, P. Van Espen, K. Janssens, Large-Area elemental imaging reveals Van Eyck's original paint layers on the Ghent Altarpiece (1432), rescoping its conservation treatment. Angew. Chem. Int. Ed. Engl. 56, 4797–4801 (2017).

21. H. Dubois, Letter to the editor. Burlingt. Mag. 160, 812 (2018).

22. E. M. Gifford, C. A. Metzger, J. K. Delaney, Jan van Eyck's annunciation. Painting materials and techniques, in Facture: Conservation, Science, Art History, D. Barbour, E. M. Gifford, Eds. (National Gallery of Art, 2013), vol. 1, pp. 128–53.

23. R. Billinge, Examining Van Eyck's underdrawings, in Investigating Van Eyck, S. Foister, S. Jones, D. Cool, Eds. (Brepols, 2000), pp. 83–96.

24. T. Holger-Borchert, K. Jonckheere, M. Martens, D. Praet, P. Schmidt. Debat: Het onthulde Lam Gods, panel discussion, in Ghent Altarpiece Second International Study Day (September 11, 2018).

25. J. R. J. Van Asperen De Boer, A scientific re-examination of the Ghent Altarpiece. Oud Holland 93, 141–214 (1979).

26. M. Martens, The creators. The role of Hubert and Jan van Eyck in the Ghent Altarpiece in The Ghent altarpiece: Van Eyck: Art, History, Science and Religion, D. Praet, M. Martens, Eds. (Hannibal, 2019), pp. 116–137.

27. M. Alfeld, K. Janssens, J. Dik, W. de Nolf, G. van der Snickt, Optimization of mobile scanning macro-XRF systems for the in situ investigation of historical paintings. J. Anal. At. Spectrom 26, 899–909 (2011).

28. P. Van Espen, K. Janssens, J. Nobels, AXIL-PC, software for the analysis of complex X-ray spectra. Chemometrics Intell. Lab. Syst. 1, 109–114 (1986).

29.   M. Alfeld, K. Janssens, Strategies for processing mega-pixel X-ray fluorescence hyperspectral data: A case study on a version of Caravaggio's painting *Supper at Emmaus*. J. Anal. At. Spectrom 30, 777–789 (2015).
30.   D. M. Conover, J. K. Delaney, M. H. Loew, Automatic registration and mosaicking of technical images of Old Master paintings. Appl. Phys. A 119, 1567–1575 (2015).

Chapter 5 **Leaded and stained-glass windows**

Although they scintillate and create mysterious spectacles under the right illumination conditions, stained-glass windows rarely receive similar attention as many other types of art.

In the first article the possible detection by means of MA-XRF of multiple 'painting' techniques applied by master stained-glass artists is discussed.

The possibility to differentiate between multiple batches/types of glass by applying semi-quantitative correlation bi-plots is discussed in the second paper. This is important because most historical panels nowadays include replacement inserts from other panels/periods.

The last paper discusses the application of MA-XRF scanning in a real restoration case as a time-efficient method to document the stained-glass window and as a technique to simultaneously provide chemical information on the objects' composition.

This chapter is a modified version of three published papers, adapted with permission from:

- J. Caen, S. Legrand, G. Van der Snickt, K. Janssens, "Macro X-ray fluorescence (MA-XRF) scanning: a new and efficient method for documenting stained-glass panels", Stained-glass: how to take care of a fragile heritage?, Paris, 8-10 July 2015, Paris, **2015**, pp. 74-81. Copyright 2015 ICOMOS France
- G. Van der Snickt, S. Legrand, J. Caen, F. Vanmeert, M. Alfeld, K. Janssens, "Chemical imaging of stained-glass windows by means of macro X-ray fluorescence (MA-XRF) scanning", *Microchemical Journal,* 124, **2016**, 615-622, 10.1016/j.microc.2015.10.010. Copyright 2016 Elsevier B.V.
- S. Legrand, G. Van der Snickt, S. Cagno, J. Caen, K. Janssens, "MA-XRF imaging as a tool to characterize the 16th century heraldic stained-glass panels in Ghent Saint Bavo Cathedral", *Journal of Cultural Heritage,* 40, 2**019**, 163-168, 10.1016/j.culher.2019.06.003. Copyright 2019 Elsevier B.V.

5.1 Macro X-ray fluorescence (MA-XRF) scanning: a new and efficient method for documenting stained-glass panels

Adapted from: J. Caen, S. Legrand, G. Van der Snickt, K. Janssens, "Macro X-ray fluorescence (MA-XRF) scanning: a new and efficient method for documenting stained-glass panels", Stained-glass: how to take care of a fragile heritage?, Paris, 8-10 July 2015, Paris, **2015**, pp. 74-81,

Abstract

In this work, we present MA-XRF scanning as an efficient spectroscopic imaging technique for stained-glass panels, allowing the simultaneous distinction of different types of glass within the same glass panel and the documentation of defects and past interventions through the collection of chemical data from the entire panel. After data processing, the results from chemical imaging are presented as a series of images, each visualizing the distribution of a chemical element. This visual way of presenting chemical data allows straightforward interpretation by conservator-restorers and art historians. From a more practical point of view, the images can also serve as working diagrams in condition and dating reports. The potential of the technique is illustrated by contrasting the results obtained on two glass panels dating from the 15th and 17th century, two different stylistic and technological eras.

5.1.1 Introduction

5.1.1.1 *Analytical technique*

Macroscopic X-ray fluorescence analysis is a non-destructive method of imaging analysis that results in a series of elemental distribution maps of the (flat) artefact examined. A mobile MA-XRF scanning instrument was developed in 2008. Since then, the elemental maps has led to new insights about the studio practice of key artists such as Jan Van Eyck, Hans Memling, Peter Paul Rubens, Vincent van Gogh, etc. (Alfeld and others 2011, p. 899; Alfeld and others 20131, pp. 165-175; Alfeld and others 2013-2, pp. 40-51) and the genesis, build-up and/or state of conservation of several of their iconic paintings. In this paper we present Macro X-ray fluorescence scanning as an efficient and effective spectroscopic imaging technique for stained-glass panels.

The first stage in every conservation process of stained-glass windows is a thorough technical examination of all components of the artefact, such as the substrate glass of the panels, the glass paints and the lead cames. This labor-intensive investigation is typically executed by means of a visual and microscopic study accompanied by photographic documentation. The collected information is subsequently translated into full size and scale diagrams of the panels for the ensuing condition report. In a limited number of high-profile cases, this descriptive research is complemented with chemical analyses, typically when an elucidation of ongoing deterioration processes is looked for.

Traditionally, spectroscopic measurements are performed on glass samples (e.g. by means of scanning electron microscopy equipped with energy-dispersive X-ray analysis [SEM-EDX], laser ablation inductively coupled plasma mass spectrometry [LA-ICPMS], etc.). These invasive investigations are aimed towards gaining information on the composition and types of glass and the applied paints, predominantly for dating and provenance purposes, but also the condition and former interventions on the glass panels are of interest. While such analyses are considered to be highly valuable for both treatment and preventive conservation, spectroscopic investigations (e.g. by SEM-EDS) are not carried out on a routine basis for a number of reasons.

Analytical techniques are not always promptly available or their implementation is not feasible within the delimited timeframe of a conservation campaign as spectroscopic analysis is both time and money consuming. Other aspects that restrain spectroscopic analyses are the necessity to extract samples and the fact that data is harvested only from a limited number of locations on the artifact. Although analytical measurements on cross-sectioned samples provide highly detailed information on the condition, type and alteration of glass and glass paints, the ensuing data only relate to a limited number of small areas. A distinct advantage of this approach is that quantitative composition data on the glass can be obtained that may be compared to data present in databases of historical glass of various periods. Apart from that, the destructive aspect of the extraction of samples can be disputed from a deontological point of view.

In contrast, MA-XRF scanning allows recording compositional data in a non-destructive way that is representative for the entire object under examination. This data can be presented in distribution images, which are interpretable by a larger public than the spectra resulting from classical spectrometric techniques. For that reason, the capability of MA-XRF scanning to differentiate between several compositional types of glass panes within the same panel is assessed in this paper. The results obtained from two panels from different technological eras are discussed: an anonymous 15th century panel from England, and a 17th century panel by Jan de Caumont from Leuven (present-day Flemish-Brabant, Belgium). Nevertheless, in comparison to the more established techniques, some limitations are associated with this new method. In the next few paragraphs, the potential and limitations of MA-XRF scanning is assessed by interpretation of the ensuing elemental distribution maps. For this purpose, the discussion primarily focuses on the maps that provide insights about aspects and characteristics of the windows that cannot be readily seen with the naked eye. This discussion is qualitative in nature; the quantitative aspects of MA-XRF and its (dis) advantages are beyond the scope of this paper.

5.1.1.2 *The Studied Panels*
The first panel (figure 1A) depicts St Matthew and was dated as an early 15th century window, based on stylistic grounds and morphological aspects of the glass. Similar panels

can still be found in English (Lincolnshire) churches and halls, as for example in Boston (Guildhall), Heydour (Church of St Michael) and North Somercotes (Locksley Hall) (Hebgin-Barnes 1996, pp. 41-49, 120-124 and 201-206). The examined panel is currently in a private collection in Belgium and underwent a conservation treatment in 2011.

The depicted saint was identified as St Matthew on the basis of his martyr attributes : a book and an axe. In this panel we see the saint as a middle-aged man with a beard wearing a blue, ochre lined, coat over a red tunic. He is standing on a tiled floor in front of a background with a floral pattern. Left and right we see two thin pillars. The glass pane composition and glass painting of this small panel (55 x 37 cm²) is executed rather clumsily and in a popular style. Besides colourless glass, a limited range of colored glass has been used: red, blue and ochre yellow. Vitreous paints have been used on both sides of the glass, as well as silver stain on the exterior side. All historical glass panes show severe weathering on both sides and also the trace lines and shades are very deteriorated.

Figure 1: – The studied glass panels from the collection J. M. A. Caen, Schoten, Belgium. **1A**: *St Matthew, England, early 15th century.* **1B**: *The Arrest of King Zedekiah, Brabant (Leuven), by Jan de Caumont (c. 1580-1659).* **1C**: *the MA-XRF instrument of the University of Antwerp during scanning of The Arrest of King Zedekiah.*

In contrast with the serene and unpretentious composition of the St. Matthew window, the second panel (figure 1B) of interest shows a lively and more intricate composition depicting the Arrest of King Zedekiah (Jeremiah 52, 6-10). The iconography shows the Babylonian troops chasing King Zedekiah and capturing him on the plains of Jericho. This panel is attributed to Jan de Caumont (c. 1580-1659), a glass painter based in Leuven who is well known for his cycle of monumental windows at the cloisters of the Park Abbey in

Heverlee (Leuven, present-day Flemish-Brabant, Belgium) (Van de Velde 1986, p. 95 and pp. 110-111). This panel can be dated in the second quarter of the 17th century and was probably made for a charterhouse in the Duchy of Brabant. Panels by the same glass painter and most likely from the same series can currently be found in Chelsea Old Church, London and St Mary the Virgin, Prittlewell (C. Berserik 2015, oral information). At present, the panel is part of the same Belgian private collection; it underwent a conservation treatment in 2012.

The Old Testament story is depicted in a very picturesque and colourful way and the panel is therefore a good example of the glass painting style commonly described as 'peinture en apprêt'. This technique is typical for the 17th century and can briefly be described as 'painting with colours on glass' instead of 'painting with coloured glass'. As a result, this somewhat larger panel (c. 48 x 71 cm²) contains mainly clear glass panes, supplemented with just a few coloured glass panes. Of particular interest is the extended range of the glass paints employed: vitreous paint on both sides, blue, blue-green and purple enamel on the interior side, two shades of silver stain on the exterior side, opaque sanguine on the interior side and translucent sanguine on the exterior side. A limited number of pieces show slight glass corrosion and slight weathering of the glass paints. Some later infillings were discerned with the naked eye by one of the authors.

5.1.2 Experimental

All stained-glass panels were analyzed in reflection mode by means of the MA-XRF scanning instrument (figure 1C) built within the AXES group of the University of Antwerp. The instrument employed is a variant of the setup described in Alfeld 2011, Alfeld 2013-1 and Alfeld 2013-2, which is capable of imaging the distribution of chemical elements present at the percentage concentration level using dwell times of less than 1 s per point. In particular, the scanner consists of an XRF measurement head mounted on a software controlled X-Y motor stage with a travel range of 57 x 60 cm² (h x v). The measurement head is equipped with two Vortex EX-90 SDD detectors that are positioned in a 20° angle with respect to the incident X-ray beam. The X-ray source is a compact 10-W Rh anode transmission tube (Moxtek, UT, USA) operated at 45 kV and 200 µA. The diameter of the primary beam was reduced by implementing a 0.8 mm lead pinhole collimator. MA-XRF scans were performed by sweeping the measuring head systematically over the glass surface, respecting a stable distance of c. 1.5 cm in between the edge of the measuring head and the panel. XRF spectra were recorded every 850 µm (step size) with a dwell time of 200 ms for each spectrum. Use of these parameters result in a total scan time of 20 hours per 1/2 m². The ensuing spectral data set was processed employing a combination of the PyMca (Solé and others 2007, pp. 63-68) and Datamuncher software packages (Alfeld and Janssens 2015, pp. 777-789). The results of this datatreatment are shown as elemental distribution images. In each pixel of these images, the intensity-value is related to the registered intensity of the element of interest at the corresponding location. For each elemental distribution, these intensities are scaled between the lowest

and highest intensity. As a result, two points in different scans with a similar composition can have a different grey value. Each glass panel was examined at both the interior and exterior sides with the aim of contrasting the resulting distribution maps stemming from both sides of the glass panes. The images recorded from the exterior side are always presented in mirror view, in order to facilitate interpretation.

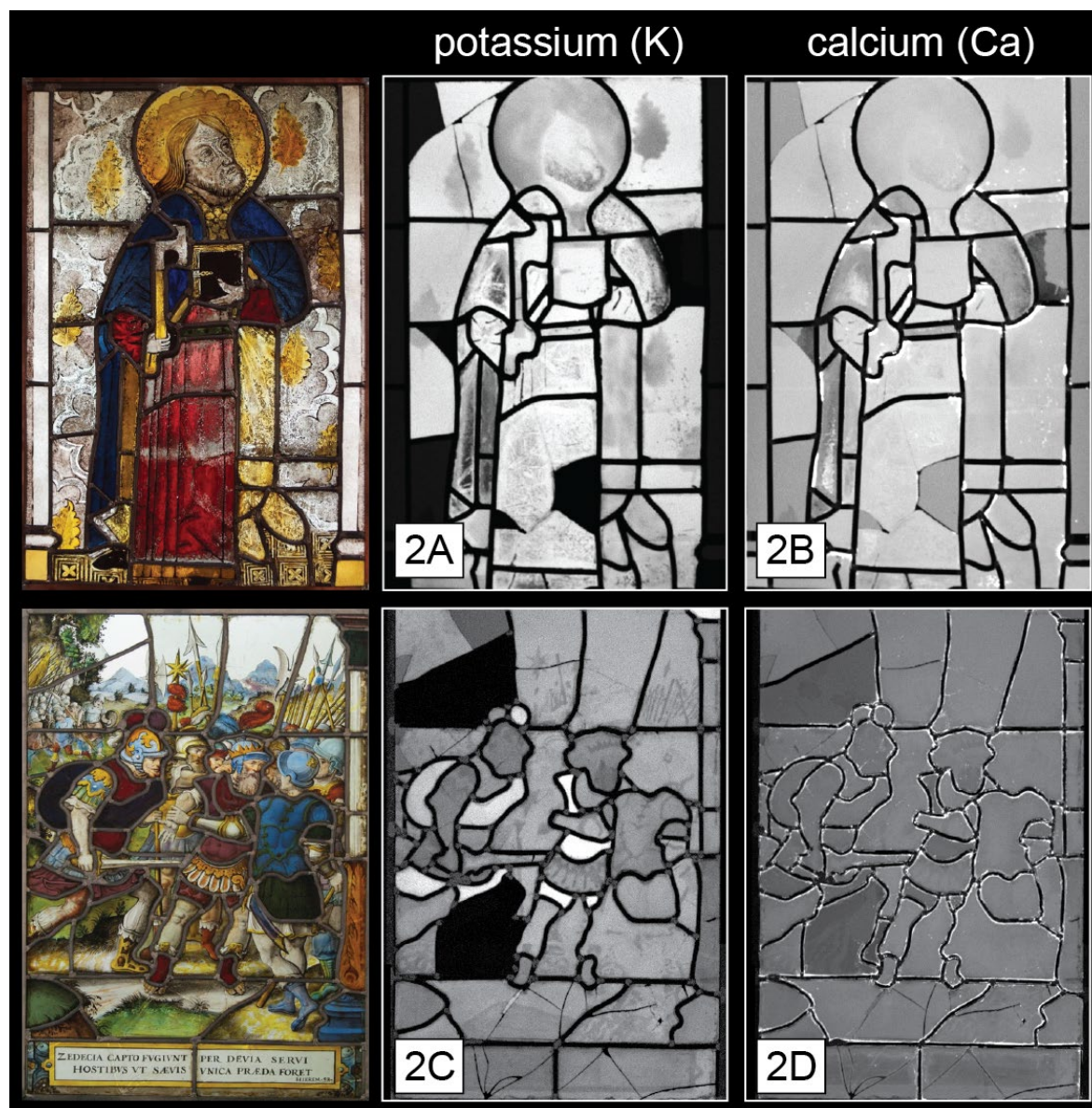
*Figure 2: – Elemental distribution images of potassium (**2A** and **2C**) and calcium (**2B** and **2D**) recorded on the exterior side of the St Matthew (**top row**) and Zedekiah (**bottom row**) panels by means of MA-XRF scanning. A lighter grey tone indicates a higher XRF intensity of the corresponding element. Modern infillings clearly show up as black areas (low in K) in the K images.*

5.1.3 Results and discussion

5.1.3.1 *Glass Composition*

Typical elements of interest are Na, K and Ca for distinguishing different types of glass (soda, potash glass, high lime - low alkali, etc.). These three elements relate to the fluxing agents and network stabilizers in the glass and are thus of special interest for distinguishing different glass types.

As the MA-XRF experiments are performed in ambient air, the low energy fluorescence radiation emitted by the low Z elements in the glass, such as Na (1.04 keV) is readily absorbed by the air path on the way to the detector. In spite of the fact that Na cannot be detected, the K distribution map collected from the exterior side of the St. Matthew window allowed differentiating between the original (late) medieval glass panes that are rich in potassium and the modern (soda-based, potassium poor) panes that were inserted during the conservation treatment in 2011. As figure 2A illustrates, the historical panes display white to light grey-values in the elemental map, indicative of a relatively high K intensity, while the modern infillings show up as dark/black areas, poor in K. A striking example of this is the large, central, fragmented glass piece in the middle of the red cloak of the saint, where two modern glass pieces were inserted in the broken pane to complement the lacunae. Additionally, a similar, but more subtle pattern can be discerned in the Ca-map (figure 2B). Figures 2C and 2D demonstrate how the modern infillings can be distinguished in an identical way in the King Zedekiah window.

Interestingly, both in the St Matthew and the King Zedekiah window, the images suggest a variation in the Ca- and K-abundance in a number of original, coloured glass panes. In particular, for the St Matthew window, the blue glass of the saint's coat exhibits a lower K- and Ca-content. For King Zedekiah, this is the case for the dark blue and purple glass panes in the clothing of the soldier stabbing Zedekiah with his sword and the purple glass of the latter. This result suggests that a different type of substrate glass was used for manufacturing specific colours (see also the next paragraph on colouring).

A firmer discrimination can be achieved by plotting against each other the net intensities of two trace elements respectively associated with potassium and calcium-rich glass: rubidium and strontium. Figure 3C shows how 'clouds' of points, each corresponding to individual measurement at one particular position on the panel, become apparent in the scatter plot. These groups are indicative of different rubidium (Rb) – strontium (Sr) concentration ratios present in the material in their turn, these ratios reflect variations in the glass composition. In figure 3C, three groups are indicated and plotted back onto a distribution image of the panel in order to facilitate interpretation. The coloured groups clearly relate to distinct groups of glass panes and signal the presence of different types of glass. Interestingly, the blue- and red-labelled group match the red and blue colored glass respectively, while the green group agrees with the colorless, historical glass.

Compared with the evaluation by the naked eye and optical microscope, one blue glass pane of the coat, situated at the right, was assessed as being the same glass as the other panes of the blue coat. Examination with MA-XRF suggests that the piece has to be related with the clear-glass panes. Most likely the blue glass pane originates from another glass sheet (made of another glass batch) or that one piece is an old reconstruction. This is a very clear example how our assessment with the naked eye can be biased and how MA-XRF can contribute to a more correct/unbiased interpretation and dating of the separate glass panes.
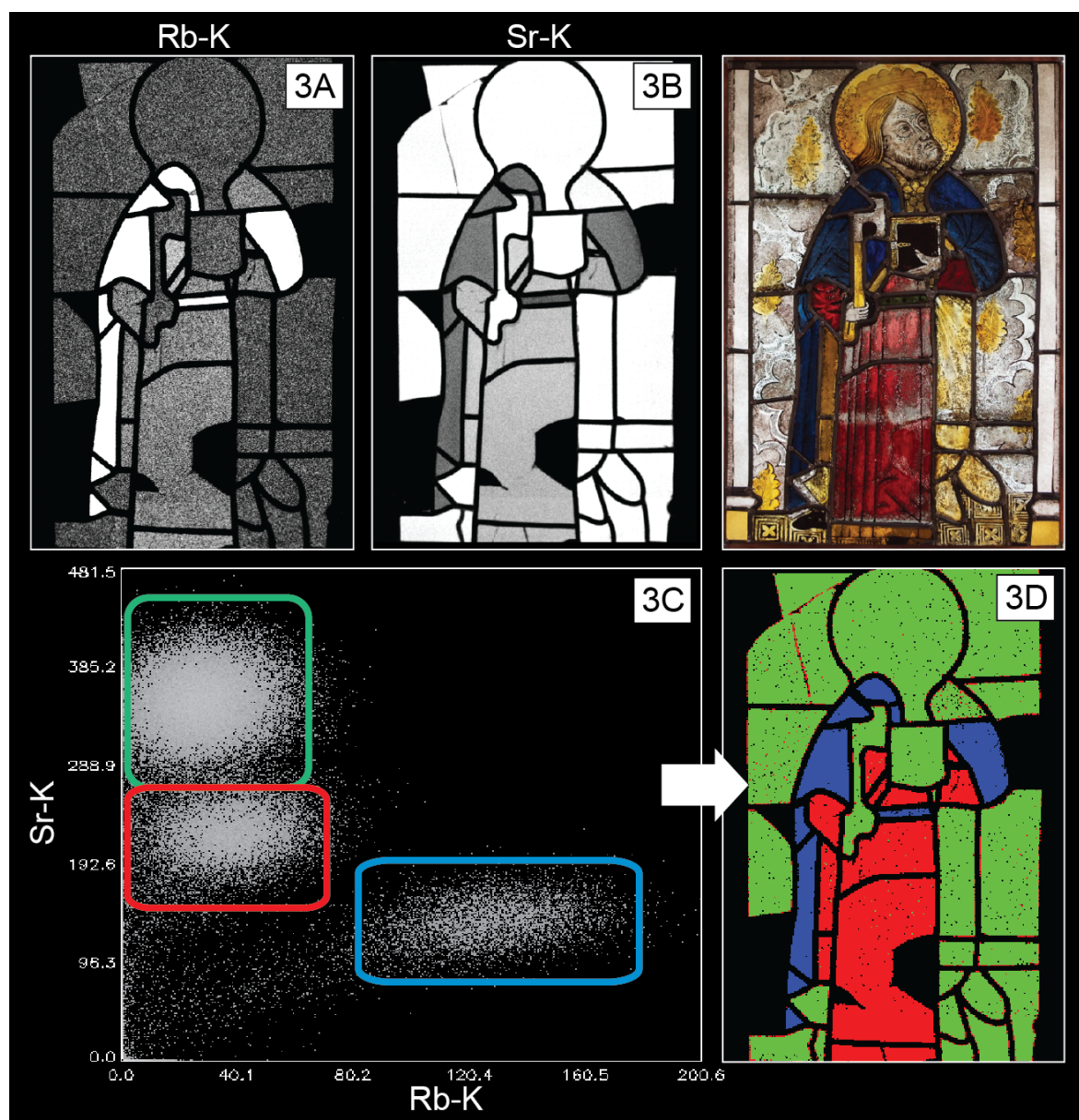

*Figure 3: – Elemental distribution of rubidium (**3A**) and strontium (**3B**) recorded on the exterior side of the St Matthew window. **3C**: scatter plot showing the net intensities of the detected Rb versus Sr XRF intensities. The three coloured rectangles indicate three groups of data points with similar rubidium (Rb-K) – strontium*

(Sr-K) intensity ratios. **3D**: *colouring of the positions belonging to the three groups on the panel allows distinguishing three historical glass types; the black areas correspond to modern infilling panes.*

5.1.3.2 *Colored glass: Pot Metal versus Flashed Glass*

It can be difficult to distinguish flashed (or marbled glass) from pot metal glass by visual inspection, especially when the glass pieces cannot be removed from the enveloping lead cames. However, scanning the glass panels from both the interior and the exterior side and a comparison of the ensuing analytical results allow for a straightforward differentiation. It is possible to determine the presence of pot metal glass panes with quite high confidence when the colouring metals (e.g., Cu, Co, *etc*.) show similar XRF intensities on both sides of the glass. For instance, blue glass is typically produced by introducing Co^{2+} ions into the batch. As a result, blue glass pieces are expected to show up in the distribution map of Co; this is the case for the blue coat of St Matthew, as illustrated by figure 4A. Moreover, the Co-signal is visible in the maps acquired both from the exterior (figure 4A) and the interior side (figure 4B) where the Co-signal in the bulk glass is outshined by the more intense Co-signals in the touched up areas. This outcome specifies that the glass is coloured throughout its entire thickness and thus of the pot metal type, as illustrated by the scheme in figure 4C. Please note that touching up with, among others, a blue Co-pigment was applied on the interior side of the window; these areas show up as well in figure 4B and largely correspond with the modern infillings that can be discerned as black areas in figure 2A.

In contrast, red glass is often manufactured by applying a thin layer of Cu-based red glass on top of clear substrate glass (flashed glass, see figure 4F). This layered structure is also detectable by comparison of the MA-XRF images of Cu corresponding to the interior and exterior side. Cu responsible for the red colour, was detected in the red glass panes on the interior side of the panel (figure 4E), while the same element appears to be absent in the same panes in the exterior map (figure 4D). Red is the most common known type of flashed glass, but more sophisticated glass stratigraphies and mixtures were produced as well in order to obtain deviating hues. For example in the King Zedekiah window, the dark blue glass pieces in the soldier's kit on the left are poorer in K than the rest of the original glass pieces. The Mn- and Co-maps (figure 5) indicate that these blue panes are rich in manganese on the exterior side, while rich in Co on the inside. This suggests a buildup of thin layers of Mn-red and Co-blue (flashed or marbled type) glass. Manganese is present as well in the purplish glass panes (also low in K), but this appears to be of the pot metal type.
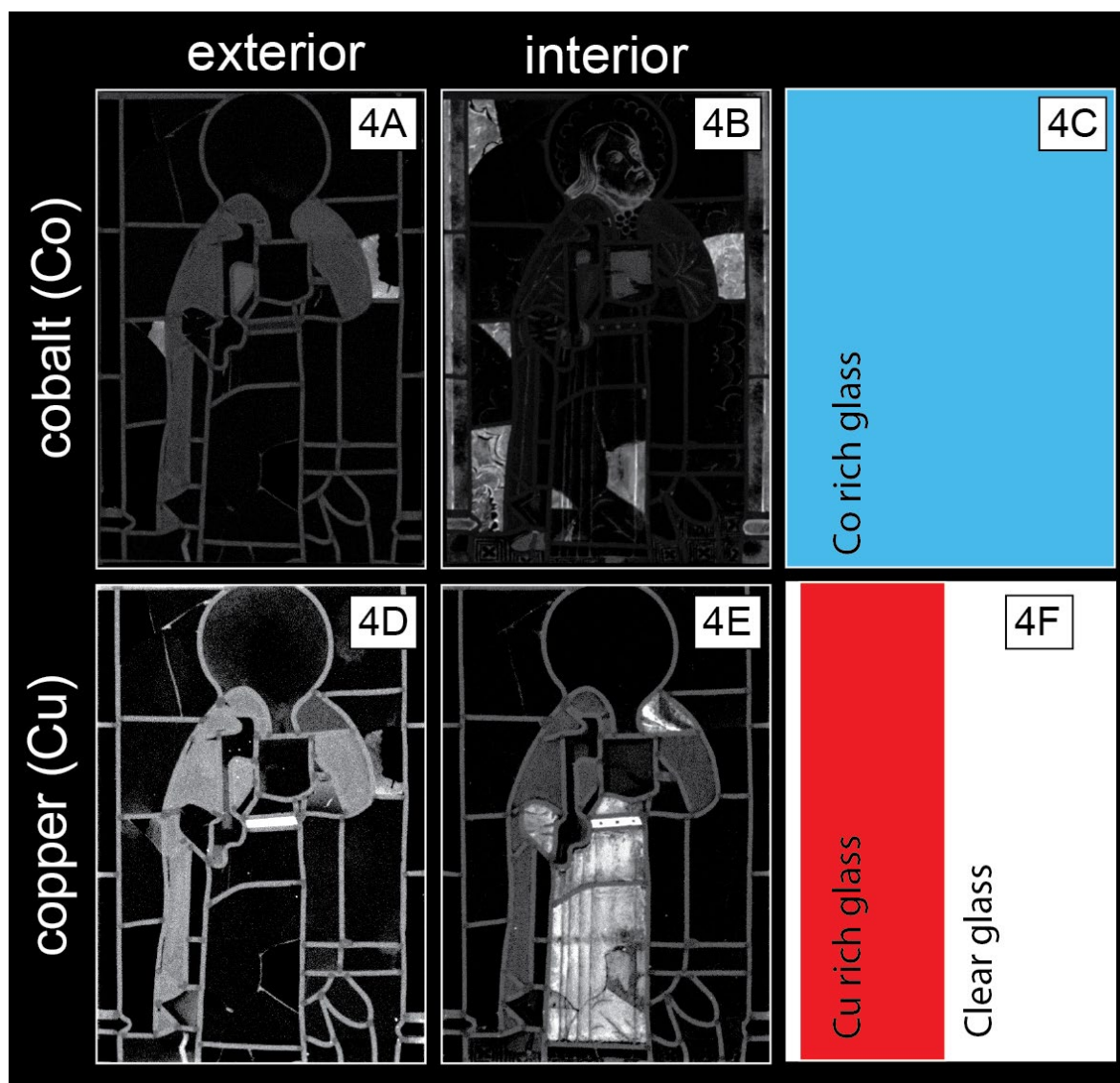
*Figure 4: – Elemental distribution images recorded on the exterior and interior side of the St Matthew panel revealing the coloring technique for the blue and red glass panes. **4A**: cobalt (Co-K, exterior). **4B**: cobalt (Co-K, interior). **4C**: cross-section scheme of blue pot metal glass. **4D**: copper (Cu-K, exterior). **4E**: copper (Cu-K, interior). **4F**: cross-section scheme of red flashed glass.*

5.1.3.3 *Tracelines and Shades*

Most glass panes were decorated with vitreous paints (grisaille) in order to realize trace lines and shades. These paints are made of a lead-rich glassy medium (figure 5C) containing metal oxides to colour the paint and to increase its opacity. Brown paints are typically obtained with Fe-oxide (figure 6D), while black paints are frequently prepared using Cu-oxides (figure 6E); often, Fe- and Cu-oxide mixtures are found (Caen 2009, pp. 251-254). Recipes with Mn-oxides are reported as well during the 16th and 17th century, resulting in more reddish paints, but this element has not been found in the panels studied. The scans show that grisaille paints were predominantly applied on the interior

side, but scanning clearly showed the presence of some shading on the backside of the glass panes as well. Although trace lines and shades can quite easily be seen by the naked eye, the MA-XRF scans yielded qualitative information on the composition of these paints as illustrated by figures 6A, 6B, 6D and 6E.
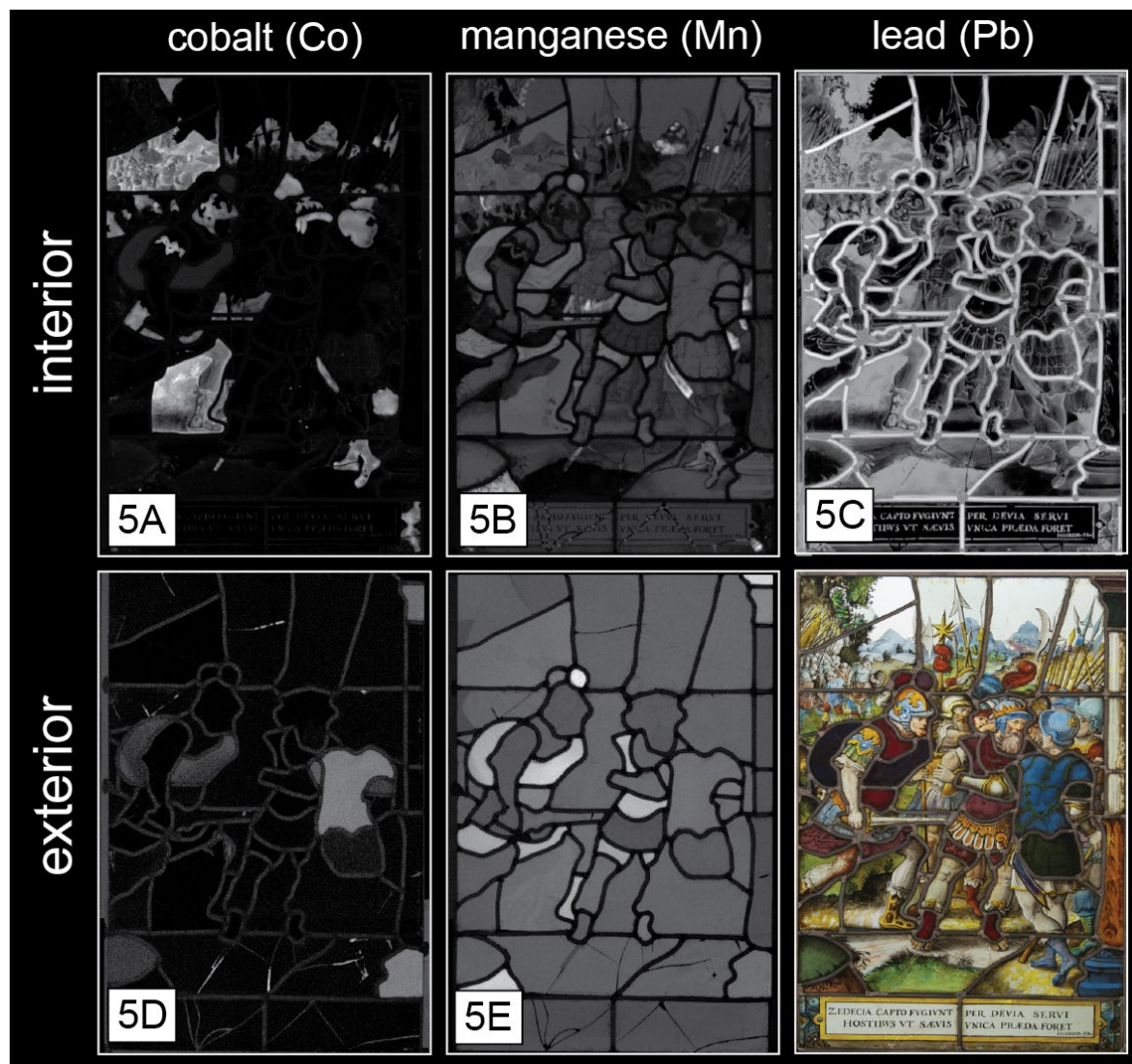
Figure 5: – Elemental distribution maps of cobalt and manganese recorded on the Zedekiah window from the interior (5A and 5B) and exterior side (5D and 5E). Comparison of interior and exterior maps allow distinguishing pot metal from flashed glass. The purplish glass of King Zedekiah is rich in Mn from both sides (5B and 5E) indicative of pot metal glass. In contrast, the soldier's kit on the left is rich in Mn on the exterior side (5E) and rich in Co on the interior side (5A), suggesting a layered structure. Please note that Mn-based purple enamel shows up in 5B as well. 5C: lead is present in the lead cames and as fluxing agent in the various vitreous paints applied on the interior side.
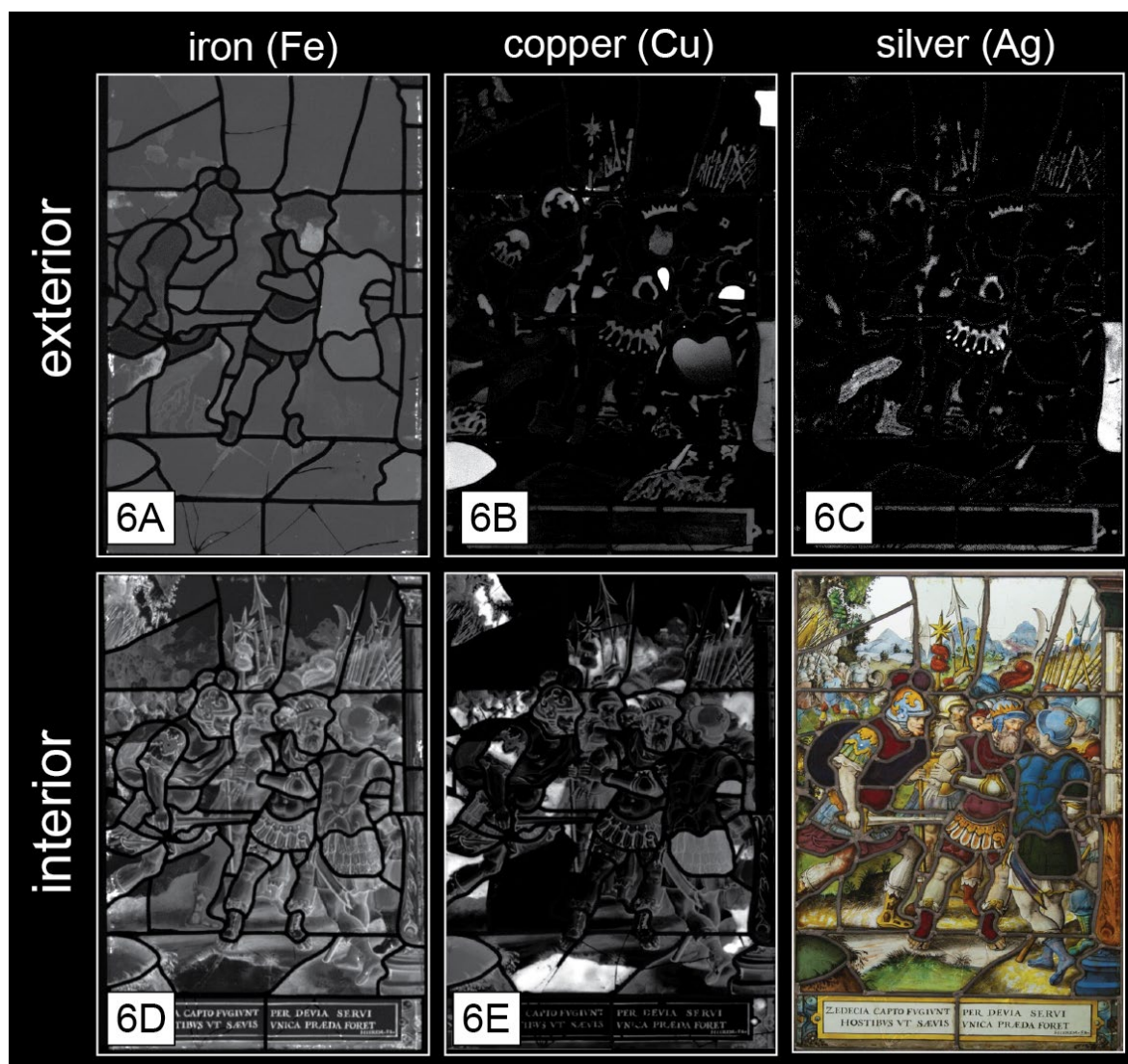
*Figure 6: – Elemental distribution maps of iron (**6A** and **6D**), copper (**6B** and **6E**) and silver (**6C**) recorded on the Zedekiah window from the interior and exterior side. 6B illustrates the abundant use of vitreous paints on the interior side, while **6A** demonstrates that a Fe-based paint was used to realize details on the exterior side. Green-blue enamels and green pot metal glass show up in the Cu image as well. **6C** visualizes the presence of silver stain whereas comparison with **6B** establishes that this paint contains copper salts as well.*

5.1.3.4 *Silver Stain*

Yellow colors can be obtained either by pot metal glass or the application of silver stain on the exterior side of glass panes. This distinction can be simply made with the naked eye, but the Ag-ions from the silver stain that diffuse in the glass matrix during firing, show up in the Ag-map as well (figure 6C). However, the previously documented ion exchange between K and Ag at the glass surface (De Vis 2000), causes a disturbance in the K-distribution image, collected on the exterior side. As shown in figure 2C, the potassium shows a distinct decrease in intensity in the areas where silver stain was applied (see figure 6C). Nevertheless, the most striking outcome concerning the silver stain was the

finding that silver salts have been combined with copper salts in the King Zedekiah window. This combination is sporadically found in stained-glass since the 16th century, resulting in yellow stains with a warmer orange to brownish colour (De Vis 2000, pp. 104-113). This insight becomes clear when comparing the Cu- and Ag-maps in figures 6B and 6C collected from the exterior side on the King Zedekiah panel.

5.1.3.5 *Enamels*

The first evidence of the use of enamels in the Low Countries dates from the last quarter of the 15th century. In spite of some initial hesitation within the guilds, these glass paints became very popular by the end of the 16th and especially during the 17th and 18th centuries (see above). (Caen 2009, pp. 255-258). During these centuries only three types were applied: blue enamel (based on Co-oxide); purple enamel (based on Mn-oxide) and blue-green enamel (based on Cu-oxide) (Van der Snickt 2006, Schalm 2009). All these enamels, even mixed among each other, have been found on the interior side of the King Zedekiah panel (figures 5D, 5E and 6E). Interesting is the clear distinction that can be made between blue Co-based enamel and blue-green (or blue-grey) Cu-based enamel. The green colours of the vegetation, on the other hand, were realized by combining Co-based enamel on one side with silver stain on the backside of the Zedekiah panel (figures 5D and 6C).

5.1.3.6 *Sanguine*

A special kind of Fe-based glass paint is sanguine. This red-brown paint existed in an opaque and translucent quality, depending on the size of coloring hematite particles. In windows in the Low Countries (initially in the County of Flanders) the paint has been applied as early as 1470, but sanguine is especially found on 17th century glass windows (Caen 2009, pp. 254-255). Usually, translucent sanguine is found on the backside of the glass panes and opaque sanguine on the interior side, but exceptions have been reported (Berserik-Caen 2007; 2011; 2014). In the King Zedekiah panel, translucent sanguine was identified on the exterior side and the use of opaque sanguine on the interior side by visual inspection and confirmed by the Fe-distribution in the maps, e.g. the beard of King Zedekiah (figure 6A).

5.1.3.7 *Glass Deterioration*

Weathering of the glass is often referred to as 'glass corrosion'. It is commonly known that salts such as metal carbonates and sulfates (gypsum, syngenite, etc.) are formed on the glass surface (Melcher and M. Schreiner, 2013, pp. 609-651). In the scanned deteriorated glass-surfaces of the St Matthew panel an increased level of calcium can be discerned in the craters of the pit corrosion (figures 7A and 7D).
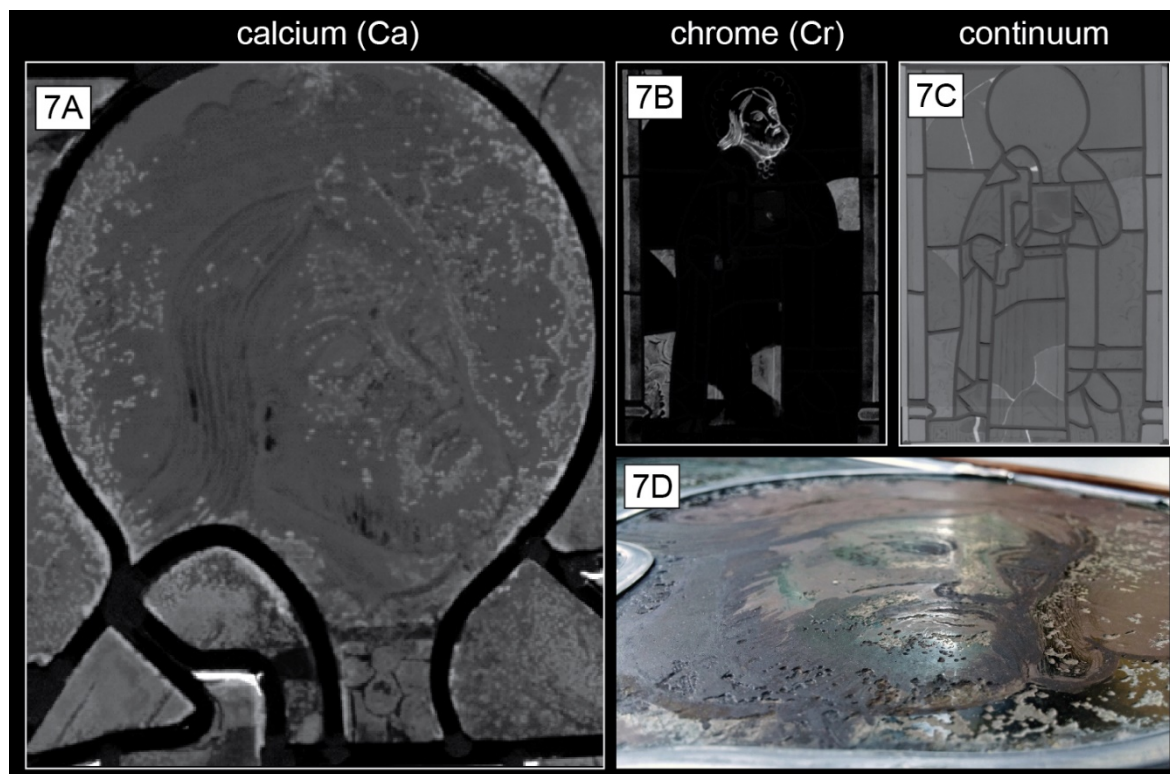
*Figure 7: – **7A**: detail of the Ca-map recorded on the head of St Matthew (interior side) reveals the pit corrosion pattern. **7B** shows the Cr signal from modern pigments used for touching up (interior side). **7C**: bonding material and modern infillings show up in the continuum image, based on divergent scattering of the incident X-rays. **7D**: detail picture of the head of St Matthew in raking light, demonstrating the pit corrosion.*

5.1.3.8 *Former Conservation Interventions*

Finally, MA-XRF maps also shed light on previous conservation interventions. Where touching up was executed with 'modern' pigments such as chrome greens, reds and/or yellows, these areas can be clearly observed in the corresponding elemental distributions. In the St Matthew panel we can clearly see evidence of the touching up of the head in the Cr-maps (figure 7B) collected from the interior side, while the areas where epoxy glue was used for bonding and infilling can be discerned in the continuum image. This map shows a high intensity at positions where low Z material efficiently backscatters the primary X-ray beam towards the XRF detector, contributing to the continuum background. As the organic glue scatters the primary X-rays to a greater extent than the glass matrix, its location is readily observed in figure 7C.

5.1.4 Conclusions

The discussion of the two case studies demonstrates how MA-XRF scanning of stained-glass panels supplies chemical information from the entire glass surface. MA-XRF turned out being a valuable technique for (a) distinguishing various glass panes with deviant compositions within the same panel, (b) characterizing glass paints and (c) documenting

deterioration propagation. In parallel, the same experiments allow supplying information on the presence of modern bonding materials (e.g. epoxy glues) and features that are difficult to discern with the naked eye such as the discrimination between deeply colored flashed glass and pot-metal glass. In this way, the scans can assist the dating and classification into distinct groups of glass panes and can be considered as a tool for benchmarking and correcting visual and microscopic observations.

During the last decades we have seen that documentation and reporting is taking more and more time and budget. The use of MA-XRF scanning in a systematic manner could generate more accurate reports in shorter time, leading in turn to a more efficient use of the available means as a function of hands-on conservation work. This scanning technique can be applied in situ, both in museums as in monuments, thus limiting costs and potential damage caused by transport and manipulations. In this way, we consider it likely that MA-XRF scanning will be able to contribute to a more efficient and cost-effective technical examination of stained-glass windows and will allow to intensify the collaboration between natural scientists and glass conservator-restorers and art historians in the near future.

References

Alfeld and others 2011: M. Alfeld and others, "Optimization of mobile scanning macro-XRF systems for the in situ investigation of historical paintings", J. Anal. At. Spectrom., v. 26, no. 5, 2011, pp. 899-909.

Alfeld and others 2013-1: M. Alfeld and others, "Scanning XRF investigation of a Flower Still Life and its underlying composition from the collection of the Kröller - Müller Museum", Appl Phys A, v. 111, no. 1, 2013, pp. 165-175.

Alfeld and others 2013-2: M. Alfeld and others, "Revealing hidden paint layers in oil paintings by means of scanning macro-XRF: a mockup study based on Rembrandt's *An old man in military costume*", J. Anal. At. Spectrom., v. 28, no. 1, 2013, pp. 40-51.

Alfeld and Janssens 2015: M. Alfeld and K. Janssens, "Strategies for processing mega-pixel X-ray fluorescence hyperspectral data: a case study on a version of Caravaggio's painting *Supper at Emmaus*", J. Anal. At. Spectrom., v. 30, 2015, pp. 777-789.

Berserik and Caen 2007; 2011; 2014: C.J. Berserik and J.M.A. Caen, "Silver-stained roundels and unipartite Panels before the French Revolution", Flanders, v. 1, Turnhout, 2007; v. 2, Turnhout, 2011; v. 3, Brussels, 2014.

Berserik 2015 C. Berserik, oral information, March 2015.

Caen 2009: J. M. A. Caen, "The Production of Stained-glass in the County of Flanders and the Duchy of Brabant from the XVth to the XVIIIth centuries: Materials and Techniques", Turnhout, Brepols, 2009.

De Vis 2000: K. De Vis, "De invloed van zilverzouten op de kleurintensiteit van zilvergeel; een analytisch onderzoek", unpublished MA-dissertation, AP Hogeschool Antwerpen, Antwerp, 2000.

Hebin-Barnes 1996: P. Hebgin-Barnes, "The Medieval Stained-glass of the County of Lincolnshire", Corpus Vitrearum Great Britain Summary Catalogue 3 Lincolnshire, Oxford, 1996.

Schalm and others 2009: O. Schalm and others, "Enamels in stained-glass windows: Preparation, chemical composition, microstructure and causes of deterioration". Spectrochimica Acta Part B: Atomic Spectroscopy, v. 64, no. 8, pp. 812-820, 2009, pp. 812-820.

Melcher and Schreiner 2013: M. Melcher and M. Schreiner, "Glass Degradation by Liquids and Atmospheric Agents", in K. Janssens, Modern Methods for Analysing Archeological and Historical Glass, Chichester, 2013, pp. 601-651.

Solé and others 2007: V. A. Solé and others, "A multiplatform code for the analysis of energy-dispersive X-ray fluorescence spectra", Spectrochim. Acta Part B, v. 62, no. 1, 2007, pp. 63-68.

Van de Velde 1986: C. Van de Velde, "17de eeuw", Gloed van Glas, exhibition catalogue, Brussels, 1986.

Van der Snickt 2006: G. Van der Snickt "Blue enamel on sixteenth- and seventeenth-century window glass - Deterioration, microstructure, composition and preparation." Studies in conservation, v. 51, no. 3, 2006, pp. 212-222.

5.2 Chemical imaging of stained-glass windows by means of macro X-ray fluorescence (MA-XRF) scanning

Abstract Since the recent development of a mobile setup, MA-XRF scanning proved a valuable tool for the non-invasive, technical study of paintings. In this work, the applicability of MA-XRF scanning for investigating stained-glass windows inside a conservation studio is assessed by analysis of a high-profile, well-studied late-mediaeval panel. Although accurate quantification of components is not feasible with this analytical imaging technique, plotting the detected intensities of K versus Ca in a scatter plot allowed distinguishing glass fragments of different compositional types within the same panel. In particular, clusters in the Ca/K correlation plot revealed the presence of two subtypes of potash glass and three subtypes of high lime low alkali glass. MA-XRF results proved consistent with previous quantitative SEM-EDX analysis on two samples and analytical-based theories on glass production in the Low Countries formulated in literature. A bi-plot of the intensities of the more energetic Rb–K versus Sr–K emission lines yielded a similar glass type differentiation and is here presented as suitable alternative in case the Ca/K signal ratio is affected by superimposed weathering crusts. Apart from identification of the chromophores responsible for the green, blue and red glass colors, contrasting the associated elemental distribution maps obtained on the exterior and interior side of the glass permitted discriminating between colored pot metal glass and multi-layered flashed glass as well. Finally, the benefit of obtaining compositional information from the entire surface, as opposed to point analysis, was illustrated by the discovery of what appears to be a green cobalt glass—a feature that was previously missed on this well-studied stained-glass window, both by connoisseurs and spectroscopic sample analysis.

5.2.1 Introduction

Within the last few years, the established synchrotron- and laboratory-based micro-XRF scanning technology was translated to a mobile instrument that allows performing in situ experiments on paintings on a macro scale [1–4]. The ability of MA-XRF scanning to visualize the distribution of elements detected at and just below the paint surface renders this spectrometric method particularly helpful for revealing hidden features such as pentimenti and overpainted compositions. Other relevant applications are the characterisation of painting materials or studio practice and the visualisation of discoloured pigments [5–7]. The main advance of this novel diagnostic method is twofold. First, compositional data is acquired from the entire paint surface by spectroscopic

analysis in a non-invasive way, as opposed to the more established point analysis on samples. Second, the outcome can be interpreted self-reliantly by art historical scholars, conservators and other non-XRF experts involved as the final result of a MA-XRF experiment does not consist in graphs or spectra, but in a set of (element-specific) images. Apart from the technological aspect, MA-XRF scanning received considerable attention because the ensuing chemical images proved pivotal arguments in the decision-making progress on (a) various art-historical and authentification issues and (b) the conservation treatment selection for iconic easel paintings [6–10].

In view of these developments, efforts are undertaken to extend the applicability of this innovative method to other types of two-dimensional objects. Experiments on illuminated manuscripts yielded promising results [11,12], while in this work we report the potential of MA-XRF scanning for studying stained-glass panels. In literature, a wide range of techniques have been surveyed for glass analysis, but most prevalent methods are XRF and scanning electron microscopy equipped with an energy dispersive X-ray detector (SEM-EDX) [13–15]. Both methods owe their popularity to the ability of detecting and quantifying a wide range of elements in a sensitive and efficient way [3,16]. A significant limitation associated with both techniques, and glass analysis in general, is the fact that it involves point measurements on samples. Collecting a consistent set of samples to address a specific research question can prove challenging for a number of reasons. Extraction of fragments can only be performed when windows are removed from their architectural setting, i.e. during a conservation treatment. Even during this limited time frame, sampling is usually highly restricted for deontological reasons as it is a particularly destructive process affecting all constituting elements of the panel (e.g. cutting up the lead came network). Apart from that, the representativeness of the ensuing results can be questioned as well since data is usually collected from only a few square mm^2, while stained-glass windows typically present surfaces of several square meters. A final disadvantage of conventional glass analysis lies in the relatively labour-intensive preparation of the samples, i.e. embedding and polishing. In response to these issues, a number of authors reported their efforts to perform point analysis directly on stained-glass panels [17–20]. In this work, we assess the potential of MA-XRF scanning for collecting compositional data from an entire glass panel inside a conservation studio and this in a non-invasive and comparatively resourceful way.

This paper focuses on the results obtained on an extraordinary late 15th century ensemble depicting Saint George and Saint Michael, shown in Fig. 1. Now part of the collection of the City Museum of Bruges (Belgium), the window was initially produced for the chapel of the Bruges guild of Saint Luke, patron of the painters and window makers. Scholars assume that the window functioned as a technical showcase for the guild. Interestingly, the end of the 15th century is considered as a period of technological transition in the Low Countries, marked by the arrival of Renaissance. The latter did not only imply that stained-glass windows started to look different from a stylistic point of view, the

evolution was also ushered by a double technological shift: glass was blown in a different way (from crown to cylinder technique) and the composition of the glass changed. In particular, the potash type was gradually abandoned in favour of what is often called 'High Lime Low Alkali' (HLLA) glass [21,22]. In essence, potash glass is sand with tree ashes added as a fluxing agent, while high lime low alkali glass is sand and tree ashes with introduction of an excess of lime to the melt, as network stabiliser. In view of these aspects, the panels were previously well-studied by connoisseurs and scientists [23–26]. In this framework, two samples were extracted and analysed by means of SEM-EDX as part of an earlier study [26]. Locations of samples M1 (clear glass) and M2 (blue glass) are indicated by means of arrows in Fig. 3. The corresponding quantified spectroscopic results presented in Table 1 can serve as a benchmark for the scanning results. As such, the panels were considered as a suitable case study for assessing the capability of MA-XRF scanning to study stained-glass windows inside a conservation studio.

Table 1: List with the concentrations of glass components in samples M1 and M2, as quantified by SEM-EDX. The sample locations are indicated in Fig. 3A.

SEM-EDX results (wt. %)		
Component	Sample M1: coloured glass	Sample M2: blue glass
Na_2O	1.4	2.3
MgO	6.7	4.0
Al_2O_3	1.1	1.6
SiO_2	55.0	52.8
P_2O_5	2.4	2.4
Cl	0.3	0.3
K_2O	14.1	6.7
CaO	17.0	27.5
MnO	1.2	1.4
Fe_2O_3	0.5	0.7
BaO	0.3	0.5

5.2.2 Experimental

5.2.2.1 *Measurement parameters*

The panel depicting Saint Michael was analysed in reflection mode by means of a MA-XRF scanning instrument (Fig. 1) that was developed within the AXES group of the University of Antwerp. This in-house device is a variant of the setup described by Alfeld et al [1] as 'Instrument B', including a compact 10 W Rh anode transmission tube (Moxtek, UT, USA) operated at 45 kV and 200 µA with an incident angle of 90° to the surface. Two Vortex EX-90 SDD detectors are positioned in a 65° detection angle with respect to the paint surface ($\vartheta 2$ in Fig. 2). The 50 mm^2 active area crystal of the detectors is 350 µm in thickness and thermoelectrically cooled to −70 °C, yielding an energy resolution of c. 170 eV at 5.9 keV (0.7 µs shaping time). X-ray photons enter the crystal via a 25 µm beryllium window. The

technical aspects of the setup, its geometry, components and spectral performances are described elsewhere [1]. The diameter of the diverging primary beam was reduced by implementing a 0.8-mm lead pinhole collimator. This XRF measurement head was mounted on a software controlled X–Y motor stage with a maximum travel range of 57 × 60 cm (h × v). MA-XRF scans were performed by sweeping the measuring head systematically over the glass surface. Careful positioning and alignment of the scanner ensured a stable distance of ca. 1.5 cm in between the snout and the panel. Retaining this void prevents fluctuation of the fluorescence signal attenuation by ambient air. During movement, XRF spectra were recorded every 850 μm (step size) with a dwell time of 200 ms for each spectrum. In this way, the panel of Saint Michael, measuring 57 × 58 cm², was measured in a single experiment (670 × 682 pixels) with a total scan time of c. 25 h (motor speed of c. 4 mm/s). The resulting spectral data cube was processed employing a combination of the PyMca [27] and Datamuncher software packages [28].
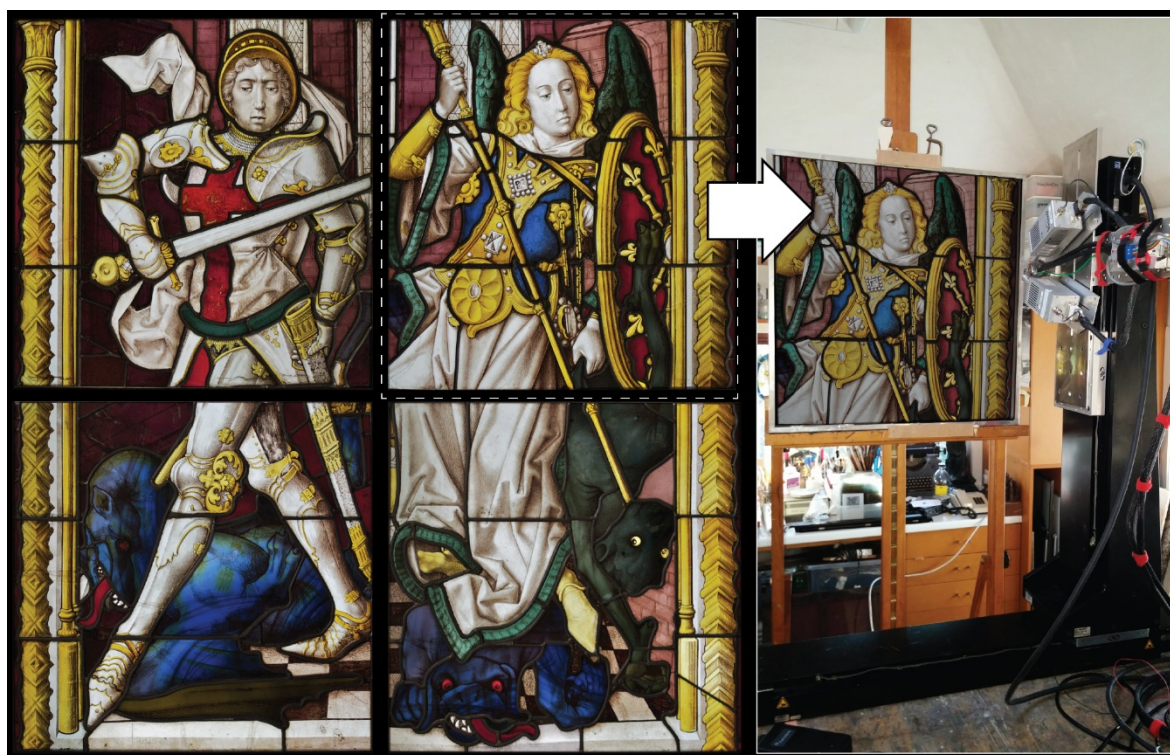
Figure 1: Stained-glass window from the collection of the City Museum of Bruges (inv. nrs. XXII.O.0081.A and B) showing Saint George on the left and Saint Michael on the right, dated c. 1490. The white rectangle indicates the panel that was analysed by means of an in-house built MA-XRF scanner, as shown on the right.

5.2.2.2 *Positioning of the measuring head: Interior versus exterior side*

Stained-glass panels resemble easel paintings in the sense that both are two dimensional and relatively flat objects with pictorial elements. Nevertheless, scanning experiments on windows necessitate a somewhat different approach as these contain pictorial and colouring elements on both the interior and exterior side. The scheme in Fig. 2, showing a

typical built-up of a stained-glass panel, illustrates that different information can be expected from scans obtained from the interior and exterior side. Hence, the position of the measuring head depends on the component that is the main subject of research. A concise review of literature reveals four key motives for glass analysis: (1) distinction of different compositional types of glass; (2) identification of the colouring metal oxides in the glass and its built-up (flashed vs. pot metal); (3) characterisation of assorted vitreous paints and (4) documentation and study of conservation problems (e.g. formation of corrosion crusts). Most technical papers focus on the discrimination of glass for provenance and dating purposes, a topic that is of particular interest to archaeologists, conservators and art-historians alike. It is habitually addressed by quantifying the network former (SiO_2), fluxing agents (Na_2O, K_2O, PbO), stabilizers (CaO) and various additives or contaminants of a corpus of samples, followed by statistical analysis of the resulting data sets [21,29]. By consequence, the potential of MA-XRF imaging for the study of stained-glass windows, will largely depend on its capability to discriminate glass types. The scheme in Fig. 2 indicates that the glass is best accessed from the exterior side for this purpose because the ensuing fluorescence spectra will be less disturbed by other superimposed components such as vitreous paints. Nevertheless, for this paper, the panel was scanned from both sides as contrasting the interior and exterior distribution maps gives rise to a more comprehensive overview of the constituent elements, as will become clear in the next few paragraphs.

Emission Line	$d_{99\%}$ (mm)
K-K_α	0.036
Ca-K_α	0.048
Rb-K_α	1.872
Sr-K_α	2.186
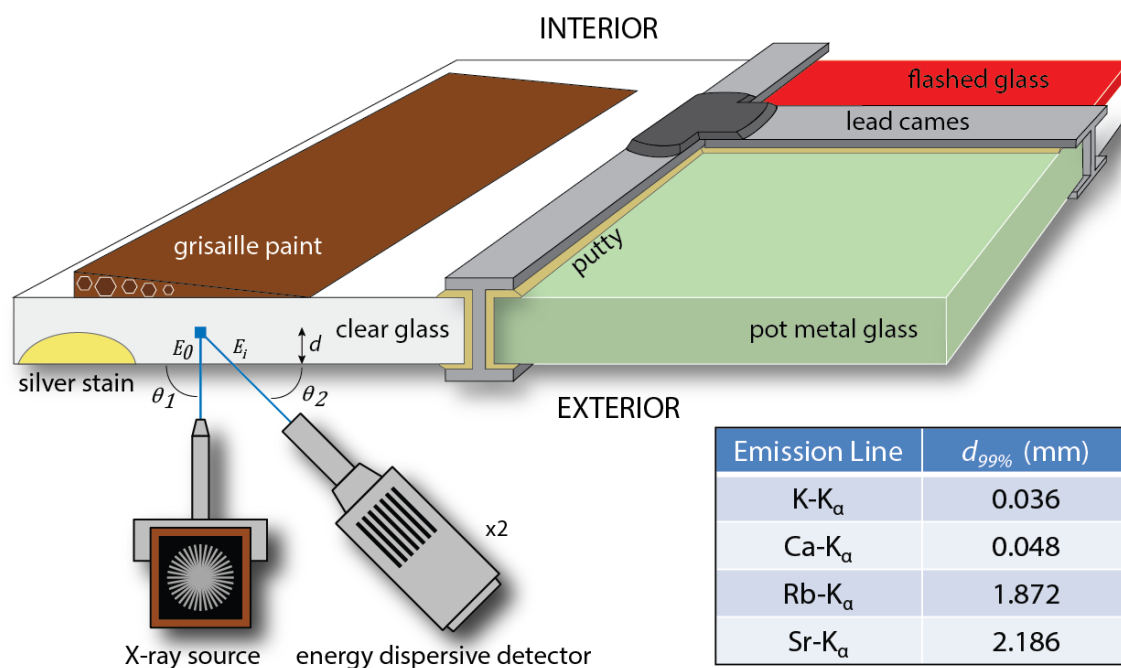
Figure 2: Scheme showing a typical built-up of a stained-glass window with the MA-XRF measuring head positioned on the exterior side of the glass. The image illustrates that the bulk of the glass is best accessed from the exterior side when differentiating compositional types of glass is aimed for, as this side is less shielded by superimposed vitreous paints. The table on the right shows an estimation of the maximum depth information (d) for a number of relevant elements.

5.2.2.3 *MA-XRF on glass fragments: Infinite thick sample*

When performing comparative XRF analyses on a set of glass pieces, it is important to consider the maximum depth from which the signal can be detected with respect to the thickness of the sample. Window glass sheets from this period vary locally in thickness between 2 and 3 mm, contain gas bubbles, and present an undulated surface. In order to assess whether the variable thickness of the glass has an influence on the detected intensities in this study, the maximum information depth from where the emitted X-rays can escape the sample was estimated according to:

$$d_{99\%} = \frac{\ln(100)}{\left[\dfrac{\mu_M(E_i)}{\sin(\vartheta_2)} + \dfrac{\mu_M(E_0)}{\sin(\vartheta_1)}\right]\rho_M}$$

The formula is derived from the Sherman equation, commonly used in quantitative XRF spectrometry, as described elsewhere [30], with $d_{99\%}$ = maximum information depth, E_0 = excitation energy of 45 keV, ϑ_1 = incident angle of 90°, ϑ_2 = detection angle of 65°, and ρ_M expressing the density of a (simplified) SiO_2 matrix (2.65 g cm^{-3}), as illustrated by Fig. 2. The parameters $\mu_M(E_i)$ and $\mu_M(E_0)$ are the mass attenuation coefficients, calculated for a (simplified) matrix consisting only of SiO_2.

Apart from the applied voltage and setup geometry, the maximum depth information is strongly dependant of the energy of the considered XRF emission lines. As shown in Fig. 2, the low energy K-lines from potassium and calcium are highly surface related. Rb–K and Sr–K at 13.3 and 14.1 keV respectively are the emission lines with the highest energies of interest for this study. The associated fluorescence signals cannot originate from deeper than 1.8 and 2.1 mm inside the glass matrix. Since window glass thinner than 2 mm mainly occurs from the seventeenth century onwards, it is safe to assume that the thickness of the glass is not substantially affecting the intensity of the fluorescence signal. As such, the glass fragments from this panel can be considered as infinite thick samples in the context of qualitative XRF analysis [26].

5.2.3 Results

The question whether MA-XRF is useful for the study of stained-glass windows will be largely answered by its capability to distinguish different glass types within the same panel. Unfortunately, an accurate quantification of the different glass ingredients as obtained from conventional XRF and SEM-EDX cross-section analysis is not feasible for a number of reasons. First of all, surface and shadowing effects are expected to occur during the scanning due to the protruding lead came network and the unpolished and weathered glass surface. Quantification necessitates direct, unobstructed access to the glass surface while many areas have some form of pigment, putty or dirt on top of them. In addition, the slight undulation of the panels is expected to affect the intensity of the

detected fluorescence signal as it causes a fluctuation of the distance between the measuring head and the glass surface in the mm range. Finally, the low energy signal from essential low Z elements such as Si and Na are largely absorbed by the air molecules on their path to the detector. Consequently, glass type differentiation must rely on spectroscopic data obtained from Z > 19 elements. For the analysis of glass from this period, this boils down to K and Ca, elements associated with a fluxing agent (K_2O) and network stabiliser (CaO) respectively.
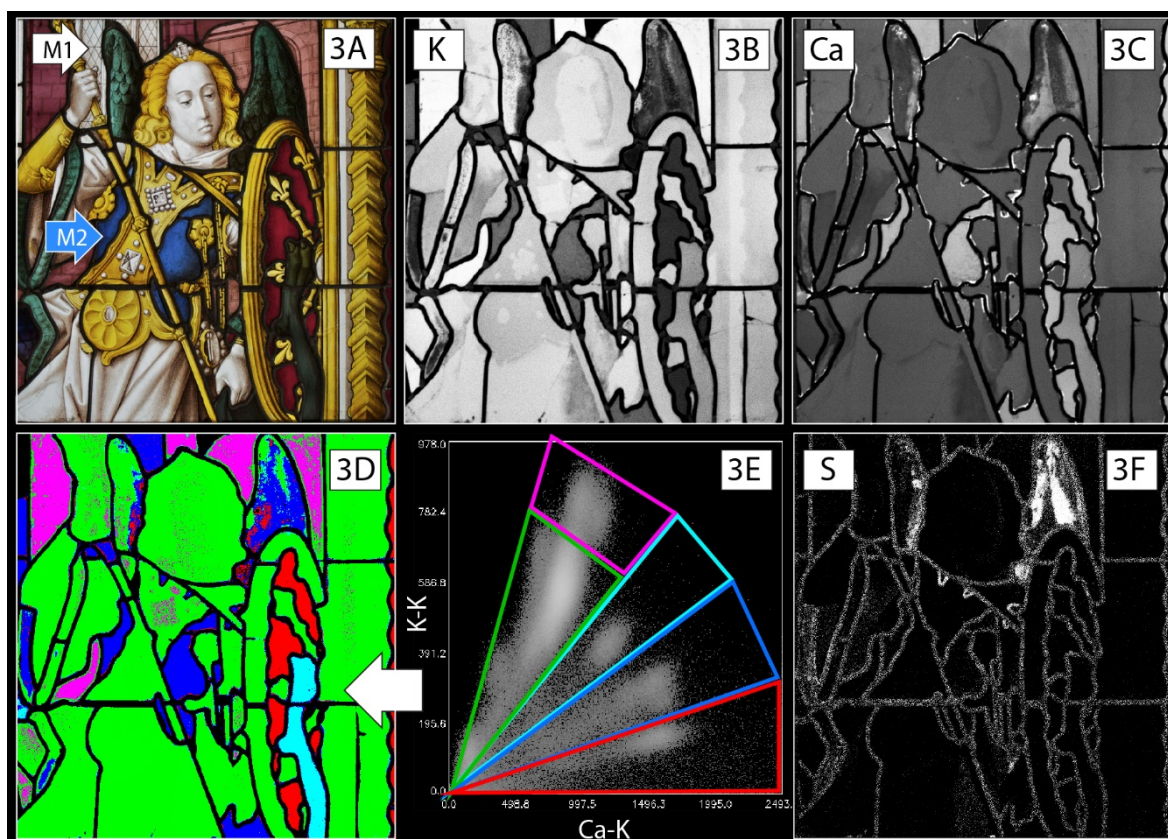
*Figure 3: Composite image showing MA-XRF results obtained on the exterior of the Saint Michael panel. **3A** is the visual image of the panel with the white arrow indicating where the colourless glass sample M1 was extracted and the blue arrow showing the location of the blue glass sample M2. Corresponding quantified SEM-EDX results are listed in Table 1. **3B**: MA-XRF image of the K–K emission line. **3C**: Ca–K map. **3D**: Coloured segmentation map presenting the five types of glass that can be distinguished on the basis of the K/Ca correlation plot displayed in **3E**. **3F**: Elemental distribution map of S–K revealing gypsum-like corrosion crust formation on the glass.*

5.2.3.1 *Differentiating compositional types of glass: Major components*

The distribution maps of the Ca–K and K–K emission lines presented in Fig. 3B and C seem promising as the glass pieces present a clear variation in grey values. This variation is indicative of divergent glass compositions and seems to corroborate with previous sample

analysis. For instance, the colourless glass, previously identified as potash glass by extraction of sample M1 (Table 1), yields a relatively high potassium intensity in the K map as it appears white in the corresponding distribution map. The MA-XRF data seems also consistent with the SEM-EDX data acquired on sample M2. This blue glass was previously identified as HLLA and the glass piece shows up as rich in Ca in Fig. 3E. In spite of these consistencies between the MA-XRF and SEM-EDX results, a more statistical approach is necessary in order to assess the scan data more accurately. For that reason, the net peak intensities of both elements were isolated from the data cube and presented in a scatter plot in order to probe for significant correlations.

As Fig. 3E demonstrates, four distinct element ratios become apparent in the resulting pixel cloud. Datamuncher software allows attributing a colour to each cluster after which the pixel groups can be plotted on to a coloured segmentation map [28]. In this way, the statistical clusters are re-associated with the visual image, a feature that facilitates visual interpretation of the results. The cluster with the highest potassium intensity versus calcium is indicated by a green triangle in Fig. 3. In the coloured segmentation image, the corresponding pixels (green in Fig. 3D) are clearly connected to distinct glass pieces and not scattered over the panel. It is safe to assume that these pieces are of the potash type, not only in view of the element ratio, but also because potash sample M1 stems from this area. Interestingly, a second sub-group can be perceived in the potash cloud, indicated in pink in Fig. 3D and E. These pixels agree with the purplish glass pieces that were decorated with a brick motive in grisaille paint. Based on their divergent glass morphology, these pieces were previously noted by connoisseurs as well, who formulated the hypothesis that these might be part of an early conservation treatment [26]. Although a different geographical origin of the glass cannot be excluded, this finding might reflect the hypothesis of Wedepohl et al. stating a gradual increase in the CaO to K_2O ratio in European potash glass towards the end of the fifteenth century. At that time, proportionally more calcium rich twigs and trunks were used for the production of wood ash at the expense of more qualitative logs [31]. Unfortunately, an accurate calculation of the CaO/K_2O ratio for allowing comparison with Wedepohl's sample-based analytical data is not feasible for the same reasons discussed in the first paragraph. Nevertheless, it can be concluded that most glass pieces in the panel are of the potash type, in particular the purplish glass, the clear glass and the deep green glass in the Saint's dress and wings.

Next to potash glass, three groups with an elevated calcium signal can be discerned. The supposition that the corresponding glass pieces are sub-groups of HLLA is confirmed by the SEM-EDX results obtained from sample M2, taken from the blue glass. Interestingly, the correlation plot reveals that the glass composition varies with colour as the cluster with the highest Ca intensity, indicated in red in Fig. 3E, confers with the red glass, while a second group with a slightly lower Ca content (indicated in blue) matches the blue glass pieces. The third cluster, associated with the green claw of the monster (indicated in turquoise), is remarkable in the sense that the other green glass pieces (i.e. in the Saint's

288

dress) were identified as potash glass. This distinction suggests that a special kind of glass was employed in order to attain a specific green hue, a finding that is substantiated below, in the section on colorants. In summary, these results infer that this late 15th century panel is mainly composed of potash glass, with addition of different sub-groups of HLLA glass for the more expensive and sophisticated colours, i.e. red, blue and the 'special' green from the claw. This MA-XRF-based finding is consistent with earlier cross section analysis as a combination of potash glass with sub-groups of HLLA within stained-glass panels from this period and geographical origin has been reported in literature [21,22].

5.2.3.2 *Differentiating compositional types of glass: Limitations*

Upon studying the coloured segmentation map in Fig. 3D, it becomes clear that the proposed Ca/K-based glass type discrimination is not absolute as a limited number of glass pieces present multi-coloured pixels. This becomes particularly clear in the wings of Saint Michael and a number of smaller pieces on the bottom left. This heterogeneity within the glass pieces is not caused by a shortcoming of the measurement technique or data processing but by the presence of corrosion products on the glass. Visual inspection reveals that a number of glass pieces are affected by the formation of whitish crusts on the exterior side. Glass deterioration products are usually caused by an ion exchange between H-ions in water that is deposited on the glass surface and Ca and/or K-ions that are leached out of the glass. The latter can react with products from the atmosphere, forming oxalate or gypsum like crusts [13]. Sulphur enriched areas appear in the S distribution map in Fig. 3F, zones that clearly agree with the ambiguous 'multi-coloured pixel' glass pieces in the segmentation image. The same areas show up in the K and Ca images where they emerge as shadows and highlights respectively. Although not critical for the panel under investigation, this finding indicates that a Ca/K-based glass differentiation will not be feasible for glass windows that are severely affected by weathering. As such, it is of interest to survey alternative (minor) elements that can serve this purpose.

5.2.3.3 *Differentiating compositional types of glass: Minor/trace components*

Although detrimental for tracing light elements (Z < 19), MA-XRF scanning holds superior minimum detection limits for elements with higher atomic numbers. In particular, MA-XRF scanning can detect elements in glass in the 10–100 ppm range with Z between 25 and 45 [1,2]. Operating in the 1000 ppm range, SEM-EDX cannot detect trace elements such as rubidium and strontium that typically occur in mediaeval glass in the 100–500 ppm range [30]. Fig. 4B and C show a clear grey value variation in the MA-XRF images showing the distribution of Sr–K and Rb–K emission lines. In particular, four clusters show up in the Rb/Sr plot. When colour coded and mapped out, these groups match the same glass pieces as for the Ca/K chart, thus confirming its consistency. The only discrepancy concerns the spectra from the enigmatic green claw of the monster that does not emerge as a separate group, but appear within the pixel cloud of the blue glass. The similarity

between the Rb/Sr and Ca/K plot can be explained by the common geological or vegetal source of Sr–Ca and Rb–K respectively, a finding that has been reported earlier [30,31]. Rubidium is likely a contamination of the potassium rich fluxing agent, while strontium is associated with the Ca source. This alternative approach is of importance as the Sr–K and Rb– K fluorescence signals are of higher energy and thus less affected by superimposed weathering crusts in comparison with the K–K and Ca– K signals discussed above.
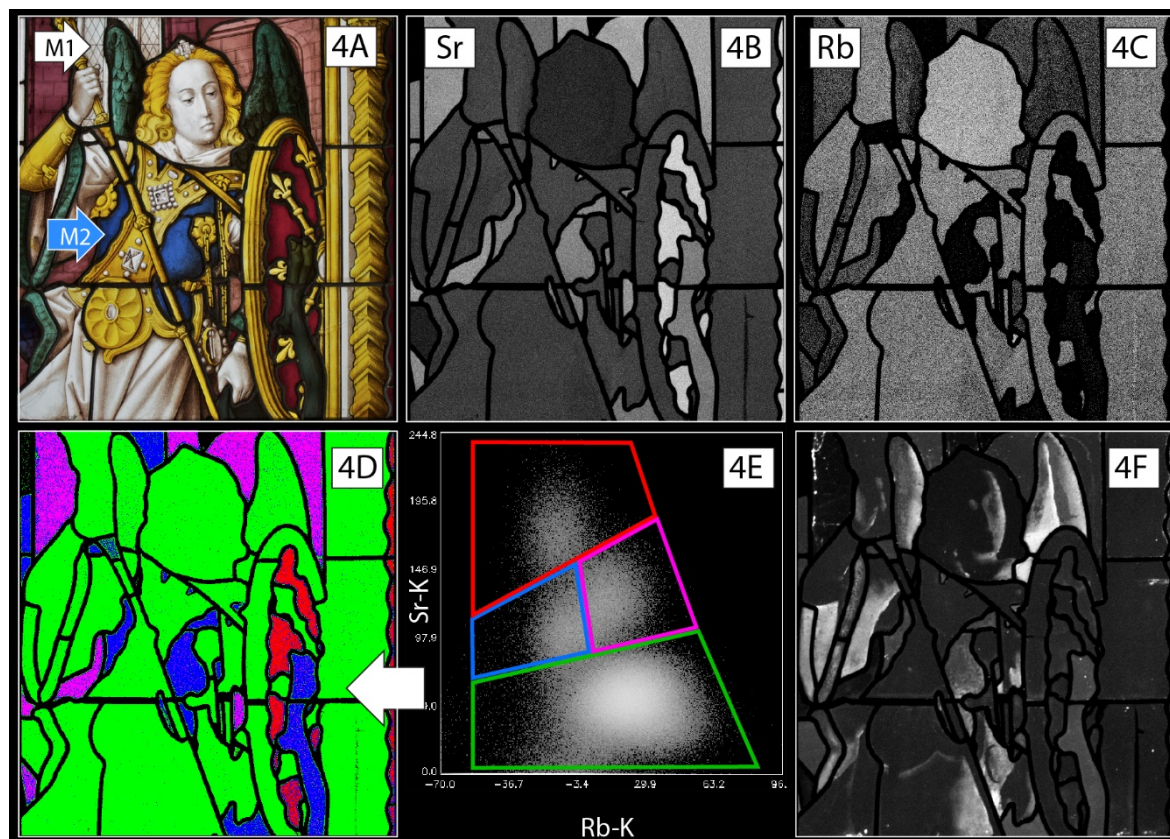
Figure 4: Composite image showing MA-XRF results obtained on the Saint Michael panel. **4A** is the visual image of the panel with indication of the M1 and M2 sampling locations (see corresponding SEM-EDX results in Table 1). **4B**: MA-XRF image of the Sr–K emission line. **4C**: distribution map of Rb–K. **4D**: Coloured segmentation map presenting the four types of glass that can be distinguished on the basis of the Sr/Rb correlation plot displayed in **4E**. **4F**: Distribution of Fe showing grisaille paint on the exterior and an elevated iron signal in the enigmatic claw. All presented MA-XRF data was recorded from the exterior side.

5.2.3.4 *Colorants: Pot metal versus flashed glass*

Apart from discriminating glass types, chromophore identification is another high-ranking motivation for glass analysis. Colours in glass are obtained by introducing specific metal ions into the batch while the resulting colour can differ if this is performed in a reducing or oxidising environment. Next to identification of the colouring metal ions, distinguishing flashed from pot metal glass is of importance as visual examination often remains

indecisive on this matter. The scheme in Fig. 2 illustrates that pot metal glass is coloured throughout its entire thickness, while the colour of flashed glass is obtained by applying a thin layer of coloured glass on top of thicker substrate of clear glass. This stratified approach was developed in mediaeval Europe in order to retain translucency in glass that contains strong light absorbing colorants. A typical example is ruby red glass that is coloured by nanoparticles of metallic copper. The coloured stratum is usually orientated towards the interior side where it is less prone to weathering. However, more sophisticated stratified structures and technologies with alternating or sandwiched red layers have been reported as well, as reviewed by Kunicki-Goldfinger et al. [26,32].
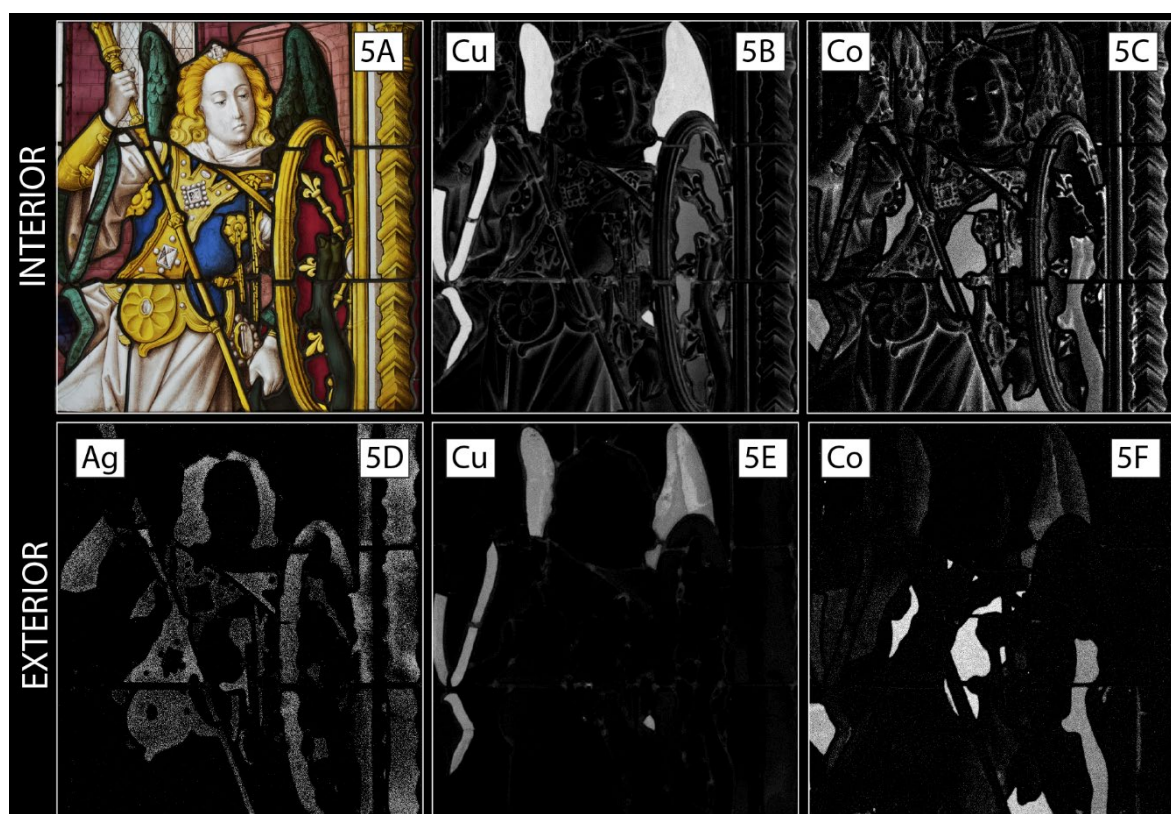
*Figure 5: Composite image opposing elemental distribution maps collected on the interior side (**top row**) and the exterior side of the glass (**bottom row**). **5A**: Visual image of the interior side; **5B** and **5E**: Cu–K from the interior and exterior side respectively; **5C** and **5F**: Co–K from the interior and exterior side respectively; **5D**: Map of Ag–K (exterior). The MA-XRF images obtained from the exterior side are displayed in mirror view to facilitate comparison.*

Flashed glass can be recognised by means of MA-XRF scanning in a straightforward way, on the basis of its stratigraphy. Contrasting the distribution maps obtained from the interior and exterior side of the glass usually reveals the presence of the colouring element on one side only. For instance, Fig. 5B demonstrates that the red glass is rich in copper on the interior side, while the same pieces appear black in the Cu–K map obtained

from the exterior side (Fig. 5E). Contrariwise, copper is equally detected on both sides of the glass in the green wings and bands of Saint's dress, indicating the use of green pot metal glass. Green glass was usually obtained by adding Cu^{2+} ions to the frit in an oxidizing furnace atmosphere. Interestingly, the enigmatic green claw is not coloured by copper ions, but appears to be rich in cobalt on both sides. Cobalt is associated with deep blue glass, as exemplified by the Co–K maps (Fig. 5C and F) and the blue glass pieces in the dress of the Saint. For the moment, it remains unclear how, but the green claw seems to be coloured in an unconventional way. The option of a combination of blue glass with yellow silver stain can be dismissed. Upon studying the Ag–K distribution map in Fig. 5D, it becomes clear that all yellow areas in the panel were obtained by applying silver stain on the exterior side of clear glass, as expected [33]. However, the claw does not come forward in this silver chart. A viable explanation is supplied by Berrie et al. [34], who reported the occurrence of 'green smalt' in Tintoretto paintings, a glassy pigment that appears rich in magnesium and iron, apart from the typical smalt components (Co, As, Bi, Ni). The magnesium fluorescence signal is not energetic enough to reach the MA-XRF detector, but the claw does seem to contain some iron, as emerges from the Fe–K map in Fig. 4F. However, apart from that, a sophisticated stratified glass with a yellow layer sandwiched in between two cobalt blue strata cannot be ruled out either. Extraction of a sample would be necessary to elucidate this matter.

5.2.4 Conclusions

The analytical imaging experiments performed on a late 15th century panel revealed that MA-XRF scanning can be a particularly useful tool for the study of stained-glass windows, in spite of a number of limitations. The major benefit is the ability to acquire compositional data from the entire surface in a completely non-destructive way, an aspect that was highlighted by the discovery of an enigmatic cobalt-based green glass in this already well-studied panel. In addition, the ensuing chemical data can be presented in a visual way, hence allowing interpretation by non-XRF specialists. The measurements performed in this work revealed that MA-XRF is not only able to identify the chromophores but can distinguish pot metal glass from flashed glass as well, simply by contrasting interior with exterior scans. However, in contrast with conventional SEM-EDX and μ-XRF point analyses on samples, MA-XRF experiments do not yield accurate quantification of the different glass components. Still, the main motive for quantification is differentiating glass types, an objective that that can be achieved by MA-XRF scanning in an alternative way. As discussed, this drawback can be largely overcome by means of Ca/K correlation plots and subsequent charting of the clusters in coloured segmentation maps. In case the Ca and K fluorescence signals are affected by overlying corrosion products, an alternative bi-plot of the more energetic Rb–K/Sr–K lines can be employed in a beneficial way for the same purposes. The resulting insights are particularly useful for conservators who are typically interested in an efficient discrimination of the historical phases in one specific window rather than exact quantification. From a practical point of view, the mobile aspect of the instrument allows performing the experiments inside a

conservation studio and the ensuing elemental distribution maps can also serve as functional 1:1 working drawings during the actual treatment. In a wider, more archaeometric perspective, the absence of absolute concentrations does prevent inter-comparison of the MA-XRF scans from different stained-glass windows. In this framework, combining the MA-XRF maps with SEM-EDX analyses on a limited number of samples is expected to be particularly relevant. Moreover, thanks to preceding MA-XRF scans sample locations can be selected in a highly substantiated way. In this way, the number of samples needed for obtaining a comprehensive compositional overview can be minimised and the resulting sample data can be extrapolated to the rest of the glass surface in a more confident way.

References
1. M. Alfeld, K. Janssens, J. Dik, W. De Nolf, G. Van der Snickt, Optimization of mobile scanning macro-XRF systems for the in situ investigation of historical paintings, J. Anal. At. Spectrom. 26 (2011) 899–909.
2. M. Alfeld, J. Vaz Pedroso, M. Van Eikema Hommes, G. Van der Snickt, G. Tauber, J. Blaas, M. Haschke, K. Erler, J. Dik, K. Janssens, A mobile instrument for in-situ scanning macro-XRF investigation of historical paintings', J. Anal. At. Spectrom. 28 (2013) 760–767.
3. K. Janssens, M. Alfeld, G. Van der Snickt, W. De Nolf, F. Vanmeert, M. Radepont, L. Monico, J. Dik, M. Cotte, G. Falkenberg, The use of X-ray based methods for the characterization of artists' pigments and paintings, Annu. Rev. Anal. Chem. 6 (2013) 399–425.
4. F.-P.h. Hocquet, H. Calvo del Castillo, A. Cervera Xicotencatl, C. Bourgeois, C. Oger, A. Marchal, M. Clar, S. Rakkaa, E. Micha, D. Strivay, Elemental 2D imaging of paintings with a mobile ED-XRF system, Anal. Bioanal. Chem. 399 (2011) 3109–3116.
5. M. Alfeld, K. Janssens, K. Appel, B. Thijsse, J. Blaas, J. Dik, A portrait by Philipp Otto Runge—visualizing modifications to the painting using synchrotron-based X-ray fluorescence elemental scanning, Z. Kunstgesch. und Konservierung 25 (2011) 157–163.
6. M. Alfeld, G. Van der Snickt, F. Vanmeert, K. Janssens, J. Dik, K. Appel, L. Van der Loeff, M. Chavannes, T. Meedendorp, E. Hendriks, Scanning XRF investigation of a Flower Still Life and its underlying composition from the collection of the Kröller–Müller Museum, Appl. Phys. A Mater. Sci. Process. 11 (2013) 165–175.
7. M. Alfeld, D.P. Siddons, K. Janssens, J. Dik, A. Woll, R. Kirkham, E. van de Wetering, Visualizing the 17th century underpainting in Portrait of an Old Man by Rembrandt van Rijn using synchrotron-based scanning macro-XRF, Appl. Phys. A Mater. Sci. Process. 111 (2013) 157–164.

8.   J. Dik, K. Janssens, M. Alfeld, K. Rickers, E. van de Wetering, in: E.v.d. Wetering (Ed.), Nouveau Regard sur Rembrandt, Local World BV, Amsterdam 2010, pp. xx–xxiv.

9.   P. Noble, A. van Loon, M. Alfeld, K. Janssens, J. Dik, Rembrandt and/or Studio, *Saul and David*, c. 1655: visualising the curtain using cross-section analyses and X-ray fluorescence imaging, Technè 35 (2012) 36–45.

10.   D. Bull, A. Krekeler, M. Alfeld, J. Dik, K. Janssens, An intrusive portrait by Goya, Burlingt. Mag. (October 2011) CLIII.

11.   N. Turner, K. Trentelman, C. Schmidt Patterson, J. Dik, G. Van der Snickt, K. Janssens, MA-XRF scanning of illuminations: an improved method for non-invasive analysis of illuminated manuscripts. Inside illuminations, Art technical research and the illuminated manuscript. Conference proceedings, June 5 2014 (In Press).

12.   S. Legrand, P. Ricciardi, G. Bertolotti, K. Janssens, MA-XRF scanning of illuminated manuscript fragments: potentialities and challenges, Microchem. J. (2015) (in this issue).

13.   K. Janssens (Ed.), Modern Methods for Analysing Archaeological and Historical Glass, John Wiley & Sons, Chichester, 2013.

14.   K. Janssens, G. Vittiglio, I. Deraedt, A. Aerts, B. Vekemans, L. Vincze, F. Wei, I. Deryck, O. Schalm, F. Adams, A. Rindby, A. Knochel, A. Simionovici, A. Snigirev, Use of microscopic XRF for non-destructive analysis in art and archaeometry, X-Ray Spectrom. 29 (2000) 73–91.

15.   O. Schalm, J. Caen, K. Janssens, Homogeneity, composition and deterioration of window glass fragments and paint layers from two seventeenth-century stained-glass windows created by Jan de Caumont, Stud. Conserv. 55 (2010) 216–226.

16.   G. Van der Snickt, W. De Nolf, B. Vekemans, K. Janssens, μ-XRF/μ-RS vs. SR μ-XRD for pigment identification in illuminated manuscripts, Appl. Phys. A Mater. Sci. Process. 92 (2008) 59–68.

17.   G. Weber, Y. Vanden Bemden, M. Pirotte, B. Gilbert, Study of stained-glass window using PIXE–PIGE, Nucl. Instrum. Methods Phys. Res., Sect. B. 240 (2005) 512–519.

18.   P. Colomban, A. Tournie, On-site Raman identification and dating of ancient/ modern stained-glasses at the Sainte-Chapelle, Paris, J. Cult. Herit. 8 (2007) 242–256.

19.   W. Meulebroeck, P. Cosyns, K. Baert, H. Wouters, S. Cagno, K. Janssens, H. Terryn, K. Nys, H. Thienpont, Optical spectroscopy as a rapid and low-cost tool for the first-line analysis of glass artefacts: a step-by-step plan for Roman green glass, J. Archaeol. Sci. 38 (2011) 2387–2398.

20.   P. Fernandes, M. Vilarigues, L.C. Alves, R.C. da Silva, Stained-glasses from Monastery of Batalha: non-destructive characterisation of glasses and glass paintings, J. Cult. Herit. 9 (2008) E5–E9.

21.   O. Schalm, D. Caluwe, H. Wouters, K. Janssens, F. Verhaeghe, M. Pieters, Chemical composition and deterioration of glass excavated in the 15th-16th century fishermen town of Raversijde (Belgium), Spectrochim. Acta B At. Spectrosc. 59 (2004) 1647–1656.

22.   O. Schalm, K. Janssens, H. Wouters, D. Caluwe, Composition of 12-18(th) century window glass in Belgium: non-figurative windows in secular buildings and stained-glass windows in religious buildings, Spectrochim. Acta B At. Spectrosc. 62 (2007) 663–668.

23.   J. Helbig, Les vitraux médiévaux conservés en Belgique 1200–1500, Corpus Vitrearum Medii Aevi, part 1, Brussels1961 199–202.

24.   L. Devliegher, Enkele Brugse Glasramen uit het einde der XVe eeuw, Belg. Tijdschr. Oudheidkunde en Kunstgeschiedenis XXVV (3-4) (1954) 201–202.

25.   Ad. Duclos, Bruges, Histoire et Souvenirs, Bruges, 1910 516.

26.   Joost Caen, The Production of Stained-Glass in the County of Flanders and the Duchy of Brabant from the XVth to the XVIIIth Centuries: Materials and Technique, Brepols Publishers, Turnhout, 2009.

27.   V.A. Solé, E. Papillon, M. Cotte, Ph. Walter, J. Susini, A multiplatform code for the analysis of energy-dispersive X-ray fluorescence spectra, Spectrochim. Acta B At. Spectrosc. 62 (2007) 63–68.

28.   M. Alfeld, K. Janssens, Strategies for processing mega-pixel X-ray fluorescence hyperspectral data: a case study on a version of Caravaggio's painting *Supper at Emmaus*, J. Anal. At. Spectrom. 30 (2015) 777–789.

29.   O. Schalm, I. De Raedt, J. Caen, K.A. Janssens, Methodology for the identification of glass panes of different origin in a single stained-glass window: application on two 13th century windows, J. Cult. Herit. 11 (2010) 487–492.

30.   J. Sherman, The theoretical derivation of fluorescent X-ray intensities from mixtures, Spectrochim. Acta 7 (1955) 283–306.

31.   K.H. Wedepohl, K. Simon, The chemical composition of medieval wood ash glass from Central Europe, Chemie Der Erde-Geochem. 70 (2010) 89–97.

32.   J.J. Kunicki-Goldfinger, I.C. Freestone, I. McDonald, J.A. Hobot, H. Gilderdale-Scott, T. Ayers, Technology, production and chronology of red window glass in the medieval period – rediscovery of a lost technology, J. Archaeol. Sci. 41 (2014) 89–105.

33.   D. Jembrih-Simburger, C. Neelmeijer, O. Schalm, P. Fredrickx, M. Schreiner, K. De Vis, M. Mader, D. Schryvers, J. Caen, The colour of silver stained-glass—analytical investigations carried out with XRF, SEM/EDX, TEM, J. Anal. At. Spectrom. 17 (2002) 321–328.

34.   B.H. Berrie, L.C. Matthew, 'New Materials on the Renaissance Artists' Palette'. Materials Issues in Art and Archaeology, 7th Symposium on Materials Issues in Art and Archeology, Vandiver, P. B. Boston (US) in 2004, 2005.

5.3 MA-XRF imaging as a tool to characterize the 16th century heraldic stained-glass panels in Ghent Saint Bavo Cathedral

Abstract MA-XRF is a novel macroscopic imaging technique originally developed for easel paintings and recently made available to glass conservators. This paper discusses the first real-life contribution of MA-XRF imaging to a conservation intervention of stained-glass panels. The six panels under study belong to the cathedral building since their creation in 1555–1559 AD. MA-XRF appeared an outstanding tool for first-line screening of stained-glass windows, providing readily interpretable information on glass type, coloring and alteration processes. In particular, the chemical imaging technique allowed distinguishing unambiguously the surviving original glass panes from later additions, thereby ensuring a correct historical understanding. From a more practical point of view, the experiments supplied accurate schemes that can be directly incorporated in condition reports and assist designing the ensuing conservation approach.

5.3.1 Introduction

Correct conservation practice of stained-glass windows includes a complete technical examination of all components, such as the substrate glass of the panels, the glass paints and the lead cames. This is a labor-intensive process and is typically done by visual and microscopic inspection. In a few cases, usually when deterioration or historical issues have to be addressed, this is complemented with chemico-physical analyses. A typical approach involves either sampling or non-invasive point measurement on each pane, for instance with portable XRF, Raman Spectroscopy or PIXE (see e.g. [1–4]). While sampling is disputable in the context of a conservation campaign, *in situ* analysis is often time and capital intensive, requires interpretation by experienced staff and is always at risk of non-representativity.

Time-effective approaches documenting complete windows, in a chemical and organized way, would be particularly welcome, as this would allow assessing the age estimates by connoisseurs, color technology and ongoing alteration processes. Therefore, a few imaging methods have been tested, starting with IR reflectography and IR photography, which have been used for preliminary assessment of the state of conservation. However, their scope is limited to surface features and provide no specificity for glass compositions[5]. UV–VIS–NIR mapping, instead, has been proposed for the investigation of (mainly) colored glasses, but also for the discrimination of different glass compositions [6]. However, in literature only point measurement analyses are reported for stained-

glass windows [7]. Redox mapping has also been tested for stained-glasses, with additional benefit for glass alteration studies, however, this being based at large scale research infrastructures, it is far from applicable in common conservation practice [8].

Macro X-ray Fluorescence (MA-XRF) scanning on the other hand, allows recording compositional data in a completely non-invasive and non-destructive way from the entire object under examination. This data can be presented in distribution images, which are interpretable by a larger public than the spectra resulting from classical spectrometric techniques. A mobile MA-XRF 2D scanning instrument for flat objects has been made available in 2011 [9] and has performed well on (iconic) paintings (see e.g. [10]). The suitability of MA-XRF as a screening technique for stained-glass windows has recently been proven [11]. While 2D scans are deemed sufficient for most conservation purposes, depth selective data collection by confocal XRF on stained-glass windows has also been reported in literature [12].

5.3.2 Research aims

This paper describes the first application of macro X-ray fluorescence (MA-XRF) on stained-glass windows in the framework of a real-life conservation-restoration intervention. The six glass panels object of this study belong to the Saint Bavo Cathedral in Ghent, Belgium. They were selected for MA-XRF scanning measurements since they were assessed by curators to belong to the Saint Bavo Cathedral building as of 1559, and therefore the only known remains of the once impressive historical glazing program of the cathedral.

The aim of the study was to provide objective evidence to the conservators on the amount of original glass panes and later additions. The extensive documentation generated with this study, consisting in chemical element distribution maps of the entire panels, is aimed at improving the understanding of the materials and processes used for their manufacture and past restorations. This, in turn, will enable a better preservation of their state of conservation.

5.3.3 Materials and methods

The six heraldic panels (57 × 60 cm^2) can be dated between 1555 and 1559 and were part of a window in the St. Landoald side chapel of Ghent Saint Bavo Cathedral. A 17th century manuscript kept in the *Rijksarchief Gent* shows the entire window and inscriptions, making clear that the window depicted the 'Resurrection' surrounded with coats of arms and the representation of the donors. All six surviving panels show typical 16th century heraldic representations: a shield of arms surrounded by decorative scrolls and the name of the family in capital letters (Figs. 1, 2A, 3A). At present, the panels are not in situ, but presented in the sacristy. Visual inspection of the panels suggested that a number of glass panes were probably replaced in the course of past restoration interventions.
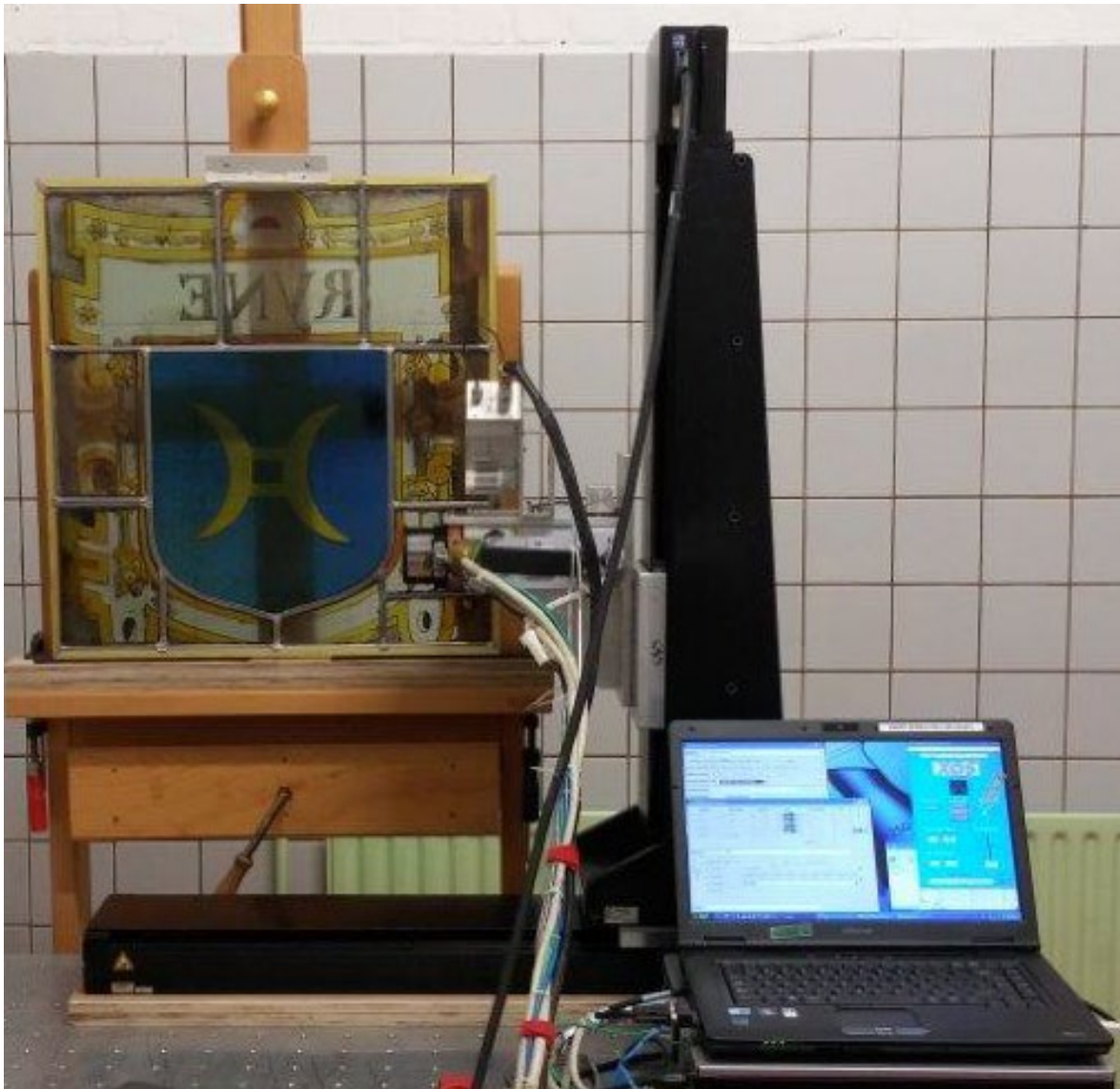
Figure 1: The MA-XRF scanning setup in front of the Ryne panel. Glass panels were scanned on their exterior side, while positioned on an easel.

For these windows, micro-sampling (e.g. under the lead cames) for quantitative SEM-EDX analyses was not permitted, due to the historical relevance of the stained-glass windows. Therefore, all stained-glass panels were analyzed in reflection mode by means of the MA-XRF scanning instrument built within the AXES group of the University of Antwerp, more details on the setup can be found elsewhere [13].

The scanner consists of an XRF measurement head mounted on a software-controlled X-Y motor stage with a travel range of about 57 × 60 cm² (h × v). The measurement head is equipped with one Vortex EX-90 SDD detector that is positioned in a 20° angle with respect to the incident X-ray beam. The X-ray source is a XOS 50 W Mo anode tube. MA-XRF scans were performed by sweeping the measuring head systematically over the glass surface, respecting a stable distance of ca. 1 cm in between the edge of the measuring head and the panel. The diameter of the primary beam was reduced to a focal spot of 50 µm at 3 mm in front of the instrument by implementing a polycapillary X-ray lens. By offsetting the distance between the optics and the panel, the divergent X-ray beam had an effective spot size of 700 µm. For each pixel in the scanned area, an XRF spectrum is collected. From these spectra, after a spectral fitting process [14], XRF maps are created for each element detected. The resulting maps, shown in Figs. 2–3, are sometimes gamma/contrast adjusted for better reading. Standard measurement parameters resulted in a total scan time of about 24 hours for each panel. Additional details on measurement conditions are available in [11]. For a more efficient narration, only the ensuing X-ray fluorescence maps, and not the spectra, are shown in the following section.

The MA-XRF setup is transportable and can be used at the location where the objects are stored or restored. Performing in situ scans on panels in their architectural setting is feasible as well, but requires supporting structures that allow for safe positioning of the equipment and the absence of physical obstructions that can hamper the movement of the measuring head. In this case, the panels were positioned on an easel for the entire duration of the measurements, while the measuring head moved across the entire surface, as shown by Fig. 1.

5.3.4 Results and discussion

The results are presented in this section according to the type of information sought. In order to keep the discussion compact, only selected results of the *Kethulle* and *Crane* panels are discussed hereafter (see Figs. 2 and 3, respectively). The data was collected from the exterior side, but for the comfort of the reader the figures are shown reversed.

5.3.4.1 *Assessment of the state of conservation*
MA-XRF scans can be used to document (the lack of) structural integrity of the window with a level of detail comparable with the scan resolution. For instance, the X-ray continuum map (Fig. 2M), which is in essence a distribution plot of primary X-rays scattered by the object under study, indicates the presence of chemical elements with low atomic number. In practice, this is especially valid for organic materials such as the polymers or glues (epoxy resins in this case) applied in the framework of a previous conservation treatment.

In the current case, the lead-came network and joints are intact, having been replaced in the course of the recent conservation intervention. However, the XRF maps of Pb and Sn in Figs. 2K–L illustrate the potential of the technique to document discontinuities in the lead came network and soldering joints. In this way, MA-XRF can be employed for performing quality checks on the results of a conservation treatment as well.

5.3.4.2 *Glass composition*

With these experiments we predominantly aimed at visualizing relative differences in glass composition, allowing distinguishing between modern (i.e., replaced in later instances) and ancient glasses, and between different glassmaking technologies.

The grey values of the panes in the maps shown in Figs. 2–3 are relative indications of the concentration of a chemical element. While black panes in the maps imply that element was not detected there, the brighter the tone, the higher is the detected X-ray intensity of that element. Pixel intensities can also be shown as bi-plots (see e.g. the Ca/K bi-plots in Fig. 2D, 3D).

Figure 2: *A. Kethulle panel - exterior side; B. K-K XRF map; C. Ca-K XRF map; D. Bi-plot of the K and Ca pixel intensities (a.u.); E. As-K XRF map; F. Mn-K XRF map; G. Ag-L XRF map; H. Fe-K XRF map; I. Co-K XRF map; J. Cr-K XRF map; K. Pb-L XRF map showing the lead came network; L. Sn-L XRF map showing the soldering; M. Continuum map showing in white likely organic material, such as polymeric filler. N. False-color map in function of As/Ca pixel intensity bi-plot. O. False-color map in function of Mn/Ca pixel intensity bi-plot.*
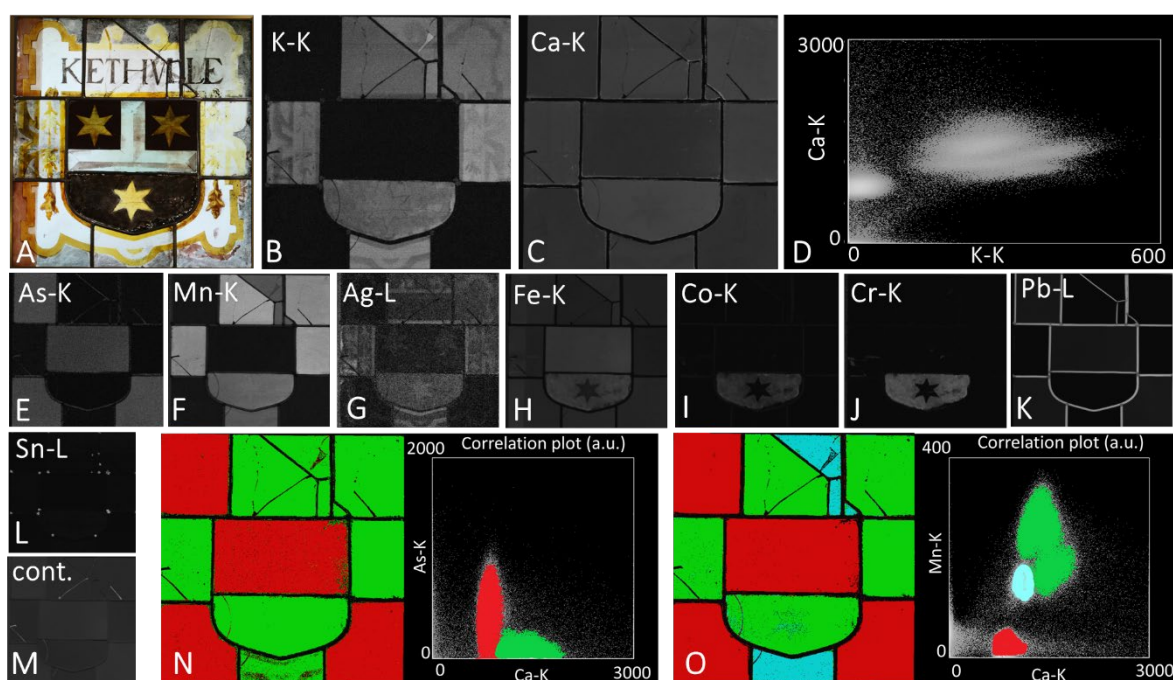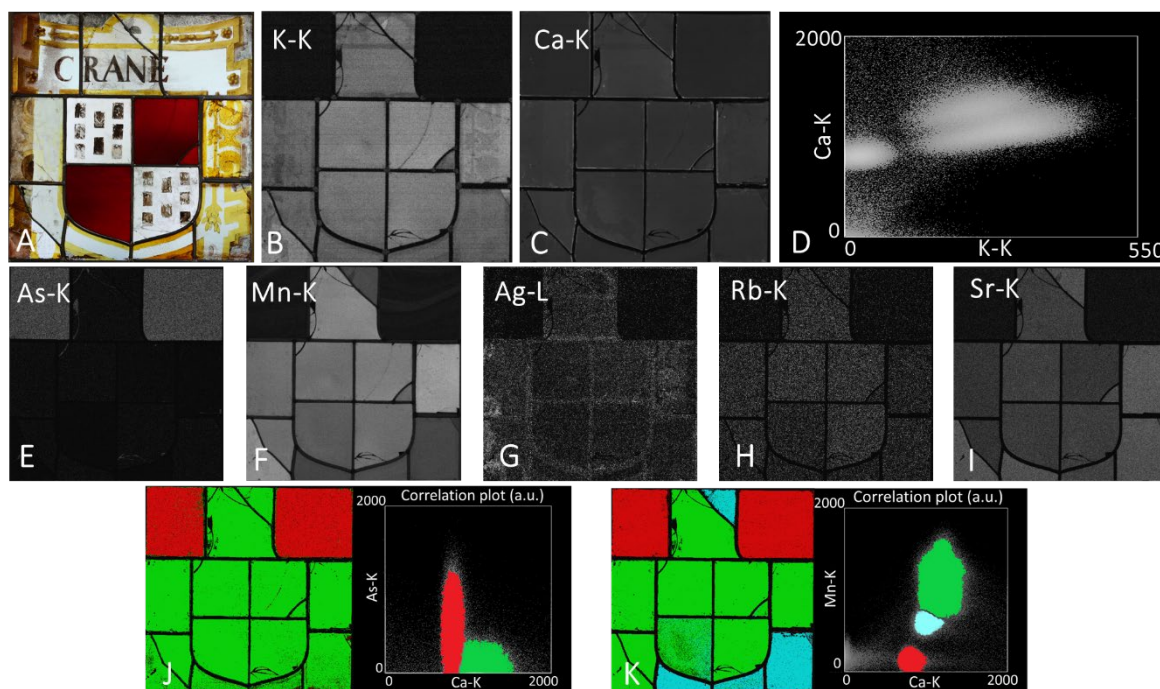
*Figure 3: **A**. Crane panel - exterior side; **B**. K-K XRF map; **C**. Ca-K XRF map; **D**. Bi-plot of the K and Ca pixel intensities (a.u.); **E**. As-K XRF map; **F**. Mn-K XRF map; **G**. Ag-L XRF map; **H**. Rb-K XRF map; **I**. Sr-K XRF map; **J**. False-color map in function of As/Ca pixel intensity bi-plot; **K**. False-color map in function of Mn/Ca pixel intensity bi-plot.*

The possible glass families expected to occur in the Saint Bavo Cathedral windows are those used for window glass in the Low Countries in the period 1555-present, i.e. potash glass, high-lime low-alkali (HLLA) glass, lead glass, vegetable ash soda glass and synthetic soda glass, the latter in case of replacements in modern times [15]. These glass families, and their hierarchical classification are summarized in Fig. 4. Further information on categories of historical window glass in other contexts can be found, e.g., in [1,15].

As shown in Fig. 4, the chemical elements allowing identifying the glass groups are Na, K, Ca and Pb. However, since MA-XRF experiments are performed in ambient air, the low energy fluorescence radiation emitted by Na is absorbed by air. Therefore, only the K, Ca and Pb distribution maps can be employed to identify these glass groups. No Pb is detected in compatible manner with its presence in the glass matrix, therefore the occurrence of lead glass can be ruled out.

When looking at the K distribution maps shown in Figs. 2B and 3B, it is striking how a number of corner panes appear to contain very low/not-detectable levels of potassium. Even if Na is not detectable, a vegetable source of soda (i.e. ash) would carry along an amount of potassium (see Fig. 4). This is a strong indication that the flux used for these panes was high purity synthetic soda, industrially produced from the late 18th century

onwards, and used for glass at a large scale from the 19th century. Therefore, such glass panes must have been replaced at a later date.
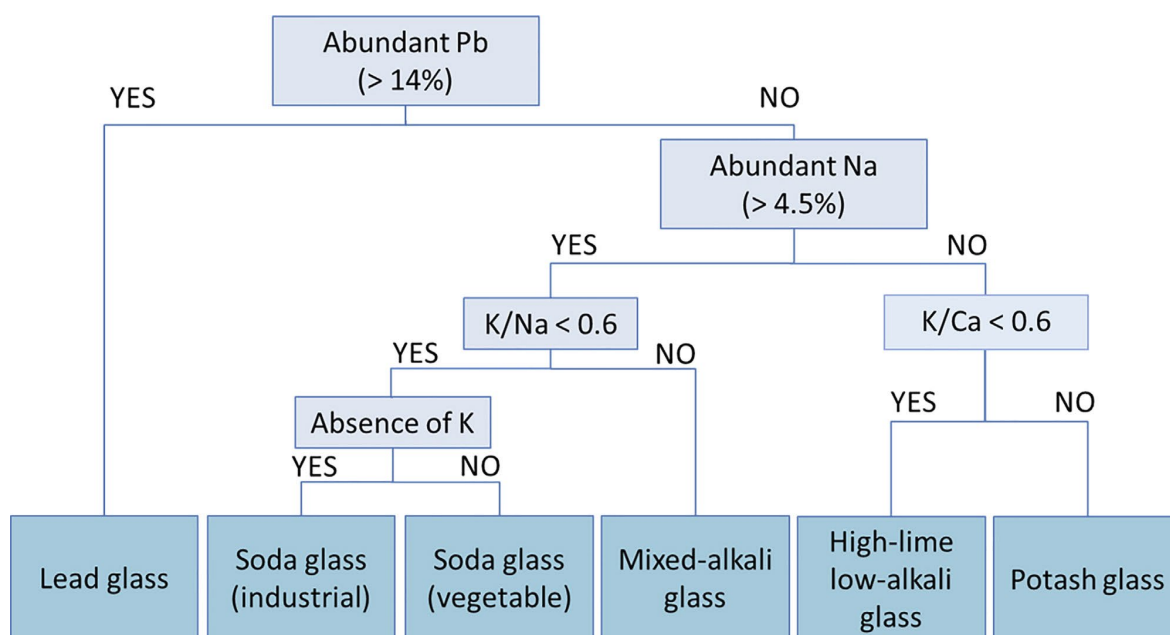

Figure 4: Window glass compositions commonly used in the Low Countries from 12th century onwards, and their hierarchical classification according to their major element content (adapted from [15]). Lead glass was introduced in England in the late 17th century, sparsely occurring in window glass of the Low Countries. Industrial soda glass appeared in the course of the 19th century, after the invention of synthetic soda, and can be found in case of replacement of glass panes. Vegetable soda and mixed alkali glass rarely occur in window glass, while they are well represented in post-medieval luxury vessel glass. High-lime low-alkali glass and potash glass are the two most widely used compositions for window glass, the first with its use peaking between the 12th and the 17th century, and the second between the 12th and the 15th century [15].

The same panes demonstrate lower intensities of Ca (Figs. 2C, 3C) and higher As levels (Figs. 2E, 3E). Arsenic was used in high quality clear glass from the 18th century onwards, and typically up until the 19th century [16]. The co-existence of synthetic soda glass and arsenic in the replaced panes thus indicates a 19th century intervention. In all the investigated windows between two and four glass panes appear to be made of modern glass.

All original glass appears to contain potassium as main fluxing agent, accompanied by relevant amounts of Ca. This would locate them in the last two categories on the right of Fig. 4 (HLLA glass and potash glass). The assessed composition of the original glass does not contradict the 1555–1559 AD date, as per conservator's judgment.

Being K and Ca adjacent elements, their characteristic X-rays undergo similar attenuation phenomena. By comparing the K/Ca intensities in Figs. 2D–3D, one could attempt a further discrimination between potash and HLLA glass, based on historical glass

compositions. The K/Ca intensity ratio appears to be 0.4 or lower, which is comparable with the average K/Ca (0.36) ratio of the most common type of HLLA-glass in use in the Low Countries in the 16th century, and far from the average ratio (0.94) of the most common potash-glass composition [15]. However, these indications would need to be corroborated by analyses on samples.

In a second step, pixel intensity bi-plots can be used to identify clusters revealing various correlations between two chemical elements. By assigning user-chosen colors to identified clusters, false colored grouping of glass panes can be visualized. As an example, in the *Kethulle* panel (Fig. 2N), two clusters of pixels are found: the first (in green) features medium to high levels of calcium and low levels of arsenic, while the second cluster (in red) has lower levels of Ca, positively correlated with As. These clusters correspond to the aforementioned original and replaced glass panes.

In the Mn/Ca bi-plot, instead (Fig. 2O), next to a cluster with low Ca and Mn (red), a large group with high Ca and Mn pixels is found (green). These correspond to replaced and original glass, respectively. In addition, a subset of the latter, with intermediate levels of Ca and Mn, can be further distinguished (light blue). These pixels belong to three small panes, with a glass composition compatible with the 16th century, but different from the green group. This could represent an indication of the use of glass of two qualities in the original windows. Two groups of HLLA glass, differentiated by their Mn content (above and below 0.2% MnO) have been identified, for instance, in English windows glass of the 16–17th Century [1].

For the *Crane* panel, similar results are obtained, but in this case, it is clear that a higher amount of original glass panes have been maintained (Fig. 3J–K).

5.3.4.3 *Glass appearance*
MA-XRF allowed to identify a single glass-pane (the centre-top pane of the *Kethulle* window), which is colored by iron, with a lightgreen tint. Since the majority of the panels is made of clear glass, no other pane shows such a uniform distribution of a coloring element (e.g. Mn for purple, or Co for blue glass).

While a comparison of MA-XRF data collected from the interior and the exterior side of the windows could also allow differentiation of flashed glass from pot metal glass [11], in this case the scans were performed from the exterior side only.

The introduction of Mn in ancient glass, when not intentional to produce purple color, was meant to counteract the light yellowgreen color caused by Fe impurities in the raw materials [17,18]. In these panels, Mn contents appears variable and allows a further distinction in two groups of original glass, as mentioned in the previous section. The modern panes with low K and high As levels, stand out as well in the Mn maps in Figs. 2F

and 3F. This modern clear glass, made with high purity raw materials, did not need manganese addition in its production process.

In the outer (original) panes of all windows, the painted decorative border and related decorations are visible at many locations in the Ag XRF maps (Figs. 2G, 3G) and, in negative in the K XRF map (Figs. 2, 3B). This is an indication that silver staining was applied on the exterior side of the window, causing a diffusion of Ag into the glass, and a corresponding depletion of alkali, in this case, potassium [19].

In the *Kethulle* panel, the star-shaped decoration in the centre bottom pane is visible in negative in the Co (Fig. 2I) and in the Fe map (Fig. 2H), and in positive in Ag map (Fig. 2G). Because of their uneven distribution, it can be deduced that cobalt and iron were applied as glass paints on the exterior side, while the star is obtained by means of silver staining on the exterior side.

Moreover, Cr signals were detected in the same glass pane (Fig. 2J), a finding that is indicative of cold-applied inpainting with modern pigments such as chrome greens, reds and/or yellows. The similar pattern of the Cr to the Co and Fe distributions seems to indicate that all elements were contained in the glass paint used to obtain the resulting brown appearance. Therefore, the investigation of glass colorants can also shed light on previous conservation interventions.

5.3.4.4 *Glass deterioration*

During glass weathering the most mobile cations (Na, K) are leached out of the glass surface due to repeated cycles of hydration/dehydration, resulting in the formation of layers of hydrated silica. In parallel, deposits of metal carbonates and sulfates are formed on the glass surface following interaction of these cations with air and atmospheric particulate matter [20–22]. These processes can be observed in the MA-XRF maps as well, through the increased level of calcium that corresponds with the observed pit corrosion craters.

Glass alteration might complicate the aforementioned glass type interpretation based on K and Ca ratios. In particular, the weathering can cause a depletion of K or formation of Ca-rich crusts, altering in this way the ratio. However, in case of significant weathering, Rb and Sr XRF signals can be used as an alternative for Ca and K [1,2,11]. Rb and Sr are largely co-occurring with K and Ca, respectively, in the raw materials used to make glass. Being more energetic, their X-ray emission can be detected even when originating from deeper in the glass, i.e. at a depth less likely to be affected by superimposed alteration. As an example, for the Crane panel, Figs. 3B–C can be compared with Fig. 3H–I.

5.3.5 Conclusion and outlook

In this real-life conservation scenario, MA-XRF supplied relevant chemical information from the entire glass surface in a time-efficient manner. The information provided by the technique is immediately usable by the conservator to answer precise historical and structural questions. In particular, MA-XRF is highly suitable for:

- assessing the structural integrity of the window;
- distinguishing groups of glass panes with a similar composition and outliers within the same panel;
- differentiate glass paints, especially modern ones;
- documenting glass alteration.

Historical stained-glass panels and windows nearly always contain several later replacement panes and infillings. Quite often it is difficult to date these only by visual examination. MA-XRF revealed unambiguously that about a quarter of the glass panes were replaced, by modern (19th C.) synthetic soda glass containing arsenic. The surviving original glass is likely high-lime low-alkali glass, which is compatible with the presumed dating (1555–1559 AD). The coloring process probably involved a mix of flashed glass, grisaille and glass paint. Modern glass paint was detected, while clear indications of silver staining were found on the original panes.

In this way, MA-XRF proved to be an important additional 'tool' for the correct dating of stained-glass and as a reliable source of information for conservators and curators. However, the qualitative nature of the technique allows only distinguishing types of panes within the same panel. Exact, quantitative information on the glass composition still requires analysis on samples.

Still, it is expected that an increased availability of this technique will favor improved knowledge on the history of stained-glass windows and their state of conservation, and therefore more accurate interventions.

References
1. D. Dungworth, Historic window glass. The use of chemical analysis to date manufacture, J. Archit. Conserv. 18 (2012) 7–25.
2. L.W. Adlington, I.C. Freestone, Using handheld pXRF to study medieval stained-glass: A methodology using trace elements, MRS Adv. 2 (2017) 1785–1800.

3.   M. Walczak, M. Kaminska, P. Karaszkiewicz, J. Szczerbinski, M. Szymonski, The preliminary results on the investigation of historic stained-glass panels from Grodziec collection, Poland, Proc. SPIE 8790 (2013), 87901 F-1.

4.   G. Weber, Y. Van den Bemden, M. Pirotte, B. Gilbert, Study of stained-glass window using PIXE–PIGE, Nucl. Instrum. Met. Phys. Res. Sect. B 240 (2005) 512–519.

5.   O. Hahn, S. Bretz, C. Hagnau, H.J. Ranz, T. Wolff, Pigments, dyes, and black enamel—the colorants of reverse paintings on glass, Archaeol. Anthropol. Sci. 1 (2009) 263–271.

6.   W. Meulebroeck, P. Cosyns, K. Baert, H. Wouters, S. Cagno, K. Janssens, Optical spectroscopy as a rapid and low-cost tool for the first-line analysis of glass artefacts: a step-by-step plan for Roman green glass, J. Archaeol. Sci. 38 (2011) 2387–2398.

7.   W. Meulebroeck, H. Wouters, K. Nys, H. Thienpont, Authenticity screening of stained-glasses, Sci. Rep. 6 (2016) [Article number: 37726].

8.   M. Hunault, C. Loisel, F. Bauchau, Q. Lemasson, C. Pacheco, L. Pichon, B. Moignard, K. Boulanger, M. Hérold, G. Calas, I. Pallot-Frossardt, Non-destructive redox quantification reveals glassmaking of rare French gothic stained-glasses, Anal. Chem. 89 (2017) 6277–6284.

9.   M. Alfeld, K. Janssens, J. Dik, W. De Nolf, G. Van der Snickt, Optimization of mobile scanning macro-XRF systems for the in situ investigation of historical paintings, J. Anal. At. Spectrom. 26 (2011) 899–909.

10.   M. Alfeld, J. Vaz Pedroso, M. Van Eikema Hommes, G. Van der Snickt, G. Tauber, J. Blaas, M. Haschke, K. Erler, J. Dik, K. Janssens, A mobile instrument for in-situ scanning macro-XRF investigation of historical paintings', J. Anal. At. Spectrom. 28 (2013) 760–767.

11.   G. Van der Snickt, S. Legrand, J. Caen, F. Vanmeert, M. Alfeld, K. Janssens, Chemical imaging of stained-glass windows by means of macro X-ray fluorescence (MA-XRF) scanning, Microchem. J. 124 (2016) 615–622.

12.   I. Mantouvalou, K. Aziz-Lange, T. Wolff, D. Grötzsch, L. Lühl, M. Haschke, O. Hahn, B. Kanngießer, A compact 3D Micro X-ray fluorescence spectrometer with X-ray tube excitation for archaeometric applications, J. Anal. Atom. Spectrom. 25 (2010) 554–561.

13.   G. Van der Snickt, S. Legrand, I. Slama, E. Van Zuien, G. Gruber, K. Van der Stighelen, L. Klaassen, E. Oberthaler, K. Janssens, In situ macro X-ray fluorescence (MA-XRF) scanning as a non-invasive tool to probe for subsurface modifications in paintings by PP Rubens, Microchem. J. 138 (2018) 238–245.

14.   M. Alfeld, K. Janssens, Strategies for processing mega-pixel X-ray fluorescence hyperspectral data: a case study on a version of Caravaggio's painting *Supper at Emmaus*, J. Anal. Atom. Spectrom. 30 (30) (2015) 777–789.

15.   O. Schalm, K. Janssens, H. Wouters, D. Caluwé, Composition of 12-18th century window glass in Belgium: Non-figurative windows in secular buildings and stained-glass windows in religious buildings, Spectrochim. Acta B 62 (2007) 663–668.

16.   J. Kunicki-Goldfinger, L. Kierzek, P. Dzierzanowski˙, A.J. Kasrzak, "Central European crystal glass of the first half of the eighteenth century." In: Annales du 16e Congrès de

l'Association Internationale pour l'Histoire du Verre, Nottingham: AIHV, 2005, pp. 258–262.

17.   A. Ceglia, G. Nuyts, W. Meulebroeck, S. Cagno, A. Silvestri, A. Zoleo, K. Nys, K. Janssens, H. Thienpont, H. Terryn, Iron speciation in soda lime silica glass: a comparison of XANES and UV–VIS–NIR spectroscopy, J. Anal. Atom. Spectrom. 30 (2015) 1552–1561.

18.   R. Arletti, S. Quartieri, I.C. Freestone, A XANES study of chromophores in archaeological glass, Appl. Phys. A Mater. Sci. Proc. 111 (2013) 99–108.

19.   D. Jembrih-Simbuerger, C. Neelmeijer, O. Schalm, P. Friedricks, M. Schreiner, K. De Vis, M. Maeder, D. Schryvers, J. Caen, The colour of silver stained-glass–analytical investigation carried out with XRF, SEM/EDX, TEM and IBA, J. Anal. Atom. Spectrom. 17 (2002) 321–328.

20.   G. Nuyts, S. Cagno, S. Bugani, K. Janssens, Micro-XANES study on Mn browning: use of quantitative valence state maps, J. Anal. Atom. Spectrom. 30 (2015) 642–650.

21.   M. Schreiner, Glass of the past: The degradation and deterioration of medieval glass artifacts, Microchim. Acta 104 (1991) 255–264.

22.   H. Roemich, S. Gerlach, P. Mottner, F. Mees, P. Jacobs, D. Van Dyck, T. Carbo, Scientific Basis for Nuclear Waste Management XXVI, 2003, pp. 97–108 (506 Keystone Drive, Warrendale, PA 15088-7563 USA).

Conclusions and perspectives

Conclusions

In this thesis a combination of advanced chemical imaging methods (mainly MA-XRF and MA-rFTIR) was used to investigate (planar) cultural heritage objects. In most cases the (combined) use of these techniques allowed to answer questions on the materials and techniques employed by the artists, the (art or restoration) history of the objects and degradation phenomena.

Although non-destructive analysis is the most desired approach for studying cultural heritage objects, micro-destructive sampling was often still necessary to clarify the remaining or emerging questions. However, when in a first step non-destructive imaging techniques were used, the number of required samples could be greatly reduced. The chemical distribution images allowed to pinpoint locations for meaningful sampling, necessary to answer the remaining questions by microscopic analytical methods.

After its initial development, MA-XRF was (and still is) mainly applied on paintings. During this work, however, not completely published, its potential use was further explored.

Illuminated manuscripts are only a small step away from canvas- and panel painting, but they do come with specific problems and questions that do not surface when scanning paintings: When these are still present in their (fragile) volume, the analysis of one page or illumination is complicated by the geometry of the object and the inherent thin pages which allow signals emerging from the backside or the following pages to reach the detector as well. However, this drawback can be an asset when cuttings (illuminations excised from their original volumes and often glued on a support) are analyzed, since visualizing the inaccessible verso side, can help to determine its location in the parent volume and to identify its authorship and place of execution.

By complementing the MA-XRF scans with MA-rFTIR measurements, it is possible to identify the pigments employed by the artist based on their spectral fingerprint and not solely by deduction, based on the elements detected and their visual appearance.

The restoration projects of Memling's *Christ with singing and Music making Angels* and the *Ghent Altarpiece* by the brothers Van Eyck allowed non-destructive macroscopic hyperspectral methods to showcase their possibilities in documenting the (sub)surface composition of paintings in a non-destructive manner. In both cases MA-XRF unveiled hidden features; delicate brocade patterns hiding under a disfiguring degradation crust in

the Memling panels and an almost completely overpainted version of the *Ghent Altarpiece*. The use of highly-specific microscopic imaging methods such as combined μ-XRF/XRPD and/or vibrational spectroscopies on a limited set of micro-samples allowed to gain a better understanding of the MA-XRF images and the layer build-up of these artworks. Thus, a far more complete overview can be constructed for the presence/usage of the various (crystalline) minerals or other pigments that were originally used to produce the painting. The new methodologies also allow us to see the *in situ* secondary products that often develop inside paint layers as they age and/or interact with their local environment.

In the case of the Memling panels, the surface crusts did not only contain dirt, but calcium oxalate salts as well. The oxalates did not appear to originate from degradation of the original paint but possibly from a combination of microbial action and a thick accumulation of dirt. The presence of intermediate varnish layer(s) between the crust and the original paint surface, indicated that the crusts were not part of the original paint stratigraphy and made it possible to remove most of them mechanically. The difficult and time-consuming removal process and its progress was carefully monitored using MA-rFTIR scanning which evidenced the almost complete removal of the calcium oxalate.

Elemental mapping by MA-XRF on the *Ghent Altarpiece* was used to objectively underpin the conservator's assertion that an extensive overpainting was present. At the same time, the chemical maps demonstrated in a quantitatively reliable manner that van Eyck's worn, overpainted composition was in sufficiently good condition to justify the full removal of the non-original layer(s).

The sensitivity of MA-XRF and infrared RIS to distinguish and map pigments is not the same and varies with the pigments used and the paint layering structure. Using both methods together, these differences can be exploited for a more robust and comprehensive identification and mapping of pigments in layered structures. Both modalities helped to visualize the facial features of the Eyckian Lamb. Together, the resulting maps and images provided the shape and position of the key facial features that defined the head and neck of the Eyckian Lamb. This example demonstrated that the combination of infrared RIS and MA-XRF, now in the vanguard of heritage science, expands the possibilities for resolving complex conservation and art historical issues. These imaging technologies can be used to predict the characteristics of specific painted features before the removal of overpaint.

The analytical imaging experiments performed on stained-glass panels revealed that MA-XRF scanning can be a particularly useful tool for the study of stained-glass windows, in spite of a number of limitations. MA-XRF turned out being a valuable technique for (a) distinguishing various glass panes with deviant compositions within the same panel, (b) characterizing glass paints and (c) documenting deterioration propagation, while the

ensuing elemental distribution maps can also serve as functional 1:1 working drawings during the subsequent treatment.

The major benefit of MA-XRF is the ability to acquire compositional data from the entire surface in a completely non-destructive way. In addition, the ensuing chemical data can be presented in a visual way, hence allowing interpretation by non-XRF specialists. The measurements performed in this work revealed that MA-XRF is not only able to identify the chromophores but can distinguish pot metal glass from flashed glass as well, simply by contrasting interior with exterior scans. In contrast with conventional SEM-EDX and μ-XRF point analyses on samples, MA-XRF experiments do not yield accurate quantification of the different glass components. Still, the main motive for quantification is differentiating between glass types, an objective that that can be achieved by MA-XRF scanning in an alternative way. This drawback can be largely overcome by means of Ca-K/K-K correlation plots and the subsequent charting of the clusters in coloured segmentation maps. In case the Ca and K fluorescence signals are affected by overlying corrosion products, glass paints or grisaille, an alternative bi-plot of the more energetic Rb–K/Sr–K lines can be employed in a beneficial way for the same purposes. The resulting insights are particularly useful for conservators who are typically interested in an efficient discrimination of the historical phases in one specific window rather than exact the quantification. Quite often it is difficult to date these phases only by visual examination. In a wider, more archaeometric perspective, the absence of absolute concentrations does prevent inter-comparison of the MA-XRF scans from different stained-glass windows. In this framework, combining the MA-XRF maps with SEM-EDX analyses on a limited number of samples is expected to be particularly relevant.

Based on these masterpieces' restoration examples, it can be expected that integral chemical imaging of paintings by chemical imaging methods will soon become a standard procedure during major restorations of painted artworks. As objectification of decisions, elaborate documentation, and public motivation of treatments become increasingly important in modern conservation, so does detailed elemental/chemical imaging of the artworks before, during, and after the conservation treatments.

As recent research projects, academic conferences and specialist publications prove, the future of heritage science as a whole lies in the application of cutting-edge non-invasive imaging methods, and on close collaboration between all parties concerned: from chemists to art historians, from conservators to imaging scientists.

Perspectives

Since both MA-XRF and MA-rFTIR use a raster scanning technique, where in each point at least one complete spectrum is recorded, it is obvious that the focus for improving of the scanning speed is at the spectral recording process.

The current MA-XRF instrument versions allow dwell times from 100 ms up to a few seconds per point. The current geometry and components allow for even shorter dwell times, while retaining acceptable counting statistics to be able to detect impurities as well, however the current control software and hardware are close to their limits keeping the correct pixel registration at maximum speed.

Meanwhile a new MA-XRF setup is under development that
● should allow for faster scanning while keeping a correct pixel registration,
● uses recent detector and multichannel analyzer electronics which allow higher count rates, while keeping a good spectral resolution,
● can probe a larger area in 1 scan, reducing the overhead of starting multiple scans and afterwards stitching the multiple subscans together,
● has a z-stage, so the optimal distance between the object and the measurement head can be maintained.

Once operational, complementary imaging techniques can be incorporated in this setup (for example, based on the reflectance of visible and infrared radiation) with the aim of corroborating the deduced paint layer sequence versus depth and collecting information on organic paint components.

The core of the MA-rFTIR instrument, the Bruker Alpha spectrometer, needs at least 1 second to record a FTIR spectrum at a resolution of 4 cm^{-1}. However, there is an additional dead time of 4 to 7 s between two consecutive measurements, resulting in a dwell time of approximately 10 s per point (3 s spectral recording, 7 s dead time). Recently a new measurement method became available that almost completely eliminates the overhead between two measurements, introducing a potential 5-10 fold increase in measurement speed. However, this came too late to be used in this thesis.

From the instrumental side, the development of more brilliant IR-sources and improved optics that capture the reflected radiation from a larger solid angle, will improve the S/N of the recorded spectra. This would be beneficial for faster scanning and applying more automated data processing.

Potentially the most improvements lie in the field of data processing, which is in most cases still done in a rather manual manner. The data reduction and automation method applied on the Neptune statue scans works well when there is a limited set of orthogonal components present. Whereas in most cases, changing mixtures of the components are present.

From the field of remote sensing and hyperspectral imaging in the UV, VIS and NIR bands, promising algorithms and data treatment processes have emerged that are potentially useful for the (semi-automatic) treatment of MA-rFTIR datasets. Currently the main holdback for their successful application, is situated finding the right pretreatment method for specular reflectance mid infrared data.

Since the future of (hyperspectral) imaging systems lies in the combination of multiple techniques/spectral ranges, the correct registration between the different datasets is essential. Currently MA-XRF, MA-rFTIR and MA-XRPD datasets or distribution images are combined after treating the different datacubes separately.

Once the multiple datacubes are merged correctly, human intervention in the data processing might be further reduced by applying deep learning algorithms or neural networks to it. This approach might be extremely beneficial for the hyperspectral data present in the UV-VIS and IR range because the spectral features present in these bands are more subtle and their exact position can shift depending on its environment, adding more complexity to the data evaluation process. This in contrast to XRF and XRPD where the spectral position of a certain signal is fixed for a given measurement condition.

In other fields artificial intelligence has already proven that it is capable of monitoring and interpreting thousands of signals simultaneously. Translated to hyperspectral imaging methods, this would mean that such systems can relate features present in multiple bands (techniques) to the components present in the objects and how these are distributed over the object.

Appendix - Publications

1.　　G. Van der Snickt, K.A. Dooley, J. Sanyova, H. Dubois, J.K. Delaney, E.M. Gifford, <u>S. Legrand</u>, N. Laquiere, K. Janssens, "Dual mode standoff imaging spectroscopy documents the painting process of the Lamb of God in the *Ghent Altarpiece* by J. and H. Van Eyck", *Science Advances,* 6 (31), **2020**, eabb3379, 10.1126/sciadv.abb3379.

2.　　G. Sciutto, <u>S. Legrand</u>, E. Catelli, S. Prati, C. Malegori, P. Oliveri, K. Janssens, R. Mazzeo, "Macroscopic mid-FTIR mapping and clustering-based automated data-reduction: An advanced diagnostic tool for in situ investigations of artworks", *Talanta,* 209, **2020**, 120575, 10.1016/j.talanta.2019.120575.

3.　　M. Hillen, <u>S. Legrand</u>, Y. Dirkx, K. Janssens, G. Van der Snickt, J. Caen, G. Steenackers, "Cluster Analysis of IR Thermography Data for Differentiating Glass Types in Historical Leaded-Glass Windows", *Applied Sciences,* 10 (12), **2020**, 4255, 10.3390/app10124255.

4.　　K.A. Dooley, A. Chieli, A. Romani, <u>S. Legrand</u>, C. Miliani, K. Janssens, J.K. Delaney, "Molecular Fluorescence Imaging Spectroscopy for Mapping Low Concentrations of Red Lake Pigments: Van Gogh's Painting The Olive Orchard", *Angewandte Chemie International Edition,* 59 (15), **2020**, 6046-6053, 10.1002/anie.201915490.

5.　　S. Cagno, G. Van der Snickt, <u>S. Legrand</u>, J. Caen, M. Patin, W. Meulebroeck, Y. Dirkx, M. Hillen, G. Steenackers, A. Rousaki, P. Vandenabeele, K. Janssens, "Comparison of four mobile, non-invasive diagnostic techniques for differentiating glass types in historical leaded windows: MA-XRF, UV–Vis–NIR, Raman spectroscopy and IRT", *X-Ray Spectrometry,* **2020**, 10.1002/xrs.3185.

6.　　G. Van der Snickt, <u>S. Legrand</u>, K. Janssens, "In situ Macro X-Ray Fluorescence (MA-XRF) imaging visualizes a scene below van Dyck's earliest self-portrait", in: J.M. Nauhaus (Ed.), Young and Famous - Anthony van Dyck's 1614/15 Self-Portrait and Other Works from the Paintings Gallery and Graphic Collection of the Academy of Fine Arts Vienna, Vienna, **2019**, pp. 179-189,

7.　　<u>S. Legrand</u>, G. Van der Snickt, S. Cagno, J. Caen, K. Janssens, "MA-XRF imaging as a tool to characterize the 16th century heraldic stained-glass panels in Ghent Saint Bavo Cathedral", *Journal of Cultural Heritage,* 40, 2**019**, 163-168, 10.1016/j.culher.2019.06.003.

8.　　L. Klaassen, G. van der Snickt, <u>S. Legrand</u>, C. Higgitt, M. Spring, F. Vanmeert, F. Rosi, B.G. Brunetti, M. Postec, K. Janssens, "Characterization and Removal of a Disfiguring Oxalate Crust on a Large Altarpiece by Hans Memling", Metal Soaps in Art, **2019**, pp. 263-282, 10.1007/978-3-319-90617-1_15.

9.　　F. Vanmeert, G. Van der Snickt, <u>S. Legrand</u>, K. Janssens, "Velázquez?: A portrait of Pope Innocent X. An X-ray imaging investigation II", in: S. Ferino-Pagden (Ed.), Velázquez – Suggestions, Proposals, Solutions, *Brepols,* **2018**, pp. 132-141,

10.   G. Van der Snickt, S. Legrand, I. Slama, E. Van Zuien, G. Gruber, K. Van der Stighelen, L. Klaassen, E. Oberthaler, K. Janssens, "In situ macro X-ray fluorescence (MA-XRF) scanning as a non-invasive tool to probe for subsurface modifications in paintings by P.P. Rubens", *Microchemical Journal,* 138, **2018**, 238-245, 10.1016/j.microc.2018.01.019.

11.   J. Peeters, G. Steenackers, S. Sfarra, S. Legrand, C. Ibarra-Castanedo, K. Janssens, G. Van der Snickt, "IR Reflectography and Active Thermography on Artworks: The Added Value of the 1.5–3 μm Band", *Applied Sciences,* 8 (1), **2018**, 10.3390/app8010050.

12.   S. Legrand, P. Ricciardi, L. Nodari, K. Janssens, "Non-invasive analysis of a 15th century illuminated manuscript fragment: point-based vs imaging spectroscopy", *Microchemical Journal,* 138, **2018**, 162-172, 10.1016/j.microc.2018.01.001.

13.   S. Legrand, P. Ricciardi, K. Janssens, "The benefits of scanning illuminated manuscripts with MA-XRF and MA-rFTIR", in: S. Panayotova, P. Ricciardi (Eds.), Manuscripts in the making - Arts and Science, *Brepols,* **2018**, pp. 169-181.

14.   J. Koldeweij, L. Hoogstede, M. Ilsink, K. Janssens, N. De Keyser, R.K. Gotink, S. Legrand, J.M. Nauhaus, G. Van der Snickt, R. Spronk, "The patron of Hieronymus Bosch's 'Last Judgment' triptych in Vienna", *Burlington Mag,* 160 (1379), **2018**, 106-111,

15.   K.A. Dooley, E.M. Gifford, A. Van Loon, P. Noble, J.G. Zeibel, D.M. Conover, M. Alfeld, G. Van der Snickt, S. Legrand, K. Janssens, J. Dik, J.K. Delaney, "Separating two painting campaigns in *Saul and David*, attributed to Rembrandt, using macroscale reflectance and XRF imaging spectroscopies and microscale paint analysis", *Heritage Science,* 6 (1), **2018**, 10.1186/s40494-018-0212-3.

16.   G. Van der Snickt, H. Dubois, J. Sanyova, S. Legrand, A. Coudray, C. Glaude, M. Postec, P. Van Espen, K. Janssens, "Large-Area Elemental Imaging Reveals Van Eyck's Original Paint Layers on the Ghent Altarpiece (1432), Rescoping Its Conservation Treatment", *Angew Chem Int Ed Engl,* 56 (17), **2017**, 4797-4801, 10.1002/anie.201700707.

17.   N. De Keyser, G. Van der Snickt, A. Van Loon, S. Legrand, A. Wallert, K. Janssens, "Jan Davidsz. de Heem (1606–1684): a technical examination of fruit and flower still lifes combining MA-XRF scanning, cross-section analysis and technical historical sources", *Heritage Science,* 5 (1), **2017**, 10.1186/s40494-017-0151-4.

18.   A.T. da Silva, S. Legrand, G. Van der Snickt, R. Featherstone, K. Janssens, G. Bottinelli, "MA-XRF imaging on René Magritte's *La condition humaine*: insights into the artist's palette and technique and the discovery of a third quarter of *La pose enchantée*", *Heritage Science,* 5 (1), **2017**, 10.1186/s40494-017-0150-5.

19.   A. Cabal, S. Legrand, B. Van den Bril, K. Toté, K. Janssens, P. Van Espen, "Study of the uniformity of aerosol filters by scanning MA-XRF", *X-Ray Spectrometry,* 46 (5), **2017**, 461-466, 10.1002/xrs.2767.

20.   G. Van der Snickt, S. Legrand, J. Caen, F. Vanmeert, M. Alfeld, K. Janssens, "Chemical imaging of stained-glass windows by means of macro X-ray fluorescence

(MA-XRF) scanning", *Microchemical Journal,* 124, **2016**, 615-622, 10.1016/j.microc.2015.10.010.

21.   P. Ricciardi, S. Legrand, G. Bertolotti, K. Janssens, "Macro X-ray fluorescence (MA-XRF) scanning of illuminated manuscript fragments: potentialities and challenges", *Microchemical Journal,* 124, **2016**, 785-791, 10.1016/j.microc.2015.10.020.

22.   K. Janssens, G. Van der Snickt, F. Vanmeert, S. Legrand, G. Nuyts, M. Alfeld, L. Monico, W. Anaf, W. De Nolf, M. Vermeulen, J. Verbeeck, K. De Wael, "Non-Invasive and Non-Destructive Examination of Artistic Pigments, Paints, and Paintings by Means of X-Ray Methods", *Top Curr Chem (Z),* 374 (6), **2016**, 81, 10.1007/s41061-016-0079-2.

23.   K. Janssens, S. Legrand, G. Van der Snickt, F. Vanmeert, "Virtual Archaeology of Altered Paintings: Multiscale Chemical Imaging Tools", *Elements,* 12 (1), **2016**, 39-44, 10.2113/gselements.12.1.39.

24.   J. Caen, S. Legrand, G. Van der Snickt, K. Janssens, "Macro X-ray fluorescence (MA-XRF) scanning: a new and efficient method for documenting stained-glass panels", Stained-glass: how to take care of a fragile heritage?, Paris, 8-10 July 2015, Paris, **2015**, pp. 74-81,

25.   S. Legrand, F. Vanmeert, G. Van der Snickt, M. Alfeld, W. De Nolf, J. Dik, K. Janssens, "Examination of historical paintings by state-of-the-art hyperspectral imaging methods: from scanning infra-red spectroscopy to computed X-ray laminography", *Heritage Science,* 2 (1), **2014**, 10.1186/2050-7445-2-13.

26.   S. Legrand, M. Alfeld, F. Vanmeert, W. De Nolf, K. Janssens, "Macroscopic Fourier transform infrared scanning in reflection mode (MA-rFTIR), a new tool for chemical imaging of cultural heritage artefacts in the mid-infrared range", *Analyst,* 139 (10), **2014**, 2489-98, 10.1039/c3an02094k.

27.   K. Janssens, M. Alfeld, G. Van der Snickt, W. De Nolf, F. Vanmeert, L. Monico, S. Legrand, J. Dik, M. Cotte, G. Falkenberg, L. van der Loeff, M. Leeuwestein, E. Hendriks, "CHAPTER 18 Examination of Vincent van Gogh's Paintings and Pigments by Means of State-of-the-art Analytical Methods", Science and Art: The Painted Surface, *The Royal Society of Chemistry,* **2014**, pp. 373-403, 10.1039/9781839161957-00373.